

[All issues](#) ▶ [Volume 327 \(2021\)](#)[◀ Previous issue](#)[Table of Contents](#)[Next issue ▶](#)[Free Access](#) to the whole issue

## E3S Web of Conferences

### Volume 327 (2021)

#### 26<sup>th</sup> Scientific Conference on Power Engineering and Power Machines (PEPM'2021)

Sozopol, Bulgaria, September 18-21, 2021

I. Nastase, A.H. Wierling, T. Totev, A. Terziev, R. Atanasova, M. Zlateva, I. Dukov and K. Filipov (Eds.)

Export the citation of the selected articles [Export](#)[Select all](#)[Open Access](#)

#### About the conference

Published online: 22 November 2021

PDF (1.01 MB)

[Open Access](#)

#### Statement of Peer review

Published online: 22 November 2021

PDF (389 KB)

- ▼ [Thermal Equipment, Heat and Mass Transfer Processes](#)
- ▼ [Renewable Energy and Environmental Protection](#)
- ▼ [Design and Technologies for Clothing and Textiles](#)
- ▼ [Hydraulic and Pneumatic Fluid Power Systems and Machinery](#)
- ▼ [Miscellaneous](#)

 [Open Access](#)

#### Preface 00001

Totyo Totev, Ilinca Nastase and August Hubert Wierling

Published online: 22 November 2021

DOI: <https://doi.org/10.1051/e3sconf/202132700001>PDF (1.571 MB) | [NASA ADS Abstract Service](#)

#### - *Thermal Equipment, Heat and Mass Transfer Processes*

 [Open Access](#)

Comparative analysis between methane and hydrogen regarding ignition and combustion in diffusive mode 01001

Lucian Mihăescu, Dorin Stanciu, Gheorghe Lăzăroiu, Ionel Pișă and Gabriel Negreanu

Published online: 22 November 2021

DOI: <https://doi.org/10.1051/e3sconf/202132701001>PDF (998.4 KB) | [References](#) | [NASA ADS Abstract Service](#)

Open Access**Energy and economic analysis of an ORC combined to steam boiler** 01002

Gabriel Mocanu, Ion V. Ion and Cristian Iosifescu

Published online: 22 November 2021

DOI: <https://doi.org/10.1051/e3sconf/202132701002>PDF (931.5 KB) | [References](#) | [NASA ADS Abstract Service](#) Open Access**Mathematical Models of the Energy Characteristics of a Backpressure Steam Turbine Based on a Simulation Study** 01003

Kaloyan Hristov and Ivan Genovski

Published online: 22 November 2021

DOI: <https://doi.org/10.1051/e3sconf/202132701003>PDF (936.9 KB) | [References](#) | [NASA ADS Abstract Service](#) Open Access**Comparative technical and economic analysis of innovative methods for waste heat recovery from flue gases for boiler type BKZ 220-100** 01004

Hristo Beloev, Iliya Iliev, Angel Terziev, Andrey Kibarin and Madina Aliyarova

Published online: 22 November 2021

DOI: <https://doi.org/10.1051/e3sconf/202132701004>PDF (2.338 MB) | [References](#) | [NASA ADS Abstract Service](#) Open Access**Moisture transfer in outer walls with layers of different density** 01005

Andrey Rymarov, Dmitriy Titkov and Aleksey Ananiev

Published online: 22 November 2021

DOI: <https://doi.org/10.1051/e3sconf/202132701005>PDF (1.604 MB) | [References](#) | [NASA ADS Abstract Service](#) Open Access**An experimental study for drying Pisum sativum on an electric dryer and a heat pump dryer** 01006

Thanh Nhan Phan, Van Hung Tran, Nikola Kaloyanov and Merima Zlateva

Published online: 22 November 2021

DOI: <https://doi.org/10.1051/e3sconf/202132701006>PDF (2.446 MB) | [References](#) | [NASA ADS Abstract Service](#) Open Access**Modelling and numerical simulation of fire in a coffee storage hall** 01007

Kalin Krumov, Nina Penkova, Boian Mladenov and Yordan Stoyanov

Published online: 22 November 2021

DOI: <https://doi.org/10.1051/e3sconf/202132701007>PDF (3.050 MB) | [References](#) | [NASA ADS Abstract Service](#) Open Access**Verification and validation of a CFD model of a fixed regenerator for heat recovery from air** 01008

Angel Penev, Lyubomir Tsokov and Momchil Vassilev

Published online: 22 November 2021

DOI: <https://doi.org/10.1051/e3sconf/202132701008>PDF (2.238 MB) | [References](#) | [NASA ADS Abstract Service](#) Open Access**Air-to-water heat pump assessment: Part 1 – Experimental setup** 01009

Nadezhda Doseva, Daniela Chakyrova, Svetoslav Stoianov and Iliia Hadhidimov

Published online: 22 November 2021

DOI: <https://doi.org/10.1051/e3sconf/202132701009>

PDF (2.298 MB) | [References](#) | [NASA ADS Abstract Service](#)

---

Open Access

**Air-to-water heat pump assessment: Part 2 – Exergetic and exergoeconomic analyses** 01010

Nadezhda Doseva and Daniela Chakyrova

Published online: 22 November 2021

DOI: <https://doi.org/10.1051/e3sconf/202132701010>

PDF (2.455 MB) | [References](#) | [NASA ADS Abstract Service](#)

---

Open Access

**Modelling and numerical simulation of the transport phenomena in water thermal energy storage tanks** 01011

Nikola Kaloyanov, Rosen Tsecov and Nina Penkova

Published online: 22 November 2021

DOI: <https://doi.org/10.1051/e3sconf/202132701011>

PDF (3.836 MB) | [References](#) | [NASA ADS Abstract Service](#)

---

Open Access

**An approach for reducing the air conditioning costs in office buildings in Vietnam** 01012

Van Hung Tran, Thanh Nhan Phan and Momchil Vassilev

Published online: 22 November 2021

DOI: <https://doi.org/10.1051/e3sconf/202132701012>

PDF (2.587 MB) | [References](#) | [NASA ADS Abstract Service](#)

---

Open Access

**Thermal-hydraulic analysis of a VVER-1000 core in MSLB conditions** 01013

Svetomir Mitkov, Ivan Spasov and Nikola Kolev

Published online: 22 November 2021

DOI: <https://doi.org/10.1051/e3sconf/202132701013>

PDF (2.363 MB) | [References](#) | [NASA ADS Abstract Service](#)

---

Open Access

**Thermodynamic and kinetic parameters of biomass from black pine (*PINUS NIGRA* ARN.)** 01014

Stanislava Tasheva, Milen Dimov, Hafize Fidan, Stanko Stankov, Lazar Lazarov, Bozidar Bozadzhev, Apostol Simitchiev and Albena Stoyanova

Published online: 22 November 2021

DOI: <https://doi.org/10.1051/e3sconf/202132701014>

PDF (180.6 KB) | [References](#) | [NASA ADS Abstract Service](#)

---

Open Access

**Investigating the kinetics at low temperature heat pump drying and conventional drying of osmotic dehydrated blueberries** 01015

Hristov Hristo, Aleksandrov Svetoslav, Petrova Todorka, Ruskova Milena, Gotcheva Velitchka and Nikolay Penov

Published online: 22 November 2021

DOI: <https://doi.org/10.1051/e3sconf/202132701015>

PDF (1.816 MB) | [References](#) | [NASA ADS Abstract Service](#)

---

## **- Renewable Energy and Environmental Protection**

Open Access

**Optimization of the distance between the rows in solar collectors' arrays** 02001

Merima Zlateva

Published online: 22 November 2021

DOI: <https://doi.org/10.1051/e3sconf/202132702001>

PDF (229.4 KB) | [References](#) | [NASA ADS Abstract Service](#)

---

Open Access

**Simulation Investigation of the Wind Load of Photovoltaic Panels** 02002

Ivaylo Stoyanov, Teodor Iliev and Grigor Mihaylov

Published online: 22 November 2021

DOI: <https://doi.org/10.1051/e3sconf/202132702002>

PDF (2.643 MB) | [References](#) | [NASA ADS Abstract Service](#)

---

Open Access

Assessing the diversification of energy mix with the methods of entropy and hierarchy of information 02003

Iliyan Petrov

Published online: 22 November 2021

DOI: <https://doi.org/10.1051/e3sconf/202132702003>

PDF (868.7 KB) | [References](#) | [NASA ADS Abstract Service](#)

---

Open Access

Renewable energies projects selection: block criteria systematization with AHP and Entropy-MOORA methods in MCDM 02004

Iliyan Petrov

Published online: 22 November 2021

DOI: <https://doi.org/10.1051/e3sconf/202132702004>

PDF (168.5 KB) | [References](#) | [NASA ADS Abstract Service](#)

---

Open Access

Influence evaluation of the ship propulsion system on the energy efficiency for small, medium and large container vessels 02005

Viktor Nikiforov and Irina Kostova

Published online: 22 November 2021

DOI: <https://doi.org/10.1051/e3sconf/202132702005>

PDF (1.562 MB) | [References](#) | [NASA ADS Abstract Service](#)

---

Open Access

Impact study of the fuel type used on the energy efficiency costs values and harmful emissions generation for small, medium and large container vessels 02006

Viktor Nikiforov and Irina Kostova

Published online: 22 November 2021

DOI: <https://doi.org/10.1051/e3sconf/202132702006>

PDF (933.5 KB) | [References](#) | [NASA ADS Abstract Service](#)

---

Open Access

A design of solar battery cleaning system by modularity method 02007

L.K. Dien and Svetlin Antonov

Published online: 22 November 2021

DOI: <https://doi.org/10.1051/e3sconf/202132702007>

PDF (1.742 MB) | [References](#) | [NASA ADS Abstract Service](#)

---

Open Access

Electronic measuring system design for photovoltaic panels analysis 02008

Krastin Yordanov, Iliya Hadzhidimov and Penka Zlateva

Published online: 22 November 2021

DOI: <https://doi.org/10.1051/e3sconf/202132702008>

PDF (4.532 MB) | [References](#) | [NASA ADS Abstract Service](#)

---

Open Access

Determination of the optimal air-fuel ratio for upgraded biogas engine operation 02009

Radostin Dimitrov and Penka Zlateva

Published online: 22 November 2021

DOI: <https://doi.org/10.1051/e3sconf/202132702009>

PDF (1.881 MB) | [References](#) | [NASA ADS Abstract Service](#)

---

Open Access

Possibilities for obtaining pellets by single-screw extrusion of biomass from black pine (*Pinus nigra* Arn.) 02010

Apostol Simitchiev, Bozidar Bozadzhiev, Lazar Lazarov, Stanko Stankov, Hafize Fidan and Albena Stoyanova

Published online: 22 November 2021

DOI: <https://doi.org/10.1051/e3sconf/202132702010>

PDF (2.069 MB) | [References](#) | [NASA ADS Abstract Service](#)

 Open Access

On the Development of a Real Time Water Monitoring System 02011

Sandel Zaharia, Gabriel Iana, Cristian Monea and Mihnea Sandu

Published online: 22 November 2021

DOI: <https://doi.org/10.1051/e3sconf/202132702011>

PDF (1.657 MB) | [References](#) | [NASA ADS Abstract Service](#)

## - Design and Technologies for Clothing and Textiles

 Open Access

Design and constructive – technological development for children's art clothing 03001

Radka Atanasova, Magdalena Pavlova and Monika Merkova

Published online: 22 November 2021

DOI: <https://doi.org/10.1051/e3sconf/202132703001>

PDF (4.287 MB) | [References](#) | [NASA ADS Abstract Service](#)

 Open Access

Development of boutique denim clothing by the "upcycling" method 03002

Magdalena Pavlova

Published online: 22 November 2021

DOI: <https://doi.org/10.1051/e3sconf/202132703002>

PDF (4.165 MB) | [References](#) | [NASA ADS Abstract Service](#)

 Open Access

Methods for personal cooling in hot environment used in clothing and wearables 03003

Atanas Vasilev, Radostina A. Angelova and Rositsa Velichkova

Published online: 22 November 2021

DOI: <https://doi.org/10.1051/e3sconf/202132703003>

PDF (2.067 MB) | [References](#) | [NASA ADS Abstract Service](#)

 Open Access

Modification of Leather Surface Using Low-Pressure Plasma and Antimicrobial Reagent 03004

Sanja Ercegović Ražić, Jadranka Akalović, Tomislav Ivanković, Anja Ludaš and Katarina Ištef

Published online: 22 November 2021

DOI: <https://doi.org/10.1051/e3sconf/202132703004>

PDF (4.560 MB) | [References](#) | [NASA ADS Abstract Service](#)

 Open Access

Tangram based technology for clothing design 03005

Boryana Georgieva-Gushtanova

Published online: 22 November 2021

DOI: <https://doi.org/10.1051/e3sconf/202132703005>

PDF (2.454 MB) | [References](#) | [NASA ADS Abstract Service](#)

 Open Access

Application of ICT in the Online Education of Apparel Design and Production within the framework of ICT-TEX project 03006

Hassan Saeed, Yordan Kyosev, Radka Atanasova, Angel Terziev and Carla Hertleer

Published online: 22 November 2021

DOI: <https://doi.org/10.1051/e3sconf/202132703006>

PDF (1.772 MB) | [References](#) | [NASA ADS Abstract Service](#)

## - *Hydraulic and Pneumatic Fluid Power Systems and Machinery*

Open Access

GA-tuning of Multivariable PID Controller for Electrohydraulic Load-Sensing Servo System 04001

Alexander Mitov, Tsonyo Slavov, Jordan Kralev and Ilcho Angelov

Published online: 22 November 2021

DOI: <https://doi.org/10.1051/e3sconf/202132704001>

PDF (2.070 MB) | [References](#) | [NASA ADS Abstract Service](#)

Open Access

Design of direct acting differential pressure control valve test bench 04002

Ognyan Bekriev and Radoslav Asenov

Published online: 22 November 2021

DOI: <https://doi.org/10.1051/e3sconf/202132704002>

PDF (1.866 MB) | [References](#) | [NASA ADS Abstract Service](#)

Open Access

Reduction of the Battery Capacity of Hybrid Electric Vehicle with the Help of Electrically Assisted Turbocharger 04003

Milen Mihaylov, Ivaylo Stoyanov and Teodor Iliev

Published online: 22 November 2021

DOI: <https://doi.org/10.1051/e3sconf/202132704003>

PDF (2.156 MB) | [References](#) | [NASA ADS Abstract Service](#)

Open Access

Experimental study of the accuracy of measuring of a central water meter 04004

Ognyan Bekriev and Aleksandar Stanilov

Published online: 22 November 2021

DOI: <https://doi.org/10.1051/e3sconf/202132704004>

PDF (426.6 KB) | [References](#) | [NASA ADS Abstract Service](#)

Open Access

Investigations of a vertical axis wind turbine with frontal cylindrical guide vane unit 04005

Valentin Obretenov and Rossen Iliev

Published online: 22 November 2021

DOI: <https://doi.org/10.1051/e3sconf/202132704005>

PDF (3.512 MB) | [References](#) | [NASA ADS Abstract Service](#)

## - *Miscellaneous*

Open Access

Modelling indoor pollutant distribution via passive scalar and virtual box approach 05001

George Pitchurov, Detelin Markov, Iskra Simova, Rositsa Velichkova, Peter Stankov and Radostina Angelova

Published online: 22 November 2021

DOI: <https://doi.org/10.1051/e3sconf/202132705001>

PDF (1.153 MB) | [References](#) | [NASA ADS Abstract Service](#)

Open Access

Parameters influencing the droplet formation in a focusing microfluidic channel 05002

Emil Grigorov, Jordan A. Denev, Boris Kirov and Vassil Galabov

Published online: 22 November 2021

DOI: <https://doi.org/10.1051/e3sconf/202132705002>

PDF (1.407 MB) | [References](#) | [NASA ADS Abstract Service](#)

Open Access

The influence of the structure of laminar flows on the characteristics of equipment 05003

Vasyl Arsirii, Oleg Kravchenko, Bohdan Savchuk and Olena Arsirii

Published online: 22 November 2021

DOI: <https://doi.org/10.1051/e3sconf/202132705003>

PDF (587.2 KB) | [References](#) | [NASA ADS Abstract Service](#)

---

Open Access

Modularity design of the bamboo plastic fiber forming machine 05004

Nguyen Thanh Nam and Nguyen Hoang Hiep

Published online: 22 November 2021

DOI: <https://doi.org/10.1051/e3sconf/202132705004>

PDF (3.237 MB) | [References](#) | [NASA ADS Abstract Service](#)

---

Open Access

A Research on The Formability of PVC Sheet in Single Point Incremental Forming (SPIF) Technology 05005

Nguyen Thanh Nam, Nguyen Hoang Hiep, Nguyen Tan Hung, Tran Trong Hy and Ho Huu Han

Published online: 22 November 2021

DOI: <https://doi.org/10.1051/e3sconf/202132705005>

PDF (2.378 MB) | [References](#) | [NASA ADS Abstract Service](#)

---

Open Access

Modularity design of instant coffee powder packaging machine 05006

Svetlin Antonov and L.K. Dien

Published online: 22 November 2021

DOI: <https://doi.org/10.1051/e3sconf/202132705006>

PDF (2.098 MB) | [References](#) | [NASA ADS Abstract Service](#)

---

**E3S Web of Conferences**

eISSN: 2267-1242



[Mentions légales](#)

[Contacts](#)

[Privacy policy](#)

*A Vision4Press website*



**Faculty of Power Engineering and Power Machines,  
Technical University of Sofia, Bulgaria**

## INVITATION

**26<sup>th</sup> Scientific Conference  
on  
Power Engineering and Power Machines  
Conference (PEPM'2021)  
of  
Faculty of Power Engineering and  
Power Machines**

# PE-PM 2021

**18-21 SEPTEMBER 2021**

**SOZOPOL, BULGARIA**

**FIRST CALL FOR PAPERS  
[www.copepm.eu](http://www.copepm.eu)**

## CHAIRS

Prof. Totyo Totev, PhD  
Assoc. Prof. Angel Terziev, PhD  
Assoc. Prof. Radka Atanasova, Ph.D  
Assoc. Prof. Kalin Filipov, PhD  
Assoc. Prof. Merima Zlateva, PhD  
Assoc. Prof. Ivan Dukov, PhD

## Organizing committee

Prof. Totyo Totev, PhD  
Assoc. Prof. Angel Terziev, Ph.D  
Chief Assist. Martin Ivanov, Ph.D  
Chief Assist. Alexander Mitov, Ph.D  
Chief Assist. Borislav Stankov

## GUEST EDITORS

Assoc. Prof. Ilinca Nastase, Ph.D  
Assoc. Prof. August Hubert Wierling, Ph.D

## SCIENTIFIC COMMITTEE

Aleksandar Georgiev (Bulgaria)  
Alexander Genbach (Kazakhstan)  
Alexander Mitov (Bulgaria)  
Alexander Stanilov (Bulgaria)  
Angel Terziev (Bulgaria)  
August Hubert Wierling (Norway)  
Boncho Bonev (Bulgaria)  
Claudio Bruzzese (Italy)  
Cristiana Croitoru (Romania)  
Daniela Sofronova (Bulgaria)  
Daniela Dzhonova Atanasova (Bulgaria)  
Detelin Markov (Bulgaria)

Domingos Viegas (Portugal)  
Donka Bodurova (Bulgaria)  
Felix Bulatbaev (Kazakhstan)  
Florin Bode (Romania)  
Gabriel Negreanu (Romania)  
Georgi Pitchurov (Bulgaria)  
George Darie (Romania)  
Hristo Petrov (Bulgaria)  
Ilia Iliev (Bulgaria)  
Ilinca Nastase (Romania)  
Ilcho Angelov (Bulgaria)  
Ion V. Ion (Romania)  
Iskra Simova (Bulgaria)  
Ivan Antonov (Bulgaria)  
Ivan Dukov (Bulgaria)  
Ivaylo Stoyanov (Bulgaria)  
Kalin Filipov (Bulgaria)  
Kostadin Fikiin (Bulgaria)  
Koycho Atanasov (Bulgaria)  
Krisztina Uzuneanu (Romania)  
Lepovasa Ristic (Serbia)  
Manuel Carlos Gameiro de Silva (Portugal)  
Martin Ivanov (Bulgaria)  
Mohamed Djemai (France)  
Milcho Angelov (Bulgaria)  
Mirjana Lakovic (Serbia)  
Merima Zlateva (Bulgaria)  
Mihnea Sandu (Romania)  
Neven Krastev (Bulgaria)  
Nikola Kaloyanov (Bulgaria)  
Nikolay Ivanov (Russia)  
Nina Penkova (Bulgaria)  
Petar Stankov (Bulgaria)  
Penka Zlateva (Bulgaria)  
Radostina Angelova (Bulgaria)  
Radka Atanasova (Bulgaria)  
Rositsa Velichkova (Bulgaria)  
Saule Savetovna SAGINTAEVA (Kazakhstan)  
Silvia Boycheva (Bulgaria)  
Siniša Bikić (Serbia)  
Teodor Iliev (Bulgaria)  
Totyo Totev (Bulgaria)  
Violeta Rasheva (Bulgaria)  
Zhivko Kolev (Bulgaria)



## Submission process

### Abstract

- ❖ Should be written in English, not exceeding 350 words;
- ❖ Full name(s) of Autor(s), their affiliation, e-mail address, contact of corresponding Author;
- ❖ Abstract template can be found on the conference website;
- ❖ To be sent to the e-mail of the conference:

[conference@copepm.eu](mailto:conference@copepm.eu)

### Full paper

- ❖ Should be submitted via on-line platform which will be further announced.
- ❖ Papers sent by e-mail will not be considered!
- ❖ Reports not complying with the mandatory layout or not received by the specified deadline shall not undergo reviewing and publishing

## Publication

- ❖ Blinded peer review process of the papers will be considered;
- ❖ **Accepted papers** will be published in E3S Web of Conferences (cited in **SCOPUS**; ISSN:2267-1242, SJR: 0,166)
- ❖ More information about the Journal can be found on the website <https://www.e3s-conferences.org> ;

## REGISTRATION FEE

Regular participant (By 31 August): 150 EUR  
Ph. D Student: 120 EUR  
Additional paper: 50 EUR  
Accompanying person: 60 EUR  
Regular participant (After 31 August): 180 EUR

No more than **2** papers per participant.

Registration fee covers: Publication of the accepted articles in E3S Web of Conferences Scientific Journal, attendance in all sessions, conference materials, all meals and Gala dinner. The Fee for other participants includes all the meals, coffee breaks and the Gala Dinner for one person.

## CONFERENCE TOPICS

Renewable Energy Technologies  
Thermodynamics, Heat and Mass Transfer  
Building Efficiency Improvements and HVAC systems  
Fundamental and Applied Fluid Mechanics  
Thermal Comfort, Indoor Air Quality  
Hydraulic and Pneumatic Fluid Power Systems  
Electrohydraulic Power and Control Systems  
Energy and Environment Protection  
Nuclear Technologies  
Control and Automation of energy processes  
Design and Technologies for Clothing and Textiles  
Advanced Fibres and Materials, Innovative Textiles  
Comfort Science, Ecological and Environmental Textiles

## PAYMENT DETAILS

The registration fee should be transferred to the bank account of Technical University-Sofia-Technologies Ltd, Technical University of Sofia, Sofia, Bulgaria

Eurobank Bulgaria AD, Sofia Branch  
1000 Sofia, 8, Kliment Ohridski, blvd  
SWIFT BIC (head quarter): BPBIBGSF  
in BGN: IBAN: BG89BPBI 79401 04613 9702  
in EUR: IBAN: BG98BPBI 79401 44613 9701

### Reason for payment:

Participation in the conference "PEPM'21".  
Also add the name of corresponding Author.  
Send a copy of the payment order to the conference email. Send invoice information.

## IMPORTANT DATES

30 March	Abstract submission
15 April	Abstract acceptance and notification
30 May	Full paper submission
30 June	Paper acceptance notification
30 Juli	"Camera ready submission"

## LANGUAGE

- ❖ Official language of the conference is English

## VENUE

- ❖ The conference will be hosted in resort town Sozopol, located on the Black sea coast;
- ❖ Conference address: ul. "Lazuren bryag" 7, Sozopol



Location of Sozopol

Coordinates:  42°25'N 27°42'E



# 2021

## PEPM Hybrid Conference AGENDA



Powered by Organizing Committee

# Conference flow

Friday, September 17

**14:00 – 18:00** Conference Registration

**19:30 – 23:00** Welcome cocktail ([Holiday house Sozopol](#))

Saturday, September 18

**9:00 – 12:00** Conference Registration

**10:00 – 10:30** Opening Ceremony  
Prof. Totyo Totev, Conference Chairman

**10:30 – 12:00** A Word from the Sponsors

**12:00 – 13:30** Lunch break (on your own)

## Saturday, September 18 Attendance session (Conference Hall)

**Session Chairman: Prof. Dr. Totyo Totev**

**13:30 – 13:40**

**ID 34:** Optimization of the distance between the rows in solar collectors' arrays

*Merima Zlateva*

**13:40 – 13:50**

**ID 36:** An approach for reducing the air conditioning costs in office buildings in Vietnam

*Momchil Vassilev; Van Hung Tran; Thanh Nhan Phan; Nikola Kaloyanov*

**13:50 – 14:00**

**ID 15:** Verification and validation of a new CFD model of fixed regenerator for heat recovery from air

*Angel Penev; Lyubomir P. Tsokov; Momchil Vassilev*

**14:00 – 14:10**

**ID 33:** Mathematical models of the energy characteristics of a backpressure steam turbine based on a simulation study

*Kaloyan Hr Hristov*

**14:10 – 14:20**

**ID 38:** Thermal-hydraulic analysis of a VVER-1000 core in MSLB conditions

*Ivan G Spasov*

**14:20 – 14:30**

**ID ...:** Modeling of unbalanced regenerators for recovery of waste heat from air: a modern overview

*Angel Penev*

**14:30 – 14:40**

**ID ...:** Influence of the return network water temperature on the production of heat and electricity from an backpressure steam turbine installation

*Ivan Genovski, Kaloyan Hristov*

**14:40 – 15:00**

*Coffee Break*

**15:00 – 15:10**

**ID 29:** Modelling indoor pollutant distribution via passive scalar and virtual box approach

*Georgi Pitchurov; Detelin Markov; Iskra S. Simova; Rositsa Velichkova; Peter Stankov; Radostina A. Angelova*

**15:10 – 15:20**

**ID 31:** Design and constructive – technological development for children’s art clothing

Radka Atanasova; Magdalena Pavlova; Monika Merkova

**15:20 – 15:30**

**ID 46:** Application of ICT in the Online Education of Apparel Design and Production within the framework of ICT-TEX project

Hassan Saeed; Yordan Kyosev; Radka Atanasova; Angel K Terziev; Carla Hertleer

**15:30 – 15:40**

Session discussions

**19:30 – 23:00**

Gala dinner ([Hotel Selena](#))

# Sunday, September 19 Online session (Virtual session 1)

Web link: [Joint the Virtual session 1 here](#)

**Session Chairman: Prof. Dr. Gabriel Negreanu**

**Topic: *Thermal Equipment***

**10:00 – 10:15**

**ID 7:** Comparative analysis between methane and hydrogen regarding ignition and combustion in diffusive mode

Gabriel P Negreanu; Lucian Mihăescu; STANCIU Dorin; Gheorghe Lazaroiu; Ionel Pisa

**10:15 – 10:30**

**ID 20:** Energy and economic analysis of an ORC combined to steam boiler

Mocanu Gabriel; Ion V. Ion; Cristian C Iosifescu; Florin Popescu

**10:30 – 10:45**

**ID 22:** Air-to-water heat pump assessment: Part 1 – Experimental setup

Nadezhda Doseva, Daniela Chakyrova, Svetoslav Stoianov, and Iliya Hadhidimov

**10:45 – 11:00**

**ID 28:** Air-to-water heat pump assessment: Part 2 – Exergetic and exergoeconomic analyses

Nadezhda Doseva, Daniela Chakyrova

**11:00 – 11:15**

**ID 37:** Comparative technical and economic analysis of innovative methods for waste heat recovery from flue gases for boiler type BKZ 220-100

Hristo Beloev, Iliya Iliiev, Angel Terziev, Andrey Kibarin, Madina Aliyarova

**11:15 – 11:30**

**ID 35:** An experimental study for drying *Pisum sativum* on an electric dryer and a heat pump dryer

Merima Zlateva; Thanh Nhan Phan; Van Hung Tran; Nikola Kaloyanov

**11:30 – 11:45**

**ID 40:** Influence evaluation of the ship propulsion system on the energy efficiency for small, medium and large container vessels

Viktor Kr. Nikiforov

**11:45 – 12:00**

**ID 41:** Impact study of the fuel type used on the energy costs values and harmful emissions generation

Viktor Kr. Nikiforov

**12:00 – 12:15**

Session discussions

**12:15 – 13:30**

Lunch (on your own)

**Sunday, September 19 Online session (Virtual session 2)**

Web link: [Join the Virtual session 2 here](#)

**Session Chairman: Assoc. Prof. Dr. Martin Ivanov**

Topic: *Thermodynamics, Heat and Mass Transfer, Building Efficiency Improvements and HVAC systems*

**13:30 – 13:45**

**ID 8:** Modelling and numerical simulation of fire in a coffee storage hall

Nina Penkova; Kalin S Krumov; Boian M Mladenov; Yordan Stoyanov

**13:45 – 14:00**

**ID 42:** The influence of the structure of laminar flows on the characteristics of equipment

Vasyl Arsirii; Oleg V Kravchenko; Bohdan SAVCHUK; Olena ARSIRII

**14:00 – 14:15**

**ID 11:** Heat transfer in outer walls with layers of different density

Andrey Rymarov; Dmitriy Titkov

**14:15 – 14:30**

**ID 43:** Modelling and numerical simulation of the transport phenomena in water thermal energy storage tanks

Nikola Kaloyanov; Rosen Tsekov; Nina Penkova

**14:30 – 14:45**

**ID 1:** Possibilities for obtaining pellets by single-screw extrusion of biomass from black pine (pinus nigra arn.)

Apostol Simitchiev

**14:45 – 15:00**

**ID 2:** Thermodynamic and kinetic parameters of biomass from black pine (pinus nigra arn.)

Stanislava Tz. Tasheva

**15:00 – 15:15**

**ID 3:** Investigating the kinetics at low temperature heatpump drying and conventional drying of osmotic dehydrated blueberries

Hristo Hristov

**15:15 – 15:30**

Session discussions and Coffee brake

Topic: *Fundamental and Applied Fluid Mechanics, Hydraulic and Pneumatic Drive and Control Systems*

**15:30 – 15:45**

**ID 32:** Parameters influencing the droplet formation in a focusing microfluidic channel

Grigorov, Jordan A. Denev, Boris Kirov and Vassil Galabov

**15:45 – 16:00**

**ID 13:** GA-tuning of Multivariable PID Controller for Electrohydraulic Load-Sensing Servo System

Alexander St. Mitov; Tsonyo Slavov; Jordan Kravev; Ilcho Angelov

**16:00 – 16:15**

**ID 18:** Reduction of the Battery Capacity of Hybrid Electric Vehicle with the Help of Electrically Assisted Turbocharger

Ivaylo Stoyanov; Milen Mihaylov; Teodor B. Iliev (University of Ruse)

**16:15 – 16:30**

**ID 24:** Modularity Design of the Bamboo Plastic Fiber Forming Machine

Nguyen Thanh Nam ; Nguyen Hoang Hiep, Vinh Long

**16:30 – 16:45**

**ID 27:** Modularity design of instant coffee powder packaging machine

Svetlin Antonov; L. K. Dien

**16:45 – 17:00**

Session discussions. Closing of panel



## Sunday, September 19 Online session (Virtual session 3)

Web link: [Joint the Virtual session 3 here](#)

Session Chairman: Assoc. Prof. Dr. Angel Terziev

Topic: *Renewable energy technologies; Hydraulic and pneumatic machines and equipment*

**13:30 – 13:45**

**ID 9:** Assessing the diversification of energy mix with the methods of entropy and hierarchy of information

Iliyan I Petrov

**13:45 – 14:00**

**ID 12:** Renewable energies projects selection: block criteria systematization with AHP and Entropy-MOORA methods in MCDM

Iliyan I Petrov

**14:00 – 14:15**

**ID 26:** A design of solar battery cleaning system by modularity method

Svetlin Antonov; L. K. Dien

**14:15 – 14:30**

**ID 10:** Investigations of a vertical axis wind turbine with frontal cylindrical guide vane unit

Rossen Sashov Iliev

**14:30 – 14:45**

**ID 25:** A research on the formability and springback phenomena of pvc sheet in single point incremental forming (spif) technology

Nguyen Thanh Nam; Nguyen Hoang Hiep, Vinh Long; Nguyen Tan Hung; Tran Trong Hy

**14:45 – 15:00**

**ID 17:** Design of direct acting differential pressure control valve test bench.

Ognyan Bekriev ; Radoslav Asenov

**15:00 – 15:15**

**ID 19:** Experimental study of the accuracy of measuring of a central water meter

Aleksandar Stanilov

<b>15:15 – 15:30</b>	<b>ID 21:</b> CFD analysis of the behavior of a submersible vehicle in multiple flow directions and elevator and rudder fin configurations Georgi Todorov; Konstantin Kamberov; Blagovest N. Zlatev
<b>15:30 – 15:45</b>	<b>ID 4:</b> Operating stress of photovoltaic panels Ivaylo Stoyanov; Teodor B. Iliev
<b>15:45 – 16:00</b>	<b>ID 47:</b> On the Development of a Real Time Water Monitoring System Sandel Zaharia, Gabriel Iana, Cristian Monea and Mihnea Sandu
<b>16:00 – 16:10</b>	Session discussions and Coffee brake

Topic: *Design and Technologies for Clothing and Textiles*

<b>16:00 – 16:15</b>	<b>ID 46:</b> Application of ICT in the Online Education of Apparel Design and Production within the framework of ICT-TEX project Hassan Saeed, Yordan Kyosev, Radka Atanasova, Angel Terziev, Carla Hertleer
<b>16:15 – 16:30</b>	<b>ID 30:</b> Modification of Leather Surface Using Low-Pressure Plasma and Antimicrobial Reagent Sanja Ercegovic; Jadranka Akalović; Tomislav Ivanković; Anja Ludaš; Katarina Ištef
<b>16:30 – 16:45</b>	<b>ID 16:</b> Tangram based technology for clothing design Boryana G Georgieva-Gushtanova
<b>16:45 – 17:00</b>	<b>ID 23:</b> Methods for personal cooling in hot environment used in clothing and wearables Atanas Vasilev; Radostina A. Angelova; Rositsa Velichkova
<b>17:00 – 17:15</b>	<b>ID 39:</b> Development of boutique denim clothing by the "upcycling" method Magdalena Pavlova
<b>17:15 – 17:30</b>	Session discussions. Closing of panel

## Poster session, September 19 **Hall conference**

Session Chairman: Assoc. Prof. Dr. Merima Zlateva

Topic: *Renewable energy technologies*

**10:00 – 17:30**

**ID 45:** Determination of the optimal air-fuel ratio for upgraded biogas engine operation

Radostin Dimitrov, Penka Zlateva

**10:00 – 17:30**

**ID 44:** Electronic measuring system design for photovoltaic panels analysis

Krastin Yordanov; Iliya Hadzhidimov; Penka Zlateva

## Statement of Peer review

In submitting conference proceedings to *Web of Conferences*, the editors of the proceedings certify to the Publisher that

1. They adhere to its **Policy on Publishing Integrity** in order to safeguard good scientific practice in publishing.
2. All articles have been subjected to peer review administered by the proceedings editors.
3. Reviews have been conducted by expert referees, who have been requested to provide unbiased and constructive comments aimed, whenever possible, at improving the work.
4. Proceedings editors have taken all reasonable steps to ensure the quality of the materials they publish and their decision to accept or reject a paper for publication has been based only on the merits of the work and the relevance to the journal.

Title, date and place of the conference

---

**26th Scientific Conference on Power Engineering and Power Machines (PEPM'2021)**

18-21 September, 2021

Sozopol, Bulgaria

Proceedings editor(s):

---

Assoc. Prof. Ilinca Nastase  
Assoc. Prof. August Hubert Wierling  
Prof. Totyo Totev  
Assoc. Prof. Angel Terziev  
Assoc. Prof. Radka Atanasova  
Assoc. Prof. Merima Zlateva  
Assoc. Prof. Ivan Dukov  
Assoc. Prof. Kalin Filipov

Date and editor's signature

---

12 November 2021



## 26<sup>th</sup> Scientific Conference on Power Engineering and Power Machines (PEPM'2021)

18 – 21 September 2021

Sozopol, Bulgaria and parallel online sessions

[www.copepm.eu](http://www.copepm.eu)

The conference is organized by the Faculty of Power Engineering and Power Machines at the Technical University – Sofia. It is held annually during the global "Days of Science" forum at the university, since 1995. For the past 26 years the conference has become a traditional annual scientific event, for meeting of Bulgarian and foreign scientists, experts and industry representatives in the field of energetics, energy efficiency, renewable energy, heat engineering, hydraulics and pneumatics, environmental protection, textile and sewing production.

The PEPM conference provides the opportunity for the young researchers (PhD and MSc students, and Post Docs), involved in these scientific areas, to present their research activities and disseminate their work, as well as to meet and discuss with well-known and recognized scientists and experts from all over the world. Academic, industry and business members are also welcomed and appreciated as key-note speakers and sponsors.

The PEPM' 2021 edition has established agreement with E3S Web of Conferences, for open access proceedings indexed by Scopus, Google Scholar, CAS, DOAJ, EBSCO, ProQuest and others. The best accepted peer-reviewed papers will be published as special conference edition issue. During the article review process, a double-blind review is followed, with minimum of two reviewers for each paper submitted. The accepted papers should justify the conference topics, comply with the general ethics, be innovative and represent high level of research quality. Each paper is verified for plagiarism, with the PlagScan Tool, set to less than 20% plagiarism. The Microsoft CMT platform (Conference Management Toolkit) is used for the event management and paper submissions and reviewing process.

### **The main topics of the Conference are:**

*Renewable Energy Technologies*

*Thermodynamics, Heat and Mass Transfer*

*Building Efficiency Improvements and HVAC systems*

*Fundamental and Applied Fluid Mechanics*

*Thermal Comfort, Indoor Air Quality*

*Hydraulic and pneumatic machines and equipment*

*Hydraulic and Pneumatic Drive and Control Systems*  
*Energy and Environment Protection*  
*Nuclear Technologies*  
*Thermal Equipment*  
*Control and Automation of energy processes*  
*Design and Technologies for Clothing and Textiles*  
*Advanced Fibres and Materials, Innovative Textiles*  
*Comfort Science, Ecological and Environmental Textiles*

For the PEPM 2021 edition are received 60 papers, distributed to 39 reviewers. 43 papers were accepted for presentation and further editing, and 17 papers were rejected or withdrawn by the authors after revision process.

Thus, the PEPM 2021 edition conference was organized in 5 tracks:

- 15 papers in section *Thermal equipment, heat and mass transfer processes*
- 11 papers in section *Renewable Energy and Environmental protection*
- 6 papers in the section *Design and Technologies for Clothing and Textiles*
- 5 papers in the section *Hydraulic and Pneumatic Fluid Power Systems and Machinery*
- 6 papers in the section *Miscellaneous*

Among the participants, and aside from the local organization representatives, the conference was attended from scientists from following foreign universities:

*Karlsruhe Institute of Technology*  
*High Performance Computing Center Stuttgart*  
*Moscow State University of Civil Engineering;*  
*University "Politehnica" Bucharest;*  
*"Dunarea de Jos" University of Galati*  
*Tashkent State Technical University;*  
*Tashkent Institute of Irrigation and Agricultural Mechanization Engineers;*  
*Almaty University of Energy and Telecommunications;*  
*Kazakh National Agrarian University;*  
*HCMC University of Technology and Education;*  
*PetroVietnam University;*  
*Wroclaw University of Science and Technology;*

On behalf of the organizing committee and as editors of this conference issue of the PEPM 2021 proceedings, we wish to express our sincere gratitude to the sponsors, plenary speakers, authors and participants, reviewers and organizing members, who have contributed in the organization of the PEPM 2021 conference! See you, in **2022!**

***Prof. Totyo Totev***

*Conference Chairman*

***Assoc. Prof. Ilinca Nastase***

***Assoc. Prof. August Hubert Wierling***

*Chief Editors of PEPM 2021 Proceedings*

# Comparative analysis between methane and hydrogen regarding ignition and combustion in diffusive mode

Lucian Mihăescu<sup>1</sup>, Dorin Stanciu<sup>1</sup>, Gheorghe Lăzăroiu<sup>2</sup>, Ionel Pișă<sup>1</sup>, and Gabriel Negreanu<sup>1,\*</sup>

<sup>1</sup>University "Politehnica" of Bucharest, Department of Technical Thermodynamics, Engines, Thermal and Refrigeration Equipments, 313 Splaiul Independenței, 060042 Bucharest, Romania

<sup>2</sup> University "Politehnica" of Bucharest, Department of Energy Generation and Use, 313 Splaiul Independenței, 060042 Bucharest, Romania

**Abstract.** The hydrogen is expected to become the energy vector of the future. If for environmental protection this concept it is obvious, the data for the design of hydrogen combustion facilities are still insufficient. This paper discusses the fundamental actions related to the design of a hydrogen burner. Numerical modelling researches using the Ansys-Fluent software has shown the link between the flow velocity in combustible gas jets together with the required air and the combustion rates. Combustion models (both analytical and numerical) allowed finding the optimal ratios between the two specified velocities (combustion and flow) compared to those for methane combustion, correlated also with the classical directions and recommendations for the burner design.

## 1 Introduction

Hydrogen is a valuable solution for the future of energy but its combustion applications still need a lot of theoretical and experimental data. Gaseous hydrogen is characterized by low calorific value, very low density, extremely high combustion rate. These three characteristics must be incorporated in combustion technologies. Very high burning speed requires first of all a very high speed at the exit of the fuel from the burner embrasure (or its channels) in order to comply with the general stability condition: the equality between the flow velocity and the combustion rate. These characteristics make hydrogen totally different from fuels in the category of hydrocarbons. High flow rates will impose a high degree of turbulence that decisively influences the entire combustion process [1-2].

Due to the increased performance of current CAD-CAE software designated to complex kinetics of combustion reactions, but also of the computing power, the numerical simulations contribute today significantly together with experiments to develop new evolved combustion technique for hydrogen.

---

\* Corresponding author: [gabriel.negreanu@upb.ro](mailto:gabriel.negreanu@upb.ro)



In this case the flame represents the interaction between the chemical reactions and the turbulent flow structure, being characterized by significant oscillations of all species variables. During combustion there is a strong variation in gas density and viscosity as a consequence of temperature variations with a significant influence on the velocities field.

The process is mirrored (in opposition) to the influence of turbulence on combustion (that improves the processes of convective mixing and diffusion). According to the data presented in paper [3] it turned out that the ignition is faster in the turbulent flow regime than in the laminar one. The research was carried out for a methane-air blend.

## 2 Methodology

### 2.1 Hypotheses regarding the combustion conditions for the studied model

The research deals with the study of hydrogen burning in comparison compared to methane for a diffusive combustion model comprising a central fuel inlet (*i*) and a peripheral air inlet (*e*) as shown in Figure 1. For an isothermal accompanied jet, the flow velocity has a hyperbolic decrease along its length

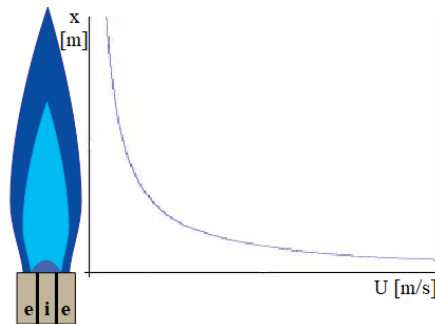


Fig. 1. Hyperbolic dependence of axial velocity  $U$  on axial distance  $x$

From the point of view of aerodynamics the model includes the flow theory of an isothermal fuel jet accompanied by a parallel air jet, without swirl.

Combustion occurs under the influence of two important factors:

- the ratio between the flow velocity and the combustion rate;
- the diffusion of air in the fuel jet.

Considering the hypothesis that the turbulent flame represent a zone of disperse reactions, in order to apply the comparison between the flow velocity and the combustion rate, the propagation of the turbulent flame can be assimilated that of the laminar flame.

The combustion stability is achieved when the following condition is met:

$$U = S_T \text{ [m/s]} \quad (1)$$

where:  $U$  – jet flow velocity;  $S_T$  – combustion rate in turbulent flow.

This condition must take into account the decrease in the flow velocity in the combustion jet so that the velocity in the output section  $u_0$  should be high enough in order

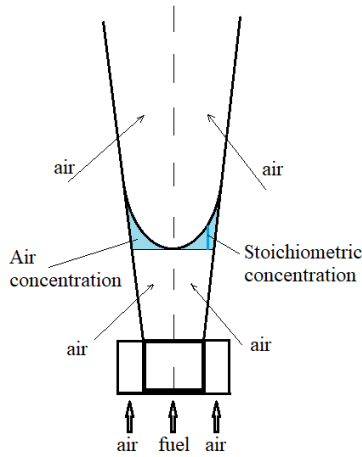
to respect the equality of stability (2) to be observed in the end zone (similar to the laminar flame).

For an isothermal accompanied jet, the variation of the velocity  $u$  in the jet axis is expressed by the equation:

$$U = U_i \cdot \frac{A}{\bar{x}} \cdot \sqrt{\frac{\rho_i}{\rho_e}}, \quad [\text{m/s}] \quad (2)$$

where:  $\bar{x} = \frac{x}{R}$ ;  $x$  – axial distance;  $R$  – radius of output section;  $\rho_i$  – density of fuel jet [ $\text{kg/m}^3_{\text{N}}$ ];  $\rho_e$  – density of accompanied jet [ $\text{kg/m}^3_{\text{N}}$ ];  $A$  – experimental constant.

From the point of view of diffusion, the gaseous hydrogen differs from methane by the ratio between thermal and mass diffusion (Lewis criterion). For hydrogen, this criterion is equal to 0.3 while for methane its value is 1. This implies strong changes in air diffusion mode in flame, moving the stoichiometry section closer to the jet fuel central axis (Fig. 2).



**Fig. 2.** Air diffusion in the fuel jet for the model studied

The turbulent combustion rate depends on the following parameters:

$$S_T = S_L \cdot \frac{\delta_L}{\delta_T} \cdot \frac{\varepsilon}{\nu}, \quad [\text{m/s}] \quad (3)$$

where:  $\delta_L$ ,  $\delta_T$  – depth of the laminar, respectively turbulent flame [m];  $\varepsilon$  – turbulent diffusion coefficient [ $\text{m}^2/\text{s}^2$ ];  $\nu$  – kinematic viscosity [ $\text{m}^2/\text{s}^2$ ].

The combustion rate on the turbulent flow regime for hydrogen requires the increase of its velocity jet  $U_i$  in the burner exit section over those of methane (where usually can be found available burner designs and operational data) with the ratio between the two combustion rates.

Table 1 shows the values of normal combustion rates for methane and hydrogen.

**Table 1.** Usual rates of combustion for methane and hydrogen.

Fuel	$S_L$ [m/s]	$S_T$ [m/s]
CH <sub>4</sub>	0.95	3.7
H <sub>2</sub>	16	26.7

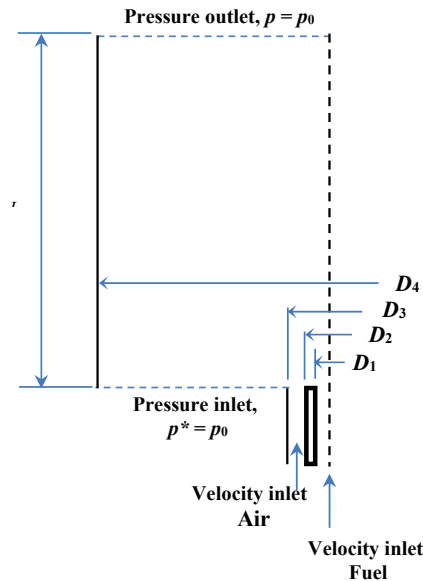
With this values the combustion rates ratios can be computed:

- $R_{\frac{H_2}{CH_4}} = 16.8$  for laminar flow;
- $R_{\frac{H_2}{CH_4}} = 7.2$  for turbulent flow.

According to these ratios, input velocities have been imposed as boundary conditions for the physical and numerical models to be further developed:

## 2.2 Physical model and boundary conditions

The computing domain is shown in Fig. 3.

**Fig. 3.** Scheme of computing domain

The fuel is entering the combustion region through the inner pipe of diameter  $D_1$ , while the air is flowing to it through the ring space formed between the  $D_2$  and  $D_3$  diameters. This is a classical coaxial jets configuration, which here is completed by a co-flow air stream, entrained by the air external jet through a ring boundary formed between the diameters  $D_3$  and  $D_4$ .

For comparing the behavior of the two diffusion flames, one must keep as much as possible flow parameters at the same values. According to van Hoot et al. [6], in the case of coaxial jets, the main flow parameters are:

- the density ratio,  $S = \rho_e / \rho_i$ ;
- the bulk velocity ratio,  $r_u = U_e / U_i$ ;
- the momentum ratio,  $M = \rho_e U_e^2 / \rho_i U_i^2$ .

In the above definitions, subscripts “e” and “i” were explained above. Obviously,

$$M = S r_u^2 \quad (4)$$

Besides, the Reynolds numbers of the jets feeding the combustion domain should be considered as parameters since their values influence the flame length.

Since the density ratio is different for the two fuel-air combinations considered in this paper, it cannot find the fuel-air velocities pairs to obtain the same values of  $r_u$  and  $M$ . As a result, we have chosen to perform our analysis at the same momentum ratio value (4).

Further, all the  $D_1$  and  $D_2$  diameters, the Reynolds number of fuels flowing inside the inner duct, and the air excess ratio  $\lambda$  are kept at the same values for both CH<sub>4</sub>-air and H<sub>2</sub>-air flames. The geometry and the boundary conditions for the CH<sub>4</sub>-air and H<sub>2</sub>-air numerical simulated flames are presented in Table 2. Note that there the mean bulk air and flow velocities are revealed. Based on these values, one has generated the fully developed velocity and turbulence profiles, which were used as boundary conditions for the inlet sections of air and fuel feeding pipes, placed at 5 cm below the combustion region.

**Table 2.** Geometry dimensions and boundary conditions for CH<sub>4</sub>-air and H<sub>2</sub>-air diffusion flames

Data	$D_1$ [mm]	$D_2$ [mm]	$D_3$ [mm]	$D_4$ [mm]	$\lambda$ [-]	$Re_{fuel}$ [-]	$Re_{air}$ [-]	$S$ [-]	$r_u$ [-]	$M$ [-]	$U_{fuel}$ [m/s]	$U_{air}$ [m/s]
CH <sub>4</sub> -air	3	4	21.3	500	1.05	7450	10000	1.91	0.2	0.07	45.0	9.0
H <sub>2</sub> -air	3	4	9.2	500	1.05	7450	17470	14.36	0.071	0.07	274.7	19.16

### 2.3 Numerical model

The reacting flows is modeled by Favre averaging Navies-Stokes system of equations. The chemistry model relies on the mixture fraction based steady flamelet approach. By using it, the fast, but finite time chemical reactions are considered. To generate the flamelet tables, one has used the GRI 1.2 reaction mechanism for CH<sub>4</sub>-air flame [7-8] and the Li et. al reaction mechanism [9-10] for H<sub>2</sub>-air flame. The NO<sub>x</sub> formation chemical mechanisms were not considered in this study. For the turbulence chemistry interaction, the k-w SST model was selected. The computations were performed under the ANSYS-FLUENT v14.0 Academic software package [4]. The pressure-based solver using the incompressible ideal gas method for density was set for the calculation. The spatial numerical discretization was second order up-wind for all properties involved in computation. After the hybrid initialization, the first 1000 iterations were performed with the aid of the SIMPLE pressure-velocity coupling algorithm, and the next ones, by using the COUPLED pseudo transient algorithm. The computations were stopped when the residuals of all computing properties were dropped at least eight order of magnitude.

## 2.4 Mesh details

In the case of CH<sub>4</sub>-air flame, the mesh contains about 40000 cells and 80000 faces. For the H<sub>2</sub>-air flame, the mesh consists of about 45000 cells and 90000 faces. In both cases the mesh was one time adapt using the gradient criterion of the fuel mixture fraction. As a result, inside the flame domain and near around it, the cell Reynolds number lies between 0.12 and 2.5. Outside these regions (i.e., near the outer wall and outflow boundary, the cell Reynolds number is around 120.

## 3 Results and discussions

### 3.1 Temperature maps

Fig. 4 shows the temperature maps of CH<sub>4</sub>-Air (up) and H<sub>2</sub>-Air (down) flames. It is noted that in the case of the hydrogen flame, the higher combustion rate and turbulence of the jet compared to methane led to a 10% shorter flame shorter. The temperature in the core of the hydrogen flame is higher than in the case of methane.

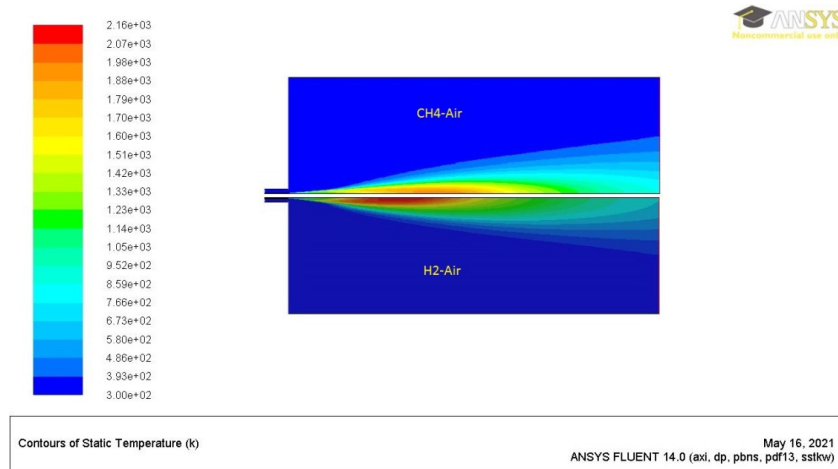


Fig. 4. Temperature maps of CH<sub>4</sub>-Air (up) and H<sub>2</sub>-Air (down) flames

### 3.2 Axial temperature profiles

Fig. 5 shows the axial variation of temperature for the two investigated flames. In absolute terms, the maximum temperature is closer to the burner embrasure for the hydrogen combustion than the methane one. The maximum temperature of the hydrogen flame is about 250 degrees higher than the homologous value of the methane flame.

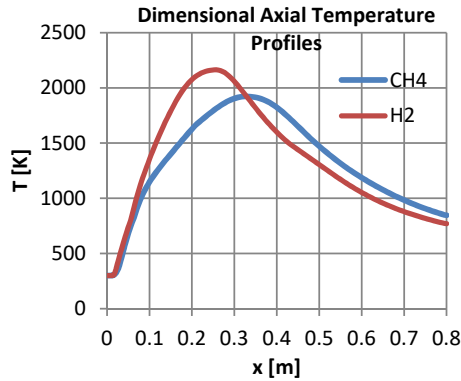


Fig. 5. Dimensional axial temperature profiles for CH<sub>4</sub>-Air and H<sub>2</sub>-Air flames

However, to compare the two flames behavior, one should find the dimensionless measure of axial length and axial flame temperature. Thus, one has chosen as dimensionless length and temperature the ratios  $x/L_{st}$ , and  $T/T_{ad}$ , respectively, where  $L_{st}$  is the stoichiometric length of the flame and  $T_{ad}$  is the adiabatic flame temperature. The stoichiometric length of the flame represents the axial length measured from the burner head at which the mixture fraction reaches the stoichiometric value. Based on the numerical simulation one found that  $L_{st} = 0.362$  m, for methane-air flame (where the stoichiometric mixture fraction is 0.55), and  $L_{st} = 0.278$  m, in the case of hydrogen-air flame (where the stoichiometric mixture fraction is 0.028). The adiabatic flame temperatures, as they are defined in chemical thermodynamics are  $T_{ad} = 2226$  K for CH<sub>4</sub>-Air flame and  $T_{ad} = 2483$  K for H<sub>2</sub>-Air flame, respectively. Fig. 6 shows the numerical simulated dimensionless axial temperature profiles.

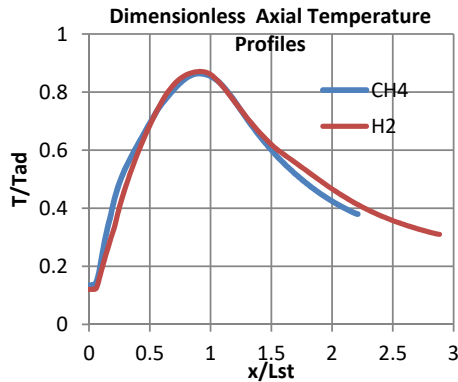


Fig. 6. Dimensionless axial temperature profiles for CH<sub>4</sub>-Air and H<sub>2</sub>-Air flames

In the dimensionless coordinates used, there is a high coincidence of the temperature profiles of the flames, along their relative length.

### 3.3 Radial temperature profiles

The radial profiles were drawn for axial lengths fractions of 1/8, 4/8 and 8/8 of  $L_{st}$ . Fig. 6 shows the radial temperature profiles for both flames.

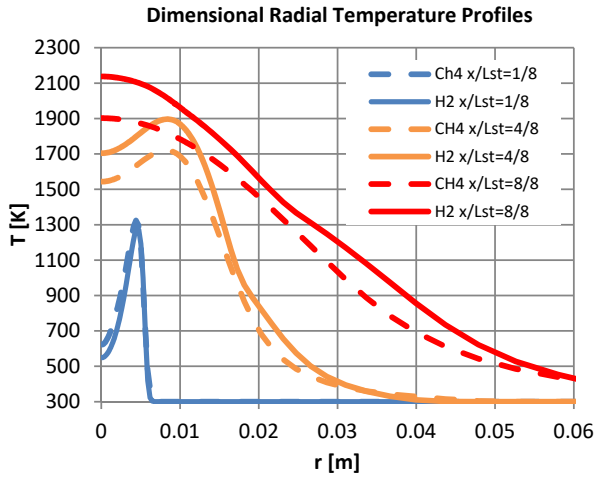


Fig. 6. Dimensional radial temperature profiles for CH<sub>4</sub>-Air and H<sub>2</sub>-Air flames

The dimensionless radial profiles are presented in Fig. 7. There the dimensionless radial coordinate is  $r/R_{cb}$ , where  $R_{cb} = 1.5$  mm is the radius of fuel feed tube, and the dimensionless temperature is expressed by  $T/T_{ad}$ , as previous defined.

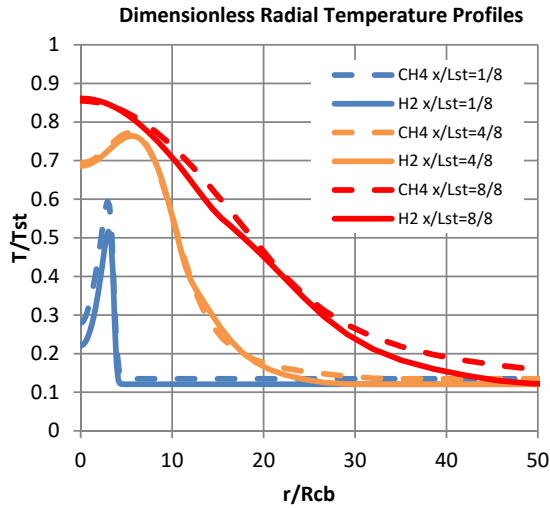


Fig. 7. Dimensionless radial temperature profiles for CH<sub>4</sub>-Air and H<sub>2</sub>-Air flames

Between the conventional and the dimensionless approach there are no significant differences between the radial temperature profiles between various dimensionless axial positions except for the final section of the flame, where the maximum deviation is 10%.

## 4 Conclusions

The paper analysed by mathematical modeling and numerical simulation the flame developed during the combustion of methane and hydrogen, respectively.

The physical model considered comprised a central jet of gaseous fuel, framed by a parallel jet of air. Jet dynamics have developed with a lower peripheral air velocity than that of fuel.

The similitude of the combustion required the choice of a common criterion, represented by the ratio of the momentum, which resulted in the input velocity of the hydrogen jet.

Excess air coefficient was chosen to the minimum possible, in correlation with current techniques for burning gaseous fuels in order to obtain maximum combustion efficiencies.

The interpretation of the resulting data showed a great similarity of the combustion of hydrogen with that of methane, both in terms of flame length and in terms of temperatures recorded in them.

The results obtained in this research can be a basis for their continuation, which will ultimately lead to the design and construction of high-performance hydrogen burners.

Future research will consider higher speeds for the air circuit and more efficient control of its diffusion.

## References

1. A. Wawrak, A. Tyliczszak, Numerical Study of Hydrogen Auto-Ignition Process in an Isotropic and Anisotropic Turbulent Field, *Energies*, (2021), **14(7)**, 1869; <https://doi.org/10.3390/en14071869>
2. F. H. Vance, Y. Shoshin, P. de Goeij, J. van Oijen, Flame Stabilization and Blow-Off of Ultra-Lean H<sub>2</sub>-Air Premixed Flames, *Energies* (2021), **14(7)**, 1977; <https://doi.org/10.3390/en14071977>
3. Y. J. Kim, B. J. Lee, H. G. Im, Hydrodynamic and chemical scaling for blow-off dynamics of lean premixed flames stabilized on a meso-scale bluff-body, *Proceedings of Combustion Institute*, Volume **37**, Issue 2, (2019), Pages 1831-1841, <https://doi.org/10.1016/j.proci.2018.05.026>
4. Ansys-Fluent, Academic Research, version 14.0
5. J. Schlup, G. Blanquart, A reduced thermal diffusion model for H and H<sub>2</sub>, *Combustion and Flame*, Volume **191**, (2018), Pages 1-8, <https://doi.org/10.1016/j.combustflame.2017.12.022>
6. R. van Hoot, S. Murugan, A. Mitra, B. Cukurel, Coaxial Circular Jets—A Review. *Fluids* 2021, **6**, 147. <https://doi.org/10.3390/fluids6040147>
7. M. Frenklach, H. Wang, C.-L. Yu, M. Goldenberg, C.T. Bowman, R.K. Hanson, D.F. Davidson, E.J. Chang, G.P. Smith, D.M. Golden, W.C. Gardiner and V. Lissianski, [http://www.me.berkeley.edu/gri\\_mech/](http://www.me.berkeley.edu/gri_mech/)
8. M. Frenklach, H. Wang, M. Goldenberg, G.P. Smith, D.M. Golden, C.T. Bowman, R.K. Hanson, W.C. Gardiner and V. Lissianski, 'GRI-Mech---An Optimized Detailed



- Chemical Reaction Mechanism for Methane Combustion,” Report No. GRI-95/0058”, November 1, (1995).
9. Li, J., Zhao, Z., Kazakov, A., and Dryer, F.L. "An Updated Comprehensive Kinetic Model for H<sub>2</sub> Combustion", Fall Technical Meeting of the Eastern States Section of the Combustion Institute, Penn State University, University Park, PA, October 26-29, (2003).
  10. Li, J., Zhao, Z., Kazakov, A., and Dryer, F.L. "An Updated Comprehensive Kinetic Model for hydrogen Combustion, *Chemical Kinetics*, **36**: 566–575, (2004).
  11. P. Jha, C. Groth, "Evaluation of Flame-Prolongation of ILDM and Flamelet Tabulated Chemistry Approaches for Laminar Flames", *Combustion Theory and Modelling*, **16(1)**, (2012), DOI:10.1080/13647830.2011.608856

# Energy and economic analysis of an ORC combined to steam boiler

Gabriel Mocanu<sup>1</sup>, Ion V. Ion<sup>1,\*</sup>, and Cristian Iosifescu<sup>1</sup>

<sup>1</sup>"Dunărea de Jos" University of Galati, 47 Domneasca St., 800008 Galati, Romania

**Abstract.** Energy and economic performance of an organic Rankine cycle (ORC) system designed to recycle waste heat of a steam boiler was analysed. Optimisation of ORC system was performed by using the Cycle-Tempo software and the REFPROP program. The selected working fluid was R245fa. For the exhaust gases temperature of 163°C and mass flow rate of 11.83 kg/s, cooling water temperature of 20°C resulted a gross efficiency of 21.02% and a cost of 2987 €/kW, an electricity levelised cost of 102 €/kWh and a payback period of 5.5 years.

## 1 Introduction

Reducing fossil fuel consumption and environmental pollution can be achieved by using renewable energy sources and by recovering waste heat from energy conversion processes. Waste heat can be recovered by using various technologies, such as: ORC, Kalina cycle, Goswami cycle, absorption refrigeration and heat pumps.

Since it was invented, in the 19th century, the steam boiler has known a continuous development, being found in all industries (food processing, chemicals, petroleum refining, pulp and paper, etc.). In the USA, steam boilers are responsible for burning about 37% of the fossil fuel consumed in industry [1]. Given the widespread use and appreciable consumption of fuels, the attention of specialists has been drawn to the increasing energy efficiency of steam boilers [2 - 6]. The thermal efficiency of steam boiler is greatly affected by the heat loss with the exhausted gases (probably the greatest heat loss). The exhaust gases from steam boilers have quite high temperatures, between 170°C and 120°C, depending on the fuel burnt, in order to minimize the risk of corrosion and to ensure the dispersion of the flue gas at a height as high as possible. For heat recovery from exhaust gases from boilers are used ORC [7] and Kalina cycle [8, 9] to generate electrical energy, absorption refrigeration [10] for cooling and heat pumps to generate heat energy [11-13].

In [7] is reported a thermal efficiency of 14.82% of an ORC system with R123 as working fluid that recovers heat from the exhaust gases from a boiler by cooling them from 135°C to 110°C (29.26 MW), the condensation temperature being 30°C.

Paper [8] presents the study on an ORC system used to recover the heat from exhaust gases from a steam boiler with a maximum gross efficiency of 18.8%, by cooling them from 180°C to 130°C (2.3 MW) and by using cooling water with temperature of 5°C.

---

\* Corresponding author: [iion@ugal.ro](mailto:iion@ugal.ro)

Heat recovery from exhaust gases from a boiler to generate electricity can be performed also by using Kalina cycle which can reach an efficiency of 14.78% by cooling them from 160°C to 105°C [10].

To generate electricity from low-temperature energy sources available at temperatures of (80-150)°C, the ORC systems are recommended [14]. Although ORC systems are a mature technology, their use is limited, mainly due to the fact that potential investors and users do not recognise the ability of these systems to conserve energy [15]. The efficiency, size and cost of an ORC system depend primarily on the working fluid, which is chosen according to the temperature of the heat source, and then on the evaporation temperature, condensation temperature and system configuration. There are many studies on working fluid selection for a particular application [14, 16-18]. In addition to the type of application and the temperature of the heat source, the selection of working fluid also takes into account the following: the auto-ignition temperature, which must be much higher than the maximum working temperature of the fluid; the enthalpy drop in the expander must be as large as possible to minimize fluid flow to the pump; in the T-s diagram, the inclination of the saturation curve must be as close as possible to the isentropic curves in order to avoid overheating; ODP and GWP to be minimal; fluid cost to be reduced; the critical temperature should be reduced because the vapour density is higher at lower temperatures. There is no fluid that meets all the criteria (environmental: ODP, GWP, flammability, toxicity; safety; physical and chemical properties; economic). The selection is finally made taking into account the international protocols that recommend fluids that are not harmful to the environment and the thermal efficiency of the cycle. In [19], working fluids are classified into six categories according to the heat source temperature. For heat source temperatures between 445 K and 465 K, the following working fluids are recommended: R600, R245fa, neopentane and R245ca. Also, in paper [20], for temperature ranges 100 – 150°C, are recommended the following fluids: butane, neopentane and R245fa.

For ORC systems with a capacity of more than 100 kW, the most suitable expansion machines are turbines [21].

When using low heat sources, it is recommended the direct heat exchange between the heat source fluid and the ORC working fluid, without using an intermediate loop, thus avoiding the reduction of the evaporation temperature and the complication of the plant.

The specific cost of ORC units is difficult to be estimated due the lack of information provided by the manufactures, but in literature can be found some indicative costs and models to calculate them. The low temperature ORC systems can have an average specific cost from about 1350 €/kW for a 250 kW-unit to 2200 €/kW for 50 kW-unit, and the high temperature ORC systems from 1000 €/kW for a 2 MW-unit, to 2000€/kW for a 500 kW-unit and up to 3000€/kW for a 150 kW-unit [22]. To the total acquisition cost ( $Z_{tot}$ ) are added the following costs: 30% from the  $Z_{tot}$  for piping and accessories, 20% for installation; 10% for instrumentation and 11% for materials necessary to build the system. Operating and maintenance costs can reach 45% from the  $Z_{tot}$  [18].

This paper aims to analyse energetically and economically the coupling of ORC to a steam boiler for heat recovery from exhaust gases.

## 2 Energy model

The steam boiler considered in this study is of type CR 12C and generates 50 t/h steam with a pressure of 36 bar and a temperature of 450°C with an efficiency of 90.5%. The boiler runs on natural gas. The properties of the exhaust gases from the boiler are given in Tab. 1.

Table 1. Flue gas properties.

Temperature, °C	Mass flow rate, kg/s	Enthalpy, kJ/kg
163	11.83	242.25
100	11.83	148.00

The ORC model was developed by using the Cycle-Tempo simulation tool. The working fluid properties were calculated by using the REFPROP program. Of the recommended working fluids for the heat source temperature of 163°C, the R245fa was chosen as it need not superheating, has low ODP, is nearly non-toxic and it does not degrade at the maximum working temperature of the cycle. The chosen expansion machine was axial turbine.

Several ORC simulations were performed with different vaporization and condensation pressures with simple cycle and with internal heat recovery cycle aiming at obtaining the maximum net power. These led to the ORC configuration shown in Fig. 1 and the representation in the *T-s* diagram in Fig. 2. The maximum net power was obtained for the evaporation pressure of 17 bar, condensation pressure of 2.6 bar and simple configuration. The pinch point temperature in evaporator and condenser was set at 10°C. The evaporator is a shell-and-tube heat exchanger and the condenser is a flat plate heat exchanger.

The ORC operation parameters of the system components are given in Table 2. The heat loss and pressure drop in pipes were neglected.

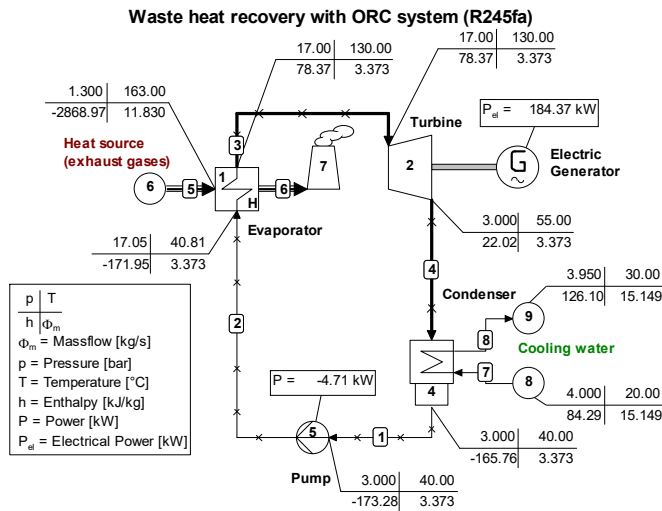


Fig. 1. ORC schematic (R245fa) (Cycle-Tempo).

The thermodynamic model is described by the following equations:

- pump power consumption:

$$W_p = \dot{m}_1 (h_2 - h_1) / \eta_{i,p} \eta_{m,p}, \text{ kW} \tag{1}$$

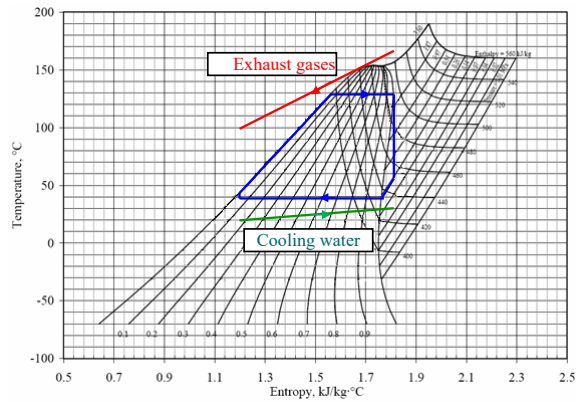


Fig. 2.  $T$ - $s$  diagram of ORC (R245fa).

Table 2. Characteristics of system apparatuses.

Parameter	Value
Turbine isentropic efficiency, $\eta_{i,T}$	0.87
Turbine mechanical efficiency, $\eta_{m,T}$	0.95
Pump isentropic efficiency, $\eta_{i,P}$	0.80
Pump mechanical efficiency, $\eta_{m,P}$	0.95
Electrical generator efficiency, $\eta_G$	0.97
Pressure loss in evaporator and condenser	0.05 bar
Evaporator overall heat transfer coefficient, $U_{ev}$	0.3 kW/m <sup>2</sup> /K
Condenser overall heat transfer coefficient, $U_c$	4 kW/m <sup>2</sup> /K

- heat transferred in evaporator:

$$\dot{Q}_{ev} = \dot{m}_{fg} (h_5 - h_6) = \dot{m}_2 (h_3 - h_2), \text{ kW} \quad (2)$$

$$\dot{Q}_{ev} = U_{ev} \cdot A_{ev} \cdot \Delta t_{ev}, \text{ kW} \quad (3)$$

where:  $A_{ev}$  is evaporator heat exchange area, m<sup>2</sup>;  $U_{ev}$  is overall heat transfer coefficient, kW/m<sup>2</sup>/K;  $\Delta t_{ev}$  is logarithmic mean temperature difference of evaporator, K;

- electric generator power output:

$$W_G = \dot{m}_1 (h_3 - h_4) \eta_{m,T} \eta_{i,T} \eta_G, \text{ kW} \quad (4)$$

- heat transferred in condenser:

$$\dot{Q}_c = \dot{m}_1 (h_4 - h_1) = \dot{m}_{cw} (h_8 - h_7), \text{ kW} \quad (5)$$

$$\dot{Q}_c = U_c \cdot A_c \cdot \Delta t_c, \text{ kW} \quad (6)$$

where:  $A_c$  is evaporator heat exchange area,  $m^2$ ;  $U_c$  is overall heat transfer coefficient,  $kW/m^2/K$ ;  $\Delta t_c$  is logarithmic mean temperature difference of evaporator,  $K$ ;  $m_{cw}$  is mass flow rate of cooling water,  $kg/s$ ;

- ORC net power output:

$$W_{net} = W_G - W_P, \text{ kW} \quad (7)$$

- ORC gross energy efficiency:

$$\eta = \frac{W_{net}}{\dot{Q}_{ev}} \quad (8)$$

### 3 Economic model

The economic model includes calculation of capital cost, levelised cost of energy and the payback period.

The purchase cost corresponding to year 2001 of the ORC system components can be calculated by using the following equations [23]:

- turbine cost as function of power output,  $W_T$ :

$$Z_T = 3.5 \cdot 10^{(2.2476 + 1.49658 \cdot \log_{10} W_T - 0.1618 \cdot (\log_{10} W_T)^2)}, \text{ €} \quad (9)$$

- cost of heat exchangers as function of heat exchange area,  $A$ :

$$Z_{HE} = 10000 + 324 \cdot A^{0.91}, \text{ €} \quad (10)$$

- pump cost as function of power capacity,  $W_P$  and operation pressure  $p$ :

$$Z_P = 10^{(3.3892 + 0.0536 \cdot \log_{10} W_P - 0.1538 \cdot (\log_{10} W_P)^2)} \cdot 10^{(-0.3935 + 0.3957 \cdot \log_{10} p - 0.0023 \cdot (\log_{10} p)^2)}, \text{ €} \quad (11)$$

- electrical generator cost as function of power output,  $W_G$ :

$$Z_G = 2775000 \left( \frac{W_G}{11800} \right)^{0.94}, \text{ €} \quad (12)$$

- total capital cost corresponding to year 2021:

$$Z_{tot} = (Z_T + Z_C + Z_P + Z_{EV}) \frac{CEPCI_{2021}}{CEPCI_{2001}}, \text{ €} \quad (13)$$

where  $CEPCI_{2001}$  and  $CEPCI_{2021}$  are the Chemical Engineering Plant Cost Index values required to convert the purchase cost from 2001 to 2021 ( $CEPCI_{2001} = 397$ ;  $CEPCI_{2021} = 637.8$ ) [24];

- capital recovery cost:

$$CRF = \frac{i(1+i)^n}{(1+i)^n - 1} \quad (14)$$

where  $i$  is annual interest rate ( $i=0.1$ ) and  $n$  is plant lifetime ( $n=25$  years);

- levelised cost of electricity:

$$LCOE = \frac{Z_{tot} \cdot CRF + C_{OM}}{N \cdot W_{net}}, \text{ €/kWh} \quad (15)$$

where  $C_{OM}$  is the annual cost of plant operation and maintenance, € ( $C_{OM} = 0.3 \cdot Z_{tot}$ ),  $N$  is annual hours of operation ( $N = 7400$  hours);

- payback period:

$$PP = \frac{Z_{tot}}{N \cdot W_{net} \cdot C_{el} - C_{OM}}, \text{ years} \quad (16)$$

## 4 Results and discussions

The developed model was verified and validated by simulating the experimental ORC system working with R245fa presented in [25] and comparing the simulation results. The results of the simulation were very close to those presented in the paper.

Following the simulations performed with Cycle-Tempo, the optimal operating parameters of the system corresponding to the maximum net power generated by the ORC were obtained. These are given in Fig. 1. The ORC system recovers 844.29 kW<sub>th</sub> from the exhaust flue gases from the boiler and generates 177.48 kW<sub>el</sub>, which means a gross efficiency of 21.02%.

In paper [10] is presented a system with Kalina cycle that recovers 2538 kW<sub>th</sub> from the exhaust gases from a steam boiler. The power generated by the system is 375.21 kW<sub>el</sub> which means an efficiency of 14.78%. If the same amount of heat with the same thermal level were recovered with the developed ORC system, 520.7 kW<sub>el</sub> would be generated, which means a system efficiency of 20.5%. It can be seen that the ORC is more efficient than the Kalina cycle for using the same heat source and the same cooling water. On the other hand the Kalina cycle has an important advantage of reacting to the heat source temperature variation by adjusting the amount of ammonia in the working fluid.

For the implementation of the ORC system, a financial effort at the level of year 2021 of 531770 € is required, which means a specific cost of 2987 €/kW<sub>el</sub>. For the annual operation and maintenance cost of € 93300, lifetime of 25 years and 7400 operating hours per year resulted in a Levelised cost of electricity of 0.115 €/kWh and a payback of 5.5 years.

Comparing the results of energy analysis as well as of the economic analysis obtained in this study with those reported in the literature, insignificant differences can be observed.

## 5 Conclusions

One way to increase the steam boiler efficiency is to recover the heat from exhaust gasses. So, the exhaust gases should be cooled down as much as it is allowed and to reintroduce it to the cycle or to convert it into electricity as efficient as possible. The ORC systems are gaining attention for waste heat recovery. There are currently a wide variety of ORC systems that differ in working fluid, expansion machine type and heat exchangers type. The correct choice of system for a particular application depends primarily on the temperature of the heat source. Cycle-Tempo is one of the tools used to simulate ORC systems. It has the advantage of allowing operation optimisation of simulated systems.

The analysis performed in this paper shows that by cooling the exhaust gases from a steam boiler into the evaporator of an ORC system allows to generate electricity with an

efficiency of 21.02%. Heat recovery for electricity generation allows an annual reduction of GHG emissions of 360 tons and an annual gain of 190436 €, obtained by selling electricity (by 0.145 €/kWh) or by reducing the electricity consumption. The generated electricity can be used to supply electric motors to drive the flue gas fan or air fan or other consumers, thus increasing the efficiency of using the energy introduced with the fuel in steam boiler.

## References

1. D. Einstein, E. Worrell, M. Khrushch, *Steam systems in industry: Energy use and energy efficiency improvement potentials* (Lawrence Berkeley National Laboratory, 2001)
2. I.V. Ion, G. Ciocea, F. Popescu, *Therm. Eng.*, **S 1** (2016)
3. I. Binev, V. Rasheva, S. Tasheva, N. Georgieva, M. Konstantinov, *ARTTE* **3** (2015)
4. Z. Kolev, P. Mushakov, P. Zlatev P., *Proceedings of Conference of University of Ruse* **57**, 1 (2018).
5. P.G. Negreanu, I. Oprea, *Proceedings of COFRET'12 Symposium*, Sozopol, Bulgaria (2012)
6. I. Iliev, A. Terziev, H. Beloiev, *E3S Web Conf.* **180**, (2020)
7. L. Qiang, *Waste Heat Recovery from Fossil-Fired Power Plants by Organic Rankine Cycles*, in *Organic Rankine Cycles for Waste Heat Recovery - Analysis and Applications* (S. Lasala, IntechOpen 2019)
8. S. Ogriseck, *Appl. Therm. Eng.* **29** 14-15 (2009)
9. K.S. Omendra, *Fuel* **267** (2020)
10. K.S. Omendra, *Renew. Energy* **143** (2019)
11. W. Maolin et al., *Appl. Therm. Eng.* **86** (2015)
12. Y. Yuan, et al., *Energy Procedia* **61** (2014)
13. M.Qu, O. Abdelaziz, H. Yin, *Energ Convers Manag.* **87** (2014)
14. H.M.D.P. Herath, M.A. Wijewardane, R.A.C.P. Ranasinghe, J.G.A.S. Jayasekera, *Energy Rep.* **6** (2020)
15. S. Lecompte, A.O. Oyeniyi, M.N. Christos, L. Marija, K. Alihan, M. van den Broek, M. De Paepe, *Energies* **10** (2017)
16. Z.Q. Wang, N.J. Zhou, J. Guo, X.Y. Wang, *Energy* **40** (2012)
17. B.T. Liu, K.H. Chien, C.C. Wang, *Energy* **29**(8) (2004)
18. L. Tocci, T. Pal, I. Pesmazoglou, B. Franchetti, *Energies*, **10** 413 (2017)
19. D. Wang, X. Ling, H. Peng, L. Liu, L.L. Tao, *Energy* **50** 1 (2013)
20. T. Kankeyan, W. Anusha, J. Saliya, R. Chathura, *Energy Procedia* **156** (2019)
21. V.O. Guillermo, C.G. Javier, D.F. Jorge, *Resources* **9**, 2; (2020)
22. B. Vanslambrouck, I. Vankeirsbilck, S. Gusev, M. De Paepe, *2nd European Conference on Polygeneration*, Tarragona, Spain (2011)
23. S. Jian, L. Ping, T. Jaime, M.N. Christos, *Front. Energy Res.* **8**:6. (2020)
24. R. Turton, R.C. Bailie, W.B. Whiting, J.A. Shaeiwitz, *Analysis, Synthesis and Design of Chemical Processes* (Pearson Education, London 2008).
25. S. Taehong, C.K. Kyung, *Energy Procedia* **129** (2017)



# MATHEMATICAL MODELS OF THE ENERGY CHARACTERISTICS OF A BACKPRESSURE STEAM TURBINE BASED ON A SIMULATION STUDY

*Kaloyan Hristov*<sup>1</sup>\*, and *Ivan Genovski*<sup>1</sup>

<sup>1</sup> Technical University of Sofia, Department of Thermal Power Engineering and Nuclear Power Engineering, 1000, 8 Kl. Ohridski Blvd, Sofia, Bulgaria

**Abstract.** The backpressure steam turbine installations for combined production generate thermal energy and electricity. The produced electricity depends on the heat load determined by consumers. Heat energy is released in the district heating system through water, which is heated with the exhausted steam in boiler-condenser (district heater). The operation regime of the installation is influenced by load of the released district heat and the temperature of the district heat water at the input and output of the boiler-condenser. The variables are heat load of the district heating system and temperature of district heat water at power plant output. The temperature of the district heat water at the boiler-condenser input is an uncontrollable variable, whose value depends on heat consumption. It influences the steam pressure in the boiler-condenser and the available enthalpy drop of the cogeneration installation. In this report, a verified simulation model is applied on a backpressure steam turbine installation, type SST-300 CE2L/V36S. A multivariate simulation is carried out, studying the performance of the installation in off-design regimes. The results obtained are used for the creation of regression models of the installation's energy characteristics. They reveal the dependence between the energy characteristics of the cogeneration steam turbine by the released heat load in the district heating system and the temperature of incoming and outgoing district heat water. The accuracy of the developed models is evaluated through multiple correlation coefficients. The mathematical models could be successfully used to optimize the operating regime of the backpressure steam turbine installation.

## 1 Introduction

The district heating systems provide the heat load to the domestic and industrial consumers connected to it. The heat load depends mainly on climatic factors, of which the air temperature is decisive [1]. Combined heat and power generation is an efficient method of

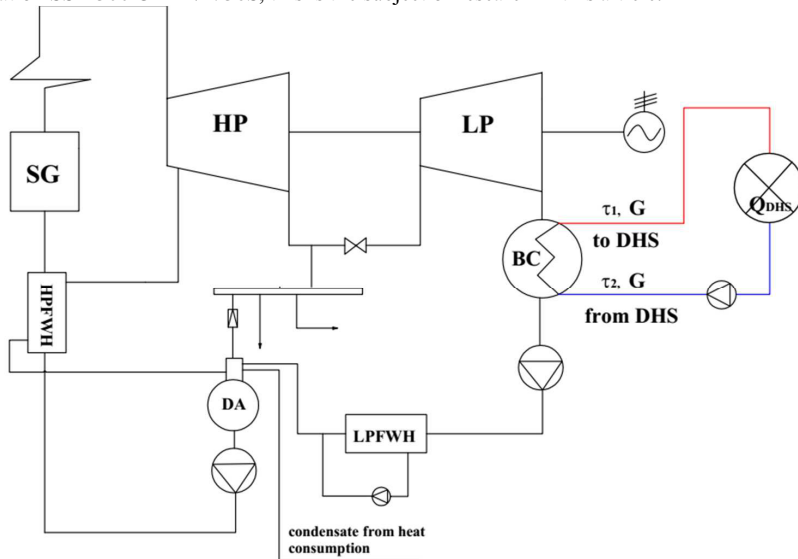
---

\* Corresponding author: [kokhris@gmail.com](mailto:kokhris@gmail.com)

using primary energy resources. This method achieves fuel savings compared to the method of separate heat and power generation.

The most widely used cogeneration technology is based on the Rankine cycle, on which steam turbines operate [2].

On the figure 1 present the technological scheme of the backpressure steam turbine installation SST-300 CE2L / V36S, this is the subject of research in this article.



**Fig. 1.** Technological scheme of backpressure steam turbine type SST-300 CE2L/V36S.

The electricity generated by the backpressure steam turbine installations depends on the size of the released heat load ( $Q_{DHS}$ ) [3], as the district water is heated with the exhaust steam, which enters after the last turbine stage in the boiler-condenser. The production of electricity in this type of turbine is also influenced by the flow of district water ( $G$ ) and the temperatures of district water inlet ( $\tau_2$ ) and outlet ( $\tau_1$ ) of the boiler-condenser. The outlet temperature after boiler-condenser depends of temperature of the district water and the magnitude of its heating ( $\Delta\tau$ ).

During operating installation for cogeneration, it is necessary to forecast the production of electrical power and fuel consumption at a certain heat load supplied to consumers in district heating systems. Present study aims to develop mathematical models for forecasting electricity power and the amount of fuel for operating the cogeneration installation.

## 2 Mathematical modeling

Mathematical modeling requires the compilation of a mathematical model that describes the properties of a real object, called plant in control theory. Usually, the mathematical model does not cover all the components and interdependencies of the plant, but only those that are most important and significant. One of the main advantages of mathematical models is that the plant can be forecasted or operated without laboratory experiments or additional tests.

The main objects of modeling are multifactorial objects, which are characterized by a set of independent or mutually influencing factors (control parameters) [4, 5].

The creation of mathematical models can be realized on the basis of experimental data from the measurement of the inlet and outlet parameters of the plant. To collect this information requires expensive equipment, human resources and technological time to prepare and perform the experiment, as well as time to process the collected data.

Experimental data collection is essentially of two types: active and passive. In the passive experimental data collection, the performer of the experiment does not have an impact on the studied object, but only registers the value of the factors changing in the process of the experiment and the magnitudes characterizing its operation. The active data collection is realized through purposeful actions on specific parameters of the plant in order to study their influence on the parameters characterizing its operation. The creation of mathematical model based on an active data collected from experiment gives a more complete description of the influence of factors on the work of the plant. It is important when performing an active data collection not to consider technological regimes that would lead to an increase in technological losses, accident or destruction of the plant.

The modern approach to the study of objects is the simulation modeling. It develops a computer model of the object by specialized software, which introduces the analytical dependences of the chemical and physical processes which govern the operation of the plant. In order to use the data from the simulation model, it is necessary for it to reflect with sufficient accuracy the considered real object, which presupposes its validation or verification. The main advantage of the simulation modeling is that its application does not violate the mode of operation of the object, and the results obtained after analysis can be used to improve its operation.

Mathematical models are most often described by polynomials, which can be linear or higher degrees. The higher degree of the polynomial makes it possible to achieve a higher accuracy of the study. On the other hand, the higher degree complicates the computational procedures in the development and use of the model. In most cases, the coefficients in the mathematical model after the quadric degrees do not have a significant impact on the final result, therefore the models up to the quadric degree are most often used.

The mathematical model used is a quadric polynomial and has the form [5]:

$$\hat{y}(X_1, X_2, X_3) = a_0 + a_1 X_1 + a_2 X_2 + a_3 X_3 + a_{11} X_1^2 + a_{22} X_2^2 + a_{33} X_3^2 + a_4 X_1 X_2 X_3 \quad (1)$$

where:

$\hat{y}$  – forecasted variable of the mathematical model;

$X_1, X_2$  and  $X_3$  - control parameters of the mathematical model;

$a_0, a_1, a_2, a_3, a_{11}, a_{22}, a_{33}, a_4$  - correlation coefficients of the mathematical model.

The accuracy of the mathematical model is determined by the multiple correlation coefficient  $R$  [4]. It is defined by the following expression:

$$R = \sqrt{1 - \frac{\sum_{i=1}^N (y_i - \hat{y}_i)^2}{\sum_{i=1}^N (\hat{y}_i - \bar{y}_i)^2 + \sum_{i=1}^N (y_i - \hat{y}_i)^2}} \quad (2)$$

where:

$N$  - number of experiments performed (obtained by measurement or simulation modeling);

$y_i$  – value of the magnitude obtained as a result of the experiment;

$\bar{y}_i$  - arithmetic mean result of the value obtained in the performed experiments.

To use the mathematical model to determine the output variables as a function of the control parameters it is necessary to determine if the coefficient of multiple correlation is significant. This estimation is performed by Fisher's criterion [5,6], as the condition for significance of the multiple correlation coefficient is:

$$F^* > F(\alpha, v_1, v_2)$$

where:

$F^*$  – variance ratio;

$F$  – critical value by Fisher's distribution;

$\alpha$  – probability associated with the Fisher's cumulative distribution;

$v_1$  – numerator degrees of freedom;

$v_2$  – denominator degrees of freedom.

### 3 Mathematical models for determination energy characteristics of cogeneration steam turbines installation

The main energy characteristics of a cogeneration installation are the electrical power and the fuel consumption for its operation. Statistically regressive mathematical models are assumed for their mathematics. For their compilation, data from multivariate calculation by the simulation software GateCycle of the developed and validated simulation model [7] of the steam turbine installation SST-300 CE2L/V36S.

The electric power ( $P$ , MW) of the steam turbine is calculated according to the following equation:

$$P = D \cdot H_i \cdot \eta_{TG} \quad (3)$$

where:

$D$  – the steam mass flow rate through steam turbine, kg/s

$H_i$  – enthalpy drop processed by the steam turbine, kJ/kg;

$\eta_{TG}$  – overall efficiency on the turbo-generator unit, including the mechanical efficiency of the steam turbine and the electrical efficiency of the generator %.

The fuel consumption during the operation of the cogeneration installation is determined by:

$$F = P \frac{3600}{LCV \cdot \eta_{el}^{chp}} + Q_{DHS} \frac{3600}{LCV \cdot \eta_Q^{chp}} \quad (4)$$

where:

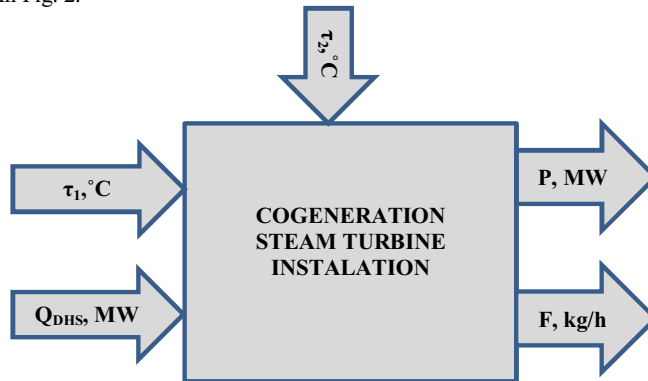
$LCV$  – low caloric value, kJ/kg;

$\eta_{el}^{chp}$  – efficiency of electricity production of the cogeneration unit, %;

$\eta_Q^{chp}$  – efficiency of heat production of the cogeneration unit, %.

The mathematical models for determining the electrical power of the cogeneration installation ( $P$ , MW) and its fuel consumption ( $F$ , kg/h) are to be determined in the present research. For the models the following control parameters are identified: the temperature of the district water at the outlet of the boiler-condenser -  $\tau_1$ , °C, the temperature of the district water returned from the district heating system for heating in the boiler-condenser  $\tau_2$ , °C

and the released heat load in the district heating system  $Q_{DHS}$ , MW. These magnitudes correspond to the control parameters of the mathematical model  $X_1$ ,  $X_2$ ,  $X_3$ . The schematic diagram of the installation for cogeneration as an object for modeling is shown in Fig. 2.



**Fig. 2** Visualization of the cogeneration steam turbine installation as an object for mathematical modeling.

The left part of fig. 2 shows the factors that are controllable for the cogeneration unit. These factors are the district water temperature at the outlet of the installation and the output heat load. At the top of the figure is the factor on which the object of study cannot have a regulatory effect. This factor is the inlet district water temperature; its value depends on the operation mode of the district heating systems. The right part of the figure shows the forecasted variables from the mathematical model - the electric power and the fuel consumption for the installation.

The multivariate calculations for obtaining the data necessary for compiling the mathematical model is performed in accordance with the modes and parameters set in the technical documentation of the steam turbine. The main technical limitations under which the calculations were performed are the following:

- Maximum district water flow through the boiler-condenser - 650 kg/s;
- Heating of the district water in the boiler-condenser ( $\Delta\tau$ ) does not exceed 50 °C;
- Steam pressure in the condenser does not exceed 0.25MPa.

The simulation calculation is performed for heat output from the boiler-condenser in the range from 60 to 90 MW, through the adjustable steam extraction no heat is released to external users. The temperature of the district water ( $\tau_2$ ), which flows into the boiler-condenser, varies from 50 to 60 °C. The change of these values is in accordance with the technical documentation of the turbine. The simulation model used a fuel with a lower caloric value - 29330 kJ / kg.

In the simulation study, the values are changed in the following steps: the district water temperature at the outlet of the cogeneration unit ( $\tau_1$ ) by 2 °C, the water temperature at the installation inlet ( $\tau_2$ ) by 5 °C and the output heat by 10 MW.

Under these conditions, 65 simulation studies for its operation were performed with the simulation model of the steam turbine installation.

The data for the simulation study, necessary to create the mathematical model for determining the electric power of the cogeneration steam turbine installation and the fuel consumption, are presented in Table 1.

**Table 1.** Data necessary to develop mathematical models for determining the electrical power and fuel consumption of cogeneration steam turbine installation

Number of experiments	$\tau_1$	$\tau_2$	$Q_{DHS}$	P	F
	°C	°C	MW	MW	kg/h
1	110	60	90	32.7	17706
2	108	60	90	33.2	17770
.....					
65	96	50	60	21.8	11775

The correlation coefficients of the mathematical model for determining the electric power of the steam turbine are determined after statistical processing of the data obtained from the multivariate calculations. The values of these coefficients are show in Table 2.

**Table 2.** Correlation coefficients for determining the electrical power of the cogeneration steam turbine installation

$a_0$	$a_1$	$a_2$	$a_3$
-18.41	$-40.39 \cdot 10^{-2}$	$55.61 \cdot 10^{-2}$	$89.16 \cdot 10^{-2}$
$a_{11}$	$a_{22}$	$a_{33}$	$a_4$
$21.68 \cdot 10^{-4}$	$-18.03 \cdot 10^{-4}$	$-86.89 \cdot 10^{-5}$	$-51.36 \cdot 10^{-5}$

The mathematical model for determining the electrical power on the cogeneration steam turbine acquires the following form:

$$P(\tau_1, \tau_2, Q_{DHS}) = -18.41 - 40.39 \cdot 10^{-2} \tau_1 + 55.61 \cdot 10^{-2} \tau_2 + 89.16 \cdot 10^{-2} Q_{DHS} + 21.68 \cdot 10^{-4} \tau_1^2 - 18.03 \cdot 10^{-4} \tau_2^2 - 86.89 \cdot 10^{-5} Q_{DHS}^2 - 51.36 \cdot 10^{-5} \tau_1 \tau_2 Q_{DHS} \quad (5)$$

In a similar way were obtained the correlation coefficients of the mathematical model for determining the fuel consumption of the cogeneration installation. Their values are presented in Table 3.

**Table 3.** Coefficients of the mathematical model for determining the fuel consumption for the cogeneration unit.

$a_0$	$a_1$	$a_2$	$a_3$
6846.49	-144.07	32.66	175.60
$a_{11}$	$a_{22}$	$a_{33}$	$a_4$
$70.00 \cdot 10^{-2}$	$98.91 \cdot 10^{-3}$	$47.89 \cdot 10^{-2}$	$-63.06 \cdot 10^{-4}$

The mathematical model for determining the fuel consumption of the cogeneration steam turbine acquires the following form:

$$F(\tau_1, \tau_2, Q_{DHS}) = 6846.49 - 144.07 \tau_1 + 32.66 \tau_2 + 175.60 Q_{DHS} + 70.00 \cdot 10^{-2} \tau_1^2 + 98.91 \cdot 10^{-3} \tau_2^2 + 47.89 \cdot 10^{-2} Q_{DHS}^2 - 63.06 \cdot 10^{-4} \tau_1 \tau_2 Q_{DHS} \quad (6)$$

The coefficient of multiple correlation for the mathematical model for determining the electrical power of the cogeneration steam turbine is  $R = 0.988$ , and the value of this coefficient for the mathematical model for obtaining the fuel consumption is  $R = 0.993$ .

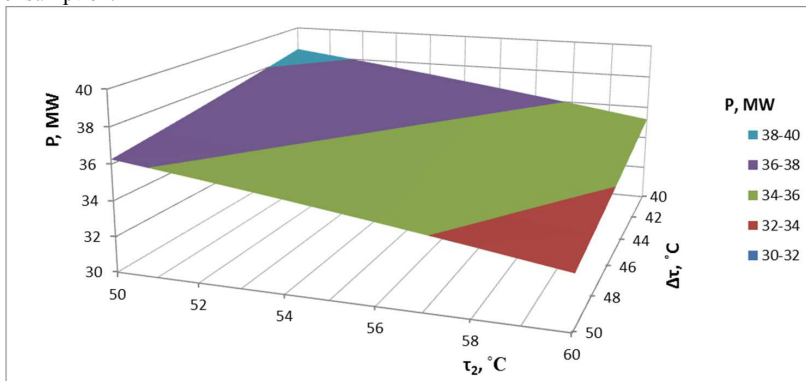
The value of the variance ratio  $F^*$  for the two mathematical models is higher than the critical value by Fisher's distribution  $F(\alpha, v_1, v_2)$ , therefore the obtained coefficients of multiple correlation are significant. The results in solving the models can be used for analysis and control of the cogeneration steam turbine installation.

#### 4 Solving the mathematical models of the steam turbine installation SST-300 CE2L/V36S.

The mathematical models are solved and the results are presented graphically depending on the heat load of the district heating system, the change in the temperature of the return district water and the magnitude of its heating in the boiler-condenser.

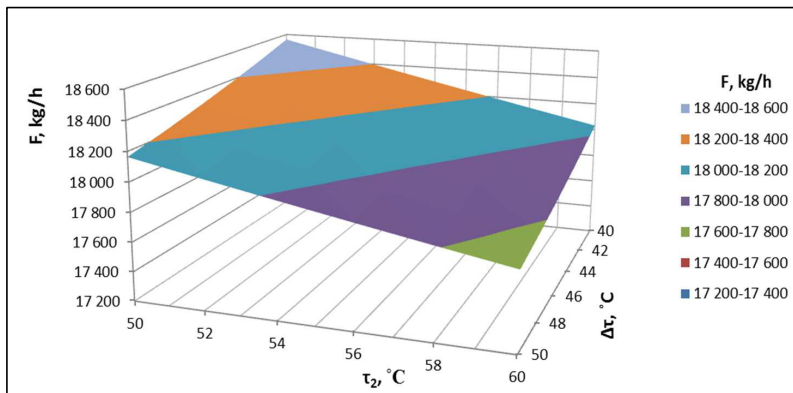
On figure 3 are shown the results of solving the mathematical model for determining the electrical power of the cogeneration steam turbine at the maximum heat load of the boiler-condenser of 90 MW.

The obtained results show that with a decrease in the temperature of the district water at the inlet of the installation and a decrease in its heating (respectively a decrease in the temperature of the district water outlet from the installation) the electric power increases. Low values of these parameters increase the available processed enthalpy drop from the steam turbine installation, which increases the electrical output obtained on the basis of heat consumption.



**Fig. 3.** Change of the electric power of the installation for cogeneration depending on the temperature of the inlet district water and the magnitude of its heating in the boiler-condenser when releasing 90 MW of heat load in the heat supply system.

The mathematical model predictions of the fuel consumption during operation of the cogeneration installation are shown in figure 4.



**Fig. 4** Change of the fuel consumption of the installation for cogeneration depending on the temperature of the inlet district water and the magnitude of its heating in the boiler-condenser when releasing 90 MW of heat load in the heat supply system

From the graphically presented results it is observed that at the same heat load of the boiler-condenser, the fuel consumption increases with lowering the temperature of the return district water and its heating. The increase in consumption is due to the increase in electricity produced based on heat consumption. These operation modes are associated with an increase of the district water flow through the boiler-condenser, and in them the installation realizes higher energy efficiency [7, 8].

The change in the electrical power and fuel consumption of the installation at other thermal loads of the boiler-condenser is subject to the same trend line as for the operation mode of maximum heat load.

## 5 Conclusion

The mathematical models for determining the electric power and fuel consumption of a backpressure steam turbine installation are developed in this study. The control parameters in the models are the magnitude of the released heat load and the district water temperatures at the inlet and outlet of the boiler-condenser.

The mathematical models were obtained by processing data from a validated simulation model of a steam turbine plant SST-300 CE2L/V36S.

The significance of mathematical models is assessed by multiple correlation coefficients according to Fisher's criterion. This allows mathematical models to be used to study the installation for cogeneration.

The results of the mathematical study show that as the temperature of the district water at the outlet of the boiler-condenser decreases, the electricity power of the steam turbine increases. This is realized by increasing the flow of district water through the boiler-condenser. The maximum flow rate depends on the throughput of the boiler-condenser.

An increase in the electrical power, while maintaining the heat load and district water temperature at the outlet of the installation, is observed at low temperatures of the district water returned from the districting heating system due to an increase in the processed available enthalpy drop for the steam turbine. The decrease of this temperature depends on the operation mode of the district heating system.



## References

1. Advanced District Heating and Cooling (DHC) Systems, Woodhead Publishing, (2016)
2. K. Sartor, S.Quoilin P.Dewallef, Simulation and optimization of a CHP biomass plant and district heating network, AE, 130, 474-483 (2013)
3. R. Smith, Steam turbine cycles and cycle design optimization: Combined cycle power plants, ASTMPP, 57-92, (2017)
4. B. N. Stankov, M. P. Vassilev, Proceedings of the XXII Scientific Conference with International Participation FPEPM 2017 (in Bulgarian), 1, pp. 134–141, (2017).
5. G. Uyanika and N. Güler, A Study on Multiple Linear Regression Analysis, *Procedia - Social and Behavioral Sciences*, **106**, 234-240, (2013)
6. D. Montgomery, E. Peck, and G. Vining, *Introduction to Linear Regression Analysis*, 5th ed, A John Wiley & Sons, inc., publication, (2012)
7. I. Genovski, and K. Hristov,. Model research of the energy efficiency of a cogeneration backpressure steam turbine installation, E3S Web Conf. **207**, 02004, <https://doi.org/10.1051/e3sconf/202020702004>, (2020)
8. I. Genovski, K. Hristov, “Optimal heat load distribution between cogeneration steam turbine installations in combined heat and power (CHP) plant”, *JMTI*, **1**, 30-46, (2014)

# Comparative technical and economic analysis of innovative methods for waste heat recovery from flue gases for boiler type BKZ 220-100

Hristo Beloev<sup>1</sup>, Iliya Iliev<sup>1\*</sup>, Angel Terziev<sup>2</sup>, Andrey Kibarin<sup>3</sup>, and Madina Aliyarova<sup>3</sup>

<sup>1</sup>University of Ruse, Bulgaria

<sup>2</sup> Technical University of Sofia, Bulgaria

<sup>3</sup>Non-commercial "Almaty University of Power Engineering and Communication" JSC, Almaty, Republic of Kazakhstan

**Abstract.** Two alternative schemes for waste heat recovery from flue gases of boiler type BKZ 220-100 in the Stepnogorsk TPP (Kazakhstan) are presented. The technical solutions are innovative because they create conditions for deep heat recovery even when using battery emulsifiers to purify the gas flow. A characteristic feature of the schemes is the purification of a small part (10-15%) of the stream by means of a bag filter and the mixing of the stream with the main gas flow consisting of moist gases after a battery emulsifier. An analysis and assessment of the technical and economic feasibility of the implementation of the two alternatives has been carried out.

## 1 Introduction

Waste heat recovery from flue gases of industrial and steam boilers is always a topical issue for industry and energy [10,14]. Each decrease in the flue gas temperature increases the rate of fuel use, reduces heat losses with the exhaust gases  $q_2$  and directly affects the efficiency of the boilers [3,5,9,10, 19]. In addition to the direct benefits of fuel economy through heat recovery both the amount of harmful components and CO<sub>2</sub> emissions are reduced.

However, it should be noted that despite the undeniable advantages of waste heat recovery methods, there are sometimes insurmountable obstacles to the implementation of such projects. For example, the sulphur content of the fuel is essential [4] to the process – it determines the permissible limit temperature to which the gases can be cooled without causing condensation and low-temperature corrosion on the heating surfaces of the disposal facilities [3]. Sometimes there are energy schemes where it is difficult at first glance to assess the technical and economic feasibility of implementing a waste heat recovery system, especially when more than one technical solution is offered [5].

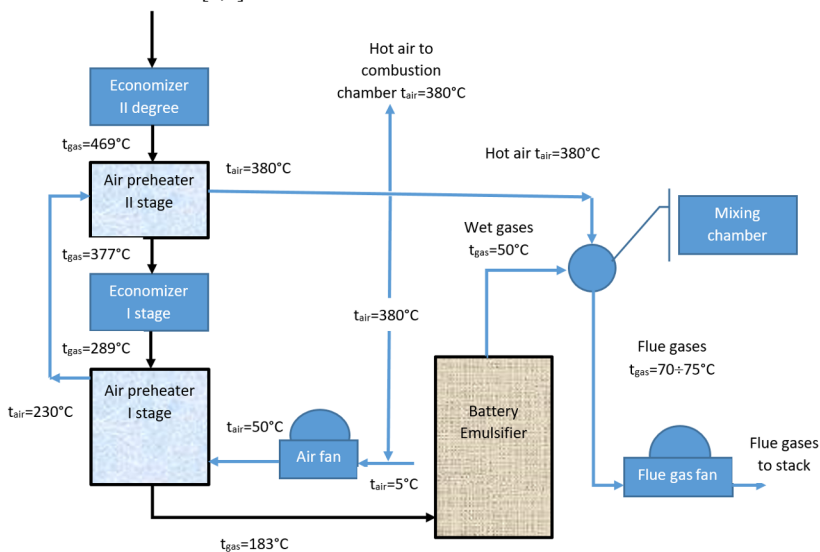
In the present work, a technical and economic analysis of two proposals for the utilization of waste heat from the exhaust gases of the steam generator BKZ 220-100F [7] in Stepnogorskaya TPP – Kazakhstan [4] is carried out.

---

\* Corresponding author: [iki@uni-ruse.bg](mailto:iki@uni-ruse.bg)

## 2 Problem description

At the Stepnogorskaya CHP, three steam generators of the BKZ 220-100F type are in operation. No. 5, 6 and 7), burning Ekibastuz coal [4, 7]. The average temperature of flue gases for the boiler No. 5 under consideration is very high, 183 °C, which leads to significant heat losses with the flue gases of up to 9 ÷ 9.5%. The average efficiency of boiler No. 5 does not exceed 84%, which gives grounds to look for opportunities to reduce the temperature of flue gases and thus increase boiler efficiency. It is also important to note that the existing emulsifier second generation [8] cleans the flue gases to a satisfactory degree and there is no reason at this stage to recommend a transition to another ash collection system. A significant disadvantage of wet ash collectors is their high-energy consumption for the circulation of flushing water. Due to the fact that humid gases after emulsifiers have a high relative humidity (in practice, 100%) heating of these is required before entering the pipe to prevent secondary condensation and subsequent sulfuric corrosion in the stack [3,6].



**Fig. 1.** Schematic diagram of the gas path after the steam generator with a battery emulsifier

A disadvantage of the presented scheme is the non-utilisation of the heat of the exhaust gases. With a high temperature of 183 °C, the gases after passing through an air preheater second stage enter a battery emulsifier which purifies the solid particles they contain. Thus, the potential from 183 to 125 °C is lost due to the wet method of gas purification used. Moreover, given that the gases purified in the emulsifier are wet (in practice their relative humidity is 100%), they should be heated additionally from 50 to 75 °C before entering the stack by mixing the flow of wet gases with part of the hot air after the air preheater 1 stage (air temperature is 380 °C). The diagram shows that the incoming air from the atmosphere is not heated by a steam heater, but this is done by mixing the outside air with part of the heated air after an air heater of the 1st stage (air temperature is 380 °C).

The preliminary assessment shows a high degree of heat loss, both with the heating air after the air heater 1st stage and with the unused potential of the flue gases before they enter the emulsifier.

### 3 The essence of the innovative method for waste heat recovery

There are two schemes for waste heat recovery from the exhaust gases, which create conditions for the elimination of the heating of the exhaust gases after the battery emulsifier [1], without using preheated air from a second stage air heater. These schemes will be analysed in detail to assess their technical and economic feasibility.

#### 3.1. Description of the proposed method for heat waste recovery (variant 1)

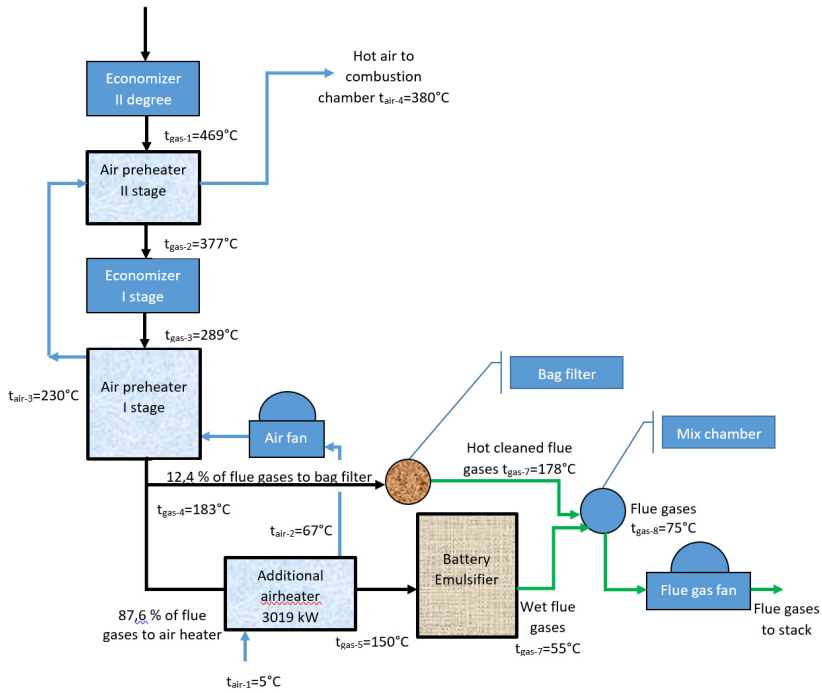
The proposed method to improve energy efficiency provides for a more complete use of thermal energy of flue gases and the elimination of the need for additional heating in front of the stack. This can be achieved by directing a portion of the gas stream (11.5%) into a bag filter, keeping the same temperature, and then mixing this portion with the main stream (88.5% from the flue gas flow) in the existing mixing chamber to achieve the desired overall temperature.

The main flow of flue gases (88.5%) after the air heater at stage 1 enters an additional air heater-utilizer, with a heat output of 3019 kW. In it the temperature of the flue gases is reduced from 183 to 150 °C, while the captured heat is used to heat the outside air from 5 to 67 °C, which should enter the stage 1 air heater. The produced heat power is able to completely eliminate the old inefficient scheme of heating the air before the air heater. However, it should be noted that the additional air heater-utilizer should be made of thermosyphons to ensure a corrosion-free regime of its heating surfaces in the winter season [6]. After the air heater-utilizer the gases enter the existing battery emulsifier for wet purification of the gases. At the outlet of the emulsifier, the temperature of the gases is reduced to 55 °C at high relative humidity (100%). Therefore, before entering the stack, the gases are mixed in a mixing chamber, with the hot stream of purified gases coming from the bag filter. The temperature of the mixture (75 °C) is normatively determined by the condition to avoid secondary condensation of the gases in the stack.

The aerodynamic resistance of the bag filter, which will be connected in parallel with the emulsifier, does not differ from the resistance of the battery emulsifier, which will allow for the use of the existing exhauster without any changes.

Thus, several positive effects are simultaneously achieved:

- Energy consumption for heating flue gases with hot air is eliminated;
- Part of the heat energy of flue gases is recovered;
- Significant cleaning of gases from ash is carried out;
- Emulsifiers are unloaded, the volume of flush water directed to the ash dump is reduced, which reduces the load on the emulsifier and flush water pumps and theoretically makes it possible to reduce their power consumption (for example, by installing a frequency control when it is economically justified by the current prices and tariffs);
- If there is market demand and economically viable transportation opportunities, baghouse ash can be sold for use in construction, agriculture or other industries.



**Fig. 2.** Diagram of the gas path after installation of an additional air heater before battery emulsifier, including bag filter.

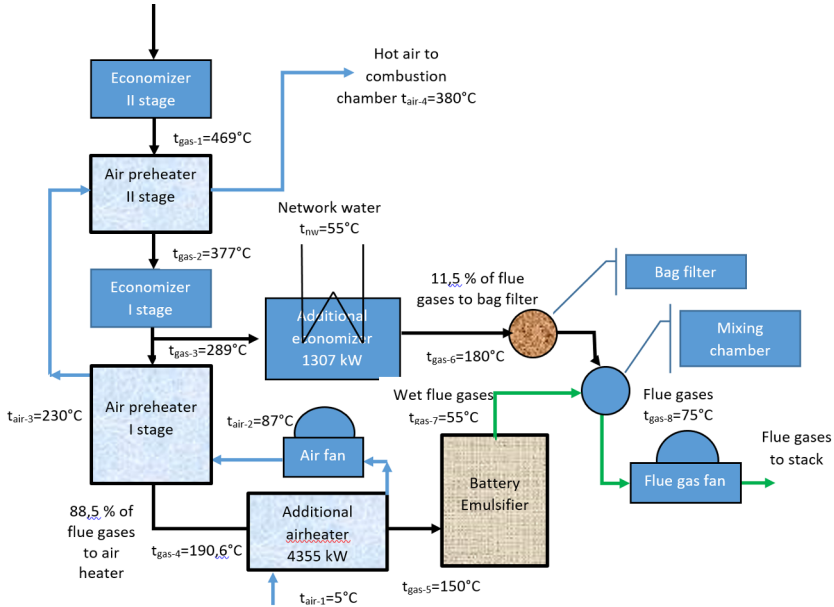
### 3.2. Description of the proposed method for heat waste recovery (variant 2)

The second option uses two energy-saving units: a water economizer and an additional air heater.

Some of the hot gases (11.5%) after the 1st stage economizer at a temperature of  $289^{\circ}\text{C}$  are fed to an additional economizer with a heat output of 1307 kW, in which the gases are cooled down to about  $180^{\circ}\text{C}$  and then enter a bag filter for gas purification. The economizer is supplied with network water with an initial temperature of  $55^{\circ}\text{C}$  and a flow rate of  $35\text{ m}^3/\text{h}$  and is heated to  $87^{\circ}\text{C}$  and is again fed to the district heating network. In order to comply with the permissible operating temperatures ( $t < 200^{\circ}\text{C}$ ) of the gases before they enter the bag filter, the water flow in the economizer acts as a regulating factor in the various operating modes. The purified gases after the bag filter at a temperature of  $178^{\circ}\text{C}$  enter a mixing chamber, where they are mixed and cooled to  $55^{\circ}\text{C}$  gases after the battery emulsifier. The mixing temperature should be in the range of  $72\text{--}75^{\circ}\text{C}$  to avoid secondary condensation in the chimney.

Due to the reduction of the gas flow (up to 88.5%) before the air heater 1st stage, the velocity of the gases in the tubular heat exchanger decreases and as a consequence the gas temperature increases from  $183$  to  $190.5^{\circ}\text{C}$ . Under these conditions, the main gas flow will enter an additional thermosyphon-type air heater with a heat output of 4355 kW, where the gases will be cooled down to  $150^{\circ}\text{C}$  before entering the battery emulsifier for purification. In this case, the air heater will heat the outside air from  $5$  to  $87^{\circ}\text{C}$  and will replace the

existing inefficient method for heating the outside air with hot air after a second stage air heater.



In Fig. 3 is a diagram illustrating the operation of the method for utilization of waste heat from gases.

**Fig. 3.** Diagram of the gas path after installation of economizer and a bag filter and additional air heater before battery emulsifier

#### 4. Analysis of results

Numerical calculations have been performed with specialized software for calculation of energy steam generators in accordance with the widely used Normative method for calculation of boilers [18].

Table 1 presents data on the technical parameters for baseline, variant 1 and variant 2 of waste heat recovery.

**Table 1.** General technical parameters

Parameter/TPP	BKZ-220-100F baseline	BKZ-220-100F First variant	BKZ-220-100F Second variant
Average steam production, $D_{av}$ , t/h (or water flow)	210	210	210
Average flue gas outlet temperature after economizer second stage, $t_{fg}^{eco}$ , °C	289	289	289
Average flue gas inlet temperature after air heater first stage $t_{fg}^{AH}$ , °C	183	183	190.6

Temperature of heated network water:			
Inlet, $t_w'$ , °C	-	-	55
Outlet, $t_w''$ , °C			87.1
Network water flow, $\dot{m}$ m <sup>3</sup> /h	-	-	35.0
Estimated heating capacity of the additional economizer, $Q$ , kW			1 307
Recovered heat of gases in additional economizer, $Q_r$ , MWh/yr.	-	-	6 928
Recovered heat of gases in additional airheater, $Q_r$ , MWh/yr.	-	16 004	23 090
Heat loss with flue gases after units implementation, $q_2''$ , %	10.38	8.44	7.02
Flue gas temperature after Heat recovery and emulsifier, $t_{em}$ , °C	55	55	55
Standard temperature of gases before entering the stack, $t_{st}$ , °C	72-75	72-75	72-75
Required heat output for heating gases after the emulsifier, $Q_{em}$ , kW	9 998	9 998	9 998
Flue gas flow via bag filter, m <sup>3</sup> /h	-	52 903	53 943
Flue gas flow via additional economizer, nm <sup>3</sup> /h	-	-	32 120
Flue gas flow via additional airheater, nm <sup>3</sup> /h	-	226 788	248 248
Boiler operation time, hours/year	5 302	5 302	5 302

The technical parameters are determined under real conditions, as the values are accepted as average for all boilers in 2020.

Full thermal calculations of the waste heat recovery units [11,12] (air preheater in combination with a bag filter and economizer) have been made, and the production, installation and commissioning costs have been estimated at European prices. The data from the calculations are presented in Table 2. The ecological payments that can be avoided as a result of the realised savings from coal are also estimated.

**Table 2.** Investments and fuel savings for different variants.

Parameters	Variant 1	Variant 2
Investment for the additional economizer, EUR	-	53 474
Investment for the back filter, EUR	61281	61281
Investment for the additional airheater, EUR	191250	255000

Total investment, EUR	252 531	369 755
Annual coal saving, t/year	6 981	10 662
Annual water savings, m <sup>3</sup> /year	37 361	37 467
Price of coal, EUR/t	7.35	7.35
Price of technical water, EUR/m <sup>3</sup>	0.134	0.134
Total savings, EUR/year	56 330	83 409
Savings due to harmful emissions reduction (based on the emission charge), EUR/year	5 092	7 776
Total cost savings and revenue, EUR/year	61 421	91 185
Specific savings, EUR/MWh	9.71	9.04

#### 4.1. Comparative analysis of economizers for different schemes of waste heat recovery

The benchmarks for selection between both variants include [16]:

- Fuel savings;
- Payback period;
- Net present value;
- Internal Rate of Return;
- Specific savings;

One of the most important criteria for assessing the feasibility of an investment related to energy efficiency is the minimum investment per unit of energy saved (EUR / MWh) min. This criterion is characterized by a high degree of objectivity, especially in countries where the price of fuels is many times lower than those on the global market. According to the data in Table 1, it can be seen that Option 1 is superior in this criterion.

The analysis shows that the most economically viable is variant 1 in which the investment for 1 MWh of saved energy is 9.71 EUR. This assessment is complex and includes a complex dependence on several criteria: fuel price, operating time of the steam generator, exhaust gas temperature, average boiler load, etc.

#### 4.2. Financial analysis

The results from the performed technical economic analysis are used to prioritize the two options proposed in Table 3.

**Table 3.** Estimated investments, savings, IRR, NPV, NPVQ and payback period

Variant of waste heat recovery method	Investment, EUR	Savings, EUR	IRR, %	NPV, EUR	NPVQ	PB, years
Variant 1 (see Fig.2)	252 531	61 421	20.6	274 089	1.09	4.11
Variant 2 (See fig.3)	369 755	91 185	21.0	412 060	1.11	4.05

This set of energy efficiency measures represents a CAPEX module, which can be used successfully by the company's management in making investment decisions [13,15,16].



In Table 2 the proposed measures (options) are prioritized based on their Internal Rate of Return (IRR) share. The following parameters are compared in the table:

- Annual net savings for the entire operational life of the project;
- Evaluation of the investment required for project implementation;
- Internal Rate of Return (IRR);
- Net Present Value (NPV);
- Net Present Value coefficient (NPVQ);
- Payback period.

The economic life has been set at 10 years for both options;

Real interest rate - set at 10% based on the conditions of bank financing in Kazakhstan; the inflation coefficient for 2020 according to data from the State Statistics Service of Kazakhstan is 6.9% [14];

The calculations have been obtained using the 'ENSI economy' v6 software product, with the results presented in Table 3.

The proposed prioritization scheme is strictly informative offering decision-makers a possibility to compare and select the most attractive option.

### 4.3. Environmental and other project benefits/impacts

The main environmental effect of installing waste heat recovery units (economizer with back filter and airheater) are the reduced CO<sub>2</sub> and NO<sub>x</sub> emissions [17]. The different options with included economizer, air heater and back filter are estimated to reduce coal consumption by 6981 to 10662 tons/year, CO<sub>2</sub> emissions from 10113 to 15445 t CO<sub>2</sub>/year and NO<sub>x</sub> emissions from 44.9 to 68.5 t NO<sub>x</sub>/year, depending on the selected technology and equipment.

The project's environmental impacts for three investment options are summarized in Table 4.

**Table 4.** Environmental impacts

Option	Units	Variant 1	Variant 2
Coal savings	t/year	6 981	10 662
Emission factor for coal	tCO <sub>2</sub> /t coal	1.4486	1.4486
Decrease of CO <sub>2</sub> from saved coal	tCO <sub>2</sub> /year	10 113	15 445
Decrease of SO <sub>2</sub> from saved coal	tSO <sub>2</sub> /year	43.8	66.9
Decrease of NO <sub>x</sub> from saved coal	tNO <sub>x</sub> /year	44.9	68.5

## 5 Conclusion

1. The proposed innovative waste heat recovery methods, comprising a combination of an additional air preheater and a bag filter or alternatively an additional economizer, air heater and a bag filter, is a topical option for steam generators and boilers using "wet methods" for flue gas purification (scrubbers, emulsifiers of the first and the second generation). Both options presented create excellent conditions for deep utilization of waste heat from the flue gases.
2. The conducted technical and economic analysis shows the expediency of the implementation of both options. There is a slight advantage of the second option in terms of simple payback period, NPV and NPVQ, but the difference is insignificant.

3. The realisation of the waste heat recovery units has high environmental impact and is estimated to reduce coal use from 6981 to 10662 tons/year, CO<sub>2</sub> emissions from 10113 to 15445 t CO<sub>2</sub>/year and NO<sub>x</sub> emissions from 44.9 to 68.5 t NO<sub>x</sub>/year, depending on the selected boilers.
4. The conclusions drawn can be used by experts in the field when making an investment decision regarding the introduction of the relevant technologies in TPP and CHP.

## References

1. N. Zlatov, S. Glazyrin, M. Zhumagulov, Z. Aidymbayeva, Wastewater Treatment of the Thermal Power Plants for Desulfurization of Flue Gas, *Journal of Engineering Science and Technology Review*, Special Issue 154-157 (2020).
2. I. Iliiev, Means and methods for waste heat recovery from low-grade gas-steam flows, Monograph, University Publishing Center at the University of Ruse, 150 p. (2013) (In Bulgarian)
3. S. Dzhakysybaev, I. Muravyev. Big coal of Ekibastuz. - M.: Nedra, (1990) .- 84 p. - ISBN 5-247-00833-2
4. K. Kostov, Determination of technical and economic indicators of thermal power stations directly from the turbine regime characteristics, *Journal EUREKA: Physics and Engineering*, **4**, (2020) DOI: 10.21303/2461-4262.2020.001358
5. I. Iliiev, K. Uzuneanu, V. Kamburova, V. Voutev, Study of integral characteristics and efficiency of a heat exchanger of thermosiphon type with finned tubes, *Thermal Science*, **5**, 20, (2016)
6. A. Askarova, S. Bolegenova, A. Georgiev, S. Bolegenova, V. Maximov, R. Manatbayev, A. Yergaliyeva, A. Nugymanova, Zh. Baizhuma.: The use of a new "clean" technology for burning low-grade coal in on boilers of Kazakhstan TPPs, *Bulgarian Chemical Communications*, **50**, Special Issue G (pp. 53 - 60) (2018).
7. V. Shtyogolev, Battery Emulsifier Swirler Unit with Replaceable Blade Machines, Patent # RU129017U1, 2013-06-20, (2013)
8. H. Zhang, Y. Dong, Y. Lai, H. Zhang, X. Zhang, Waste heat recovery from coal-fired boiler flue gas: Performance optimization of a new open absorption heat pump, *Applied Thermal Engineering*, **183**, Part 1, (2021), <https://doi.org/10.1016/j.applthermaleng.2020.116111>.
9. J. Liu, X. Gong, W. Zhang, F. Sun. Wang, Q. Experimental Study on a Flue Gas Waste Heat Cascade Recovery System under Variable Working Conditions. *Energies* (2020), **13**, 324. <https://doi.org/10.3390/en13020324>
10. M. Hongqiang, N. Liang, N. Zhang, X. Luo, C. Hou, G. Wang, Simulation of a novel waste heat recovery system with sulfide-containing flue gas, *Applied Thermal Engineering*, **187**, (2021), 116556, ISSN 1359-4311, <https://doi.org/10.1016/j.applthermaleng.2021.116556>.
11. H. Jouhara, N. Khordehgah, S. Almahmoud, B. Delpech, A. Chauhan, S. Tassou, Waste heat recovery technologies and applications, *Thermal Science and Engineering Progress*, **6**, (2018), Pages 268-289, ISSN 2451-9049, <https://doi.org/10.1016/j.tsep.2018.04.017>.
12. A. Ayoub, A. Gaigneux, N. Le Brun, S. Acha, N. Shah, The development of a low-carbon roadmap investment strategy to reach Science Based Targets for commercial

- organisations with multi-site properties, *Building and Environment*, **186**, (2020), <https://doi.org/10.1016/j.buildenv.2020.107311>.
13. Agency for Strategic planning and reforms of the Republic of Kazakhstan Bureau of National statistics, official website <https://stat.gov.kz/>
  14. I. Iliev, A. Terziev, H. Beloev - Condensing economizers for large scale steam boilers, E3S Web of Conferences, **180**, 01004 (2020), <https://doi.org/10.1051/e3sconf/202018001004>
  15. K. Kostov, I. Ivanov, K. Atanasov, Development and analysis of a new approach for simplified determination of the heating and the cooling loads of livestock buildings, EUREKA, Physics and Engineering, 2021, 2021(2), pp. 87–98
  16. V. Popa, I. Ion, C. Popa. (2016). Thermo-Economic Analysis of an Air-to-Water Heat Pump. Energy Procedia. **85**. DOI: 10.1016/j.egypro.2015.12.221
  17. Paraschiv S.L., Paraschiv S., Ion V.I., Vatachi N., Techno-economic Analysis of the Emissions Reduction Technologies in the Thermal Power Plants in Romania, Journal of Environmental Protection and Ecology (JEPE), **14**, No 2 (2013), pp. 770-780. <https://docs.google.com/a/jepejournal.info/viewer?a=v&pid=sites&srcid=amVwZS1qb3VybmFsLmluZm98amVwZS1qb3VybmFsGd4OjZkYzNmZWYzYTFmZWE1OGI>
  18. Thermal calculation of the boiler (Normative method), 1998, St. Petersburg, 259 p.
  19. Zlateva, P., Penkova, N., Krumov, K. (2020) Analysis of combustion efficiency at boilers operating on different fuels, 7th International Conference on Energy Efficiency and Agricultural Engineering - Proceedings, Art. number 9278784, DOI: 10.1109/EEAE49144.2020.9278784

# Moisture transfer in outer walls with layers of different density

*Andrey Rymarov*<sup>1\*</sup>, *Dmitriy Titkov*<sup>1</sup>, and *Aleksey Ananiev*<sup>2</sup>

<sup>1</sup>National Research Moscow State University of Civil Engineering, 129337, Moscow, Yaroslavskoe highway, 26, Russia

<sup>2</sup>Institution Research Institute of Building Physics of the Russian Academy of Architecture and Building Sciences, 127238, Moscow, Lokomotivny driveway, 21, Russia

**Abstract.** The need to protect external walls from excess moisture to improve heat-shielding properties is an urgent task. If the outer wall is created from expanded clay concrete blocks, then the most interesting are the blocks created by layer-by-layer moulding, in which each layer can have its own given density. In such blocks, each layer has its own coefficients of thermal conductivity and vapor permeability, which allows you to select the required heat transfer resistance and vapor permeability of the outer wall for a specific region, taking into account the characteristics of the climate. The ability to have external walls with different material densities inside makes it possible to implement energy saving tasks in the building. The article discusses options for external walls made of expanded clay concrete blocks with layers with different densities and coefficients of thermal conductivity and vapor permeability. Changing the location of layers with different densities inside the blocks changes the local values of the vapor permeability resistance, which leads to a different nature of the movement of water vapor inside the wall in winter. It is good when water vapor does not accumulate in the wall; it does not condense and freely goes into the external environment. A dry wall is more durable, it loses less heat in winter. Changes in partial pressures at full saturation and with existing humidity inside the expanded clay concrete block for layers of different densities in winter are considered to determine the possible condensation from water vapor inside the wall. Layer-by-layer moulding of building materials improves their properties to increase resistance to heat transfer and to form a dry and more durable outer wall.

## 1 Introduction

Cellular concretes, which were well studied earlier, are now used less often due to the growing requirements for the thermal protection of buildings to solve energy-saving problems. New properties of expanded clay concrete blocks appear during layer-by-layer moulding [1], when the layers of the material have different densities and, accordingly, different values of the coefficients of thermal conductivity and vapour permeability. Reducing the flow of moisture through expanded clay concrete blocks with layers of different

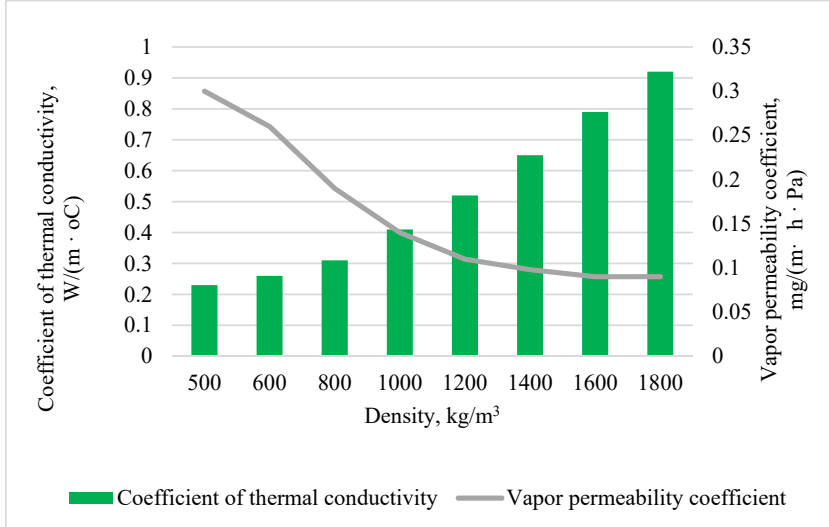
---

\* Corresponding author: [rymarov@list.ru](mailto:rymarov@list.ru)

densities during operation increases the resistance to heat transfer and allows you to save heat energy by reducing heat losses of the building in the winter season. As well as monitoring the resistance to vapour penetration, it will allow the outer wall to be kept in a dry state, which will increase its durability.

## 2 Problem statement

In the cold season, moisture moves from the room through the outer wall to the outside air, so when forming expanded clay concrete blocks in layers, it is useful to have denser layers closer to the inner surface of the wall. This approach will allow the water vapor located in the internal air not to enter the wall, which becomes dry in the winter season and more durable. And also at the same time, the resistance to moisture transfer and heat transfer of the wall increases, which reduces heat losses in the winter time by the premises of the building.



**Fig. 1.** Change in the coefficients of thermal conductivity and vapor permeability depending on the density of expanded clay concrete.

The dependence of the thermal conductivity coefficient and the vapor permeability coefficient of aerated concrete with a material moisture content of about 10% of the density is nonlinear (Fig. 1), which is associated with the presence of solid elements of expanded clay concrete and air between them [2]. Studies of changes in temperature, partial pressures at full saturation and at the existing humidity inside the expanded clay concrete block on expanded clay sand in the outer wall at an outdoor air temperature of  $-8.7\text{ }^{\circ}\text{C}$  and a relative humidity of 83% and an indoor air temperature of  $+20\text{ }^{\circ}\text{C}$  and a relative humidity of 55%. The calculations were carried out for the climatic conditions of the city of Moscow. Moisture transfer through building materials takes about a month, so the estimated outside air temperature is taken as the average for the coldest month, and for the city of Moscow it is January. The number of layers with which the blocks are formed is 7, each layer has a thickness of 0.07 m. If necessary, the thickness of the layers can be formed differently. The total thickness of the block is 0.49 m. The ability of expanded clay concrete to absorb moisture depends on its density [3]. 6 variants of expanded clay concrete blocks with different layering of layers with different material density inside are considered. The first

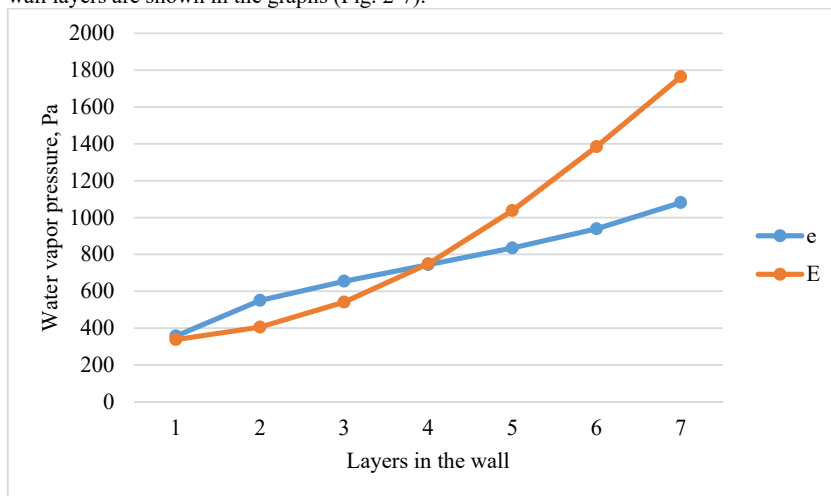
version of the wall consists of seven layers with a density of 1000 kg / m<sup>3</sup>, 600 kg / m<sup>3</sup>, 500 kg / m<sup>3</sup>, 500 kg / m<sup>3</sup>, 600 kg / m<sup>3</sup>, 800 kg / m<sup>3</sup>, 1000 kg / m<sup>3</sup>. The second version of the wall consists of seven layers with a density of 500 kg / m<sup>3</sup>, 500 kg / m<sup>3</sup>, 500 kg / m<sup>3</sup>, 600 kg / m<sup>3</sup>, 800 kg / m<sup>3</sup>, 800 kg / m<sup>3</sup>, 1000 kg / m<sup>3</sup>. The third version of the wall consists of seven layers with a density of 1000 kg / m<sup>3</sup>, 800 kg / m<sup>3</sup>, 600 kg / m<sup>3</sup>, 500 kg / m<sup>3</sup>, 500 kg / m<sup>3</sup>, 500 kg / m<sup>3</sup>, 500 kg / m<sup>3</sup>. The fourth version of the wall consists of seven layers with a density of 500 kg / m<sup>3</sup>, 500 kg / m<sup>3</sup>, 800 kg / m<sup>3</sup>, 1000 kg / m<sup>3</sup>, 800 kg / m<sup>3</sup>, 600 kg / m<sup>3</sup>, 600 kg / m<sup>3</sup>. The fifth version of the wall consists of seven layers with the same density of 1000 kg / m<sup>3</sup>. The sixth version of the wall consists of seven layers with the same density of 500 kg / m<sup>3</sup>.

The data on the coefficients of thermal conductivity and vapor permeability are taken in accordance with the current regulatory document SP 50.13330.2012 "Thermal protection of buildings. Updated edition of regulatory document 23-02-2003". Calculations of the temperature distribution inside the outer wall were carried out according to the method based on one-dimensional stationary thermal conductivity in a homogeneous material of each layer, which is described by the Fourier equation known in engineering practice. Calculations of the partial pressure of water vapor are carried out based on the total resistance to vapor penetration of the outer wall. This resistance consists of the resistance to vapor penetration of all layers of the outer wall and the resistance to moisture exchange on its surfaces.

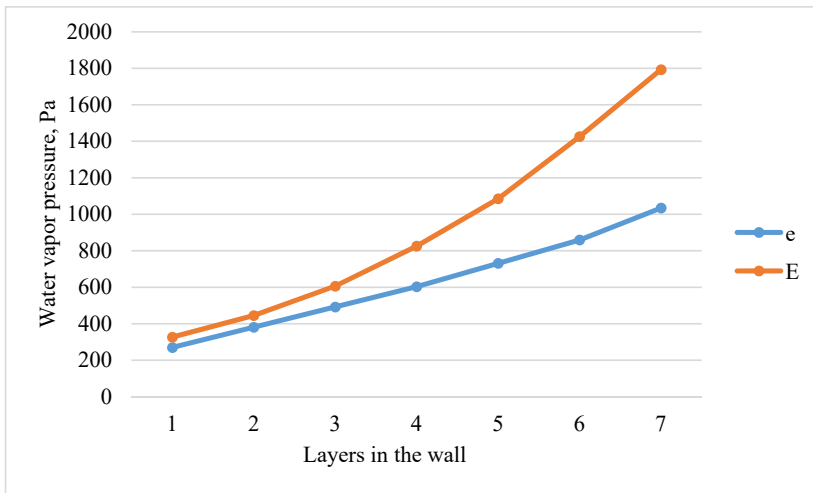
There is no need to prevent the penetration of rain moisture into the layers of the wall close to the outer surface [4, 5] and, therefore, forming them more dense.

### 3 Result of research

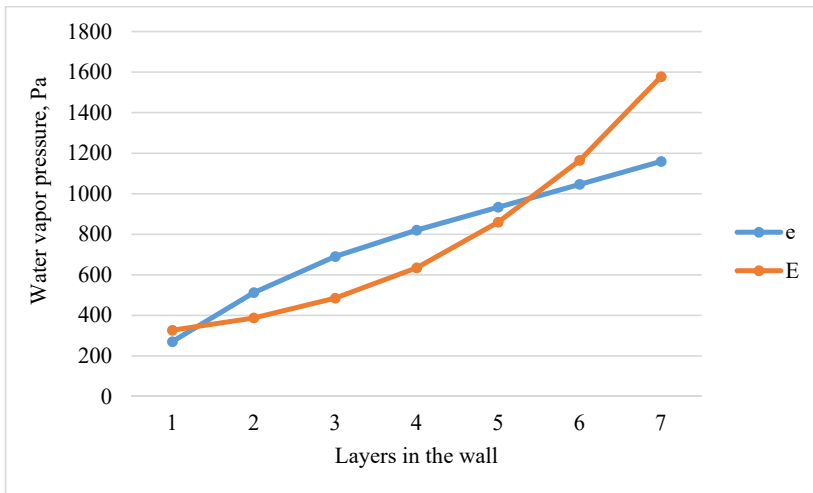
The results of calculations of changes in partial pressures at full saturation and at the existing humidity inside the expanded clay concrete block for all 6 variants of the density of the outer wall layers are shown in the graphs (Fig. 2-7).



**Fig. 2.** Change in partial pressures at full saturation (E) and with existing humidity (e) inside the outer wall for option 1.



**Fig. 3.** Change in partial pressures at full saturation (E) and at existing humidity (e) inside the outer wall for option 2.

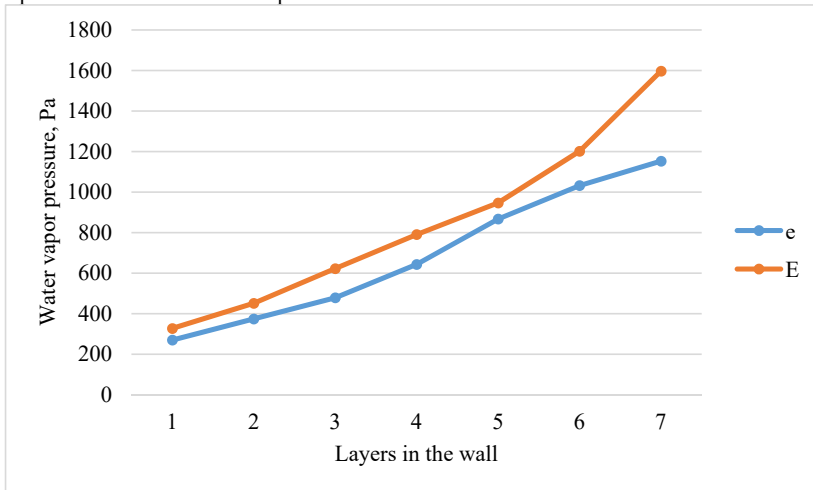


**Fig. 4.** Change in partial pressures at full saturation (E) and at existing humidity (e) inside the outer wall for option 3.

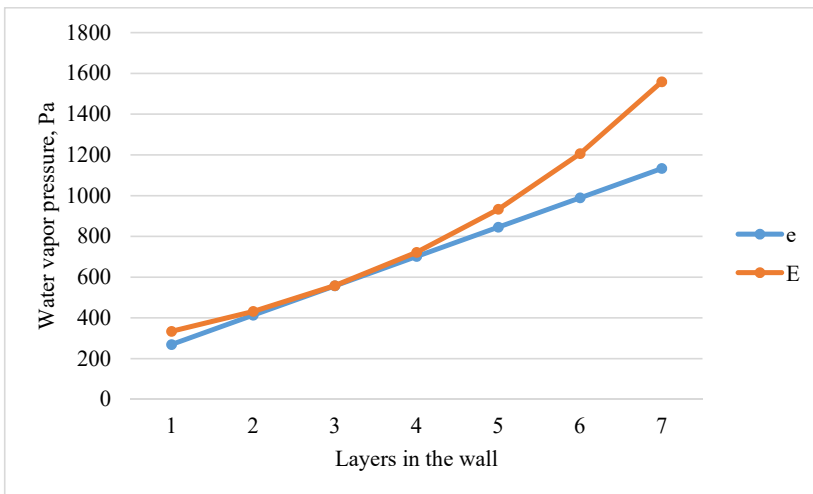
The figures show the intersection or non-intersection of the curves of the partial pressure lines at full saturation and at the existing humidity, which allows us to draw conclusions about the quality of the decisions made on the formation of layers of expanded clay concrete with different densities inside the wall.

In fig. 2, 4 (options 1 and 3), it can be seen that the lines of partial pressures at full saturation and at the existing humidity intersect twice, which indicates the condensation of moisture inside the wall in winter, which will freeze and then thaw, destroying the material

and reducing the durability of the outer walls, which is not acceptable. Such wall options require the use of additional vapor barrier on the inner surfaces of the outer walls.



**Fig. 5.** Change in partial pressures at full saturation (E) and at existing humidity (e) inside the outer wall for option 4.



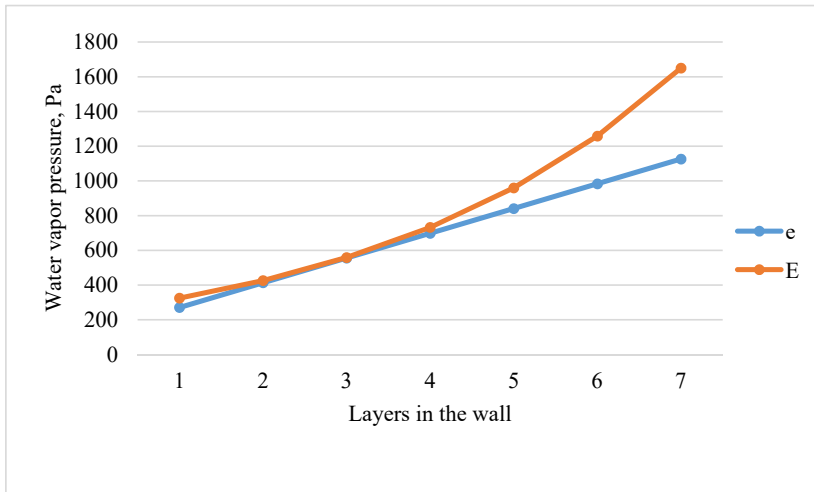
**Fig. 6.** Change in partial pressures at full saturation (E) and with existing humidity (e) inside the outer wall for option 5.

With options 2 and 4 (Fig. 3 and 5), the curves of the partial pressure lines at full saturation and at the existing humidity do not intersect, which means that the wall is dry and there is no moisture condensation in it, such a wall can be suitable for use in building.

In fig. 6 and 7 (options 5 and 6), the curves of the partial pressure lines at full saturation and at the existing humidity for a number of layers inside the wall merged together into a

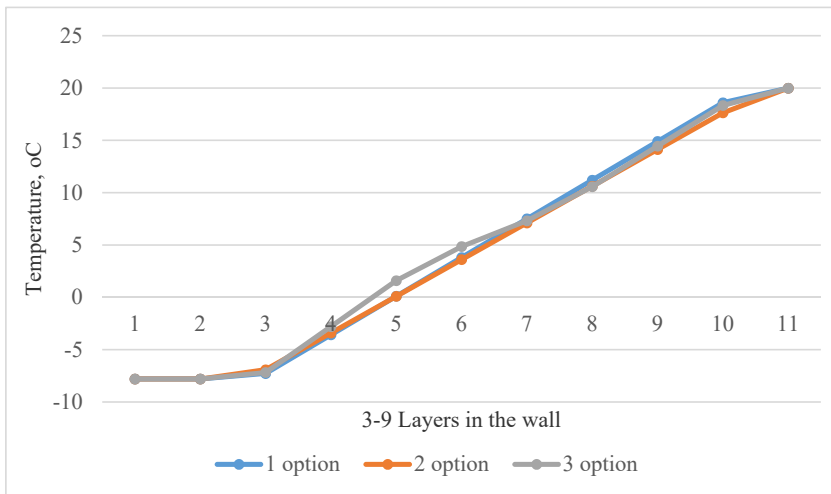


single line. Which indicates a possible condensation inside the wall and these wall options are also not suitable without additional vapor barrier for the inner surface of the outer walls.



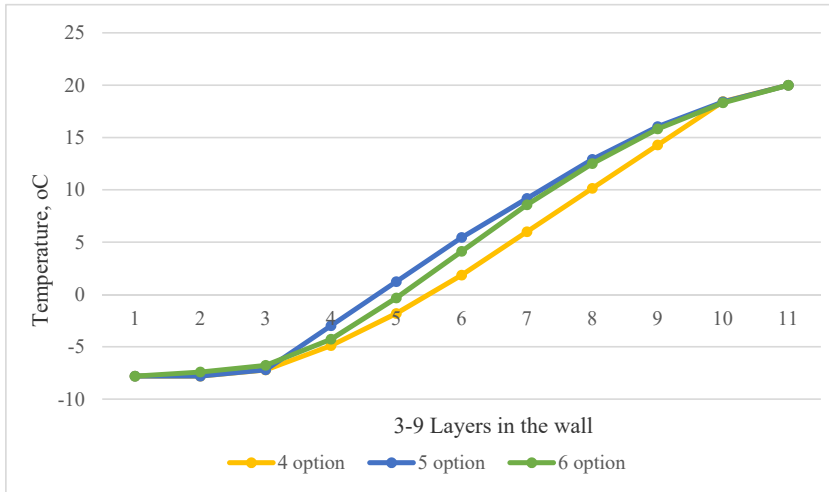
**Fig. 7.** Change in partial pressures at full saturation (E) and at existing humidity (e) inside the outer wall for option 6.

In fig. 8 shows, the temperature change inside the wall for options 1, 2 and 3; on the horizontal axis 3-9 - 7 layers inside the wall, 1, 2 - the temperature on the outer surface and in the outdoor air, 10, 11 - the temperature on the inner surface and in the indoor air.



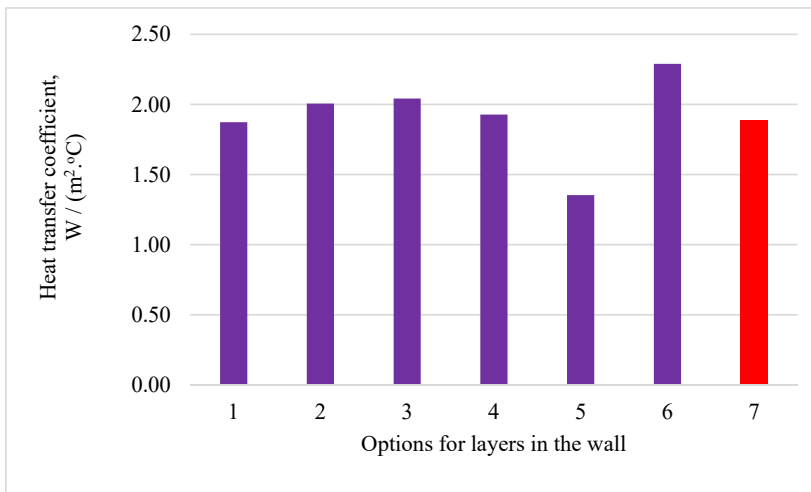
**Fig. 8.** Change temperature inside the wall for options 1, 2 and 3, where 3-9 - 7 layers inside the wall, 1, 2 - the temperature on the outer surface and in the outdoor air, 10, 11 - the temperature on the inner surface and in the indoor air.

In fig. 9 shows, the temperature change inside the wall for options 4, 5 and 6; on the horizontal axis 3-9 - 7 layers inside the wall, 1, 2 - the temperature on the outer surface and in the outdoor air, 10, 11 - the temperature on the inner surface and in the indoor air.



**Fig. 9.** Change temperature inside the wall for options 4, 5 and 6, where 3-9 - 7 layers inside the wall, 1, 2 - the temperature on the outer surface and in the outdoor air, 10, 11 - the temperature on the inner surface and in the indoor air.

In fig. 10 shows, the resistance to heat transfer of the outer wall with 6 considered options for the density of layers inside the wall.



**Fig. 10.** Change in the resistance to heat transfer of the outer wall with the considered 6 options for the thickness and density of layers in the thickness of the wall, 7 - the standard value of the resistance to heat transfer for the city of Moscow.

The low moisture content in the layers of blocks increases the resistance to heat transfer of the outer wall, which is useful for solving the problems of energy saving in buildings [6, 7]. The obtained values of the resistance to heat transfer for options 2 and 4 satisfy the requirements of the norms for thermal protection and protection against excessive moisture of the outer walls of buildings [8].

## 4 Conclusions

Layer-by-layer moulding of expanded clay foam concrete blocks allows obtaining blocks for external walls with new properties.

When forming expanded clay concrete blocks in layers, layers can be made with a given density and coefficients of thermal conductivity and vapour permeability.

Of course, you can create an outer wall from layers of different materials, but a single block with a single moulding concept is still better for installing and maintaining the outer walls, since dealing with fewer materials on the construction site is better for increasing construction speed. The durability of a single building material is also higher.

It is possible that it would be possible to form blocks or bricks from other materials also layer by layer, using the layers necessary for the construction of a particular building.

With the right combination of thermal conductivity and vapor permeability coefficients, as well as density and strength properties, it is possible to obtain an outer wall capable of saving energy with low heat loss, capable of being dry in winter, to increase the durability of the building.

## References

1. A.I. Ananiev, A.G. Rymarov, N. A. Denshchikov, *Industrial and civil engineering*, **1**, 28-34 (2021)
2. I. YA. Kiselev, *Building materials*, **7**, 17-18 (2003)
3. S.V. Kornienko, *Energy security and energy saving*, **4**, 12-17 (2015)
4. I.L. Shubin, A.I. Anan'ev, *Industrial and civil engineering*, **3**, 57-59 (2013)
5. O.I. Lobov, A.I. Anan'ev, A.G. Rymarov, *Industrial and civil engineering*, **11**, 67-71 (2016)
6. O.I. Lobov, etc., *Urban planning*, **4**, 61-65 (2010)
7. O. Brukhanov, A. Rymarov, A. Malysheva, D. Titkov, *IPICSE 2016*, 04028 (2016)
8. A.G. Rymarov, *Academia. Architecture and construction*, **5**, 362-364 (2009)

# An experimental study for drying *Pisum sativum* on an electric dryer and a heat pump dryer

Thanh Nhan Phan<sup>1,2,\*</sup>, Van Hung Tran<sup>1,2</sup>, Nikola Kaloyanov<sup>3</sup>, and Merima Zlateva<sup>3</sup>

<sup>1</sup>Ho Chi Minh City University of Technology (HCMUT), 268 Ly Thuong Kiet Street, District 10, Ho Chi Minh City, Vietnam

<sup>2</sup>Vietnam National University Ho Chi Minh City, Linh Trung Ward, Thu Duc District, Ho Chi Minh City, Vietnam

<sup>3</sup>Technical University of Sofia, Power Engineering and Power Machines Department, 8 Kliment Ohridski Blvd., 1000 Sofia, Bulgaria

**Abstract.** A study of drying parameters on the drying process of *Pisum Sativum* bean was carried out. The effects of drying temperature of moisture air from 40°C to 80°C on the drying time and on the drying kinetics were demonstrated not only on conventional electric dryers but also on heat pump dryers. Besides, checking the steady operation of the heat pump dryer was also considered. The results show that, when temperature rises, the shorter time and the faster removal of moisture content can be obtained for both dryer systems. Drying in an electric heater at 80°C took only 1 hour 45 minutes, but the broken skin of pea seeds happened. The comparison of heat pump dryer and electric dryer was presented with the shorter drying time on heat pump than electric dryer as a result of removing water vapor from moisture air at the evaporator of heat pump, it led to the reduction of specific humidity of air entering the drying chamber. And the last impressive result which can be seen is that the drying rate of a heat pump is higher than an electric dryer at the same drying temperatures beside the energy consumption of electric dryer is 2.76 times as much as that of heat pump dryer.

## 1 Introduction

The scientific name of Pea seeds is *Pisum sativum* with very rich nutrient contents around 25% protein and also rich of vitamins A, B and D. It is hard to store safely for long time due to the germination of seed with very high moisture content on the fresh seeds, with experimental test to store the fresh *sativum* seed for this research, just only 4 days after harvest in the environment while 5 days stored in refrigerator, the pea seeds would be germinated. So, drying is the best method to preserve products.

Many Drying technologies have been investigated and developed from the past to now, which were suitable for every product such as hot air dryer, heat pump dryer, freeze dryer, vacuum dryer. The influence of drying parameters on the drying process is one of the most important and interesting topics [1-5]. With the *Pisum sativum*, the research considered

---

\* Corresponding author: [phannhan@hcmut.edu.vn](mailto:phannhan@hcmut.edu.vn)

about the drying kinetics and colour of dried product had been done by Kayisoglu [1], the group of Siddique et al [2] was approached by the influence of drying time and temperature on the moisture percentage and quality of seeds. Also, some other group researchers keep working in this method for some other products such as pepper and so on. The effect of drying temperature on the quality of red bell pepper has been done by Vega-Galves et al [4], and studies about the drying characteristics and quality of difference maturity stages of pepper products were presented by Getahun et al [5].

Some researchers determined that at low temperature, the quality of dried products would be improved so they presented the new technology as a promised and new generations for drying technique, heat pump. Liu et al [6] presented the design and thermal analysis for heat pump dryer which is suitable for food products while Strommen et al [7] introduced the new drying method at low dryer temperature and they stated that drying at low temperature on heat pumps is the new generations to get the dried product with very high quality.

The purpose of this paper is to investigate the drying behaviour of thin layer drying of pea seeds, especially the drying curve and drying rate curve. Besides, the comparison of the efficiency of the drying process between an electric dryer and a heat pump dryer is considered, and the analysis of the comparison of water removal and energy performances of conventional dryer (electric dryer) and heat pump dryer is presented.

## 2 Methodology

### 2.1 Sample preparation

The Pea seeds (*Pisum sativum*) (Fig. 1) used for this test are a special product planted in Dalat City, Lamdong Province, the central highland in the middle of Vietnam. After harvesting, they are separated from the seed-pod by hand and stored in a refrigerator at 5°C until applied in experiments.



Fig. 1. Pea seeds (*Pisum sativum*).



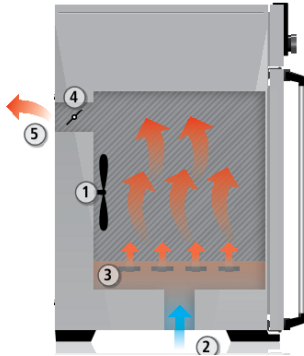
Fig. 2. Sample analysis dryer - MX-50 WinCT – Moisture.

The initial moisture content of pea seeds is analysed by repeated drying of the samples in sample analysis dryer AND MX-50 with 0.1% accuracy as in Fig. 2. After 7 times repeated with around 5 grams of random samples, the initial moisture content of pea seeds is found to be  $W_o = (54.12 \pm 0.95) \%$ . The dried moisture content of pea seeds material is  $W_e = 14 \%$ .

### 2.2 Experimental apparatus

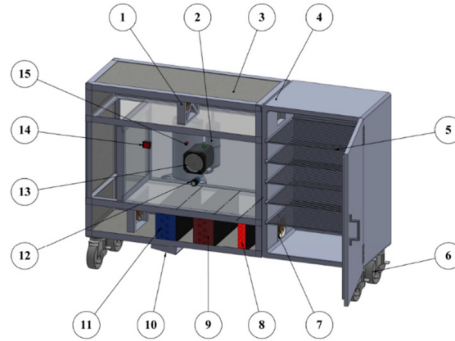
The two dryer machines that have been used in this study are electric dryer and heat pump dryer. The electric dryer (Fig.3) was purchased with a power of 2 kW, volume 108 liters

and dimensions 560x480x400 mm. The control temperature of the machine can remain the temperature in the drying chamber with the accuracy is  $\pm 0.5^\circ\text{C}$ . The Heat pump dryer is designed, and manufactured by our research group with 0.746 kW power of compressor, R407a refrigerant, 3 kW evaporator, 3.746 kW of condenser as shown in Fig. 4.



**Fig. 3.** Electric dryer.

1-fan, 2-inlet air, 3- electric heater, 4- damper, 5-outlet air



**Fig. 4.** Heat pump dryers.

1- exhaust air fan, 2-compressor, 3- drying trolley, 4- drying chamber, 5-drying tray, 6-wheels, 7- entrance air fan, 8-electric heater, 9-condenser, 10- drain water, 11- evaporator, 12-control temperature, 13-timer, 14- switch on/off-, 15-lamp alert.

Humid ambient air flows through the evaporator (10) to reduce the temperature and due to the lower dew point temperature, condensed water would be removed so as to influence the specific humidity of air. After that, the air stream keeps moving to the condenser (9), the temperature of air increases to the drying temperature, if the heat released from the condenser is not enough to raise the air temperature, a sub-electric heater is used. The air at drying temperature with lower specific humidity flows to the drying chamber (4) and takes moisture from the drying material as a drying process and absorbs moisture from the material for drying.

**Instruments:** the instruments used to measure the experimental parameters during the test are presented in Table 1 with their accuracy.

**Table 1.** The list of instruments.

Measure	Instrument	Accuracy
Air velocity	Testo 425	$\pm 0.3$ m/s
Temperature	Datalogger TC type K	$\pm 0.1^\circ\text{C}$
Humidity of air (dry-wet bulk temperatures)	PH721	$\pm 3\%$
Mass of material	Weight	$\pm 10$ gam
Moisture of material	AND MX-50	$\pm 0.1\%$

**Experimental test:** The test focuses on the kinetic drying due to the effect of temperature and the efficiency of a heat pump dryer compared to an electric dryer. Then the working range of experiment is shown in table 2 below:

**Table 2.** Experimental working conditions.

<b>Velocity</b>	2m/s
<b>Temperature</b>	40, 45, 50, 55, 60, 70, 80°C
<b>Type of dryers</b>	electric dryer, heat pump dryer

### 2.3 Moisture content and drying rate of Pea seeds

In order to determine data reduction, experiment parameters of pea seeds were used in each experiment as below:

$M_o = 2$  kg: mass of fresh product;

$W_o = 54.12\%$ : initial moisture content of fresh product;

$W_e = 14\%$ : moisture content of dried product;

Data reduction:

$$Water = M_o - M_e \quad (1)$$

$$Water = M_o \cdot \frac{W_o - W_e}{100 - W_e} \quad (2)$$

$$W_e = W_o - Water \cdot \frac{100 - W_o}{M_e} \quad (3)$$

$W_t$ : Moisture content of product at a drying time  $t$

$$W_t = W_o - Water \cdot \frac{100 - W_o}{M_t} \quad (4)$$

Drying rate (DR) of pea seeds was determined:

$$DR = \frac{M_{t+\Delta t} - M_t}{\Delta t} \quad (5)$$

Where:  $M_t$ : mass of product after drying period time  $t$ ;

$\Delta t$ : time interval;

DR: drying rate.

## 3 Result and discussion

### 3.1 Drying pea seeds on electric dryer

Experimental tests have been done on electric dryers with a vary of temperature from 40°C to 80°C with the fresh pea seeds from 54.12% initial moisture content to 14%. The Data results show in Fig. 5, at drying temperature of 40°C a very long period of time was spent to dry pea seeds product, while at 80°C a very short time was used. More detail, it took 6 hours to dry pea seeds at 40°C, at 55°C it did take 3.5 hours and at 80°C it took only 1 hour and 45 minutes. But one important thing to get from data results is that the phenomenon of

breaking the skin seed cover around the seed happened at a drying temperature of 80°C. It could be explained that due to the fast removal of moisture from the surface of seed in the short period of time, the skin layer is dried so fast.

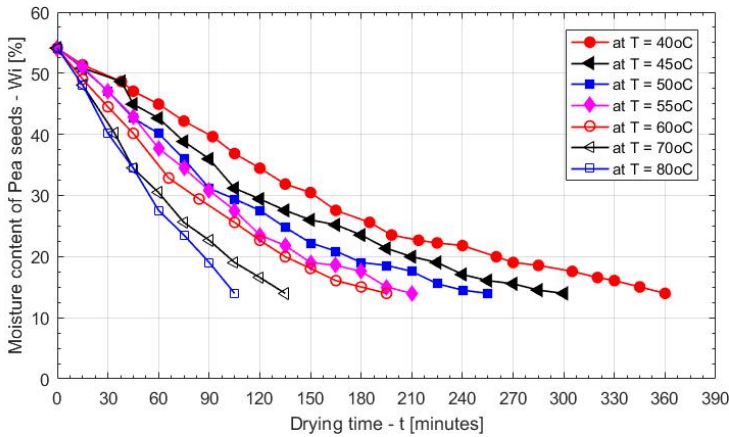


Fig. 5. Drying curves of Pea seeds on an electric dryer.

### 3.2 Drying pea seeds on heat pump dryer

The experiments have been performed at three different temperatures as follows: 45°C, 50°C and 55°C. As could be seen in Fig. 6, the reducing of moisture content during drying time follow by difference temperature. At the end of the series of 55°C temperature, the time is 2h45min and the product is dried to 14% moisture content, but at that time if drying temperature is 45°C the moisture content will remain 20% and needs one more hour to get the dried product. And at the last period of time at 45°C drying temperature, it can be seen that the remaining moisture in the seed is very hard to remove, that is why the reduction of the moisture content from 20% to 14% at 45°C takes one more hour and around 30 minutes at 50°C.

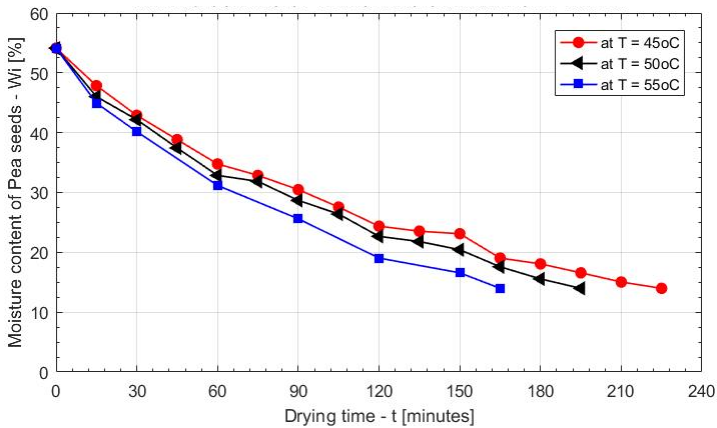


Fig. 6. Drying curves of Pea seeds on Heat pump dryer.



### 3.3 Comparison of the processes of drying pea seeds by electric dryer and heat pump dryer

#### 3.3.1 Comparison of drying curves and energy consumption

Fig. 7 represents the comparison of drying pea seeds on electric dryer and heat pump dryer at the same drying temperatures. It is clear to see that drying in a heat pump is faster than in an electric dryer at all comparing temperatures.

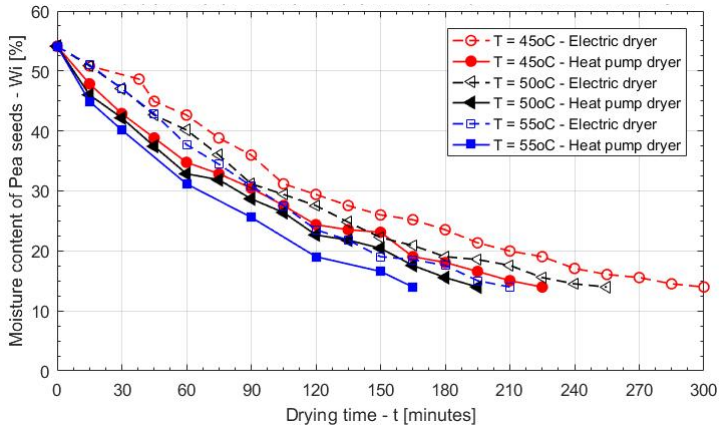


Fig. 7. Comparison of drying curves of Pea seeds on electric and Heat pump dryers.

At 50°C, drying in the electric dryer took 4 hours and 15 minutes while the heat pump took 3 hours and 15 minutes. It could be seen in Fig 8, about the steady of running heat pump system, the humid ambient air at  $29.5 \pm 0.4^\circ\text{C}$ , around 77% humidity flows through evaporator, moisture air moves out of evaporator at  $22 \pm 0.4^\circ\text{C}$  then moves to condenser to rise temperature again to  $51.1 \pm 0.9^\circ\text{C}$  (take as working drying temperature  $50^\circ\text{C}$ ) before flows to drying chamber. So that the drying air flows to the drying chamber at  $51.1^\circ\text{C}$ , specific humidity  $d = 0.015 \text{ kgw/kg}$  instead of at specific humidity  $d = 0.020 \text{ kgw/kg}$  if working with an electric dryer in the same environment.

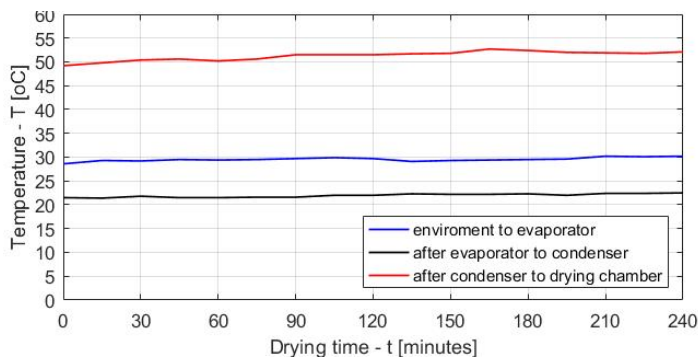


Fig. 8. The steady heat pump system.

**Consider about energy consumption:** The comparison of water removal and energy performances of conventional dryer (electric dryer) and heat pump dryer, a specific moisture extraction ratio (SMER) would be applied as a standard comparison to determine the performances of the electric dryer and heat pump dryer

$$SMER = \frac{\text{Water removal}}{\text{electric consumption}} \quad (6)$$

Electric consumption of each experiment was recorded by using power instrument ATA AT-NL01, it presented total energy consumption of each experiment (kWh).

Water removal could be determined with the mass of fresh product and the mass of dry product at the end of experiment.

**Table 3.** The comparison of the performance of the electric dryer and heat pump dryer

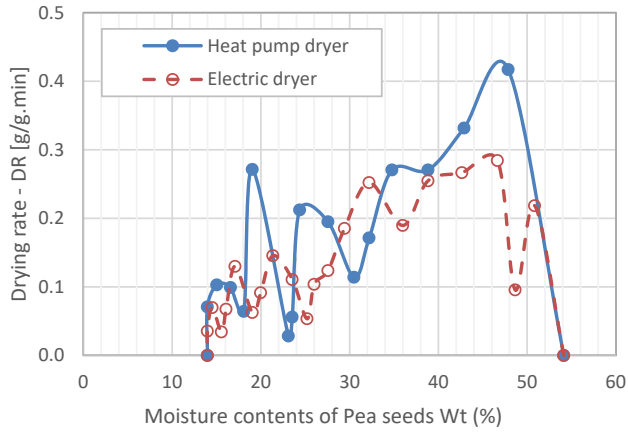
Performance	Unit	Electric dryer	Heat pump dryer
Heating capacity	kW	2	3.746
Cooling capacity	kW	-	3
Shaft work	kW	-	0.746
COP	-	-	4.02
Mass of fresh product	kg	2	2
Drying temperature	°C	50	50
Water removal	kgw	0.933	0.933
Working time	hours	4.25	3.5
Electric consumption	kWh	7.86	2.84
SMER	Kgw/kWh	0.12	0.33

The comparison of the performance in table 3 present at the same drying temperature at 50°C, for an input of 1kWh, the electric dryer removes 0.12 kg water, while the heat pump dryer removes 0.33 kg water. In addition, the amount of energy consumption of a heat pump is only 2.84 kWh, whereas the electric dryer uses 7.86 kWh.

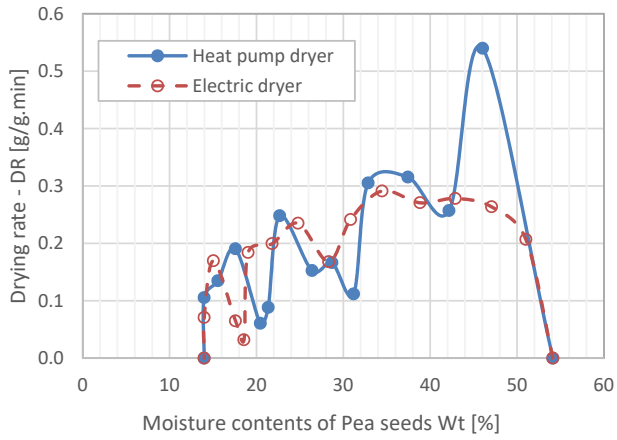
### 3.3.2 Comparison of drying rate curves:

About the drying rate, the comparison between drying in an electric dryer and heat pump at 45°C and 50°C could be observed in Fig. 9 and Fig. 10. It could take the drying at 45°C as an example, at the first drying time, when the moisture content of pea seeds is still high (at 54%) the drying rate of heat pump is greater than 0.4 and decreases gradually, while with electric dryer it is only about 0.2 to 0.3 at the same moisture content. It could be observed that during the drying process, the drying rate on the heat pump is always larger than on an electric heater.

In Fig. 11, the dried products from the experiments were collected with very good results and will be stored in the environment and in a refrigerator for a long time to check the stored time of products.



**Fig. 9.** Drying rate curves at 45°C.



**Fig. 10.** Drying rate curves at 50°C.



**Fig. 11.** Dried Pea seeds products.

## 4 Conclusion

Experimental research for drying of pea seeds has been done with the consideration of drying temperature affected on the drying time and quality of products for both systems: electric dryer and heat pump dryer. The steady working operation of the heat pump also checked during the drying process and confirmed that the system works well. The comparisons between electric dryer and heat pump dryer were considered under the drying curve and drying rate of the drying process of pea seeds at the same temperature conditions. The result shows that the efficiency of the heat pump is better than the electric dryer.

We would like to thank The Ho Chi Minh City University of Technology (HCMUT), VNU-HCM for the support of time and facilities for this study.

## Nomenclature

$M_o$  [kg]: mass of fresh product;  
 $M_e$  [kg]: mass of dry product;  
 $M_t$  [kg]: mass of product after drying period time  $t$ ;  
 $\Delta t$  [s]: time interval;  
 $W_o$  [%]: initial moisture content of fresh product;  
 $W_t$  [%]: moisture content of product at the drying time  $t$ ;  
 $W_e$  [%]: moisture content of dried product;  
DR: drying rate;  
SMER: specific moisture extraction ratio

## References

1. S. Kayisoglu, Lat. Am. Appl. Res., **50**(3), pp. 235-240, (2020).
2. A. B. Siddique, D. Wright, Asian J. Plant Sci., **2**(13), pp. 978-982, (2003).
3. R. F. Mechlouch, B. Mahdhaoui, W. Elfalleh, A. Mahjoubi, A. B. Brahim, Int. J. Energy Eng., **4**(2A), pp. 25-32, (2014).
4. A. Vega-Galvez, R. Lemus-Mondaca, C. Bilbao-Sainz, P. Fito, A. Andres, J. Food Eng., **85**, pp. 42-50, (2008).
5. E. Getahun, M. A. Delele, N. Gabbiye, S.W. Fanta, M. Vanierschot, Case Stud. Therm. Eng., **26**, 1001052, (2021).
6. H. Liu, K. Yousaf, K. Chen, R. Fan, J. Liu, S. A. Soomro, Sustainability, **10**(9), 3216, (2018).
7. I. Strommen, T. M. Eikevik, O. Alves-Filho, K. Syverud, O. Jonassen, *The 2<sup>nd</sup> Nordic Drying Conference*, Copenhagen Denmark, June 25th -27th 2003, ISBN 82-594-2550-5 (2003).

# Modelling and numerical simulation of fire in a coffee storage hall

*Kalin Krumov*<sup>1</sup>, *Nina Penkova*<sup>1\*</sup>, *Boian Mladenov*<sup>1</sup>, and *Yordan Stoyanov*<sup>1</sup>

<sup>1</sup>University of Chemical Technology and Metallurgy, Department of Silicate Technology, Blvd. Sv. Kliment Ohridski 8, 1756 Sofia, Bulgaria

**Abstract.** An approach for modelling of fire in halls at solid materials burning, based on gas phase combustion models in ANSYS/CFX, is proposed. The models are suitable for quick prediction of the flue gases distribution and thermal loads on the building envelopes at a design stage. They were applied for numerical simulation of such processes in a coffee storage hall at different fire positions and forced anti-smoke ventilation. The thermal, fluid flow and concentration field were obtained at the modelled scenarios. Maximal thermal loads on the building envelopes are established at the case of fire near their non-streamlined parts.

## 1 Introduction

The prediction of smoke and heat distribution at the cases of fire is important for the sizing and mounting of the building components and materials, smoke vents, sprinkler and ventilation systems [1]. The modeling and computer simulation are convenient ways for analysis of possible burning processes in the buildings [2, 3, 4]. Different CFD techniques are used for fire modeling: Direct Numerical Simulation (DNS), Large Eddy Simulation (LES) and Reynolds-Averaged Navier-Stokes (RANS) [2].

DNS requires very fine spatial and temporal resolutions (about 1 mm or less). It is convenient for low Reynolds number flows and simple geometries and is not practical for large-scale fire simulations. LES is suitable for “large eddies” modeling at relatively coarse space meshes. It is the base of the computational code Fire Dynamics Simulator (FDS), widely used for fire analysis at large-scale buildings [1, 5 -7]. The software allows numerical simulations of low-Mach flows, driven by the released combustion heat and the buoyancy via the coupled LES, combustion and radiation models [8].

The CFD techniques, based on RANS also allow solutions of combustion models by finite volumes method. Such models for gaseous and liquid fuels are well developed and proved [9]. However, the computational models of solid material burning at fire are still in the process of development, validation and verification.

The aim of the present study is to develop and test a model for quick numerical simulation of fires in buildings at burning of solid materials, based on RANS and gas phase combustion models, available in ANSYS. An idea for such modeling is mentioned in [10]. Here it is

---

\* Corresponding author: [nina@uctm.edu](mailto:nina@uctm.edu)

developed in details for numerical simulation of released smoke and heat at burning of coffee in a storage hall.

## 2 Modeling of fire in buildings at burning of solid materials

The models below allow numerical simulation of quasi-stationary fire at moments of the unsteady burning. They are based on the idea for a modeling of the burning of solid materials by gas fuel combustion at the same released heat and smoke flows. The possible fire locations are modeled as sources of gas mixture, containing combustible and noncombustible components: methane, carbon monoxide, hydrogen sulfide and water vapor. The mass fractions of these components and the gas mass flow are computed in order to release equal emissions as at the solid burning:

- heat flows and heat release rate;
- mass flows of the products of the reactions  $\text{CO}_2$ ,  $\text{SO}_2$  and  $\text{H}_2\text{O}$ .

The first acceptance is not new. It is the base of the so-called Pyrolysis model of FDS: the mass flow of a chosen in advance hydrocarbon gas fuel is computed and applied on the "burning area" at known heat release rate of the burning solid materials [8].

That approach allows numerical simulation of fire at solid material burning with RANS based software as CFX (ANSYS), using the available gas phase combustion models for the computations of the correspondent mixing and chemical reactions. The radiation heat transfer at solid materials burning can be modeled via calibration of the radiation model in order to ensure equal flame emissivity for the both types of fuels. The formation, moving and dissipations of the eddies are represented by the turbulent viscosity, kinetic energy and energy dissipation rate, computed by turbulence models. The finer meshes and the smaller real and physical time steps allow obtaining of sufficiently accurate information for the distribution of the released flue gases and heat in the building space at a case of fire.

A three-dimensional geometrical model of the internal space of the hall is generated. The doors, windows, smoke vents and the possible fire locations present in the model as merged surfaces on the walls. Different scenario of fire can be simulated moving the fire locations in the geometrical model. The internal building space is discretized by a mesh of finite volumes in order to solve numerically the system of partial differential equations:

- continuity equation;
- momentum equations at non zero gravity to model the buoyancy;
- thermal energy equation;
- $k$ - $\epsilon$  or  $k$ - $\omega$  turbulence model;
- gas phase combustion model;
- radiation model.

The air, gas fuel mixture and the product of the reactions are accepted as ideal gases: their density are computed by the corresponding equations of the state. Possible boundary conditions are summarized in Table 1.

**Table 1.** Boundary conditions.

Boundary	Variable
Fire locations (inlets)	Gas mixture mass flow, mass fractions of the components, gas temperature.
Vertical opened windows and doors (opening boundaries)	Wind pressures with positive values at the windward facades and negative on the leeward ones, the ambient temperature.
Openings for forced air supply in a case of fire (inlets)	Average velocity or mass flow of the airflow, temperature.

Smoke vents on the roofs (opening boundaries)	Local atmospheric pressure, computed according to the altitude, ambient temperature.
Heat exchanging boundaries: closed doors, windows walls, roofs and floors	Coefficients of heat transfer from the internal surface to the outdoor environment: $U = \frac{1}{R_{se} + \sum_{i=1}^n R_i}$ , $\text{Wm}^{-2}\text{K}^{-1}$ ; emissivity of the internal surfaces and ambient temperature.

The variables  $R_{se}$  and  $R_i$  in the equation in Table 1 are the thermal resistances of the external boundary layer and solid layers of the wall/roof/floor,  $\text{m}^2\text{KW}^{-1}$ . The overall coefficient of thermal transmittance of the windows and transparent doors  $U$  can be used in the last boundary condition with a sufficient accuracy for the engineering purposes.

The mass fractions of the components of the gas fuel and its mass flow are computed at the common solution of the equations (1-5).

$$\dot{Q} = \dot{m}_{s,m} LHV_{s,m} = \dot{V}_{g,f} LHV_{g,f}, \text{ kW} \quad (1)$$

$$\dot{V}_{CO_2} = \dot{m}_{s,m} V_{CO_2}^{s,m} = \dot{V}_{g,f} V_{CO_2}^{g,f}, \text{ m}^3\text{s}^{-1} \quad (2)$$

$$\dot{V}_{H_2O} = \dot{m}_{s,m} V_{H_2O}^{s,m} = \dot{V}_{g,f} V_{H_2O}^{g,f}, \text{ m}^3\text{s}^{-1} \quad (3)$$

$$\dot{V}_{SO_2} = \dot{m}_{s,m} V_{SO_2}^{s,m} = \dot{V}_{g,f} V_{SO_2}^{g,f}, \text{ m}^3\text{s}^{-1} \quad (4)$$

$$CH_4 + CO + H_2S + H_2O = 100, \% \quad (5)$$

where  $\dot{Q}$  = heat flow, released at the combustion, kW;  $\dot{m}_{s,m}$  = solid material mass, burned per unit time,  $\text{kg}\text{s}^{-1}$ ;  $\dot{V}_{g,f}$  = volumetric flow of the gas fuel at normal physical conditions,  $\text{m}^3\text{s}^{-1}$ ;  $\dot{V}_{CO_2}$ ,  $\dot{V}_{H_2O}$  and  $\dot{V}_{SO_2}$  = volumetric flows of the components of the flue gases at normal physical conditions,  $\text{m}^3\text{s}^{-1}$ ;  $LHV_{s,m}$  = lower heating value of the burning solid material,  $\text{kJkg}^{-1}$ ;  $V_{CO_2}^{s,m}$ ,  $V_{H_2O}^{s,m}$  and  $V_{SO_2}^{s,m}$  = specific volumes of the component of the flue gases at solid materials burning,  $\text{m}^3\text{kg}^{-1}$ ;  $LHV_{g,f}$  = lower heating value of the gas fuel,  $\text{kJm}^{-3}$ ;  $V_{CO_2}^{g,f}$ ,  $V_{H_2O}^{g,f}$  and  $V_{SO_2}^{g,f}$  = specific volumes of the component of the flue gases at the combustion of fuel gas,  $\text{m}^3\text{m}^{-3}$  (Table 2).

**Table 2.** Lower heating values and flue gases components [11]

Solid material	Gas fuel mixture
Components (mass percentages): $C, H, O, N, S, A$ (ash), $W$ (water content), %	Components (volumetric percentages): $CH_4, CO, H_2S, H_2O$ , %
$LHV_{s,m} = 4.187(81C + 246H - 26(O - S) - 6W)$ , $\text{kJkg}^{-1}$	$LHV_{g,f} = 358.17CH_4 + 126.35CO + 235.52H_2S$ , $\text{kJm}^{-3}$
$V_{CO_2}^{s,m} = 0.01855C$ , $\text{m}^3\text{kg}^{-1}$	$V_{CO_2}^{g,f} = 0.01(CO + CH_4)$ , $\text{m}^3\text{m}^{-3}$
$V_{H_2O}^{s,m} = 0.112H + 0.0124W$ , $\text{m}^3\text{kg}^{-1}$	$V_{H_2O}^{g,f} = 0.01(2CH_4 + H_2S + H_2O)$ , $\text{m}^3\text{m}^{-3}$
$V_{SO_2}^{s,m} = 0.000685S$ , $\text{m}^3\text{kg}^{-1}$	$V_{SO_2}^{g,f} = 0.01H_2S$ , $\text{m}^3\text{m}^{-3}$

The parameters of the solid material burning process in Table 2 are computed at a known material composition. The unknown variables  $CH_4$ ,  $CO$ ,  $H_2S$ ,  $H_2O$  and  $\dot{V}_{g,f}$  can be obtained at the use of the expressions for the parameters of the gas mixture combustion (Table 2) in

equations (1-5). Then the mass flow of the gas fuel  $\dot{m}_{g,f}$  and the mass fractions  $g$  of the components can be computed:

$$\dot{m}_{g,f} = \dot{m}_{CH_4} + \dot{m}_{CO} + \dot{m}_{H_2S} + \dot{m}_{H_2O} = \frac{CH_4}{100} \dot{V}_{g,f} \rho_{CH_4} + \frac{CO}{100} \dot{V}_{g,f} \rho_{CO} + \frac{H_2S}{100} \dot{V}_{g,f} \rho_{H_2S} + \frac{H_2O}{100} \dot{V}_{g,f} \rho_{H_2O}, \text{ kgs}^{-1} \quad (6)$$

$$g_{CH_4} = \frac{\dot{m}_{CH_4}}{\dot{m}_{g,f}}, \quad g_{CO} = \frac{\dot{m}_{CO}}{\dot{m}_{g,f}}, \quad g_{H_2S} = \frac{\dot{m}_{H_2S}}{\dot{m}_{g,f}}, \quad g_{H_2O} = \frac{\dot{m}_{H_2O}}{\dot{m}_{g,f}} \quad (7)$$

where  $\rho_{CH_4}$ ,  $\rho_{CO}$  and  $\rho_{H_2O}$  are the densities of the correspondent gases at normal physical conditions.

### 3 Numerical simulation of fires in a coffee storage hall

The models above are solved numerically to simulate fire at a design stage of a coffee storage hall at a case of forced ventilation for evacuation of the smoke and the heat. The sizes of the building are width=9.85m, length=42.1m and average height = 8.24 m (fig. 1). There are not windows on the facades. The higher long wall borders with another building. It is accepted as adiabatic boundary in the model. The coffee is stored in bags arranged near the floor. Three locations of burning are accepted on the floor in order to simulate 3 scenario of fire.

The finite volumes mesh is consisted of 1253580 elements, sharing 222856 nodes. The average size of the elements is 0.3m. The mesh is finer near the door, vents and fire locations. An air flow with volumetric flow of  $27.5 \text{ m}^3\text{s}^{-1}$  and ambient temperature of  $30 \text{ }^\circ\text{C}$  is supplied through the open door on fig. 1 in order to dilute and evacuate the smoke through the vents. The air exchange rate per hour (ARCH) is  $29\text{h}^{-1}$ . It is obtained according to [12] at a thermal load of  $840 \text{ kWhm}^{-2}$  at burning of coffee and an accepted height of the smokeless space lower than 50% of the average height of the hall. The vents on the roof are sized at the same conditions.

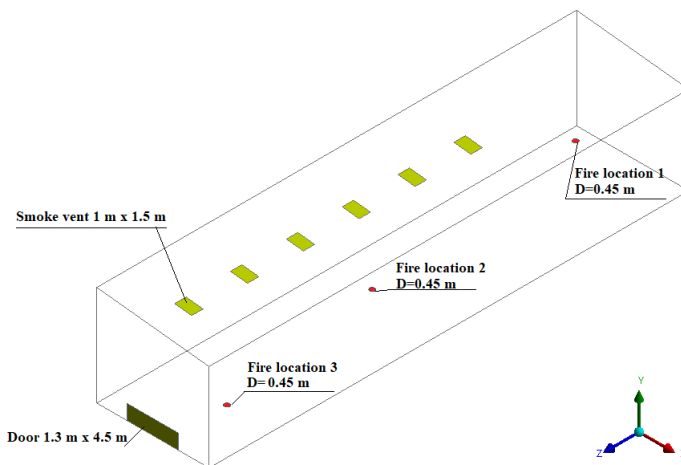


Fig. 1. Common view of the hall.



The coffee composition is accepted according to [13], assuming that the spent coffee ground and the coffee have approximately the same compositions. The equilibrium moisture content of the coffee is accepted as 8%. Details about the combustion process are given in Table 3. The computed flow of SO<sub>2</sub>, released at the combustion is relatively small and its concentration in the hall can be neglected at the high ARCH. So a zero concentration of H<sub>2</sub>S is accepted and the volumetric flow  $\dot{V}_{SO_2}$  is added to  $\dot{V}_{CO_2}$  at the computing of the fuel gas composition. This step simplify the combustion modelling and enables using a two step model of combustion Methane Air WD2 NO PDF, available in CFX. The gas mixture of the model contains all possible component of the gases in the hall. The model also allows computing of nitrogen oxide if there are suitable conditions for its formation. *k-ε* model is used to simulate the turbulence effects. The buoyancy is modelled at density differences between the local and the reference density of the ambient air. The radiation heat transfer is neglected due to the negligible concentration and subsequent emissivity of the radiating gases (CO<sub>2</sub>, H<sub>2</sub>O and CH<sub>4</sub>) in the hall space.

**Table 3.** Components of the fuels, lower heating values and flows

Coffee	Gas fuel mixture
Components (mass percentages): $C=39.43\%$ , $H=7.89\%$ , $S=1.47\%$ ; $O=41.63\%$ , $N=1.28\%$ , $A=0.30\%$ , $W=8.00\%$	Components (volumetric percentages): $CH_4=30\%$ , $CO=40\%$ , $H_2S=0\%$ , $H_2O=30\%$
$\dot{Q} = 258 \text{ kW}$	
$LHV_{s,m} = 16916 \text{ kJkg}^{-1}$	$LHV_{g,f} = 15799 \text{ kJm}^{-3}$
$\dot{m}_{s,m} = 0.0167 \text{ kgs}^{-1}$ (corresponding to 1 kg coffee burning per minute)	$\dot{V}_{g,f} = 0.0178 \text{ m}^3\text{s}^{-1}$ ; $\dot{m}_{g,f} = 0.0170 \text{ kgs}^{-1}$
	$g_{CH_4} = 0.224$ ; $g_{CO} = 0.523$ ; $g_{H_2O} = 0.252$
$\dot{V}_{CO_2} = 0.024 \text{ m}^3\text{s}^{-1}$ ; $\dot{V}_{H_2O} = 0.013 \text{ m}^3\text{s}^{-1}$ ; $\dot{V}_{SO_2} = 0.0002 \text{ m}^3\text{s}^{-1}$	$\dot{V}_{CO_2} = 0.025 \text{ m}^3\text{s}^{-1}$ ; $\dot{V}_{H_2O} = 0.013 \text{ m}^3\text{s}^{-1}$ ;

**Table 4.** Boundary conditions for numerical simulation of fires in a coffee storage hall

Boundary	Variable
Fire locations (inlets)	$\dot{m}_{g,f} = 0.0170 \text{ kgs}^{-1}$ ; $g_{CH_4} = 0.224$ ; $g_{CO} = 0.523$ ; $g_{H_2O} = 0.252$ ; $t_{gas}=20^\circ\text{C}$
Opened door (inlet)	Velocity, normal to the boundary $V_n=4.3 \text{ m/s}$ (at the supplied air flow through the door); ambient temperature of $30^\circ\text{C}$ .
Smoke vents on the roofs (opening boundaries)	Average gauge pressure 0 Pa; ambient temperature of $30^\circ\text{C}$ .
Heat exchanging boundaries: walls, roof and floor	Heat exchange at $U=0.3 \text{ Wm}^{-2}\text{K}^{-1}$ for all building envelopes (floor, roof, floor); walls and roof: ambient temperature of $30^\circ\text{C}$ ; floor: ambient temperature of $10^\circ\text{C}$
Wall, bordering with an adjacent building	Adiabatic boundary

The models were solved numerically at the conditions above for the chosen fire locations and are validated by mass and energy balances on the base of the obtained results. The differences between the mass flows, entering and leaving the hall are less than 1 %. The

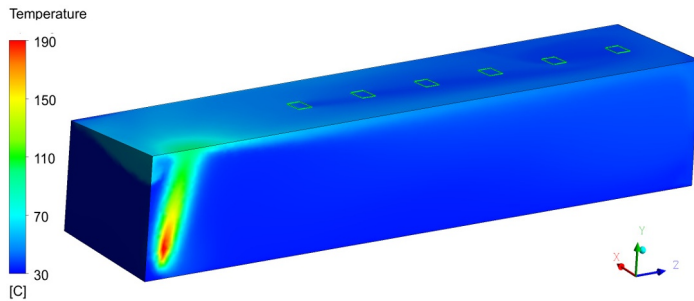
differences between the input heat flow (released at the combustion) and sum output heat flows, including the thermal losses through the building envelopes and the heat flow of the exhaust gas mixture, are below 2 %. So the obtained results can be accepted as reliable in order to estimate the processes at the modelled variants.

The computed temperatures, mass fractions of  $\text{CO}_2$  and fluid flow fields are visualised on the figures below. The space orientations of the building are chosen in order to ensure good view of the fires.

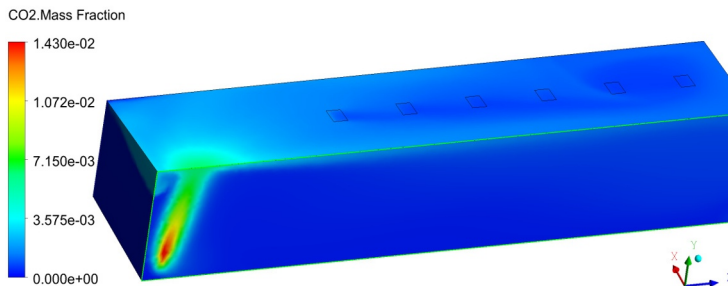
The established concentration of  $\text{CO}$  and  $\text{CH}_4$  at the openings are negligible at all modelled scenarios. Therefore, the combustion processes proceeded completely. The  $\text{CO}_2$  distribution is similar to the temperature one (fig. 2 and 3).

Higher thermal loads on the building walls are established at the fire location 1 (fig. 2). In this case, the main airflow distorts the flame and the mixing of the ventilation air and the flue gases is strained (fig. 5). The temperature on the vertical wall near the fire reaches 190 °C. The temperature gradients on the hot zones are relatively high. That will cause thermal stresses and damages if the wall is not fire resistant.

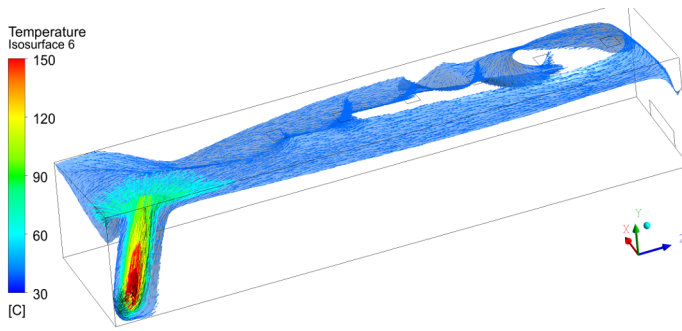
At the other fire locations, the fresh airflows dilute well the flue gases (fig. 7 and 9) and the concentration of  $\text{CO}_2$  is negligible in the overall internal space. The temperature fields on the building envelopes are more even and the temperatures and their gradients on the internal wall surfaces are smaller (fig. 6 and 8).



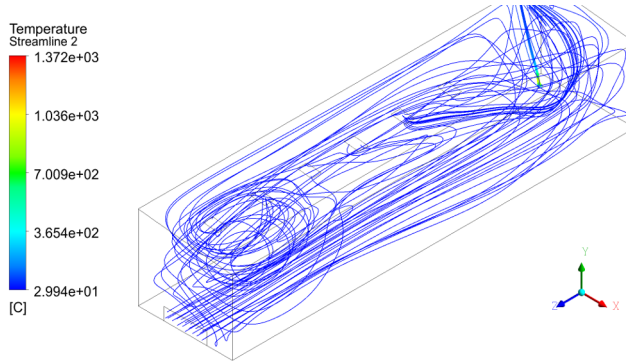
**Fig. 2.** Temperature field of the internal surfaces of the walls at fire location 1.



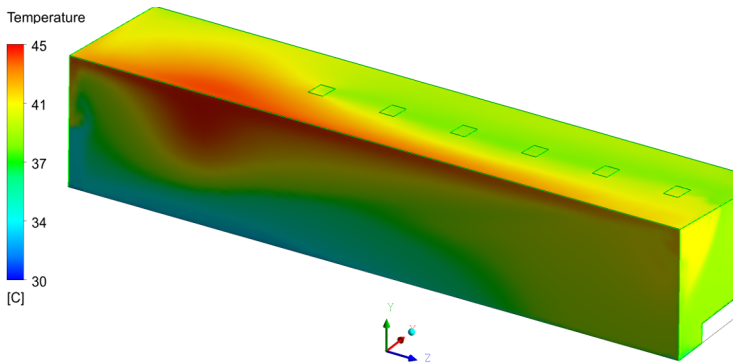
**Fig. 3.** Mass fraction of  $\text{CO}_2$  near the internal surfaces of the walls at fire location 1.



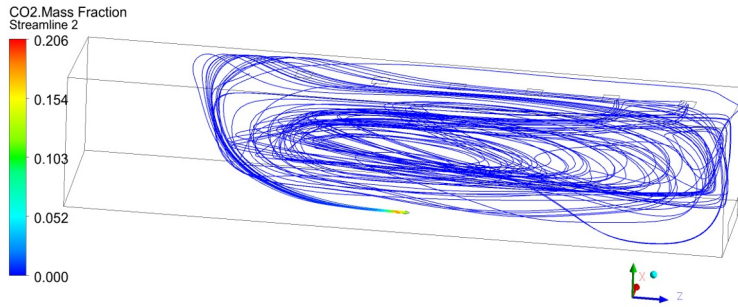
**Fig. 4.** Isothermal surfaces (40, 60, 80, 100, 120 and 150 °C) and vectors, belonging on them at fire location 1.



**Fig. 5.** Streamlines at fire location 1.

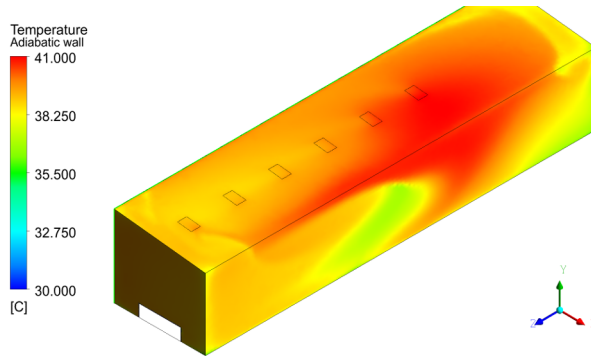


**Fig. 6.** Temperature field of the internal surfaces of the walls at fire location 2.

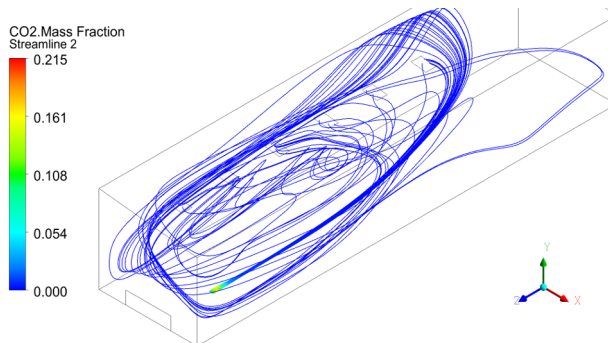


**Fig. 7.** Streamlines, starting from fire location 2, coloured by the mass fraction of CO2.

In the all analyzed cases, the smoke is collected and retained due to the buoyancy in the zones above the smoke vents. Therefore, the chosen positions of the smoke openings are not suitable -they must be located in the highest parts of the roof and have to be evenly distributed along the length of the building.



**Fig. 8.** Temperature field of the internal surfaces of the walls at fire location 3.



**Fig. 9.** Streamlines, starting from fire location 3, coloured by the mass fraction of CO2.

## 4 Conclusions

The proposed concepts for modeling and numerical simulations allow analyses of different fire scenarios in buildings, changing the fire locations, solid material quantity and compositions, and organization of forced ventilations. For proper analyses, the simulations must be done at a pre-estimated maximal burning rate of the materials.

The results allow assessments of the efficiency of the vents position and ventilation mode, and determinations of suitable arrangements of the combustible solids in the storage halls.

The thermal load analyses of the building envelope at different fire scenarios enable proper choice of the materials for the internal layers of the walls.

This study has been financially supported by the project BG05M2OP001-1.001-0008: National Centre of Mechatronics and Clean Technologies, funded by Operational Programme for Science and Education for Smart Growth at EU Funds.

## References

1. V. Dréan, B. Girardin, E. Guillaume and T. Fateh, *Fire and Materials* **47**, 7, 839-856 (2019)
2. K.B. Mcgrattan, *Fire Safety Science*, **8**, 53-68 (2005)
3. A.C.Y. Yuen, G.H. Yeoh, R.K.K. Yuen and T. Chen, *Procedia Engineering*, **52**, 3-12 (2013)
4. Z. Vass, A.B. Şimon-Marinică and S. Stănilă, *MATEC Web of Conferences, EDP Sciences*, 305, 00024, (2020)
5. W.K.Chow, C. L. Chow, and S. S. Li, *Modelling and Simulation in Engineering*, **2011**, Article ID 781252 (2011)
6. K. Prasad, R. Kramer, N. Marsh, M. Nyden, T. Ohlemiller and M. Zammarano, Fire research division, BFRL, NIST annual fire conference (2009)
7. A. Rahmani and M. Salem, *Electron J Gen Med*. 2020, **17** (3), em200 (2020)
8. K. McGrattan, S. Hostikka, R. McDermott, J. Floyd, C. Weinschenk, and K. Overholt, *Fire dynamics simulator - Technical reference guide*, Volume 1: Mathematical model, NIST special publication, **1018 (1)**, (2013)
9. *ANSYS Release 16* - © SAS IP, Inc. (2016)
10. S. Deliev, V. Iliev, M. Hristova, N. Penkova, *Proceedings of XXIII scientific conference with international participation FPEPM 2018*, 138-144 (2018)
11. I. Kassabov and L. Zashcova, *Technical thermodynamics and thermal techniques*, (in Bulgarian), Martilen (1991)
12. Bulgarian regulation No 1h 1971/2009 on building/technical regulations and fire safety standards (2018)
13. G.A. Kristanto and H. Wijaya, *IOP Conference Series: Earth and Environmental Science*, **195 (1)**, 012056 (2018)

# Verification and validation of a CFD model of a fixed regenerator for heat recovery from air

Angel Penev<sup>1,\*</sup>, Lyubomir Tsokov<sup>1</sup>, and Momchil Vassilev<sup>1</sup>

<sup>1</sup>Technical University of Sofia, Thermal and Refrigeration Engineering Department, Sofia, Bulgaria

**Abstract.** The article presents verification and validation of a numerical model of conjugated heat and mass transfer processes and aerodynamics in a fixed "honeycomb" type regenerator with square channels for heat recovery from the exhaust air of a local ventilation system. The processes in the regenerator are simulated by the CFD method. The influence of the processes of condensation and evaporation of moisture in the humid air on the efficiency of the regenerator has been investigated through these simulations and is shown in the article. The calculations of the fixed regenerator's thermal efficiency and pressure losses are made by known analytical models and the results are compared with those of the numerical model. The article compares the model simulation results with experimental data and data from reference sources.

## 1 Introduction

Regenerative heat exchangers are often used to recover heat from the exhaust air to the supply air in ventilation and air conditioning systems. A wide range of regenerators is available on the market in terms of operating mode, geometry, and heat storage material. Standardized tests are used to determine the parameters of the air flows and the thermal efficiency of the regenerators. These tests use stationary conditions - constant temperatures, humidity, and flows. Usually, the duration of the regeneration cycle is chosen by the manufacturers. The regenerative heat exchangers, built into the air conditioning units, operate under not constant conditions. In such devices, the parameters of hot and cold airflow vary depending on the climate and conditions in the room. This unbalances the operation of the heat exchanger and affects its efficiency, which is evidenced by measurements performed on-site and published in various articles, [1-3]. Mathematical modeling and numerical simulation under different conditions and durations of the regenerator cycle can be used to study and analyze the operation of such regenerators. The tasks that can be solved by using sufficiently accurate and flexible models of such heat exchangers are important for the optimization of the devices in which these regenerators are mounted.

The article presents the verification and validation of a new CFD model of a fixed bed regenerator, [4]. The accuracy of the model is shown and a comparison is made with the results of well-known methods for calculating such regenerative heat exchangers. The

---

\* Angel Penev: [gartz@tu-sofia.bg](mailto:gartz@tu-sofia.bg)

comparison allows evaluating the possibilities of these methods to be used in the design of regenerators operating in similar conditions.

## 2 Methods statement

### 2.1 Analytical method

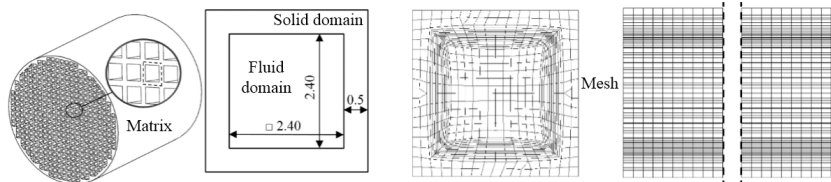
The paper uses the well-known analytical method to determine the efficiency of the regenerator – the “ $\Lambda$ -II” method developed by Hausen, [5, 6]. The “ $\Lambda$ -II” method is specifically aimed at fixed regenerators with periodic mode, which correspond to the dimensionless variables “ $\Lambda$ ” for reduced length and “II” for the reduced period. This method allows the evaluation of the efficiency of the regenerator with engineering accuracy in the operation of the regenerator with dry air. It is obtained on the basis of solutions of simplified one-dimensional differential models of the processes, with constant average thermophysical properties of the air and the matrix. The average values of the heat transfer coefficient between the matrix and the hot and cold air flows participate as parameters in the equations of the analytical model. They are calculated by appropriate criterion equations for the Nusselt number, [7-9].

### 2.2 Numerical method

For the computer simulations, a physical-mathematical model of a fixed regenerator with a counterflow arrangement was used. The model describes a complex transient conjugate process of heat and mass transfer. It can be used for moist air with and without processes of condensation and evaporation on the surface of the wall of the matrix channel, but without fog formation in the flow, [10, 11]. To solve the system of differential equations, the CFD method was used, namely the Finite Volume Method, [12]. The numerical procedure was implemented through the ANSYS - Fluent software, [13].

#### 2.2.1 Geometry and mesh

The adiabatic symmetry of the matrix allows being reduced to a single channel with the half-thickness of its walls, Fig.1. The front surfaces of the solid walls are also assumed to be adiabatic. The fine mesh contains 1 880 855 nodes and 439 560 elements, recommended for the correct Courant number. The setup for meshing is “inflation” with connections between solid domain and fluid domain. This mesh is recommended for Eulerian wall film model. The number of time steps is 0.01.



**Fig. 1.** The matrix, computational domains and mesh.

#### 2.2.2 Algorithm of the model

The algorithm of the computerized model provides automatic switching of the heating and cooling periods to reach a quasi-steady-state solution, Fig.2. The flow is laminar.

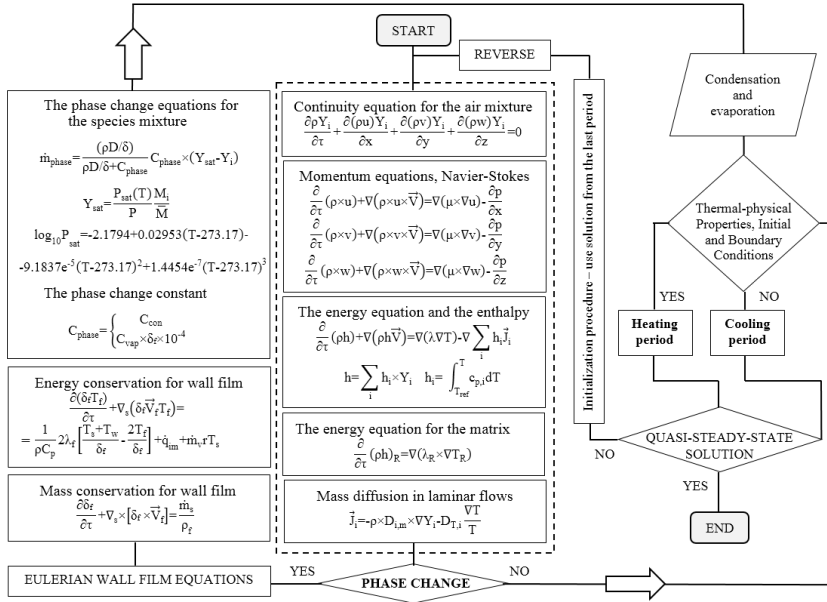


Fig. 2. Algorithm of the new CFD model.

The descriptions of the variables from the system equations are given in Table 1.

Table 1. Nomenclature of the numerical model.

Variable	Descriptions and dimensions, [unit]
$V, u, v, w$	vector of the velocity of the airflow and its orthogonal projections, [m/s]
$\rho, \lambda, c_p, \mu, d$	density, [kg/m <sup>3</sup> ], thermal conductivity, [W/m.K], heat capacity at p=const, [J/kgK], and dynamic viscosity, [N.s/m <sup>2</sup> ], specific humidity, [g/kg]
$\rho_r, \lambda_r, c_r$	density of the regenerator matrix, [kg/m <sup>3</sup> ], thermal conductivity of the regenerator, [W/m.K], and heat capacity of the regenerator, [J/kgK]
$Y_i$	mass fraction for i-th species, [kg <sub>i</sub> /kg <sub>mixture</sub> ]
$J_i$	mass diffusion flux for laminar flow, [kg/m <sup>2</sup> s]
$D, D_{i,m}, D_{T,i}$	mass diffusion coefficient, mass diffusion coefficient for i-th species and thermal mass diffusion coefficient, [m <sup>2</sup> /s]
$P_{sat}, P$	saturation pressure and absolute pressure, [Pa]
$T, T_r, T_s, T_f$	temperature of the flow, temperature of the regenerator, temperature of the film, average temperature of the film, [K] or [°C]
$\delta, \delta_f$	distance from the grid cell center to the wall and the film height, [m]
$M_i, M$	molecular weight of the vapour species and the mixture, [kg/kmol]
$\dot{m}_{phase}, \dot{m}_s, \dot{m}_v$	rate of phase change, rate of mass source per unit wall area due to droplet collection, mass rate of the evaporation and the condensation, [kg/m <sup>2</sup> s]
$h, h_r$	specific enthalpy of the species mixture and the regenerator, [J/kg]
$C_{phase}, C_{con}, C_{vap}$	phase change constant, condensation constant and evaporation constant
$\dot{q}_{im}$	source term due to liquid impingement from the bulk flow to the surface
$r, q$	latent heat associated with the phase change, [J/kg], heat flux, [W/m <sup>2</sup> ]



### 2.2.3 Initial and boundary conditions

The boundary conditions of the heat transfer between the airflow and the regenerator's matrix are as follow:

$$T_w = T_{r,w} \quad (1)$$

where:  $T_w, T_{r,w}$  are the temperatures of the air and the matrix on the surface of the channel.

The simulation starts from the state of heat-mass equilibrium:

$$T_r(x,y,z,0) = T(x,y,z,0) = T_o, \quad Y_{wv}(x,y,z,0) = Y_{wv,o} \quad 0 \leq x \leq L \quad (2)$$

For each flow switching, the temperature field in the regenerator and the air at the end of the heating or cooling half-cycle period are saved and set as the initial condition for the next half-period. The process of periodic heating and cooling of the matrix continues until reaching a quasi-steady-state solution. The time required to switch is negligibly small.

$$T_{r,h}(x, y, z, \tau_h) = T_{r,c}(x, y, z, \tau_{h,0}=0) \quad T_{r,h}(x, y, z, \tau_{h,0}=0) = T_{r,c}(x, y, z, \tau_c) \quad (3)$$

The boundary conditions have periodic-flow conditions with constant inlet parameters during the heating/cooling period.

$$T_h(0,y,z, \tau_{h,\tau}) = T_{h,i} \quad Y_{wv,h}(0,y,z, \tau_{h,\tau}) = Y_{wv,h,i} \quad u_{i,h}(0,y,z, \tau_{h,\tau}) = u_{i,h} \quad 0 \leq \tau \leq \tau_h \quad (4)$$

$$T_c(L,y,z, \tau_{c,\tau}) = T_{c,i} \quad Y_{wv,c}(L,y,z, \tau_{c,\tau}) = Y_{wv,c,i} \quad u_{i,c}(L,y,z, \tau_{c,\tau}) = -u_{i,c} \quad 0 \leq \tau \leq \tau_c \quad (5)$$

where:  $u$  is the velocity of the flow  $x=0$  and  $x=L$ , m/s; subscripts "i" and "o" – inlet and outlet; subscript "m" indicates the average value for the flow and "τ" indicates the current moment of the period; subscripts "c" and "h" indicate cold and hot flow and „wv" indicates water vapour of mass fraction; "i" – sequence number of the cycle.

### 2.2.4 Values of the initial and boundary conditions

Equal initial temperatures of the regenerator and the air in the channel  $T_o = T_r = T = 0^\circ\text{C}$  are set zero,  $T_o = T_r = T = 0^\circ\text{C}$ . The outlet gauge pressure during the heating and cooling period is zero,  $p = 0$  Pa. Constant inlet temperatures during the heating and cooling period are  $T_{h,i} = 20^\circ\text{C}$  and  $T_{c,i} = 0^\circ\text{C}$ . Constant inlet mass fractions of water vapour during the heating and cooling period are  $Y_{h,i} = 0.00321$  and  $Y_{c,i} = 0.00213$ , which simulate dry conditions with approximately indoor relative humidity 25% and outdoor relative humidity 53%. The equal durations of the two half-periods are  $\tau_h = \tau_c = 90\text{s}$ .

### 2.2.5 Physical properties of air and honeycomb matrix

The average physical properties of the humid air at absolute pressure  $p = 94659$  Pa for the temperature range of  $0.0 \leq T \leq 20.0$  and the inlet humidity range of  $2.14 \leq d \text{ g/kg} \leq 11.7$  and the thermal properties of ceramic materials are shown below in Table 2.

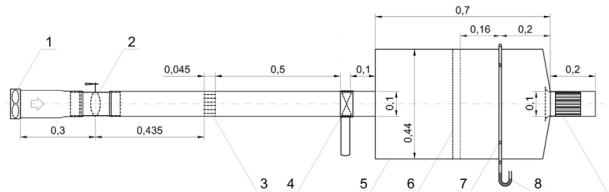
**Table 2.** Thermal properties of the air and matrix materials.

Name / Unit	$\rho$ , kg/m <sup>3</sup>	$c_p$ , J/kgK	$\lambda$ , W/mK	$\mu$ , Pa.s
Humid Air	$\rho = p/RT$	$c_p = 1010$	$\lambda = 0.02517$	$\mu = 1.676e-5$
Water Vapour	$\rho = p/RT$	$c_p = 1896$	$\lambda = 0.01721$	$\mu = 9.461e-6$
Water Liquid	$\rho = 999$	$c_p = 4196$	$\lambda = 0.5803$	$\mu = 1.306e-3$
Dense Cordierite	$\rho_r = 2100$	$c_r = 900$	$\lambda_r = 1.5$	-
Ceramic – NiCrBSi	$\rho_r = 2107$	$c_r = 495$	$\lambda_r = 5.7$	-

## 2.3 Experimental equipment

### 2.3.1 Aerodynamic characteristics test bench

A test bench complying with the requirements of the AMCA 210 standard (ISO 5801) is used to measure the aerodynamic characteristics of the regenerator - flow rate and pressure drop, [14]. A drawing of the test bench is presented in Fig.3.

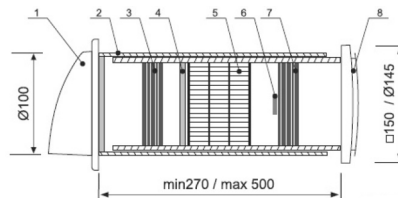


**Fig. 3.** The test bench for regenerator pressure drop measurement.

The airflow through the channel of the test bench is induced by fan 1. The value of the airflow can be set by the control valve 2 and after passing the airflow rectifier 3 is measured with an anemometer 4, with an accuracy of  $\pm 3\%$ . The pressure drop through the regenerator 9 is measured at position 8 with a differential pressure gauge to within  $\pm 1\%$ .

### 2.3.2 Thermal efficiency test equipment

The air handling unit for heat recovery from the exhaust air is shown in Fig.4. The ventilation device consists of two fans, position 3 for the exhaust fan and position 7 for the supply fan, and the ceramic matrix of the regenerator, position 5. The dimensions of the matrix are diameter  $\varnothing 93$  mm, length 99 mm, and square channels 2.4mm x 2.4mm with wall thickness around 1 mm.



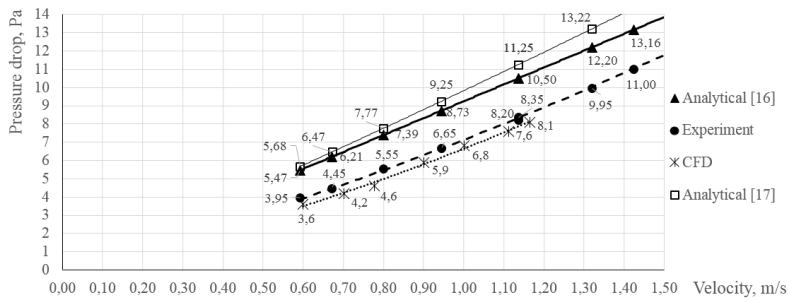
**Fig. 4.** The regenerative device for heat recovery from air: 1 – outdoor grid, 2 - thermally insulated air duct, 3 – exhaust fan, 4 – filters, 5 – matrix, 6 – ionizer, 7-supply fan, 8 – indoor grid.

In order to experimentally determine the thermal efficiency of the regenerator, the device was mounted in a wall separating two spaces with different air temperatures, [15]. The air temperature in the low-temperature volume is not kept constant. For this reason, in the process of the experiment, the inlet temperature of the cold flow increases very smoothly due to the exchange of air between the two spaces. Temperatures are measured with low inertia temperature sensors. The time step in the temperature measurement is 0.5s.

## 3 Results

### 3.1 Assessment of the aerodynamic

This section compares the aerodynamic characteristics of the regenerator, obtained in three different ways - known analytical equations [16, 17], numerical results from computer simulations, and experimental measurements described above. The results for the pressure drop in the regenerator depending on the airflow rate, obtained in the three ways, are presented in the graph in Fig.5.



**Fig. 5.** Correlations of the pressure drop vs the flow rate of the regenerator

The error of the analytical correlations with respect to the result of the experiment reaches 50% for the low flow rates. The difference between the results of the CFD calculations and the experimental data at the same flow rate is minus 9%, but the CFD solution does not include local pressure losses at the inlet and outlet of the matrix. The analytical solutions include all pressure losses in the channel.

### 3.2 Assessment of the thermal efficiency

In this section, a comparison is made of the values of thermal efficiency of the regenerator, obtained by three different methods - analytical, numerical, and experimental. The evaluation of the thermal efficiency by all three methods refers to the operation of the regenerator with humid air, but without the occurrence of phase transition processes in the channels of the matrix.

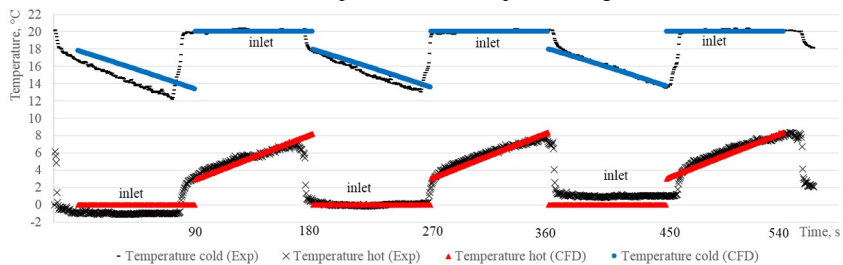
The physical properties of the regenerative matrix were selected from reference data by the measured value of the dense cordierite density (Table 2).

Experimental thermal efficiency data were obtained for an unbalanced regenerator. The velocities of unbalanced airflows in the matrix during the half-periods are:

$$u_{i,h}(0,y,z, \tau_{h,\tau}) = u_{i,h} = 0.6 \quad 0 \leq \tau \leq 90 \quad (6)$$

$$u_{i,c}(L,y,z, \tau_{c,\tau}) = -u_{i,c} = -0.5 \quad 0 \leq \tau \leq 90 \quad (7)$$

The inlet and outlet temperatures on both sides of the regenerator, obtained as a result of the numerical simulations and the experiment, are compared in Figure 6.



**Fig. 6.** Flow temperature curves on both sides of the regenerator

The visual comparison of the temperature curves shows a very good match. It can be seen that the difference between the amplitudes of the temperature curves is due to the slow increase in the inlet temperature of the cold flow, as noted in section 2.3.2. The discrepancy of the curves over time is due to the fact that the switching of the flows in the experiment is not instantaneous.

The calculated values of thermal efficiency by the three methods (analytical, numerical, and experimental) are shown on the bar chart in Fig.7.



Fig. 7. Bar diagram of thermal efficiency

The bar chart shows three different values of thermal efficiency, calculated by "Λ-Π" method for three different values of the Nusselt number, obtained from three equations for laminar flow in a channel, of Hausen ( $Nu = 3.76$ ), Perkins ( $Nu = 3.61$ ), Shah and London ( $Nu = 3.19$ ), where the values of  $Nu$  are averaged over the two heating and cooling half-periods.

### 3.3 Influence of phase change on the thermal efficiency

The influence of the phase transition processes in the matrix channels on the regenerator efficiency was evaluated approximately by upgrading the validated model and under the same boundary conditions as in section 2.2.3 with several differences. The differences are in the thermal properties of ceramic NiCrBSi (Table 2), the inlet velocities ( $u_{i,h} = u_{i,c} = 0.7$ ), and the mass fraction of the water vapor of the exhaust air, which corresponds to a relative humidity of the air in the room 73%.

$$Y_{wv,h}(0,y,z, \tau_{h,\tau}) = Y_{wv,h,i} = 0.0116 \quad 0 \leq \tau \leq 90 \quad (8)$$

$$Y_{wv,c}(L,y,z, \tau_{c,\tau}) = Y_{wv,c,i} = 0.00213 \quad 0 \leq \tau \leq 90 \quad (9)$$

Under these conditions, there is no water accumulation in the periods and the condensate was completely evaporated during the cooling period.

The inlet and outlet temperatures on both sides of the regenerator, obtained as a result of the numerical simulations with and without phase change of the moisture in the matrix channel, are compared in Figure 8.

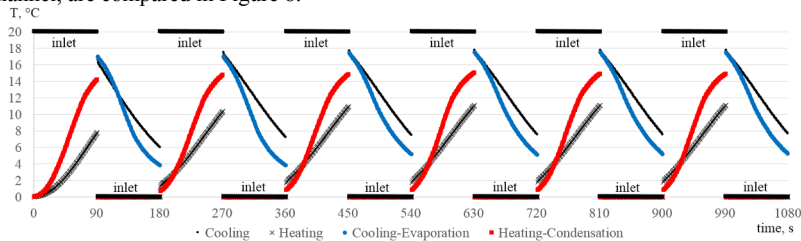


Fig. 8. Flow temperature curves on both sides of the matrix for air with and without phase change.

Condensation and evaporation processes under these conditions reduce the thermal efficiency of the regenerator from 67.8% to 58.2%. This decrease is due to the complex heat and mass transfer in the matrix channels and the different heat transfer coefficients, which the existing analytical methods cannot take into account. It should be noted that the validation of the simulation results with the presence of a phase transition has not been performed. The differential mathematical model used does not include the formation of fog in the airflow, but allows an increase in relative humidity above 100%, simulating supersaturated vapour. The used computational model was verified by comparing the results of simulations with similar ones from the article, [18].

## 4 Conclusion

A CFD model of fixed matrix regenerative heat exchanger for decentralized ventilation for humid air with and without water vapour condensation on the wall of the channels is presented. The article shows that the CFD model of the processes in the regenerator significantly surpasses the analytical models not only in terms of the range of boundary conditions, but also in terms of accuracy. The computational model was tested by analytical solutions and validated by experimental data and it was found that the results of the simulation for humid air without condensation and evaporation are quite accurate and reliable. The results of simulations with the phase change in the channels are not validated but the model is verified with similar solutions. They are indicative and show that the reduction in thermal efficiency under the boundary conditions used is about 10% and depends on the thermal properties of the regenerator's material, [19].

This article is subject of the study of the author's PhD dissertation.

## References

1. A. Mikola, R. Simson, J. Kurnitski, *Energies*, **12**(13), 2633, (2019).
2. A. Merzkirch, S. Maas, F. Scholzen, D. Waldmann, *The 45. International HVAC&R Congress, Zbornik Međunarodnog kongresa o KGH*, **45**(1), (2017).
3. A. Penev, L. Tsokov, *6th International Symposium on Environment-Friendly Energies and Applications*, IEEE, **116**(6), pp. 154-159, (2021).
4. W. L. Oberkampf, T. G. Trucano, *Prog. Aerosp. Sci.*, **38**(3), pp. 209-272, (2002).
5. H. Hausen, *Heat Transfer in Counterflow, Parallel Flow and Cross Flow*, McGraw-Hill Book Company, (1983).
6. K. Thulukkanam, *Heat exchanger design handbook*, CRC press, (2013).
7. R. K. Shah, A. L. London, *Laminar flow forced convection in ducts: a source book for compact heat exchanger analytical data*, Academic press, (2014).
8. W. H. Mcadams, *Heat Transmission: 3d Ed.*, McGraw-Hill, (1954).
9. A. Penev, L. Tsokov, *The Scientific Journal of BulCToMM, Varna*, **124**, (2020).
10. A. Penev, L. Tsokov, N. Penkova, *J. Chem. Technol. Metall.*, **55**(5), (2020).
11. A. Penev, L. Tsokov, *6th International Symposium on Environment-Friendly Energies and Applications*, IEEE, **116**(6), pp. 164-170, (2021).
12. J. D. Anderson, *Computational fluid dynamics. The basic with application*. New York, McGraw-Hill, Inc., (1995).
13. Fluent, *ANSYS Fluent user's guide*, Ansys Inc, (2009).
14. M. Vassilev, L. Tsokov, *XXI Scientific Conference with International Participation FPEPM, Sozopol*, pp. 169-174, (2016).
15. L. Tsokov, N. Kaloyanov, *XX National Scientific Conference with International Participation FPEPM, Sozopol*, pp. 333-337, (2015).
16. R. K. Shah, D. P. Sekulic, *Fundamentals of heat exchanger design*. John Wiley & Sons, (2003).
17. N. Monarkin, S. Lukin, Y. M. Anurov, B. A. Tihomirov, G. A. Agasiant, S. M. Galileev, and T. R. Akhmetov, *IOP Conf. Ser.: Earth Environ. Sci.*, **337**, (2019).
18. M. Nizovtsev, V. Borodulin, V. Letushko, *Appl. Therm. Eng.*, **111**, (2017).
19. A. Penev, L. Tsokov, *E3S Web Conf.*, **207**, 01001, (2020).

# Air-to-water heat pump assessment: Part 1 – Experimental setup

Nadezhda Doseva<sup>1,\*</sup>, Daniela Chakyrova<sup>1</sup>, Svetoslav Stoianov<sup>1</sup>, and Ilia Hadhidimov<sup>1</sup>

<sup>1</sup>Varna Technical University, Heat Technology Department, 9000 Varna, Bulgaria

**Abstract.** This paper is part 1 of the investigation on the exergetic and exergoeconomic parameters of an existing system with an air-to-water heat pump unit as a heat source. Part 1 presents the used experimental setup. The main aim of the conducted experimental tests is to develop a model of produced heat transfer rate and energetic *COP* at different ambient conditions. The obtained data is used in Part 2 of the study where the exergetic and exergoeconomic assessment is carried out. The performance of the considered system is evaluated using Seasonal Exergy Efficiency. Moreover, Part 2 of the study has presented the formulation of the cost of the product, and cost allocation within the heat pump unit based on exergy.

## 1 Introduction

In the reference literature, there is a wide discussion about the performance parameters of air-to-water heat pumps (AWHP). In many studies is conducted experimental and theoretical research on the factors that affected the coefficient of performance (*COP*) of an aerothermal heat pump and consumed electrical energy. For example, Zhao *et al.* [1] conduct the experimental study of an aerothermal heat pump and they establish the influence of the water temperature in the tank on the observed *COP* of the heat pump when the external air temperature remains almost constant.

Morrison *et al.* [2] determined experimentally the consumed electrical energy and instantaneous heat capacity for the considered in cited investigation types of the heat pump system. The experiment is carried out for a range of ambient temperature and relative humidity conditions and the aim of the study is to demonstrate the procedure for seasonal performance rating of air-source heat pump water heaters. Ji *et al.* [3] conduct a laboratory test of an AWHP with the utilization of the rejected heat in cooling mode. The experiment is conducted to validate the developed model of the system's performance. Another part of studies in reference literature deals with experimental and theoretical research of novel air-to-water heat pump systems [4-6].

While many authors are conducting experiments to establish specific dependencies, which characterized air-to-water heat pumps, little is known about necessary output data for the conduction of dynamic exergy and exergoeconomic analysis of a real aerothermal heat pump system. Ozturk *et al.* [7] investigated experimentally an AWHP from the exergy point of view. The objective of the experimental test is to collect the data for the

---

\* Corresponding author: [nadezhda.doseva@abv.bg](mailto:nadezhda.doseva@abv.bg)

thermodynamic properties of the working fluids of the system at specific states and to evaluate the exergy destruction of the system's components at varying ambient conditions.

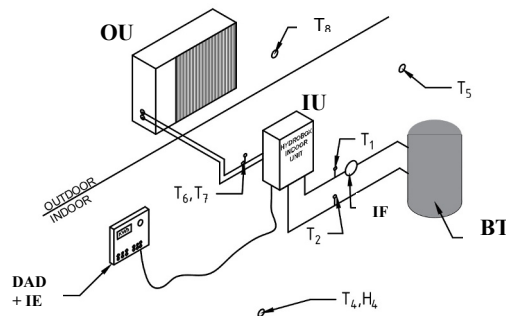
In this regard, the current paper suggests the simplified method for experimental research of an existing AHP system, considering the system as a black-box with defined inputs and outputs. Thus, the used equipment, instruments, and realized measurements are minimized, because the parameters at the internal state of the refrigerant are not necessary to know. The study aims to establish the dependencies between specific system performance parameters (produced heat transfer rate and energetic *COP*) and dynamic changing ambient conditions. The obtained data is used in Part 2 of the study where the exergetic and exergoeconomic assessment is carried out.

## 2 Air-to-water heat pump experimental setup

To determine the electrical energy input to the AHP unit and produced heat transfer rate at different ambient conditions, an air-to-water heat pump experimental platform is developed. The experimental setup consists of instruments for the AHP operating parameters data acquisition and displaying in real-time. The measurements were implemented in the period 09.02-22.02.2020. The general view of the system and schemes of the AHP experimental setup are shown in Figure 1, 2 and 3, respectively.

### 2.1 Description of the equipment and instruments for the AHP operating parameters data acquisition and displaying in real-time

The AHP system (Figure 2) is an existing system located in Varna Technical University, Bulgaria – at the laboratory of the Heat Technology Department. The AHP unit is split type, model PUHZ-SW75VHA(-BS)\ERSC-MEC (Mitsubishi). The heat pump unit is the inverter-driven, reversible type and with a variable outlet (according to the classification of EN 14825:2019). The outdoor (OU) and the ERSC-MEC indoor (IU) units are mounted on both sides of the laboratory's eastern facade. The refrigerant is R410A. The heat transfer medium is a 30% water solution of propylene glycol.



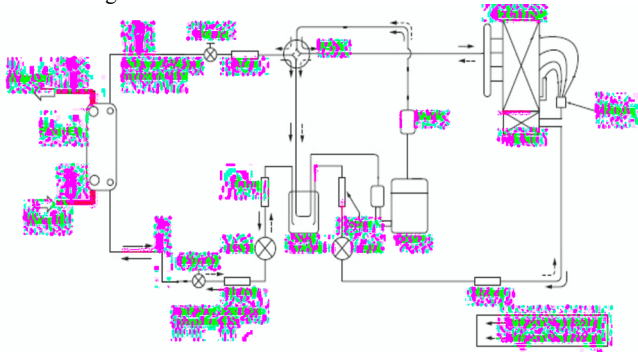
**Fig. 1.** Scheme of the AHP experimental platform: DAD+IE –instruments for data acquisition and displaying in real-time + static single-phase electric meter; BT – buffer tank with 80 litres volume; OU – outdoor heat pump unit; IU - indoor heat pump unit; IF – water flow meter with Hall effect sensor; T<sub>1</sub>, T<sub>2</sub>, ..., T<sub>8</sub> – digital thermometers; H<sub>4</sub> – relative humidity sensor.



**Fig. 2.** General view of the AHP system.

In addition, the AHP system consists of four fan coil units with a nominal heat transfer rate of 5.7 kW (i.e., at the nominal value of logarithmic mean temperature difference  $\Delta T_{nom} = 50\text{ K}$  or at  $75^\circ\text{C}/65^\circ\text{C}/20^\circ\text{C}$ ).

Figure 2 presented the location of the all of the used digital thermometers and equipment. The wire digital thermometers provide from 9-bit to 12-bit Celsius temperature measurements.  $T_1$  and  $T_2$  measure the temperature of the glycol solution inlet and outlet to the indoor unit (i.e., they measure the temperatures  $t_{w,e}$  and  $t_{w,i}$ , respectively). The digital thermometers  $T_1$  and  $T_2$  are mounted on the supply and return pipe - before the buffer tank (BT). The digital thermometers  $T_6$  and  $T_7$  quantify the temperature of refrigerant flows. The scheme of the observed AHP unit and location of the digital thermometers  $T_1$ ,  $T_2$ ,  $T_6$ , and  $T_7$  is presented in Figure 3.



**Fig. 3.** Scheme of the observed AHP unit [8]: HEX - heat exchanger; Comp - compressor; LEV-A and LEV-B - linear expansion valve; REV/V - reversible valve;  $T_1$  and  $T_2$  - digital thermometers measured water-glycol solution temperature;  $T_6$  and  $T_7$  - digital thermometers measured refrigerant temperature



The indoor air temperature is measured in two points: near to the wall ( $T_5$ ) and into the room – through combined humidity and temperature sensor ( $T_4, H_4$ ). The outdoor air digital thermometer ( $T_8 = t_e$ ) is located on the eastern facade of the room, and it is protected from direct solar radiation and wind.

The flow rate of the glycol solution is measured by a single jet, dry dial liquids flow meter with a Hall effect sensor. The flow meter is velocity type, with the impeller mounted in radial position within the body of the flowmeter, whereas the incidence of the liquid flow is tangential. The liquids flow meter is mounted in the circuit of the indoor unit and buffer tank, on the supply water pipe of the system – in a horizontal position. The maximum pressure loss of the liquids flow meter is 0.63 bar (i.e.,  $\Delta p$  63) at volumetric flow rate with value within the interval of the minimal ( $Q_1=40$  l/h) and permanent flow rate ( $Q_3=4$  m<sup>3</sup>/h). Therefore, the measuring range of the liquids flow meter is  $Q_3 / Q_1 = 100$  (R100-H). The declared maximum permissible error (MPE) on volumes between the minimum flow rate ( $Q_1$ ) and the transitional flow rate ( $Q_2 = 64$  l/h) is  $\pm 5\%$ , whereas on volumes between the transitional flow rate ( $Q_2 = 64$  l/h) and the overload flow rate ( $Q_4 = 5$  m<sup>3</sup>/h) the declared MPE is  $\pm 3\%$ . The temperature range of the flow meter is  $30\div 90^\circ\text{C}$ .

The consumed electrical energy from the AWHP unit and the auxiliary elements is measured through the static electric meter. It is designed for the measurement and registration of active energy in single-phase two-wire networks for direct connection. The rated voltage of the electric meter is 230V and the basic (reference) current is  $I_b = 10$  A. The electric meter has a built-in LED indicator, reproduces a pulse with a width of 40ms when it read 1Wh electrical energy. The electrical pulse enters the instruments for data acquisition and displays in real-time.

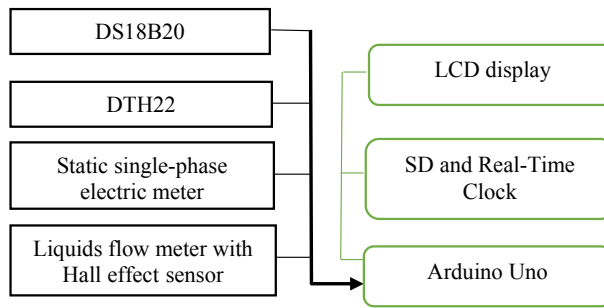
The accuracy and tolerance of the used types of equipment are summarized in Table 1.

**Table 1.** The accuracy and tolerance of the used equipment.

Equipment	Symbol	Declared accuracy	Full scale	Model
Digital thermometers	$T_1, T_2, T_3, T_5, T_6,$ and $T_7$	$\pm 0.1^\circ\text{C}$	$-10^\circ\text{C} \div 85^\circ\text{C}$	DS18B20
Combined digital thermometer and humidity sensor	$T_4, H_4$	Humidity: $\pm 2\%$ ; Temperature: $\pm 0.5^\circ\text{C}$	Humidity: $0\% \div 100\%$ Temperature: $-10^\circ\text{C} \div 85^\circ\text{C}$	DHT22
Liquids flow meter with Hall effect sensor	IF	$\pm 3\%$ at $64 \text{ l/h} < Q < 5 \text{ m}^3/\text{h}$ $\pm 5\%$ at $40 \text{ l/h} < Q < 64 \text{ l/h}$	$40 \text{ l/h} \div 4 \text{ m}^3/\text{h}$	B-METERS GSD8-RFM
Static single phase electric meter	IE	$\pm 2\%$ at $0.1I_b < I < I_{\max}$	$0.5 \text{ A} \div 85 \text{ A}$ $0.8U_n \div 1.25U_n$	ISKRA ME161

The system for data acquisition and displaying in real-time is based on the Arduino UNO platform, consisting of an 8-bit AVR microcontroller. A schematic diagram of the system is shown in Figure 4. The system consists of the following additional elements:

- SD and Real-Time Clock – this module can record data on an SD card, while the clock acquisition data about time and date;
- 16x2 LCD display and keyboard - the module is used for displaying the data in real-time. It allows the selection of visualization of another operation parameter using the keys on the keyboard.



**Fig. 4.** Scheme of the system for data acquisition and displaying in real-time.

The measured parameters were recorded every 1 minute. The ultimate operating parameters are the average statistics for the 30 minutes.

## 2.2 Identifying the outliers

In the current paper, for outliers filtering is used Chauvenet's criterion. To identifying the outliers, first, the data is grouped according to the outside air temperature,  $t_e$ . Within the  $i$ -th external air temperature bin,  $t_e \pm 0.5^\circ\text{C}$ , it is observed  $n$  measurements of  $x_i$  ( $i = 1, 2, \dots, n$ ) that have a mean,  $\bar{x}$ , and sample standard deviation,  $S$ . From point of view of Chauvenet's criterion, the measurements that should be rejected are those that have the probability of obtaining their deviation from the mean is less than  $1/(2n)$ . This statement is expressed by the equation [9]:

$$if \left| \frac{x_i - \bar{x}}{S} \right| < \tau_{max}, \text{ then reject } x_i \quad (1)$$

The maximum acceptable normalized deviation,  $\tau_{max}$ , for various values of the number of measurements ( $n$ ) is determined according to the look-up table [10].

In equation (1), the terms mean,  $\bar{x}$ , and sample standard deviation,  $S$ , are determined as follow [10]:

$$\bar{x} = \frac{x_1 + x_2 + \dots + x_n}{n} = \sum_{i=1}^n \frac{x_i}{n} \quad (2)$$

$$S = \sqrt{\frac{\sum_{i=1}^n (x_i - \bar{x})^2}{(n-1)}} \quad (3)$$

## 2.3 Uncertainty analysis

After the outliers were identified and rejected, the uncertainty analysis of the obtained mean values was conducted. The current experimental measurements aim to establish the mathematical models of the produced heat power and energetic  $COP$  of the observed AWHP. Consequently, the objective of this analysis is to assess the translation of the uncertainties from the individual measurement into the uncertainty in the final results for  $Q$  and  $COP$  at an external air temperature bin,  $t_e \pm 0.5^\circ\text{C}$ .

In the current paper, the data from individual measured variables  $x_1, x_2, \dots, x_n$  are combined to determine the final results for  $Q$  and  $COP$ . Therefore, the systematic uncertainty of the mean values of the parameter  $R$  is determined through the conceptual basis of the root of the sum of the squares [10]:

$$B_R = \left\{ \sum_{i=1}^N \left( B_i \frac{\partial R}{\partial x_i} \right)^2 \right\}^{1/2} \quad (4)$$

According to the equation (4), the systematic uncertainty of the mean values of the  $Q$  and  $COP$  is:

$$B_Q = \left[ \left( B_V \frac{\partial Q}{\partial V} \right)^2 + \left( B_{T_{wi}} \frac{\partial Q}{\partial T_{wi}} \right)^2 + \left( B_{T_{we}} \frac{\partial Q}{\partial T_{we}} \right)^2 + \left( B_{\rho} \frac{\partial Q}{\partial c_p \rho} \right)^2 \right]^{1/2} \quad (5a)$$

$$B_{COP} = \left[ \left( B_V \frac{\partial COP}{\partial V} \right)^2 + \left( B_{T_{wi}} \frac{\partial COP}{\partial T_{wi}} \right)^2 + \left( B_{T_{we}} \frac{\partial COP}{\partial T_{we}} \right)^2 + \left( B_{c_p} \frac{\partial Q}{\partial c_p \rho} \right)^2 + \left( B_{W_{el}} \frac{\partial COP}{\partial W_{el}} \right)^2 \right]^{1/2} \quad (5b)$$

In equations (5a) and (5b) the partial derivatives  $\partial Q / \partial \rho c_p$  and  $\partial COP / \partial \rho c_p$  are involved because they are not considered as a constant when the temperature of the water-glycol solution vary. The similar approach is used in [11]. It is important to note, that the volumetric flow rate,  $V$ , temperatures of the heat transfer medium,  $T_{we}$  and  $T_{wi}$ , and electrical power,  $W_{el}$ , were determined from the measurements. The physical properties of the water-glycol solution, such as density,  $\rho$ , and specific heat capacity,  $c_p$ , were taken from a table. Moreover, each partial derivative  $\partial R / \partial x_i$  was calculated by using the average values of the measured parameters. The systematic uncertainties of the measurements of the volumetric flow rate ( $B_V$ ), temperature ( $B_{T_{wi}}$  and  $B_{T_{we}}$ ), and electrical power ( $B_{W_{el}}$ ) are presented in Table 1. The accuracies of the readings of the  $c_p$  and  $\rho$  are  $\pm 1$  kJ/(kgK) and  $\pm 0.01$  kg/m<sup>3</sup>, respectively [11].

The results from the systematic uncertainty estimation of the results for  $Q$  and  $COP$  are presented in Table 2. The  $B_{COP}$  decreases with the outdoor temperature increasing. Moreover, the consumed electrical power decreasing gives rise to a decline in the systematic uncertainty of  $COP$ . A similar result is reported in [11]. Therefore, the partial derivative  $\partial COP / \partial W_{el}$  and accuracy of the electrical energy measurements have a major contribution to the results for  $B_{COP}$ . Contrarily, there is no clear tendency in the variation of  $B_Q$ . It can be concluded that the systematic uncertainty in the  $Q$  is around 12% when the external air temperature is in the range of 2.03°C to 11.13°C. The noticeable slight increases in  $B_Q$  can be explained by the fact that at certain values of the outside air temperatures (for example,  $t_e = 3.07^\circ\text{C}$ ,  $t_e = 5.06^\circ\text{C}$ ,  $t_e = 5.99^\circ\text{C}$ , and  $t_e = 7.9^\circ\text{C}$ ) the difference in the temperature of the heat transfer medium in the supply and return pipe decreases due to the slight increase in the flow rate.

**Table 2.** Results from systematic uncertainty estimation of the mean values of the  $Q$  and  $COP$ .

Average external air temperature	Systematic uncertainty of COP	Systematic uncertainty of Q	Mean COP	Mean Q, kW $\pm\%$
$t_e$ [°C]	$B_{COP}$	$B_Q$		

2.03	0.0708	0.1208	2.421±7.1%	4.58±12.1
3.07	0.0849	0.1241	2.475±8.5%	4.42±12.4
4.03	0.0924	0.1198	2.727±9.2%	4.30±11.98
5.06	0.0889	0.1238	2.858±8.9%	4.07±12.4
5.99	0.1041	0.1247	3.237±10.4%	3.90±12.5
7.00	0.1183	0.1241	3.461±11.8%	3.68±12.4
7.90	0.1292	0.1242	3.477±12.9%	3.35±12.4
8.99	0.1507	0.1222	3.548±15.1%	2.90±12.2
9.92	0.1548	0.1217	3.505±15.5%	2.73±12.2
11.13	0.1487	0.1168	3.406±14.9%	2.65±11.7
11.78	0.1636	0.1098	2.804±16.4%	2.10±10.98

### 3 MATHEMATICAL MODELS OF THE PRODUCED HEAT POWER AND ENERGETIC COP

As a result of collecting experimental data of the AHP system, the experimental modeling of the produced heat transfer rate and energetic COP was carried out. These models are used as input data in Part 2 of the current investigation where the exergy and exergoeconomic assessment of the system is conducted.

The prediction of the produced heat transfer rate by the AHP was implemented using linear regression of the experimental data. The measured mean values of the heat output rate were plotted as a function of external air temperature (Figure 5) and the obtained linear relationship is:

$$Q_i = -0.2495 \cdot t_e + 5.2602, \text{ kW} \quad (6)$$

To define the operating modes of the considered AHP system, it is assumed that up to a certain external air temperature, the heat pump unit produces heat output that fully satisfies the requirements for the heating of the building. At this external air temperature (called bivalent temperature), the partial load ratio,  $PLR = Q/Q_{max}$ , of the AHP unit is equal to 1. Otherwise, at outdoor air temperature equal to the balance temperature,  $PLR$  is zero. Then, at  $PLR = 0$  the heat loss of the building is equal to the internal and external heat gains.

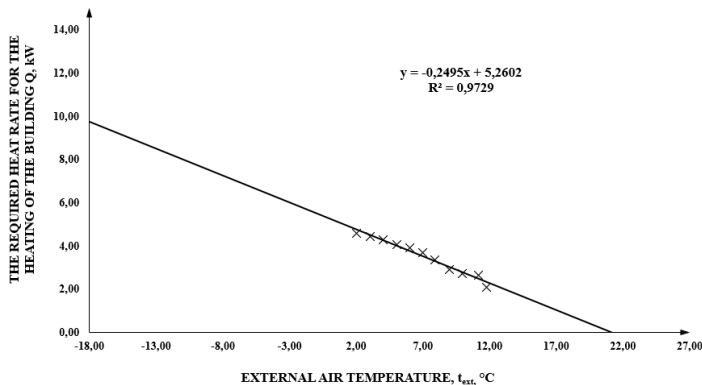


Fig. 5. Produced heat power by the AHP as a function of external air temperature.

Conducting a two-dimensional linear regression of the data for produced heat transfer rate at maximum inverter frequency,  $Q_{max,i}$ , is obtained the equation:

$$Q_{max,i} = 14.781 + 0.18175 \cdot t_e - 0.15908 \cdot t_{w,e}, \text{ kW} \quad (7)$$

During the period of the experimental measurements, it was not observed conditions lead to the operation of the AWHP at maximum inverter frequency. As a result, the data for  $Q_{max}$  is according to the technical documentation of the unit [8].

According to the equations (6) and (7), the partial load ratio can be expressed as :

$$PLR = Q_i / Q_{max} = \frac{-0.2495 \cdot t_e + 5.2602}{14.781 + 0.18175 \cdot t_e - 0.15908 \cdot t_{w,e}} \quad (8)$$

Therefore, from equation (7) can be state that the current AWHP system is characterized by the bivalent temperature  $t_{biv} = -5.73^\circ\text{C}$  (at  $PLR = 1$ ) and the balance temperature is around  $t_{balance} = 21.08^\circ\text{C}$  (at  $PLR = 0$ ). The analysis of the technical data suggests that the AWHP will operate in on-off cycles when the  $PLR$  is less than 0.29 or at an external air temperature higher than  $8.99^\circ\text{C}$ .

From Table 2 it can be seen that at external air temperatures higher than  $t_{on-off} = 8.99^\circ\text{C}$ , the mean values of COP slightly decrease. A significant drop is designated at  $t_e = 11.78^\circ\text{C}$  (Table 2). These results can be explained by the on-off cycling energy losses. Moreover, in a previous study [12] was established that the electrical consumption during the on-off operation mode might exceed 12% of the overall electric energy consumed by the system due to the on-off cycling losses. The authors [12] supplement that these results are observed when an AWHP is sized to cover a large fraction of the design building peak load and the volume of the thermal storage is small. These prerequisites are present in the current case.

As a result of a limited number of measurements at outdoor external air temperatures higher than  $8.99^\circ\text{C}$ , the on-off operation mode of the AWHP unit is not considered in the current paper and the followed exergetic and exergoeconomic analyses.

In conclusion, within the interval of values of the external air temperature  $t_e = -5^\circ\text{C} \div 8^\circ\text{C}$ , the AWHP will operate in partial load, and it will fully satisfy the requirements for the heating of the building, i.e.  $Q_i = Q_{building,i}$ . At external air temperature equals  $-5.73^\circ\text{C}$ , the AWHP will operate at maximum inverter frequency.

The heat output rate of the considered AWHP unit is a function of the external air temperature, and the temperature of the produced heat transfer medium,  $t_{w,e}$ . Therefore, it is necessary to establish a procedure for analytical determination of  $t_{w,e}$  as a function both of the required heat transfer rate for the heating of the building,  $Q_{building,i}$ , and external air temperature,  $t_{e,i}$ . This study suggests the using of the following expression [13, 14]:

$$t_{w,e} = \left( \frac{Q_{building,i}}{N_{FC} \cdot Q_{FC,nom}} \right)^{\frac{1}{n}} \cdot \Delta T_{nom} + \frac{\sigma}{2} + \theta_{int,des} \quad (9)$$

where:

$Q_{FC,nom} = 5.7 \text{ kW}$  - nominal heat transfer rate of fan coil units;

$Q_{building,i}$  - required heat transfer rate for the heating of the building at  $i$ -th external air temperature, kW;

$N_{FC} = 4$  - count of the fan coil units ;

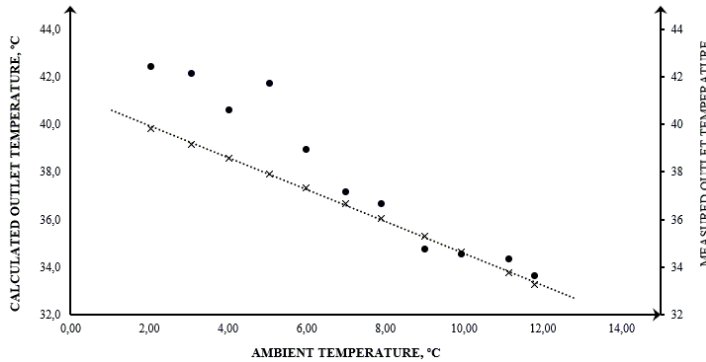
$\Delta T_{nom} = 50 \text{ K}$  - logarithmic meant temperature difference at standard conditions ( $75^\circ\text{C}/65^\circ\text{C}/20^\circ\text{C}$ );

$\sigma = 5 \text{ K}$  - design temperature difference between the temperature of the heat transfer medium in supply and return pipe;

$\theta_{int,des} = 21^{\circ}C$  - design temperature of the indoor air;

$n = 1.4$  - exponent to characterize the type of heat emission system (radiators, convectors, floor heating, etc.) [13].

Figure 6 illustrates the difference between the measured mean values of the temperature of the produced heat transfer medium and the calculated by equation (9) data for  $t_{w,e}$ . It was observed 11 test points were defined by the mean value of the external air temperature within a temperature bin  $t_e \pm 0.5^{\circ}C$ . The average difference between the measured  $t_{w,e}$  and the predicted values is around 3.6%. The larger deviations can be noticed at lower outdoor air temperatures.



**Fig. 6.** Comparison of the measured and predicted outlet temperatures of the heat transfer medium.

In order to predict accurately energetic  $COP$  of the AWHP at partial load operating mode, the following mathematical model is used:

$$COP_i = \frac{PLR_i}{Z_i} \cdot COP_{max,i} \quad (10)$$

where:

$PLR_i = Q_i / Q_{max,i}$  – partial load ratio at  $i$ -th external temperature bin;

$Z = W_{el,i} / W_{el,max,i}$  – the ratio of the consumed electrical power at part load operating mode and at full load (at the same outlet temperatures of the heat transfer medium,  $t_{w,e}$ );

$COP_{max,i}$  - energetic coefficient of performance at  $i$ -th external temperature bin and  $j$ -th temperature of outlet heat transfer medium.

The conducted experimental measurements indicate a linear relationship between  $PLR_i = Q_i / Q_{max,i}$  and  $Z = W_{el,i} / W_{el,max,i}$ . The  $Z$  was correlated in terms of  $PLR$  as shown in equation (11):

$$Z = 0.8332 \cdot PLR + 0.1086 \quad (11)$$

A graphical representation of relationship from equation (11) is presented in Figure 7.

According to the equation (10) and (11), for energetic  $COP$  at partial operation mode can be formulate the expression:

$$COP_i = \frac{PLR_i}{0.8332 \cdot PLR + 0.1086} \cdot COP_{max,i} \quad (12)$$

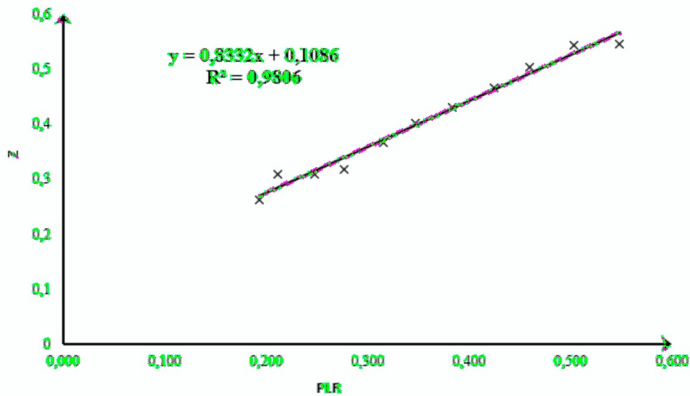


Fig. 7.  $Z = W_{e,il} / W_{el,max,i}$  as a function of the partial load ratio (PLR).

### 3 Validation and verification of the obtained mathematical models

The assessment of the adequacy and accuracy of all presented models was performed according to the rules of regression analysis.

First, the validity of the obtained regression model proved the high value of the coefficient of determination,  $R^2$  ( $R^2 = 0.97$  for the linear regression of  $Q$  and  $R^2 = 0.98$  for  $Z$ ). On the other hand, the adjusted  $R^2$  values are 96.7% and 97.8% in the case of the relationships of  $Q$  and  $Z$ , respectively. Therefore, over 96% of the variance of  $Q$  and  $Z$  can be explained by the variance of the  $t_e$  and  $PLR$ , respectively. In conclusion, the obtained mathematical models can be considered statistically significant.

In addition, using the tools of MS Excel is analyzed the variance of the suggested models. The obtained results are presented in Table 3 and Table 4.

Table 3. Results from analysis of variance of linear regression of  $Q$ .

Parameter	Coefficients	Standard Error	t- Stat	P-value	Lower 95%	Upper 95%
Intercept	5.2601	0.1063	49.48	$2.8 \cdot 10^{-12}$	5.01968	5.500
$t_e$	-0.2495	0.0139	-17.97	$2.3 \cdot 10^{-8}$	-0.2809	-0.218

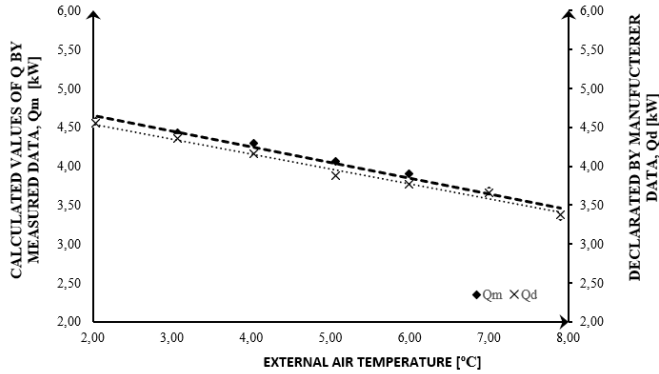
Table 4. Results from analysis of variance of linear regression of  $Z = W_{e,i} / W_{el,max,i}$ .

Parameter	Coefficients	Standard Error	t- Stat	P-value	Lower 95%	Upper 95%
Intercept	0.1086	0.01458	7.448	$3.9 \cdot 10^{-5}$	0.07562	0.142
$PLR$	0.8332	0.03907	21.33	$5.15 \cdot 10^{-9}$	0.74477	0.922

The results from Tables 3 and 4 designate that the intercepts in equations (6) and (11) are statistically significant at a 95% confidence level. This is evidenced by the results of  $P$ -values. In both cases, they are significantly lower than the assumed level of significance ( $2.8 \cdot 10^{-12} \ll 0.05$  and  $3.9 \cdot 10^{-5} \ll 0.05$ ). Moreover, the slopes of the equations (6) and (11) are also statistically significant at a 0.05 level of significance.

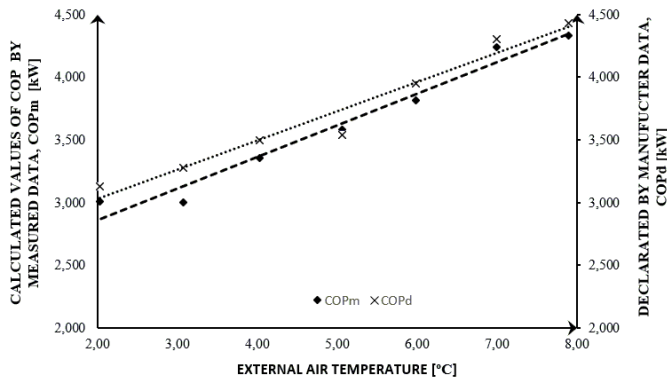
As verification of the obtained models, a comparison of the calculated values for the  $Q$  and  $COP$  through the measured data with those published by the manufacturer [8] is carried

out. The results are shown in Figures 8 and 9. There is a little difference between the values of  $Q$  obtained by the experiment and those declared by the manufacturer. These differences can be explained in part by the distinction in conditions at which the heat power was measured by the manufacturer [8]. Another possible explanation for this result is differences in the physical properties of the used heat transfer medium.



**Fig. 8.** Comparison of heat power determined using the measurement data,  $Q_m$ , and the values declared in [8],  $Q_d$ .

In [8] manufacturer presents the COP values characterized only by the AWHF, whereas in the current paper are presented the values for COP describe the whole system. Due to the lack of exact information about consumed electricity power by auxiliary equipment (fans, pumps, etc.) in the various operation modes of the system, in Figure 9 the values of COP obtained by the experiment are compared the data for COP of the unit at an outlet temperature of heat transfer medium equal to 45°C and minimum inverter frequency (15 Hz). Thus, it is possible to assess the convergence of the obtained results. The experimental and declared data are approximated by a linear function. It can be concluded that the COP values determined using the measurement data have good convergence with declared in [8] values of the COP.



**Fig. 9.** Comparison of the COP values determined using the measurement data and the values declared in [8].



## 4 Conclusions

In Part 1 of the current investigation, an AWHP system was modeled and the obtained experimental results were evaluated. The objective of the paper was to establish the dependencies between produced power and energetic  $COP$  and dynamic changing ambient conditions. The developed mathematical models of  $Q$  and  $COP$  are used in Part 2 of the investigation.

This study has identified that the system uncertainty value of  $COP$  is in interval  $\pm (7.1\div 16.4)$  %, whereas the system uncertainty of  $Q$  varying in interval  $\pm (10.98\div 12.5)$  %. However, the conducted regression analyses confirmed the statistical significance of the regression models and their coefficients. In this case, it is not necessary to consider a larger number of measurements. It is proved that it is not necessary to add other parameters to the obtained models.

Moreover, an analytical procedure for the determination of the outlet temperature of the produced heat transfer medium is presented. It has proved that the obtained results about  $t_{w,e}$  describe with high accuracy the actual behavior of the AWHP units with variable outlet. Therefore, the  $COP$  and  $t_{w,e}$  models obtained in the current study for a particular application of the analyzed model AWHP unit can be used again in different applications of the same model heat pump.

The question raised by this study is how to achieve the maximum exergy content of the product of the AWHP system and is there a significant difference in the exergetic and exergoeconomic performance parameters of the AWHP system in different operations modes of the AWHP unit and backup heater. An attempt at a comprehensive answer to these questions is presented in Part 2 of the current investigation.

## References

1. H. Zhao, E. Long, X. Zhang, Q. Liu, Z. Jin, F. Liang, *Procedia Engineering* **205**, 2055 (2017).
2. G. Morrison, T. Anderson, M. Behnia, *Sol Energy* **76**, 147 (2004).
3. J. Ji, G. Pei, T. Chow, W. He, A. Zhang, J. Dong, H. Yi, *Appl Energy* **80**, 307 (2005).
4. Y. Ding, Q. Chai, G. Ma, Y. Jiang, *Energy Convers Manage* **45**, 2393 (2004).
5. D. Wang, Y. Liu, Z. Kou, L. Yao L, Y. Lu, L. Tao, et al., *Int J Refrig* **106**, 628 (2019).
6. P. Byrne, R. Ghouali, *Appl Therm Eng*, **149**, 414 (2019).
7. M. Ozturk, B. Doğan, L. Erbay, *Sustain. Energy Technol. Assess.*, **42** (2020).
8. Mitsubishi Electric Corporation. *Ecodan data book*, 4 (2018), [Online], available at <https://www.mitsubishi-les.info/database/servicemanual/files>.
9. A. Rochim, *Chauvenet's Criterion, Peirce's Criterion, and Thompson's Criterion (Literatures Review). 2nd Quantitative and Qualitative Analysis Course Homework*, 21 March 2016.
10. A. Wheeler, A. Ganji *Introduction to engineering experimentation* (3rd Edition, Pearson, 2009).
11. A. Kahraman, A. Çelebi, *Energies*, **2**, 697, (2009).
12. G. Bagarella, R. Lazzarin, M. Noro. *Int J Refrig* **65**, 183, (2016).
13. prEN 15316-4-2:2006 *Heating system in buildings – Method for calculation of system energy requirements and system efficiencies – Part 4-2: Space heating generation systems, heat pump systems*.
14. St. Stamov, *Heating, air conditioning and cooling handbook. Part II: Heat and gas supply*, (Tehnika, Sofia, 2001).

# Air-to-water heat pump assessment: Part 2 – Exergetic and exergoeconomic analyses

Nadezhda Doseva<sup>1,\*</sup>, and Daniela Chakyrova<sup>1</sup>

<sup>1</sup>Varna Technical University, Heat Technology Department, 9000 Varna, Bulgaria

**Abstract.** This study is part 2 of the investigation on the exergetic and exergoeconomic parameters of an existing system with an air-to-water heat pump unit as a heat source. Part 1 presents the used experimental setup. The main aim of the conducted experimental tests is to develop models of produced heat rate and energetic COP at different ambient conditions. The obtained data is used in Part 2 of the study where the exergetic and exergoeconomic assessment is carried out. The exergetic and exergoeconomic analysis was performed at dynamically changing ambient parameters. The considered operation modes of the air-to-water heat pump (AWHP) unit and backup heater (BUH) were evaluated based on Seasonal Exergetic Efficiency. For the exergoeconomic analysis, the SPECO method is used. Thus, this paper provides an exhaustive understanding of the exergy and exergoeconomic performance of the considered air-to-water heat pump system.

## 1 Introduction

To perform an objective thermo-economical assessment of an energy conversion system, for example, in addition to the quantity of the energy flows, it is necessary to consider and their quality. The main reason for such an approach to the problem lies in the fundamental consequence from the Second Law of Thermodynamics: the different energy forms do not have the same value; they differ in the part that can be converted into another energy form able to do work. Then, the main goal in the design and operation of heating systems should be achieving the maximum exergy content of the product of the analyzed system. On the other hand, in the case of the air to water heat pump (AWHP) system, the higher energy content of the product suggests a higher exergy cost of heating. Therefore, it is necessary to use a method that involves a comprehensive evaluation accounting for the quantities of energy, exergy, and monetary cost. Such an approach is an exergoeconomic method for assessment.

Previous researches [1-6] has established solutions for many problems in the field of the energy performance of AWHP and they provide good practices for the optimal design of air-to-water heat pump systems. However, these investigations provide valuable insights about the rational use of the whole energy flows in the AWHP systems, but, at the same

---

\* Corresponding author: [nadezhda.doseva@abv.bg](mailto:nadezhda.doseva@abv.bg)

time, they cannot give an accurate description of how this energy is being used and what are the monetary cost of the irreversibility of the conducted real processes.

The application of the exergetic and exergoeconomic methods to the heat pump systems is not a novelty in the reference literature. For example, many studies consider geothermal and solar-assisted heat pumps [7-10]. Suleman *et al.* [9] conduct comprehensive energy and exergy analyses of the integrated solar and heat pump system. The obtained results show that the coefficient of performance on an energy basis (*COP*) of the heat pump cycle is 3.54 whereas the exergy efficiency is 42.5%. Dong, X. *et al.* [10] prove the statement that the exergy efficiency of the considered in their study solar integrated air source heat pump is 7.9% higher than the exergy efficiency of the same type of conventional air source heat pump.

The application of the exergoeconomic method is a rarity in the case of the AWHP systems. Bingjie *et al.* [11] adopt the conventional exergy analysis to the air source heat pump water heater and demonstrate that from an exergetic point of view, the most major component of the system is the compressor because its exergy loss coefficient is the largest in the system (26.12%). The object of the exergetic analysis in [12] is an air source transcritical carbon dioxide heat pump. The authors of this paper consider the exergy efficiency as a function of the refrigerant charge, and they conduct classical economic and environmental analyses. Although the main aim of these studies is different, they are similar in one thing: the calculated values of the exergy efficiency of the considered AWHP systems are moment's values because they were determined at specified conditions of the reference environment. In this regard, Ozturk *et al.* [13] perceive a quite different approach: the authors consider the exergy destruction of the AWHP unit components at dynamic change ambient conditions in the heating period. The results in [13] show the variation of exergy destruction through the entire heating period and thus, it can determine the operating conditions of every component for minimizing the irreversibilities.

The idea for the seasonal exergy efficiency of the heat pump unit was introduced by Lizarraga *et al.* [14]. However, there is a need to apply this concept to the concrete AWHP system and thereby investigate the usefulness of this method for exergy assessment. Therefore, the objective of the current paper is to provide the methodology combining the concept for the seasonal exergetic efficiency of the AWHP systems with the exergoeconomic method. For this purpose, first, in Part I of the investigation, the basic energy characteristics of the observed AWHP system (such as energetic *COP* and produced heat transfer rate) were examined experimentally under dynamically changing parameters of the environment. Then, the method for calculation of the seasonal exergetic efficiency of the AWHP systems is proposed. This method involves the basic insights from previous publications [14-16]. Finally, the method for the determination of the seasonal exergy efficiency of the AWHP systems is supplemented with an approach for exergoeconomic evaluation.

## 2 Method

### 2.1 Seasonal Exergetic Efficiency of the AWHP

In the process of conduction of the exergy analysis, the AWHP unit is considered as a Grassman's thermodynamic box shown in Figure 1 with  $n$  input and  $m$  output exergy rate flows. In this analysis, the environment is no meaning to the corresponding concept of thermodynamics, because its parameters (temperature, pressure, humidity) are variable.

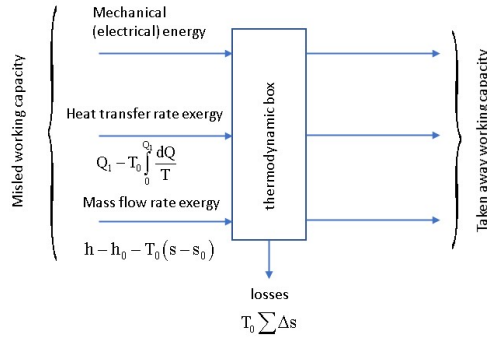


Fig. 1. Grassman's thermodynamic box.

To drive a heat pump can be used mechanical or electrical energy. The rate of these energy flows can be considered equal to the exergy rate of the mechanical or electrical energy flows [15], i.e.,  $\dot{W}_{el} = \dot{E}x_{W,el}$  and  $\dot{W}_{mech} = \dot{E}x_{W,mech}$ . On the other hand, waste heat or heat is taken from the environment can be used as a heat source. In AWHP, from the heat source is taken only energy, because, in this case, the exergy transfer accompanying heat transfer is zero,  $\dot{E}x_{Q_0} = 0$ . Therefore, the moment's value of the exergy efficiency ( $\eta_{ex,i}$ ) of an AWHP is:

$$\eta_{ex,i} = 1 - \frac{\dot{E}x_{D,AWHP}}{\sum \dot{E}x_{in}} = \frac{\sum \dot{E}x_{out}}{\sum \dot{E}x_{in}} = \frac{\dot{E}x_{QN}}{\dot{E}x_{W,el} + \dot{E}x_{Q_0}} = \frac{\dot{E}x_{QN}}{\dot{W}_{el}} = \frac{\dot{E}x_{QN}}{\dot{Q}_N - \dot{Q}_0}, \quad (1)$$

where:  $\dot{E}x_D$  - exergy destruction rate within the AWHP unit, W;

$\dot{E}x_{QN} = \left(1 - \frac{T_0}{T_N}\right) \cdot \dot{Q}_N$  is the exergy of the produced heat power rate, W;

$T_0$  - temperature of the heat source, K;

$T_N$  - temperature of the heat sink, K;

$\dot{Q}_N$  - produced heat rate, W;

$\dot{Q}_0$  - ambient heat rate used as the heat source of the heat pump, W.

After a mathematical transformation of equation (1) is obtained:

$$\eta_{ex,i} = \frac{\dot{E}x_{QN}}{\dot{Q}_N - \dot{Q}_0} \Bigg| \frac{\dot{Q}_N}{\dot{Q}_N} \quad (2)$$

$$\eta_{ex,i} = \frac{(T_N - T_0)/T_N}{1 - \omega} = \frac{(T_N - T_0)/T_N}{1 / COP_{eff}}$$

where:  $\omega = \dot{Q}_0 / \dot{Q}_N = (\dot{Q}_N - \dot{W}_{el}) / \dot{Q}_N = 1 - (1 / COP_{eff})$ ;

$COP_{eff}$  - effective coefficient of performance on the energy basis.

The value of the  $COP_{eff}$  depends on the operating mode of the heat pump mode (i.e., full load, partial load, or on-off cycles) and the method of its calculation is detailed

discussed in a previous study [17]. The used approach for the determination of energetic  $COP$  and  $Q_N$  of currently considered AWHP is presented in Part 1 of the study. Here, the developed mathematical models are used to perform the calculations by equations (3) and (4).

In eq. (2), the term  $(T_N - T_0)/T_N$  is nothing but the coefficient of performance of the ideal heat pump cycle. Therefore:

$$\eta_{ex,i} = \frac{COP_{eff}}{COP_{CARNOT}} = 1 - \frac{Ex_{D,AWHP,i}}{\dot{W}_{el,i}} \quad (3)$$

where:  $Ex_{D,AWHP,i}$  – exergy destruction within the system at  $i$ -th ambient temperature, W.

Equation (3) gives the moment's value of the exergetic efficiency of the considered AWHP system because it is calculated at specified conditions of the environment. In the current investigation, this moment's values are used to determine the seasonal exergetic efficiency of the AWHP system.

Based on the views of other authors [14], the seasonal exergetic efficiency of the AWHP unit can be written:

$$S\eta_{EX} = \frac{\sum Ex_{Q_N}(i)}{\sum W_{el}(i)} \quad (4)$$

where:  $\sum W_{el}(i) = \sum_{i=1} (\dot{W}_{el,i} \cdot \tau_i)$  – electrical energy input to the AWHP unit in the heating period, kWh;

$\sum Ex_{Q_N}(i) = \sum_{i=1} (\eta_{ex,i} \cdot \dot{W}_{el,i} \cdot \tau_i)$  – the exergy of the produced heat rate in the heating period

or heating exergy demand of the building, kWh;

$\tau_i$  – the duration of the  $i$ -th outdoor temperature bin, h.

## 2.2 Methodology for exergoeconomic analysis of AWHP systems

In this study, the exergoeconomic analysis consists of the conventional exergy analysis and economic analysis. The aim is to reveal the process of cost formation and evaluate the exergy cost of the produced useful heat. This calls for the formulation of cost rate balances for the considered AWHP system. For an AWHP unit operating during the heating period with duration  $\tau_{HP}$  can be written:

$$\begin{aligned} c_{p,HP} \cdot \frac{\sum Ex_{Q_N}(i)}{\tau_{HP}} &= \dot{Z}_{AWHP,HP} + c_F \cdot \frac{\sum W_{el}(i)}{\tau_{HP}} \\ c_{p,HP} \cdot \frac{S\eta_{EX} \cdot \sum W_{el}(i)}{\tau_{HP}} &= \dot{Z}_{AWHP,HP} + c_F \cdot \frac{\sum W_{el}(i)}{\tau_{HP}} \end{aligned} \quad (5)$$

where:  $Z_{AWHP,HP}$  is levelized costs of the capital investment, operating and maintaining of the AWHP system per unit time (hour) during the heating period, €/h;

$c_{p,HP}$  and  $c_F$  – seasonal exergetic cost of the product of the system and of the fuel, respectively, €/kWh.

The levelized costs of the capital investment, operating and maintaining of the AWHP system per unit time (hour) during the heating period are determined as follow:

$$\dot{Z}_{AWHP,HP} = (PEC_{HP} \cdot CRF \cdot \varphi) / \tau_{HP} \quad (6)$$

where:  $PEC_{HP}$  – the initial investment costs for the heat pump unit. It is defined according to the official price list of the manufacture [18], €;

$$CRF = \frac{i \cdot (i+1)^n}{(i+1)^n - 1} - \text{capital recovery factor [19];}$$

$i = 6\%$  - the real discount rate;

$n$  - the economic life of the heat pump system. It is assumed to be  $n = 15$  years;

$\varphi = 1.06$  - maintenance factor [19];

$\tau_{HP}$  - duration of the heating period, h.

According to the previous investigation of the authors [20], it is proved that the duration of the heating period in Varna, Bulgaria is  $\tau_{HP} = 4582$  h.

### 2.3 Climatic data

Because the experiment in Part 1 of the investigation is carried out for a range of ambient temperature ( $t_e = 2.03^\circ\text{C} \div 11.78^\circ\text{C}$ ), to obtain a complete picture of the exergetic and exergoeconomic behavior of the AWHP system, it is necessary to be considered a wider external air temperature range.

In the current paper, the heat exergy requirement of the building,  $EX_{QN}$ , dependent on the temperature operating conditions is determined after by assessment of the ambient temperature. This evaluation consists of obtaining the cumulative frequency of the external air temperature within a typical heating period. For this purpose, the data for the frequency of the external air temperature within the heating period is used. The input data used (i.e., the frequency of the external air temperature) for Varna, Bulgaria is published in a previous study [20].

The cumulative frequency for Varna, Bulgaria is obtained by summed-up bin-by-bin the frequency of the external air temperature within the heating period:

$$N_k = \sum_{i=1}^k n_i \quad (7)$$

where :

$N$  – cumulated number of hours;

$k$  – number of the considered bin;

$n_i$  – number of hours for the considered bin.

The cumulative frequency of the external air temperature is shown in Figure 2.

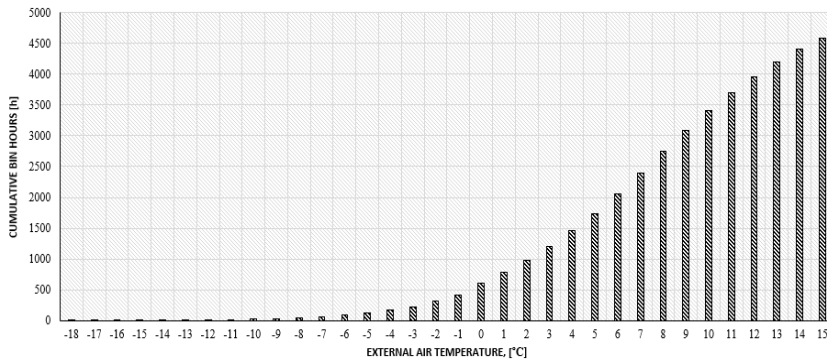
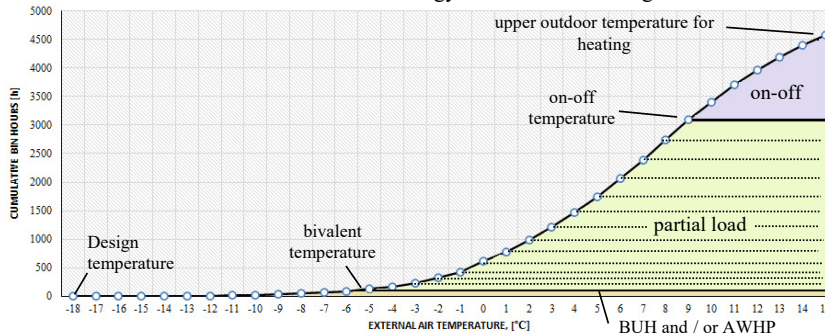


Fig. 2. Cumulative frequency of the external air temperature in the heating period – Varna, Bulgaria

In the context of the obtained in Part 1 of the study results regarding PLR, the operation modes of the AWHP can be defined. In case it is assumed that the design temperature is the lowest of the observed values, i.e.  $-18^{\circ}\text{C}$ , from Figure 3 follows that 2676 h the AWHP unit will be operated at part load. At the same time, there is 89.2 h in which the heat capacity of the AWHP will be insufficient to meet the energy needs of the building.



**Fig. 3.** Bin hours for alternate or partly parallel operation mode of the back-up heater (BUH) – Varna, Bulgaria

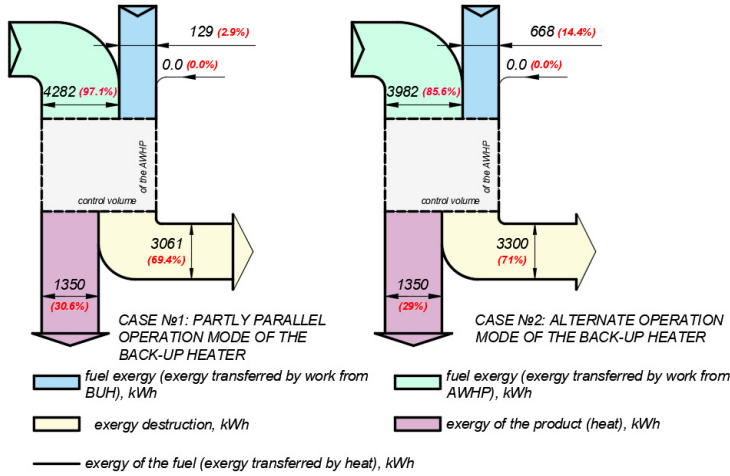
Moreover, according to the methodology for determination of outlet temperature of the heat transfer medium (presented in Part 1 of current investigation), it is predicted that at ambient temperatures  $t_e < -14^{\circ}\text{C}$ , the outlet temperature,  $t_{w,e}$ , will be in the range  $49^{\circ}\text{C} \pm 51^{\circ}\text{C}$ . At these operating conditions (i.e., the values of  $t_e$  and  $t_{w,e}$ ), however, the operating limit temperature ( $TOL$ ) of the AWHP unit is  $-15^{\circ}\text{C}$ . This allows the conduct of exergetic and exergoeconomic analyses for two different cases: partly parallel and alternate operation mode of the backup heater.

In the current paper is assumed that at alternate operation mode of the back-up heater (BUH), the AWHP unit is switched-off at bivalent temperature  $t_{biv} = -5.73^{\circ}\text{C}$ , and only the BUH covers the full energy requirement of the building. At partly parallel operation mode of the BUH, the AWHP is not switched-off at  $t_{biv} = -5.73^{\circ}\text{C}$ . The AWHP unit and the BUH operate in parallel mode up to  $TOL$ , and at an ambient temperature lower than  $-15^{\circ}\text{C}$  only the BUH operates.

It is important to note, that the AWHP on-off operation mode is not considered in the current investigation. The reason is the limited number of measurements within an interval  $t_e > 9^{\circ}\text{C}$ . Therefore, the obtained model of energetic  $COP$  does not cover this operation mode. In addition, the previous part of the investigation established that the balance temperature is  $t_{balance} = 21.08^{\circ}\text{C}$ . This is the ambient temperature at which  $PLR = 0$ . However, in part 2 of the study is assumed that the upper outdoor temperature for heating is  $15^{\circ}\text{C}$ . Thus, the performed analysis is closer to the real conditions under which the heating of buildings is realized.

### 3 Results and discussion

According to the concept of seasonal exergetic efficiency expressed by equation (4), the considered operation modes of the BUH and the AWHP were evaluated. The results are presented in Figure 4 using Grassman's diagrams. From this data, it can see that the alternate operation mode of the BUH results in the lower value of the seasonal exergetic efficiency:  $S\eta_{EX} = 30.6\%$  in the case of the partly parallel operation mode of the BUH and  $S\eta_{EX} = 29\%$  for alternative operation mode, respectively.

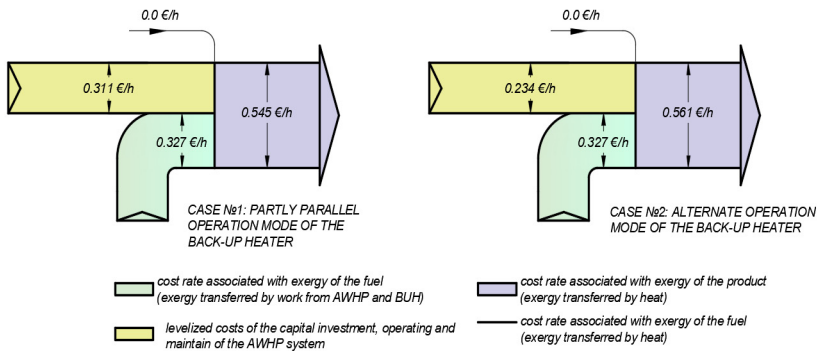


**Fig. 4.** Grassman's diagram of exergy flows considering the heating season.

This leads to the conclusion that if the AWHP unit operated for a longer period in the heating season, this is more efficient from an exergetic point of view.

Figure 5 provides information about the cost rate associated with the exergy of the fuel (electrical energy) and the product (heat). As can be expected, due to the higher value of  $S\eta_{EX}$  in Case №1 (the partly operation mode of the BUH), the cost rate associated with the product,  $\dot{C}_p$ , is lower than the one in Case №2 (the alternate operation mode of the BUH).

The unit exergy cost of the product,  $c_p$ , during the considered heating period is 1.11 €/kWh in Case №1 and 1.14 €/kWh in Case №2, respectively.



**Fig. 5.** Cost flow diagram of the AWHP system operating during the heating season.

Overall, the presented results suggest the statement that the switch-off temperature of the AWHP unit plays a vital role in the seasonal efficiency of the system. The seasonal exergetic coefficient of performance rise around 5.16 % when the switched-off temperature



is decreased from  $t_e = -5.73\text{ }^\circ\text{C}$  to  $t_e = -15\text{ }^\circ\text{C}$ , whereas the cost rate associated with the product of the AWHP system realize a 3.1% drop.

A closer inspection of the moment's values of the  $\eta_{EX}$  at partial operation mode of the AWHP as a function of the external air temperature (Figure 6) indicates an unexpected outcome: there is a maximum value of  $\eta_{EX}$ . The highest moment's values of the  $\eta_{EX}$  at partial operation mode is equal to 34.1 % and it is observed at external air temperature  $t_e = -2.573^\circ\text{C}$  and temperature of the produced heat transfer medium  $t_{w,e} = 42.54^\circ\text{C}$ .

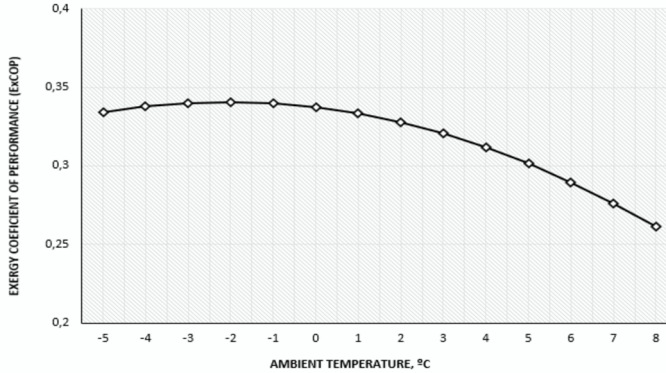


Fig. 6. Moment's values of the exergetic efficiency at partial operation mode of the AWHP as a function of ambient temperature.

The maximum of  $\eta_{EX}$  can be explained considering the derivative of exergy efficiency. From the graph in Figure 7, it can be seen that the derivative of the exergy efficiency changes its sign, which indicates the presence of an extremum of the function. The value for the outside air temperature at which the extremum is obtained is calculated from the equation of the derivative. Physically, this phenomenon is explained by the fact that the rates of decreasing of the exergy used in the heated space and the external exergy inputted into the process are different. The input exergy has a significantly higher rate of decreasing than the produced exergy, which at some point changes the tendency of change of the exergy efficiency. On the contrary, the energetic  $COP$  gradually rises with the external air temperature increase.

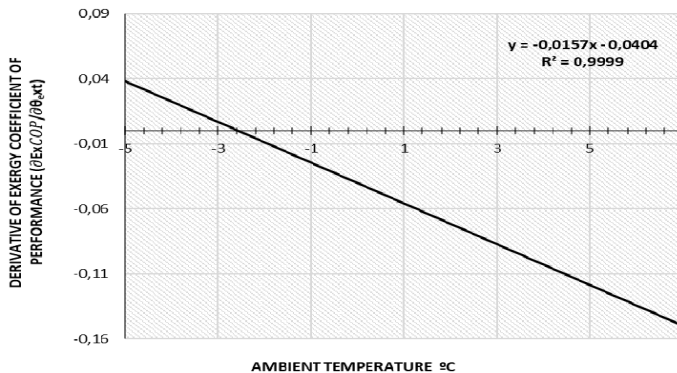


Fig. 7. Derivative of exergy performance coefficient ( $\partial\eta_{EX}/\partial t_{ext}$ ) as a function of the ambient temperature.

## 4 Conclusions

The main objectives of Part 1 and Part 2 of the current investigation were to provide a methodology for seasonal exergetic and exergoeconomic assessment of air-to-water heat pump systems using the experimental data. The obtained results demonstrate the usefulness of the exergy-based assessments.

Furthermore, this study is indicative that from a thermodynamic point of view, there is no heat transferred from a renewable energy source. The second law of thermodynamic said that all heat transferred processes are spontaneous or non-spontaneous. Therefore, the use of all so-called renewable energies becomes possible because of the realization of heat transfer in a spontaneous process between the environment and the considered thermodynamic system. A clear example of this statement is the use of solar energy in thermal engineering systems. However, the current paper can be considered as a demonstration of the exception to the rule described above. That exception is in the case of heat pumps: the utilizing of aerothermal energy by a heat pump is possible after occurring a non-spontaneous heat transfer process. At this non-spontaneous process between the environment and control volume (the AWHP unit), the exergy of the fuels (electrical energy) is consumed to produce the useful heat (exergy of the product) and to cover exergy destruction within the system. The produced heat power, on the other hand, consists of the exergy and anergy. The exergy content of the product is used to maintain the indoor air temperature, whereas the anergy (the irreversible part of the heat) taken from the ambience is returned to the environment in form of heat loss through the building envelope. A consideration of the heat pump systems in similar aspect can bring additional insights into the thermodynamic description of their operating modes as well as into the aims in the process of their optimization.

## References

1. Dongellini, M., Naldi, C., Morini, M. IBPC 2015, **78** (2015).
2. Naldi, C., Dongellini, M., Morini, M. ATI 2014, **81** (2015).
3. Naldi, C., Dongellini, M., Morini, M. IBPC 2015, Energy Procedia **78** (2015).
4. Vocale, P., Morini, G., Spiga, M. ATI2013 **45** (2014).
5. Dongellini, M., Naldi, C., Morini, G. J. Appl. Therm. Eng. **114** (2017).
6. Dongellini, M., Impala, V., Morini, G., 16th International Conference on Sustainable Energy Technologies – SET 2017 (2017).
7. A. Hepbasli, O. Akdemir, Energ Convers Manage, **45**, 737 (2004).
8. Y. Bi, X. Wang, Y. Liu, H. Zhang, L. Chen, Appl Energ, **86**, 2560 (2009).
9. F. Suleman, I. Dincer, M. Agelin-Chaab, Appl Therm Eng, **73**, 559 (2014).
10. X. Dong, O. Tian, Z. Li, Energ Buildings, **142**, 128 (2017).
11. M. Bingjie, L. Qinghai, C. Guojie, 4th International Conference on Sensors, Measurement and Intelligent Materials (ICSMIM 2015), 197 (2016).
12. Y. Wang, Z. Ye, Y. Song, X. Yin, F. Cao, Energ Convers Manage, **223**, (2020).
13. M. Ozturk, B. Doğan, L. Erbay, Sustainable Energy Technologies and Assessments, **42**, (2020).
14. J. Lizarraga, A. Picallo-Perez, *Exergy Analysis and Thermoeconomics of Buildings. Design and Analysis for Sustainable Energy Systems* (Book, Elsevier, 2020).

15. W. Eder, F. Moser, *Die Wärmepumpe in der Verfahrenstechnik* (Bulgarian edition, 1984).
16. D. P. Gohshteyn, *Modern methods of thermodynamic analysis of power plants*, (Energiya, Moscow, 1969).
17. N. Doseva, D. Chakyrova, E3S Web of Conferences, 207, (2020), Article number 01014 25th Scientific Conference on Power Engineering and Power Machines, PEPM 2020; Sozopol; Bulgaria, 2020.
18. ClimaCom. *Ecodan Price List 2020/2021* (2020). [Online], available at <https://climacom.com/en/price-lists>
19. Bejan A, Tsatsaronis G, Moran M., *Thermal design and optimization* (Wiley, New York, 1996).
20. D. Chakyrova, N. Doseva, N. Kalcheva, CIEES International Conference, (2020) <https://iopscience.iop.org/article/10.1088/1757-899X/1032/1/012024> ISSN 1757 899X

# Modelling and numerical simulation of the transport phenomena in water thermal energy storage tanks

Nikola Kaloyanov<sup>1</sup>, Rosen Tsecov<sup>1</sup> and Nina Penkova<sup>2,\*</sup>

<sup>1</sup>Technical university of Sofia, Department of Thermal and Refrigeration Engineering, Blvd. Sv. Kliment Ohridski 8, 1756 Sofia, Bulgaria

<sup>2</sup>University of chemical technology and metallurgy, Department of Silicate Technology, Blvd. Sv. Kliment Ohridski 8, 1756 Sofia, Bulgaria

**Abstract.** Mathematical model for numerical simulation of the transient heat transfer and fluid flows in water thermal energy storage tanks is developed. The model allows analysis of the thermal fields in the accumulators at different schemes and modes of charging and discharging. It was verified and validated based on experimentally obtained information about the temperature stratification at charging of a thermal accumulator at a laboratory solar system. The proposed approach for numerical study of the thermal energy storage is convenient for parametrical estimation and improvement of the efficiency of the thermal systems.

## 1 Introduction

The thermal energy storage (TES) in the form of sensible heat in insulated water tanks is the most widely used method at systems where the periods of energy production and consumption do not coincide. The water heat accumulators are key elements for the efficiency of the solar heating systems, thermal power generation and industrial systems [1]. The temperature stratification in the liquid domain due to the buoyancy can increase the performance of these technologies:

- the upper water levels can be enough hot at lower accumulated amount of heat and the thermal losses through the tank walls are smaller in comparison to the unstratified accumulators;
- the cooler water in the bottom of the tanks leads to a higher temperature difference in the heat exchangers at the energy source and to more efficient heat transfer in them.

Many investigations aiming enhancement of the temperature stratification in water thermal accumulators are known from the literature. The first of them are based on experimental measurements, balance equations and one-dimensional analytical models of the temperature field [2, 3]. They allow relatively accurate prediction of the temperature variation along the axis of vertical cylindrical tanks. The advanced software for computational fluid dynamics (CFD) and heat transfer (CHT) allows numerical simulation of the three-dimensional

---

\* Corresponding author: [nina@uctm.edu](mailto:nina@uctm.edu)

transient fields in the accumulating media in order to increase the efficiency of the thermal systems [4 - 6]. Such investigation are oriented to improvements of the accumulator shape [7], locations and geometries of the inlets and outlets [8], internal constructions for better temperature stratification [9] and charging and discharging flow parameters. The optimization of the design and the operation mode depends of the thermal systems where the thermal accumulator is integrated. These problems are not fully solved at the various technologies and applications of heat accumulators, obvious from the continuous research oriented on the topic.

The aim of the investigations in the present paper is a precise model for numerical simulation of the 3D transient fields in water tanks for TES, allowing prediction and improvement of the efficiency of thermal systems for domestic applications.

## 2 Conceptions for modeling of the transient fluid flow and heat transfer in water thermal accumulators

A three-dimensional geometrical model of the accumulator is generated, including all inlet and outlet pipes. Different scenarios of charging and discharging of the tank can be simulated accepting them as open or closed (walls). The pipe walls do not influence significantly on the processes and can be modeled as boundary interfaces [6]. The walls of the tank are also excluded from the geometrical model. The heat transfer through them can be modeled according to the boundary conditions in Table 1. The water and pipe domains are discretized by a mesh of finite volumes in order to solve numerically the system of partial differential equations:

- continuity equation;
- momentum equations at non zero gravity to reflect the buoyancy;
- thermal energy equation;
- turbulence model.

The initial numerical solutions of the model for the thermal accumulator, described in the next part of the paper, proved the advantage of Renormalization Group (RNG) k-epsilon turbulence model – it leads to a quicker convergence than the standard one. That is in accordance to the tips for the modeling of the turbulence in [10] and the conclusions of other research of turbulence flows with swirls [11]. The influence of the buoyancy on the turbulence is taken into account using Boussinesq buoyancy model in the production and dissipation terms in the RNG k-epsilon model.

The boundary conditions are summarized in Table 1.

**Table 1.** Boundary conditions.

Boundary	Variable
Inlet of the hot flow at charging	Velocity or mass flow and temperature variation with the time.
Inlet of the cold flow at discharging	Velocity or mass flow and temperature.
Outlets	Mass flow or gauge pressure.
Tank walls (heat exchanging boundaries)	Coefficient of heat transfer from the internal surface to the ambient environment: $U = \frac{1}{R_{se} + \sum_{i=1}^n R_i}$ , $Wm^{-2}K^{-1}$ ; ambient temperature $t_{amb}$ .
Pipe walls in the water domain (interfaces between the tank and pipe domains)	Thermal resistance of the wall $R_w$ . $R_w = \frac{d_{ex} - d_{in}}{2\lambda}$ , $m^2KW^{-1}$ at $\frac{d_{ex}}{d_{in}} \leq 2$

The variables in the equations in Table 1 are:  $R_{se}$  and  $R_i$  - thermal resistances of the external thermal boundary layer and solid layers of the tank envelopes,  $m^2KW^{-1}$ ;  $d_{ex}$  and  $d_{in}$  - external and internal diameters of the walls, m;  $\lambda$  = thermal conductivity of the pipe wall,  $Wm^{-1}K^{-1}$ .

The initial conditions include:

- initial temperature field in the water domain. It can be uniform or obtained as result of previous numerical simulation of charging or discharging of the tank;
- zero initial velocity and turbulence ratio;
- initial pressure distribution  $p_{in}$  taking into account hydrostatic pressure variation in the tank. For example at vertical tank parallel on  $z$  direction and  $z=0$  at the bottom:

$$p_{in} = \rho_w g(H - z), Pa$$

where  $H$  = the vessel height, m;  $\rho_w$  = water density,  $kgm^{-3}$ ;  $g$  = gravity acceleration,  $ms^{-2}$ .

For better convergence, the transient processes are simulated numerically at time steps at which the average Courant number is smaller than one at the correspondent mesh size. As finer is the mesh as smaller are time steps.

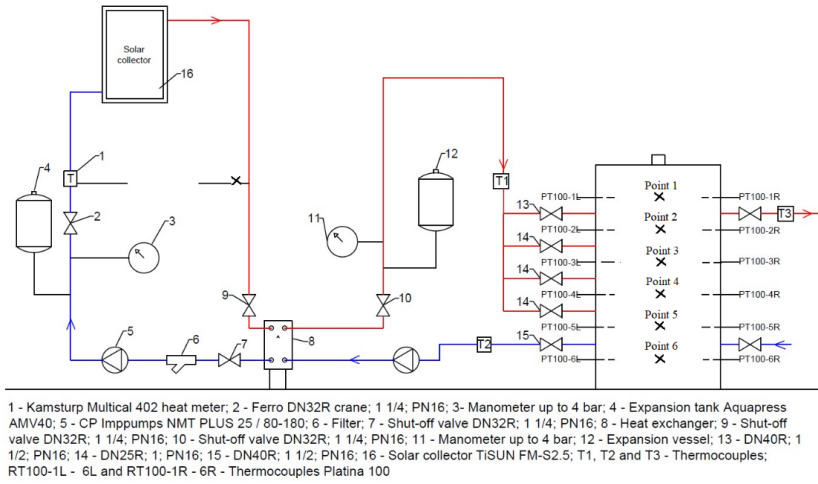
### 3 Experimental tests and numerical study of transport phenomena in a water accumulator, integrated in solar system

#### 3.1 Object of investigation

The thermal accumulator is a part of a laboratory solar installation situated on the territory of Technical University of Sofia (fig. 1). The water tank is thermally charging indirectly via heat exchanger. The internal diameter and height of the water tank (fig. 2) are correspondently 0.788 m and 2.114 m. The water volume is 1000 l. The tank envelopes, made by carbon style are insulated.

Twelve thermocouples Platina 100 measure the temperatures in the tank at different levels. They are localized radially: six in the "right" side (PT100-1R – 6R) and six on the "left" side (PT100-1L - 6L). The temperatures, measured by them are written and averaged at each level. The temperatures on the inlet and the outlets are also measured by thermocouples T1, T2 and T3. The level of the inlet at the thermal charging of the accumulator can vary but it is always higher according to the outlet in order to ensure temperature stratification in the axial direction.

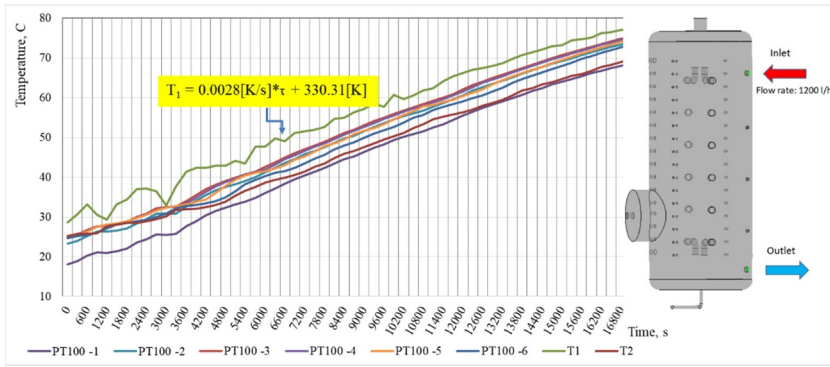
Different regime of charging and discharging are implemented varying the mass flows and the charging level of the supplied water flow. Detail information of the measurements at variations of the daily solar irradiation and the regime parameters is given in [12]. A part of that information for three modes of thermal charging of the water tank (Scenario 1, 2 and 3) is used at the boundary conditions for the numerical simulation of the processes and for validation of the models. Figures 3-4 show the measured temperature variations at the inlets, outlets and the different levels of the accumulator space for these scenarios. The higher temperatures in Point 1 in comparison to the bottom and outlet temperatures are probably caused by insufficient calibrations or other problems at the upper sensors. The numerical simulations, discussed in the next section showed that the temperatures in Point 1 have to be higher according to the outlet temperature.



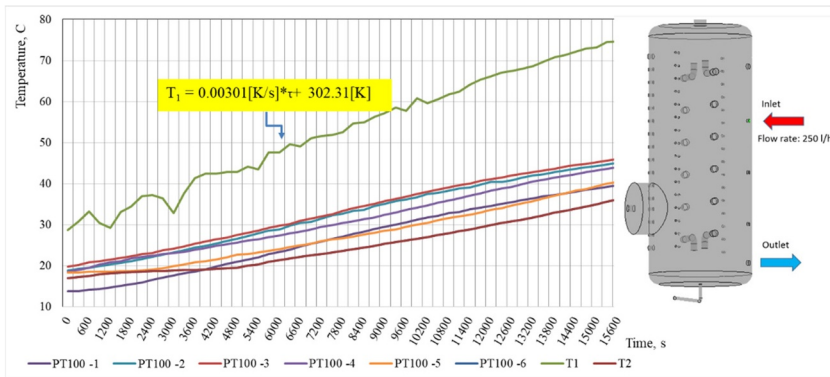
**Fig. 1.** Scheme of a solar thermal installation with water thermal energy storage tank



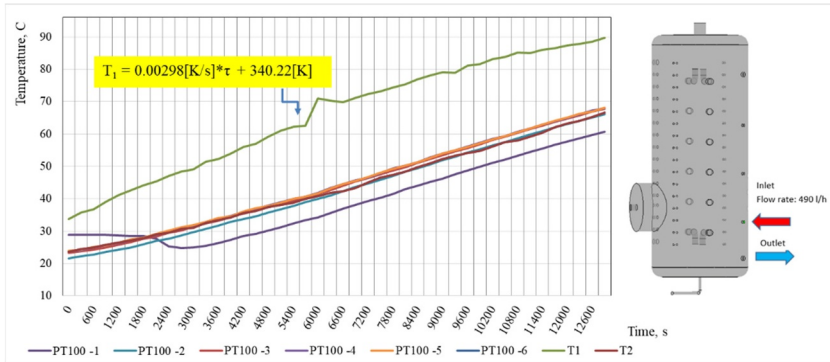
**Fig. 2.** Water tank for thermal energy storage (a) and its geometrical model (b)



**Fig. 3.** Temperatures in the water tank, inlet and outlet pipes at supplied flow rate of 1200 l/h (Scenario 1)



**Fig. 4.** Temperatures in the water tank, inlet and outlet pipes at supplied flow rate of 250 l/h (Scenario 2)



**Fig. 5.** Temperatures in the water tank, inlet and outlet pipes at supplied flow rate of 490 l/h (Scenario 3)



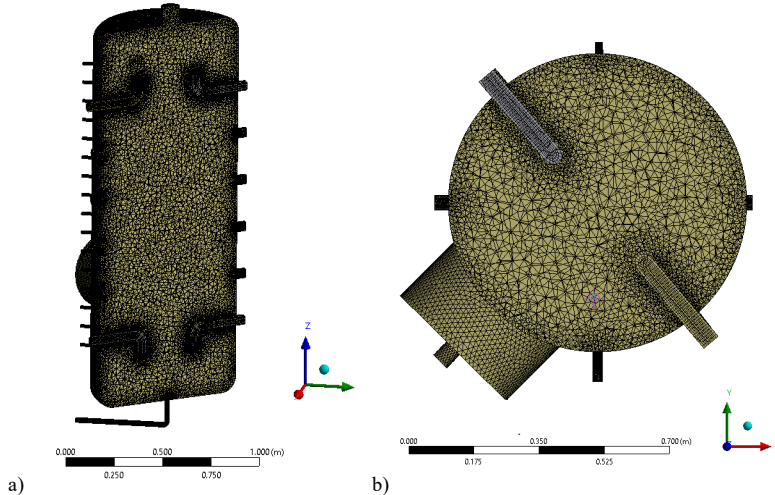
### 3.2 CFD analysis and validations of the models

The geometrical model contains all features of the real object although some of them are not used. It is discretized by a finite volumes mesh, consisted of 302613 nodes and 1522587 elements (fig. 6). The nodes on the interfaces between the pipe and accumulator space are common for the two domains.

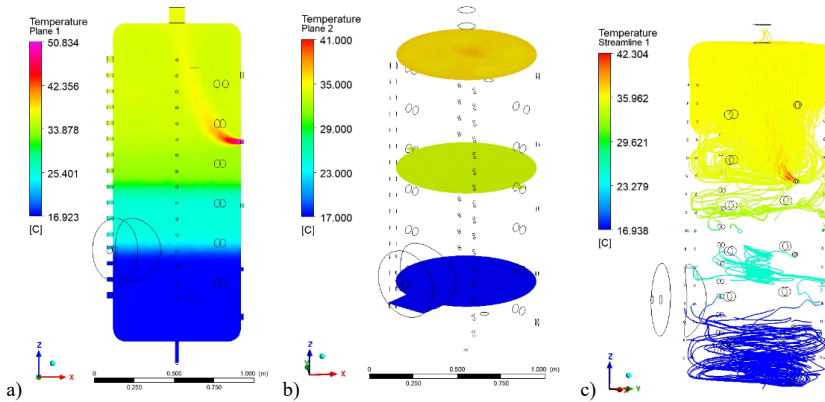
Three scenarios of charging are simulated numerically by ANSYS 19/CFX. The maximal time steps, allowing sufficient convergence at the transient computations are 0.6 seconds. That led to a relatively long computational time. So parts of the processes on figures 3-5, enough for the model validations are simulated. The heat transfer through the tank envelopes are not taken into account to check the possibility for its neglecting. Temperature fields and the streamlines in the water domain are shown on the next figures. Clear temperature stratification and relatively uniform temperatures at the horizontal cross sections are obvious at the case of low flow rate at the upper level of the inlet at Scenario 2 (fig. 7). In contrast the temperature stratification is almost absent at Scenario 3. Recirculating flows due to the buoyancy and the forced outflowing of the water at the bottom level are established at this case. They occupied the entire volume of the accumulator and cause unstratified temperature field in the water domain (fig. 8).

Water motions in the unused external pipe spaces are not established at the modeled scenarios, excepting the space near the flange at the bottom of the tank. So the geometrical model can be simplified by ignoring its unnecessary components with a total volume less than 2% of the volume of the tank. This will decrease the computational time and will allow flexible analyses without reducing the accuracy of the results.

Comparisons between the average temperatures at the levels of the internal thermocouples PT 100 and the temperatures, obtained at the numerical simulations at the same places are shown on figures 9-11. The maximal differences between the experimentally obtained and the computed temperatures are about 3 % at Point 1 for all simulated scenarios. The possible reasons for these differences are the established errors at the upper sensors. Therefore, the models for numerical simulations of the transient processes in the water accumulators are reliable and applicable for analysis of different modes of their thermal charging.



**Fig. 6.** Finite elements mesh at vertical (a) and horizontal (b) cross-sections

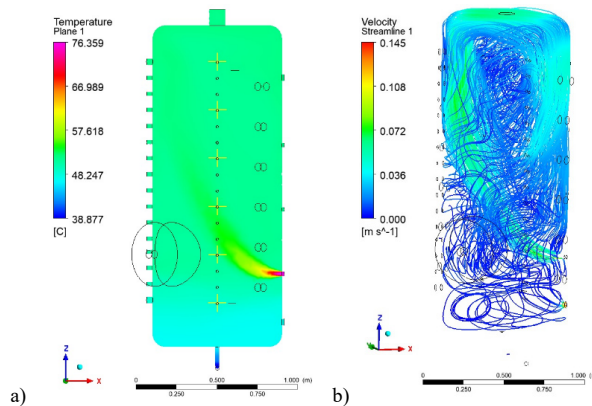


**Fig. 7.** Temperature fields in vertical and horizontal cross sections (a, b) and streamlines (c) at a moment of Scenario 2 (7200 s)

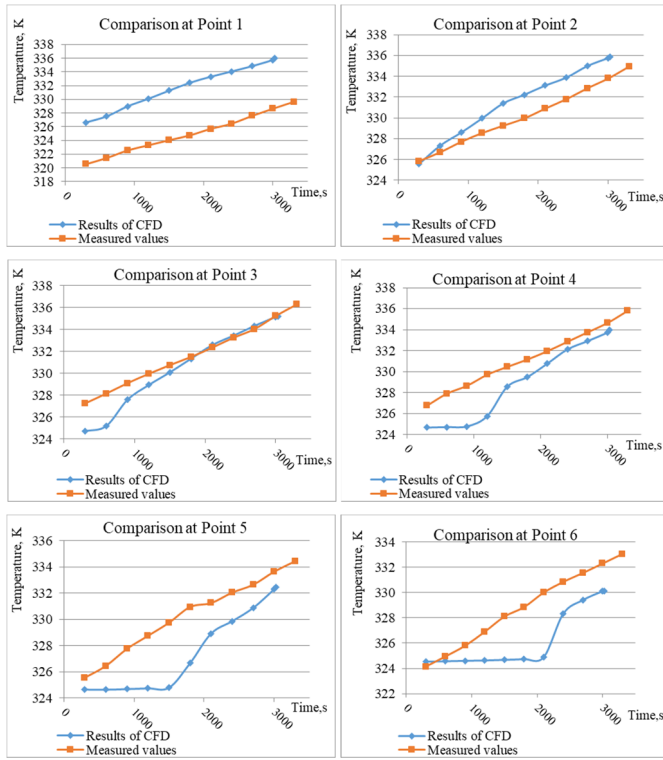
Other probable reasons for the deviation of the obtained at the simulations temperatures according to the experimental data are:

- the lower turbulence in the model comparing to the real object – the platina thermocouples are fixed by metal pins in the space of the laboratory accumulator that probably caused local turbulence eddies. These pins do not present in the geometrical models.
- the neglecting of the thermal losses through the accumulator envelopes leads to higher temperature stratification in the modelled object at the lower flow rates and velocities.

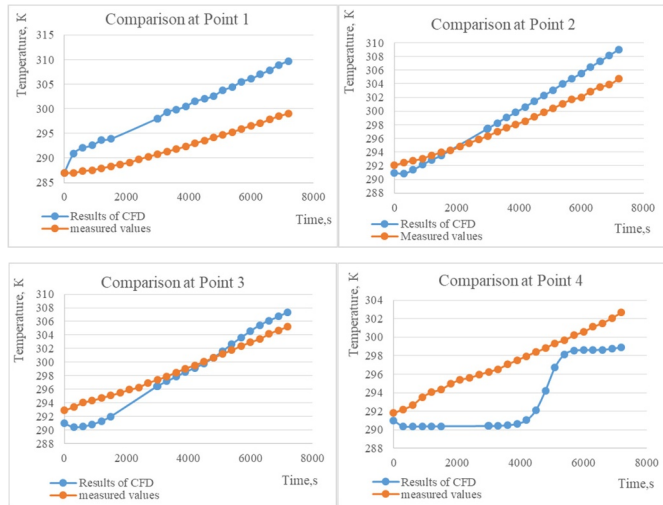
Despite the mentioned inaccuracy, CFD allows detail analyses of parameters about the transient thermal and fluid flow fields in the accumulator space that cannot be obtained experimentally: streamlines, turbulence characteristics, heat transfer coefficients and other.

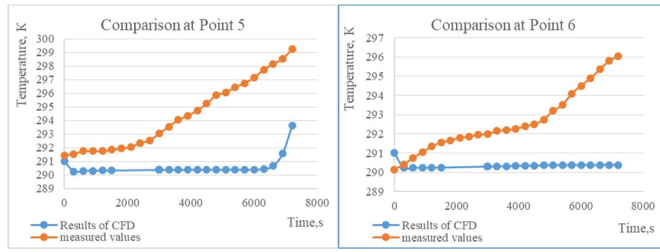


**Fig. 8.** Temperature fields in vertical cross section (a) and streamlines (b) at a moment of Scenario 3 (3200s)

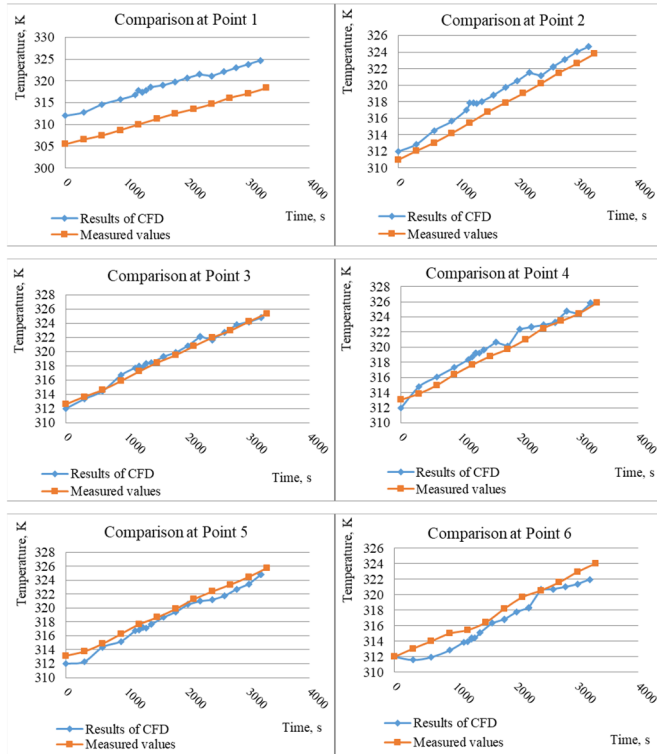


**Fig. 9.** Comparisons between the obtained at the measurements and the numerical simulations temperatures along the axis of the tank at Scenario 1





**Fig. 10.** Comparisons between the obtained at the measurements and the numerical simulations temperatures along the axis of the tank at Scenario 2



**Fig. 11.** Comparisons between the obtained at the measurements and the numerical simulations temperatures along the axis of the tank at Scenario 3

## 4 Conclusions

The numerical solution of the proposed mathematical model allows detailed information about the transient three-dimensional thermal and fluid flow fields in water accumulators at different configurations and charging schemes. This approach is suitable for prediction and control of the temperature stratification and the accumulated heat in order to achieve efficient

operation mode of the thermal systems according to the characteristics of the energy sources and consumers.

Further testing and validation of the models at thermal discharging and simultaneous charging and discharging of the thermal accumulator are forthcoming. For better accuracy, it is necessary to take into account the heat transfer through the envelopes of the tank.

This study has been financially supported by the project BG05M2OP001-1.001-0008: National Centre of Mechatronics and Clean Technologies, funded by Operational Programme for Science and Education for Smart Growth at EU Funds.

## References

1. Z. Wang, H. Zhang, B. Dou, H. Huang, W. Wu and Z. Wang, *Renewable Energy*, **111**, 353-371 (2017)
2. R. I. Loehrke, M. K. Sharp, H. N. Gari and R. D. Haberstroh, *Thermal Stratification Enhancement for Solar Energy Applications*, Colorado State University Fort Collins Dept. of Mechanical Engineering (1977)
3. N. Kaloyanov, *Analysis and synthesis of low potential combined heat systems*, PhD Thesis, Technical University of Sofia (1990)
4. C. Pagkalos, G. Dogkas, M. K. Koukou, J. Konstantaras, K. Lymperis and M. G. Vrachopoulos, *International Journal of Thermofluids*, **1**, 100006 (2020)
5. Y. Ahmed, *International Journal of Advanced Engineering and Business Sciences*, **2(2)**, 33-50 (2021)
6. N. Penkova and N. Harryzanov, In *Proceedings at 5th International Conference on Energy and Sustainability* 469-477 (2014)
7. Z. Yang, H. Chen, L. Wang, Y. Sheng and Y. Wang, *Renewable Energy*, **85**, 31-44 (2016)
8. Z. Wang, H. Zhang, B. Dou, H. Huang, W. Wu and Z. Wang, *Renewable Energy*, **111**, 353-371 (2017)
9. T. Bouhal, S. Fertahi, Y. Agrouaz, T. El Rhafiki, T. Kousksou and A. Jamil, *Numerical modeling and optimization of thermal stratification in solar hot water storage tanks for domestic applications: CFD study*. *Solar Energy*, **157**, 441-455 (2017)
10. ANSYS Release 16 - © SAS IP, Inc. (2016)
11. Q. Hou, and Z. Zou, *ISIJ international*, **45(3)**, 325-330 (2005)
12. R. Tsecov N. Kaloyanov and S. Chervenkov, *Proceedings of 25-th International Conference of Power Engineering and Power Machines (in Bulgarian)*, 29-39 (2020), <http://copepm.eu/documents/2020.pdf>

# An approach for reducing the air conditioning costs in office buildings in Vietnam

*Van Hung Tran*<sup>1,2,\*</sup>, *Thanh Nhan Phan*<sup>1,2</sup>, and *Momchil Vassilev*<sup>3</sup>

<sup>1</sup>Ho Chi Minh City University of Technology (HCMUT), 268 Ly Thuong Kiet Street, District 10, Ho Chi Minh City, Vietnam

<sup>2</sup>Vietnam National University Ho Chi Minh City, Linh Trung Ward, Thu Duc District, Ho Chi Minh City, Vietnam

<sup>3</sup>Technical University of Sofia, Power Engineering and Power Machines Department, 8 Kliment Ohridski Blvd., 1000 Sofia, Bulgaria

**Abstract.** According to statistics from the Ho Chi Minh Energy Saving Center, the electricity costs of the air conditioning system for office buildings are about 70% of the electricity costs. There are many solutions that have been proposed to reduce the operating costs of the air conditioning systems, this article discusses a method of accumulating cold to reduce the cost of electricity for the air conditioning system of an office building.

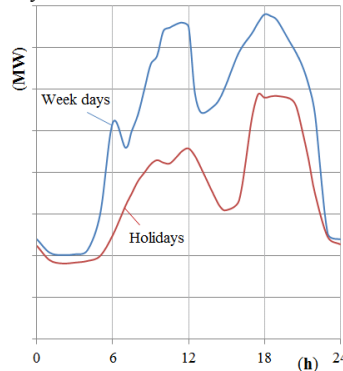
## 1 Introduction

Nowadays, the consumption of electricity for an air conditioning system in an office building is one of the most important issues not only for the owners but also for the electricity suppliers. The cooling needs of the building are not constant, and the price of electricity at different times of the day also has a different value. There is a lot of research on saving electricity costs by different methods. One approach to reducing air conditioning costs is to reduce energy consumption by applying the active cooling method [1]. Another approach is the accumulation of cold. The accumulation of cold is used not only to save on electricity costs but is also used for other purposes. According to the research of D. Shlichkov [2], a chilling system with a storage tank, in which the ice freezes on the outer surface of the heat exchange tubes of the evaporator, leads to a significant reduction in electricity costs for air conditioning systems. The combined method between cold accumulators and cryocoolers has been considered by Arkhipov et al [3] in order to increase the life of the cryogenic cooling system. According to R. Sekret et al [4], the cold accumulator is applied by using the latent heat of a phase-change material in a layer of capsules with diameters of 80 mm, 70 mm, and 60 mm, the optimal working conditions according to the study are when using capsules with a diameter of 70 mm and a mass flow rate of 0.084 kg/s. In Vietnam, a study by Nguyen The Bao [5] also mentioned the melting of ice outside the pipes used in the cold storage battery in air conditioning systems.

---

\* Corresponding author: [tvhung@hcmut.edu.vn](mailto:tvhung@hcmut.edu.vn)

In Vietnam, as in other countries, consumption in the national electricity grid for one day is not stable (Figure 1), so the Vietnamese Electricity Company (EVN) sets three prices to stimulate the reduction of electricity consumption during the main peak periods and to encourage the use of electricity in the low hours.



**Fig. 1.** Electricity consumption in weekdays and holidays [6].

According to EVN, the price of electricity at the peak hours is 4,586 VND/kWh (19.80 \$cent/kWh), in normal hours the price is 2,666 VND/kWh (11.51 \$cent/kWh) and in the low hours the price is 1,662 VND/kWh (7.18 \$cent/kWh). The peak hours are during the intervals 10:00 ÷ 12:00 and 17:00 ÷ 20:00. The normal hours are in the intervals 4:00 ÷ 10:00, 12:00 ÷ 17:00 and 20:00 ÷ 22:00. The low hours are in 22:00 ÷ 4:00.

An opportunity for savings arises if at night, when the price of electricity is lowest, the cooling system works and the produced cold accumulates, and in other periods, when the price is higher, this accumulated cold is used to cool a building. The accumulation of cold not only reduces the electricity costs of the air conditioning system but also stabilizes the national electricity grid. Ho Chi Minh City is an economic and commercial centre not only in Vietnam but also in Southeast Asia and is known for its large number of large office buildings. These buildings do not work at night (when the price of electricity is lowest), which is why an office building was chosen as the subject of this study.

## 2 Modelling office building and conditioning system

The pilot building is an office building, located in Ho Chi Minh City. It has 3 basements for parking, 22 floors for offices and total area of 19,800 m<sup>2</sup>. The mode of operation of the building is only on weekdays, from 7:00 to 17:00.

The air conditioning system is designed according to Vietnamese norms. The designed indoor temperature and relative humidity are  $t = 26^{\circ}\text{C}$ ,  $\phi = 65\%$ .

The cooling load of the building is calculated by the Carrier method, according to which the total heat load is calculated by:

$$Q_o = \sum Q_{ht} + \sum Q_{at} = Q_{11} + Q_{21} + Q_{22} + Q_{23} + Q_{31} + Q_{32} + Q_{4h} + Q_{4a} + Q_{Nh} + Q_{Na} + Q_{5h} + Q_{5a} \quad (1)$$

where:

- $\sum Q_{ht}$ : Total sensible heat load of the building, kW;
- $\sum Q_{at}$ : Total latent heat load of the building, kW;
- $Q_{11}$ : Heat from solar radiation through the transparent area, kW;
- $Q_{21}, Q_{23}$ : Heat transfer through the roof and through the floor, kW;

- $Q_{22}$ : Heat transfer through the walls, doors and windows, kW;
- $Q_{31}$ ,  $Q_{32}$ : Heat from lighting systems and from equipment, kW;
- $Q_{4h}$ ,  $Q_{4a}$ : Sensible and latent heat of people, kW;
- $Q_{Nh}$ ,  $Q_{Na}$ : Sensible and latent heat of fresh air, kW;
- $Q_{5h}$ ,  $Q_{5a}$ : Sensible and latent heat of infiltration air, kW.

The cooling load of the building is  $Q_o = 3128$  kW (894 tons of refrigeration). The air conditioning system is designed with 3 chillers Model RTHD – D2G2G1 (RTHD 300 – 350 Tons – built for Industrial and Commercial Application), with Refrigerant R134a.

### 3 The cold accumulation systems

Currently, there are many cold accumulation technologies and schemes, divided of two groups:

- Sensible cold accumulation storage;
- Latent cold accumulation storage (ice cold storage, eutectic salt cold storage and etc.).

In this study, Cristopia's technology was chosen to represent the second group. Cristopia technology offers the accumulation of cold in phase-change materials. The phase change temperature ( $-33^{\circ}\text{C} \rightarrow 27^{\circ}\text{C}$ ) can be selected according to the user's needs (Table 1).

**Table 1.** Properties of phase change materials according to Cristopia's technology [7, 8].

Nodule type	Phase change temperature °C	Latent heat Ql kWh/m <sup>3</sup>	Sensible heat solid Qss kWh/°C	Sensible heat liquid Qsl kWh/°C	Heat transfer PCM crystallisation Kvor kW/°C	Heat transfer PCM fusion Kvfufu kW/°C	Nodule weight kg	Toxicity LD50 value in mg/kg a	Operating temperature limits °C
SN.33	- 33	44.6	0.7	1.08	1.6	2.2	724	2,600	-40°C to +60°C
SN.29	- 28.9	39.3	0.8	1.15	1.6	2.2	681	1,200	
SN.26	- 26.2	47.6	0.85	1.2	1.6	2.2	704	1,200	
SN.21	- 21.3	39.4	0.7	1.09	1.6	2.2	653	1,300	
SN.18	- 18.3	47.5	0.9	1.24	1.6	2.2	706	2,700	
IN.15	- 15.4	46.4	0.7	1.12	1.6	2.2	602	8,400	-25°C
IN.12	- 11.7	47.7	0.75	1.09	1.6	2.2	620	5,000	
IN.10	- 10.4	49.9	0.7	1.07	1.6	2.2	617	11,000	
IN.06	- 5.5	44.6	0.75	1.1	1.6	2.2	625	18,000	
IN.03	- 2.6	48.3	0.8	1.2	1.6	2.2	592	58,000	to
IC.00	0	48.4	0.7	1.1	1.6	2.2	558	85,000	+60°C
AC.00	0	48.4	0.7	1.1	1.15	1.85	560	85,000	
IC.27	+ 27	44.5	0.86	1.04	1.6	2.2	867	2,500	

#### 3.1 Cristopia's technology

With this technology, the phase change material is contained in nodules with structure (Figure 2) as follows:

- A sphere one millimetre thick, obtained by blow moldings of a blend of polyolefins. This material is neutral towards the heat transfer fluids;
- Phase Change Material (PCM) [9]. It could be organic (paraffin and fatty acids for example) or inorganic (hydrated salts), depending on temperature;
- Air pocket for expansion, the effect is a low stress on the nodule shell;
- Plug.



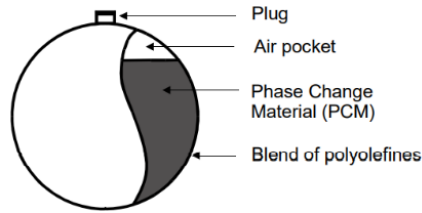


Fig. 2. The structure of a nodule.

The cold accumulation tank (STL – *le stockage latent* in French [10], or Storage of Latent heat) is made of steel or concrete and is well thermally insulated. The heat exchange between the spherical nodules and the system is by a liquid, in this case water. The tank can be horizontal or vertical (Figure 3).

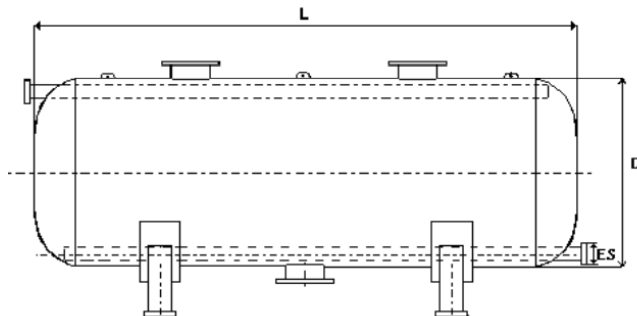


Fig. 3. A cold accumulator tank (storage of thermal latent - STL).

### 3.2 Principle of operation of the cold accumulation system

The principle of operation can be represented by five operating modes of the system.

- **STL charging:** At hours when the price of electricity is the lowest and there is no cooling load, the chillers work and the produced cold accumulates as the energy of the phase change (from liquid to solid phase) of the substance in spherical nodules (Figure 4.a).

- **The chillers work for building's cooling needs:** In off-peak hours, the chillers work for air conditioning system and there is no flow through the STL (Figure 4.b).

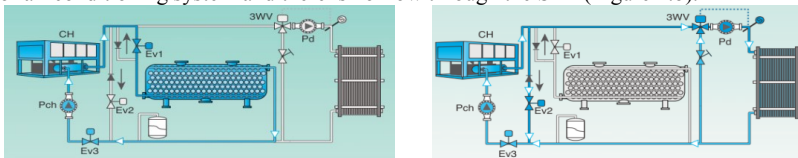
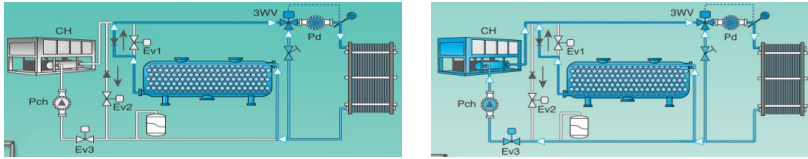


Fig. 4. a) STL charging; b) Chillers work for cooling needs.

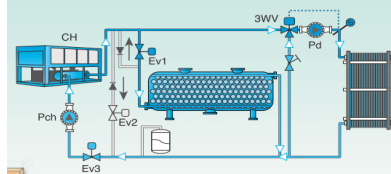
- **STL discharging:** At peak hours, when the price of electricity is highest, the chillers do not work and the air conditioning system uses accumulated cold from STL (Figure 5.a).

- **In case of overload of the air conditioning system or some of chillers are damaged:** STL can also be used when the air conditioning system is overloaded or some of chillers are damaged, to share cooling power (Figure 5.b).



**Fig. 5.** a) STL discharging; b) The chillers working and STL discharging.

-The chillers work for cooling needs and charge the STL (Figure 6).



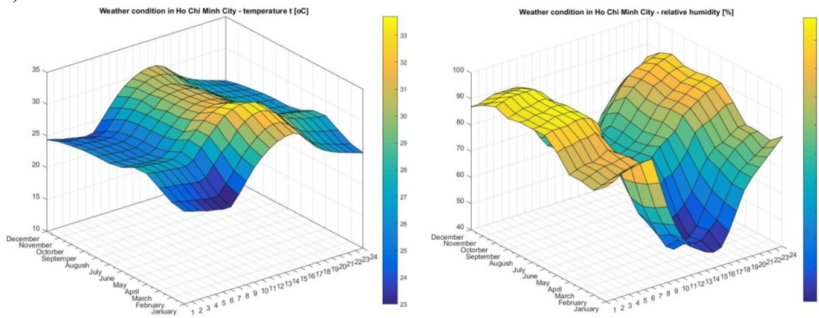
**Fig. 6.** Chillers work for cooling needs and charge the STL.

### 4 Analysis of the options for cold accumulation

Principle of operation: The STL system accumulates a sufficient amount of cold in hours when the price of electricity is the lowest. This accumulated cold will satisfy 100% of the required cold at peak hours and part of the required cold at normal hours.

Three steps to determine electricity costs:

- Step 1: Calculation of the cooling load of the building for each hour according to the Carrier method with the climatic data of Ho Chi Minh City. The climatic data includes the hourly values of temperature, relative humidity and solar radiation on horizontal and 8 vertical surfaces [11]. The temperature and relative humidity could be seen below (Figure 7).



**Fig. 7.** Hourly values of outdoor temperature and relative humidity of Ho Chi Minh City.

- Step 2: Determination of electricity consumption for each hour, by a calculated EER:

$$EER = \frac{Q_0 - N_2 - N_3 - N_6}{N_1 + N_2 + N_3 + N_4 + N_5 + N_6} \tag{2}$$

where:

- $Q_0$  - Cooling capacity of chiller, kW;
- $N_1$  - Electric power of chiller, kW;
- $N_2$  - Electric power of the pump for the first circulation circuit, kW;
- $N_3$  - Electric power of the pump for the second circulation circuit, kW;

- $N_4$  - Electric power of the cooling tower fans, kW;
- $N_5$  - Electric power of fans in AHU and FCU, kW;
- $N_6$  - Electric power of fresh air fans, kW.

- Step 3: According to the calculated electricity consumption for each hour of a typical day of the month from January to December, the annual saved electricity costs can be calculated using the following options:

- Option 1: The accumulated cold in STL is used only during the peak hours. In other periods, the cooling load is provided by the chiller system.
- Option 2÷7: The total consumption of cold at peak hours and 10% to 60% of the cooling demand at normal hours are provided by STL.

The calculation for Option 1 for January is shown below in Table 2, the same calculations are made for each month. Summarizing the results for all months leads to a result for the whole year.

In option 1, the distribution of cooling power for a typical day in January is shown in Figure 8. At peak hours (10:00 ÷ 12:00), when the price is highest, the demand for cooling of the building is satisfied by the accumulated cold in the STL tank. This accumulated cold is produced in the low hours (22:00 ÷ 4:00) when the price is the lowest.

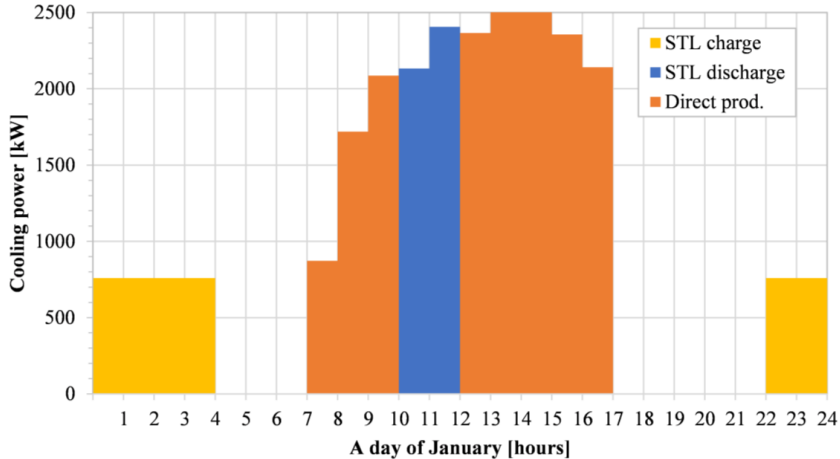


Fig. 8. Distribution of the cooling power of January (Option 1).

The saved electricity costs for a typical day of the month are calculated using the electricity costs for systems with and without STL as shown below.

- Calculation of electricity costs for a chilling system without STL:

Based on the hourly climate data, the required cooling capacity for each hour is calculated. Therefore, the electricity consumption and electricity costs of the chilling system for each hour can be calculated.

- Calculation of electricity costs for the chilling system with STL:

The required chiller capacity for each hour, electricity consumption, and electricity costs of the chilling system in normal hours (7:30÷10:00, 12:00÷17:00) are calculated as without STL. Electricity consumption from the chilling system and electricity costs in peak hours are calculated at the lowest price of electricity (Table 2).

The difference between the total amount of daily electricity costs without STL (717.73 USD) and the total amount of electricity costs with STL (571.13 USD) is the savings for one day: 146.60 USD.

**Table 2.** Analysis of a typical day of January in Option 1.

A day of January (22 workdays)							
Time	Without STL			With STL			
	Required cooling capacity (kW)	Hourly electricity consumption of the chiller system, (kWh)	Electricity costs (USD)	Accumulated cold in STL (kWh)	Required cooling capacity (kW)	Hourly electricity consumption of the chiller system (kWh)	Electricity costs (USD)
0h ÷ 1h				2,270.1	756.7	193.53	13.89
1h ÷ 2h				3,026.8	756.7	193.53	13.89
2h ÷ 3h				3,783.5	756.7	193.53	13.89
3h ÷ 4h				4,540.2	756.7	193.53	13.89
4h ÷ 5h				4,540.2			
5h ÷ 6h				4,540.2			
6h ÷ 7h				4,540.2			
7h ÷ 8h	872.2	223.07	25.68	4,540.2	872.2	223.07	25.68
8h ÷ 9h	1,719.2	439.69	50.61	4,540.2	1,719.2	439.69	50.61
9h ÷ 10h	2,086.0	533.50	61.41	4,540.2	2,086.0	533.50	61.41
10h ÷ 11h	2,133.6	545.68	108.05	2,406.6			
11h ÷ 12h	2,406.6	615.50	121.88				
12h ÷ 13h	2,366.0	605.12	69.66		2,366.0	605.12	69.66
13h ÷ 14h	2,521.4	644.86	74.23		2,521.4	644.86	74.23
14h ÷ 15h	2,506.0	640.92	73.78		2,506.0	640.92	73.78
15h ÷ 16h	2,356.2	602.61	69.37		2,356.2	602.61	69.37
16h ÷ 17h	2,142.0	547.83	63.06		2,142.0	547.83	63.06
17h ÷ 18h							
18h ÷ 19h							
19h ÷ 20h							
20h ÷ 21h							
21h ÷ 22h							
22h ÷ 23h				756.7	756.7	193.53	13.89
23h ÷ 0h				1,513.4	756.7	193.53	13.89
<b>Total</b>	-	<b>5,398.78</b>	<b>717.73</b>	-	-	<b>5,398.78</b>	<b>571.14</b>

Based on the saved electricity costs for a typical day of January and the number of working days per month, the saved electricity costs for one month are calculated. The same calculations are made for other months. Summarizing the results for all months, the saved electricity costs for the whole year are calculated.

To calculate the effectiveness of each option, it is necessary to calculate the investment. Based on the summary of the accumulated cold (kWh) each month for the option, the volume of the STL tank is calculated from the data in Table 1 (kWh/m<sup>3</sup>). So the investment for the option is also calculated. The result of option 1 is shown in Table 3.

**Table 3.** Analysis of option 1.

	Low hours	Normal hours	Peak hours	Total for year
Price of electricity (\$cent/kWh)	7.18	11.51	19.8	
1. Air conditioning system without STL				
Power consumption of chiller system (kWh)	0	1,033,973	283,327	1,317,300
Electricity costs (USD)	0	119,023	56,103	175,126
2. Air conditioning system with STL				
Power consumption of chiller system (kWh)	283,327	1,033,973	0	1,317,300
Electricity costs (USD)	20,332	119,023	0	139,355
3. Result				
Annual saved electricity costs (USD/year)	35,771			
Investment costs for STL system (USD)	96,058			
Payback time (year)	2.7			

Options 2 to 7 explore the greater potential for cold accumulation. This inevitably leads to larger investments, which must be assessed through technical and economic analysis.

Figure 9 shows the distribution of cooling power in January for option 4 when the total cold consumption at peak hours and 30% of the cold consumption at normal hours are used by STL. Compared to option 1, the accumulated cold (kWh) is larger, so the volume of STL is larger and therefore the investment is also larger.

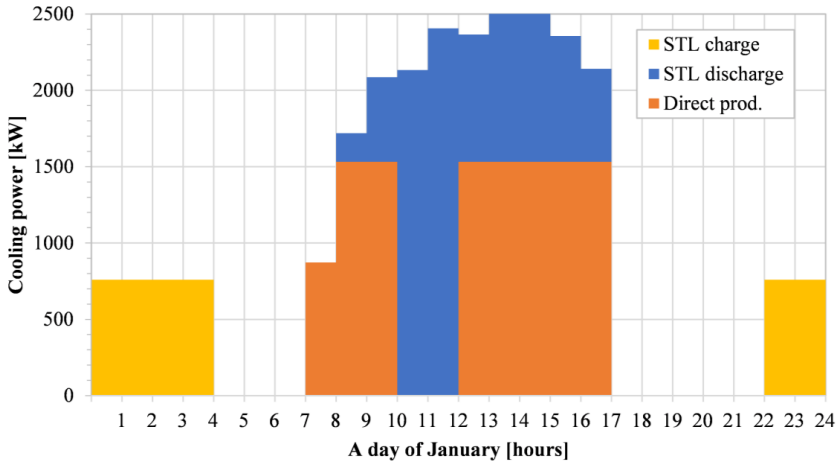


Fig. 9. Distribution of the cooling power of January (Option 4, peak hours + 30% normal hours).

Technical and economic analysis was made for all seven considered options. Nominal interest rate (8% for Vietnam) and inflation (3% last year) are taken into account. The economic life for all options is 15 years. The results of the analysis are shown in Table 4.

Table 4. Summary results for all options (calculated using the software *ENSI Economy*).

Printed from the *ENSI Economy* Software

Project: <b>Summary results</b>									
All Measures									
Real interest rate: 4,9 %									
Measures	*)	Investment [USD]	Net savings [USD/Year]	Lifetime [Year]	PB [Year]	PO [Year]	IRR [%]	NPV [USD]	NPVQ
Peak hours only		96.058	35.771	15	2,7	3,0	37	278.914	2,90
Peak hours +10% of normal hours		131.113	44.742	15	2,9	3,2	34	337.898	2,58
Peak hours +20% of normal hours		166.166	44.559	15	3,7	4,2	26	300.925	1,81
Peak hours +30% of normal hours		201.224	49.047	15	4,1	4,7	23	312.915	1,56
Peak hours +40% of normal hours		236.279	53.500	15	4,4	5,1	21	324.539	1,37
Peak hours +50% of normal hours		271.334	57.952	15	4,7	5,4	20	336.152	1,24
Peak hours +60% of normal hours		306.390	62.405	15	4,9	5,7	19	347.775	1,14

PB = Payback, PO = Pay-off, IRR = Internal Rate of Return, NPV = Net Present Value, NPVQ = Net Present Value Quotient

The analysis shows that option 1 has the best: Pay-off, Internal rate of return and Net present value quotient. Another advantage of this option is the lowest space required to install facilities.

## 5 Conclusion

The use of a cold storage system can reduce the electricity costs of air conditioning systems for office buildings in Ho Chi Minh City. With the option to accumulate cold only at peak hours (Option 1), the annual savings are \$ 35,771, while the investment costs are \$ 96,058 and the Pay-off period is 3.0 years. The Pay-off period for other options is from 3.2 to 5.7 years. The pilot building works only 5 days/week, from 7:00 to 17:00 (working hours include only 1 peak period/day) and for buildings with more working days/week, as well as including the second peak period (17:00 ÷ 19:00), the Pay-off period will be even less.

We would like to thank Ho Chi Minh City University of Technology (HCMUT), VNU-HCM for the support of time and facilities for this study.

## References

1. M. Zlateva. *Proceedings of the XXI Scientific Conference with International Participation FPEPM 2016 (in Bulgarian)*, **1**, pp. 199 – 204, (2016).
2. D. Shlychkov. *E3S Web of Conferences*, **135**, 03071, ITESE-2019, (2019).
3. V. T. Arkhipov, V. F. Getmanets, A. Ya. Levin, R. S. Mikhailchenko, H. Stears. *Cryocoolers*, **10**, pp. 689-696, (1999).
4. R. Sekret, P. Starzec. *Energies*, **14**(9):2703, (2021).
5. T. B. Nguyen, H. A. Truong. *Sci. Tech. Dev. J.*, **10**, No.02, (2007).
6. Tran Thanh Ky, Nhà máy nhiệt điện, Trường ĐH Bách Khoa TPHCM, (1998).
7. *Technical manual*. Cristopia Energy Systems, (2000).
8. Cristopia Energy Systems. Thermal energy storage. <https://www.ciat.uk.com/wp-content/uploads/2017/02/cristopia-brochure.pdf>, (2017).
9. A. Amer, V. Lebedev. *Int. J. Sci. Eng. Res.*, **9**(5), (2018).
10. I. Dincer, M. A. Rosen. *Thermal energy storage: systems and applications - 2<sup>nd</sup> ed.*, Wiley, (2011).
11. Vietnam Building code, Natural Physical and Climatic data for construction QCXDVN 02: 2015/BXD, (2015).

# Thermal-hydraulic analysis of a VVER-1000 core in MSLB conditions

*Svetlomid Mitkov<sup>1</sup>, Ivan Spasov<sup>2\*</sup>, and Nikola Kolev<sup>1</sup>*

<sup>1</sup> Reactor Physics Laboratory, Institute for Nuclear Research and Nuclear Energy – Bulgarian Academy of Sciences, Bulgaria

<sup>2</sup> Department of Thermal Power Engineering and Nuclear Power Engineering, Technical University of Sofia, Bulgaria

**Abstract.** The objective of this paper is to analyze the ability of a VVER-1000 core and its control system to cope with a hypothetical main steam line break (MSLB) accident in case of multiple equipment failures. The study involves the use of advanced 3D core calculation models benchmarked and validated for reactivity accidents in preceding studies. A MSLB core boundary condition problem is solved on a coarse (nodal) mesh with the coupled COBAYA/CTF neutronic/thermal hydraulic codes. The core thermal-hydraulic boundary conditions are obtained from a preceding full-plant MSLB simulation. The assessment of the core safety parameters is supplemented by a fine-mesh (sub-channel) thermal-hydraulic analysis of the hottest assemblies with the CTF code using information from the 3D nodal COBAYA/CTF calculations. Thirteen variants of a pessimistic MSLB scenario are considered, each of them assuming a number of equipment failures aggravated by eight control rods stuck out of the core after scram at different locations in the overcooled sector. The results (within the limitations of the adopted modeling assumptions) show that the core safety parameters do not exceed the safety limits in the simulated aggravated reactivity accidents.

## 1. Introduction

A major concern in a main steam line break (MSLB) reactivity accident is the risk of core overheating. In the computational analysis of such accidents the safety parameters of particular interest are the fuel centerline temperature, the departure from nucleate boiling ratio (DNBR) and the fuel rod cladding temperature. The fuel temperature should be kept well below the UO<sub>2</sub> melting temperature which can significantly vary depending on the fuel burnup. As a VVER-1000 core can contain once, twice, three or four times burnt fuel assemblies, it is of practical interest to analyze the consequences of such an asymmetric reactivity accident at the end of core life and for various combinations of equipment failure.

This paper presents results from the analysis of thirteen variants of a hypothetical MSLB scenario, each of them assuming a number of equipment failures plus eight control rods stuck out of the core after scram at different radial locations in the overcooled sector.

---

\* Corresponding author: [spasov@tu-sofia.bg](mailto:spasov@tu-sofia.bg)

The main objective is to demonstrate the use of state-of-the-art 3D core calculation models which have been benchmarked and partly validated for VVER-1000 reactivity accidents in preceding studies. A specific objective is to make a step in the analysis of the ability of a VVER-1000 core and its control system to cope with such an accident without exceeding the safety limits. Uncertainty analysis is beyond the scope of this work.

## 2. Methodology

### 2.1 Accident scenario

The considered accident scenario is based on aggravated variants of the pessimistic scenario in the OECD/NEA VVER-1000 MSLB benchmark (V1000CT-2) [1]. The task is to solve a MSLB core boundary condition problem using coupled 3D neutronic/thermal hydraulic codes, given the core thermal-hydraulic (TH) boundary conditions as obtained from a full plant simulation. The core boundary conditions (BCs) are taken to be as specified in the V1000CT-2 benchmark [1, 2]. The plant transient is initiated at hot full power by a large guillotine type break of steam line #4 outside the containment, upstream of the steam intercept valve. The reference core is a real Kozloduy-6, Cycle 8 three-year batch core at 270.4 EFPD [1]. The core contains once, twice and three times burnt  $\text{UO}_2$  fuel of initial enrichment 4.23 w/o and 4.4 w/o. The steam generator feed-water valve in the faulted loop fails to close on MSLB signal and remains open. The main coolant pump (MCP) in the faulted loop fails to trip on MSLB signal and all MCP remain in operation. The steam generator in the faulted loop continues uncontrolled cooling till the complete evaporation of the secondary water. A cooler sector is formed at the core inlet, with overcooling of up to 80°C. During the transient eight peripheral control rod clusters (CR) are assumed to remain stuck out of the core after scram, all of them in the overcooled sector. Thirteen cases with different radial combinations of the stuck rods are to be analyzed to assess the values of the core safety parameters.

### 2.2 Codes and methods

#### 2.2.1 Full-core nodal calculation

Full-core coarse-mesh (nodal) simulations for each CR configuration were carried out with the coupled COBAYA4/CTF neutronic/thermal-hydraulic codes.

COBAYA4 [3, 4] is a 3D multi-scale core physics code using transport-corrected multi-group diffusion approximation. It is developed by the Universidad Politecnica de Madrid and benchmarked for VVER-1000 calculations [5, 6] in the frame of the EU NURISP [7] and NURESAFE [8] projects. At the nodal level the analytical coarse-mesh finite-difference (CMFD) method [9] is used. The code has radial mesh refinement capability.

COBRA-TF (CTF) [10, 11] is a recent version of the COBRA-TF thermal-hydraulic (TH) code which uses a two-fluid, three-field modeling approach and has sub-channel capabilities.

The COBAYA4/CTF coupling method [12] for VVER-1000 is based on the MED Coupling libraries in the Salome platform [13]. The coupling and the coupled models have been tested for VVER MSLB in preceding studies [5, 14]. The modeling assumptions in the coupled COBAYA4/CTF VVER-1000 calculation models are briefly summarized below:

- Coarse-mesh COBAYA 3D neutron kinetics with:
  - 30 axial nodes in the heated region;
  - 2 nodes in each axial reflector;



- 6 triangles per hexagon.
- Use of a realistic VVER-1000 multi-parameter two-group cross-section library [15] for reactivity accident analysis which has been generated with the APOLLO2 code [16] and validated in the frame of the NURESAFE project [8];
- Use of time-dependent assembly-by-assembly MSLB thermal-hydraulic core boundary conditions (inlet temperatures, inlet mass flow rates, and outlet pressures) obtained from a full plant simulation involving a quasi-3D reactor pressure vessel TH model [17];
- Coarse-mesh CTF thermal-hydraulic model with one channel per assembly and 30 axial nodes in the heated part;
- Fuel model with 9 radial rings in the fuel, one for the gas gap and one for the cladding;
- Temperature-dependent fuel and cladding thermal-physical properties [18];
- The spacer grids are not explicitly modeled and are taken into account by the vertical pressure loss coefficients;
- The gas gap conductance coefficient is taken constant, equal to 3070 W/m<sup>2</sup>K, as estimated at average core burnup of 26.6 MWd/kgHM [1];
- Chen's model of nucleate boiling [19] and the W-3 critical heat flux (CHF) correlation [20] with non-uniform power distribution.

### 2.2.2 Sub-channel assembly calculations

Two variants of the transient having the most risky values of the core safety parameters were selected for sub-channel TH calculations of the hottest assemblies. Such simulations were carried out for the hottest assemblies and assemblies next to them so that the analysis includes once, twice or three times burnt fuel. The main modeling assumptions were as follows:

- Assembly thermal-hydraulic problems were solved with inlet/output TH BCs from the plant system simulation, and assembly powers and axial power profiles as obtained from the full-core nodal simulation with COBAYA4/CTF;
- Radial pin-power distribution taken such as at hot full power for the hottest assemblies, and with artificially imposed 5% radial tilt for the considered adjacent assembly of higher burnup;
- Coolant-centered radial spatial mesh with 660 sub-channels per assembly;
- Axial mesh with 30 nodes in the heated region;
- Fuel model with 9 radial rings in the fuel pellet, 1 for the gap and 1 for the cladding. The central hole is taken into account, and conduction in radial and axial direction is considered;
- The bypass of 2.2% through the control rod guide tubes in the un-rodged assemblies is not explicitly modeled and is taken into account by decreasing the active coolant flow;
- The spacer grids are not explicitly modeled and are taken into account by the vertical pressure loss coefficients;
- User defined coolant mixing coefficient of 0.01 (and exploratory option of 0.03 to study the impact of higher coefficients);
- Use of the W-3 CHF correlation with non-uniform power distribution;
- Use of both Chen's [19] and Thom's [21] models of nucleate boiling, to compare the performance;
- Constant fuel gap conductance coefficient equal to 3070 W/m<sup>2</sup>K as estimated at average core burnup of 26.6 MWd/kgHM [1];
- Temperature-dependent fuel and cladding thermal-physical properties [18].

Details of the sub-channel input model for VVER assemblies can be found in ref. [22].

### 3. Results

#### 3.1 Full-core nodal calculations

**Table 1** Summary of the coarse-mesh computed core configurations and safety parameters

Case #	Stuck CR, #	Max return to power MW	Hottest assembly # & Adjacent assembly #	Assembly burnup MWd/kgHM	Fxy	Max T <sub>fuel</sub> , °C	T <sub>melt</sub> UO <sub>2</sub> , °C	Max T <sub>clad</sub> , °C	Min DNBR
1	90,91,105, 106,117, 118,130, 140	1098	104 / 117	15.3/ 31.0	7.694/ 6.958	2015/ 2018	2745/ 2650	335.5	4.21/ 4.27
2	82,90,91, 105,106, 117,118,130	889.8	104 / 117	15.3	8.927/ 7.470	1851/ 1580		313.2/ 298.8	4.69/ 5.98
3	79,90,91, 105,106, 117,118, 130	986.8	104 / 90	15.3	8.303/ 6.964	1976/ 1661		319 / 303	4.23/ 5.57
4	63,90,91, 105,106, 117,118, 130	991.2	104 / 90	15.3	8.421/ 7.440	1912 / 1680		319.2/ 307.4	4.31/ 5.29
5	63,82,90, 91,105, 106,117, 118	891.9	104 / 90	15.3/ 24.1	8.986/ 8.076	1826 / 1630		313.4/ 303.7	4.72/ 5.60
6	105,106, 117,118, 130,140, 142,151	1051	129 / 140	15.45 / 24.2	8.013/ 7.605	1944 / 1831	2745/ 2690	320.2 / 315.2	4.31/ 4.71
7	64,90,91, 105,106, 117,118, 130	933.5	104 / 117	15.3	8.703/ 7.219	1902 / 1609		316.3 / 301	4.46/ 5.80
8	90,91,94, 105,106, 117,118,130	957.3	104 / 117	15.3	8.388/ 7.036	1912 / 1642		316 / 302	4.46/ 5.69
9	90,91,105, 106,117, 118,120, 130	984.4	104 / 90	15.3	8.112/ 6.704	1926 / 1584		316./ 299.	4.43/ 5.96
10	91,105, 106,117, 118,120, 130,140	1005	129 / 140	15.45	8.141/ 6.887	1957/ 1665		318.8 / 304	4.27/ 5.53
11	91,94,105, 106,117, 118,130, 140	963.7	129 / 117	15.45	8.301/ 6.989	1882 / 1636		315.4 / 301.5	4.54/ 5.70
12	91,105, 106,117, 118,130, 140,151	1035	129 / 140	15.45	8.115/ 7.319	1906 / 1702		320 / 310.	4.30 / 5.11
13	91,105, 106,117, 118,130, 140,142	955.9	129 / 140	15.45	8.503/ 7.293	1884/ 1623		316.4 / 302.7	4.48/ 5.67
	Limiting values			0.0			2840	1200	1.45*
	of the safety parameters			49.0			2540	1200	1.45*

\* When using the W-3 DNB correlation

Table 1 summarizes the suite of 13 variants of the MSLB scenario and the corresponding coarse-mesh computed core safety parameters. In each case, the parameters of the hottest assembly (which appears to be once burnt) and those of an adjacent assembly (twice or three times burnt) with high  $F_{xy}$  power peaking factor are shown.

The nodal simulation results show that the highest return to power after scram and the highest radial peaking factors occur in Case 1 and Case 6.

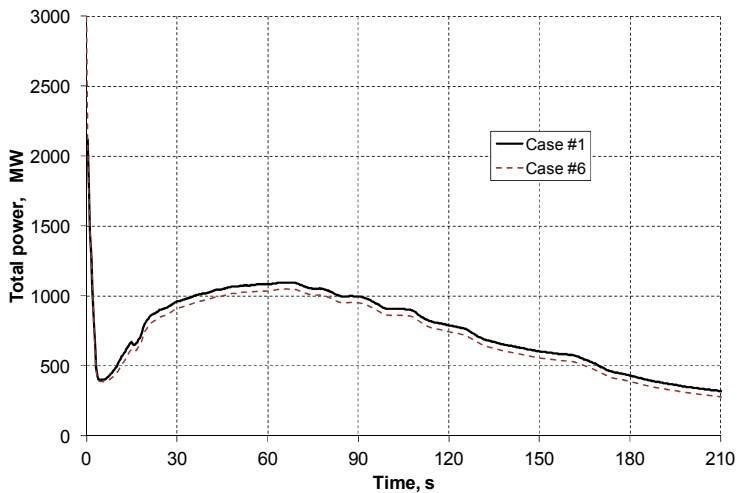
Figure 1 shows the time history of the total core power in Case 1 and Case 6 of the transient. The corresponding maximum return to power after scram is 1098 MW, respectively 1051 MW, at 67s from the onset of the transient.

Figure 2 illustrates the computed relative assembly powers at time of max return to power (67s) in Case #1. The radial locations of the fully inserted control rod clusters are marked in blue and those of the stuck rods – in beige. The hottest assembly is the unrodded #104, marked in brick.

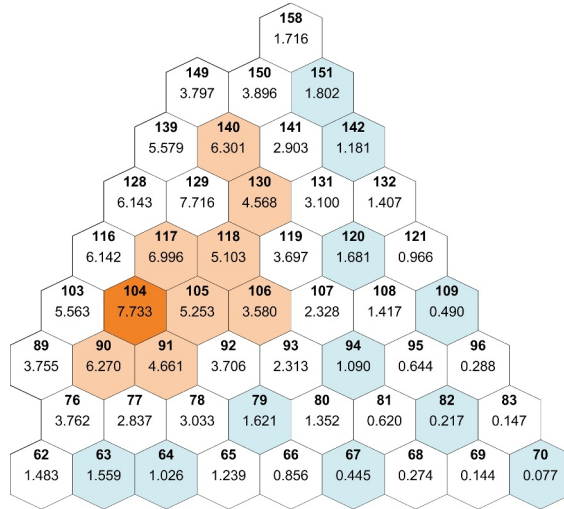
Figure 3 illustrates the computed relative assembly powers at time of max return to power (67s) in Case #6. The core map format is as in Figure 2. The hottest assembly is the unrodded #129, marked in brick.

The assembly-wise power distributions show that a big part of the core power is released in the region of stuck rods in the overcooled core sector. The peak of the 3D power distribution in the disturbed sector is near the core periphery. Correspondingly, Case 1, assembly #104 (15.3 MWd/kgHM) and the adjacent #117 (31.0 MWd/kgHM), as well as Case 6, assembly #129 (15.45 MWd/kgHM) and the adjacent #140 (24.1 MWd/kgHM) were selected for additional sub-channel thermal-hydraulic analysis.

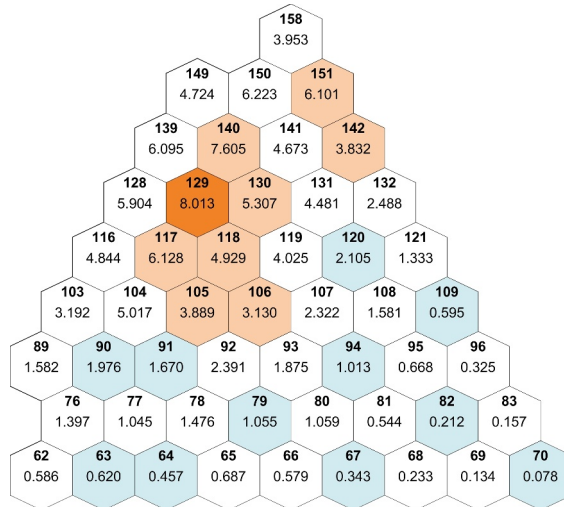
Figure 4 illustrates the coarse-mesh computed axial power distributions at time of max return to power - core-averaged and assembly-wise for the assemblies of interest for sub-channel analysis.



**Fig. 1** Time history of the total core power



**Fig. 2** Case #1 : Computed relative assembly powers at time of max return to power (67s)



**Fig. 3** Case #6: Computed relative assembly powers at time of max return to power (67s)

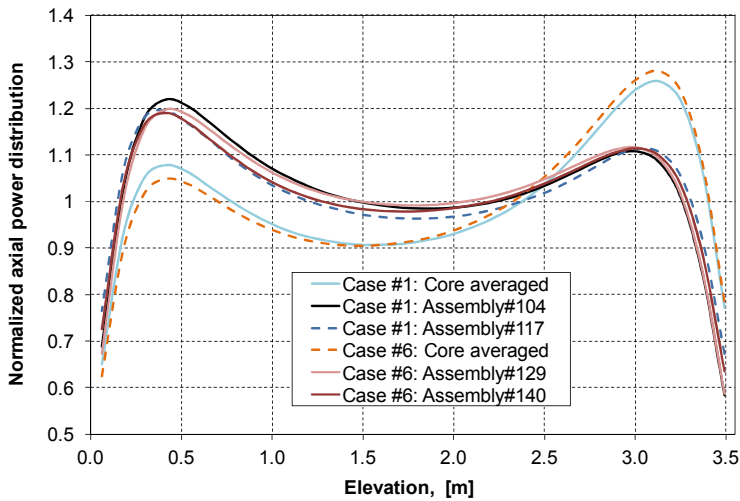


Fig. 4 Computed axial power distribution at time of max return to power

### 3.2 Sub-channel thermal-hydraulic calculations

In Case 1, sub-channel TH analysis was carried out for the hottest assembly which is #104 (15.3 MWd/kgHM) and for the adjacent #117 (31.0 MWd/kgHM).

In Case 6, sub-channel calculation was performed for the hottest #129 assembly (15.45 MWd/kgHM) and the assembly #140 (24.1 MWd/kgHM) next to it.

In both cases the assembly inlet and outlet TH boundary conditions at time of max return to power are nearly the same. The inlet temperatures for Case 1, assembly #104 and #117 are 207.62 °C, and for Case 6, assembly #129 and #140 are 207.7 °C and 207.66 °C respectively. The corresponding inlet mass flow rates are nearly the same.

It should be noted that some preliminary sub-channel results for Case 1, hot assembly #104 have been reported in ref. [23], and this study extends the sub-channel analysis to more cases and various assemblies including such of higher burnup, where the UO<sub>2</sub> melting temperature is lower.

The peak of the 3D power distribution in the disturbed sector is near the core periphery and corresponds to the radial location of the hottest assembly. For such a configuration and in the lack of full-core pin-by-pin calculation, it is reasonable to assume a hot full power-like radial pin-power distribution for the hottest assembly (#104 in Case 1, and #129 in Case 6). An approximate tilt of  $\pm 5\%$  across the assembly section is assumed for the adjacent assemblies.

Figure 5 illustrates the adopted pin-power distribution at hot full power (HFP).

Details of the computed distributions are illustrated in Figures 6 through 14.

Table 2 summarizes the sub-channel results for the core safety parameters, obtained with the Chen and Thom options of the nucleate boiling model in CTF. The results in this table and the figures below (except for Figure 12) are obtained with user defined cross-channel mixing coefficient of 0.01. A small value is specified because this coefficient is not yet validated. Thus, the cross-channel mixing is mainly gradient driven. See Figures 11 and 12 for a parametric study of the impact of higher values of the user defined mixing coefficient on the vapor volume fraction.

0.000  
 1.001 1.001  
 1.000 1.000 1.000  
 0.998 0.997 0.000 0.998  
 0.992 0.984 0.993 0.994 0.992  
 0.000 0.990 0.992 0.993 0.992 0.000  
 0.982 0.986 0.988 0.000 0.988 0.987 0.983  
 0.971 0.973 0.975 0.985 0.985 0.975 0.973 0.971  
 0.985 0.978 0.976 0.979 0.979 0.979 0.976 0.978 0.985  
 1.015 1.002 0.998 0.993 0.995 0.995 0.994 0.998 1.002 1.015  
 1.078 1.057 1.046 1.041 1.040 1.038 1.040 1.054 1.046 1.057 1.078

**Fig. 5** PERMAK [24] computed radial pin power distribution in a fuel assembly at hot full power

**Table 2** Sub-channel computed core safety parameters

Case	Assembly # / Burnup, MWd/kgHM	Fxy	5% tilt of the radial pin-power distribution	Hot cell exit vapor volume fraction, %	Max T fuel, °C	T melt UO <sub>2</sub> , °C	Max T clad, °C	Min DNBR
1	104 / 15.3	7.733	no	0.32	2506	2745	333.1	2.66
1	117 / 31.0	6.996	yes	0.20	2367	2650	328.3	2.96
6	129 / 15.45	8.013	no	0.30	2456	2744	332.7	2.69
6	140 / 24.2	7.605	yes	0.31	2439	2690	332.4	2.71
6	140 / 24.2	7.605	no	0.16	2341	2690	327	3.03
6*	129 / 15.45	8.013	no	0.12	2456	2744	330.1	2.69
6*	140 / 24.2	7.605	no	0.05	2341	2690	327	3.03

\*When using the Thom nucleate boiling correlation

In Table 2, the limiting values of the core safety parameters are as follows:

- Tmelt UO<sub>2</sub>, °C: 2840 °C for fresh fuel and 2540 °C for burnt fuel (at 50 EFPD for the considered VVER fuel);
- T clad: 1200 °C;
- Min DNBR: 1.45 (when using the W-3 DNB correlation).

The predicted values of the core safety parameters (within the limitations of the modeling assumptions) do not exceed the safety limits. However, the impact of the 5% tilt of the radial assembly pin power distribution is considerable and indicates that this issue requires further attention using full-core pin-by-pin coupled calculations.

Figures 6 and 7 show the sub-channel results for Case 1, assembly #104 obtained with HFP pin-power distribution and Chen's nucleate boiling model.

Figure 8 illustrates the results for Case 1, assembly #117, obtained with 5% tilt in the pin-power distribution across the hexagonal section and Chen's nucleate boiling model.

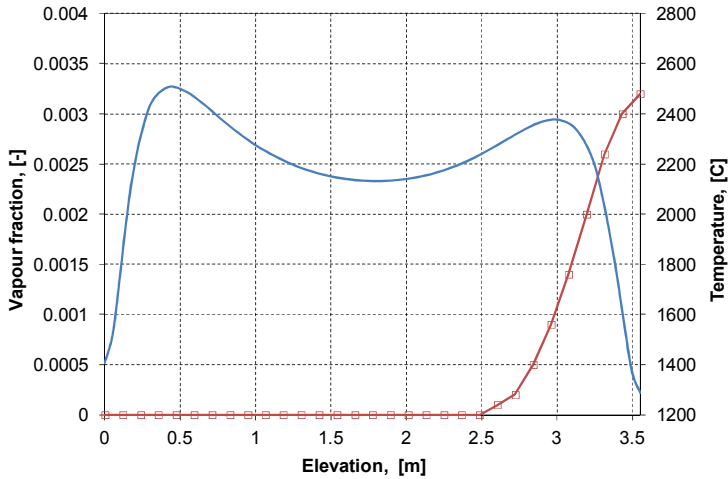
Figures 9 through 12 show the results for Case 6, hot assembly #129 (15.45 MWd/kgHM). The results are obtained using HFP pin-power distribution. The comparison of the sub-channel liquid fraction maps in Figures 11 and 12 shows the impact of using higher values of the cross-channel mixing coefficient (0.03) – the sub-cooled boiling area shrinks toward the assembly center.

Figures 13 and 14 show the results for Case 6, assembly #140 (24.2 MWd/kgHM), obtained with ±5% tilt in the pin-power distribution across the hexagon and Chen's nucleate boiling model.

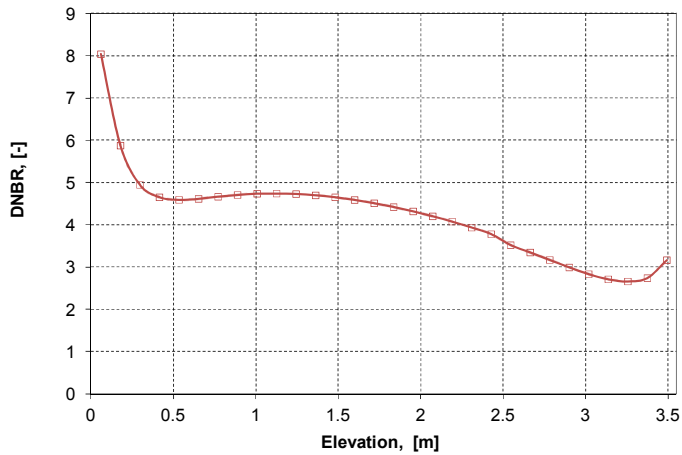
The results in Figures 6, 8, 9 and 13 show that despite the high power peaking factors in the hottest assemblies only subcooled boiling and small vapor volume fraction in the upper part of the assemblies is predicted, because of the low inlet temperatures.

Figure 9 shows that the use of Chen's nucleate boiling model predicts higher vapor void fraction in the subcooled region compared to that obtained with the Thom correlation.

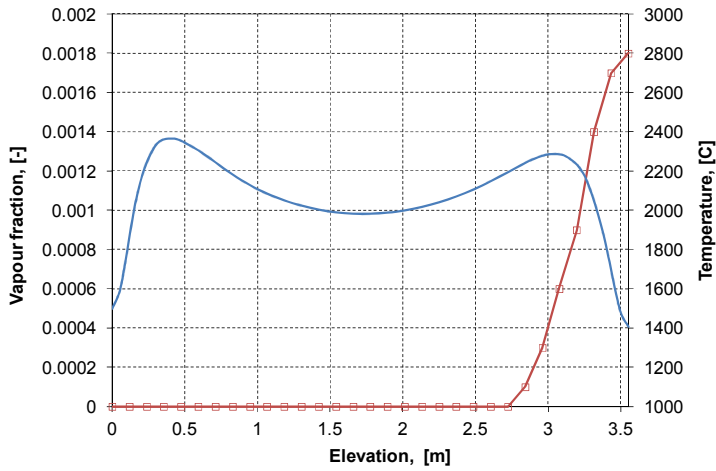
Both Chen's and Thom's correlations predict nearly the same axial profiles of the fuel centerline and cladding temperatures (see Figure 10).



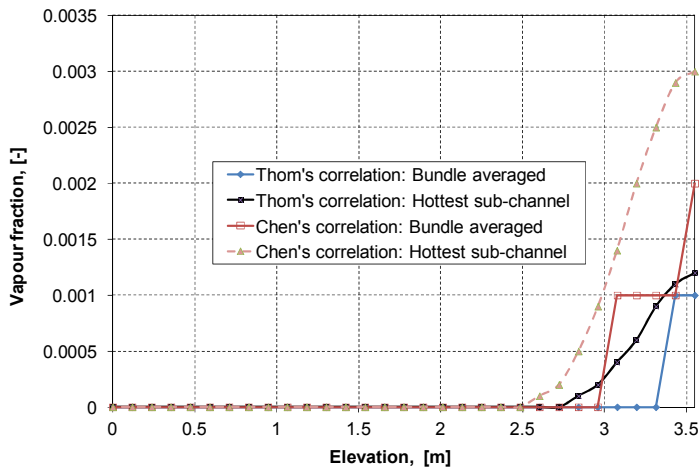
**Fig. 6** Case #1, Assembly #104: Computed hottest pin centerline temperature and hot cell vapor volume fraction at max return to power, when using the Chen nucleate boiling model



**Fig. 7** Case #1, Assembly #104: Computed DNBR (z) using the W-3 correlation and HFP pin power distribution, at max return to power

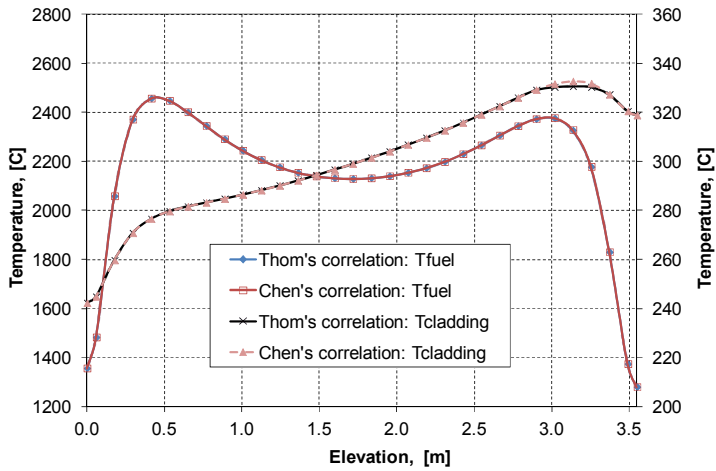


**Fig. 8** Case #1, Assembly #117: Computed hottest pin centerline temperature and hot cell vapor volume fraction at max return to power, when using the Chen nucleate boiling model

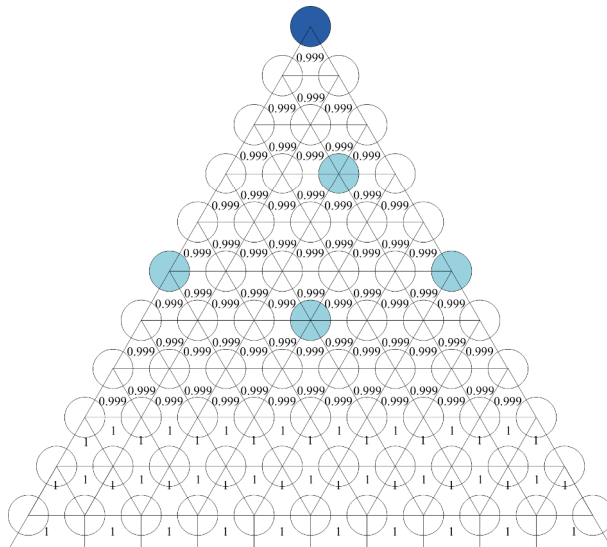


**Fig. 9** Case #6, Assembly #129: Computed axial distribution of the bundle averaged and hot cell vapour volume fractions

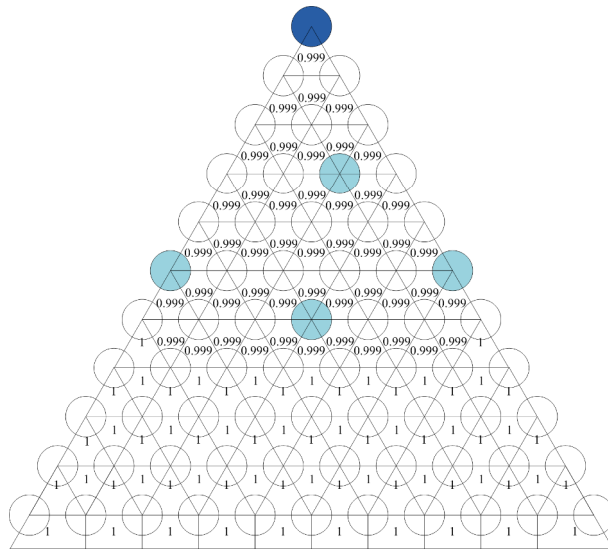




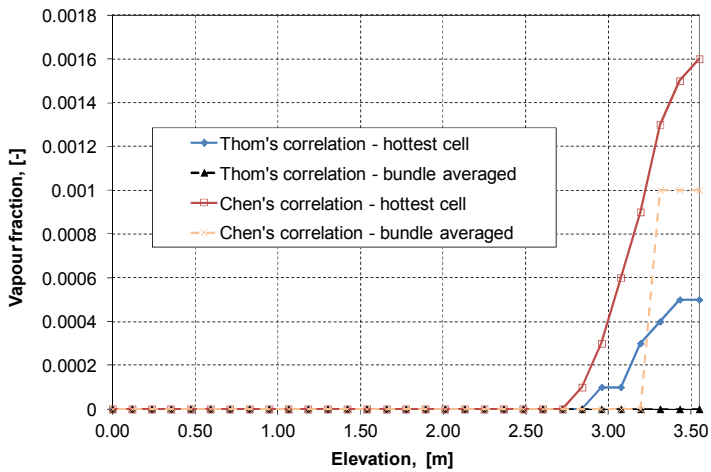
**Fig. 10** Case #6, Assembly #129 : Computed hottest pin centerline and cladding temperatures.  $T_{max, fuel}=2456,4\text{ C}$  ,  $T_{max, clad-Chen} = 332,7\text{ °C}$  ,  $T_{max, clad-Thom} = 330,6\text{ °C}$



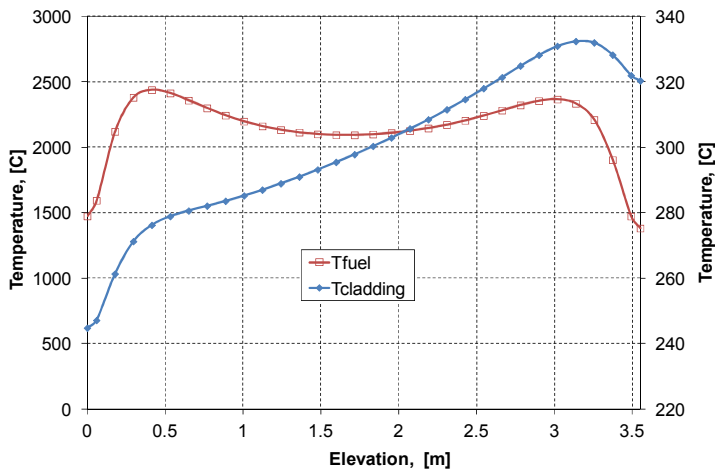
**Fig. 11** Case #6, Assembly #129 at max return to power: Computed exit liquid volume fraction, with user defined mixing coefficient of 0.01 and Thom's nucleate boiling model



**Fig. 12** Case #6, Assembly #129 at max return to power: Computed exit liquid volume fraction, with user defined mixing coefficient of 0.03, and Thom's nucleate boiling model



**Fig. 13** Case #6, Assembly #140: Computed vapor volume fraction with pin-power distribution tilt



**Fig. 14** Case #6, Assembly #140 : Computed hottest pin centerline and cladding temperatures using Chen's nucleate boiling model and pin-power tilt.  $T_{\max, \text{fuel}} = 2439 \text{ }^{\circ}\text{C}$ ,  $T_{\max, \text{clad}} = 332.4 \text{ }^{\circ}\text{C}$

#### 4. Summary and conclusions

The safety parameters of a VVER-1000 core near the end of life were analyzed for a suite of pessimistic MSLB accident scenarios. For this purpose, coupled full-core COBAYA4/CTF neutronic/ thermal-hydraulic simulations at the nodal level were supplemented by CTF sub-channel calculations for the hottest assemblies of different burnup in the most risky cases.

In the CTF sub-channel assembly simulations, modeling options in the modeling assumptions with the Chen and Thom nucleate boiling models and with different user-specified cross-channel mixing coefficients were compared.

The results show that:

- In all cases the predicted fuel cladding temperature at time of max return to power is far below the limiting value of  $1200 \text{ }^{\circ}\text{C}$ ;
- The predicted sub-cooled boiling in the upper part of the hottest sub-channels is insignificant, even in the worst cases. The Chen model of nucleate boiling predicts higher vapor volume fraction compared to that obtained with Thom's model (as observed in other LWR assembly calculations);
- The minimum DNBR value of 2.66 predicted in the worst Case 1, Assembly #104 is well above the limiting value of 1.45 when using the W-3 CHF correlation;
- The predicted fuel centerline temperature in the hottest assemblies has a moderate margin of about  $237 - 251 \text{ }^{\circ}\text{C}$  to the burnup dependent  $\text{UO}_2$  melting temperature. Because of its importance, and of its strong dependence on the local pin power distribution and on the gap conductance coefficient, the assessment of this safety parameter deserves further attention.
- In case of boiling in the assembly, the user-defined cross-channel mixing coefficient in sub-channel CTF needs further validation on measured assembly

data because of its impact on the void fraction distribution. In the meantime, small values or not using this coefficient produce more conservative results.

The results (within the limitations of the adopted modeling assumptions) show that the core safety parameters do not exceed the safety limits in the simulated aggravated reactivity accidents.

Further improved analyses are expected to include a coupled pin-by-pin neutronic/thermal-hydraulic calculation, at least for a mini-core of seven assemblies around the hottest one, as well as a dynamic gap conductance coefficient, a DNBR from VVER-specific CHF skeleton tables in CTF, and uncertainty quantification.

## 5. References

1. N.P. Kolev et al: VVER-1000 Coolant transient benchmark Phase II (V1000CT-2), Vol.2, Final Specifications of the VVER-1000 MSLB problem. NEA/NSC/DOC 2006(6) © OECD (2010)
2. N.P. Kolev, I. Spasov, Tz. Tzanov, E. Royer: VVER-1000 Coolant Transient Benchmark: Phase 2 (V1000CT-2) Volume 4: Summary results of coupled 3D kinetics/core-vessel thermal hydraulics and core-plant MSLB simulation. NEA/NSC/DOC (2011)3, Paris © OECD (2011)
3. COBAYA team: COBAYA4 user's guide. UPM Report, Madrid, (2015)
4. C. Ahnert: Capacities and achievements of the COBAYA4 code after the NURES SAFE project. NURES SAFE Open General Seminar, Brussels, November 4-5, (2015).
5. N.P. Kolev, I. Spasov, N. Zheleva, G. Todorova, N. Petrov, P. Ivanov, S. Mitkov, O. Kamenscic, J. Hadek, L. Vyskocil, J. Jimenez, V.H. Sanchez, S. Sanchez-Cervera, N. Garcia-Herranz, A. Sabater, D. Cuervo: Higher-resolution VVER MSLB simulation – Final Report. *NURES SAFE D14.41 report*, Feb (2016)
6. B. Chanaron, C. Ahnert, N. Crouzet, V. Sanchez, N. Kolev et al, “ Advanced multi-physics simulation for reactor safety in the framework of the NURES SAFE project”, *Annals of Nuclear Energy*, **Volume 84**, pp. 166-177, doi:10.1016/j.anucene.2014.12.013, (2015)
7. B. Chanaron, C. Ahnert, D. Bestion, M. Zimmermann, N. Crouzet: The European Project NURISP for Nuclear Reactor Simulation. *Proc. 2010 Annual Meeting of the American Nuclear Society*, San Diego, CA, 13-17 June, (2010)
8. B. Chanaron: Overview of the NURES SAFE European Project, *Nuclear Engineering and Design*, **Vol. 321**, pp.1-7 DOI: 10.1016/j.nucengdes.2017. 09.001, (2017)
9. Juan-Andrés Lozano, Javier Jiménez, Nuria García-Herranz, José-María Aragonés: Extension of the analytic nodal diffusion solver ANDES to triangular-Z geometry and coupling with COBRA-IIIc for hexagonal core analysis, *Annals of Nuclear Energy*, **37** pp. 380–388, (2010)
10. M. Avramova, R. Salko et al.: COBRA-TF (CTF) 2013 User's Guide. Pennsylvania State University, PA, Nov (2013)
11. R.K. Salko, M. Avramova: COBRA-TF Sub-channel Thermal Hydraulic Code (CTF) Theory Manual, CASL-U-2016-1110-000, Pennsylvania State University, May 25 (2016).
12. N. García-Herranz, D. Cuervo, A. Sabater, G. Rucabado, S. Sánchez-Cervera, E. Castro: Multi-scale neutronics/thermal-hydraulics coupling with COBAYA4 code for pin-by-pin PWR transient analysis. *Nuclear Engineering and Design*, **Volume 321**, pp. 38-47, September (2017)

13. Salome 6: <http://www.salome-platform.org/>
14. I. Spasov, S. Mitkov, N.P. Kolev, S. Sanchez-Cervera, N. Garcia-Herranz, A. Sabater, D. Cuervo, J. Jimenez, V.H. Sanchez, L. Vyskocil: Best-estimate simulation of a VVER MSLB core transient using the NURESIM platform codes. *Nucl. Eng. and Design*, **Vol. 321**, pp.26-37, (2017)
15. N. Petrov, I. Spasov, N.P. Kolev, S. Sanchez-Cervera, N. Garcia-Herranz: Nodal level XS library v2 for VVER parameterized for MSLB. *NURESAFE D14.25-Rev2 report*, Jan (2015)
16. R. Sanchez: APOLLO2 Year 2010. *Nuclear Engineering and Technology*, **Vol.42**, No.5, pp 474-499, October (2010)
17. I. Spasov, N.P. Kolev, J. Donovan, L. Sabotinov: CATHARE Multi-1D Modeling of Coolant Mixing in VVER-1000 for RIA Analysis. *Science and Technology of Nuclear Installations*, **Vol.2010**, Article ID 457094, Hindawi, New York, open access j., doi: 10.1155/2010/457094, (2010)
18. N.P. Kolev, I. Spasov, G. Todorova: VVER MSLB Specification: Vessel mixing tests and N/TH simulation at the nodal level. *NURESAFE D14.11.1 report*, (2014)
19. J.C. Chen: A Correlation for Boiling Heat Transfer to Saturated Fluids in Convective Flow. *BNL-6672*, <https://doi.org/10.2172/4636495>, (1962)
20. L.S. Tong: Prediction of Departure from Nucleate Boiling for an Axially Non-Uniform Heat Flux Distribution. *Journal of Nuclear Energy*, **Vol. 21**, pp 241-248, (1967)
21. JRS Thom, WM. Walker, T.A. Fallon, GFS Reising: Paper 6: Boiling in Sub-Cooled Water during Flow up Heated Tubes or Annuli. *Proceedings of the Institution of Mechanical Engineers, Conference Proceedings*, **180(3)**, pp 226-246, (1965)
22. I. Spasov, S. Mitkov, N. Kolev: Sub-channel FLICA4 and COBRA-TF input models qualified for VVER. *NURESAFE D14.23 Report*, 14 June (2014)
23. S. Mitkov, I. Spasov, N.P. Kolev: Simulation of a hypothetical MSLB core transient in VVER-1000 with several stuck rods. *Kerntechnik*, **83**, pp. 389-395, (2018)
24. P.A. Bolobov, A.P. Lazarenko, M.Ju. Tomilov: Development of the code package KASKAD for VVER calculations. 2011 [www.iaea.org/inis/collection/.../Public/40/.../40059695.pdf](http://www.iaea.org/inis/collection/.../Public/40/.../40059695.pdf)

# Thermodynamic and kinetic parameters of biomass from black pine (*PINUS NIGRA* ARN.)

Stanislava Tasheva<sup>1</sup>, Milen Dimov<sup>2</sup>, Hafize Fidan<sup>3</sup>, Stanko Stankov<sup>3</sup>, Lazar Lazarov<sup>4</sup>, Bozidar Bozadzhiev<sup>5</sup>, Apostol Simitchiev<sup>6</sup>, and Albena Stoyanova<sup>4</sup>

<sup>1</sup>University of Food Technologies, Department of Heat Engineering, Bulgaria

<sup>2</sup>Trakia University, Department Food Technology, Bulgaria

<sup>3</sup>University of Food Technologies, Department of Tourism and Culinary Management, Bulgaria

<sup>4</sup>University of Food Technologies, Department of Tobacco, Sugar, Vegetable and Essential Oil, Bulgaria

<sup>5</sup>University of Food Technologies, Department of Cereals, Fodder, Bread and Confectionery Products, Bulgaria

<sup>6</sup>University of Food Technologies, Department of Machines and Apparatuses for Food and Biotechnological Industry, Bulgaria

**Abstract:** The aim of the present study was to determine the thermodynamic and kinetic parameters of biomass obtained from black pine (*Pinus nigra* Arn.). The biomass, consisting of twigs with needles and needles alone of black pine, was used. Ultimate analysis with the elemental composition of the biomass with respect to the main components such as carbon (C), hydrogen (H), nitrogen (N), and sulfur (S) of the biomass before and after water distillation was made. The high heating value (HHV) and low heating value (LHV), energy density and fuel value index were determined. Thermodynamic (Gibbs energy, enthalpy, and entropy) and kinetic (activation energy, the rate constant of the process, and reaction order) parameters of the biomass were calculated.

## 1 Introduction

Conventional energy sources are based on the earth's deposits of coal, peat, natural gas, and oil [1, 2]. Residues from these natural energy sources are increasingly declining due to increased consumption of fuels and electricity [1-4, 6]. Natural sources of energy formed nanocomposite tissue systems, which in different plant species have specific structural and functional properties [3, 4]. Improving the physical and chemical characteristics of coniferous biomass increased its energy density and positively affected its industrial application.

According to the European Union's (2014) climate and energy targets, it was necessary to reduce conventional energy sources and use renewable energy sources to a greater extent by 2030. Using renewable energy sources will reduce CO<sub>2</sub> emissions and reduce energy

---

\* Corresponding author: [st\\_tasheva@abv.bg](mailto:st_tasheva@abv.bg)

consumption by 20% (through effective saving measures), and generate 20% of primary energy from renewable energy sources [4-5].

Renewable energy sources are solar energy, geothermal heat, wind energy, and biomass (plant and animal). Plant biomass is divided into primary (natural wood, straw, crop stems, etc.) and secondary (with mechanical treatment - compaction of pellets and briquettes or with chemical treatment - vegetable oil, alcohol, paper, etc.) [1, 6-9].

Wood is a renewable energy source; it is a product of photosynthesis, i.e., carbohydrates from solar energy [1, 3, 7]. The use of wood as fuel allows saving energy sources (oil, natural gas, coal, and uranium), whose reserves are limited and whose distribution is very uneven. The main advantage of energy from wood is that it does not contribute to the greenhouse effect. The amount of carbon dioxide produced by burning wood is comparable to what is naturally produced by its decomposition. This amount of CO<sub>2</sub> corresponds to what was absorbed by photosynthesis while the tree was growing. In this way, equilibrium is achieved [1, 3, 7].

Based on certain kinetic parameters, the thermodynamic values of torrefaction of the isothermal biomass are calculated and analyzed.

In applied thermodynamics, it has been found that geographical location can affect the energy characteristics of plant biomass [2, 6-7]. This can be useful in determining the thermodynamic and kinetic parameters and optimize pyrolytic processes in bioreactors. Therefore, the aim of the present study was to determine the thermodynamic and kinetic parameters of the biomass obtained from black pine (*Pinus nigra* Arn.).

## 2 Materials and methods

### 2.1 Materials

The needles with thin twigs of black pine (*P. nigra* Arn.) growing in Bulgaria were used. The raw material was collected during the spring of 2020. The species has been identified in Agricultural University, Plovdiv. Before processing, the raw material was cut into particle size 1.5-2.5 cm. It was processed by hydrodistillation into a laboratory distillation. Ash, moisture and cellulose content were determined for the studied biomass [10].

The infrared spectrum was recorded using a Nicolet iS 50 Thermo Scientific FT-IR spectrometer in the frequency region of 4000–400 cm<sup>-1</sup>, with the samples embedded in KBr matrixes.

### 2.2 Elemental analysis

Biomass was analyzed before and after hydrodistillation for the main components carbon (C), hydrogen (H), nitrogen (N) and sulfur (S) by elemental analysis using elemental analyzer Euro EA3000, Type (CHNSO).

### 2.3 Calculations

The upper heating value (HHV) was determined by the following equations [1, 11]:

$$\text{HHV} = [33.5 \cdot C + 142.3 \cdot H - 15.4 \cdot O - 14.5 \cdot N] \cdot 10^{-2}, \text{KJ} \cdot \text{kg}^{-1} \quad (1)$$

and

$$Q_g^p = Q_d^p + \left( \frac{9 \cdot \text{HP}}{100} + \frac{\text{WP}}{100} \right), \text{KJ} \cdot \text{kg}^{-1} \quad (2)$$

where: C is the carbon content in the biomass, %;  
 H is the hydrogen content in the biomass, %;  
 O is the oxygen content in the biomass, %;  
 N is the nitrogen content in the biomass, %;  
 W is the moisture content in the biomass, %;  
 $Q_d^p$  is the lower operating heat of combustion,  $\text{KJ.kg}^{-1}$   
 $Q_g^p$  is the upper operating heat of combustion,  $\text{KJ.kg}^{-1}$

and the low heating value (LHV) and the lower operating heat of combustion  $Q_d^p$  are calculated by the following equation [1-2]:

$$\text{LHV} = \text{HHV} - 2.447 \cdot \left(\frac{\text{H}_A}{100}\right) \cdot 9.011, \text{MJ.kg}^{-1} \quad (3)$$

and

$$Q_d^p = 339.39 \cdot C^p + 1257 \cdot H^p + 108.94(S^p - O^p) - 25 \cdot (9 \cdot H^p + W^p), \text{KJ.kg}^{-1} \quad (4)$$

The value of the fuel index is calculated, which is a parameter for classifying tree species as fuels. The value of the fuel index is calculated according to the following equation [2,12-13]:

$$FVI = \frac{\text{HHV} \cdot \rho}{A \cdot 100}, \text{KJ.cm}^{-3} \quad (5)$$

where: HHV - upper heating value of the fuel (biomass),  $\text{KJ.g}^{-1}$ ;  
 $\rho$  is the biomass density,  $\text{g.cm}^{-3}$ ;  
 A is the ash content in the fuel, %.

The energy density of the fuel was calculated using black pine needles with a measured bulk density of  $0.243 \text{ g.cm}^{-3}$  and a mixture of black pine needles and branches with a measured bulk density of  $0.297 \text{ g.cm}^{-3}$ , by the following equation [2, 12] :

$$E = \text{LHV} \cdot \rho, \text{MJ.cm}^{-3} \quad (6)$$

or

$$E_d = \frac{1}{3600} \cdot \text{LHV} \cdot \rho, \text{MWh} \quad (7)$$

where: LHV lower heating value of fuel / biomass,  $\text{KJ.g}^{-1}$ ;  
 $\rho$  is the bulk density of the biomass,  $\text{g.cm}^{-3}$ ;  
 $\frac{1}{3600}$  is the conversion factor from MJ to MWh.

The thermodynamic parameters: Gibbs energy, enthalpy, and entropy are calculated according to the equations presented in [9, 14]:

$$\Delta G = \Delta H - \Delta S \cdot T \quad (8)$$

$$\Delta G = -\ln K \cdot R \cdot T \quad (9)$$

$$\Delta H = E_a - R \cdot T \quad (10)$$

$$E_a = 2,31 \cdot t \cdot g \alpha \cdot R \cdot T \quad (11)$$

where:  $\Delta G$  is the free energy of Gibbs,  $\text{KJ.mol}^{-1}$ ;  
 $\Delta H$  is the enthalpy,  $\text{KJ.mol}^{-1}$ ;  
 $\Delta S$  is the entropy,  $\text{KJ.mol}^{-1} \cdot \text{K}^{-1}$ ;



K is the equilibrium constant;  
 R is the universal gas constant,  $\text{KJ.mol}^{-1}.\text{K}^{-1}$ ;  
 T is the absolute temperature, K;  
 Ea is the activation energy,  $\text{KJ.mol}^{-1}$ ;  
 $\alpha$  is the slope determined from  $\ln K$  vs  $1/T$ .

The kinetic parameters are also calculated - activation energy, process rate constant and biomass reaction order depending on moisture, ash and cellulose content, according to the Arrhenius equation from [9, 14]:

$$k = A \cdot e^{-\frac{E_a}{RT}}, s \quad (12)$$

where: k is the rate constant of the reaction, s;

A is the Arrhenius constant.

### 3 Results and discussion

The infrared spectra of needles and twigs with needles are presented in Table. 1. The analysis of FT-IR represented mainly strong vibrations of the components before and after treatment. The data demonstrated that all four samples had a characteristic absorption band for the H - bond in the OH group (bands 3421, 3432, 3420 and 3423  $\text{cm}^{-1}$ ). It is also noteworthy that the fluctuation band of the conjugated double bond  $\gamma\text{C} = \text{C}$  for needles (1618  $\text{cm}^{-1}$ ) and twigs with needles (1617  $\text{cm}^{-1}$ ) before distillation was absent in the same samples after distillation. On the other hand, characteristic bands for cis - HRC = CR'H (alkene) appear in the samples after distillation for needles (1637  $\text{cm}^{-1}$ ) and twigs with needles (1636  $\text{cm}^{-1}$ ). These changes were probably due to the high temperature (100 °C), which influences the regrouping of the double bonds in the studied samples.

**Table 1.** Infrared spectra

Characteristic stripes ( $\text{cm}^{-1}$ )					Group type
Needles		Twigs with needles		Data from the directory	
before	After	before	after		
3421	3432	3420	3423	3590 – 3420	$\gamma\text{OH}$ intramolecular H – bond
2922	2924	2922	2925	2940 – 2915	$\gamma_{\text{as}} - \text{CH}_2 -$
-	2361	2852	2362	3110 – 2362	$\gamma_{\text{s}} - \text{CH}_2 -$
1735	-	1732	1735	1740 – 1720	R – CHO $\gamma\text{C}=\text{O}$ characteristic band for aldehyde carbonyl group
-	-	1694	-	1740 – 1650	valence fluctuation of the $\gamma\text{C}=\text{O}$ group
-	1637	-	1636	1665 – 1635	characteristic band for cis - HRC = CR'H
1618	-	1617	-	1625 – 1600	band of valence oscillation of the conjugated double bond $\gamma\text{C}=\text{C}$ , flat with high intensity

1514	-	1514	1517	1525 – 1475	a band with variable intensity characteristic of an aromatic nucleus, oscillations for $\gamma$ C=C
1450	-	1455	1458	1480 – 1450	linear -CH <sub>2</sub> - groups
1377	1384	1384	1375	1385 – 1370	stripes corresponding to a structural fragment of type C(CH <sub>3</sub> ) <sub>2</sub>
1264	-	1266	1262	1275 – 1200	$\gamma$ C-O type connection band (hydroxyl group)
-	-	1158	-	1175 – 1125	monosubstituted 1,3 C-H in the aromatic nucleus
1035	1030	1035	1031	1070 – 1000	planar deformation oscillations 1,2,4 substituted C-H in aromatic nucleus

The data of the biomass content (before and after treatment) are presented in Fig. 1 and Fig. 2, as the biomass composition is recalculated to 100% of the total amount of raw material used.

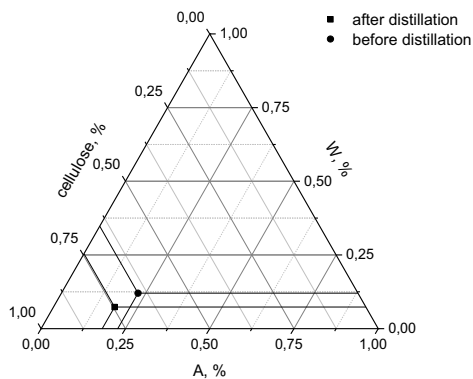


Fig. 1. Ash, moisture and cellulose content in black pine needles

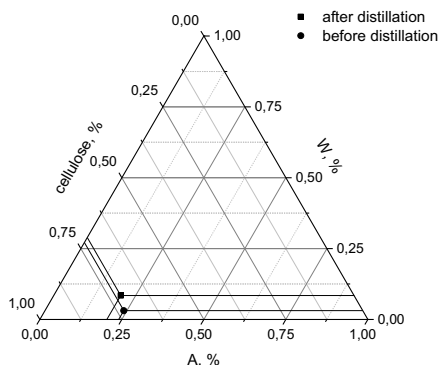


Fig. 2. Content of ash, moisture and cellulose in needles and twigs of black pine

Table 2 shows the defined elemental composition of black pine biomass - needles and twigs with needles, before and after distillation.

**Table 2.** Elemental composition of black pine biomass

Sample	C	H	N	S	O
Needles before distillation	51.44 ± 0.32	7.28 ± 0.24	1.55 ± 0.24	0.10 ± 0.02	27.17±0.72
Needles after distillation	50.53 ± 0.30	7.58 ± 0.25	1.82 ± 0.29	0.10 ± 0.02	30.01±0.72
Twigs with needles before distillation	53.21 ± 0.33	7.67 ± 0.27	1.35 ± 0.23	< 0.10	19.35±0.72
Twigs with needles after distillation	52.76± 0.38	7.48 ± 0.10	1.75 ± 0.20	< 0.10	27.29±0.71

C - carbon content,%; H - hydrogen content,%; N - nitrogen content,%; S - sulfur content,%; O - oxygen content,%. The oxygen content is calculated based on the elemental analysis of the biomass, as the ash and moisture contents are predicted according to [11-12,15-17].

The oxygen content was calculated according to the presented studies for the elemental composition (in Table 2) and the basis of the elemental composition given up to 100% in [11-12,15-17], taking into account the ash and moisture content. The obtained values of the elemental composition of biomass for black pine are approximately close to the composition of pinewood and sawdust reported by other authors [8, 18], stem, branches, needles, and tips of pine [6, 9-10]. Biomass contains cellulose, lignin and hemicellulose in different proportions depending on the type of plant parts (branches, tops, wood) and the plant age, as described in [15, 19]. The difference in the values of the tested components could be explained by the influence of the high temperature during distillation (100 °C), associated with the course of different chemical processes between the different functional groups of the compounds.

The energy characteristics of black pine biomass for black pine needles and twigs were calculated before and after biomass distillation (Table 3).

**Table 3.** Energy characteristics of black pine biomass

Sample	HHV, MJ.kg <sup>-1</sup>	LHV, MJ.kg <sup>-1</sup>	$Q_g^p$ , MJ.kg <sup>-1</sup>	$Q_d^p$ , MJ.kg <sup>-1</sup>	E, MJ.cm <sup>-3</sup>	FVI.10 <sup>-3</sup> , kJ.cm <sup>-3</sup>	E <sub>d</sub> , kWh
Needles before distillation	23.18	16.26	23.66	21.82	3.95	13.07	1.10
Needles after distillation	22.82	18.04	23.42	21.54	4.38	19.39	1.22
Twigs with needles before distillation	25.56	8.12	25.60	23.68	2.41	6.02	0.67
Twigs with needles after distillation	23.86	18.71	24.35	22.48	5.56	18.58	1.54

HHV - upper heating value, MJ.kg<sup>-1</sup>; LHV - low heating value, MJ.kg<sup>-1</sup>;  $Q_g^p$  - upper operating heat of combustion, MJ.kg<sup>-1</sup>;  $Q_d^p$  - lower operating heat of combustion, MJ.kg<sup>-1</sup>; E - energy density, MJ.cm<sup>-3</sup>; FVI - value of fuel index, kJ.cm<sup>-3</sup>; E<sub>d</sub> - energy density, kWh.

The data for the energy characteristics of the biomass from needles and twigs with black pine needles reported in a previous study were in the range of 16.75-16.88 kJ.kg<sup>-1</sup> [10]. Many authors have studied the energy values of different types of pine and different parts of pine wood (needles, branches, bark, tree part, and cones) [2, 12-14, 16-17, 20]. The values for the

upper heat of combustion were in agreement with those reported in this study, regardless of the equation used for its calculation. There is a difference in calculating the lower heat of combustion, depending on the equation used.

The energy density of wood is a characteristic that gives an indication of the biomass' storage and transport. According to [15], high destiny and high LHV values have more energy per unit volume. Pelletizing significantly increases the energy density, which in turn reduces storage needs. The energy density with the other characteristics of the wood and the installation, in which it will be processes, will be influenced mainly by the equipment and its compaction, which therefore will determine the produced pellets' bulk density [2].

The fuel index is a parameter for assessing the quality of wood biomass. The increasing of the fuel index leads to the better biomass's fuel quality [15]. The fuel index value is regarded as a standard parameter for identifying suitable tree species for firewood production [15, 21-22].

According to [9], as the ash content in the biomass increases, the value of the fuel index and its energy density decreases. Energy density is an indicator used in the storage and transport of biomass [15].

Table 4 presents the thermodynamic parameters of black pine biomass for needles and twigs after a distillation process.

**Table 4.** Thermodynamic parameters of black pine biomass

Sample	Content, %		t, s	$\Delta G$ , kJ.mol <sup>-1</sup>	$\Delta S$ , kJ.mol <sup>-1</sup> .K <sup>-1</sup>	$\Delta H$ , kJ.mol <sup>-1</sup>	k.10 <sup>3</sup> , s
Black pine needles	Moisture	7.17	10800	-5929.57	-35.04	7144.76	0.29
	Ash	2.86	10800	-2107.31	-24.80	7144.76	0.40
	Cellulose	29.24	10800	-5014.39	-32.59	7144.76	1.61
Black pine twigs and needles	Moisture	7.55	10800	-8339.94	-41.50	7144.76	0.14
	Ash	3.12	10800	2590.04	-12.21	7144.76	2.00
	Cellulose	26.16	10800	-8279.01	-41.33	7144.76	0.50

t - duration of process, s;  $\Delta G$  - the free energy of Gibbs, kJ.mol<sup>-1</sup>;  $\Delta S$  - the entropy, kJ.mol<sup>-1</sup>.K<sup>-1</sup>;  $\Delta H$  - the enthalpy, kJ.mol<sup>-1</sup>; k - the rate constant, s.

From the representation of values of thermodynamic parameters, it could be concluded that the distillation process was stable and proceeded irreversibly and spontaneously. The negative values of entropy confirmed that the process is irreversible and spontaneous. The enthalpy obtained in distillation from biomass of needles and twigs of black pine was equal in value to the activating energy with the opposite sign. The positive values obtained for enthalpy indicated an endothermic process, i.e., in order to carry out the process, introduction of heat was required. The value obtained for the activating energy is  $E_a = -7144.76$  kJ.mol<sup>-1</sup>, which means that it is necessary to introduce heat during the distillation process in order to carry out this process. The order of the reaction was determined by the differential method; the reaction was of zero-order, the values of the calculated rate constants were given in the Table 4.

## 4 Conclusion

The ash, moisture, and cellulose contents of black pine samples (needles and branches with needles) were determined in this study. Elemental analysis of the combustible elements has been made. The upper and lower combustion thickness, fuel index, and energy density of the considered samples were calculated. Thermodynamic parameters (gypsum energy, enthalpy, and entropy energy) and kinetic parameters (activating energy, rate constant, and reaction order) were also calculated. From the representation of values of thermodynamic parameters, it could be concluded that the distillation process was stable and proceeded irreversibly and spontaneously. The negative values of entropy confirmed that the process is irreversible and spontaneous. The enthalpy obtained in distillation from biomass of needles and twigs of black pine was equal in value to the activating energy with the opposite sign. The positive values obtained for enthalpy indicated an endothermic process, i.e., in order to carry out the process, introduction of heat was required. The value obtained for the activating energy is  $E_a = -7144.76 \text{ kJ}\cdot\text{mol}^{-1}$ , which means that it is necessary to introduce heat during the distillation process in order to carry out this process. The order of the reaction was determined by the differential method; the reaction was of zero-order.

The authors acknowledge the support by the National Science Fund of Bulgaria, project No KP-06-H36/14.

## References

1. G. Valtchev, *Fuel technics and technologies*, (EDP UFT-Plovdiv, second edition, (2011).
2. T. Miranda, I. Montero, F. Sepulveda, J. Arranz, C. Rojas, S. Nogales- Materials, **8**, 1413, (2015).
3. G. Boyadzhieva, B. Baykov, B. Angelov, *Ecologization*, NBU, **40**, (2012).
4. 2030 Climate and Energy Goals for A Competitive, Secure And Low-Carbon Eu Economy. European Commission—Ip/14/54, (2014).
5. Directive 2009/28/Ec of The European Parliament And Of The Council of 23 April 2009 On The Promotion of The Use Of Energy From Renewable Sources and Amending And Subsequently Repealing Directives 2001/77/Ec And 2003/30/Ec. Official Journal of The European Union: Brussels, Belgium, (2009).
6. S. Soltani, S. M. S. Mahmoudi, M. Yari, M. A. Rosen, *Appl. Therm. Eng.*, **59**, 60, (2013).
7. P. McKendry, *Bioresource Technology*, **83**, 37, (2002).
8. O. Olatunji, S. A. Akinlabi, M. P. Mashinini, S. O. Fatoba, O. O. Ajay, *IOP Conf. Series: Materials Science and Engineering* **423**, 012175, (2018). doi:10.1088/1757-899x/423/1/012175
9. Colomba Di Blasi, *PECS*, **34**, 47, (2008).
10. H. Fidan, S. Stankov, N. Petkova, B. Bozadziev, M. Dimov, L. Lazarov, A. Simitchiev, A. Stoyanova, *Proceedings of 9<sup>th</sup> European Conference on Renewable Energy System*, 408, (2021). [www.ecres.net](http://www.ecres.net)
11. R. Moya, C. Tenorio, *Biomass & Energy*, **56**, 14, (2013).
12. Y. Sing, P. Mahanta, U. Bora, *Renewable Energy*, **103**, 490, (2017).
13. B.P. Bhatt , J.M.S. Tomar, K.M. Bujarbaruah, *Renewable Energy*, **29**, 1401, (2004).
14. T. Sen, S. Afroze, H. Ang, *Water Air Soil Pollut*, doi: 10.1007/s11270-010-0663-y.

15. H. Viana, A. Rodrigues, R. Godina, J. Matias, L. Nunes, *Sustainability*, **10**, 2877, (2018).
16. K. Motghare, A. Rathod, K. Wasewar, N. Labhsetwar, *Waste Management*, **47**, 40, (2016).
17. V. Petkov, E. Mihailov, N. Kazakova, *Journal of Chemical Technology and Metallurgy*, **49**(1), 94, (2014).
18. O. Olatunji, S. Akinlabi, O. Ajayi, P. Mashinini, M. Nkosinath, *IOP Conf. Series: Materials Science and Engineering*, **413**, 012054, (2018). doi:10.1088/1757-899x/413/1/012054
19. M. Brebu, C. Vasile, *Cellulose Chemistry and Technology Cellulose Chem. Technol.*, **44** (9), 353, (2010).
20. B.P. Bhatt, J.M.S. Tomar, *Biomass and Bioenergy*, **23**, 257, (2002).
21. S.B.Meetei, E.J.Singh, A.K. Das, *J. Environ. Biol.*, **36**, 1007, (2015).
22. V.Saravanan, K.T.Parthiban, P.Kumar, P.V.Anbu, P.G. Pandian, *Res. J. Agric. For. Sci.*, **1**, 8, (2013).

# Investigating the kinetics at low temperature heat pump drying and conventional drying of osmotic dehydrated blueberries

Hristo Hristov<sup>1\*</sup>, Svetoslav Aleksandrov<sup>2</sup>, Todorka Petrova<sup>2</sup>, Milena Ruskova<sup>2</sup>, Velitchka Gotcheva<sup>3</sup>, and Nikolay Penov<sup>4</sup>

<sup>1</sup>Department of Machines and apparatuses for food industry<sup>1</sup>, University of food technologies, Plovdiv, Bulgaria

<sup>2</sup>Institute of food preservation and quality, Plovdiv, Bulgaria

<sup>3</sup>Department of Biotechnology, University of food technologies, Plovdiv, Bulgaria

<sup>4</sup>Department of Food preservation and refrigeration technology, University of food technologies, Plovdiv, Bulgaria

**Abstract.** The possibilities for low-temperature heat pump and conventional drying of blueberries during preliminary osmotic dehydration was studied. A full factor experiment of type 2<sup>2</sup>+3 was performed. The kinetics of the process during variation of the main mode parameters: inlet temperature and thickness of the drying layer (load on the scaffolding) was studied. The curves of the drying process  $U = f(\tau)$  and the curves of the drying speed  $dU / d\tau = f(U)$  were constructed. The influence of the regime parameters on the drying time was established. Regression models of the drying coefficient during the second period of drying were presented.

## 1 Introduction

The fruits of the blueberry family (*Vacciniaceae*) which in Bulgaria are presented by bilberry (*V. myrtillus L*), blueberry (*V. uliginosum*), cranberry (*V. Vitis - idaea*) and Caucasian bilberry (*V. Arctostaphylos*). Their dry substance content varies in the range from 12 to 18 %. Depending on the type and degrees of maturity, the amount of carbohydrates in blueberries is about 15 %, of which reducing sugars predominate (about 10 %), and the fiber content can reach 0,9 %. The detected concentration of total organic acids is from 0,5 to 1,7 mg/100 g. Polyunsaturated fats (0,15 g/100g) predominate. The ash content of blueberries varies from 0,19 to 0,24 % [1].

Blueberries are a source of biologically active substances, such as phenolic compounds, tannins, stilbenes, flavonoids, anthocyanins, vitamin A and calcium, which have a positive effect on human health and have protective properties against diseases such as memory loss, cancer, heart disease, urinary tract infections, impaired vision and cell aging [2].

\*corresponding author: [h\\_geo@mail.bg](mailto:h_geo@mail.bg)

About 90 percent of the world's blueberry production is in North America, with more than 42000 tons produced annually, according to the United Nations Food and Agricultural Organization.

About 50 % of all blueberries produced are available on the market fresh, with a shelf life of 2 to 3 weeks. Based on research and implemented industrial practices, drying and osmotic dehydration have been found to be effective ways to ensure the consumption of blueberries out of season [3]. When using osmotic dehydration, a large part of the water is released without causing changes in the phases, including a cost-effective ingredient (sugar) in an expensive fruit, which increases the weight of the product.

Various methods have been used to preserve freshly and osmotically dehydrated blueberries to a state of stable low moisture content.

The drying of fresh, frozen or osmotically dried blueberries has been studied, but nevertheless the main task before preserving these fruits is to determine technological solutions, through which to preserve the most heat-sensitive biologically active substances and the color of the final product [4].

The main goal of the present investigation is to study the drying kinetics of low temperature heat pump and conventional drying of osmotically dehydrated blueberries.

## 2 MATERIALS AND METHODS

### 2.1. Materials

Pre-osmotically dehydrated blueberries were used.

### 2.2. Methods

#### 2.2.1. Determination of dry substance content

A weighting method was used to determine the dry substance content.

#### 2.2.2. Investigation of drying kinetics of pre-osmotically dehydrated blueberries

The curve of drying process is constructed -  $U_c=f(\tau)$ , after which the drying speed curve is derived from it -  $\frac{dU^c}{d\tau}=f(U_c)$  and  $\ln(U^c - U_p^c) = f(\tau)$  [5], where:  $U$  –moisture content, kg  $H_2O/kg$  dry substance;  $\tau$  - drying time, min.

The speed coefficient of the drying process is determined by the equation of the drying process curve:

$$-\frac{dU^c}{d\tau} = K_c(U^c - U_p^c), \quad (1)$$

$U_p^c$  – equilibrium moisture content, %;

$U^c$  - current moisture content, %;

$K_c$  – speed coefficient of the drying process,  $min^{-1}$ .

#### 2.2.3. Planning of experiment

A full factorial experiment (ANOVA) of the type  $2^2$  with three replicates in the center of experiment was used. The response surface method was applied to determine the influence of the independent variables [6,7].



### 3 Results and discussion

#### 3.1. Matrix for conducting the experiment and results of the conducted researches

After preliminary studies, the main independent variables influencing the kinetics of the drying process are determined:

- The temperature of the drying agent –  $t$ , °C;
- Thickness of the drying layer (load on the scaffolding) -  $\sigma$ , kg/m<sup>2</sup>.

The levels of variation of the independent variables for the two types of drying are presented in table 1.

**Table 1.** Variation levels and names of the independent variables in heat pump and conventional drying of osmotically dehydrated blueberries

Variables	heat pump		conventional	
	t, °C	$\sigma$ , kg/m <sup>2</sup>	t, °C	$\sigma$ , kg/m <sup>2</sup>
High level, $z_j^h(x_j^h)$	50	15	70	15
Low level, $z_j^l(x_j^l)$	40	5	50	5
Center of the plan, $z_j^0(x_j^0)$	45	10	60	10
Interval of variation, $\Delta z_j$	5	5	10	5

**Table 2.** Plan of the experiment (Anova 2<sup>2</sup>+3)

№	Drying		Heat pump		Conventional	
	X <sub>1</sub> (t, °C)	X <sub>2</sub> ( $\sigma$ , kg/m <sup>2</sup> )	t, °C	$\sigma$ , kg/m <sup>2</sup>	t, °C	$\sigma$ , kg/m <sup>2</sup>
	coded		natural		natural	
1.	-	-	40	5	50	5
2.	+	-	50	5	70	5
3.	-	+	40	15	50	15
4.	+	+	50	15	70	15
5.	0	0	45	10	60	10
6.	0	0	45	10	60	10
7.	0	0	45	10	60	10

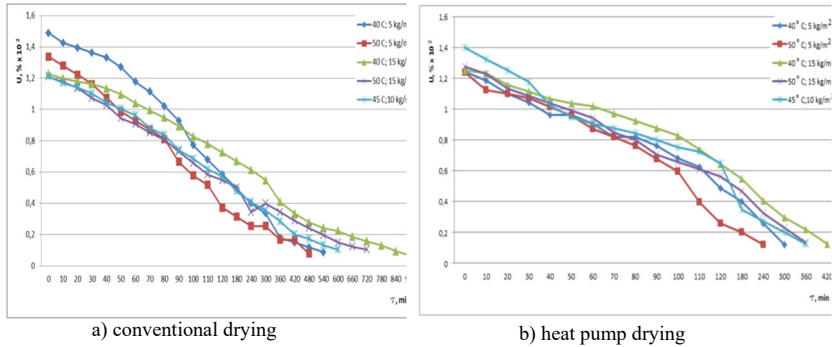
#### 3.2. Kinetics of the drying process of osmotically dehydrated blueberries under different technological regimes of drying

Figures 1 a and b show the drying curves –  $U=f(\tau)$  in two methods – low temperature heat pump and conventional drying of osmotically dehydrated blueberries. Depending on the temperature of the drying agent and the load on the scaffolding, the time for conventional drying varies from 8 to 15 hours, and for low-temperature heat pump drying from 4 to 6 hours. It is noteworthy that the time to reach equilibrium humidity in conventional drying is about twice as long as the heat pump.

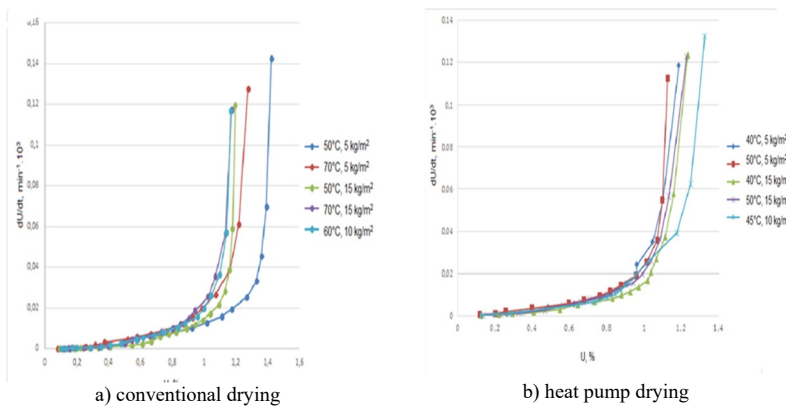
When analyzing the graphs, the absence of the first period (period of constant drying speed) is noticed. For all curves obtained, a period of reduction of the drying speed is

reported. The nature of the drying curves during this period depends on the composition, structure and size of the product, as well as on the form of binding of the water in it.

Figures 2 a and b show the drying rate curves ( $\frac{dU^c}{d\tau} = f(U_c)$ ) by two methods – low temperature heat pump and conventional drying of osmotically dehydrated blueberries. They express the drying speed as a function of the moisture content of the product. Analysis of the drying speed curves shows that the above mentioned trends are observed. Impressive are the lack of a period of constant drying speed and the presence of a period of decreasing drying speed. The experimentally obtained results for heat and mass transfer, presented by drying speed curves, are comparable to those of [8] in convective drying of osmotically dehydrated pieces of papaya.



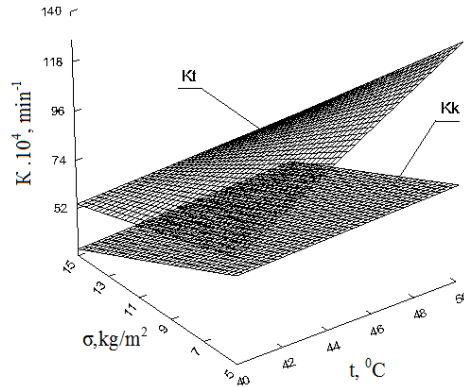
**Fig. 1.** Drying curves of osmotically dehydrated blueberries



**Fig. 2** Drying curves of osmotic dehydrated blueberries

In figures 2 a and b, the presence of a second critical point can be established in all variants of the experiment. This is characteristic of this part of the curves in capillary-porous colloidal bodies. In this case, two sub periods stand out: a sub period of uniform deceleration and a sub period of non-uniform deceleration. They can be used to judge the nature of evaporation of the bound water in material. The explanation for this fact can be found in the complex nature of the structure of the solid skeleton of the product, the ratio of different forms of bound moisture, the mechanism of its transfer, as well as the pretreatment of the

product (osmotic dehydration). Figure 3 show the response surfaces of the obtained regression equations of the speed drying coefficients.



**Fig. 3.** Speed drying coefficients

$$K_{t.104} = -255.6 + 8.6 \cdot t + 18.5 \cdot \sigma - 0.52 \cdot t \cdot \sigma, \text{ min}^{-1} \quad R^2 = 97\% \quad (2)$$

$$K_{k.104} = 71.0 + 0.4 \cdot t - 4.4 \cdot \sigma + 0.02 \cdot t \cdot \sigma, \text{ min}^{-1} \quad R^2 = 94\% \quad (3)$$

In both drying methods, the maximum values of the drying coefficients are obtained at variant №2 (table 2). The maximum value for heat pump drying  $K_t=0,138, \text{ min}^{-1}$  is about twice as high as the convective speed drying coefficient  $K_k=0,075, \text{ min}^{-1}$ .

## 4 Conclusion

A combined drying method with pre-osmotic treatment is applied, as a result of which the free moisture is released. As a result of the osmotic treatment dried blueberries in both methods have an increased sugar content. This allows the dried blueberries to have a higher moisture content with a water activity lower than 0,6. This guaranties the safety of the final product, as well as its better organoleptic properties. The time to reach equilibrium humidity in conventional drying of osmotically dehydrated blueberries is about twice as long (8 to 15 hours) compared to the heat pump drying (4 to 6 hours). Absence of a constant drying speed and presence of a period of decreasing drying speed was reported. A second critical point was also found during this second drying period, and two sub periods were reported: a sub period of uniform deceleration and a sub period of non-uniform deceleration.

## References

1. K. Skupieñ, J. Oszmiañski, J. Agricultural and Food Science, **16** (1), 46-55 (2007)
2. X. Wu, L. Gu, L. Prior, S. McKay. Journal of Agricultural and Food Chemistry, **52** (26), 7846-7856 (2004)
3. J. Shi, Z. Pan, T. McHugh, D. Wood, E. Hischberg, D. Olsonc. Food Science and Technology, **41** (10), 1962-1967 (2008)

4. G. Skrede, E. Wrolsta, R. Durst. *Journal of Food Science*, **65** (2), 357-364 (2000)
5. K. Kolarov, *Processes and apparatus in Food processing industry*, Plovdiv, Publishing house Hr. Danov, 429-432 (1985) (In Bulgarian)
6. B. Bozhanov, I. Vutchkov, *Statistical methods for modelling and optimization of multifactor objects*, P.H Technika, Sofia, 1983 (in Bulgarian)
7. A. Lambrev, *Basics of engineering experiment in terms of study of machines and apparatus in food industry*, 1994 (in Bulgarian)
8. K. Park, A. Bin, F. Brod. *Journal of Food Engineering*, **56**, 97-103 (2002)

# Optimization of the distance between the rows in solar collectors' arrays

Merima Zlateva<sup>1\*</sup>

<sup>1</sup>Technical University of Sofia, Department of Heating and Refrigeration Engineering, 1000 Sofia, Bulgaria

**Abstract.** The article presents some results of the analysis of the influence of the distance between the collectors' rows in thermal solar systems on the degree of self-shading. For the purposes of the study, the dimensionless ratio  $K_s$  between the required minimum distance between the rows, guaranteeing the absence of self-shading, and the height of the collectors, was used. A simulation study was performed for specific climatic conditions and the annual solar radiation incident on the collectors' array at different degrees of self-shading was determined. Its annual financial equivalent for various alternative heat sources (electricity, natural gas, wood pellets, district heating and gas oil) was assessed, as well as the necessary investment costs for construction of the solar system. A regression relationship between the coefficient of net present value NPVQ and  $K_s$  was derived and its optimal values were established, which ensure the achievement of maximum economic efficiency of the system operation for the considered replaced heat sources.

## 1 Introduction

Solar energy is utilized via thermal [1] and photovoltaic solar systems. In solar systems designed to provide large capacities it is necessary to divide the collector's array in more than one row. Often in such cases, the available surface on the building roof or the ground is limited and shading between the rows is inevitable. In such circumstances, determining the degree of self-shading of all rows behind the first one is a prerequisite for correct assessment of the solar radiation incident on the array. This applies to both thermal and photovoltaic solar systems [2].

In [3] is presented a mathematical optimization procedure for thermal solar systems, used to obtain the field and collectors' design parameters (number of rows, distance between collector rows, collector height, and collector inclination angle). The aim of the optimisation procedure is to minimize the periodic cost of a solar plant, producing a given amount of annual energy, and the unit cost of energy. The optimal deployment of the collectors is presented as a function of daily energy demand, with the cost of land and collector efficiency as parameters.

---

\* Corresponding author: [mzlat@tu-sofia.bg](mailto:mzlat@tu-sofia.bg)

The degree of self-shading depends on the distance between the rows  $R$ , the height of the collectors  $L$ , their slope angle to the horizon  $\beta$ , the latitude  $\varphi$  and the position of the sun, defined by the solar altitude  $\alpha_s$  and azimuth  $\gamma_s$  angles (Fig. 1). According to data from various sources, e.g. [3, 4], the length of the rows does not have a noticeable effect on the solar radiation falling on the collectors' array, which is confirmed by the author's research, carried out with the simulation software Transol [5].

## 2 Theoretical considerations

The parameters characterizing the mutual position of two adjacent collectors' rows and necessary for estimating the degree of self-shading for southern orientation are shown in Fig. 1. To ensure maximum irradiation of the surface at a certain solar attitude, the angle  $\nu$  between the horizon and the line connecting the upper and lower edges of two successive collectors' rows have to meet the following condition:

$$\nu \leq \alpha_s \quad (1)$$

The solar altitude  $\alpha_s$  is determined by the ratio of the lengths of the sides of the triangles in Fig. 1 and expressed by (2):

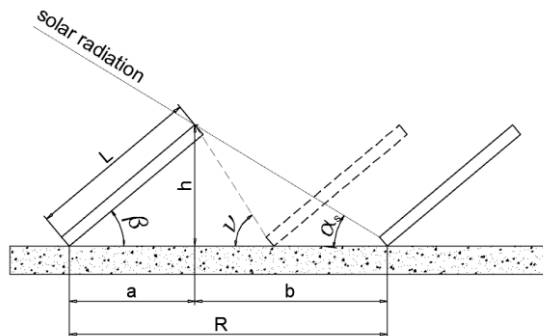
$$\operatorname{tg} \alpha_s = h \cdot b^{-1} \quad (2)$$

Where  $b$  and  $h$  are the projections on the horizontal and vertical surfaces of the line connecting the upper and lower edges of the successive collectors' rows.

For distance between the rows  $R=a+b$  and collector height  $L$ , the following trigonometric dependences are valid:

$$\sin \beta = \frac{h}{L} \Rightarrow h = L \cdot \sin \beta \quad (3)$$

$$\cos \beta = \frac{a}{L} = \frac{R-b}{L} \Rightarrow R-b = L \cdot \cos \beta \Rightarrow b = R - L \cdot \cos \beta \quad (4)$$



**Fig 1.** Shading of south-facing collectors' rows.

After substituting (3), (4) and (2) in (1), the condition of absence of self-shading of two consecutive rows can be presented with (5) and is reduced to determining the minimum

allowable value of  $R$ , expressed as a linear function of the height of the collectors  $L$ , the angle  $\beta$  and the tangent of the angle  $\nu = f(\alpha_s)$ :

$$R \geq L \cdot \left( \cos \beta + \frac{\sin \beta}{\operatorname{tg} \nu} \right) \quad (5)$$

In [6] the dimensionless criterion  $K_s(\tau)$  is defined as a function of time  $\tau$ :

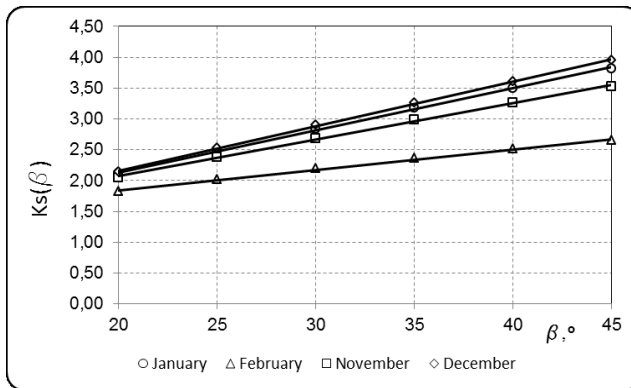
$$K_s(\tau) = R_1^{\min}(\tau) \cdot L^{-1} \quad (6)$$

The criterion  $K_s(\tau)$  is interpreted as a coefficient of proportionality between the required minimum distance between the rows of the collectors' array  $R_1^{\min}(\tau)$ , ensuring the absence of self-shading and the height of the collectors  $L$ . For  $K_s(\tau)$  the author has derived a generalized functional dependence on the type:

$$K_s(\varphi, \beta) = a \cdot \varphi^b \cdot \beta^c \Big|_{m=\text{const}} \quad (7)$$

Where  $m$  is the month of the year;  $a$ ,  $b$  and  $c$  are constants the monthly values of which depend on the latitude  $\varphi$  and the angle  $\beta$ .

The geographical location of Bulgaria, with a relatively small range of variation of  $\varphi$ , does allow simplification of dependence (7) and its representation as a function only of the angle  $\beta$ . In Fig. 2 is shown the change of the parameter  $K_s$  for the months from November to February, for values of the angle of inclination of the collectors in the range  $\beta = 20^\circ \div 45^\circ$ . The graph is constructed using (7) for the medium latitude of Bulgaria with relative error  $< 1,5\%$



**Fig. 2.** Coefficient of proportionality  $K_s(\beta)$ .

The fulfillment of (8) for the month of December, during which the solar altitude angle has minimum values, is a condition for year-round prevention of self-shading of the collectors' rows:

$$R_1^{\min} \geq L \cdot K_s(\beta) \quad (8)$$

The decrease in the ratio  $K_s$  causes an increase in the shading which has a significant effect mainly on the direct solar radiation, as its maximum instantaneous values are in the hours immediately after sunrise and before sunset during the winter, when the intensity of the solar radiation is low. However, with a certain area available for the collectors' array, the reduction of  $K_s$  allows the placement of a larger number of collectors' rows and an increase of the annual solar radiation, despite the negative effect of self-shading. This gives reason for different authors, e. g. [3], to look for the optimal distance between the collectors' rows based on energy and economic criteria.

### 3 Optimal distance between the rows in solar collectors' arrays

The annual solar radiation falling on a collectors' array at different degrees of self-shading is determined with the help of the software Transol [5] for the climatic conditions of the city of Varna. An array with 8 flat-plate collectors is considered as a reference. The collectors' parameters are as follows: height  $L = 2,07 \text{ m}$ , width  $B = 1,0 \text{ m}$ , optical efficiency  $\eta_0 = 0,82$  and heat loss coefficient  $a_0 = 3,65$ , slope angle  $\beta = 43^\circ$ . To avoid shading, it is necessary to fulfil the condition  $K_s = 4$  and the required area of the terrain is  $A_{ca, K_s^* = 4} = 39,2, \text{ m}^2$ .

As an alternative, collectors' arrays with a different degree of self-shading are considered, for which the condition is fulfilled  $A_{ca, K_s = var} \leq A_{ca, K_s = 4}$  ( $A_{ca, K_s = var}$  - surface of the terrain occupied by the alternative collectors' arrays).

The annual solar radiation on the collectors' array  $H_{sh,a}, \text{ MWh/a}$  with  $K_s = [1; 1.5; 2; 2.5; 4]$  is shown on Fig.3. The annual financial equivalent of the incident solar radiation, determined for different alternative heat sources  $B = f(K_s)$ , taking into account the efficiency of the system, is shown in Fig. 4.

The results presented in Fig. 4 are obtained according to the typical prices of the replaced energy sources [8]. The equivalent annualized value  $I_a(K_s)$  of the investment costs for the solar system is also shown.

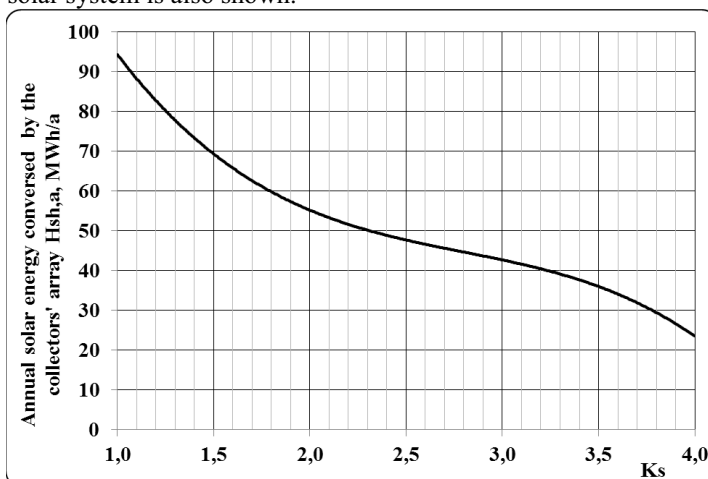


Fig. 3. Annual solar energy converted by the collector array.



The presented dependencies  $B = f(K_s)$  and  $I_a(K_s)$  clearly illustrate the different rates of change of each. This allows to formulate the hypothesis that there is an optimal value of the criterion "net present value ratio", defined by (9) and showing the net income from the operation of the system for an investment of BGN 1.

$$NPVQ = \frac{NPV}{I(K_s^*)} \quad (9)$$

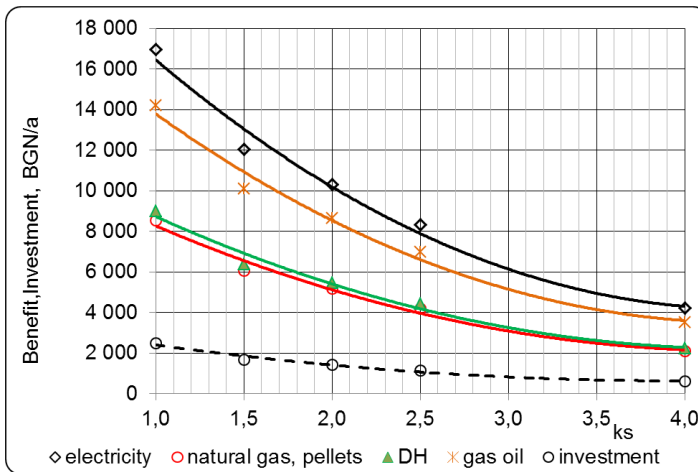
Where  $NPV = B \frac{1 - (1 + r)^{-n}}{r} - I_a$  is the net present value, BGN;

$B$  - financial equivalent of the energy recovered by the solar system, BGN;

$I_a$  - annuitizes investment costs, BGN;

$n$  - time period of the analysis;

$r$  - discount rate.



**Fig. 4.** Benefit and annual investment cost for the solar system.

The net present value ratio for the different types of substitute heat sources at values of  $K_s$  in the range  $K_s^* = [1 \div 4]$  is shown in Fig. 5. The obtained regression dependencies  $NPVQ = f(K_s^*)$  were studied in order to find the optimal values of the ratio  $K_{s,opt}$  at which the maximum value of  $NPVQ = f(K_s)$  is achieved.

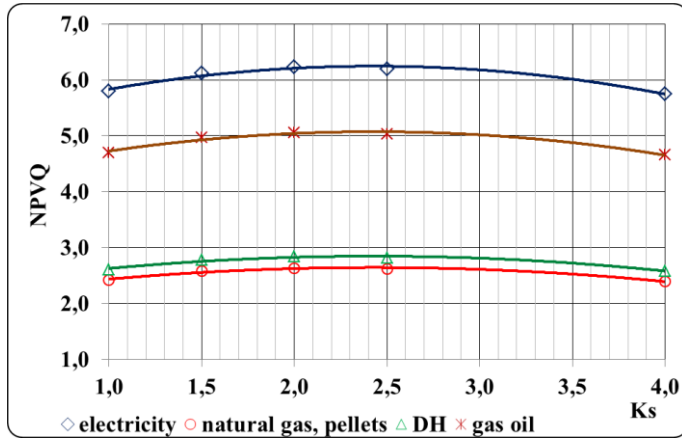


Fig. 5. Net present value ratio depending on the factor  $K_s$ .

The functional dependences  $NPVQ = f(K_s)$  are summarized in Table 1. The table also shows the values of the ratio  $K_{s,opt}$ .

Table 1. Functional dependence and optimal values of  $NPVQ = f(K_s)$ .

	Functional dependence	$NPVQ_{max}$	$K_{s,opt}$
<b>Electricity</b>	$NPVQ = -0,16 \cdot K_s^2 + 0,79 \cdot K_s + 3,84$	6,03	2,5
<b>Gas oil</b>	$NPVQ = -0,14 \cdot K_s^2 + 0,66 \cdot K_s + 3,06$	4,85	2,4
<b>District heating</b>	$NPVQ = -0,09 \cdot K_s^2 + 0,42 \cdot K_s + 1,57$	2,70	2,3
<b>Natural gas, pellets</b>	$NPVQ = -0,08 \cdot K_s^2 + 0,40 \cdot K_s + 1,43$	2,54	2,5

## 4 Conclusions

The study shows that with the accepted financial parameters and prices of the replaced energy sources, the functional dependencies  $NPVQ = f(K_s^*)$  are approximated with a high degree of accuracy (multiple correlation coefficients  $R^2 = 0,97$ ) by second degree polynomials.

In the studied range of change of the ratio  $K_s = [1 \div 4]$ , the net present value ratio  $NPVQ > 1$ , which guarantees the efficiency of the financial resources invested for the construction of the system. For the considered energy sources, its maximum values are achieved at  $K_{s,opt} = 2,5$  for electricity, natural gas and pellets;  $K_{s,opt} = 2,4$  for gas oil and  $K_{s,opt} = 2,3$  in case of energy from district heating.

Despite the small range of values of  $K_{s,opt}$ , the maximum values of the net present value ratio  $NPVQ_{max}$  vary considerably: 6.03 for electricity; 4.85 for gas oil; 2.7 for district heating and 2.54 for natural gas and pellets.

For the efficient operation of thermal solar systems, it is necessary, right at the design stage, to determine correctly the degree of shading of the collectors' array. The optimal distance between the rows must be determined on the basis of energy and economic criteria, taking into account the specific financial conditions.

## References

1. N. Kaloyanov, L. Tsokov, R. Tsekov, M. Vassilev, Ts. Bozhkov. *Proceedings of the XXIII Scientific Conference with International Participation FPEPM 2018 (in Bulgarian)*, pp. 72 – 77, (2018)
2. S. Omidreza et al., *Malaysia Advances in Environment, Biotechnology and Biomedicine*, pp 100 – 106 (2012)
3. D. Weinstock, J. Appelbaum, *Jour. of Sol. En. Eng.*, **129**, pp 363 – 370 (2007)
4. S. Stamov et al., *Handbook on Heating, Air conditioning and Cooling. Part II. Heating, heat and gas supply*, (2001)
5. *Sistems Avancats d'Energia Solar Termica Transol for Windows*
6. J. A. Duffie, W Beckman, *Solar Engineering of Thermal Processes*, (2013)
7. N. Kaloyanov, *Analysis and synthesis of low-potential combined systems*, (1989)

# Simulation Investigation of the Wind Load of Photovoltaic Panels

Ivaylo Stoyanov<sup>1\*</sup>, Teodor Iliev<sup>2</sup>, and Grigor Mihaylov<sup>3</sup>

<sup>1</sup>University of Ruse, Department of Electrical Power Engineering, 7017 Ruse, Bulgaria

<sup>2</sup>University of Ruse, Department of Telecommunications, 7017 Ruse, Bulgaria

<sup>3</sup>University of Telecommunications and Posts, 1700 Sofia, Bulgaria

**Abstract.** In this article, a simulation and evaluation of the mechanical stress exerted by the wind on photovoltaic panels is performed. The stresses of the solar cells in a PV module are calculated using the finite element method, taking into account the wind pressure and the allowable mechanical stresses, according to the regulatory requirements. Seven different operating positions of the photovoltaic panel during its rotation from 0° to 90° are considered. In each of these positions, a distributed load for computer simulations is 1 kN/m<sup>2</sup>. It is clear from them that for all operating positions of the panel, the maximum stresses are obtained in its frame. These stresses in different cases vary around the value of 50 MPa and are not dangerous for the structure.

## 1 Introduction

In order to achieve Bulgaria's national target for the share of energy from renewable sources in gross final energy consumption by 2030, it is set that 30.33% of electricity should be produced from renewable energy sources (RES). This corresponds to an increasing trend of 0.55 - 1.24 percentage points per year [1]. In this regard, a number of normative documents have been adopted, which support the faster and wider introduction of RES at national and regional level. On the other hand, it is known that in Bulgaria there are favorable conditions for electricity production using the photovoltaic system (PVS). Thus, a number of researchers have focused their efforts on improving their efficiency and improving the quality of electricity [2, 3, 4, 5]. The introduction of these new technologies leads to a number of problems related to customer relationships, facility and utility management, surge protection, etc. [6, 7, 8]. However, one of the main problems is the mechanical sizing depending on the method of installation of PVS. For example, installation on the roofs of industrial buildings. But this increases the risk of leaks, and photovoltaic panels must withstand the high wind forces that act on them. There is also a wind load in the ground stationary and monitoring systems.

Damage to photovoltaic systems can be divided into electrical and mechanical damage [9]. In turn, mechanical damage occurs under the influence of climatic factors, defects in production and installation, and force majeure circumstances. The greatest influences of

---

\* Corresponding author: [stoyanov@uni-ruse.bg](mailto:stoyanov@uni-ruse.bg)

climatic factors have the load of wind and snow, temperature, hail and ultraviolet rays [10, 11, 12]. The analysis shows for the load from wind and snow that the structures on a sloping roof have with relatively the least load, and the structures on a flat roof - with the highest (due to the height of the building). Higher mechanical loads are observed in open terrains and in PVS with a larger area of the modules. Therefore, different methods are applied to study PVS using modeling and simulation [13, 14, 15, 16]. All of them are based on the data accumulated during the operation of PVS [17]. All this saves time and costs, and helps designers to find appropriate technical solutions in the construction and operation of PVS.

## 2 Material and methods

The main elements of the task for the manufacture of a metal structure for mounting photovoltaic modules are:

- Overall dimensions:
  - length - 1245 mm;
  - width - 635 mm;
  - thickness - 7 mm;
  - weight - 12 kg.
- Construction to allow easy installation and maintenance;
- Convenient and easy connection of measuring instruments;
- Ergonomically designed and meeting the conditions for safe work and system;
- Resistance to snow and wind loads;
- Corrosion resistance;

The modules are from Solarpro Holding AD [18].

The construction consists of two stands connected to each other by a pipe to which the panel frame is welded. The schematic diagram of the respective structure and its overall dimensions are shown in Fig.1.

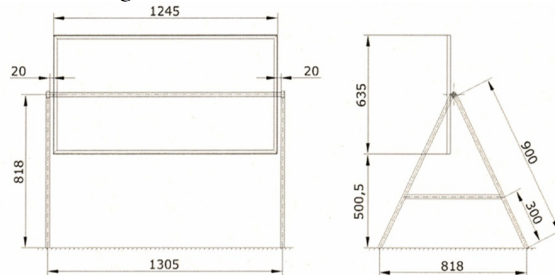
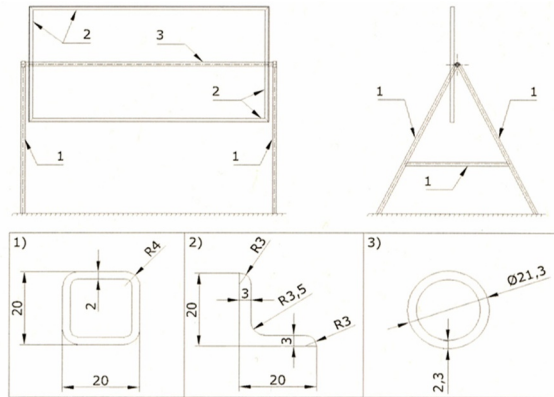


Fig. 1. Schematic diagram of the structure.

The structural elements used for the construction of this structure are shown in Fig. 2. . A square tube with a cross section of 20x20x2 mm was used for the stands (Fig. 2,1). The solar panel with dimensions is attached to a frame made of L-shaped profiles with a cross section of 20x20x3 mm (Fig. 2,2). The frame is reinforced in the middle by a pipe with a diameter  $\Phi 21,3$  mm (Fig. 2,3), mounted at both ends to the stand.

### 2.1. Mechanical load on the structure

The predominant force acting on the supporting structure of the solar panel is wind. It is determined in accordance with Ordinance № 3 of 21 July 2004 on the basic provisions for the design of construction structures and the impacts on them [19]. The load from the own weight of the structure and the panel is not taken into account, as it is negligible compared to the wind load.



**Fig. 2.** Structural elements.

According to the Ordinance, the wind load on buildings and facilities is defined as the sum of its average (so-called static) and pulsation component. The normative value of the static component of the wind load  $W_n$ , в  $\text{kN/m}^2$  at height  $z$  above the terrain is calculated by the formula:

$$W_n = W_m \cdot k_z \cdot c \cdot \gamma_f, \quad (1)$$

where  $W_m$  is the normative value of the pressure (speed) of the wind. For the region of Ruse  $W_m = 0.5 \text{ kN/m}^2$ ;

$k_z$  - the coefficient by which the change in pressure in height is taken into account. The value of the coefficient for buildings up to 10 m e 1;

$c$  - the aerodynamic coefficient. For free-standing flat solid wall constructions  $c = 0.8$  ;

$\gamma_f$  - the private impact factor ( $\gamma_f = 1.4$  for wind loads).

After taking into account all the coefficients, the value of the static component of the wind load is obtained:

$$W_n = 0,5 \cdot 1,0 \cdot 0,8 \cdot 1,4 = 0,56 \text{ kN/m}^2. \quad (2)$$

The normative value of the pulsation component of the wind load  $W_p$  at height  $z$  is determined by:

$$W_p = W_n \cdot \zeta \cdot v, \quad (3)$$

where  $W_n$  is the static component of the wind load ( $W_n = 0,56$ );

$\zeta$  - the coefficient for pulsation of the wind pressure at height  $z$ . It assumes a value of 0.76 for buildings up to 10 m high;

$v$  - coefficient for spatial correlation of wind pressure pulsations,  $v = 0,89$ .

After taking into account all the coefficients, for the value the component of the wind load is obtained:

$$W_p = 0,56 \cdot 0,76 \cdot 0,89 = 0,38, \text{ kN/m}^2, \quad (4)$$

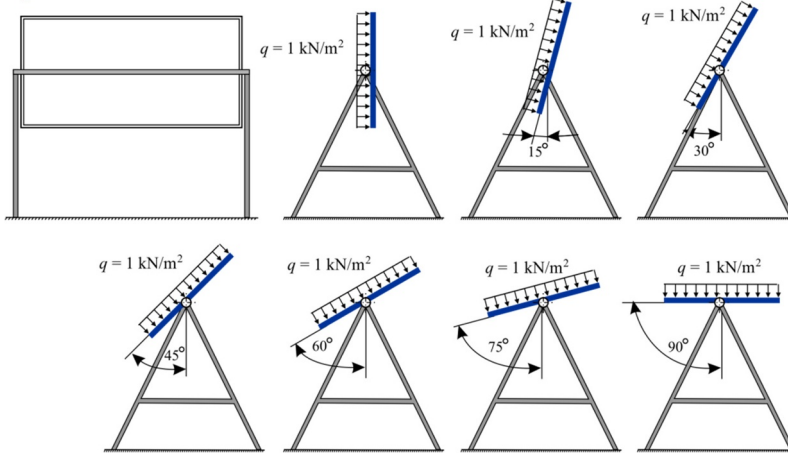
and for the total wind load:

$$W = W_n + W_p = 0,56 + 0,38 = 0,94 \text{ kN/m}^2. \quad (5)$$

When performing computer simulations, the wind load is rounded to 1  $\text{kN/m}^2$ .

## 2.2. Stimulation investigation

Seven different operating positions of the photovoltaic panel during its rotation from  $0^\circ$  to  $90^\circ$  are considered. In each of these positions, a distributed load  $q$  with an intensity of  $1 \text{ kN/m}^2$  is normally applied to the surface of the panel. The positions for which a strength check of the model has been performed are shown in Fig. 3. To fasten the model, a clamp is accepted at the lower end of the stands.



**Fig. 3.** Diagram of the seven operating positions of the photovoltaic panel

The geometric model shown in Fig. 1, is built of profiles (Fig. 2) and a surface recreating the solar panel. Steel BCr3кп was chosen for the profiles (Table. 1.).

**Table 1.** Technical characteristics of used steel.

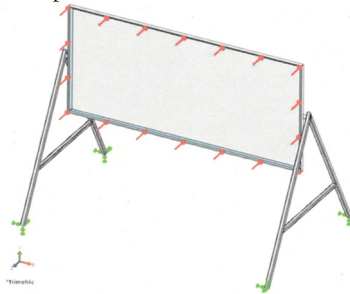
Features	Designation	Units	Value
Density	P	$\text{kg/cm}^3$	7850
Modulus of elasticity	E	MPa	$2,06 \cdot 10^5$
Poisson's ratio	P	—	0,3
Angular deformation modulus	G	MPa	$0,79 \cdot 10^5$
Normative resistance of tensile strength	Run	MPa	370
Calculated tensile, compressive and bending resistance from Run	Ru	MPa	335
Normative resistance to tension, pressure and bending from the city of traction	Ryn	MPa	225
Calculated tensile, compressive and bending resistance from Ryn	Ry	MPa	205

The stimulation task is solved using the finite element method (FEM). For this purpose, a three-dimensional model was built in the SolidWorks program (Fig. 4), which was subsequently analyzed using the COSMOSWorks application. The SolidWorks Office Premium package is used to solve the task [15].



**Fig. 4.** Three-dimensional model of the experimental circuit with the photovoltaic module

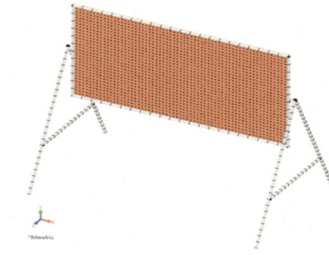
For the surface representing the glass panel, standard material from the COSMOS Works library built into the program was used. It has a modulus of elasticity  $E = 6,89.10^4$  MPa and a Poisson's ratio  $\mu = 0,23$ . The aim of the task is to study the load-bearing capacity of the structure. The surface of the photovoltaic panel is created in the model to transmit the load on the frame. In this regard, the strength of the protective surface glass of the panel is not considered. In solving the problem, it is assumed that all components of the structure are fixedly connected to each other. The whole structure is fixed by tightening the lower ends of the stands (Fig. 5). A wind load is applied to the model, applied to the surface of the panel as a distributed load with an intensity of  $1 \text{ kN/m}^2$ . In Fig. 5, the applied load and the fastening of the model are shown. The places where the structure will be attached to pre-cast concrete "steps" in the ground are shown with a fixed clamp. The metal rods will be attached to them with anchor bolts, three per step, with dimensions. This will ensure that the structure does not react to lifting forces. Wind forces will act on the panels. Since they will be located at a not very high height from the ground, the lifting forces will not be so great. There will be no large side load. Only wind blowing against the panels would create pressure on the entire structure.



**Fig. 5.** Applied load and attachment of the model.

The network of finite elements needed to solve the task is created automatically by the COSMOSWorks program after the type of elements and their size are selected. A mixed network of beam and shell finite elements has been created. In this case, two-node beam end elements were used to represent the beams. Each two-node beam element has six degrees of freedom in each node: three translations and three rotations. At the discretization of the glass surface, triangular shell elements of the second row were used. Each triangular element in the second row has six knots: three knots in its vertices and three knots in the middle of its sides. When solving the problem, the nominal size of the element is set to 20 mm. The resulting network of finite elements is shown in Fig. 6.

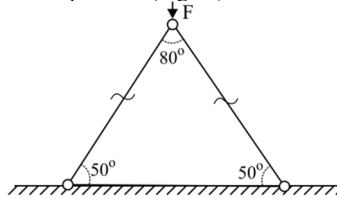




**Fig. 6.** Created network of finite elements.

The calculations are done for one panel.

It is obvious that when expressing the cutting forces, the triangular part of the structure, as well as the base, is loaded with pressure (Fig. 7.).

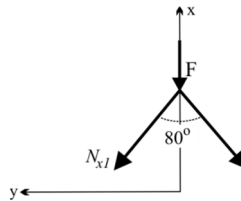


**Fig. 7.** Pressure load.

The force with which the structure is loaded is:

- force from the weight of the panel  $F_1 = m \cdot g = 17,9,81 \approx 167$  N;
- force generated by the wind  $F_2 = 140 \cdot S \cdot g = 140,1,27,9,81 \approx 1750$  N;
- total strength  $F = F_1 + F_2 = 1917$  N.

A x-y coordinate system is introduced, according to which the normal cutting forces will be decomposed (Fig. 8.)



**Fig. 8.** Shear forces.

The following equations are solved to calculate the stresses in the structure:

$$\begin{aligned} \sum x_i &= 0; \sum y_i = 0; \\ N_{x_1} \sin 40^\circ - N_{x_2} \sin 40^\circ &= 0, \Rightarrow N_{x_1} = N_{x_2}; \\ -N_{x_1} \sin 40^\circ - N_{x_2} \sin 40^\circ - F &= 0, \Rightarrow N_{x_1} \approx 1438 \text{ N}. \end{aligned} \quad (6)$$

The normal shear force has a negative sign, which indicates that the structure is under pressure.

In the cross-section of the structure acting only normal voltages  $\sigma_x$ , which are evenly spaced and have a value:

$$\sigma_x = \frac{N_x}{S} = \frac{1438}{0,231} \approx 6225 \text{ Pa}. \quad (7)$$

Checking the stresses in the bars (square tubes) at the allowable stress  $[\sigma]$  is performed using the strength condition:

$$[\sigma] = \frac{\sigma_s}{n} = \frac{240}{3} = 80 \text{ MPa} \tag{8}$$

where  $\sigma_s$  is the allowable stress for the material is equal to 240MPa;

$n$  - the coefficient of security. The selected value is 3.

The condition is  $\sigma_x < [\sigma]$ , or  $6225 < 80 \cdot 10^6 \text{ Pa}$ .

The large difference in allowable stresses indicates that the structure will withstand compressive forces much greater than anticipated.

Determination of support reactions (Fig. 9).

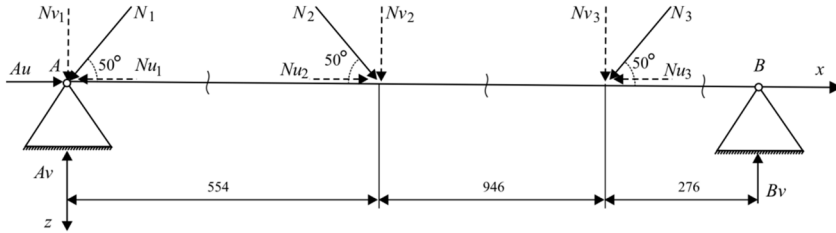


Fig. 9. Support reactions of the experimental model

To find the reference reactions  $A_u, A_v$  and  $B_v$  respectively on the entered  $x - z$ , coordinate axes, the following equations are solved:

$$\begin{aligned} \sum x_i &= 0; \\ A_u - N_{u1} + N_{u2} - N_{u3} &= 0; \\ A_u - N_1 \cdot \cos 50^\circ + N_2 \cdot \cos 50^\circ - N_3 \cdot \cos 50^\circ &= 0; \\ A_u &= N_3 \cdot \cos 50^\circ \approx 925 \text{ N}. \end{aligned} \tag{9}$$

$$\begin{aligned} \sum M_{Bi} &= 0; \\ -1,8 \cdot A_v + 1,8 \cdot N_{v1} + 1,2 \cdot N_{v2} + 0,28 \cdot N_{v3} &= 0; \\ -1,8 \cdot A_v + 1,8 \cdot \cos 40^\circ N_1 + 1,2 \cdot \cos 40^\circ N_2 + 0,28 \cdot \cos 40^\circ N_3 &= 0; \\ A_v &\approx 3478 \text{ N}. \end{aligned} \tag{10}$$

$$\begin{aligned} \sum M_{Ai} &= 0; \\ 1,8 \cdot B_v - 1,5 \cdot N_{v3} - 0,554 \cdot N_{v2} &= 0; \\ 1,8 \cdot B_v + 1,5 \cdot \cos 40^\circ N_3 + 0,554 \cdot \cos 40^\circ N_2 &= 0; \\ B_v &\approx 1258 \text{ N}. \end{aligned} \tag{11}$$

The diagrams of the cutting forces are constructed on axes parallel to the geometric axis of the beam (Fig. 10.). It is clear from the diagram that there are no strong jumps in the concentrated forces and moments.

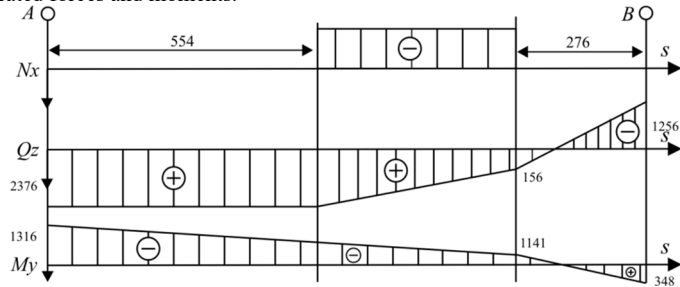
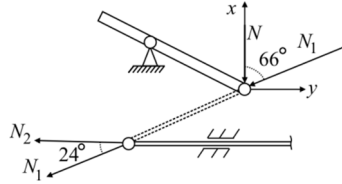


Fig. 10. Diagram of shear forces

The inclination of the photovoltaic panel is done by a lever mechanism driven by an electric motor for a satellite dish. The maximum angle of rotation of the panels is from 0° to 90°. The main parameters of the drive mechanism are: maximum stroke: 53 cm; static load: 450 kg; dynamic load: 250 kg; speed of movement: 5.6 mm/s ; supply voltage: 36 V (Fig. 11).



**Fig. 11.** Kinematic diagram for determining the loads on the drive motor.

We know that the force of gravity of the panel ( $N$  in the figure) amounts to 167 N. To find the force  $N_1$ , at an inclination in the rendered direction, the following equation is solved:

$$N_1 = \frac{N}{\cos 66^\circ} = \frac{167}{0,407} = 410 \text{ N.} \tag{12}$$

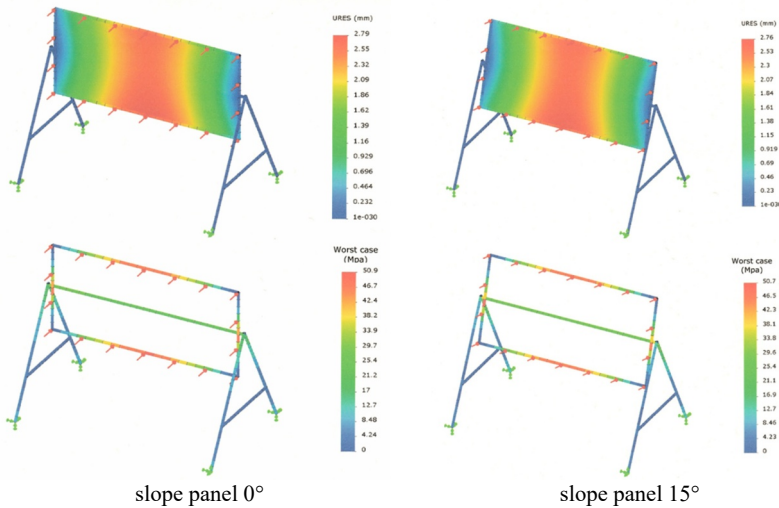
It can be seen that the force  $N_1$  is transmitted to the lower part of the structure by means of the lever. Again, by solving equation, we find the force  $N_2$ , which acts directly on the engine:

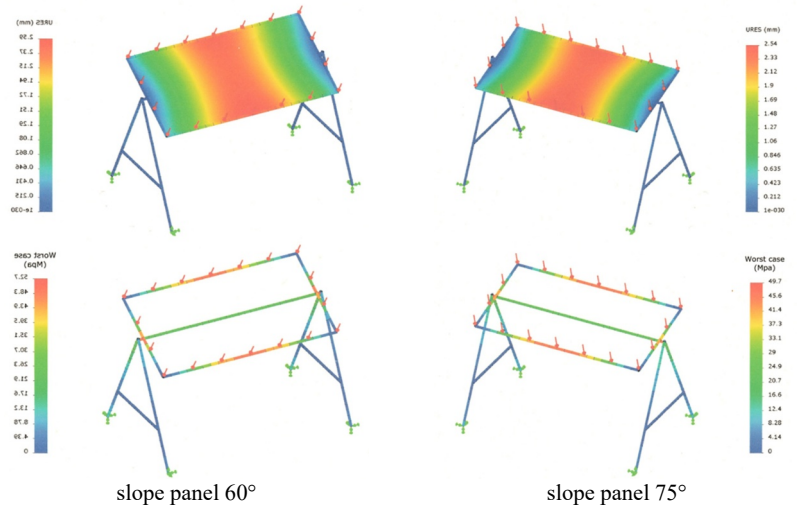
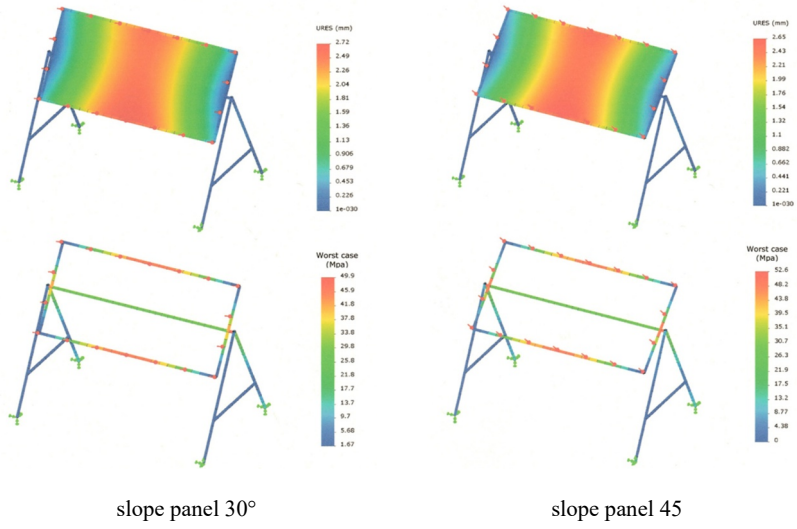
$$N_2 = N_1 \cos 24^\circ = 374 \text{ N} = 37 \text{ kg.} \tag{13}$$

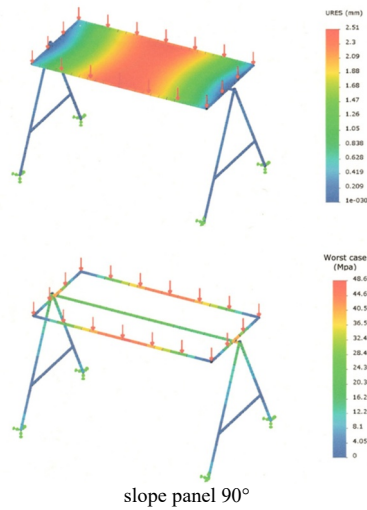
Therefore, under both static and dynamic loads, the motor will withstand the load.

### 3 Results and Discussion

Finite element strength (FEM) strength analysis was also performed for seven operating positions of the solar panel (from 0° to 90° with a step of 15°). The results obtained for each of the cases are presented in graphical form in Fig. 12.







**Fig. 12.** Displacements and maximum stresses in the beams at different slopes of panel.

The results obtained for each of the cases are presented in graphical form in Figure 12. It is clear from them that for all operating positions of the panel, the maximum stresses are obtained in its frame. These stresses in different cases vary around the value of 50 MPa and are not dangerous for the structure. The maximum stresses for each of the considered cases are presented in a Table 2.

**Table 2.** Maximum stresses obtained for operating positions from 0° to 90°

Working position	0°	15°	30°	45°	60°	75°	90°
Maximum mechanical stress (MPa)	50,9	50,7	49,9	52,6	52,7	49,7	48,6

The analysis of the obtained results shows that the greatest load is in the middle area of the photovoltaic panel. It has a maximum at a perpendicular position of the panel relative to the wind direction, which corresponds to a sloping panel 0°. This load leads to an URES of 2.79 mm, which shows how much the photovoltaic module deforms under the influence of wind force. The least wind load on photovoltaic panels is shown when they are successfully oriented on the earth's surface. This corresponds to a 90° inclined panel.

## 4 Conclusions

It has been established that the load-bearing structure and the photovoltaic panel must be able to withstand mechanical loads both from their own weight and from snow and wind. The obtained results for the conditions of the city of Ruse, Bulgaria show that for all working positions of the panel the maximum stresses are obtained within its framework. These voltages in different cases vary around the value of 50 MPa and are not dangerous for both the structure and the photovoltaic panel. The greatest load on the panel and the frame is observed in the middle part, with the maximum being at a perpendicular position of the panel with respect to the wind direction, which corresponds to an inclined panel of 0°, and the least of an inclined panel of 90°.

## References

1. Republic of Bulgaria. Ministry of Energy. Ministry of the Environment and Water. *Integrated energy and climate plan of the republic of Bulgaria 2021–2030*. (2020) [https://ec.europa.eu/energy/sites/default/files/documents/bg\\_final\\_necp\\_main\\_en.pdf](https://ec.europa.eu/energy/sites/default/files/documents/bg_final_necp_main_en.pdf)
2. T. Pavlovic, P.T. Tsankov, N.D. Cekić, I.S. Radonjić Mitić, Photovoltaic solar energy conversion, *The Sun and Photovoltaic Technologies* (2020) DOI: 10.1007/978-3-030-22403-5
3. I. Stoyanov, T. Iliev, An integrated approach for improvement of the efficiency of the photovoltaic system by using cogeneration, Bulgarian Chemical Communications, **Volume 52, Special Issue C**, pp. 46-52, (2020) DOI: 10.34049/bcc.52.C.0102.
4. M. Mehmed-Hamza and P. Stanchev, Overcurrent Protection Against Faults in Smart Grids, *11th Electrical Engineering Faculty Conference BulEF* (2019), pp. 1-4, DOI: 10.1109/BulEF48056.2019.9030744
5. Zlatov, N., Iliev, I., Terziev, A., Kamburova, V., Estimation of the photovoltaic modules energy production in respect of the PV inclination angle (2014) art. no. 6920446, DOI: 10.1109/REM.2014.6920446
6. P. Hristov, T. Hristova, Explaining The DLT Applications in The Context of a Customers, Facility Managements and Utility Companies Relationship, *16th Conference on Electrical Machines, Drives and Power Systems ELMA* (2019), pp. 1-5, DOI: 10.1109/ELMA.2019.8771693
7. M. Pandursi, F. Tsvetanov, Journal of Engineering Science and Technology Review SI, pp. 32-36 (2020)
8. C. Osterwald, T. McMahon, History of Accelerated and Qualification Testing of Terrestrial Photovoltaic Modules: A Literature Review. Prog. Photovolt: Res. Appl., 11-33 (2009)
9. O. Al-Habahbeh, B. Al-Hrout, E. Al-Hiary, S. Al-Fraihat, Reliability Investigation of Photovoltaic Cell Using Finite Element Modeling, *Proceedings of 9th International Symposium on Mechatronics and its Applications* (2013)
10. M. Kempe, D. Holsapple, K. Whitfield, N. Shiradkar, Standards development for modules in high temperature micro-environments, *Progress in Photovoltaics: Research and Applications*, 10.1002/pip.3389, **29**, **4**, pp. 445-460 (2021)
11. P. Zlateva, L. Yordanov, R. Petkova-Slipets, A study of the thermal properties of an alternative straw-containing building material. E3S Web Conf., 207 (2020) 01004, <https://doi.org/10.1051/e3sconf/202020701004>
12. A. Terziev, Analysis of the terrain specifics and roughness factor on the wind shear over complex terrains, (2019) 595 (1), art. no. 012043, DOI: 10.1088/1757-899X/595/1/012043, ISSN: 17578981
13. I. Stoyanov, T. Iliev, G. Mihaylov and E. Ivanova, Synthesis and design of virtual measurement system for investigation on photovoltaic modules, *10th International Symposium on Advanced Topics in Electrical Engineering ATEE* (2017), pp. 915-918, doi: 10.1109/ATEE.2017.7905070.
14. A. Sinha, D. B Sulas-Kern, M. Owen-Bellini, L. Spinella, S. Uličná, S. Pelaez, S. Johnston, L. T Schelhas, Glass/glass photovoltaic module reliability and degradation: a review, Journal of Physics D: Applied Physics, 10.1088/1361-6463/ac1462, **54**, **41**, 413002 (2021)
15. M. Owen-Bellini, P. Hacke, D. C. Miller, M. D. Kempe, S. Spataru, T. Tanahashi, S. Mitterhofer, M. Jankovec, M. Topič, Advancing reliability assessments of photovoltaic

- modules and materials using combined-accelerated stress testing, *Progress in Photovoltaics: Research and Applications*, 10.1002/pip.3342, **29**, **1**, pp. 64-82, (2020)
16. J. H. Wohlgemuth, Development of Accelerated Stress Tests, *Photovoltaic Module Reliability*, 10.1002/9781119459019, pp. 55-65, (2020)
  17. J. Fonseca, F. Oliveira, C. Prieb, A. Krenzinger, Degradation analysis of a photovoltaic generator after operating for 15 years in southern Brazil, *Solar Energy*, 10.1016/j.solener.2019.11.086, **196**, 196-206 (2020)
  18. <https://solarpro.bg/>
  19. Ordinance № 3 of 21 July 2004 *on the basic provisions for the design of construction structures and the impacts on them* (in Bulgarian). Source: <https://www.mrrb.bg/bg/naredba-3-ot-21-yuli-2004-g-za-osnovnite-polojeniya-za-proektirane-na-konstrukciite-na-stroejite-i-za-vuzdejstviyata-vurhu-tyah/>

# Assessing the diversification of energy mix with the methods of entropy and hierarchy of information

Iliyan Petrov<sup>1</sup>

<sup>1</sup>Bulgarian Academy of Sciences, Institute of Information and Communication Technologies, Dep. "Information Processes and Decision Support Systems", akad. Georgi Bonchev srt., bl. 2, 1113 Sofia, Bulgaria

**Abstract.** Energy systems are a typical example of complex and dynamic systems and the study of their structure is of particular interest in theoretical and practical terms. Becoming the main trend of diversification and, renewable energies play important role in the evolution and dynamics of energy balances at the international, national, and local levels. Usually, natural sciences use Information Theory and the concept of entropy to assess diversity, uncertainty, and chaos in systems with a high number of components. An alternative approach to assess system complexity is to consider these issues from point of view of the concentration of resources, dominance, and hierarchy in the interactions between system components. This report presents an original method developed by the author for assessing the hierarchy in energy mix structures and the role of renewable energies. The author's studies in the field of energy explore the evolution of markets and energy balances (energy mixes) on an international, regional and national level with a special focus on the European Union and Bulgaria. The hierarchy approach provides results in a more logical, objective, and balanced format and improves the analysis in terms of energy security and diversification. In this paper, is presented a research on the structure of the energy mix in Bulgaria.

## 1 Introduction

Assessing the complexity and interactions in dynamical systems is a challenging process that requires logically defined methods and tools. Traditionally, as a first step (Level 1) in this process, the primary data for relative weights or probabilities ( $p$ ) of the individual system's components are processed with some basic transformation function in terms of two alternative concepts: entropy  $e(p)$  as a representation of diversity and uncertainty, and, hierarchy  $h(p)$  – in the context of order, security, and domination. As a second step (Level-2), the transformed output results from Level-1 for all individual components are summed to

---

\* Corresponding author: [petrovindex@gmail.com](mailto:petrovindex@gmail.com)



obtain an aggregation characterizing the complexity of the system as a whole. In symmetrical configurations, the parts “ $p$ ” of all “ $n$ ” components are equal ( $\sum_{i=1}^n \frac{1}{n} = 1$ ), and, in these cases, the entropy of the system is maximal and the hierarchy is minimal. To individualize the various indicators or models, we use the first letter of the author's surname, placing it as an index to the symbol for entropy or hierarchy: "SE" - for "Shannon's Entropy" [1]; "RE" for Reni's Entropy" [2]; "HC" - for " Herfindahl Concentration (Hierarchy)" [3, 4], "PH" for " Petrov Hierarchy".

The summarized results at the macro level for all system configurations and distributions of relative weights can be classified in the Harrington's scale for psychophysical classification. This scale contains 6 phases and is a more detailed version of the traditional scale proposed by E. Harrington [5], which in its original form contains three or five classification intervals (0-0.2-0.37-0.63-0.8-1). Table 1 presents the 6 levels of structural space assessment in the Harrington-Petrov scale.

**Table 1.** Petrov Hierarchy in Harrington's assessment and classification scale

Hierarchy labels	Quantitative scale	Qualitative scale
Concentrated oligopoly (Mono-Duo-Tripoly)	0.80-1.00	Extremely high
Classic oligopoly	0.63-0.80	Very high
Enlarged Oligopoly	0.50-0.63	Higher than average
Polipoly	0.37-0.50	Lower than average
Multipoly	0.20-0.37	Very low
Hyperpoly	0.00-0.20	Extremely high

The combination of quantitative and psycho-physical assessments improves information perception and shows the opposite concepts of the two approaches and the relationship between them. When we measure hierarchy we get an indirect idea of entropy: i.e., high hierarchy means low entropy and vice versa.

## 2 Novel approach to Hierarchy as a complement to Entropy

To improve the methods and tools for measuring the system complexity, we offer an original approach to assessing order and security, called "*Petrov Logistic function Hierarchy (PLH)*". The basic function for transforming empirical data for component's parts is defined as follows:

$$plh = \frac{i}{1 + \left( \frac{\sum_{j=1}^J \log_{R_j} p_i}{J} \right)^c} \quad (1)$$

where:  $plh$  - individual hierarchy at micro-level;  $p_i$  - component's part (relative weight or probability);  $p_i$  [0, 1];  $R_j$  - "reference (etalon) weight" or "Reference Structural Thresholds (RST)";  $R_j$  [0, 1];  $J$  - number of  $R_j$ ;  $c$  - power factor, modelling the nonlinearly the structural interaction,  $c$  [0, 1]. We experimented with different values for " $R_j$ ", " $J$ " and " $c$ " for optimizing the basic function in equation (1). In a combination of ( $J = 2$ ;  $R_1 = 0.001$ ;  $R_2 = 0.25$ ;  $c = 2$ ) the basic function is defined as:

$$plh = \frac{p_i}{1 + \left( \frac{\log_{0.001} p_i + \log_{0.25} p_i}{2} \right)^2} \quad (2)$$

Figure 1 includes visualisation on the following values and graphs:

- 1) The basic function of the PLH (0.001; 0.25);
- 2) Scenario "Equalization in each population", in which the set of points for symmetrical configurations is linked by a series of "transit paths" consisting of points with

successive sub-symmetrical configurations forming the boundary of "minimum cumulative hierarchy";

- 3) Scenario "Single leader's dominance in all populations" in which asymmetric configurations are used to model the cumulative "maximum working hierarchy";
- 4) Scenario "Average working hierarchy", formed by the arithmetic mean of cumulative "minimum hierarchy" and "maximum working hierarchy".

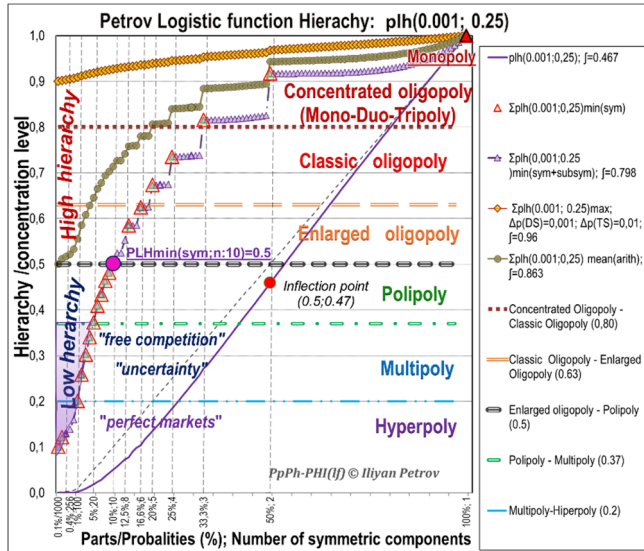


Fig. 1. Structural evolution in Petrov Logistic Hierarchy

### 3 Traditional complexity indicators v/s Petrov Hierarchy

The quality of entropy and hierarchy indicators can be assessed by comparing the integrals values of their basic functions. Graphically, this means comparing the surface (quadrature) that respective functions in the structural space. All basic transformation functions are continuous in the interval [0, 1] and the determination of the values of their integrals by symbolic calculations is possible with maximum accuracy. At this level of analysis, the conclusion is obvious: the undisputed leader is the Petrov Hierarchy, followed by the Shannon Entropy, while the Herfindahl Concentration (Hierarchy) seems to be less effective tool for universal structural assessments. The symbolic calculations of basic functions integral in *Maple 17* and *Python 3.9* produced equivalent results, presented in Table 2.

Table 2. Integrals' Quadrature of system complexity indicators

Entropy and Hierarchy Indicators (basic functions)	$\int_0^1 f(p_i); (dx=0.01)$
Petrov Logistic Hierarchy (PLH): equation (1)	0.467
Shannon Entropy (SE): $-p_i \cdot \log_2 p_i$	0.361
Herfindahl Concentration (HC): $p_i^2$	0.333
Shannon Entropy: $-p_i \cdot \ln p_i$	0.241
Shannon Entropy (SE): $-p_i \cdot \log_{10} p_i$	0.101

Figure 2 presents the basic functions of the indicators of Petrov and Herfindahl Concentration (Hierarchy) and Shannon Entropy (in three logarithmic forms - with binary,

decimal, and normal logarithm). The graphical analysis shows that the distribution of information in the integrals is also in favour of the Petrov Logistic Hierarchy (PLH).

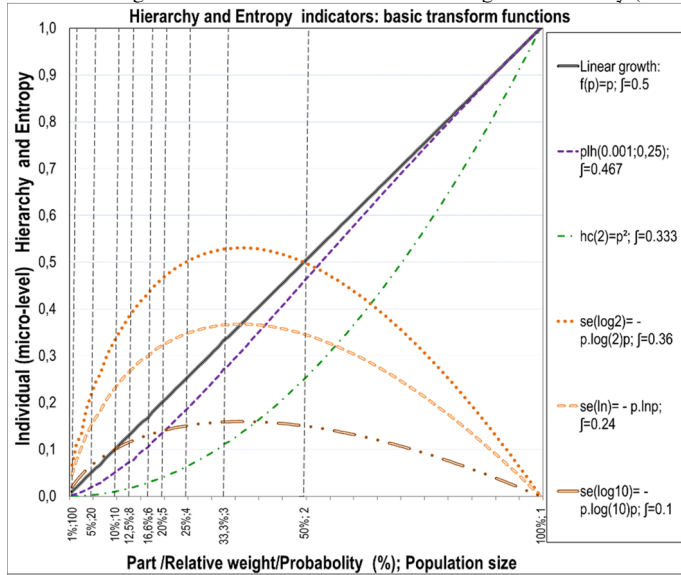


Fig. 2. Basic transform functions of Hierarchy and Entropy indicators

#### 4 Structural evolutions in national and world energy balances

**Sources of information and methodology.** This study of energy markets and balances is based publicly available sources and up-to-date information provided in some of the most reliable and detailed annual publications in the field of energy – “*IEA World Energy Outlook 2019*” [9] and “*BP Statistical Review of World Energy 2020*” [10]. In this paper, the analysis of the structure of energy balances is made based on Petrov Logistic Hierarchy as in methodology terms it is more logical, intuitive and balanced in comparison with Shannon Entropy and Herfindahl Concentration (Hierarchy). The empiric data for all energies are recalculated (normalized) from the absolute comparable physical values in relative weights for each year, country and region.

**Energy balances.** The energy industry is a typical example of a complex system composed of several inter-dependent and very dynamic sub-systems, each of which employs different technologies and requires intensive and large-scale financial investments in huge industrial and infrastructure projects. Over the last five years (2015-2019), as a result of technological advances in the RES sector and climate change control policies, structural changes have become increasingly visible. During this period the hierarchy in the structure of the energy balance of the world energy calculated by the method of Petrov Logistic Hierarchy (PLH) decreased from 0.76 to 0.74. And although traditional fossil fuels (oil, coal, and gas) still maintain their position as the three leading energy sources in most countries, their shares are gradually declining in favour of the RES sector.

This study explored the evolution of energy systems by groups of countries. The Petrov Hierarchy in variant  $PLH(0.001;0.25)$  allowed to obtain an objective quantitative assessment and qualitative classification of the dynamics in the structure of the energy balances since

2014. The results of the study are summarized in Table 3 in classification phases and according the types of energy types and also on local and imported resources.

**Table 3.** Evolution of Energy Mix structures

Energy mix Phase:	Countries	Types of energy	2014	2019	2020
Concentrated Oligopoly (PLH=0.8-1)	<b>Energy exporters</b>				
	Trinidad	2 (O, G)	0.955	0.95	0.95
	Turkmenistan	2 (O, G)	0.927	0.92	0.95
	Kuwait	2(O, G)	0.92	0.92	0.92
	Qatar	2 (G, O)	0.93	0.92	0.92
	Saudi Arabia	2 (O,G)	0.92	0.91	0.91
	Iraq	3 (O, G, H)	0.92	0.91	0.91
	Azerbaijan	3 (O, G, H)	0.87	0.90	0.90
	Uzbekistan	4 (C, O, G, H)	0.91	0.90	0.90
	UAE	4 (O, G, R)	0.92	0.88	0.875
	Venezuela	4 (O, G, H, )	0.82	0.81	0.83
	Iran	5 (O, G, H, C, N)	0.90	0.89	0.895
	Egypt	5 (O, G, H, C, R)	0.87	0.86	0.87
	Norway	5 (O, G, H, C, R)	0.85	0.81	0.815
	Netherlands	5 (O, G, H, C, R)	0.822	0.81	0.81
	<b>Energy importers (less than 50% of own resources in EM)</b>				
	Singapore	3 (O, G, R)	0.94	0.93	0.93
	Israel	4 (O, G, C, R)	0.82	0.91	0.91
	Lithuania	5 (O, G, H, C, R)	0.92	0.915	0.91
	Belorussia	5 (O, G, H, C, R)	0.91	0.88	0.85
Thailand	5(O, G, H, C, R)	0.83	0.81	0.805	
Taiwan	5 (O, G, H, C, R)	0.84	0.81	0.805	
Classic Oligopoly (PLH = 0.63-0.8)	<b>Energy exporters</b>				
	Vietnam	5 (O, G, H, C, R)	0.78	0.78	0.78
	Russia	6 (O, G, H, C, N, R)	0.78	0.76	0.765
	Canada	6 (O, G, H, C, N, R)	0.72	0.71	0.72
	<b>Energy importers (more than 50% own resources in EM)</b>				
	Denmark	5 (O, G, H, C, R)	0.76	0.79	0.785
	UK	6 (O, G, H, C, N, R)	0.77	0.76	0.76
	USA	6 (O, G, H, C, N, R)	0.74	0.73	0.735
	Brazil	6 (O, G, H, C, N, R)	0.78	0.72	0.73
	France	6 (O, G, H, C, N, R)	0.75	0.72	0.72
	Romania	6 (O, G, H, C, N, R)	0.72	0.68	0.675
	Bulgaria	6 (O, G, H, C, N, R)	0.71	0.68	0.685
	Finland	6 (O, G, H, C, N, R)	0.67	0.66	0.655
	<b>Energy importers (less than 50% of own resources in EM)</b>				
	Ireland	5(O, G, H, C, R)	0.82	0.79	0.785
	Greece	5 (O, G, H, C, R)	0.82	0.78	0.78
	Poland	5 (O, G, H, C, R)	0.82	0.78	0.78
	Italy	5 (O, G, H, C, R)	0.79	0.77	0.775
	Turkey	5 (O, G, H, C, R)	0.745	0.71	0.70
	Austria	5 (O, G, H, C, R)	0.74	0.71	0.71
	India	6 (O, G, H, C, N, R)	0.79	0.80	0.81
	China	6 (O, G, H, C, N, R)	0.85	0.77	0.76
	South Korea	6 (O, G, H, C, N, R)	0.79	0.75	0.75
	Hungary	6 (O, G, H, C, N, R)	0.75	0.74	0.74
	Japan	6 (O, G, H, C, N, R)	0.775	0.73	0.73
	Spain	6 (O, G, H, C, N, R)	0.72	0.73	0.73
	Ukraine	6 (O, G, H, C, N, R)	0.755	0.73	0.735
	Germany	6 (O, G, H, C, N, R)	0.71	0.71	0.71
	Belgium	6 (O, G, H, C, N, R)	0.78	0.71	0.71
	Czech Republic	6 (O, G, H, C, N, R)	0.73	0.71	0.71
	Sweden	6 (O, G, H, C, N, R)	0.72	0.70	0.71
	Slovakia	6 (O, G, H, C, N, R)	0.69	0.68	0.685
EU	4-5-6	0.75	0.73	0.73	
OECD	4-5-6	0.75	0.72	0.725	

Aggregates	World	2-3-4-5-6	0.76	0.74	0.74
------------	-------	-----------	------	------	------

Legend: C – coal; O – oil; G – gas; N – nuclear; H – hydro; R – renewables.

In most national energy systems that use only two or three types of traditional fossil fuels, the hierarchy of energy balances is traditionally very high and is classified in the phase *Concentrated Oligopoly (0.8-1)*, which in reality reflects the following types of structure: monopoly, duopoly or tripoly. In most of the case these structures are based on the dominance of oil and gas - in some of them, the hierarchy levels slowly decrease, but remain above the lower limit (0.8) and a transition to the phase of *Classical oligopoly (0.63-0.8)*. In most cases, this is due to the production of one, two, or three low-cost local energy resources, which are often actively exported on international markets. These countries are forced to develop and maintain large-scale and capital intensive projects in the extracting and infrastructure sectors and this limits their possibilities for developing the sector RES.

At this stage, for oil, gas and coal-producing and exporting countries, the very high level of hierarchy in the energy balance seems not to generate problems for their energy independence and security. At the same time, the sharp changes in world energy markets and the high volatility of international prices often lead to significant reductions of foreign exchange earnings and generate critical stress and critical situations in their social, financial, and economic systems. Particularly sensitive in this regard are Venezuela, Russia, Nigeria, Algeria, Egypt, Iran, Iraq, and other countries. At the same time, S. Arabia, Qatar, Kuwait, Oman, and the UAE, in which hydrocarbons are extracted at very low costs have accumulated significant gold and foreign exchange reserves compared to their gross domestic products and social budgets, and, subsequently are significantly less exposed to market risks. A different trend is observed in countries that use more than four types of energy but cannot achieve full or significant energy independence at the expense of their own resources. Investments in renewable energies are particularly active in countries where local traditional energy sources account for less than 50% of energy consumption. The level of hierarchy of their energy balances is steadily declining, but remains in the range of the *Classical oligopoly phase (0.63-0.8)* and only very few of them (Finland, Sweden) are approaching the phase of *Enlarged Oligopoly (0.5-0.63)*.

In all countries, the yearly structural changes have an evolutionary character and are expressed within apparently very limited deviation of hierarchy values - about  $\pm 0.0025-0.005$  on yearly basis. In energy exporting countries and big economies (USA, Japan, Germany, UK, Italy, Russia) the EM structures are more static than in smaller countries (Belgium, Greece, Romania, Bulgaria). However, the RES begin to play a more important role in the energy importing countries. In this respect, the structures of the energy mix of China, Brazil, South Korea, Turkey noticeably evolved since 2014 and contributed to the evolution in the EM structure of the World. The economies of developed countries have traditionally more diversified economies with a significant share of the services sector, in which electricity consumption is significant. As a result, at this stage, the investments in renewable energy sources are concentrated in the production of electricity from large photovoltaic and wind farms and, recently, from micro mezzo local capacities at the level of households and companies.

## 5 Energy balances under COVID-19

In the EU the main factors for diversification of the energy balance structure are the environmental policies and the active stimulation of investments in the field of RES. Unfortunately, not all RES have reached the required level of technological maturity and economic efficiency. On the positive side, the direct production of electricity by RES is becoming more dynamic and more efficient [11]. At the same time, the highly anticipated technologies for the production and use of hydrogen in transport and many industrial sectors

need further development [12, 13]. The EU's ambitions to reduce carbon emissions within the so-called "Green Deal" of 50% by 2030 and up to 0% by 2050 are not yet supported by clear programs and plans. This can lead to significant shocks in the coal and nuclear energy sectors in some countries (Germany, France, Bulgaria, Poland, the Czech Republic, Slovakia, and other countries), where these industries traditionally represent a significant share of the energy system [14]. Despite the ambitious political declarations, the unfavourable development of the COVID-19 pandemic and the economic crisis of 2020-21 adds further uncertainty in the plans for accelerated decommissioning of coal and nuclear power plants [15] and efficient development of the RES sector. Under conditions of COVID-19 and economic crisis, the energy sector is stagnating on World basis, with a substantial decrease in energy consumption in several industry sector like transport, construction, tourism, recreation. In most developed countries, due to the containment measures on social mobility this trend is partially mitigated by a higher electricity consumption on the level of households related to the new formats of home working and distance education. In this situation, the lower utilisation of fossil fuels was compensated by higher utilisation of RES. Unfortunately, the main RES (photovoltaics and wind farms) that depend on natural factors are not flexibly scalable and available with constant capacity. A major challenge for many countries and regions in the future will be the matching of decentralized consumption with the ambitions of close major power plants based on coal. As a result, the decrease of hierarchy of national balance was not as dynamic as expected.

Taking into account the objective lack of financial resource in big and small countries, we may expect that economic recovery will have to rely on the most accessible and locally available fossils - oil in the USA; coal in China, India, Poland, South Africa; oil and gas in OPEC and other exporting countries. In this situation, the EU is facing increasing pressure to balance between climate control and competition policies. Important changes can be expected as a result of completion of major nuclear power plants or infrastructure projects which are already under construction in a limited number of countries such as Belorussia, Finland, Hungary, Turkey, while in other countries (Japan, Bulgaria, Czech Republic) the prospective of similar projects are still under discussion.

## 6 Conclusions and further research

The results of the research show that in the theoretical aspect the approach of Petrov Hierarchy offers effective methods and tools for analysis of the dynamic systems and processes in the energy sector. The analysis of the development of energy balances in the period 2011-2019 proves the still insufficient technological development in the field of RES. In this sense, in the foreseeable future, world and national energy balances are not expected to reach the notion of a "perfect structure" and move to the "polypoly" phase with a hierarchy level below 0.5 by the method of the Petrov Hierarchy.

Of particular interest for future research are the analysis and forecasting of the structure of the RES sector. On the one hand, in the generalized statistics all types of new RES (photovoltaics, wind generators, solar heat generators, biotechnologies, hydrogen, etc.) are traditionally summarized in one group. On the other hand, the prospects for their development differ significantly. In the near future, when the share of some types of RES will reach 4-5%, it would be appropriate to divide them into separate items in a timely and clear manner and to start considering them as separate items in the energy balances. In this respect the analysis of energy security and diversification in the "E-6" format (i.e. based on six types of energy) would appear over-simplified and misleading. Such a format would reflect an incomplete picture of the real distribution and prospects for the development of production and consumption in the energy sector by countries and regions. It is possible, for example, to present the existing types of RES as 10 separate items (RES-10): 1) hydro-

electricity; 2) photovoltaic electricity; 3) wind electricity; 4) solar heating (heat pumps); 5) geothermal energy for heating or cooling; 6) biomass; 7) biogas; 8) biofuel; 9) "green" hydrogen (electrolysis of water through RES); 10) "blue" hydrogen (pyrolysis of natural gas). As a result, the number of energy types increases from "6" to "14" (E-14).

Another promising direction is to explore the structural evolution of energy markets and balances not only in physical but also in economic indicators, reflecting the cost and prices of different energy sources. Such an approach may unveil some privileges for projects related to traditional energy sources or accelerated introduction of RES at unreasonably high prices which could lead to unfair competition and economic unavailability of energy in many industries and regions. An objective analysis will be particularly important in the EU for attaining not only effectively but also efficiently the targets for low carbon emissions and not to the detriment of economic competitiveness.

This research is supported by the Bulgarian FNI fund through the project "Modeling and Research of Intelligent Educational Systems and Sensor Networks (ISOSeM)", contract KP-06-H47/4 from 26.11.2020.

## References

1. C. Shannon, W. Weaver., *The Bell Sys. Tech. J.* **27**, 379–423 (1948)
2. A. Renyi, On measures of information and entropy., *Proceedings of the fourth Berkeley Symposium on Mathematics, Statistics and Probability* 547–561 (1961)
3. O. Herfindahl, *Concentration in the U.S. Steel Industry* (dissertation, Colum. Univ., 1950)
4. E.H. Simpson, *J. Nature* **163 (4148)**, 688 (1949)
5. E. Harrington, The desirability function. *Ind. Qual. Contr.* **21(10)**, 494-498 (1965)
6. I.I. Petrov, *J. Econ. Altern.* **1**, 5–15 (2016)
7. Guidelines on the assessment of horizontal mergers under the Council Regulation on the control of concentrations between undertakings (2004/C 31/03) /Section "HHI levels" paragraph 19-20; Off. J. of EU (05.02.2004) [https://eur-lex.europa.eu/legal-content/EN/TXT/PDF/?uri=CELEX:52004XC0205\(02\)](https://eur-lex.europa.eu/legal-content/EN/TXT/PDF/?uri=CELEX:52004XC0205(02))
8. I.I. Petrov, I.I., *Structural Evolution of World and European energy markets and the development of gas pipeline networks in South-East Europe with participation* (Ph.D. dissertation, Russian State University for oil and gas, Moscow, 2015).
9. BP Stat. Rev. of W. En.: - Statistical Review of World Energy – all data, 1965-2019 (2020)
10. IEA World Energy Outlook - 2020, *Int. En. Outlook* (2020)
11. Agora Energie<sup>2</sup>wende (2020): "The European Power Sector in 2019: Up-to-Date Analysis on the Electricity Transition", [https://www.agora-energiawende.de/fileadmin2/Projekte/2019/Jahresauswertung\\_EU\\_2019/172\\_A-EW\\_EU-Annual-Report-2019\\_Web.pdf](https://www.agora-energiawende.de/fileadmin2/Projekte/2019/Jahresauswertung_EU_2019/172_A-EW_EU-Annual-Report-2019_Web.pdf) (2020)
12. Dickel, R., *Blue hydrogen as an enabler of green hydrogen: the case of Germany* (Oxford Institute for Energy Studies, ISBN978-1-78467-159-4, (2020)
13. Stahl Business Association (2020): *National hydrogen strategy in delay*, <https://www.stahl-online.de/index.php/nationale-wasserstoffstrategie-in-verzug/> (17.0.3.2020)
14. German Coal Commission: "Growth, Structural Change and Jobs Commission: Final report"; [https://www.bmwi.de/Redaktion/DE/Downloads/A/abschlussbericht-kommission-wachstum-strukturwandel-und-beschaefigung.pdf?\\_\\_blob=publicationFile](https://www.bmwi.de/Redaktion/DE/Downloads/A/abschlussbericht-kommission-wachstum-strukturwandel-und-beschaefigung.pdf?__blob=publicationFile) ((2019)

<sup>2</sup> Corresponding author: [petrovindex@gmail.com](mailto:petrovindex@gmail.com)

15. Energate Messenger (2020): “Corona shakes up coal phase-out schedule”, 6 April 2021  
<https://www.energate-messenger.ch/news/201586/corona-bringt-zeitplan-fuer-kohleausstieg-ins-wanken?media=print>



# Renewable energies projects selection: block criteria systematization with AHP and Entropy-MOORA methods in MCDM

Iliyan Petrov<sup>1</sup>

<sup>1</sup>Bulgarian Academy of Sciences, Institute of Information and Communication Technologies, Dep. "Information Processes and Decision Support Systems", akad. Georgi Bonchev str., bl. 2, 1113 Sofia, Bulgaria

**Abstract.** EU countries face two major challenges in the energy sector – the control of carbon emissions and the high dependence on imported primary energy sources. Both European Commission and national governments actively develop, update and upgrade strategies and plans for the energy sector. They aim to ensure the gradual reaching of consecutive targets for increasing the weight of Renewable Energies (RE) in the European primary energy mix. The selection of Renewable Energy investment projects in these sectors involves different groups of experts who have to consider the specifics of different countries, regions, and technologies. The Decision-making process becomes more complicated, as in addition to political goals it has to ensure the efficiency and competitiveness of European economies. Several conflicting objectives have to be balanced with complex social, economic, technological, and environmental factors. Our study explores the application of combined methods and evaluation techniques for improving the assessment and selection of prospective RE projects. We implement an innovative integration of the Analytical Hierarchy Process (AHP) for block criteria systematization combined with objective Shannon Entropy in the MOORA evaluation.

## 1 Introduction

Multi-Criteria Decision Making (MCDM) is one of the main disciplines in operations analysis which employs different subjective (expert-dependant) and objective (data-driven) methods for assessing the quality and performance of complex systems in many areas. On one hand, the risks of relying on experts' opinions are determined by the subjectivity of human experiences and preferences, while, on the other hand, the data-driven selections depend on the quality of data and practically neglect the users' needs. One-sided subjective or analytical methods may lead to uncertainty in the evaluation decision-making process.

---

\* Corresponding author: [petrovindex@gmail.com](mailto:petrovindex@gmail.com)

The Multi-Objective Optimization with Ratio Analysis (MOORA) is a popular approach with a compensatory concept for handling complex tasks for the assessment of numerous alternatives with multiple controversial criteria [1-6]. It is more transparent, intuitive, and easy for computation than other concepts, such as TOPSIS [7] and VIKOR [8], and allows to combine it easily with other methods without over-engineering the calculations.

RE energy projects can be based on different technologies and management systems and their functioning can be assessed with different criteria and methods [9-13].

## 2 Objective definition of criteria weights with Entropy-MOORA

A combination of MOORA with the Information Entropy concept allows performing an objective definition of weights for evaluation criteria [14-16]. It is used for different MCDM problems and includes several consecutive steps. In this paper, we use the essentials of common MCDM methodology aspects developed in our previous work [24].

**Step 1.** This step prepares the data for the selection process in the following sub-steps:

**Step 1.1.** Definition of the *Basic Decision Matrix (BDM)* comprising a list of “*m*” target alternatives (*A<sub>i</sub>*) which are evaluated with a set of “*n*” independent criteria (*C<sub>j</sub>*):

$$BDM_{m \times n} = [x_{ij}]_{m \times n}, \text{ where } i = 1, 2, \dots, m; j = 1, 2, \dots, n \quad (1)$$

In this study, we use an existing data-set [17] containing 13 alternatives RE projects and 7 selection attributes shown in Table 1.

**Table 1.** Target alternatives and evaluation criteria for selection of RE projects

Alternative RE projects		Criteria		Unit	
WA1	Wind power $P \leq 5$ MW	C1	P	Power	MW
WA2	Wind power $5 \leq P \leq 10$ MW	C2	OH	Operating Hours/year	1000 h/y
WA3	Wind power $10 \leq P \leq 50$ MW	C3	UP	Utilisation Period	years
HA4	Hydroelectric $P \leq 10 \leq$ MW	C4	tCO2/y	Avoided CO2 emissions	Mt/y
HA5	Hydroelectric $10 \leq P \leq 25$ MW	C5	IR	Investment Ratio	€/KW
HA6	Hydroelectric $25 \leq P \leq 50$ MW	C6	CP	Construction period	years
SA7	Solar Thermo-electric $P \geq 10 \geq$ MW	C7	O&MC	Oper. & Mainten. Cost	€/MWh
BA8	Biomass (energetic cultivations) $\leq 5$ MW				
BA9	Biomass (forest & agro wastes) $P \leq 5$ MW				
BA10	Biomass (farm industry wastes) $P \leq 5$ MW				
BA11	Biomass (forest industry wastes) $P \leq 5$ MW				
BA12	Biomass (co-comb.in conv. central) $P \geq 50$ MW				

The number of alternatives “*m*” is not limited, but it is preferable to perform a preliminary selection according to the preferences and restraints of DM. This data-set contains projects of different scales based on mature and widely accessible technologies based on four types of RE for producing electricity: wind power (W), hydropower (H), solar (S), and biomass (B). Table 2 contains the *Normalized Decision Matrix (NDM)*

**Step 1.2.** Calculating the proportions of relative “basic weights *p<sub>ij</sub>*” for each value of *x<sub>ij</sub>* in *C(i)* and formation of *Normalized Decision Matrix (NDM)* with  $\sum_{i=1}^m p_{ij} = 1$ :

$$p_{ij} = x_{ij} / \sum_{i=1}^m p_{ij} \quad (2)$$

$$NDM = [p_{ij}]_{m \times n} = \begin{bmatrix} p_{11} & p_{1n} \\ p_{m1} & p_{mn} \end{bmatrix}, \text{ where } i = 1, 2, \dots, m; j = 1, 2, \dots, n. \quad (3)$$

**Step 1.2.** Calculation of the total nominal Shannon Entropy [18] for each criterion vector-column “*j*” as a sum of the “*i*” individual entropies for the “*m*” target alternatives:

$$SEnom_j = -\sum_{i=1}^m se_j = -\sum_{i=1}^m p_{ij} \cdot \log_2(p_{ij}) \quad (4)$$

**Step 1.3.** Calculation of maximal Shannon Entropy value for a set of “*m*” alternatives in which all elements have equal relative weights, i.e.  $p_{ij} = 1/m$ :

$$SEmax(m) = -\sum_i^m (1/m \cdot \log_2 1/m) = \log_2 m \quad (5)$$

Step 1.4. Normalization of nominal entropy  $SEnom_j$  by comparing it to  $SEmax(m)$ :

$$SEnorm_j = e_j = SEnom_j / SEmax(m) = -(\log_2 m)^{-1} \sum_{i=1}^m p_{ij} \cdot \log_2(p_{ij}) \tag{6}$$

Step 1.5. Calculation of the sum of the normalized criteria entropies  $e_j = SEnorm_j$  and defining their real entropy criteria weights ( $recw_j$ ) for each criterion  $C_j$ :

$$recw_j = e_j / \sum_{i=1}^n e_j \tag{7}$$

**Table 2.** Basic Decision Matrix (BDM)

Criteria (n)	C1	C2	C3	C4	C5	C6	C7
	P	OH	UP	tCO2/y	IR	CP	O&MC
Alternatives (m)	MW <i>Benefit</i>	1000h/y <i>Benefit</i>	years <i>Benefit</i>	Mtons/ <i>Benefit</i>	€/KW <i>Cost</i>	years <i>Cost</i>	€/MWh <i>Cost</i>
WA1	5	2,35	20	1929936	937	1	1,470
WA2	10	2,35	20	3213560	937	1	1,470
WA3	25	2,35	20	9649680	937	1	1,510
HA4	5	3,10	25	472812	1500	1,5	1,450
HA5	20	2,00	25	255490	700	2	0,700
HA6	35	2,59	25	255490	601	2,5	0,600
SA7	50	75,00	25	482856	5000	2	4,200
BA8	5	75,00	15	2524643	1803	1	7,106
BA9	5	75,00	15	2524643	1803	1	5,425
BA10	5	75,00	15	2524643	1803	1	5,425
BA11	5	7500	15	2524643	1803	1	2,813
BA12	56	75,00	20	4839548	856	1	4,560
BA13	2	7,00	20	5905270	1503	1,5	2,512

Based on additional data treatment whose aim is to substitute the genuine results from the transformation of empiric data with the “idea” to enhance the difference between criteria through a “divergence parameter”  $d_j$  which represents an arithmetic difference between the normalized maximal entropy  $SEmax(m)$  expressed as “1” minus  $SEnorm_j$  expressed as “ $e_j$ ” as defined in eq. (6-7):

$$d_j = 1 - e_j \tag{8}$$

$$decw_j = d_j / \sum_{i=1}^m d_j = (1 - e_j) / \sum_{i=1}^m (1 - e_j) \tag{9}$$

The results of Steps 3.1-6 are displayed in Table 3.

**Table 3.** Real and differed entropy weights in stand-alone Entropy approach

Criteria	P	OH	UP	tCO2/y	IR	CP	O&MC
WA1	0,121	0,038	0,285	0,22	0,206	0,236	0,178
... BA13	0,060	0,090	0,285	0,42	0,279	0,304	0,254
$SEnom$	3,033	2,858	3,672	3,15	3,431	3,612	3,376
$SEmax$	3,700	3,700	3,700	3,700	3,700	3,700	3,700
$SEnorm=e_j$	0,820	0,772	0,992	0,852	0,927	0,976	0,912
$recw_j$	0,131	0,124	0,159	0,136	0,148	0,156	0,146
$d_j=1-e_j$	0,180	0,228	0,008	0,148	0,073	0,024	0,088
$decw_j$	0,241	0,305	0,010	0,197	0,097	0,032	0,117

The substitution of the genuine objective “real entropy criteria weights ( $recw_j$ )” with another “concentration-like set” of “differed entropy criteria weights ( $decw_j$ )” produces very different results without taking into account the needs and preferences of users. If the discussion was purely theoretical, such extraction treatment might be regarded as an experiment. However, in any real situation, such artificially created reality dramatically transforms the positioning of all criteria distancing them from input empiric data. While the values of “ $recw_j$ ” are quite even, the values of “ $decw_j$ ” become very unequal. As a result, only 2 technical criteria (“Power” and “Operating hours”) concentrate 54,6% of the total weights, while the “Utilization period” (1%) and the “Construction period” (3,2%) are practically neglected. In principle, in this treatment, the losers in a diversity context are

transformed into winners in a concentration context. Such perturbation in many cases may be regarded as “data treatment”, but in our opinion, the concept of “information extraction” from relative weights is illusive. If there are doubts about the capacity of the entropy approach a logical way-around would be to replace it with an approach that measures directly the opposite of diversity. In other words, to measure the concentration of information in each criterion rather than trying indirectly to “extract data” from entropy for judging about concentration. Actually, both approaches are purely technical and they may look non-transparent and technocratic. In fact, the most important task in MCDM is to focus on those parameters or functions which objectively correspond to the needs and preferences of users, as shown below in Section 3.

**Step 2.** Calculation of “normalized weighted values “ $v$ ” with real weights ( $r_{ij}.recw_j = rv_{ij}$ ) and with differed weighs ( $r_{ij}.decw_j = dv_{ij}$ ) for constructing the respective Normalized Weighted Matrices  $NWM$  with real and differed entropy criteria weights:

$$NRWM_{m \times n} = [r_{ij}.recw_j]_{m \times n} = [rv_{ij}]_{m \times n} \quad (10)$$

$$NDWM_{m \times n} = [r_{ij}.decw_j]_{m \times n} = [dv_{ij}]_{m \times n} \quad (11)$$

**Step 3.** Classification of criteria in “benefit (profit)” and “non-benefit (cost)” depending on how their attribute or save resources and performance. The optimization for “benefit (profit)” is expressed in maximal values and for “non-benefit(cost)” - in minimal values. Criteria C1-C4 are “benefit (profit)” type, while C5-C7 are “non-benefit (cost)” type.

**Step 4.** Calculation of MOORA Alternatives Assessments ( $AA_j$ ) for each alternative. In our case, we perform a comparison between the sets of  $recw_j$  and  $dcew_j$ :

$$AA_{recw_j} = \sum_{j=1}^g rv_{ij} - \sum_{j=g+1}^n rv_{ij} \quad (12)$$

$$AA_{dcew_j} = \sum_{j=1}^g dv_{ij} - \sum_{j=g+1}^n dv_{ij} \quad (13)$$

**Step 5.** Ranking the assessment results  $MAA_j$  in descending order.

For better visualization, the results of Steps 5-8 for calculations in the traditional “SE-MOORA” approach are displayed in Table 8, Section 4, here below.

### 3 Optimizing AHP by systemizing the evaluation criteria in blocks

The stand-alone Entropy approach described in Section 2 is data-driven and, in principle, excludes the participation of experts in defining the weights of evaluation criteria. However, a professional expertise is needed in many aspects – defining needs, pre-selecting target alternatives, selecting criteria, and applying evaluation methods. This report has not the possibility to explore the variety of topics related to expert activities, which are well discussed in numerous publications [19-22]. Our studies are focused on improving the traditional “Entropy & MOORA” approaches by decomposing the initial set of criteria into smaller blocks for optimizing the assessment procedures and finding solutions that allow reflecting the users’ needs and preferences.

In the algorithm of Section 2, an additional *Step 1.0* is integrated for defining the weights of a limited number of blocks “ $b$ ” ( $b > 1$  and, in our opinion, preferably  $b \leq 5$ ) with the Analytical Hierarchy Process (AHP) method [23-24]. Such systematization allows to organize the expression of experts’ opinions and to frame the subjectivity of individual judgments up to the stage of defining the importance of blocks. In case discussed in this paper, all criteria are grouped in 3 blocks:

1) “Technical - Block 1” - for all technical parameters ( $C_1, C_2, C_3$ );

2) “Ecology - Block 2” - for ecology and pollution control parameters ( $C_4$ );

3) “Costs - Block 3” - for financial and time parameters related to the realisation

of the project ( $C_5, C_6, C_7$ ).

The logical systematization of criteria in blocks(groups) reduces the number of “pairs-comparisons” and facilitates the hierarchical ranging of priorities, allowing to express with less confusion the individual preferences of DM. To define block weights a quadratic *Hierarchy Preference Matrix*  $HPM_{(b \times b)}$  is constructed in which the values reflect the judgments of DM according to the traditional AHP scale. The values of “1-3-5-7-9” correspond to pivot verbal judgments “equal importance - moderate importance - strong importance - very strong importance - top importance”. Interim values (2-4-6-8) can be used for more precision. The comparison of a single block ( $b_e$ ) with itself results in “1”, so the main diagonal’s cells in  $HPM_{(b \times b)}$  are fixed to “1”. If the *hierarchy preference* “hp” of “Technical v/s Energy” is judged as “strong”, it is quantified in “ $hp=5$ ”. The reciprocal comparison “Energy v/s Technical” results in “ $hp=1/5$ ”. An important advantage of the “AHP(blocks)” approach allows to model flexibly the values  $HPM_{(b \times b)}$  with less computational efforts, less subjectivity, and better consistency in defining the *hierarchy preferences*. The block weights ( $bw$ ) are calculated as:

$$bw_e = (\prod_{e=1}^b hp_{ee})^{1/b} / (\sum_{e=1}^b (\prod_{e=1}^b hp_{ee})^{1/b}), \text{ where } e = 1, \dots, b. \quad (14)$$

$$\sum_{e=1}^b bw_e = 1 \quad (15)$$

For better results and simplified presentation a simulation of 3 variants of  $HPM$  with different user’s preference are proposed in Table 4.

**Table 4.** AHP Hierarchy Preference Matrices (HPM) for block weights definition

Preferences Blocks	Balanced preferences				Ecology-driven preference				Cost-driven preferences			
	B1	B2	B3	weight	B1	B2	B3	weight	B1	B2	B3	weight
B1: Technical	1	1/2	1/2	0.2	1	1/4	1/2	0.143	1	1/2	1/4	0.143
B2: Ecology	2	1	1	0.4	4	1	2	0.571	2	1	1	0.286
B3: Costs	2	1	1	0.4	2	1/2	1	0.286	4	2	1	0.571
Consistency	CR=0% (excellent)				CR=0% (excellent)				CR=0% (excellent)			

To define objectively the weights of criteria in the blocks with more than one criterion (Block 1) the Entropy transformation is calculated as described in Step 3 of Section 2.

The definition of weights for the variant “Balanced preferences” is presented in Table 5.

**Table 5.** Entropy weighting of criteria with balanced “Ecology-to-Costs (1:1)” preferences

AHP Blocks	Block 1 - Technical			Block 2 - Ecology		Block 3 - Costs			
Block weights	0.2			0.4		0.4			
Criteria	P	OH	UL	tCO2/y			IR	IP	O&M C
$S_{Enorm} = e_j$	0,820	0,772	0,992	0,852			0,927	0,976	0,912
rebw (Blocks)	0,317	0,299	0,384	0,400			0,329	0,347	0,324
recw (Criteria)	0,063	0,060	0,077	0,400			0,132	0,139	0,130
$d=1-e$	0,180	0,228	0,008	0,400			0,073	0,024	0,088
debw (Blocks)	0,434	0,548	0,018	0,400			0,394	0,130	0,476
decw (Criteria)	0,087	0,110	0,004	0,400			0,158	0,052	0,190

The definition of weights for the “Ecology-driven preferences” is presented in Table 6.

**Table 6.** Entropy weighting of criteria with Ecology-driven preferences /Ecology-to-Costs (2:1)/

AHP Blocks	Block 1 - Technical			Block 2 - Ecology		Block 3 - Costs			
Block weights	0.143			0.571		0.286			
Criteria	P	OH	UL	tCO2/y			IR	IP	O&M C
$S_{Enorm} = e_j$	0,820	0,772	0,992	0,852			0,927	0,976	0,912
rebw (Blocks)	0,317	0,299	0,384	0,571			0,329	0,347	0,324
recw (Criteria)	0,045	0,043	0,055	0,571			0,094	0,099	0,093
$d=1-e$	0,180	0,228	0,008	0,571			0,073	0,024	0,088
debw (Blocks)	0,434	0,548	0,018	0,571			0,394	0,130	0,476
decw (Criteria)	0,062	0,078	0,003	0,571			0,113	0,037	0,136

The definition of weights for the “Cost-driven preferences” is presented in Table 7.

**Table 7.** Entropy weighting of criteria with Cost-driven preferences /Ecology-to-Costs (1:2/)

AHP Blocks	Block 1 - Technical			Block 2 - Ecology	Block 3 - Costs		
Block weights	0.143			0.286	0.571		
Criteria	P	OH	UL	tCO2/y	IR	IP	O&M C
SEnorm = e <sub>j</sub>	0,820	0,772	0,992	0,852	0,927	0,976	0,912
rebw (Blocks)	0,317	0,299	0,384	0,286	0,329	0,347	0,324
recw (Criteria)	0,045	0,043	0,055	0,286	0,188	0,198	0,185
d=1 - e	0,180	0,228	0,008	0,286	0,073	0,024	0,088
debw (Blocks)	0,434	0,548	0,018	0,286	0,394	0,130	0,476
decw (Criteria)	0,062	0,078	0,003	0,286	0,225	0,074	0,272

In the hybrid “AHP-block &Entropy”, approach the “real entropy criteria weights (recw)” are logical and directly deducted from primary data to reflect the real distribution of information. In opposite, the artificial calculation of “differed entropy criteria weights (decw)” creates important redistribution of information in Block 1 and Block 3 which contain more than one criterion. In Block 1 the importance of “Utilization Life (UL)” is reduced to a neglected level: in the Balanced policy from 0.077 to 0.004 (19.25 times); in the Ecology-driven policy from 0.055 to 0,003 (18,3 times); and in the Cost/Efficiency-driven policy - from 0.055 to 0,003 (18,3 times). The situation is very similar in Block 3: the importance of “Construction period” is reduced in “Balanced policy” from 0.139 to 0.052 (2,7 times); in the Ecology-driven policy from 0.099 to 0.037 (2.7 times); and in the Cost/Efficiency-driven policy - also from 0.198 to 0,074 (2.7 times). Data treatments depend on the researcher’s concept and responsibility, but in real conditions they should be undertaken with common sense since such “differed content” may have serious consequences for users.

### 4 Results and Discussion

The ranking of results for best alternatives with MOORA in the four variants of weighs for the 3 different selection policies is displayed in Table 8. The stand-alone entropy method “SE” is 100% data-driven and it cannot take into account the users’ preferences. Logically however the perturbation of results between “recw” and “decw” is very important – except for t #1, #2 and #4 ranks all other results are different.

**Table 8.** Final ranking of MOORA assessment results for selection of RE projects

Approach	Hybrid AHP Block & Shannon Entropy						Stand-alone Shannon Entropy	
	recw			decw			recw	decw
Preference	B	E	C	B	E	C	Single variant	Single variant
WA1	6	6	5	6	12	5	6	12
WA2	4	4	4	4	10	4	3	10
WA3	1	1	1	1	2	1	2	2
HA4	12	12	11	12	13	9	11	13
HA5	11	11	7	10	11	8	7	11
HA6	10	10	8	7	8	6	5	8
SA7	13	13	13	13	3	13	13	3
BA8	9	9	12	11	7	12	12	7
BA9	7	7	9	8	5	10	9	5
BA10	7	7	9	8	5	10	9	5
BA11	5	5	6	5	4	7	4	4
BA12	2	2	2	2	1	2	1	1
BA13	3	3	3	3	9	3	8	9

Legend: B – Balanced policy (Ecology/Costs); E – Ecology-driven policy; C – Cost-driven policy

In contrast, thanks to the block systematization in the combined “AHP-block & Entropy” approach the policy preferences can be taken into account flexibly and correctly. Although

values of AHP(blocks) weights were adjusted for modelling different preferences, the selections in the 3 variants of preferences in *real entropy criteria weights (recw)* are very similar. In this case, this was predetermined by the empirical information contained in the original data-set. The top 4 alternatives with “*recw*” for all 3 preference have the same ranking and are based on the more mature wind and biomass technologies (WA3>BA12>BA13>WA2).

The final assessments with the combined “AHP(blocks) & Entropy” and MOORA approaches in our study are in accordance with the basic findings in the study of J.R. San Cristobal [17] received initially on the same data-set with the application of the classical AHP and VIKOR methods.

One of the purposes of our studies is to explore the repercussions of the “differed entropy” generated in eq. (8-9) on the robustness of MCDM process. The advantages of the combined “AHP(blocks) & Entropy” method are confirmed by simulating selections in three different variants of preferences and assessments with the MOORA technique. The systematization of criteria in blocks allocates defined “quota” of importance to each block and this is space in which the “differed entropy” is limited redistribute the weights of criteria. If needed, additional AHP(blocks) decompositions can be performed for creating sub-blocks in selections with more criteria. This is often the case in MCDM for complicated investment projects with numerous technical, financial, social, and other criteria. A major advantage of such an approach is that at the sub-block levels the participation of experts can be very well structured to improve the consistency of their opinions. In addition, the DMs’ involvement becomes more feasible and effective. At the same time, the application of artificially calculated weights risk to completely disregard the real needs of users and to increase uncertainty. For this reason, the data-driven methods based on a logical systematization should be preferred to the substitution of empiric facts by “differed reality”.

## 5 Conclusion and further research

The methodological improvements and experiments in this study confirm that the enlargement of the traditional “Entropy” approach with the “block weighting” of criteria in AHP(blocks) provides an additional logical and accessible approach for multi-criteria analysis and effective support for the decision-making process. The comparative analysis of the variants with real and differed weights of criteria confirm our preferences for direct measuring of diversity based on real data and sets a basis for further research in other areas and evaluation techniques used in MCDM.

From a practical point of view, this study provides a useful basic framework for analyzing RE investment projects and improving the MCDM process with approaches tailored to preferences and budgets of different users, regions, and technologies under conditions of pandemic and economic restraints. Another result is the confirmation that benefits from economies of scale are well expressed in the all types of technologies based on different RE sources. This is important for convincing the users to be orientated for more performant equipment if they can be realized in their region, and at the same time to have a flexible and portfolio-oriented policy. The combination of projects based on different technologies will be critical for building diversified and reliable energy-generating systems. The data set employed in this system includes alternatives that were ranked without controversies in the preference profiles. In practice, the real situation is expected to become more uncertain with the progress in the different technologies and the increase of competition between manufacturers of different systems and equipment, which would require considering larger numbers of criteria and alternatives with increased number of experts.

Further applied research should include the application of “AHP(blocks) & Entropy”-approach with different final evaluation techniques, such as TOPSIS, VIKOR, WPN,

ELECTRE, and others which will provide integrated and more reliable methods for selecting investment projects. Taking into account that the migration to “zero carbon emissions” energy model can be achieved during a reasonable transition period of 20-30 years, the future research should include other technologies (hydrogen, gas, coal, nuclear or hybrid projects) depending on the specifics of different countries and geographical regions.

This research is supported by the Bulgarian FNI fund through the project “Modeling and Research of Intelligent Educational Systems and Sensor Networks (ISOSeM)”, contract P-06-H47/4 from 26.11.2020.

## References

1. Brauers, W., *Optimization methods for a stakeholder society* (Boston: Kluwer Academic, 2004)
2. Barzilai, J., *Springer. Int. Ser. in Oper. Res. & Man. Sci.* **142**, pp. 57-86 (2010)
3. Saaty, T., *Principia Mathematica Decernendi: Mathematical Principles of Decision Making* (Pittsburgh, Pennsylv.: RWS Publ., 2010)
4. Zavadskas E., Turskis Z., *Tech. and Econ. Devel. of Econ.* **17(2)** pp.397–427 (2011).
5. Genova, K., Kirilov, K., Guliashki, V., *Cyber. and Inf. Tech.*, **2**, pp. 3-22 (2015)
6. Petrov, P., Kostadinov, G. and al., *Int. Conf. Automat. and Inform. (ICAI)*, Varna, Bulgaria, pp. 1-5, (2020) doi: 10.1109/ICAI50593.2020.9311351
7. Opricovic, S., Tzeng, G.H., *Eur. J. Oper. Res.*, **156**, pp. 445-55 (2004)
8. Hwang, C.L., Yoon, K. *Multi-attribute decision making: methods and applications*. Berlin: Springer-Verlag; (1981)
9. Georgopoulou, E., Lalas, D., Papagiannakis, L., *Eur. J. Oper. Res.* **103(1)**, pp. 38-54 (1997)
10. Golabi, K., Kirkwood, C.W., Sicherman, A., *Manag. Sci.*, **22(2)**, pp. 174-89, (1981)
11. Lee, A.H.I., Chen, H.H., Kang, H.Y., *Renew. Ener. J.*, **34**, (2009).
12. Ilchev, S., Petkov, D., Andreev, R., Ilcheva, Z., *J. Cyb. and Inf. Tech.*, **19 (3)**, pp. 137-153, (2019)
13. Alexandrov, A., Andreev, R., Ilchev, S., Batchvarov, D., Boneva, A., Ivanov, S., Doshev, J., in *HPC 2019 Conf., Stud. in Comp. Intel.* **902**, (2020)
14. Brauers, T., Zavadskas, E., *Tech. and Econ. Devel. of Econ.*, **15(2)**, pp.352-375 (2009)
15. Anysz, H., Nica, A., and al., *J. Symmetry*, **1/46**, (2021),
16. Attri, R., Grover, S., *Int. J. of Sys. Ass. Eng. and Man.*, **5(3)**, pp. 320-328 (2014)
17. San Christobal, J.R., *Renew. Energ. J.* **36**, pp.498-502 (2011)
18. Shannon, C., *Bell Sys. Tech. J.* **27(3)**, pp.379–423 (1948)
19. Saaty, T., Peniwati, K., *Group Decision Making: Drawing out and Reconciling Differences* (Pittsburgh, Pennsylv. RWS Publ., 2008)
20. Borissova, D., *Comptes rend. de l'Acad. Bulg. des Scien.*, **71(11)**, pp. 1520-1527 (2018)
21. Korsemov, D., Borissova, D., *Adv. Model. and Optim. J.*, **20(1)**, pp. 101-112 (2018), ISSN: 1841-4311
22. Saaty, S., *Decision Making for Leaders: The Analytic Hierarchy Process for Decisions in a Complex World* (Pittsburgh, Pennsylv. RWS Publ., 2008) ISBN 978-0-9620317-8-6
23. Forman, E., Saul, G., *Oper. Res. J.*, **49 (4)**, pp. 469–487 (2001) doi: 10.1287/opre.49.4.469.11231
24. Petrov, I., in *Conf. “TechSys 2021”*, 27-29 May 2021, Plovdiv, Bulgaria. 8 pages, in print., <http://techsys.tu-plovdiv.bg/index.html#HOME>



# Influence evaluation of the ship propulsion system on the energy efficiency for small, medium and large container vessels

Viktor Nikiforov<sup>1,\*</sup>, Irina Kostova<sup>1</sup>

<sup>1</sup>Technical University of Varna, Department of Naval Architecture and Marine Engineering, 9000 Varna, Bulgaria

**Abstract.** The transportation of goods worldwide has a vital meaning for the entire of humanity. The seaborne transport is considered to be the most efficient – economically and environmentally friendly way to convey large amount of goods when compared to the other transport options available. Marine vessels contribute for the carriage of about 90 percent of the worldwide trade and a significant part of the goods delivered by sea are performed by container vessels. Even considered as the most efficient way of transportation the negative aspects of the shipping should not be neglected. The fuels intended for the ship propulsion generating enormous amounts of Greenhouse gases (GHG) and harmful emissions which are directly released into the atmosphere. When it comes to Energy Efficiency of the ships, the proper selection of the propulsion system and the fuel type used are essential with regard to achieve the best values. In the current paper a diverse alternative propulsion system options in order to achieve maximum Energy Efficiency on various sizes of container vessels will be analyzed.

## 1 Introduction

The basic goal set in front of the today's worldwide shipping is to reduce the negative effect caused by the generation of the GHG and harmful gases produced when ship's operation. The goods transportation via ships is considered for about 90 percent of the global trade and the main ships type involved in it is the container class.

In terms of value, global seaborne container trade is believed to account for approximately 60 percent of all world seaborne trade, which was valued at around 12 trillion U.S. dollars in 2017 [1].

The GHG emissions — including carbon dioxide (CO<sub>2</sub>), methane (CH<sub>4</sub>) and nitrous oxide (N<sub>2</sub>O), expressed in CO<sub>2</sub>e — of total shipping have increased from 977 million tonnes in 2012 to 1,076 million tonnes in 2018 (9.6% increase). In 2012, 962 million tonnes were CO<sub>2</sub> emissions, while in 2018 this amount grew 9.3% to 1,056 million tonnes of CO<sub>2</sub> emissions. The share of shipping emissions in global anthropogenic emissions has increased from 2.76% in 2012 to 2.89% in 2018 [2].

The values for global CO<sub>2</sub> emissions and the share that falls for the shipping industry in the period of 2012÷2018 are given in Table 1 (*units are in million tonnes*).

---

\* Corresponding author: [v.nikiforov@tu-varna.bg](mailto:v.nikiforov@tu-varna.bg)

**Table 1.** Total Global and Shipping CO<sub>2</sub> Emissions (Source – IMO GHG Study 2020)

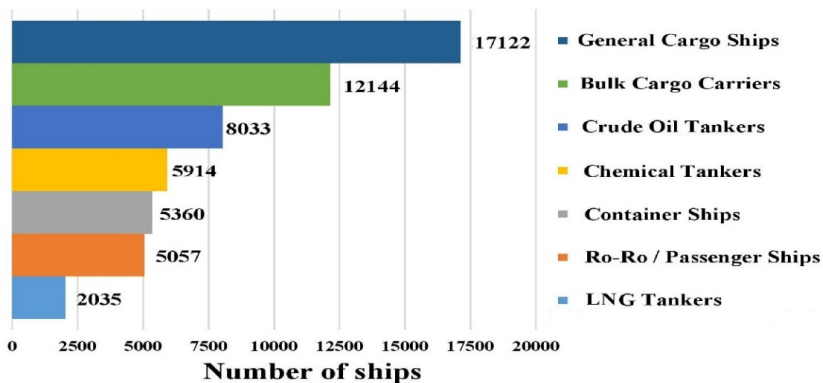
Year	Global CO <sub>2</sub> Emissions	Shipping CO <sub>2</sub> Emissions	Shipping as percentage of global
2012	34 793	962	2.76
2013	34 959	957	2.74
2014	35 225	964	2.74
2015	35 239	991	2.81
2016	35 380	1 026	2.90
2017	35 810	1 064	2.97
2018	36 573	1 056	2.89

Despite the shipping industry could be classified as the most environmentally friendly and economically profitable way to transport a large amount of goods the negative effect of the industry should also be considered. Annually the worldwide shipping uses a large amount of fossil fuels to operate the available fleet.

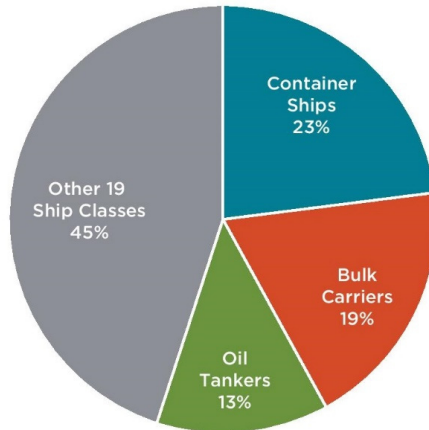
Even with the newly adopted requirements known as IMO 2020 which limits the sulphur content in the fuels used onboard of the ships to 0.50 % outside Emission Control Areas (ECAs) and 0.10 % inside ECAs, the ships equipped with devices for exhaust gas treatment are still able to use heavy fuel oils (HFO) with high sulfur content whose burning in the main engines lead to serious environmental pollution.

Of the around 56,000 merchant ships trading internationally, some 5400 are container ships, thus means that the container class accounts for about 10% of the global merchant fleet.

In Figure 1 is shown the number of the ships included in the global merchant fleet and the shares respectively for each ship's class engaged in the worldwide trading until 1st January 2020.

**Fig. 1.** Shares by ship's class involved in the global merchant fleet (Source - [www.statista.com](http://www.statista.com))

Three ship classes accounted for 55% of the total shipping CO<sub>2</sub> emissions: container ships (23%), bulk carriers (19%), and oil tankers (13%), also these three ship classes accounted for 84% of total shipping transport supply (deadweight tonne nautical miles, or dwt-nm) [3]. In Figure 2 are depicted the CO<sub>2</sub> emissions generation depending on the ship's class (Source – [3]).



**Fig. 2.** Shares of CO<sub>2</sub> emissions by ship's class

With purpose to achieve better Energy Efficiency and state of the environment improvement, the International Maritime Organization (IMO) and Marine Environment Protection Committee (MEPC) established some requirements in connection with reducing the GHG generated by the industry.

In 2011, IMO adopted mandatory technical and operational energy efficiency measures which are expected to significantly reduce the amount of CO<sub>2</sub> emissions from international shipping. These mandatory measures (EEDI/SEEMP) entered into force on 1 January 2013. IMO has adopted important guidelines aimed at supporting implementation of the mandatory measures to increase energy efficiency and reduce GHG emissions from international shipping, paving the way for the regulations on EEDI and SEEMP to be smoothly implemented by Administrations and industry [4].

The EEDI represents a non-prescriptive, performance- based mechanism that leaves the choice of technologies to use in a specific ship design to the industry. As long as the required energy efficiency level is attained, ship designers and builders would be free to use the most cost-efficient solutions for the ship to comply with the regulations. EEDI is requiring a minimum energy efficiency level for new ships by stimulating continued technical development of all the components influencing the fuel efficiency of a ship and by separating the technical and design-based measures from the operational and commercial ones [5].

The ship's energy efficiency could be represented as a function of its main and auxiliary engines power and the work fulfilled (cargo transported for certain time). The required speed of the ship and the engines power can be reached by various types of propulsion systems.

In order to comply with the IMO requirements regarding the GHG generation, the ship engine manufacturers developed much more efficient engine types which are able to work either with gaseous or with conventional fuels. Increasingly wider applications are finding the so-called Dual-Fuel Engines, which are able to operate with gaseous fuels and a small portion of diesel as a pilot fuel.

The energy efficiency of the ship could be improved and therefore the GHG emitting reduced by applying some of the various ways listed below:

- **Pay more attention on the proper engine selection;**
- **Using fuels with lower carbon content;**
- **Speed reduction with purpose to decrease the Specific Fuel Oil Consumption (SFOC);**
- **Implementation of innovative and renewable technologies reducing the CO<sub>2</sub> emissions.**

If we consider the service speed of the ship and its deadweight as a constant value, we have to pay much more attention when choosing the propulsion system with purpose to select the proper one which leads to EEDI improvement and GHG reduction.

The aims set in the current paper is to describe a methodology for selecting the proper propulsion system type for small, medium and large container vessels based on calculations of various systems, comparing the energy efficiency achieved with each and choosing the most efficient one with regard to fulfill the IMO requirements intended to GHG Emissions.

In the current article will be observed three types of container vessels – Feeder, Post-Panamax, and ULCV which could be classified respectively as small, medium and large ships. The distribution of the observed ships is approximately 55.2% of the total container ships by 2019.

In Figure 3 is shown the distribution of the container vessels by their size (Source – [6]).

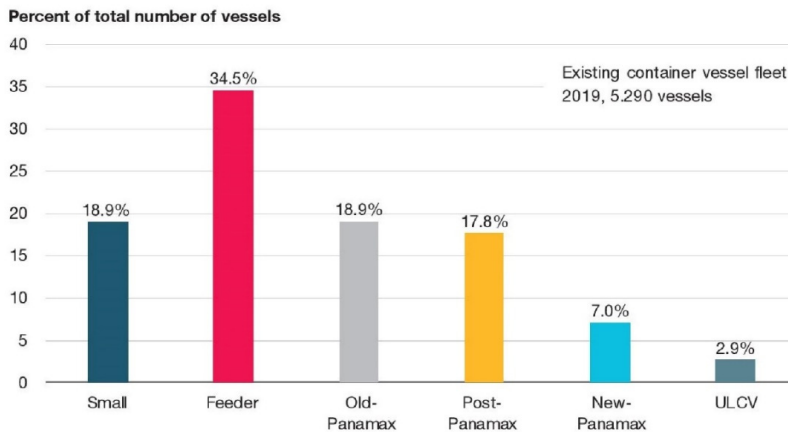


Fig. 3. Container vessels distribution by 2019

## 2 Marine propulsion system types

Nowadays there are a various options to configure a ship's propulsion system. The fuel oil consumption of the propulsion system mainly describing its cost efficiency is only the one side of the coin, but the other one is the ecology and the energy efficiency offering the use of each system type.

Today, ship propulsion is not just about successful movement of the ship in the water. It also includes using the best mode of propulsion to ensure a better safety standard for the marine ecosystem along with cost efficiency [7].

The common arrangement of the container ships propulsion system consists of a Main Engine (ME) and Diesel Generators (DG), but usually one ME and up to 3 DG are involved.

With the constantly tightening requirements regarding the ecology the ships have to comply with, the shipping industry have to adapt and implement new technologies.

One of the methods to comply with the requirements is to run the fleet with engines using fuels with lower or none carbon content in comparison with the widely used conventional fuels like HFO and MDO.

The engines used in the ship's propulsion arrangement could be classified by various features, some of them listed below:

- *By working cycle accomplishment – 2-stroke and 4-stroke engines;*
- *By their speed – Low-speed, Medium-speed and High-speed engines;*
  - *By the fuel type used – Diesel or Dual-Fuel engines.*

In the past decade, dual-fuel marine diesel engines using LNG as a secondary fuel, from either an LNG fuel tank or boil-off-gas, were developed and applied on board merchant vessels as an option to fulfil the IMO NO<sub>x</sub> Tier III regulations [8].

On Figure 4 is shown the typical arrangement commonly used in the container ship propulsion systems.

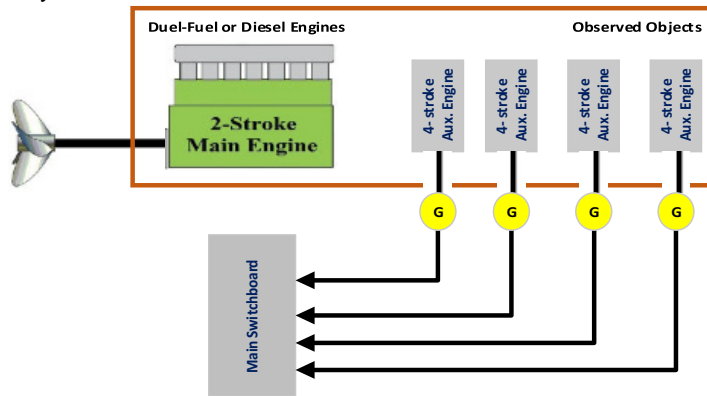


Fig. 4. Typical container ship propulsion system arrangement

In the current article will be considered various options for propulsion system arrangements for small, medium and large container vessels. This will be achieved by comparison of diverse propulsion systems using diesel or dual-fuel engines working on 2 or 4-stroke cycle. The comparison of the propulsion systems will be performed based on the achieved EEDI values depending on the fuel type used.

### 3 Attained and Required EEDI calculation methodology

The seaborne transport represents the most effective way of transport used nowadays, but the GHG and harmful emissions produced by the fossil fuels used in the internal combustion engines is a quite serious issue. Basically, the ship's energy efficiency is measured by the amounts of emissions radiated in the atmosphere and this effect could be accounted by calculating the ship's Attained EEDI and after that comparing it to the Required EEDI strictly depending on the ship's specific type and its capacity.

#### Attained EEDI

EEDI is mandatory for each new-built ship with gross tonnage equal to or above 400 GT and could be considered as the most valuable indicator for her energy efficiency GHG emission level. EEDI is expressed in grams CO<sub>2</sub> per tonne mile.

The methodology and requirements for Attained EEDI calculation for new ships are published by MEPC in [9].

The formula intended for Attained EEDI calculation of the ship includes CO<sub>2</sub> emissions generated by the work done by the main and auxiliary engines, shaft motor and shaft generators and the reduction derived by the implementation of innovative energy efficient technologies. Thus, all is divided by the transport work done which could be represented as the multiplication of the ship's deadweight and her service speed.

The simplified formula for Attained EEDI calculation is listed below:

$$Attained\ EEDI = \frac{(P_{ME(i)} \times C_{FME(i)} \times SFC_{ME(i)}) + (P_{AE} \times C_{FAE} \times SFC_{AE})}{f_i \times f_c \times f_1 \times Capacity \times f_w \times V_{ref}} \quad (1)$$

Where:

$P_{ME(i)}$  – 75% of the rated installed power for each main engine (i);

$P_{AE}$  – is the required auxiliary engine power to supply normal maximum sea load including necessary power for propulsion machinery/systems and accommodation;

$C_{FME(i)}$  – conversion factor between fuel consumption and CO<sub>2</sub> emissions for main engine(s);

$C_{FAE(i)}$  – conversion factor between fuel consumption and CO<sub>2</sub> emissions for auxiliary engine(s);

$SFC_{ME(i)}$  – specific fuel consumption of main engine at 75% of the rated power of the engine;

$SFC_{AE}$  – specific fuel consumption of auxiliary engine at 50% of the rated power of the engine;

Capacity – for container vessels 70% of deadweight should be used as capacity;

$V_{ref}$  – ship's speed at 75% power of the main engine;

$f_i$  – capacity factor;

$f_c$  – cubic capacity conversion factor;

$f_1$  – factor for general cargo ships equipped with cranes and other cargo related gear;

$f_w$  – weather factor.

If Power Take In / Power Take Off devices (PTI/PTO) and/or renewable energy efficiency technologies are used in composition of the ship propulsion system, their effect should also be accounted. This is achieved by supplementing the numerator of equation (1) with equation (2):

$$\left( (f_j \times P_{PTI(i)} - f_{eff(i)} \times P_{AEeff(i)}) C_{FAE} \times SFC_{AE} \right) - (f_{eff(i)} \times P_{eff(i)} \times C_{FME} \times SFC_{ME}) \quad (2)$$

Where:

$f_j$  – correction factor for specific ship specific design elements;

$P_{PTI(i)}$  - 75% of the rated power consumption of each shaft motor divided by the weighted average efficiency of the generator(s);

$f_{eff(i)}$  - the availability factor of each innovative energy efficiency technology;

$P_{AEeff(i)}$  – is the auxiliary power reduction due to innovative electrical energy efficient technology;

$P_{eff(i)}$  - the output of the innovative mechanical energy efficient technology for propulsion at 75% main engine power;

The required auxiliary engine power to supply normal maximum sea load including necessary power for propulsion machinery/systems and accommodations could be found by the following two principles:

For ships with a total propulsion power of 10000 kW or above,  $P_{AE}$  have to be defined as follows:

$$P_{AE} = \left( 0.025 \times \left( MCR_{ME(i)} + \frac{P_{PTI(i)}}{0.75} \right) \right) + 250 \quad (3)$$

For ships with a total propulsion power below 10000 kW,  $P_{AE}$  have to be defined as follows:

Where:

$MCR_{ME(i)}$  – maximum continuous rating of the main engine;

$$P_{AE} = \left( 0.05 \times \left( MCR_{(i)} + \frac{P_{PTI(i)}}{0.75} \right) \right) \quad (4)$$

Generally, the full formula consisting of equations (1) and (2) could be simplified to much easier for understanding equation (5) as follows:

$$EEDI = \frac{CO_2 \text{ Emissions Generated}}{\text{Transport work}} \quad (5)$$

More specific information regarding the calculation methodology, parameters and coefficients used for calculation of the EEDI for each ship could be found in [7].

### Required EEDI

According to the requirements adopted by IMO and MEPC, each new-built ship EEDI value have to be in compliance with the reference value calculated for the corresponding ship type.

The REEDI is going to be decreased gradually and this is planned to be achieved in three phases as the last one has to be introduced in force from 1st January 2025 and aims for a reduction of REEDI by 30%.

On Figure 5 are shown the reduction phases of REEDI thru the years [Source – [10]]

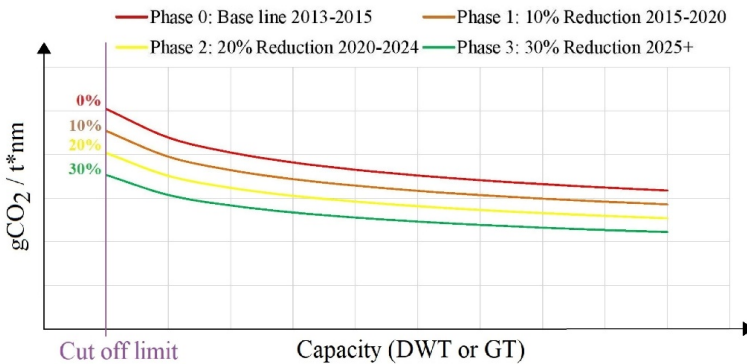


Fig. 5. REEDI reduction phases

The formula for calculating the REEDI is listed below:

$$REEDI = a \times b^{-c} \quad (6)$$

In equation (6) the parameters “a” and “c” are determined from the regression curve fit and they are specified in [9] and [10], the parameter “b” expresses the deadweight of the ship.

## 4 Calculations and study results

With regard to fulfil the goals set in this paper and to perform the necessary calculations for the propulsion systems which we intend to observe, first we have to choose some real ships or projects. For the purpose of this paper, we have chosen real container vessels of MSC company, which is one of the biggest companies in this field. The initial data necessary for the purpose of the calculations and for the size of the ships are presented in Table 2. More detailed information regarding the chosen ships could be found in [14].

Table 2. Initial data for small, medium and large container vessels

MSC AMY	
ME	MAN B&W, 6L70MC, 16 980 kW at 108 rpm
DG	MAN B&W, 4 x 6L23/30H, 1050 kW each
TEU	1 683

Deadweight	22 308 t
Speed	Max 20.5 knots
<b>MSC ATHENS</b>	
ME	MAN B&W, 9SME-C8.2, 47 430 kW at 78 rpm
DG	MAN B&W, 2 x 8L32/40 – 4000 kW each, 2 x 9L32/40 – 4500 kW each
TEU	8 827
Deadweight	95 380 t
Speed	Max 22.0 knots
<b>MSC HAMBURG</b>	
ME	MAN B&W, 11S90ME-C9, 59 780kW at 82 rpm
DG	MAN B&W, 4 x 9L32/40, 4500 kW each
TEU	16 652
Deadweight	184 100 t
Speed	Max 23.0 knots

For the purpose of this paper, we substitute the main components of the propulsion system (ME and DG) of each considered ship with alternative modern engines with equivalent power working on the Dual-Fuel principle. The rest of the ship's parameters remain unchanged.

In Table 3 are shown the chosen alternative options for each observed ship.

**Table 3.** Alternative propulsion options for small, medium and large container vessels

<b>MSC AMY</b>	
ME	MAN B&W, 7G60ME-C10.5-GI, 16 980 kW at 98 rpm
DG	MAN B&W, 4 x 8L23/30DF, 1000 kW each
<b>MSC ATHENS</b>	
ME	MAN B&W, 9G90ME-C10.5-GI, 47 430 kW at 78 rpm
DG	MAN B&W, 2 x 8L35/44DF + 2 x 9L35/44DF, 4080 kW + 4590 kW each
<b>MSC HAMBURG</b>	
ME	MAN B&W, 11G95ME-C10.5-GI, 59 780 kW at 82 rpm
DG	MAN B&W, 4 x 9L35/44DF, 4590 kW each

For both – initial and alternative propulsion systems identical calculations for determination of the Attained EEDI have been conducted.

The calculations are performed according to the requirements exposed in Section 2 of the current article. The information concerning the specific fuel oil consumption of the ME and DG is based on the relevant engines project guides and with the help of CEAS (Computerized Engine Application System) application provided for free use on the official website of the company MAN B&W.



The reference speed of the observed ships at the relevant engine load necessary for EEDI calculations is estimated based on the equation (8) listed below:

$$P_B = c \times V^i \quad (8)$$

Where:

$P_B$  – ME Power, [kW];

$c$  – constant;

$V$  – Ship's speed, [knots];

$i$  – exponent, depending on the ship's size. For first estimations widely used in the practice is the adoption of  $i=3$ .

In Table 4 are given the full input data necessary for the calculations performed in the current article for Attained and Required EEDI.

**Table 4.** Input data necessary for the calculations of EEDI and REEDI for the observed ships

Ship	MSC AMY	MSC ATHENS	MSC HAMBURG
ME Power at 75% load, [kW]	12735	35572.5	44835
ME SFOC at 75% (initial), [g/kWh]	170.5 (HFO)	159.5 (HFO)	159.1 (HFO)
ME SFOC at 75% (alt.), [g/kWh]	128.2 (LNG) 3.34 (MDO)	126.9 (LNG) 3.36 (MDO)	121.5 (LNG) 3.70 (MDO)
DG Power (Equation 3), [kW]	568.38	1435.75	1744.5
DG SFOC at 50% (initial), [g/kWh]	196.5 (MDO)	197.0 (MDO)	197.0 (MDO)
DG SFOC at 50% (alt.), [g/kWh]	206.1(LNG) 3.60 (MDO)	193.5(LNG) 3.80 (MDO)	193.5(LNG) 3.80(MDO)
$C_F$ (HFO)	3.114		
$C_F$ (MDO)	3.206		
$C_F$ (LNG)	2.750		
Deadweight, [tonnes]	22308	95380	184100
Ref. Speed, [knots]	18.63	19.99	20.9
Coeff. „a“	174.22		
Coeff. „c“	0.201		

In Tables 5 and 6 are shown the calculated data regarding the Required and Attained EEDI for each ship using respectively the initial and the alternative proposed propulsion options.

**Table 5.** REEDI and AEEDI for the observed ships equipped with the initial propulsion systems

Ship	MSC AMY	MSC ATHENS	MSC HAMBURG
Base REEDI (2013÷2015)	23.28	17.39	15.23
Phase 1 (2015÷2020)	20.96	15.65	13.71

Phase 2 (2020÷2024)	18.63	13.91	12.19
Phase 3 (2025+)	16.30	12.17	10.66
Attained EEDI	24.7	13.94	8.65

**Table 6.** REEDI and AEEDI for the observed ships equipped with the alternative propulsion systems

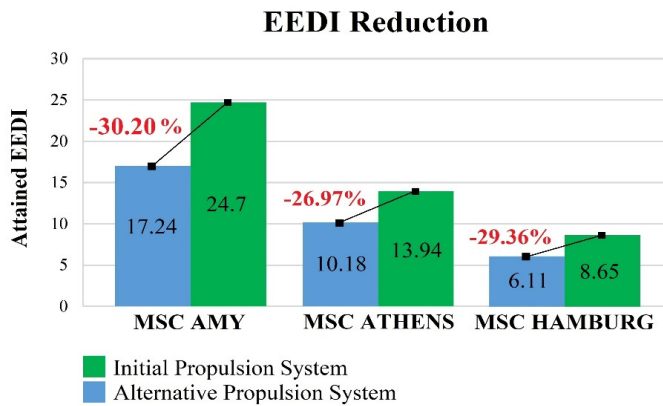
Ship	MSC AMY	MSC ATHENS	MSC HAMBURG
Base REEDI (2013÷2015)	23.28	17.39	15.23
Phase 1 (2015÷2020)	20.96	15.65	13.71
Phase 2 (2020÷2024)	18.63	13.91	12.19
Phase 3 (2025+)	16.30	12.17	10.66
Attained EEDI	17.24	10.18	6.11

**Note:**

- Green color - In compliance;
- Red color – Non-compliance.

In Figure 6 is shown the reduction in percentages between the Attained EEDI for initial and alternative propulsion systems.

Depending on the reduction percentages could be done a basic estimation of the positive effect rendered only by the propulsion system type.



**Fig. 6.** EEDI reduction in percentages due to alternative propulsion system use

On Figures 7, 8 and 9 are graphically illustrated the calculated values for Attained EEDI regarding the observed in the current article ships respectively for the initial equipped and alternative propulsion systems proposed.

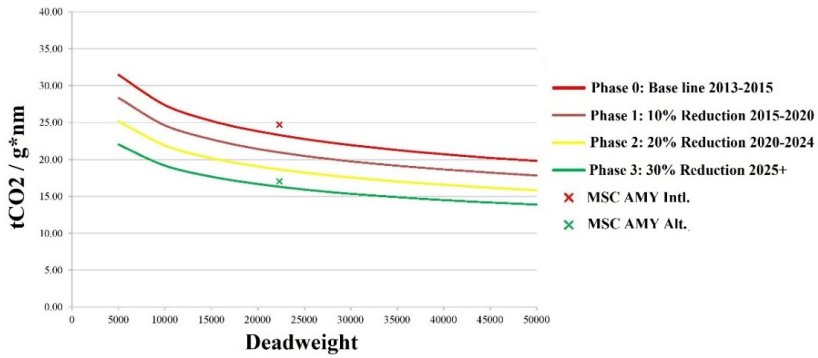


Fig. 7. Attained EEDI for small container vessel

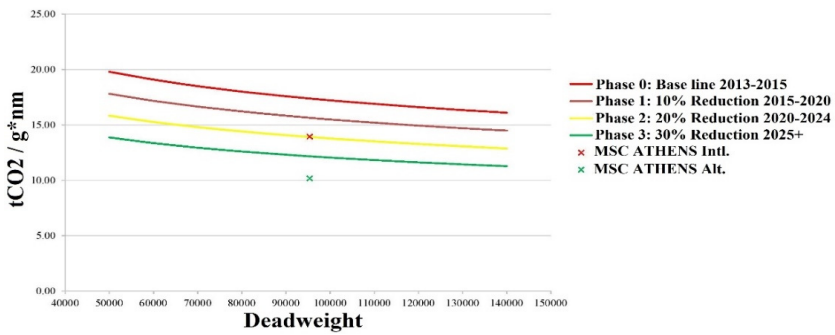


Fig. 8. Attained EEDI for medium container vessel

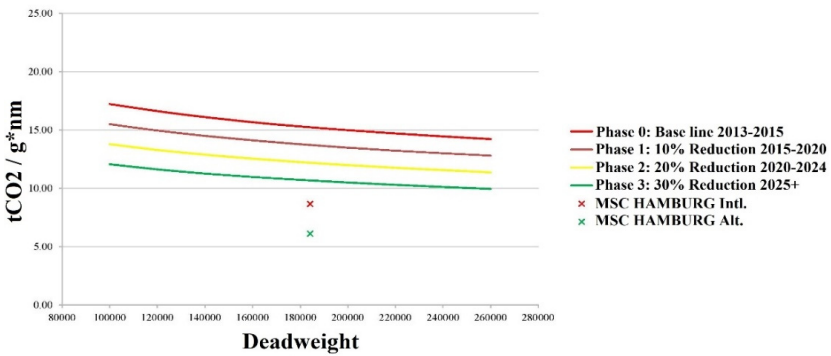


Fig. 9. Attained EEDI for large container vessel

## 5 Conclusions

In the current paper had been observed three types of container vessels depending on their size – small, medium and large respectively. For the analyzed ships have been considered their initial equipped propulsion systems and then alternative modern options for the propulsion working on the Dual-Fuel principle have been proposed.

Based on the calculations performed in Section 3 of the present paper, first for the initial propulsion systems and then for the alternative options a significant improvement of the Attained EEDI has been found for each ship.

The improvement of the EEDI amounts to 30.20% for small, 26.97% for medium and 29.36% for large container vessels respectively. Average EEDI enhancement of 28.84% has been accounted for the three types of vessels observed.

Thanks to the switching to modern propulsion systems working on Dual-Fuel principle the observed ships are able to fulfil the stricter energy efficiency requirements introduced by IMO.

This work was performed within Project NP8/2021 from the Research Plan of the Technical University of Varna, financed by the State Budget. The first author has been funded in the frame of the Bulgarian National Science Program “Young Scientists and Postdoctoral Students 2021” (Council of Ministers’ Decisions No. 577 / 16.08.2018).

## References

1. <https://www.statista.com/topics/1367/container-shipping/> (visited November, 2021)
2. Fourth IMO GHG Study 2020, Executive Summary - IMO
3. N. Olmer, B. Comer, B. Roy, X. Mao, D. Rutherford, Greenhouse gas emissions from global shipping, 2013–2015 (International Council on Clean Transportation 2017)
4. <https://www.imo.org/en/OurWork/Environment/Pages/AirPollution-Default.aspx>, (visited November, 2021)
5. Edmund Hughes (IMO), New Chapter for MARPOL Annex VI – requirements for technical and operational measures to improve the energy efficiency of international shipping (2013)
6. MAN Energy, Solutions Propulsion Trends in Container Vessels (2019)
7. [www.marineinsight.com](http://www.marineinsight.com), Different Types of Marine Propulsion Systems Used in the Shipping World (2021)
8. H. Xing, St. Spence, H. Chen, A Comprehensive Review on Countermeasures for CO2 Emissions from Ships (2019)
9. Resolution mepc.245(66), 2014 Guidelines on the method of calculation of the attained energy efficiency design index (eedi) for new ships
10. IMO, Train the Trainer (TTT) Course on Energy Efficient Ship Operation, Module 2 - Ship Energy Efficiency Regulations and Related Guidelines
11. Resolution mepc.203(62), Amendments to the annex of the protocol of 1997 to amend the international convention for the prevention of pollution from ships, 1973, as modified by the protocol of 1978 relating thereto
12. Resolution mepc.251(66), amendments to the annex of the protocol of 1997 to amend the international convention for the prevention of pollution from ships, 1973, as modified by the protocol of 1978 relating thereto
13. Resolution mepc. 231(65), 2013 guidelines for calculation of reference lines for use with the energy efficiency design index (eedi)
14. <https://www.scheepvaartwest.be/CMS/index.php/containerships> (visited November, 2021)

# Impact study of the fuel type used on the energy efficiency costs values and harmful emissions generation for small, medium and large container vessels

Viktor Nikiforov<sup>1,\*</sup>, and Irina Kostova<sup>1</sup>

<sup>1</sup>Technical University of Varna, Department of Naval Architecture and Marine Engineering, 9000 Varna, Bulgaria

**Abstract.** Annually a large amount of goods has been transported over the world and the most of the transportation is carried by seaborne. Although the seaborne trade is considered to be the most efficient – economically and environmentally friendly way of transportation an enormous amount of fossil fuels is used to fulfil the operation of the merchant fleet. Although we are living in times where efforts are directed to improvement of the state of the environment and reduction of the negative impact of the Greenhouse Gases, the fossil fuels still remain the main energy source used to run the internal combustion engines widely used in the ships nowadays. A well-known fact is that the fuel burning leads to significant harmful emissions generation causing a serious negative effect on the surrounding us environment. The introduced by IMO and MEPC requirements regarding the Greenhouse Gases (GHG) imposes for development and application of new criteria when selecting the ship's propulsion plant. In the current article will be observed three ship groups consisting of real container vessels. The purpose is to analyse the impact caused by the fuel type used in the ship's engines on the GHG generation and the economic indicators related with fuel costs

## 1 Introduction

The seaborne trade is a constantly evolving area developing and incorporating new technologies with purpose to turn the shipping into one much cleaner and environmentally friendly industry.

Annually the worldwide shipping uses a large amount of fossil fuels to run the available fleet, which burning in the ship engines is resulting in enormous GHG generation negatively reflecting on the surrounding us environment.

The GHG emissions — including carbon dioxide (CO<sub>2</sub>), methane (CH<sub>4</sub>) and nitrous oxide (N<sub>2</sub>O), expressed in CO<sub>2</sub>e — of total shipping have increased from 977 million tonnes in 2012 to 1,076 million tonnes in 2018 (9.6% increase). In 2012, 962 million tonnes were CO<sub>2</sub> emissions, while in 2018 this amount grew 9.3% to 1,056 million tonnes of CO<sub>2</sub> emissions. The share of shipping emissions in global anthropogenic emissions has increased from 2.76% in 2012 to 2.89% in 2018 [1].

The values for global CO<sub>2</sub> emissions and the share that falls for the shipping industry in the period of 2012÷2018 are given in Table 1 (*units are in million tonnes*).

---

\* Corresponding author: [v.nikiforov@tu-varna.bg](mailto:v.nikiforov@tu-varna.bg)

**Table 1.** Total Global and Shipping CO<sub>2</sub> Emissions (*Source – IMO GHG Study 2020*)

Year	Global CO <sub>2</sub> Emissions	Shipping CO <sub>2</sub> Emissions	Shipping as percentage of global
2012	34 793	962	2.76
2013	34 959	957	2.74
2014	35 225	964	2.74
2015	35 239	991	2.81
2016	35 380	1 026	2.90
2017	35 810	1 064	2.97
2018	36 573	1 056	2.89

With the development of the modern engine building there is a real opportunity to equip the newbuilding ships or to retrofit the existing fleet (if possible) with new more efficient engines, using fuels which differ from the conventional ones widely used in the shipping nowadays. It is important to note that the modern engines are characterized with lower specific fuel consumption (SFC) when compared to the previous generations. This leads to fuel costs reduction for each separate voyage as well as for each operational period of the ship.

The mentioned fact has two really important aspects for the ship's operation:

- First one could be considered as purely economic – reducing the operational costs related to the fuel, which constitutes a main part from the total expenditures.
- The second one is related to the regulations from harmful emissions generated by shipping, which at the present moment are very strict. Therefore, when taking a decision regarding the main engine type selection it is mandatory to account not only the technical and economic indicators, but the ecological ones as well.

With purpose to reduce the volume of GHG and to improve the state of the environment, the International Maritime Organization (IMO) and Marine Environment Protection Committee (MEPC) established some requirements in connection with the GHG generated by the shipping industry.

In 2011, IMO adopted mandatory technical and operational energy efficiency measures which are expected to significantly reduce the amount of CO<sub>2</sub> emissions from international shipping. These mandatory measures (EEDI/SEEMP) entered into force on 1 January 2013. IMO has adopted important guidelines aimed at supporting implementation of the mandatory measures to increase energy efficiency and reduce GHG emissions from international shipping [2].

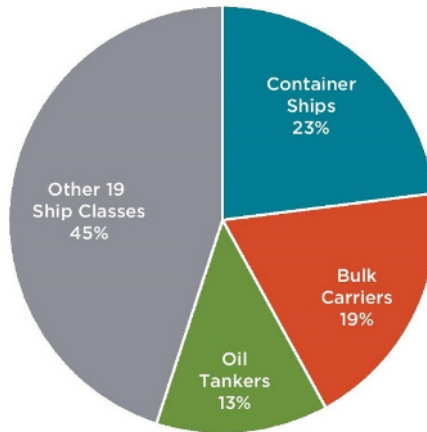
In 2018, IMO adopted an initial strategy on the reduction of GHG emissions from ships, setting out a vision which confirms IMO's commitment to reducing GHG emissions from international shipping and to phasing them out as soon as possible [3].

In order to comply with the requirements, set out by the organizations, the ship engine manufacturers developed much more efficient engine types, able to operate with gaseous and conventional fuels, or a combination of them. Increasingly wider applications are finding the so-called Dual-Fuel Engines, which are able to operate with gaseous fuels as LNG and a small portion of diesel oil used as a pilot fuel.

One of the advantages with gas-fuelled vessels is the ability to adjust operation when the fuel prices rise and modern exhaust-emission limits tighten. Indeed, service experience shows that the dual-fuel engine delivers significant reductions in CO<sub>2</sub>, NO<sub>x</sub> and SO<sub>x</sub> emissions [4].

Three ship classes accounted for 55% of the total shipping CO<sub>2</sub> emissions: container ships (23%), bulk carriers (19%), and oil tankers (13%). These three ship classes also accounted for 84% of total shipping transport supply (deadweight tonne nautical miles, or dwt-nm) [5].

In Figure 1 are depicted the CO<sub>2</sub> emissions generation depending on the ship's class (Source – [5]).



**Fig. 1.** Shares of CO<sub>2</sub> emissions by ship's class

In the current article will be observed three types of container vessels – Feeder, Post-Panamax, and ULCV which could be classified respectively as small, medium and large ships.

The aim set out in the current article is to analyse the possibilities for utilizing the dual-fuel technology in the composition of the ship power plants and to account the benefits following due to such an intervention. With the calculation performed in the current paper we aim to help for the facilitation in connection with the ship power plant selection.

With purpose to perform that we will use as example existing ships and a substitution of their power plants will be done with regard to account the improvement in GHG emitting only due to the proper engine selection.

## 2 Dual-Fuel technology

Today, ship propulsion is not just about successful movement of the ship in the water. It also includes using the best mode of propulsion to ensure a better safety standard for the marine ecosystem along with cost efficiency [6].

Nowadays a wide range of options intended for the ship propulsion are available. The typical arrangement includes two stroke diesel engines as a prime mover and a number of electric generators propelled by diesel engines ensuring the electrical production

With the stricter requirements introduced by IMO and MEPC regarding the energy efficiency of the ships and the GHG emitting, the shipping industry had been forced to act in direction leading to efficiency improvement of the components used in the ship's propelling systems.

In the past years the marine engine manufacturers introduced modern engines working on the dual-fuel principle able to operate with fuels different from the well-known

conventional fuels like HFO, MDO and MGO. These engines are able to operate with gaseous fuels like LNG which are considered much cleaner than the conventional ones.

Essentially, the dual-fuel engines don't differ from the well-known diesel engines widely spread in the shipping industry. Like the diesel engines they also provide a wide range of power and speeds ensuring the possibility to propel each ship class available.

There are two main engines concepts for LNG: high and low-pressure. In the high-pressure dual-fuel LNG concept, the LNG is injected under high pressure and ignited by a small quantity of diesel. This produces virtually complete combustion of the gas, and thus virtually no un-combusted methane. In the low-pressure system, the LNG is injected under low pressure and ignited by a small amount of diesel. This produces low NO<sub>x</sub> emissions that meet IMO Tier III, the strictest NO<sub>x</sub> requirements, while high-pressure LNG requires additional abatement technologies to satisfy IMO Tier III [7].

The main pros when using dual-fuel engines is the opportunity to run the engines with much cleaner fuel like LNG which almost fully eliminate the sulphur oxides (SO<sub>x</sub>) and Particulate Matter (PM), and also substantially reduce the nitrous oxides (NO<sub>x</sub>) generated due to the fuel burning in the marine engines.

The common arrangement of the container ships propulsion system consists of a Main Engine (ME) and Diesel Generators (DG), usually one ME and up to 3 DG are involved.

On Figure 2 is shown the typical arrangement commonly used in the container ship propulsion systems.

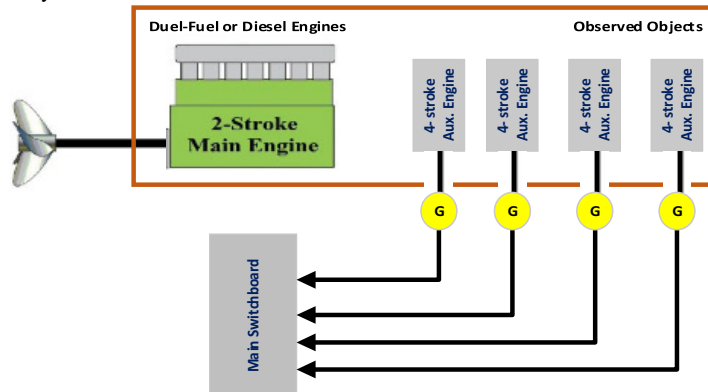


Fig. 2. Typical container ship propulsion system arrangement

### 3 Study scenario and calculation methodology

In the current paper will be observed 3 types of container vessels – small, medium and large respectively. To account the benefits achieved by the dual-fuel propulsion, calculations will be performed first for the initial equipped propulsion systems of each ship, and then for the alternative modern propulsion systems.

For the purpose of current article, we have chosen real container vessels of MSC company, which is one of the biggest companies in the field of container seaborne trade. The initial data necessary for the purpose of the calculations and for the size of the ships are presented in Table 2, more detailed information regarding the chosen ships could be found in [8].



**Table 2.** Initial data for small, medium and large container vessels

<b>MSC AMY</b>	
ME	MAN B&W, 6L70MC, 16 980 kW at 108 rpm
DG	MAN B&W, 4 x 6L23/30H, 1050 kW each
TEU	1 683
Deadweight	22 308 t
Speed	Max 20.5 knots
<b>MSC ATHENS</b>	
ME	MAN B&W, 9SME-C8.2, 47 430 kW at 78 rpm
DG	MAN B&W, 2 x 8L32/40 – 4000 kW each, 2 x 9L32/40 – 4500 kW each
TEU	8 827
Deadweight	95 380 t
Speed	Max 22.0 knots
<b>MSC HAMBURG</b>	
ME	MAN B&W, 11S90ME-C9, 59 780kW at 82 rpm
DG	MAN B&W, 4 x 9L32/40, 4500 kW each
TEU	16 652
Deadweight	184 100 t
Speed	Max 23.0 knots

With regard to fulfil the goals set, we substitute the main components of the propulsion system (ME and DG) of each considered ship with alternative modern engines with equivalent power working on the Dual-Fuel principle. The rest of the ship's parameters remain unchanged.

In Table 3 are shown the chosen alternative options for each observed ship.

**Table 3.** Alternative propulsion options for small, medium and large container vessels

<b>MSC AMY</b>	
ME	MAN B&W, 7G60ME-C10.5-GI, 16 980 kW at 98 rpm
DG	MAN B&W, 4 x 8L23/30DF, 1000 kW each
<b>MSC ATHENS</b>	
ME	MAN B&W, 9G90ME-C10.5-GI, 47 430 kW at 78 rpm
DG	MAN B&W, 2 x 8L35/44DF + 2 x 9L35/44DF, 4080 kW + 4590 kW each
<b>MSC HAMBURG</b>	
ME	MAN B&W, 11G95ME-C10.5-GI, 59 780 kW at 82 rpm
DG	MAN B&W, 4 x 9L35/44DF, 4590 kW each

### Energy Costs Calculation

Amongst the most important parameters which each marine engine could be described with are its power, speed and specific fuel consumption (SFC).

The fuel consumption represents the basic value used to account the economy of each marine propulsion system.

The main power propulsion plant selection primarily affects the fuel/lubricating oil expenses and maintenance costs i.e., 57% of the operating cost [9]

To calculate the amount of fuel used for the observed period, the following formulas has been used:

$$FC_{(S)} = (\tau_S \times 24 \times P_{B(ME)} \times SFC_{ME}) \times 10^{-6} + (\tau_S \times 24 \times P_{B(AE)} \times SFC_{AE} \times \sum AE) \times 10^{-6} \quad (1)$$

Where:

$FC_{(S)}$  – total fuel consumption of the ship in sailing period, [tonnes];

$\tau_S$  – time spent at sea, [days];

$P_{B(ME)}$  – main engine power, [kW];

$SFC_{ME}$  – main engine fuel consumption, [g/kWh];

$P_{B(AE)}$  – auxiliary engine power, [kW];

$SFC_{AE}$  – auxiliary engine fuel consumption, [g/kWh].

$$FC_{(P)} = (\tau_P \times 24 \times P_{B(AE)} \times SFC_{AE} \times \sum AE) \times 10^{-6} \quad (2)$$

Where:

$FC_{(P)}$  – total fuel consumption at port stay, [tonnes];

$\tau_P$  – time spent at port, [days].

$$FC_{(T)} = FC_{(S)} + FC_{(P)} \quad (3)$$

Where:

$FC_{(T)}$  – total fuel consumption for the observed period, [tonnes].

With purpose to find the energy costs regarding the fuel type used for the observed in the current paper period, the following equation has been used:

$$EC = FC_{(T)} \times PR_{FO} \quad (4)$$

Where:

$EC$  – energy costs [USD];

$PR_{FO}$  – fuel price, [USD].

With purpose to the calculations performance, the following assumptions have been considered:

- ME power and SFOC at 75%;
- Diesel ME operates with HFO, Dual-Fuel ME operates with LNG and MDO as Pilot Fuel;
- DG power and SFOC at 50%.
- Diesel Generators operates with MDO, Dual-Fuel Generators operates with LNG and MDO as Pilot Fuel;
- ME in operation only when sailing;
- Number of DG in operation when sailing – 2 x 50% Power;
- Number of DG in operation at port stay – 2 x 50% Power;
- Observed period – 1 year;
- Time spent at sea – 80% or approximately 292 days;

- Time spent at port – 20% or approximately 73 days.

The calculations concerning the energy costs strictly depends on the fuel prices. The fuel prices vary depending on the sailing region and ports visited. For the purpose of our calculations will be considered the global average prices for the last six months (01.12.20÷31.05.21) for HFO and MDO based on [10], and the average prices for the same period for LNG at Henry Hub based on [11].

The information concerning the specific fuel oil consumption of the ME and DG is based on the relevant engines project guides and with the help of CEAS (Computerized Engine Application System) application provided for free use on the official website of the company MAN B&W.

In Table 4 are given the input data necessary for the calculations regarding the amount of fuel used and the energy costs for the observed period.

All of the values are according to the assumptions set earlier in the current paper.

**Table 4.** Input data necessary for the calculations of fuel consumption and energy costs for the observed ships

Ship	MSC AMY	MSC ATHENS	MSC HAMBURG
$P_{B(ME)}$ , [kW] at (75%)	12735	35572.5	44835
$SFC_{ME}$ (intl.), [g/kWh] at 75%	170.5 (HFO)	159.5 (HFO)	159.1 (HFO)
$SFC_{ME}$ (alt.), [g/kWh] at 75%	128.2 (LNG) 3.34 (MDO)	126.9 (LNG) 3.36 (MDO)	121.5 (LNG) 3.70 (MDO)
$P_{B(AE)}$ , [kW] at (50%)	525	2125	2250
$SFC_{AE}$ (intl.), [g/kWh] at 50%	196.5 (MDO)	197.0 (MDO)	197.0 (MDO)
$SFC_{AE}$ (alt.), [g/kWh] at 50 %	206.1 (LNG) 3.60 (MDO)	193.5 (LNG) 3.80 (MDO)	193.5 (LNG) 3.80 (MDO)
HFO Price [\$/tonne]	402.50		
MDO Price [\$/tonne]	577.50		
LNG Price [\$/tonne]	168.35		

### Harmful Emissions Quantification

The FC and the energy costs arising from the former are only the one side of the coin. The other side is the ecology and the influence on the surrounding us environment rendered by the fuel burning in the internal combustion engines. The aim set in front of each shipping company and the shipping society at all is to reduce the harmful emissions generation and therefore the negative impact caused by them.

Quantification of the CO<sub>2</sub>, NO<sub>x</sub>, SO<sub>x</sub> and PM are based on the fuel total fuel consumption calculated and the values for estimation the harmful emissions given in [8] and [9].

With purpose of the calculations performed, the following assumptions have been considered:

- HFO with sulfur content 3.5%;
- MDO with sulfur content 0.5% when sailing;
- MDO with sulfur content 0.1% at port stay;
- LNG Calorific Value – 48 000 kJ/kg;

- ME considered as slow-speed engine;
- AE considered as medium-speed engine.

With purpose to estimate the GHG emissions emitted by the observed ships for the period set, the following formulas has been used:

$$CO_2 = (FC_{(T,ME)} + FC_{(T,AE)}) \times E_{F(CO_2)} \quad (5)$$

Where:

CO<sub>2</sub> – carbon dioxide emissions, [t];

FC<sub>(T,ME)</sub> – total FC of main engine, [t];

FC<sub>(T,AE)</sub> – total FC of auxiliary engine, [t];

E<sub>F(CO<sub>2</sub>)</sub> – emission factor for CO<sub>2</sub> [kg/t fuel].

$$SO_x = (FC_{(T,ME)} + FC_{(T,AE)}) \times E_{F(SO_x)} \quad (6)$$

Where:

SO<sub>x</sub> – sulfur oxides emissions, [t];

E<sub>F(SO<sub>x</sub>)</sub> – emission factor for SO<sub>x</sub> [kg/t fuel].

$$NO_x = (FC_{(T,ME)} + FC_{(T,AE)}) \times E_{F(NO_x)} \quad (7)$$

Where:

NO<sub>x</sub> – nitrogen oxides emissions, [t];

E<sub>F(NO<sub>x</sub>)</sub> – emission factor for NO<sub>x</sub> [kg/t fuel].

$$PM = (FC_{(T,ME)} + FC_{(T,AE)}) \times E_{F(PM)} \quad (8)$$

Where:

PM – particulate matters emissions, [t];

E<sub>F(PM)</sub> – emission factor for PM [kg/t fuel].

In Table 5 are given the emission factor values in necessary for GHG estimation. Values are based on [12] – Table 3 and [13] – Table C.5.

**Table 5.** Fuel emission factors

/	HFO	MDO	LNG
E <sub>F(CO<sub>2</sub>)</sub>	3170	3170	2688
E <sub>F(SO<sub>x</sub>)</sub>	20 x S%	20 x S%	0.027
E <sub>F(NO<sub>x</sub>), Slow Speed</sub>	87	87	8.16
E <sub>F(NO<sub>x</sub>), Medium Speed</sub>	57	57	5.35
E <sub>F(PM)</sub>	7.6	7.6	0.21

## 4 Study results

In Table 6 are shown the results attained by equations (1), (2) and (3) regarding the fuel used for the parameters set in Chapter 3.

**Table 6** Fuel consumption for operation the vessels for period of 1 year

<b>MSC AMY</b>		
	ME FC [tonnes]	AE FC [tonnes]
Initial	15217 HFO	1445 MDO
Alternative	11441 LNG + 298 MDO	3033 LNG + 53 MDO
<b>MSC ATHENS</b>		
	ME FC [tonnes]	AE FC [tonnes]

Initial	39762 HFO	11735 MDO
Alternative	31635 LNG + 838 MDO	11526 LNG + 226 MDO
<b>MSC HAMBURG</b>		
	ME FC [tonnes]	AE FC [tonnes]
Initial	49990 HFO	12425 MDO
Alternative	38176 LNG + 1163 MDO	12204 LNG + 240 MDO

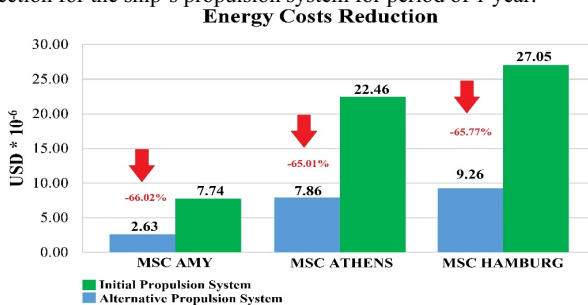
In Table 7 are shown the energy costs regarding the fuel used for operation the ships in a period of 1 year. The results are derived by equation (4)

**Table 7.** Energy costs for operating the ships in a period of 1 year with both propulsion options

<b>MSC AMY</b>			
Initial	HFO Costs [\$]	MDO Costs [\$]	Total Costs [\$]
	6 124 681	1 612 212	<b>7 736 893</b>
Alternative	LNG Costs [\$]	MDO Costs [\$]	Total Costs [\$]
	2 436 797	195 716	<b>2 632 513</b>
<b>MSC ATHENS</b>			
Initial	HFO Costs [\$]	MDO Costs [\$]	Total Costs [\$]
	16 004 241	6 542 207	<b>22 456 448</b>
Alternative	LNG Costs [\$]	MDO Costs [\$]	Total Costs [\$]
	7 266 249	593 169	<b>7 859 410</b>
<b>MSC HAMBURG</b>			
Initial	HFO Costs [\$]	MDO Costs [\$]	Total Costs [\$]
	20 120 899	6 927 038	<b>27 047 937</b>
Alternative	LNG Costs [\$]	MDO Costs [\$]	Total Costs [\$]
	8 481 505	781 743	<b>9 263 248</b>

*Note: The fuel costs may vary depending on the sailing region of the ships, therefore the energy costs savings could be quite different.*

In Figure 3 is depicted the percentage reduction of the energy costs achieved due to the fuel type selection for the ship's propulsion system for period of 1 year.



**Fig. 3.** Energy costs reduction level in percentages

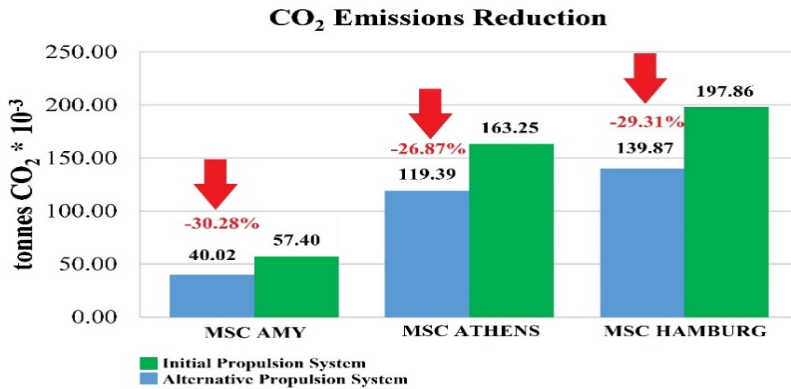
In Table 8 are given the quantified values for harmful gases and substances emitted into the atmosphere due to the fuel burning. The calculations are performed by equations (5), (6), (7) and (8).

**Table 8.** GHG Emissions separated due to the operation of the ships for period of 1 year

Observed object	CO <sub>2</sub>	SO <sub>x</sub>	NO <sub>x</sub>	PM
MSC AMY Initial	57403.8	1082.5	1488.7	137.6
MSC AMY Alternative	40020.6	3.7	129.6	5.7
MSC ATHENS Initial	163245.5	2853.8	4128.2	391.4
MSC ATHENS Alternative	119391.1	10.9	380.5	17.2
MSC HAMBURG Initial	197855.5	3573.8	5057.4	474.4
MSC HAMBURG Alternative	139867.0	14.4	402.1	21.2

*Note: All units are in metric tonnes.*

In Figures 4, 5, 6 and 7 is depicted the percentage reduction of the GHG emissions achieved due to the fuel type selection for the ship's propulsion system for period of 1 year.



**Fig. 4.** CO<sub>2</sub> Emissions reduction level in percentages

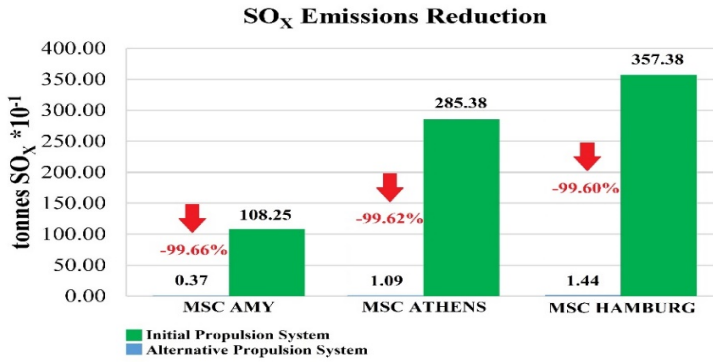


Fig. 5. SO<sub>x</sub> Emissions reduction level in percentages

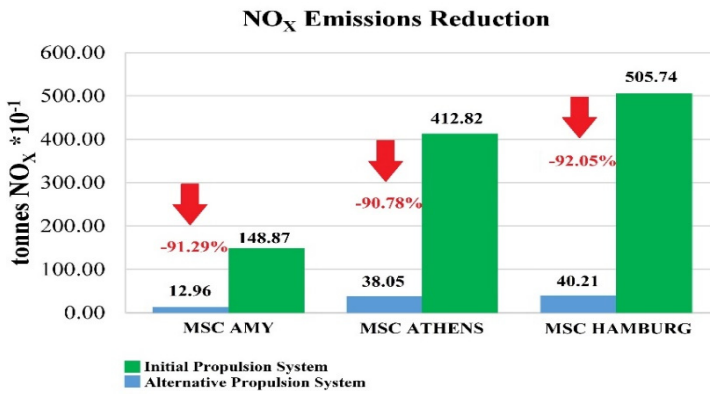


Figure 6. NO<sub>x</sub> Emissions reduction level in percentages

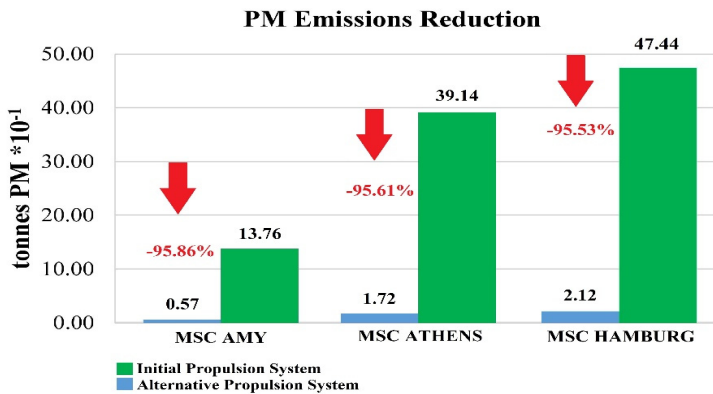


Fig. 7. PM Emissions reduction level in percentages

## 5 Conclusions

In the current study three types of container vessels has been observed. For each ship the initial equipped and alternative modern propulsion systems has been studied. Calculations regarding the energy costs and GHG emitting has been performed with purpose to make an assesment of the ecology performance of each ship.

Based on the calculation methodology set out in Chapter 3 a significant advantages of the modern dual-fuel engines over the conventional diesel engines widely used in the shipping has been found.

The fuel consumption forming a major part of the energy costs of each ship is significant reduced due to using a dual-fuel technology. An average reducing of the energy costs with 65.6% is observed based on the results published in Chapter 4.

Along with the notable annual fuel consumption and energy costs reduction, the less environment pollution rendered due to use of less polluting fuels should not be neglected.

Due to the methodology set out in Chapter III also and remarkable GHG reduction has been accounted. An average reduction of main GHG gases like CO<sub>2</sub>, SO<sub>x</sub>, NO<sub>x</sub> and PM respectively with 28.82%, 99.63%, 91.37% and 95.67% is observed. The results from the conducted study displaying a significant reducing of the CO<sub>2</sub> and NO<sub>x</sub>, and also almost full elimination of the SO<sub>x</sub> and PM when using dual-fuel engines.

Owing to the switching to modern propulsion systems working on Dual-Fuel an option is given to the shipowners to significantly reduce their fuel expenditures as along with that to help for state of the environment improvement. Dual-Fuel technology likewise contributes to fulfil the stricter energy efficiency requirements introduced by IMO.

This work was performed within Project NP8/2021 from the Research Plan of the Technical University of Varna, financed by the State Budget. The first author has been funded in the frame of the Bulgarian National Science Program "Young Scientists and Postdoctoral Students 2021" (Council of Ministers' Decisions No. 577 / 16.08.2018).

## References

1. IMO, Fourth IMO GHG Study 2020, Executive Summary (2020)
2. <https://www.imo.org/en/OurWork/Environment/Pages/AirPollution-Default.aspx>
3. <https://www.imo.org/en/MediaCentre/HotTopics/Pages/Reducing-greenhouse-gas-emissions-from-ships.aspx>
4. MAN Energy Solutions, *MAN B&W ME-GI Installation in Very Large or Ultra Large Container Vessels* (2018)
5. N. Olmer, B. Comer, B. Roy, X. Mao, D. Rutherford, *GREENHOUSE GAS EMISSIONS FROM GLOBAL SHIPPING, 2013–2015* (International Council on Clean Transportation 2017)
6. Sharda, [www.marineinsight.com](http://www.marineinsight.com), *Different Types of Marine Propulsion Systems Used in the Shipping World* (2021)
7. E. Lindstad, T. Ingebrigtsen Bo, *Potential Power Setups, Fuels and Hull Designs Capable of Satisfying Future EEDI Requirements* (2018)
8. <https://www.scheepvaartwest.be/CMS/index.php/containerships>
9. G. M. Saha, *The Technical and Economical Aspect of Marine Engine Selection* (1996, World Maritime University)
10. <https://shipandbunker.com/>: visited July 2021
11. <https://www.eia.gov/dnav/ng/hist/rngwhhdM.html>: visited July 2021



12. K. Spoof-Tuomi, S. Niemi, *Environmental and Economic Evaluation of Fuel Choices for Short Sea Shipping* (2019)
13. Entec UK Limited, *Quantification of Emissions from Ships Associated with the Ship Movements Between Ports in European Community* (2002, Final Report)

# A design of solar battery cleaning system by modularity method

L.K. Dien<sup>1,\*</sup>, and Svetlin Antonov<sup>2</sup>

<sup>1</sup>Saigon Technology University (STU), Faculty of Mechanical Engineering, Vietnam

<sup>2</sup>Technical university of Sofia, Faculty of telecommunications, Bulgaria

**Abstract.** According to the World Bank statistical report, Vietnam has an average of 1,600-2,700 hours of sunshine and normal direct radiation averaging 4-5 kWh per square meter a day. Before 2017, solar energy was considered worthless in Vietnam's energy development strategy, but by the end of 2019, Vietnam overtook Malaysia and Thailand to become the country with the largest solar panel installation capacity in Southeast Asia. The photovoltaic projects in Vietnam has reached 5 gigawatts (GW), far exceeding from the target of 1 GW that proposed by the Government in 2020 [1]. The strong development of solar energy from industry to civil activities has led to the development of ancillary services such as installation, maintenance and commerce. To ensure the productivity, all solar panels must be cleaned to absorb solar energy as much as possible. In the paper, we mention on the design of a solar panel cleaning robot that has a compact size, easy to move through the panels, taking advantage of domestic factors to have an edge price. The highlight point in that work is our application of the modularity method to gain the best competition with the other existing products on the market.

## 1 Introduction

The application of modularity method for design of mechanical products has developed rapidly in recent years [1]. At present, it has become a perfect and effective method that can help the design to overcome so many proposed conditions such as: low price, high productivity, interchangeability ... [2, 3]. Due to the trend of the diversification of customers' demands, small product batches with high varieties, the modular design has been applied widely [4] in this paper.

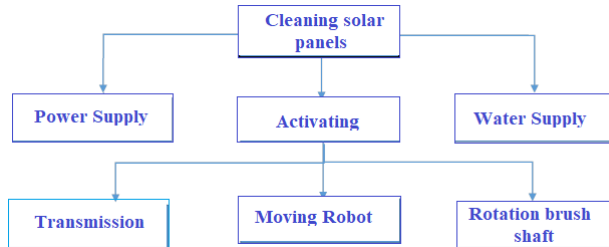
From the above demands, the application of modular design of the mechanical systems is indispensable. The objective of the modularization design in the article is the solar panel cleaning system or solar panel cleaning robot [5, 6] that could gain the following competitive points: compact size, effective working on effective clean panel surfaces, easy to activate, and lowest price by taking advantage of domestic factors.

---

\* Corresponding author: [dien.lekhanh@stu.edu.vn](mailto:dien.lekhanh@stu.edu.vn)

## 2 Method of design process

Application of the functional analysis [7] for solar battery cleaning system, from the above complete general demands, we divided the sub-functions as in the Fig. 1.



**Fig. 1.** Functional schema of solar battery cleaning system.

Proposing ideas for the design problem [7]: Deploy ideas for each function, systematically combine ideas, we get 4 ideas for the design of cleaning solar panels as in Table 1.

**Table 1.** Implementation ideas for each function.

Function	Idea 1	Idea 2	Idea 3	Idea 4
Power supply	Power supply from solar panels	Power supply from outside source	Power supply from solar panels	Power supply from outside source
Water Supply	Pump	Pump	Pump	Pump
Transmission	Transmission by coupling and gears	Transmission by coupling and belt	Transmission by gearbox and belt	Transmission by coupling and gears
Rotation Brush Shaft	Motor	Belt	Belt	Motor
Moving robot	Servo motor DC	Servo motor DC	Servo motor DC	Servo motor DC

Preliminary concept evaluation for designed product [7]: The ideas are listed on the first horizontal row of the selection matrix. The selection criteria are arranged along the left column of the matrix. Choose one of the above ideas as a base. Analysis of each idea: ideas are compared with base one according to the selection criteria and scored in the corresponding box (Table 2). From the above ideas we consider that the ideas 1 and 3 are feasible when design the robot.

Calculating the ideal scores for the final product design [7]: Decision matrix with additional weight column. Selection criteria are assigned a weight (in percentage), which are determined by consensus of the design team. Analysing each idea: the ideas are compared with the standard idea according to the selection criteria and scored in the corresponding box. Calculate the total score of each idea by the formula:

$$S_j = \sum_{i=1}^n r_{ij} w_i, \quad (1)$$

where:  $r_{ij}$  - the first criterion point of idea  $j$ ;  $w_i$  -the weight of the  $i^{\text{th}}$  criterion;  $n$  -total number of criteria;  $S_j$  - total score for idea  $j$ .

Rank the ideas by total score are showed in Table 3.

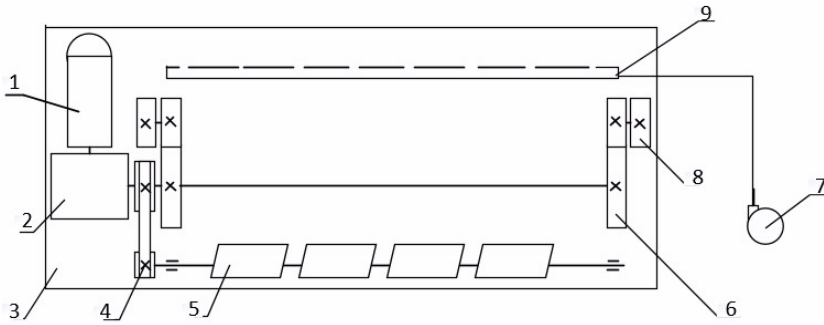
**Table 2.** Matrix of evaluation the ideas.

Criteria	Ideas			
	1(selected as base)	2	3	4
Logical productivity	+	0	0	+
Effective hygiene	+	0	0	+
Facility to activate	-	+	+	-
Saving resources	0	0	0	-
High longevity, high reability	+	0	+	+
Ease to maintenance	+	0	+	+
Applicable remote control technology	+	+	+	+
Logical price	0	+	+	-
Use recyclable materials	+	+	+	+
Total marks (+)	6	4	6	6
Total marks (0)	3	5	3	0
Total marks (-)	1	0	0	3
Ultimate total marks	5	4	6	3
Range	2	3	1	4
Continue or stop	Yes	No	Yes	No

**Table 3.** Matrix of scoring and selection of ideas.

Criteria	Weights(%)	Ideas			
		3		4	
		Marks		Marks	
		Coarse	Multipled to weight	Coarse	Multipled to weight
Hygenic effect	10%	4	0.4	3	0.3
Easy to activate	6%	2	0.12	4	0.24
Resource saving	15%	3	0.45	3	0.45
High longevity, high reability	16%	3	0.48	5	0.8
Easy maintenance	10%	4	0.4	5	0.5
Application of remote control technology	6%	3	0.18	3	0.18
Logical price	22%	3	0.66	4	0.88
Use recyclable materials	5%	3	0.15	3	0.15
Total marks	100	3.24		3.8	
Ranking		2		1	
Continues?		No		Yes	

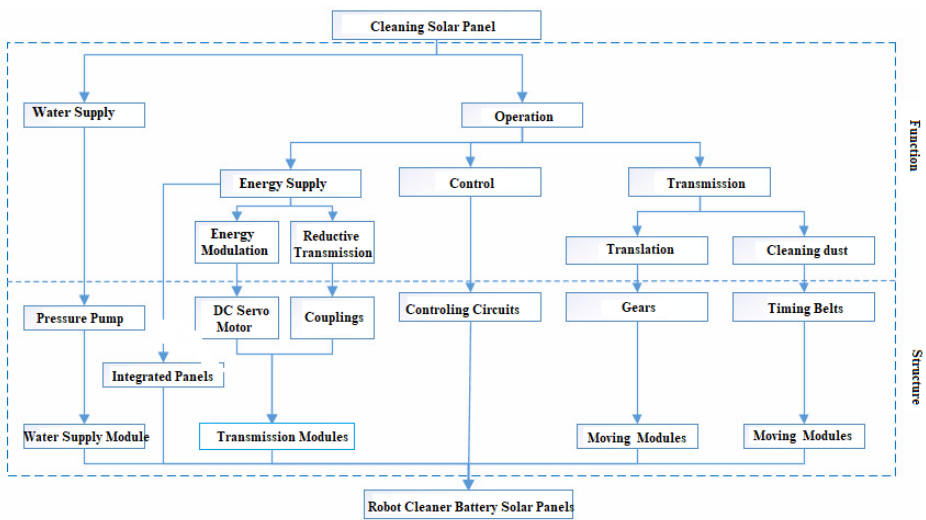
Based on the scoring matrix, the design team chooses an idea as a design concept. Solar battery cleaning system principle diagram as follows:



**Fig. 2.** Theoretical schemas of solar battery cleaning system: 1- servo motor; 2- gear box; 3- machine frame; 4- belt conveyor; 5- brush shaft; 6- Gear; 7- pressure pump; 8- wheels; 9- water pipes.

### 3 Results and discussion

After application of the design product modularization method [8] to design the system after analysing the demands of customer and choosing a design concept for the product, we combine the functional analysis diagrams and the design concepts in one structural – functional diagram that is illustrated in the following diagram:



**Fig. 3.** Schema of structure and function of solar battery cleaning system

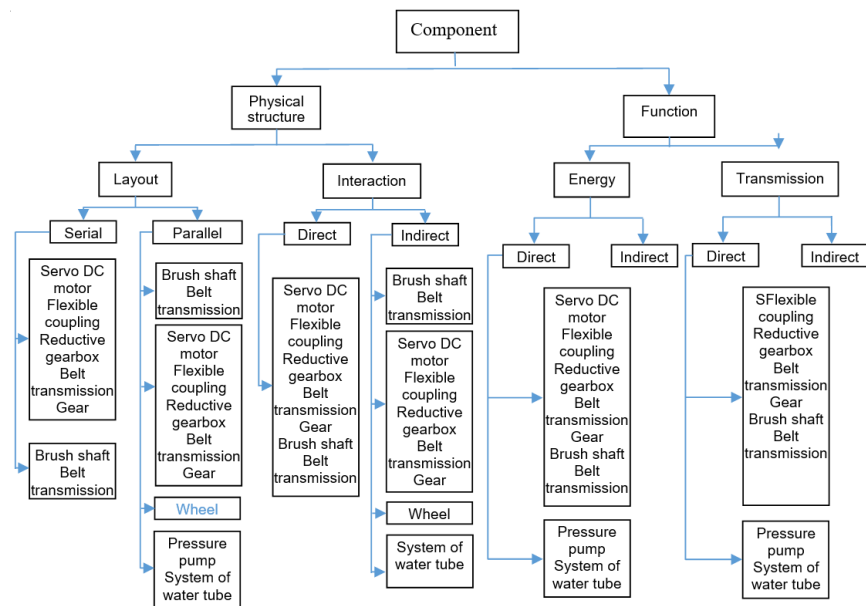
List of the components and symbols is shown in Table 4:

**Table 4.** Parts designation solar battery cleaning system.

	Components	Designation
1	Servo DC motor	DDC
2	Flexible coupling	NTD
3	Reductive gearbox	HGT
4	Gear	BR
5	Belt transmission	BTD
6	Wheel	BX
7	Brush shaft	TC
8	Pressure pump	BAS
9	System of water tube	HTN

The system-level specifications of the product are orderly sorted in a hierarchical structure in where the physical structure is divided according to the arrangement and the interactive state (direct or indirect), while the functional structure is divided according to the flow of energy, materials and information as in Figure 4.

Establishing the relationships of the details in the system [8] through the properties of physical structure and function of the system (Table 5), number 1 represents interaction, 0 represents no relationship system; NT- serial; SS- parallel; TT- direct interaction; GT- indirect interaction.

**Fig. 4.** Schema of structure and function of solar battery cleaning system

**Table 5.** The relationships of the details in the system.

Mechanical details/ Cluster of details		Structure				Function			
		Arrangement		Interaction		Energy		Transmission	
		NT	SS	TT	GT	TT	GT	TT	GT
DDC	NTD	1	0	1	0	1	0	1	0
	HGT	1	0	0	1	0	1	0	1
	BR	1	0	0	1	0	1	0	1
	BTD	1	1	0	1	0	1	0	1
	BX	0	1	0	1	0	1	0	1
	TC	0	0	0	1	0	1	0	1
	BAS	0	0	0	0	0	0	0	0
NTD	HTN	0	0	0	0	0	0	0	0
	HGT	1	0	1	0	1	0	1	0
	BR	0	1	0	1	0	1	0	1
	BTD	0	1	0	1	0	1	0	1
	BX	0	0	0	1	0	1	0	1
	TC	0	0	0	1	0	1	0	1
	BAS	0	0	0	0	0	0	0	0
HGT	HTN	0	0	0	0	0	0	0	0
	BR	1	0	1	0	1	0	1	0
	BTD	1	0	1	0	1	0	1	0
	BX	0	1	0	1	0	1	0	1
	TC	0	1	0	1	0	1	0	1
	BAS	0	0	0	0	0	0	0	0
BR	HTN	0	0	0	0	0	0	0	0
	BTD	0	0	0	0	0	0	0	0
	BX	1	0	1	0	1	0	1	0
	TC	0	0	0	0	0	0	0	0
	BAS	0	0	0	0	0	0	0	0
BTD	HTN	0	0	0	0	0	0	0	0
	BX	0	0	0	0	0	0	0	0
	TC	1	0	1	0	1	0	1	0
	BAS	0	0	0	0	0	0	0	0
BX	HTN	0	0	0	0	0	0	0	0
	BAS	0	0	0	0	0	0	0	0
	TC	0	0	0	0	0	0	0	0
TC	HTN	0	0	0	0	0	0	0	0
	BAS	0	0	0	0	0	0	0	0
BAS	PTB	1	0	1	0	1	0	1	0

Determining the influence of System – Level Specification (SLS) on General Functional Requirements (GFR) [8]:

To determine the effect of the properties of machine on the functional requirements, we use a relationship matrix between machine design requirements and importance factors value:

1: the desired impact value;

0: the insignificant impact value;

-1: the undesirable effect value.

Then we build a matrix of relationships between Systems – Level Specification on General Functional Requirements (Table 6).

**Table 6.** Relationship matrix between SLS and GFR.

<i>System – Level Specifications (SLS)</i>	<i>General Functional Requirements (GFR)</i>		
	<i>Ease of Service</i>	<i>Compactness</i>	<i>Performance</i>
<i>Serial arrangement</i>	1	1	0
<i>Parallel arrangement</i>	0	1	1
<i>Direct interaction</i>	1	1	1
<i>Indirect interaction</i>	0	0	0
<i>Direct Energy</i>	1	1	0
<i>Indirect Energy</i>	1	0	1
<i>Direct transmission</i>	1	1	0
<i>Indirect transmission</i>	1	0	1
<i>Weight</i>	1	1	1

Applying Cluster Identification Algorithm (CIA) [8], we can determine the matrix of functional (Table 7), structural (Table 8) and overall similarity (Table 9).

**Table 7.** The structural similarity matrix.

	DDC	NTD	HGT	BR	BTD	BX	TC	BAS	HTN
DDC		5	2	2	2	2	2	0	0
NTD	5		5	2	2	0	0	0	0
HGT	2	5		5	5	2	2	0	0
BR	2	2	5		0	5	0	0	0
BTD	2	2	5	0		0	5	0	0
BX	2	0	2	5	0		0	0	0
TC	2	0	2	0	5	0		0	0
BAS	0	0	0	0	0	0	0		5
HTN	0	0	0	0	0	0	0	5	

**Table 8.** The functional similarity matrix.

	DDC	NTD	HGT	BR	BTD	BX	TC	BAS	HTN
DDC		4	4	4	4	4	4	0	0
NTD	4		4	4	4	4	4	0	0
HGT	4	4		4	4	4	4	0	0
BR	4	4	4		0	4	4	0	0
BTD	4	4	4	0		0	4	0	0
BX	4	4	4	4	0		0	0	0
TC	4	4	4	4	4	0		0	0
BAS	0	0	0	0	0	0	0		4
HTN	0	0	0	0	0	0	0	4	

**Table 9.** The general similarity matrix.

	DDC	NTD	HGT	BR	BTD	BX	TC	BAS	HTN
DDC		9	6	6	6	6	6	0	0
NTD	9		9	6	6	4	4	0	0
HGT	6	9		9	9	4	4	0	0
BR	6	6	9		0	9	4	0	0
BTD	6	6	9	0		0	9	0	0
BX	6	4	4	9	0		0	0	0
TC	6	4	4	4	9	0		0	0
BAS	0	0	0	0	0	0	0		9
HTN	0	0	0	0	0	0	0	9	



Combine details into modules: use Cluster Identification Algorithm CIA identification algorithm to cluster details. Details in the product are shown in the table below:

**Table 10.** Product details.

N0	Clusters denomination	Design for selection	Design for manufacturing
1	Servo DC motor	✓	
2	Coupling	✓	
3	Reductive gearbox	✓	
4	Belt transmission	✓	
5	Gears	✓	
6	Wheels		✓
7	Brush shaft		✓
8	Roller bearings	✓	
9	Pressure pump	✓	
10	Machine frame		✓

### 3 Conclusion

The results show that the modules of physical structure and function are suitable: Module 1: Wheel and brush drive function; Module 2: Function of water supply for cleaning process. Seven clusters are designed for selection (purchasing from market), three parts are designed for manufacturing by ourselves. Modular design improved the design efficiency, product quality and reliability, good maintainability. Solar panel cleaning module provides an economic and effective method for cleaning the solar panel.

### 4 References

1. Thời báo Ngân hàng, *Triển vọng phát triển năng lượng tại Việt Nam*, <https://thoibaonganhng.vn/trien-vong-phat-trien-nang-luong-mat-troi-tai-viet-nam-106420.html> (2020)
2. Z. M. Bi, Y. T. Sherman Lang, V. Marcel, P. Orban, *Development of reconfigurable machines*, Int. J Adv. Manuf. Technol (2007)
3. R. Shang, Y. F. He, Z. Zhang, *Study on Evaluation System Based on the Reconfigurable and Modular Design*, App. Mec and Mat. (2012)
4. R. Rahul, R. Ronald, C. P. Ignasious, J. Ignatius, R. Zachariah, *Design and Fabrication of a Fully Automated Solar Panel Cleaning Module with Microfiber Brush*, Emerging Technologies for Sustainability (2020)
5. N. Maindad, A. Gadhave, S. Satpute, B. Nanda, *Automatic Solar Panel Cleaning System*, Int. Conf. on Communication and Information Processing (ICCIP-2020), Elsevier (2020).
6. N. Sugiarta, I. G. N. Ardana, I. M. Sugina, I. B. G. Widiyantara, I. N. Suparta, I. K. Adi, *Preliminary Design And Test Of A Water Spray Solar Panel Cleaning System*, iCAST-ES 2019, J. of Phys.: Conference Series (2019)
7. Nguyễn Thanh Nam, *Giáo trình phương pháp thiết kế kỹ thuật*, Nhà xuất bản đại học quốc gia Tp. Hồ Chí Minh (2010)
8. A. K. Kamrani, S. M. Sahlhied, *Product design for modularity*, Second edition (2002)

# Electronic measuring system design for photovoltaic panels analysis

Krastin Yordanov<sup>1,\*</sup>, Iliya Hadzhidimov<sup>1</sup>, and Penka Zlateva<sup>1</sup>

<sup>1</sup>TU Varna, Department of Thermal Engineering, 1 Studentska Str., 9010 Varna, Bulgaria

**Abstract.** The article presents the design and manufacture of an electronic measuring system based on an ESP32 microcontroller equipped with LORA E32 wireless data transceivers, a SD card for data recording and a computer with application for photovoltaic panels testing. Under environmental conditions the system has been experimentally tested to determine the efficiency of photovoltaic panels, which depends primarily on solar radiation and ambient parameters. In addition, the current, voltage and surface temperatures on the back side of the panels have been measured. The measuring sensors are selected in order to achieve the goal set, as well the durability of the system. The rising of the surface temperature of the photovoltaic panels have a significant effect on module's efficiency, increasing the risk of losing energy production. In the experimental study, temperature, solar radiation, current and voltage have been measured to refine the effect on a monocrystalline and polycrystalline structure of photovoltaic panel. The test has been performed on the experimental field of the Technical University of Varna, Bulgaria. Also, the ambient meteorological parameters during the experiment are reported by a weather station mounted on the experimental field, which transmits data online in the global meteorological database Wunderground with name IVARNA50.

## 1 Introduction

The recent years have seen an increasing need for the use of solar energy, dictated by the gradual depletion of conventional energy resources, such oil, natural gas and coal, on the one hand, and by environmental protection considerations, on the other hand. At the end of the 20th century, scientists from all over the world focused their efforts on the development and implementation of technologies for energy production from so-called "renewable sources" [1-3]. The major part of the endeavors related to renewable energy sources is aimed at the development of converters of solar energy into electricity, i.e. photovoltaic panels (PV) [4].

Over the past years, the photovoltaic panels market has been developing and expanding at increasing rates. The beginning of the 21st century saw the worldwide installation of power plants of a new capacity exceeding 3600 MWp [5, 6]. When installing a photovoltaic system, the photovoltaic panels account for about half of the investment. They are an important part of the photovoltaic system and their financing depends primarily on their energy performance. [7, 8] Photovoltaic panels still feature relatively low conversion efficiencies.

---

\* Corresponding author: [krastin\\_yordanov@tu-varna.bg](mailto:krastin_yordanov@tu-varna.bg)

Thus, when designing PV systems, it is very important that the panel control ensures maximum power delivery (Maximum Power Point Tracker - MPPT). The power varies depending on the change of solar radiation and the temperature of the module, which differ for the different times of the day and depend on the environmental parameters. The implementation of the MPPT processes requires various methods, which are of different complexity depending on the results expected [9, 10]. With simpler interference and observation methods, the point of maximum power is determined by directly controlling the power calculated from the measurements of the current and the voltage of the module as an initial value. As technology advances, fuzzy logic and controllers are increasingly used in the MPPT process. Their main advantage is that mathematical models are not required to control the power. High accuracy is rather achieved through using a significant amount of information from preliminary research to determine the functions of affiliation of linguistic terms, the base rules, etc. [11-13]

Other methods for tracking the MPP point with their respective advantages and disadvantages are also employed. Some of them are based on measuring the solar radiation and the panel temperature, while others use voltage and current [14-16]. Only a few of the methods take into account the multiple local power peaks obtained as a result of partial shading of the PV panels, which can be a real obstacle to the MPPT functionality [17-19]. When it reaches and works at a local maximum, significant energy loss occur due to the tracking of the local, instead of the global MPP, as experts claim. However, some of the methods require additional initial steps to avoid this set of local maxima and achieve proximity to the true MPP [20, 21].

The present study aims at determining the efficiency of photovoltaic panels, which depends primarily on the global solar radiation density and environmental parameters. A measuring electronic system is designed and manufactured based on a microcontroller with wireless transmission, reception, and recording of data on an SD card and a computer with an application for photovoltaic panel analysis, and experimental testing and testing in a real working environment are conducted.

## 2 Methods and materials employed

### 2.1 Methods

The choice of measurement methods involves meteorological approach to the processing of the results obtained from the electronic measuring system sensors installed, i.e. the calculation of the average value  $\bar{x}$  of the measurements:

$$\bar{x} = \frac{\sum_{i=1}^n x_i}{n} \quad (1)$$

where: where:

$x_i$  – the value measured in every one second;

$n$  – number of measurements for the selected period.

This averages the result of  $n$  measurements and facilitates their processing.

The measured physical quantities that will participate in the system design are the temperature  $t$ , solar radiation  $SR$ , voltage  $U$ , current  $I$ , ambient temperature  $t_{amb}$ , relative humidity  $RH$  and barometric pressure  $P_b$ . These values are combined with microcontroller ESP32.

For measuring the temperature of the photovoltaic panels' inside, a digital temperature sensor DS18B20 of the company MAXIM with a range of temperature measurement from -55°C to +125°C is chosen. The measurement accuracy of 0,5°C is in the range from -10 to

+ 85°C. It has a 9 to 12-bit conversion resolution and various functions for monitoring temperatures in degrees Celsius (°C). One of the good features of the selected sensor is the opportunity to combine up to 1023 sensors connected to one wire, depending on the microcontroller resolution.

The solar radiation contacting photovoltaic panels surface is measured by a BPW34 photodiode, in which the incident coming sunlight induce a direct current. It can be measured with the ADC converter of the measuring module. To obtain the solar radiation SR as a quantity, the following equation is used:

$$SR = \frac{U_s \cdot U_{in} \cdot 1000}{4095} \cdot K_{SR}, W/m^2, \quad (2)$$

where:

$U_s$  – sensor voltage;

$U_{in}$  – supply voltage 3,3 V;

4095 – 12-bit rate of the microcontroller's ADC converter;

$K_{SR}$  – conversion factor, experimentally determined.

The current and voltage produced by the photovoltaic panels are measured with a precision current amplifier MAX471 produced by MAXIM with a measuring range up to 36 V and a current of 3 A. The amplifier provides a linear dependence of the measured quantities by the following equations:

Voltage measurement:

$$U = \frac{U_s \cdot U_{in} \cdot 0,1875}{1000}, V, \quad (3)$$

Current measurement:

$$I = \frac{U_s \cdot 0,1875}{1000}, A, \quad (4)$$

where:

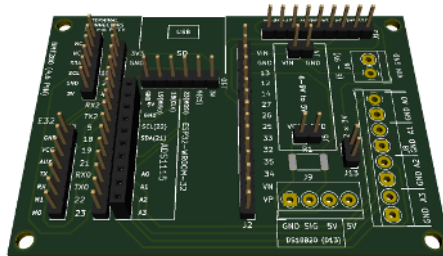
$U_s$  – sensor voltage, V;

$U_{in}$  – input voltage 4,98 V;

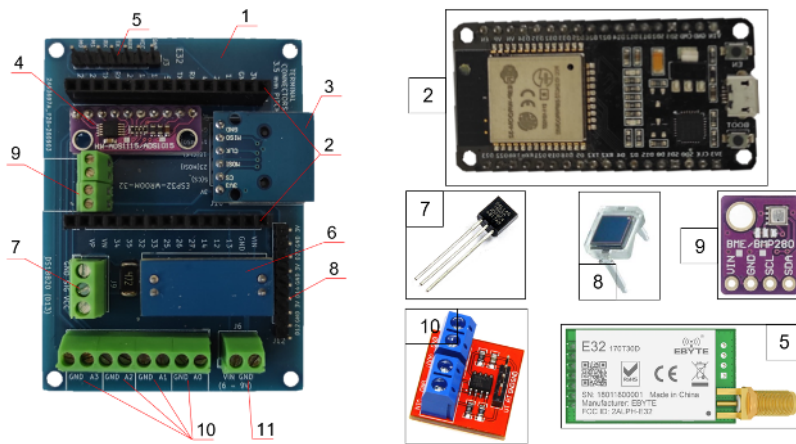
0,1875 – 16-bit rate of ADC converter with a programmable amplifier.

Environmental parameters, such as ambient temperature, relative humidity, and barometric pressure are measured with BOSCH's BME280. The sensor manufacturer has provided compensation formulas to ensure the accurate results of the quantities measured [22].

The methods described above are employed for the design (Fig. 1) and manufacture (Fig. 2) of a circuit board accommodating the pins required for the electronic elements and a data recorder with wireless transmission.



**Fig. 1.** Design of the data logger with wireless transmission.



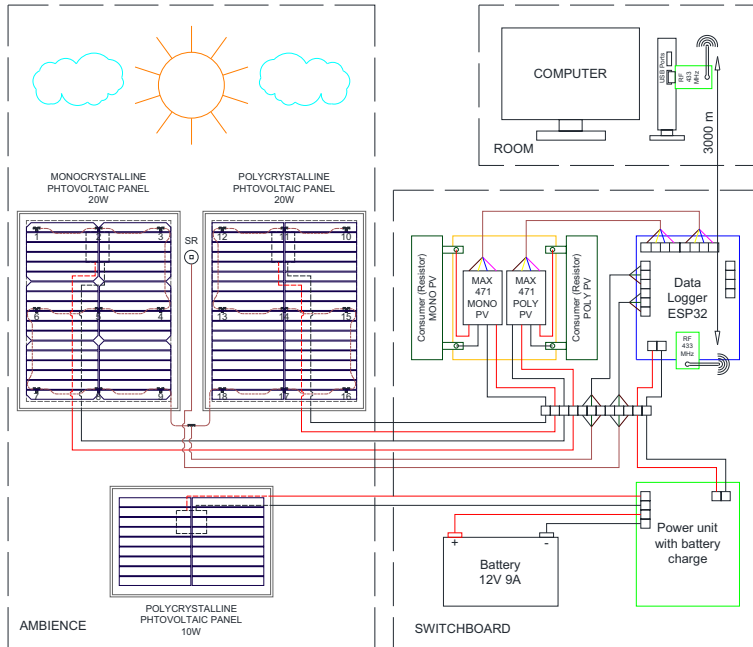
**Fig. 2.** Prototype board for data recording with wireless transmission: 1) circuit board, 2) microcontroller ESP32 WROOM, 3) SD card slot, 4) four-channel 16-bit analog-to-digital converter (Analog-to-Digital Converters – ADCs), 5) wireless transmitter E32, 6) linear voltage regulator AMS1117, 7) digital temperature sensors, 8) solar radiation sensor BPW34, 9) sensor BME280, 10) voltage and current sensors MAX 471, 11) power supply from 6 to 15 V.

## 2.2 Materials

The components used to create the electronic measuring system for the analysis of the photovoltaic panels are shown in the connection diagram in Fig. 3, which consists of the following elements:

- Photovoltaic panels - monocrystalline  $P_{max} = 20 \text{ W}$  and polycrystalline  $P_{max} = 20 \text{ W}$ . When choosing the panels, measures are taken to ensure that they are approximately of the same area and overall dimensions of the photovoltaic cells and the frame, from the same manufacturer and one batch. The parameters of the monocrystalline photovoltaic panel at maximum power are: voltage  $U_{mp} = 18,6 \text{ V}$  and current  $I_{mp} = 1,08 \text{ A}$ , and with the polycrystalline panel, at maximum power, the voltage is  $U_{mp} = 18,2 \text{ V}$  and the current is  $I_{mp} = 1,12 \text{ A}$ ;
- A photovoltaic panel for battery charging - polycrystalline  $P_{max} = 10\text{W}$  with maximum power - voltage  $U_{mp} = 17,4 \text{ V}$  and current  $I_{mp} = 0,57 \text{ A}$ ;
- Digital temperature sensors DS18B20 - 18 pieces – 9 pcs installed at the bottom of each photovoltaic panel;
- A rechargeable battery for autonomous operation of a system with voltage 12 V and current 9 A, placed in the electrical panel;
- A manufactured module with precision-mounted two MAX 471 amplifiers and two consumers (resistances  $R = 30,2 \Omega$ ). In this case, the energy produced by the photovoltaic panels is converted into heat energy given out in the electrical panel, which has a ventilation air grille;
- A wireless transmission data logger in the electrical panel;
- A power supply unit with input AC voltage from  $\sim 15 \text{ V}$  to  $\sim 22 \text{ V}$ , output DC voltage from 10 V to 14 V, and output current up to 3 A. The module is used to switch the power supply to the data logger automatically from the photovoltaic panel or the battery. When the data logger does not consume power, some of it is stored in the battery. The power supply is mounted in the electrical panel;

- A computer system with internet connection placed in a room at a distance less than 3000 m and direct visibility with the measurement equipment provides receiving and control of the data.



**Fig. 3.** Diagram of the measuring electronic system for analysis of photovoltaic panels

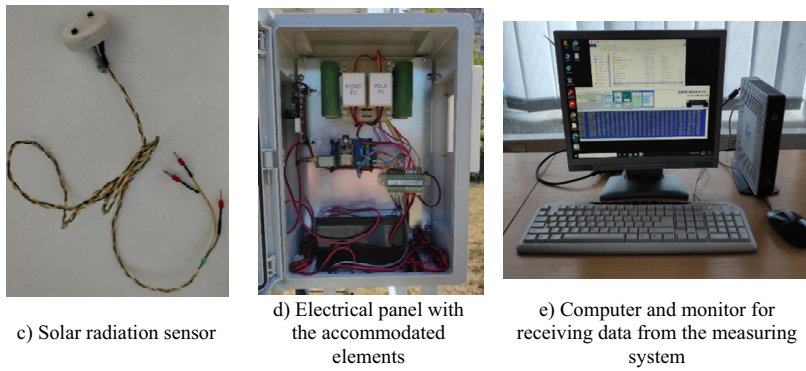
The created electronic measuring system for analysis of photovoltaic panels is shown in Fig. 4. It is installed on the territory of Technical University – Varna on the university experimental field and oriented to north-south. The installation is accomplished on a steel structure of L profiles at a height of 1,5 m and the panels are oriented to the south. The photovoltaic panels fixation is at angle of  $32^\circ$  to the horizontal plane. The solar radiation sensor is fitted in the same plane as the panels, between them. This aims to ensure its movement to the same angle of the panels after changing the latter.



a) South view



b) Arrangement of the panels on the structure



**Fig. 4.** Photos of the electronic measuring system for photovoltaic panels analysis on the experimental field of Technical University – Varna



**Fig. 5.** Meteorological station located in the experimental field of Technical University – Varna

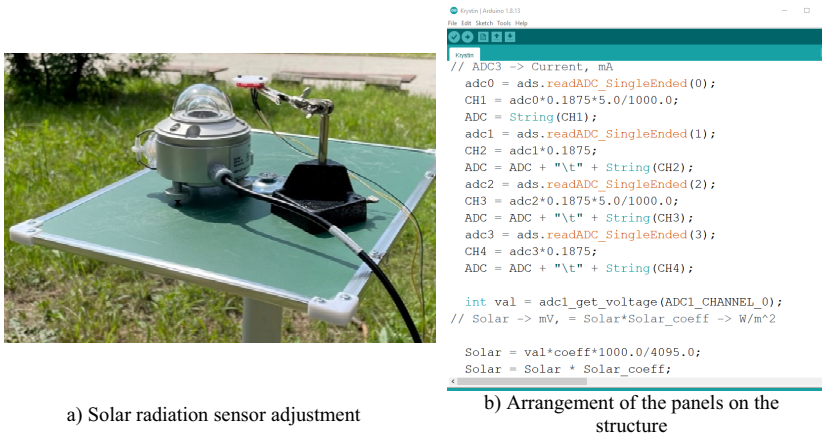
The meteorological station MISOL, model MS-2600-1 is located in the experimental field, 6 m away from the measuring system. It serves to take readings of the meteorological data required for the analysis of photovoltaic panels. The data obtained are included in the Wunderground global database, and the name under which it can be found on the site is IVARNA50 - Fig. 5.

### 3 Results and discussion

The results obtained are based on the experiments conducted.

The first experiment carried out involves adjustment of the solar radiation sensor and its calculation as per 2.1  $K_{SR}$  or the conversion factor calculation. The adjustment has been performed with a standard Kipp & Zonen CM11B pyranometer in the time range between 11 and 16 hours on a clear day, in every 5 minutes - Fig. 6 a). The conversion factor after processing the data collected is obtained as  $K_{SR} = 0,572$ . Fig. 6 b) illustrates part of the program from the ESP32 microcontroller memory.

The photovoltaic cell areas are constant, the monocrystalline photovoltaic panel being  $A_M = 0,108312 \text{ m}^2$ , and for the polycrystalline one it is  $A_P = 0,109512 \text{ m}^2$ . The difference in areas is determined by the geometry of the cells manufactured by different technologies.

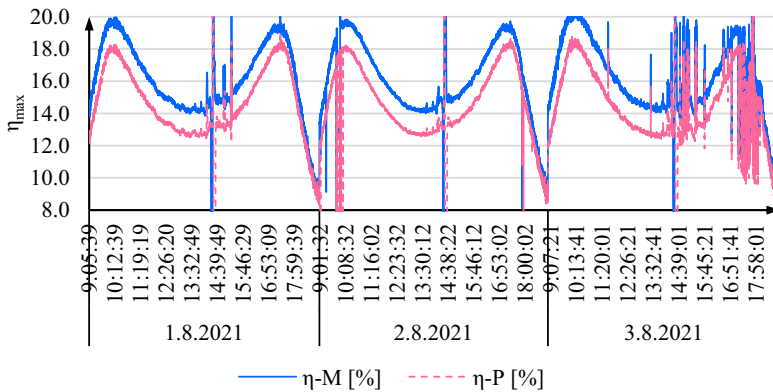


**Fig. 6.** Solar radiation sensor adjustment

The second experiment consists of a three-day measurement of the maximum efficiency of the photovoltaic panels in relation to the parameters measured:

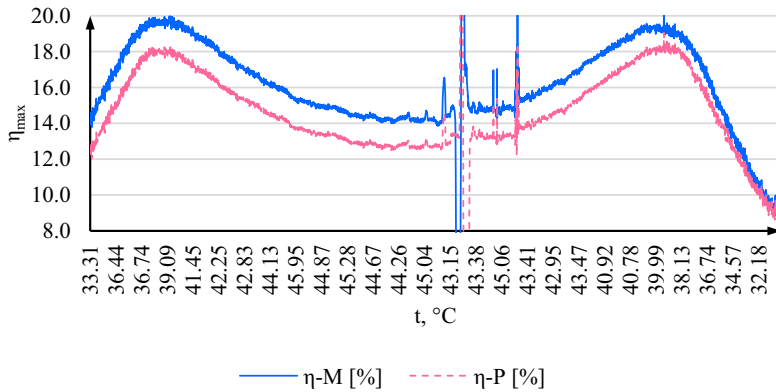
$$\eta = \frac{P}{SR \cdot A} \quad (4)$$

The time for conducting the experiment is from 01.08.2021 to 03.08.2021 in the time interval from 09:00 to 19:00 hours. The results are recorded every 10 seconds, the measurements are taken every 1 second and when the results of 10 are accumulated, it is averaged and recorded. The readings are presented graphically in Fig. 7, indicating the clear decreasing character of the panel efficiencies at noon. In this case, the more efficient of the two is the monocrystalline panel, which for this period of time achieves an average efficiency of  $\eta_M=16,06\%$ , and the polycrystalline features an efficiency of  $\eta_P=14,60\%$ . Fig. 8 presents the results as a function of the temperature relative to the efficiency of the panels for 01.08.2021. The graph indicates that in both types of panels, the efficiency drops after  $40^\circ\text{C}$ .



**Fig. 7.** Efficiency of the panels over the 3 days of the experiment.





**Fig. 8.** Efficiency of the panels in relation to their average temperature taken from 9 temperature sensors for 1 day.

The results of the measurements presented in Fig. 7 and Fig. 8 show clearly expressed disturbances. They are simultaneous, or this is the time period from 14:20 to 14:30 hours. This is due to the location of the experimental arrangement near the meteorological mast, which shades first the monocrystalline panel and then the polycrystalline panel. The other disturbances result from clouds in the atmosphere, which are most pronounced on 03.08.2021 in the afternoon.

## 4 Conclusions

1. The electronic measuring system records the data and processes the results in real-time to determine the efficiency and the average surface temperature of a monocrystalline and polycrystalline photovoltaic panels. The results are transmitted properly even at intervals as short as 10 seconds via 433 MHz radiofrequency at a distance of 300 m with indirect vision.
2. The analysis of the results leads to the conclusion that it is possible to establish the true behavior of the photovoltaic panels efficiency in terms of the temperature they acquire and the environmental parameters during the experiments.
3. The outcomes can be improved and the arrangement can be developed by extending the time for conducting the experiments and taking images of the surface with an infrared camera for comparison with the average contact sensors temperature of the photovoltaic panels underside.

The investigations in that paper have been implemented with the financial support of National Programme “Young scientist and postdoctoral students”, funded by Bulgarian Ministry of Education.

## References

1. B. Knopf, P. Nahmmacher, E. Schmid, *Energy Policy*, **85** (2015)
2. IRENA, *Global Renewables Outlook: Energy transformation 2050* (2020)
3. EC, *General and regional statistics* (Eurostat Database (2020)
4. EC, *In focus: Renewable energy in Europe, Energy*, (Brussels, 2020)

5. Eurostat, *Electricity production, consumption and market overview* (2020)
6. M. Pacesila, S.G. Burcea, S.E. Colesca, *Renew. and Sust. En. Rev.*, **56** (C) (2015)
7. J. Cubas, S. Pindado, C. de Manuel, *Energies*, **7** (2014)
8. B. Amouche, A. Guessoum, M. Belhamel, *Appl. Energy*, **91** (2012)
9. M. Catelani, L. Ciani, L. Cristaldi et al., *The IEEE Int. ENERGYCON* (2012)
10. A.R. Amelia, Y. Irwan, W. Leow et al., *Int. J. Adv. Sc., Eng. Inf. Tech.*, **6** (2016)
11. E. Meyer, *International Journal of Photoenergy*, art. ID: 8479487 (2017)
12. P.K. Dash and N.C. Gupta, *Int. J. of Eng. Res. and Appl.*, **5** (2015)
13. I. S. Stoyanov, T. B. Iliev, G. Y. Mihaylov and E. P. Ivanova, (*ATEE*), 2017, pp. 915-918, doi: 10.1109/ATEE.2017.7905070.
14. G. Takyi, F. Nyarko, *Journal of Power and Energy Engineering*, **8** (2020)
15. N. Suwapaet, P. Boonla, *Energy Procedia*, **52** (2014)
16. Y.M. Irwan, A.R. Amelia, M. Irwanto, et al., *Appl. Mech. Materials*, **793** (2015)
17. B.K. Indra, *Journal of Nepal Physical Society*, **3** (2015)
18. G. Sahin. *Journal of Basic and Applied Physics*, **5** (2016)
19. S. Chander, A. Purohit, A. Sharma et al., *Energy Reports*, **1** (2015)
20. N. Zlatov, I. Iliev, A. Terziev, V. Kamburova, *15th Int. Workshop on REM*, **1** (2014)
21. A. Genbach, D. Bondartsev, I. Iliev, A. Terziev, *E3S Web Conf., EENVIRO*, **85** (2019)
22. Bosch, *Combined humidity and pressure sensor* (Germany, 2020)

# Determination of the optimal air-fuel ratio for upgraded biogas engine operation

Radostin Dimitrov<sup>1,\*</sup>, and Penka Zlateva<sup>2</sup>

<sup>1</sup>Technical University of Varna, Department Transport Engineering and Technologies, 1 Studentska Str., 9010 Varna, Bulgaria

<sup>2</sup>Technical University of Varna, Department of Thermal Engineering, 1 Studentska Str., 9010 Varna, Bulgaria

**Abstract.** The paper reveals a study about air-fuel ratio variation of spark-ignition engine running on upgraded biogas (biomethane). Using biogas as internal combustion engine fuel and external mixture formation is a new approach to decrease harmful exhaust gas emissions. To obtain minimum concentrations of exhaust gases harmful emissions the engine must work with optimal air-fuel ratio. This research contains analysis of many test engine adjusting characteristics to determine optimal air-fuel ratio for each working regime and to obtain maximum effective working process by the use of biomethane as a fuel. Three-dimensional graphics of air-fuel ratio variation across the rpm and load range were made. In conclusion based on performed experiments, a table with values of air-fuel ratio for all engine operating modes and dependence on rpm and load of the engine is proposed.

## 1 Introduction

The ever-increasing environmental requirements and regulations for exhaust gas determined by European legislation dictate the growing use of alternative fuel sources [1-3]. Using alternative fuels is one of the most feasible options to reduce CO<sub>2</sub> emissions is by using alternative fuels. For Spark-Ignition engines, these alternative fuels can be: LPG (liquid petroleum gas), CNG (compressed natural gas), different types of alcohols and biogas [4].

The new method for decreasing exhaust gas emission involves the use of biogas. Biogas is alternative fuel derived from Renewable Energy Sources, containing basically methane and carbon dioxide. Its composition depends on the type of raw material used for its production [5]. The methane concentration in biogas is between 50 and 80% [6]. The biogas obtained needs to be further purified in order to be used as fuel for internal combustion engines [7].

The resultant mixture is composed mainly of methane and is called biomethane. To enable an engine to operate with maximum efficiency, it is necessary to determine the optimal ratio of mixture of biomethane and air entering into the cylinder [8].

As an alternative fuel, biomethane is of growing interest due to its lowest exhaust gas emissions when burnt in the engine [9]. The fuel systems developed for methane operation

---

\* Corresponding author: [r\\_dimitrov@tu-varna.bg](mailto:r_dimitrov@tu-varna.bg)

are characterized by the additional large weight of the fuel tank and the lower power output upon engine retrofitting, which are advantages to be taken into account. On the other hand, this fuel has better environmental performance and low cost, which justifies the tendency toward its use [10-13].

Since the different nature of methane as a fuel, it requires a greater quantity of air for achieving its complete combustion. Thus, 17.19 kg air is necessary to burn 1 kg biomethane as compared to the amount of air required for the engine when running on conventional gasoline fuel, i.e. 14.7 kg air for burning 1 kg gasoline. These factors dictate the need for the determination of air-fuel ratio for each operating mode of the engine when using methane as a fuel [14-17].

This study aims at establishing the optimal air-fuel ratio for achieving the highest efficiency of the engine operation working on biomethane over the whole speed and load range of operation.

## 2 Experimental methodology

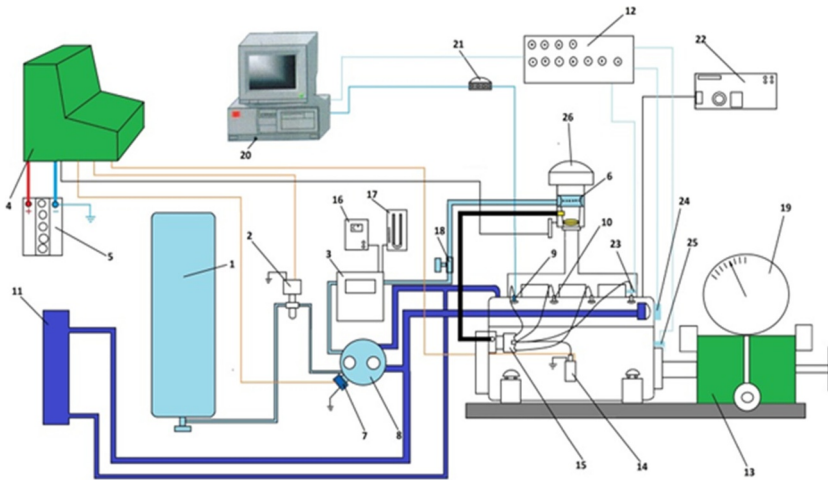
Table 1 shows the parameters of the Spark-Ignition engine used for conducting the experiments included in the study:

**Table 1.** Test engine parameters.

№	Parameter	Value
1	Volume [dm <sup>3</sup> ]	1.275
2	Cylinder diameter [mm]	70.61
3	Stroke [mm]	81.28
4	Compression ratio	9.75
5	Nominal power/ crankshaft speed [kW/ min <sup>-1</sup> ]	46/5500
6	Nominal torque/ crankshaft speed [Nm/ min <sup>-1</sup> ]	95/3000

The Biomethane fuel system is conventionally equipped with a reducer-evaporator, which facilitates the adjustment of the air-fuel ratio of the mixture. The engine is connected to an electric DC current dynamometer. The multitude characteristics established for the air-fuel adjustment parameters are employed to find the optimal parameters promoting the highest efficiency of the combustion process. Also, for each point of measurements, an indicator diagram was drawn using a piezo-quartz sensor of the Kistler brand.

A schematic diagram of the laboratory unit is shown in Fig. 1, where:



**Fig. 1.** Experimental apparatus.

- |                          |                              |                          |
|--------------------------|------------------------------|--------------------------|
| 1 – biomethane bottle;   | 2 – magnetic valve;          | 3 – flow meter;          |
| 4 – control panel;       | 5 – battery;                 | 6 – mixer;               |
| 7 – stop magnetic valve; | 8 – reducer-evaporator;      | 9 – pressure sensor;     |
| 10 – spark plugs;        | 11 – cooling engine system;  | 12 – BNC adapter;        |
| 13 – dynamometer;        | 14 – ignition coil;          | 15 – distributor;        |
| 16 – thermometer;        | 17 – pressure gauge;         | 18 – gas regulator;      |
| 19 – brake force scale;  | 20 – PC system;              | 21 – amplifier;          |
| 22 – gas analyzer;       | 23 – ignition system sensor; | 24 – hall effect sensor; |
| 25 – hall effect sensor; | 26 – air filter.             |                          |

### 3 Experimental data and results

Fig. 2 illustrates an excerpt of the results obtained from the experiments. The variation of the air-fuel ratio as a function of the brake power is shown for different load modes at a crankshaft rotation speed of  $4500 \text{ min}^{-1}$ . The figure shown represents only part of the results of the research conducted at only one crankshaft rotation speed. According to results in Fig. 2, the optimal values of air-fuel ratio are determined for a given crankshaft rotation speed. The 3D-view of the determined values of air-fuel ratios for all regimes of operation of engine are shown in the next figure.

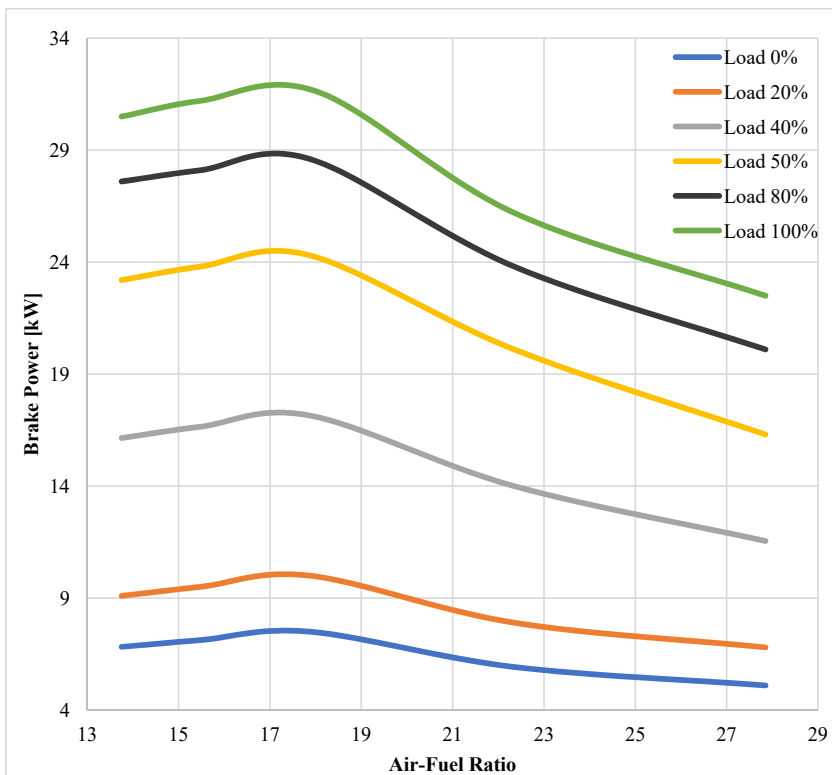


Fig. 2. Variation of Air-fuel ratio in function of Brake Power at a crankshaft rotation speed of 4500  $\text{min}^{-1}$ .

The adjustment characteristics obtained refer to the entire load range (from a closed throttling valve, i.e. zero load to a fully open throttling valve, i.e. full load) at crankshaft rotation speeds of 1000  $\text{min}^{-1}$ , 2000  $\text{min}^{-1}$ , 3000  $\text{min}^{-1}$ , 3500  $\text{min}^{-1}$ , 4500  $\text{min}^{-1}$ , 5500  $\text{min}^{-1}$ , and 6000  $\text{min}^{-1}$ .

The experimental results for the variation of the air-fuel ratio are shown in table 2.

Table 2. Experimental results.

Crankshaft rotation speed [1/min]	% Opening throttle valve					
	0	20	40	50	80	100
1000	15.13	15.30	15.13	15.30	15.30	15.30
2000	15.13	15.47	15.13	14.96	15.47	14.96
3000	16.33	15.47	15.81	14.96	15.13	15.81

<b>3500</b>	17.02	17.19	17.36	17.53	17.36	16.85
<b>4500</b>	17.53	17.88	18.05	17.88	17.88	18.05
<b>5500</b>	17.02	18.05	18.22	17.53	17.88	18.05
<b>6000</b>	16.85	18.05	17.88	18.39	18.57	17.96

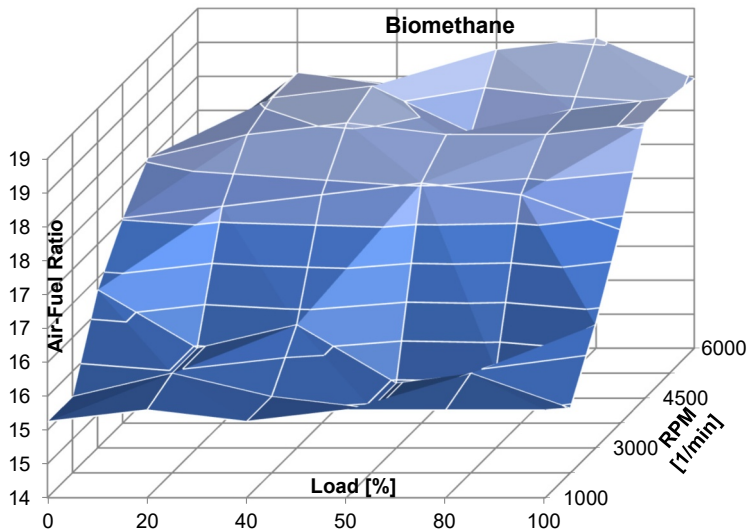
In order to be able to determine whether the mixture is rich or lean, it is necessary to convert the values shown in table 2 into equivalence air-fuel ratio –  $\alpha$  (alfa) using the following equation:

$$\alpha = \frac{AFR_{actual}}{AFR_{ideal}}, \quad (1)$$

where:  $AFR_{actual}$  are values from table 2,  $AFR_{ideal}$  is 17.19.

If the equivalence air-fuel ratio is less than 1, the mixture is rich, and respectively, if the equivalence air-fuel ratio exceeds 1, the mixture is lean. If the equivalence air-fuel ratio is equal to 1, the mixture is stoichiometric.

To provide a clearer visualization, the data obtained are illustrated as a 3D diagram in Fig. 3.



**Fig. 3.** 3D graph of results.

The figure shows the variation of optimal Air-Fuel ratio for all regimes of engine operation, depending on the variation of engine load and rotation speed over the whole

operating range of the engine. By presenting the graph in 3D format, it is possible to understand the results of the experiment more clearly and to analyze the experiment results.

## 4 Conclusions

1. The highest efficiency of the engine requires an air-fuel ratio of approximately 15.3 at crankshaft rotation speeds or reach mixture for crankshaft rotation speed up to 2000 min<sup>-1</sup>.
2. For crankshaft rotation speeds up to the nominal crankshaft rotation speed, the air-fuel ratio is to be equal to or little more than 17.19, corresponding to the stoichiometric mixture.
3. The change of air-fuel ratio of the mixture depends mainly on the crankshaft rotation speed rather than on the engine load.
4. The determination of the optimal air-fuel ratio of an engine running on biogas allows the engine to operate with maximum efficiency and minimized concentrations of harmful emissions in the exhaust gases.

## References

1. EC, *General and regional statistics* (Eurostat Database, 2020)
2. EC, *In focus: Renewable energy in Europe, Energy* (Brussels, 2020)
3. IRENA, *Global Renewables Outlook: Energy transformation 2050* (2020)
4. A. A. Yontar, Y. Dogu, *Int. J. Engine Res.*, **21** (2020)
5. J. Heywood, *Internal Combustion Engine Fundamentals* (McGraw Hill, 1988)
6. J. Brodny, M. Tutak, P. Bindzár, *Energies*, **14**, 3765 (2021)
7. S. Iliev, *Processes*, **9**, 1322 (2021)
8. G. A. Sorin, E. Anca, *Energy*, **147** (2020)
9. L. Sitnik, Z. J. Sroka, M. K. Andrych-Zalewska, *Energies*, **14**, 41 (2021)
10. E. Sosnina, A. Shalukho, L. Veselov, *Proc. of UralCon*, art. no.9216233 (2020)
11. D. Y. Damara, M. D. Dermawan, *Proc. of ICT-PEP*, 9249898 (2020)
12. M. Mouftahi, N. Tlili, N. Hidouri et al., *Processes*, **9**, 48 (2021)
13. J. S. Byun, J. Park, *J. Natural Gas Sci. Eng.*, **22** (2015)
14. E. Porpatham, A. Rameshand, B. Nagalingam, *Fuel*, **87** (8–9) (2008)
15. K. Biernat, I. Samson-Brek, Z. Chłopek, M. Owczuk, *Energies*, **14**, 3356 (2021)
16. N. O'Connell, A. Röhl, R. Lechner, T. Luo, M. Brautsch, *Ren. Ener.*, **143** (2019)
17. S. Lee, U.H. Yi, H. Jang, C. Park, C. Kim, *Energy*, **220**, 119766 (2021)



# Possibilities for obtaining pellets by single-screw extrusion of biomass from black pine (*Pinus nigra* Arn.)

Apostol Simitchiev <sup>1\*</sup>, Bozidar Bozadzhiev <sup>2</sup>, Lazar Lazarov <sup>3</sup>, Stanko Stankov <sup>4</sup>, Hafize Fidan <sup>4</sup>, and Albena Stoyanova <sup>3</sup>

<sup>1</sup>University of Food Technologies / Department of Machines and Apparatuses for Food and Biotechnological Industry, Bulgaria

<sup>2</sup>University of Food Technologies / Department of Cereals, Fodder, Bread and Confectionery Products, Bulgaria

<sup>3</sup>University of Food Technologies / Department of Tobacco, Sugar, Vegetable and Essential Oil, Bulgaria

<sup>4</sup>University of Food Technologies / Department of Nutrition and Tourism, Bulgaria

**Abstract.** The aim of the present study was to investigate the possibilities for obtaining pellets by single-screw extrusion of black pine (*Pinus nigra* Arn.) biomass. Two fractions of black pine needles – 1) with  $d_p \geq 500 \mu\text{m}$  and bulk density  $\rho_n = 0.243 \text{ g/cm}^3$  and 2) black pine twigs with  $d \geq 500 \mu\text{m}$  and  $\rho_n = 0.297 \text{ g/cm}^3$ , were obtained. Wheat bran with  $d_p \geq 500 \mu\text{m}$  and bulk density  $\rho_n = 0.258 \text{ g/cm}^3$  in a ratio of 1:1 was added to the obtained fractions. The experiments showed that getting pellets by single-screw extrusion of biomass from twigs and needles of black pine was possible when mixing them in a 1:1 ratio with wheat bran. The addition of wheat bran improved the smoothness and homogeneity of the produced pellets and increased their density. High-density pellets with a low sectional expansion index were produced during extrusion. The productivity of extruding mixtures of black pine twigs with wheat bran was 30% higher than that made from a mix of black pine needles and wheat bran. The pellets obtained after mixing biomass from black pine and wheat bran had over 13% higher density than those produced entirely from wheat bran. The presence of black pine biomass increased the quality of the final product while at the same time having a positive effect on both productivity and specific energy consumption.

## 1 Introduction

Renewable natural sources, including waste raw materials from the timber and processing industry, could be used as an alternative energy source [1]. Their utilization was in granular

\*corresponding author: [asimitchiev@gmail.com](mailto:asimitchiev@gmail.com)

form, which created preconditions for disruption of the flow due to adhesion and the appearance of cracks [2-4].

Coniferous species and, in particular, black pine (*Pinus nigra* Arn.) are sources of biomass, not only in Bulgaria but also worldwide. The biomass of plant species was characterized by low energy density and high water content, requiring its pre-treatment (extrusion). Many physical and energy characteristics of black pine biomass, such as density, strength, calorific value, and others, were essential in the bioenergy market. The mechanical properties of the biomass used for extrudates are strongly influenced by the distribution and size of the individual particles in the system [5-7]. There were no standard methodologies in the literature for the properties of extrudates (granules) and values for the coefficients of friction, a slip of black pine biomass with different moisture values.

The density of the obtained granules was an essential parameter for evaluating the mechanical characteristics, as it also determines the pressure used to obtain the pellets [2, 8]. New conditions are created during the increase of the pellet's density to create close interaction between the system's components. This condition lowered the moisture content by decreasing the mass and significantly reducing transport and storage costs [9-11]. The creation of a dense structure of extrudates may also cause a decrease in their mechanical stability due to solid compaction [12].

Granulated biomass absorbed less moisture from the environment [9], but pellet extrudates require higher amounts of energy [13].

Some authors [6, 14] used waste products from soybean processing, sugar cane, eucalyptus wood, wheat straw, algae, willow, and cork in the composition of the extrudates. Their analyzes have identified several energy characteristics of biomass. The determination of mechanical parameters such as hardness assesses the quality of the pellets.

Most of the biomass obtained from processing, and agricultural production comprises lignocellulose, a composite of cellulose, hemicellulose, and lignin. Each of the polysaccharides involved in the biomass composition determined the different binding methods between the particles, which was the main factor determining the heat of combustion. The use of an unsuitable extruder or incorrectly selected extrusion conditions may cause lignin flow and migration of some substances to the surface. All these changes influenced the quality of the obtained extrudates [14].

Coniferous species used for timber, such as black pine, fall into the group of large amounts of biomass. Different energy characteristics were observed between the various anatomical parts of the coniferous species. The higher lipid content and volatile substances in the biomass increased the calorific value of the obtained extrudates used for combustion. For this reason, during drying or extrusion, some representatives of lipids and volatile components were lost, which negatively affected the energy potential of biomass [15].

Because of the increased interest in using bioenergy resources and applying the principles of the green economy in several industries, knowledge of their application is needed. Black pine in Bulgaria is a widely used species in the timber, wood processing, and essential oil industries. The large scale of the waste raw materials obtained during its processing contains materials with a composition that suggests many possibilities for their inclusion in the bioenergy sector. The case of its wide application is influenced by the fact that the black pine species is not a protected species in Bulgaria. To the best of our knowledge, this is the first scientific study evaluating the usage of raw waste products by black pine to produce pellets. Therefore, the aim of this study was to determine the options of obtaining pellets by single-screw extrusion of black pine biomass (*P. nigra*) obtained after extraction of the essential oil.

## 2 MATERIALS AND METHODS

### 2.1. Materials

Biomass (needles and twigs with needles) from black pine (*P. nigra*) which was obtained after extraction of the essential oil by water distillation was used in this study. The raw material was collected during the summer season (May - June 2020) in Central Balkan Nature Park, Bulgaria. After distillation, the biomass was dried at a temperature of  $20 \pm 2$  °C and an air velocity of 0.5 m/s.

The wheat bran (obtained from soft wheat) was purchased from the commercial network (Claremont company).

### 2.2. Methods

#### 2.2.1. Biomass grinding

The raw material was grounded by a hammer mill [1]. The grinding rate for biomass was  $d_p \geq 500 \mu\text{m}$  and bulk density was  $\rho_n = 0.243 \text{ g/cm}^3$  (for needles) and  $\rho_n = 0.297 \text{ g/cm}^3$  (for twigs with needles), respectively (Fig.1).



**Fig.1.** *P. nigra* biomass.

#### 2.2.2. Determination of moisture

The moisture content [5] for needles, twigs with needles and wheat bran biomass were determined as follows  $7.10 \pm 0.87\%$ ,  $7.50 \pm 0.13\%$ , and  $6.12 \pm 0.81\%$ .

#### 2.2.3. Ash content

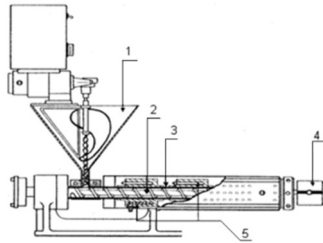
The mineral composition of the samples was  $2.86 \pm 0.12\%$  (needles),  $3.12 \pm 0.03\%$  (twigs with needles), and  $6.64 \pm 0.09\%$  (wheat bran).

#### 2.2.4. Determination of cellulose

The cellulose content of needles ( $29.20 \pm 1.56\%$ ), twigs with needles ( $26.10 \pm 2.18\%$ ), and wheat bran biomass ( $8.15 \pm 0.12\%$ ) was determined according to the method described by Simitchiev et al. [1].

### 2.2.5. Extrudates obtaining

The experiments were carried out on a single-screw laboratory extruder “Brabender 20 DN” (Germany) with a working screw diameter of 20 mm, equipped with a measuring facility for torque  $\Pi_n$ , N.m, the temperature of the material in the die and pressure inside the die. All data were obtained directly from the control unit display of the extruder (Fig. 2).



**Fig. 2.** Single-screw laboratory extruder “Brabender 20 DN”.

1. Feeding device. 2. Screw 3. Cylinder 4. Die with nozzle and heater. 5. Heating devices

Cylinder diameter 20.05 mm

Cylinder length 406.5 mm

L/D 20:1

Cooling air, water

The obtained pellets are characterized by the following indicators:

Productivity of the extrusion process ( $Q_m$ ), kg/h - is determined by calculating the mass of the amount of expired product per unit time according to the following equation:

$$Q_m = \frac{m}{t}, \quad (1)$$

where:  $m$  – mass of biomass, kg;

$t$  – time, min.

Sectional expansion index (SEI) – was defined as the ratio of the average diameter of the extrudate from each experiment ( $D_e$ ) to the diameter of the hole of the matrix nozzle ( $D_o$ ) by the following equation:

$$SEI = \frac{D_e}{D_o} \quad (2)$$

where:  $D_e$  – the average diameter of the extrudate for ten samples, mm;

$D_o$  – diameter of the die nozzle hole, mm.

Specific mechanical energy (SME), (kJ/kg) - determined by the following equation:

$$SME = \frac{\pi \cdot M_n \cdot n}{30 \cdot Q_m} \cdot 3,6, \quad (3)$$

where:  $M_n$  – torque, N.m. It is recorded from the display of the power supply unit of the laboratory extruder;

$n$  – the speed of the working screw,  $\text{min}^{-1}$ ;

Density of pellets ( $\rho$ ), ( $\text{g}/\text{cm}^3$ ) - is determined by measuring the mass and the average diameter of the same amount of extrudates (10 pcs.) of the same length. Calculate the volume of each extrudate, assuming that its shape is close to cylindrical. The density is calculated by the following equation:

$$\rho = \frac{M(1 - \frac{W}{100})}{V - M \frac{W}{100}}, \quad (4)$$

where:  $M$  – the mass of biomass, g,

$V$  – sample volume,  $\text{cm}^3$ ,

$W$  – the moisture of biomass, %.

The moisture of the products was determined by drying for 24 h at  $105^\circ\text{C}$ .

Volumetric flow rate ( $\text{cm}^3/\text{h}$ ) - determined by the following equation:

$$Q_v = \frac{Q_m}{\rho} \cdot 10^3 \quad (5)$$

All experiments were performed with an initial humidity  $W = 10\%$ , determined by drying for 24 h at a temperature of  $105^\circ\text{C}$  (EN ISO 712:2010) [16].

### 3 Results and discussion

The main difficulty during extrusion processing was to reach optimal operating modes in order to obtain a product with the best physical and mechanical properties. Therefore, it was always necessary to perform preliminary experiments in which the basic parameters were changed during extrusion [3, 4, 17]. Needles and needle twigs contained resinous substances which melted at temperatures above  $40^\circ\text{C}$ . At the same time, the resistance moment and the pressure in the system increased and the molten product was not able to pass through the die. The same problem occurred without additional heating in the three zones of the extruder. Due to the friction forces from the rotation of the screw in the cylinder of the extruder, the temperature increased again to the extent that the resin liquefied and the extruder closed [3, 4, 8, 9].

In order to prevent this negative phenomenon, wheat bran was added to the two black pine biomass (Fig. 3) with the following parameters:  $d_p \geq 500 \mu\text{m}$ , bulk density  $\rho_n = 0.258 \text{ g}/\text{cm}^3$ . The biomass ratio of black pine: wheat bran is 1:1.



**Fig.3.** Wheat bran

New difficulties related to the clogging of the extruder confirmed the binding potential of the bran used [3, 4].

Another problem was the inner diameter of the nozzle through which the pellets come out. Preliminary experiments have shown that if this diameter was less than 8 mm, the product is not able to be extruded. The reason is that the inner hole of the die through which the product passes before reaching the nozzle is 8 mm in diameter. If the nozzle that was mounted to it was smaller, then the product encounters great resistance along the way. This leads to an increase in the resistance moment and the pressure in the extruder, accompanied by an increase in the coefficient of friction between the product and the nozzle. In order to reduce friction, experiments have been performed to increase the humidity of the input raw materials, but the results were unsatisfactory. After numerous experiments, operating modes have been established in which pellets with the best physical and mechanical properties were obtained:

Inner diameter of the nozzle was determined as  $D_0 = 8$  mm; the degree of compression of the screw was  $K = 5:1$ ; the temperatures in the three zones of the extruder was  $t_1 = 30^\circ\text{C}$ ;  $t_2 = 30^\circ\text{C}$ ;  $t_3 = 40^\circ\text{C}$ ; the dosing screw speed was  $N_f = 100 \text{ min}^{-1}$ ; and the speed of rotation of the working screw was  $n = 250 \text{ min}^{-1}$ .

The experimental preparation was performed at ambient temperature  $t_a = 20.5^\circ\text{C}$ . Five parallel experiments were performed in the modes of operation described above with a mixture of biomass from black pine needles and wheat bran (sample 1), twigs with needles, and wheat bran (sample 2) and only wheat bran (control sample). The results are presented in Table 1.

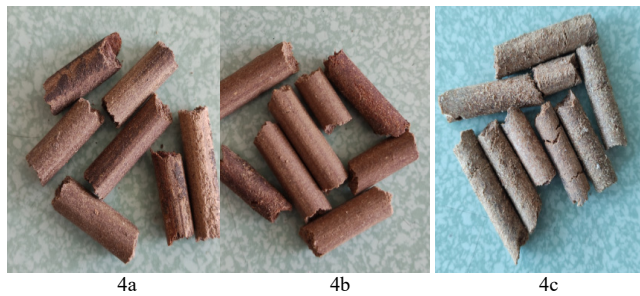
**Table 1.** Physical characteristics of the pellets.

	EI	Mass flow $Q_m$ , kg/h	Specific mechanical energy SME, kJ/kg	Volume flow $Q_v$ , cm <sup>3</sup> /h	Density, $\rho$ , g/cm <sup>3</sup>	Pressure, MPa
Sample 1	1.02 $\pm 0.005$	2.187 $\pm 0.016$	1077.36 $\pm 13.572$	1701.95 $\pm 66.212$	1.285 $\pm 0.018$	3.6 $\pm 0.112$
Sample 2	1.06 $\pm 0.025$	3.123 $\pm 0.046$	1146.79 $\pm 14.148$	2248.38 $\pm 102.014$	1.389 $\pm 0.026$	4.3 $\pm 0.132$
Control sample	1.02 $\pm 0.014$	2.012 $\pm 0.021$	1311.60 $\pm 16.162$	1804.48 $\pm 72.046$	1.115 $\pm 0.022$	2.8 $\pm 0.094$

The data values are expressed as the mean  $\pm$  SD (standard deviation (n = 5))

The obtained values for the individual parameters of the extrudates were not in agreement with previously reported [3, 4, 9], as the differences in the indicators of the initial biomass - a type of biomass, moisture of the raw material, and type of extruder used could be the reason for the differences. The data obtained in this study showed that the inclusion of wheat bran in the composition of the biomass improved the density, increasing the extruder's productivity.

Figures 4a, 4b, and 4c showed the images of the pellets obtained. They show the good smoothness, homogeneity, and density of sample 1 and sample 2. In contrast, the control sample showed an apparent porosity. There were also microcracks, which indicated poor sealing of the control sample at the exit and from the nozzle.



**Fig. 4.** Pellets obtained after single-screw extrusion of biomass from black pine and wheat bran: 4a - sample 1; 4b - sample 2; 4c – control sample.

The sectional expansion index indicated the increase in the size of the extruded product after it left the nozzle. Index values were greater than or equal to 1 (one) due to the transition from high pressure from the pressing of the product in the cylinder to atmospheric pressure at its exit after the nozzle. It was mainly influenced by the humidity and chemical composition of the extruded product and the temperature regimes, and the rotational speed of the working screw. The obtained results showed that the extruded pellets had low expansion. In this case, the low expansion index was not a negative phenomenon. Instead, it was an indicator of the products' good compaction in the matrix, expressed by the homogeneity and strength of the obtained pellets. Mixtures with twigs with black pine needles (sample 2) had a higher expansion index than those with black pine needles (sample 1) and wheat bran (control). It could be explained by the higher bulk density of sample 2, which allowed for better dosing of the product and led to a more optimal filling of the inter-turn space of the screw with the product and an increase in pressure.

The lower bulk density of the product (sample 1) led to problems with its dosing to the working screw. Therefore, the resistance moment and the pressure in the cylinder acquired lower values than those recorded in the experiments with sample 2. As a result, the productivity and the sectional expansion index of the obtained pellets were affected. A problem with dosing also occurred in the control sample, which affected both the productivity and the density of the pellets.

The density of the pellets is a major indicator on which their hardness and strength depend. It also characterizes the changes in the structure of the product during its movement in the cylinder of the extruder. During the extrusion of pure black pine biomass, the resulting extrudates decomposed when leaving the nozzle and were characterized by high friability and low density. The addition of wheat bran to the two black pine samples positively affected the quality and density of the pellets obtained. A parallel could be made with previous experiments for obtaining pellets from distilled juniper [1, 17]. The pellets obtained in the experiments with a mixture of wheat bran and black pine were characterized by three times higher density than those with a main component of juniper.

On the other hand, the pellets obtained after mixing biomass from black pine and wheat bran had a higher density than those produced with the control sample. Therefore, the presence of black pine biomass increased the quality of the final product while positively affecting both productivity and density. Biomass compaction systems were adapted depending on the moisture of the feedstock, the particle size, and the protein and lignin content, which had a very strong effect on the binding potential between the individual particles. The lignin fraction in the biomass determined the necessity to use technological solutions, such as the inclusion of steam, steam explosion, torrefaction in order to improve

the quality of extrudates. The inclusion of natural or synthetic adhesives in the production of low lignin extrudates reduced the specific energy of compaction [17], while improving the index of density and strength, bulk density, moisture and calorific value of extrudates.

Volume productivity is an indicator that represents the ratio between the productivity expressed by mass flow to the density of the pellets. In the present study, the volumetric productivity of the pellets from sample 1 was about 25% higher than that obtained from sample 2. The total volumetric productivity of the product obtained from mixtures of black pine and wheat bran was lower than that obtained in pellets from distilled juniper [1, 3, 4, 16, 17]. It could be explained by the different extrusion modes and the higher density of the mixtures of black pine and wheat bran, due to which the speed of the pellets coming out of the nozzle was lower. Sample 2 had more than 8% higher volumetric productivity than the control sample due to the better filling of the screw inter-turn space with the product [17].

Productivity and energy consumption are essential technical and economic indicators that characterize each production process. In the present experiment, they had a rather indirect influence due to the type of extruder used to produce pellets in this study. Therefore, the calculated productivity was low, with relatively low energy consumption. The results showed a higher energy consumption when working with sample 2. This was mainly due to higher productivity (over 30% higher than sample 1), higher resistance moments, and a higher pressure during extrusion. When using an industrial turbo extruder operating at high pressure, the obtained productivity would be significantly higher, which was a prerequisite for further experiments in this direction. In the control sample, the energy consumption was over 12% higher than that obtained in the other samples. This was due to the lower pressure during the extrusion treatment, which affected the torque and the flow rate of the product from the nozzle of the extruder.

## 4 Conclusion

The results obtained in this study showed that the production of pellets produced by single-screw extrusion of biomass from needles and twigs with black pine was possible by mixing them with wheat bran in a ratio of 1:1. The addition of wheat bran improved the smoothness and homogeneity of the pellets and increased their density. Extrusion regimes have been established in which high-density pellets with a low sectional expansion index were produced. The productivity of extruding mixtures of twigs with black pine needles with wheat bran (sample 2) was 30% higher than that made from a mix of black pine needles and wheat bran (sample 1).

The pellets obtained after mixing the black pine biomass and wheat bran had over 13% higher density than those produced entirely from wheat bran. This showed that the presence of black pine biomass increased the quality of the final product while at the same time having a positive effect on both productivity and specific energy consumption. The experiments carried out in our study emphasized that the energy performance of the sample increased the quality of the final product. The energy characteristics of black pine biomass will be the subject of future research, because of the potential possibilities for application as an energy source.

The authors acknowledge the support by the National Science Fund of Bulgaria, project No 0P-06-H36/14.



## References

1. A. Simitchiev, L. Lazarov, H. Fidan, B. Bozadzhiev, A. Stoyanova, IOP Conf. Series: Materials Science and Engineering, **1031**, (2021)
2. M. Stasiak, M. Molenda, M. Banda, J. Horabik, J. Wiacek, P. Parafiniuk, J. Wajs, M. Gancarz, E. Gondek, A. Lisowski, Materials, **13**, 3567 (2020)
3. G. Wang, Y. Luo, J. Deng, J. Kuang, Y. Zhang, Chin. Sci. Bull., **56**, 1442-1448 (2011)
4. D. Medic, M Darr, A. Shah, B. Potter, J. Zimmerman, Fuel, **91**, 147-154 (2012)
5. M. Gil, P. Oulego, M. Casual, C. Pevida, J-J. Pis, F. Riviera, Bioresour. Technol, **101**, 8859-8867 (2010)
6. M. Scatolino, L. Neto, T. Protaslo, A. Carneiro, C. Andrade, J. Guimaraes Junior, L. Mended, Waste Biomass Valor, (2017)
7. V. Kazimirova, L. Kubik, J. Chrastima, T. Giertl, Agron. Res., **15**, 1906-1917 (2017)
8. M. Rabacal, U. Fernandez, M. Costa, Renew. Energ., **51**, 220-226 (2013)
9. H. Li, X. Liu, R. Legros, X.T. Bi, C.J. Lim, S. Sokhansanj, Appl. Energy, **93**, 680-685 (2012)
10. W. Stelte, J. Holm, A. Sanadi, S. Barsberg, J. Ahrenfeldt, U. Henriksen, Fuel, **90**, 3285-3290 (2011)
11. J.S. Tumuluru, C.T. Wright, J.R. Hess, K.L. Kenney, Biofuels Bioprod. Biorefin., **5**, 683-707 (2011)
12. N. Kaliyan, R.V. Morey, Biomass Bioenergy, **33**, 337-359 (2009)
13. C. Wang, J. Peng, H. Li, X.T. Bi, R. Legros, C.J. Lim, S. Sokhansanj, Bioresour. Technol. **127**, 318-325 (2013)
14. A. Demirbas, T. Ozturk, M.F. Demirbas, J Energy Sources, **28**, 1473-1482 (2006)
15. P. Lehtikangas, Biomass Bioenergy, **20**, 351-360 (2000)
16. BDS EN ISO 712:2010
17. J.S. Tumuluru, T. Cristopher, J. Wright, R. Hess, K.L. Kenney, Biofuels, Bioprod. Bioref., **5**, 683-707 (2011)

# On the Development of a Real Time Water Monitoring System

*Sandel Zaharia*<sup>1,\*</sup>, *Gabriel Iana*<sup>1</sup>, *Cristian Monea*<sup>1</sup>, and *Mihnea Sandu*<sup>2</sup>

<sup>1</sup>MIRA Technologies Group, Romania Bucharest, Romania

<sup>2</sup>Technical University of Civil Engineering Bucharest, Romania

**Abstract.** The goal of the paper starts from the need for real-time monitoring of both running water and its affluents and urban sewerage systems with a role in discharging wastewater. The idea is to assess water quality and to determine the sources of pollutants resulting from human activity. The data quality will be obtained by purchasing them with a high resolution, both spatial and temporal, using multi-parametric sensors on a hardware platform of its own multisensory acquisition. The acquired data is stored in CLOUD or local server for storage, analysis and interpretation. There will be a software application based on artificial intelligence technologies that serves to identify and classify different polluted areas, locate pollution sources, predict their extinction, degree of pollution and help make decisions based on real-time detection. A web application will provide all the data collected in the field and it can be accessed on a common online platform. This allows researchers or employees of relevant agencies as well as city sewer system operators to validate the quality of data purchased from sensors and end users to be sure of their correctness.

## 1 Introduction

River water is the main source of drinking water for most localities in our country and it is obvious that their quality level directly influences the drinking water treatment and the water distribution systems in populated centers. Rivers and their tributaries are subject to high dynamics that change both in time and space. In addition to daily and seasonal natural variations [1], the rivers are influenced by changing discharge regimes (flow, rainfall) and very often, unpredictably, by the impact of different types of pollutants resulting from human activity [2]. Basically, the pollution is more harmful to the ecological and chemical status of the river the smaller the river is. It should also be borne in mind that the quantity of pollutants coming from small tributaries accounts for most of the pollution in large running waters. Another very important factor that leads to the increase of the degree of pollution of the running waters in Romania is the discharges of the insufficiently treated wastewater. There are two main categories of wastewater, insufficiently or not treated urban wastewater in urban environment or industrial wastewater treatment plants. The industrial wastewater is characterized by loads of specific pollutants which can be discharged untreated both in urban sewage systems and directly into running water. The

---

\* Corresponding author: [mihnea.sandu@utcb.ro](mailto:mihnea.sandu@utcb.ro)

latter are particularly dangerous if they are accidentally or intentionally spilled, often leading to real environmental disasters.

In Europe, since 2000, based on the requirements of the European Commission, the situation of small and medium-sized rivers has been analyzed according to the "EU-Water Framework Directive" (WFD) [3]. Assessing the impact of pollution on running water is done through a combined approach that involves analyzing the different sources of pollution and how they drain. It is necessary to identify the sources and routes of pollutants in running water in order to allow a correct planning of measures to eliminate them and to improve the chemical and ecological status of the water. In Romania there are maximum values of the concentrations of pollutants that can be discharged into natural waters, based on the NTPA001 norms, and maximum values of the concentrations of pollutants that can be discharged into the urban sewerage networks based on the NTPA002 norms. The traditional approach to water quality monitoring is achieved by the laboratory testing of water samples collected both in the case of natural running water and in the case of sewerage systems. This technique offers a full range of testing, including biological, chemical and physical parameters. Due to the high dynamics, non-linear behavior in time and space of running water as well as sewerage systems, traditional sampling methods fail to identify sources of pollution in real time.

To identify and monitor pollutants in real time, it is necessary to take samples using automated systems; they provide information on the water quality of a river or sewer system and allow the detection of both short-term events and long-term changes. Moreover, they allow the distinction of different paths and sources of pollution that can be categorized to be point or diffuse.

Currently, in many countries, running water is monitored by permanent stations specializing in monitoring standard physic-chemical parameters of water quality, administered by public agencies. The main parameters monitored are physical - pH, temperature, color, turbidity, conductivity, radioactivity and bio-chemicals - biological oxygen consumption, chemical oxygen consumption, dissolved oxygen, solid suspensions, nitrates, nitrites, sulfates, phosphates, various dissolved elements. Among these elements, total nitrogen, ammoniacal nitrogen, total phosphorus, lead, cadmium, total chromium, hexa-valent chromium, tri-valent chromium, copper, nickel, zinc, manganese can be listed as the main industrial pollutants. chlorides. An important part of these pollutants are the heavy metals (listed above) that have already reached the city treatment plants and they will be found in the composition of the sludge resulting from the treatment process, making it considerably more difficult to process. Many of the necessary sensors, especially electrochemical ones, require continuous maintenance, frequent calibration procedures and cleaning to ensure safe and accurate data. In addition, various problems may arise when integrating them into a common software platform (data collection, processing, etc.), which has implications for the end user in making decisions about water quality and how to act in the event of an incident.

## **2 State of the art**

Nowadays there are different systems that monitor the water quality from the point of view of its pollution level. Some of these are made only for pollutants from the agricultural sector, especially for the flow of nutrients from rivers [4]; other systems focus on assessing the ecological status of rivers or the impact of river pollution on drinking water. Most studies have been performed using in-situ sensor placement [5]. However, the precision water monitoring devices, such as chemical analysers, are not widely used due to the high investment and maintenance costs, as they are used to monitor river basins through analysis

stations of national agencies [6]. These types of analysers are used, for example, to determine the amount of phosphorus in water. However, ammoniacal nitrogen (NH<sub>4</sub>-N) and organic carbon (TOC) are of significant relevance to the chemical and ecological status of rivers, as well as to the identification of their sources.

## 2 System description

This paper describes the conception of a system dedicated to the acquisition and the interpretation of an extensive set of data from several types of pollutants, the characterization and the classification of the full spectrum of pollution sources, using the latest methods and technologies. The system architecture could be presented from the hardware or software point of view. Generally, the system is composed from the following subsystems (see figure 1):

- Multi-sensor hardware platforms that read the water quality parameters and send them to the data storage, processing and analysis software application;
- Weather station that provides data necessary to increase the accuracy of prediction of analysis algorithms;
- River pollution monitoring software application that ensures the storage, processing and analysis of purchased data (resident in a cloud or local server) and recognition using artificial intelligence algorithms;
- Web software application for visualizing the state of the equipment in the composition of the system, in order to manage and maintain them;
- Research software application that provides all the data collected by the multi-sensor hardware platforms for the research institute and the university, visualization and production of reports, statistics and predictions on pollution events;
- Alert service software application used to transmit real-time pollution events to the authorities.

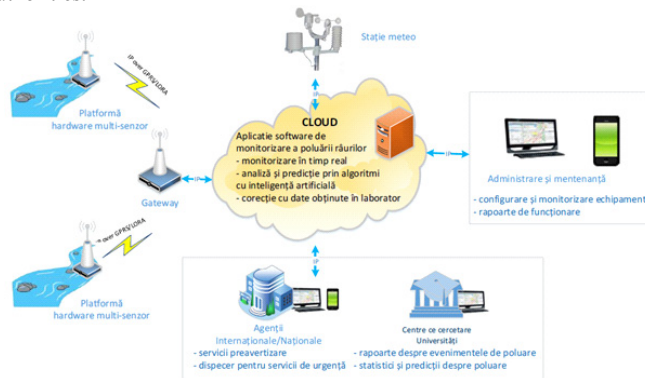


Fig 1. General architecture of the system

The general tasks of the system are described below:

- real-time monitoring of water pollution
- storage of data purchased from multi-sensor hardware platforms.
- preprocessing and analysis of data taken from multi-sensor hardware platforms;
- data fusion from all data from multi-sensor hardware platforms;

- generating information for pre-warning services;
- generating alerts for emergency services;
- allows access to raw data and results from their processing and analysis to make detailed statistics and predictions about pollution, and provide reports on pollution events;
- allows the connection of a wide range of sensors, in order to collect and record data from them;
- allows its programming so that the software interface can be interfaced with the connected sensors;
- communicate through several communication technologies;
- allows the configuration of smart sensors connected by the user;
- allows the calibration of the sensors connected by the user;
- allows monitoring the status of all component hardware equipment.

We will describe below the role and the architecture of the main components of the system.

#### *Multi-sensor hardware platform*

The role of multi-sensor hardware platforms is to take data from sensors that measure water quality parameters and transmit them to the data storage, processing and analysis software application. The hardware architecture of a multi-sensor platform is illustrated in Figure 2.

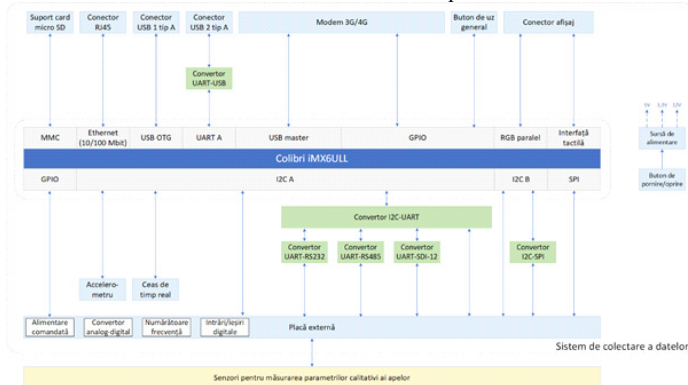


Fig 2. Hardware architecture of the platform

The multi-sensor platform consists of two main components: (1) the system for collecting data from sensors and (2) sensors for measuring water quality parameters. The data collection system is built with a Toradex Colibri iMX6ULL module. It is a system-on-module (SoM) microsystem that provides the digital interfaces, computing power and power consumption necessary to meet the functional requirements of the platform. It also ensures the flexibility of software programming by offering the possibility to access low-level digital interfaces (eg SPI, I2C, etc.) and to allow programming using high-level languages (eg C #, Python, etc.).

In general, the data collection system consists of the following components: central unit (Colibri iMX6ULL), sensor interfaces (RS-232, RS-485, SDI-12, I2C, SPI, UART, analog, digital, power supply), communication interfaces (USB slave, USB master, Ethernet, 3G / 4G modem, WiFi), memory (micro SD card, flash), display.

The functions of its components are the following:

- Micro SD card - for local storage of data from sensors; this function is particularly important when the communication link with the server on which the data storage,

processing and analysis software application resides cannot be established; the micro SD card is connected to the MMC interface of the SoM;

- RJ45 connector - to ensure Ethernet communication at speeds from 10 to 100 Mb / s; it is connected to the Ethernet interface of the SoM;
- 2 USB connectors - to offer the possibility of local download of data stored on the micro SD card on an external memory support;
- 3G / 4G modem - it ensures communication with the server through mobile data networks, having the possibility to operate in 4G networks, but also 3G when there is no 4G coverage in the areas where the platform is installed;
- General purpose button - for performing software configurable functions (eg system reset); it is connected to the GPIO port of the SoM;
- Accelerometer - it has the role of detecting if the platform has changed its installation position; this can happen in case of theft or fall of the platform;
- Real time clock - it is responsible for maintaining the system time;
- I2C-UART converter - the converter has the role of providing several serial communication ports to ensure flexibility regarding the types of sensors that can be connected to the data logger;
- I2C interface B - is used to allow the connection of digital sensors with I2C interface;
- I2C-SPI converter - it is used to allow the connection of digital sensors;
- Power supply - ensures the supply of the system with the necessary voltages and currents;
- Start / stop button - allows the system to start / stop;
- External board - it is located in the vicinity of the data logger, it is connected to it by ribbon cable;
- Analog-to-digital converter - this block contains the analog-to-digital converters used for interfacing with analog sensors;
- Frequency counters - allow the reading of data from sensors that provide them in the form of pulses;
- Digital inputs / outputs - for interfacing with sensors; they are connected to the GPIO port of the SoM;
- Sensors for measuring water quality parameters - they can be digital or analog.

The multi-sensor hardware platform must perform the following functions:

- allows the transmission and reception of settings to / from a software application resident on a server;
- communicate via standard protocols so that it can interface with any software application;
- allows the user access through a display in order to calibrate the sensors, enter the data, respectively view the recorded data and its settings;
- is able to detect when his position has changed (eg, fell from the stand, was stolen) and record this event;
- allows the setting of different parameters for each channel (sensor) - independent channels;
- allows the monitoring of limit values, with several thresholds for a single sensor;
- allows the transmission of alarms when the threshold values are exceeded and the measurement and data transmission range is changed;
- allows the transmission of alarms via SMS;
- allows the synchronization of his watch with that of the 3G / 4G network;
- allows remote configuration;
- allows the firmware update;
- allows data to be downloaded and deleted;

- allows the deactivation of the LEDs to reduce energy consumption.

*Software application for river pollution monitoring, data storage, processing and data analysis*

This application is intended for real-time pollution monitoring. This application is resident on a server or cloud and can be this by:

- web application software for alerting services
- web application for research

The functional requirements are as follows:

- retrieval and storage of data from multi-sensor hardware platforms
- preprocessing of acquired data
- data analysis using specific algorithms
- merging data from all multi-sensor hardware platforms (simulated platforms)

*Web application for alerting services*

This application is made on a web platform for its accessibility to any electronic device such as (computers, tablets, smartphones). It is dedicated to pre-warning services, respectively emergency services.

The functional requirements are as follows:

- Communication with river pollution monitoring application, data storage, processing and analysis
- Arranging through the web interface the information necessary for pre-warning services
- Disposition via the web interface of the information necessary for the emergency services
- Displaying alerts on the web interface with the signaling of the location where the detection was made (station), of the type of alert (exceeding the threshold, technical alert, etc.) and of the registered values.
- Recording alerts in a history and the possibility to navigate through the history
- Acknowledge an alert after a plan of action has been completed
- Sending alerts via SMS or e-mail to a list of operators.

*Web application for research*

This application is made on a web platform for its accessibility to any electronic device such as (computers, tablets, smartphones). It is dedicated to institutes and universities in order to take the raw data on pollution to make detailed statistics and predictions about pollution, reports on pollution events.

The functional requirements are as follows:

- Display data as dashboard charts embedded in a web page,
- Possibility to configure the dashboard by changing the position of the viewers (tables, graphs) in the dashboard and by changing the viewer
- Possibility to import data in a csv format that can then be displayed in excel.

*A. Web application for administration and maintenance*

This application is made on a web platform for its accessibility to any electronic device such as (computers, tablets, smartphones). It is dedicated to ensuring the configuration and monitoring of system equipment.

The functional requirements are as follows:

- Configuring the component equipment of the SmartMonWater system,
- Monitoring the component equipment of the SmartMonWater system,
- Generation of operation reports

- Possibility to generate technical alerts in case certain SmartMonWater components have operating problems
- Recording technical alerts with details on the time, type of equipment and the problem that occurred.

### 3 Conclusions and perspectives

The system architecture is now ready to use in laboratory conditions at the beginning and in natural environment lately. The data quality will be obtained by purchasing them with a high resolution, both spatial and temporal, using multi-parametric sensors on a hardware platform of its own multisensory acquisition. The acquired data is stored in CLOUD or local server for storage, analysis and interpretation. A software application based on artificial intelligence technologies that serves to identify and classify different polluted areas, locate pollution sources, predict their extinction, degree of pollution and help make decisions based on real-time detection. A web application will provide all the data collected in the field and it can be accessed on a common online platform. The next step is the connection to the sensors and the validation of data.

This work was supported by a grant of UEFISCDI – 54PTE/2020 – Intelligent System for Water Quality Monitoring – SmartMonWater.

### References

1. D. Yang, X. Shi, and P. Marsh, “Variability and extreme of Mackenzie River daily discharge during 1973–2011,” *Quat. Int.*, vol. 380–381, pp. 159–168, 2015, doi: <https://doi.org/10.1016/j.quaint.2014.09.023>.
2. P. O. Ukaogo, U. Ewuzie, and C. V Onwuka, “21 - Environmental pollution: causes, effects, and the remedies,” P. Chowdhary, A. Raj, D. Verma, and Y. B. T.-M. for S. E. and H. Akhter, Eds. Elsevier, 2020, pp. 419–429.
3. E. Mostert, “The European Water Framework Directive and water management research,” *Phys. Chem. Earth, Parts A/B/C*, vol. 28, no. 12, pp. 523–527, 2003, doi: [https://doi.org/10.1016/S1474-7065\(03\)00089-5](https://doi.org/10.1016/S1474-7065(03)00089-5).
4. L. Xiao, J. Liu, and J. Ge, “Dynamic game in agriculture and industry cross-sectoral water pollution governance in developing countries,” *Agric. Water Manag.*, vol. 243, p. 106417, 2021, doi: <https://doi.org/10.1016/j.agwat.2020.106417>.
5. S. Pasika and S. T. Gandla, “Smart water quality monitoring system with cost-effective using IoT,” *Heliyon*, vol. 6, no. 7, p. e04096, 2020, doi: <https://doi.org/10.1016/j.heliyon.2020.e04096>.
6. H. Kim *et al.*, “Fluorescent sensor array for high-precision pH classification with machine learning-supported mobile devices,” *Dye. Pigment.*, vol. 193, p. 109492, 2021, doi: <https://doi.org/10.1016/j.dyepig.2021.109492>.



# Design and constructive – technological development for children's art clothing

Radka Atanasova <sup>1,\*</sup>, Magdalena Pavlova <sup>1</sup>, and Monika Merkova <sup>1</sup>

<sup>1</sup>Technical University of Sofia, Department of Textiles, 1000 Sofia, Bulgaria

**Abstract.** The present study directs research and creative activity towards the realization of a design and constructive-technological concept for children's art clothing. The collection consists of clothes that are inspired by the children's imaginary world - fairy tale characters, animals, fruits. The educational function of the clothing is sought. The choice of models is subject to comfort and freedom of movement. The artistic design of the products in the collection is realized with the help of software for creating and processing images. The process of construction and modelling is algorithmized and performed automatically using a specialized CAD clothing system. The technological and operational maps are algorithmized and developed on CorelDraw. The designed constructions can be used for modelling a wide range of clothing for children.

## 1 Introduction

For millennia, children have been dressed the same way as adults. The children's costume was a scaled-down copy of the adult costume. The creation of clothing for children as a separate segment in fashion develops in parallel with the evolution of the consciousness of adults. Children's clothing, as an independent segment of adult fashion, began to develop only in the transition to modern society in the late eighteenth and early nineteenth centuries. The status of childhood changed for almost 200 years, and this process continued throughout the 19th century and ended in the 20th century - a century that is sometimes called the "age of the child". In the second half of the 19th century, light industry began to develop and marketing increasingly turned its attention to children's fashion. Children's stores appear and with their opening they begin to flourish. This is the period in which haute couture began to show interest in differentiating a particular segment of fashion - clothing designed specifically for children [1].

In the 21st century, children's clothing is a way for them to present themselves in the society [2]. Children's fashion is oriented to the image of the child and his life and to the spheres of his activity. The widespread perception of Sigmund Freud's concept that childhood is the most important stage in a person's development and his future depends on his first five years also changed children's fashion.

At the beginning of the 21st century, parents are starting to pay more attention to clothing as a way for a child to communicate with the world. The dynamics of today bring

---

\* Corresponding author: [ratanasova@tu-sofia.bg](mailto:ratanasova@tu-sofia.bg)

out the way of dressing as a necessary condition for self-realization. Clothing is becoming part of a system of nonverbal communication. Children's clothing is a way for them to make their own free choice, to stand out as members of society with an independent opinion, to state and affirm their individuality. The child is the object of various spiritual influences, he communicates with art in a specific cultural environment. In this direction, the attitude towards the colors of children's clothing is developing more and more, which have their specific influence on the development, temperament and emotions of children. In addition, children's clothing must take into account the peculiarities of growth, the specifics of hygiene habits and, above all, the psychological need for freedom of movement.

## 2 Methods and Results

### 2.1 Creative development of children's collection (fashion sketches, technical drawings)

The present children's collection consists of twenty art garments that are inspired by the children's imaginary world - fairy tale characters, animals, fruits. Fashion sketches of the products in the collection are presented on Fig. 1. The choice of models is subject to comfort and freedom of movement.

The educational function of the clothing is sought. The first ten models direct children to healthy nutrition. The fruits and vegetables used for inspiration, which the clothes remind of, are rich in vitamins and microelements and provoke children to try their taste. Some of them carry additional symbolism. Model 1. **Avocado**. It is an Aztec symbol of love and fertility, most likely because the trees grow in pairs. Model 2. **Pineapple**. It has become a popular traditional feng shui symbol of wealth, luck and prosperity. Model 3. **Strawberry**. The fruit is considered a symbol of Venus, the goddess of love, because of its heart shape and bright red color. Model 4. **Pear**. Pears, which evoke an association with a



Model 1. Avocado



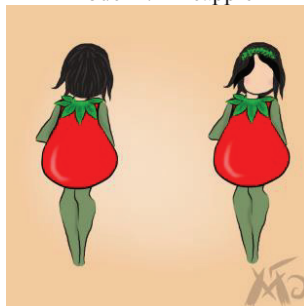
Model 2. Pineapple



Model 3. Strawberry



Model 4. Pear



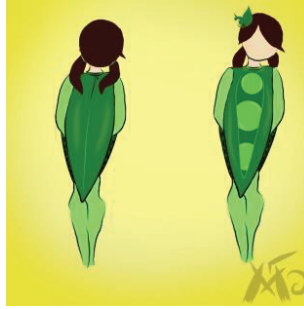
Model 5. Tomato



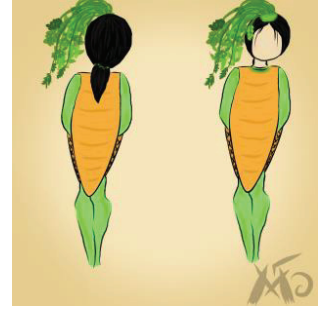
Model 6. Watermelon



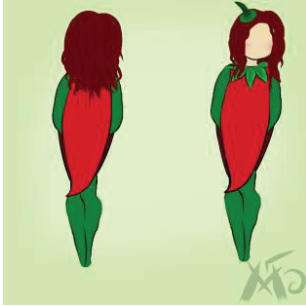
Model 7. Pumpkin



Model 8. Peas



Model 9. Carrots



Model 10. Red pepper



Model 11. Bee



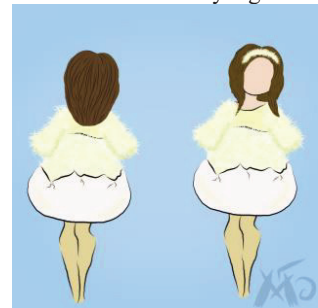
Model 12. Ladybug



Model 13. Butterfly



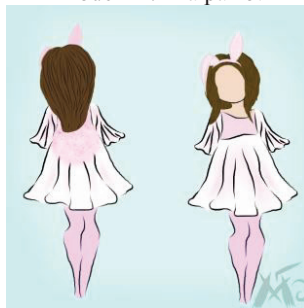
Model 14. Ara parrot



Model 15. Chicken



Model 16. Fox



Model 17. Rabbit



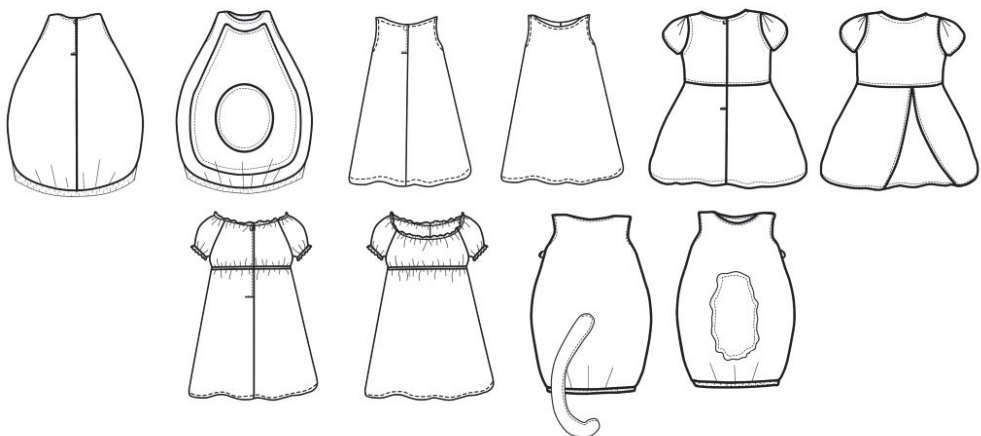
Model 18. Bear



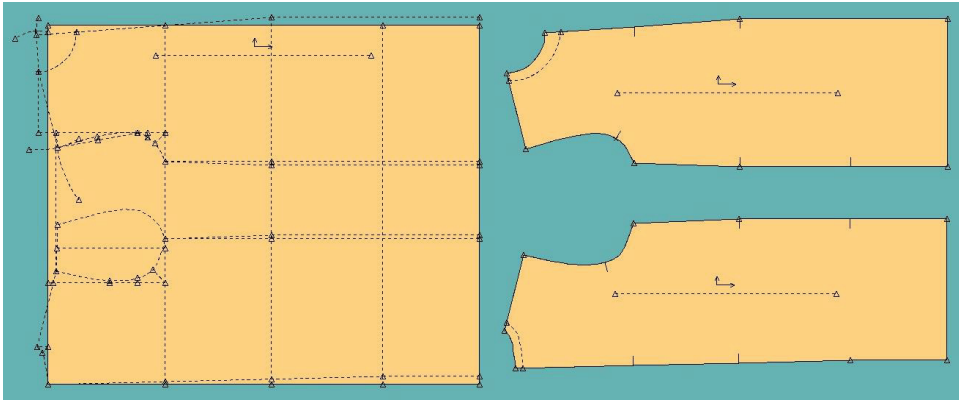
**Fig. 1.** Fashion sketches of the garments from the designed collection.

woman's body, play an important cult role in the rituals of the holidays dedicated to pregnancy, childbirth and motherhood. Model 5. **Tomato**. Model 6. **Watermelon**. Symbolizes fertility, abundance, well-being. Model 7. **Pumpkin**. Symbol of good health, permanence, immortality. In the Catholic diaspora there is a cult presence in the rituals of All Saints' Day. Model 8. **Peas**. In China, this vegetable is a symbol of fertility and wealth. Model 9. **Carrots**. Model 10. **Red pepper**. For Neapolitans, the red pepper is a symbol of happiness, success, luck and money when it is given as a gift, and it often happens that shopkeepers give such gifts to passing tourists.

The second ten models direct children to the world of fairy tales and animals. Since the lives of humans and animals are intertwined in everyday life, quite logically animals embody certain qualities that children want to have. The fairy-tale characters also pay attention to some negative traits of the character, which facilitates the parents in the educational process. Awareness of nature protection can also be nurtured through animals. Model 11. **Bee**. Bees are a symbol of hard work, and honey - abundance. Model 12. **Ladybug**. The presence of the ladybug is connected with the family, protection and fulfillment of various wishes. Model 13. **Butterfly**. The butterfly is emblematic of transformation and significant change. Model 14. **Ara parrot**. They cultivate a taste for a combination of bright colors and sociability due to the nature of these birds. Model 15. **Chicken**. Symbol of new life, home and care. Model 16. **Fox**. The cunning fox has a



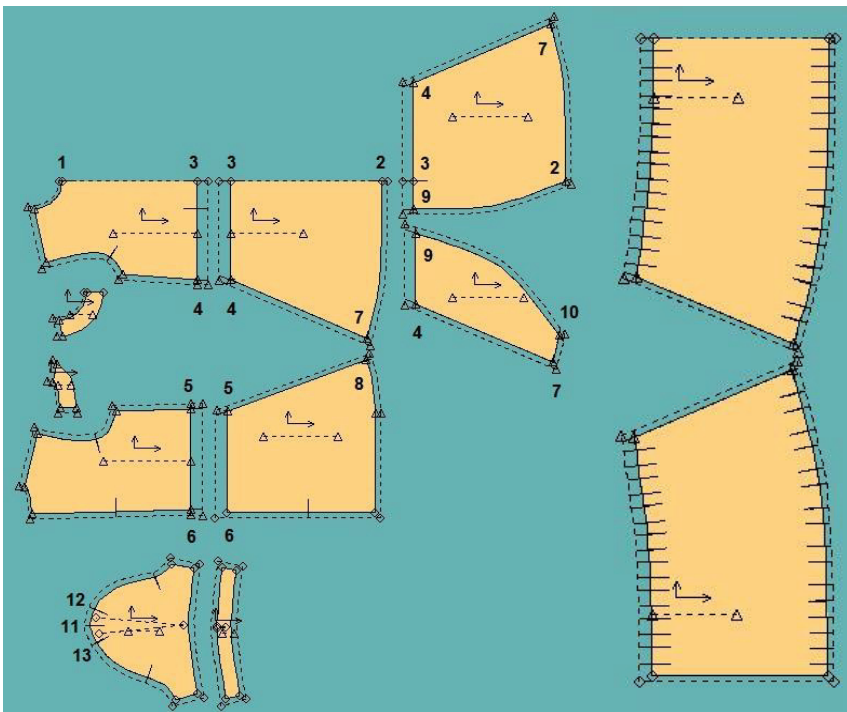
**Fig. 2.** Technical drawing of the garments, selected for sewing samples (from top left to bottom right side): Model 1. Avocado, Model 3. Berry, Model 6. Watermelon, Model 12. Ladybug, Model 20. Cat.



**Fig. 3.** Basic construction of children's dress 116/60/67,4.

reputation for being a cunning and deceitful character. Model 17. **Rabbit**. Always on-the-move, the rabbit is known for its alert nature. Model 18. **Bear**. It regarded as the symbol of resurrection and coming of new life. Another meaning associated with the bear is strength and power. Model 19. **Mouse**. It symbolizes modesty and innocence. Model 20. **Cat**. It varies from negative aspects such as being linked to witchcraft to very positive characteristics such as independence and intuition [3].

The artistic design of the products in the collection is realized with the help of software for creating and processing images FireAlpaca. This program is free digital painting software that is compatible with both Mac and Windows [4]. Technical drawings of the garments, selected for sewing samples, are presented on Fig. 2: Model 1. Avocado, Model 3. Berry, Model 6. Watermelon, Model 12. Ladybug, Model 20. Cat.



**Fig. 4.** Production patterns of Style 6. Watermelon.

## 2.2 Computer development of the production patterns





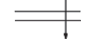
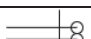

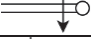




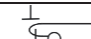
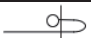



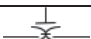
The object of the study was a child figure of a girl from the first height group with values of the main body dimensions as follows: height 116.0 cm, chest circumference 60.0 cm, hip circumference 67,4 cm. The basic construction of a children's dress without darts is calculated and developed, using 12 body dimensions by methodology [5]. The front and the back pieces of the basic construction of the dress are shown in Fig. 3. According to the features of the model, five selected garments from the collection are constructed. The graphic part was developed with automated use of the capabilities [6] of the specialized clothing software AccuMark, version V10 of Gerber Technology, USA. An example algorithm for making the patterns of Style 6. Watermelon is given in Table 1, and the corresponding production patterns are presented in Fig. 4. In the process of modeling the dress is separated along the waist line, widen by 20,0 cm along the hem line and in the bottom front part two asymmetrical details for the outer layer of the skirt are formed. The sleeves are short and puffed. The gathered element is a double-side fold at the shoulder area.


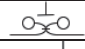




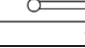

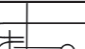


**Table 1.** Algorithm for construction modelling of Style 6. Watermelon.

No	Name of the step	Function in the CAD system	Parameters/ Elements of the drawing
1	2	3	4
1	Reshape the front middle line	Create/Ln/ 2 Pt/ 2 Pt	1-2
2	Replace the contour line	Modify/Ln Act/ Replace	
3	Rotate the front piece	Modify/Piece Act/ Rotate	Perform X- alignment
4	Reorient the direction of the grain line	Modify/Piece Act/ Realign grain	FR
5	Split the front and the back piece along the waist line	Modify/Piece Act/ Split Vertical	FR: 3-4 BK: 5-6
6	Measure the length of the side seam at the bottom part	Verify/Measure/ Ln Length	Dist: 27,0 cm
7	Widen the bottom part from the side seam	1. Create/Ln/ Circles/ Center 2. Modify/Ln Act/ Clip 3. Create/Ln/ 2 Pt/ 2 Pt 4. Modify/Ln Act/ Replace	Radius: 27,0 cm  End: 10,0 cm 2-7-4
8	Transform the front as a symmetrical piece	Modify/Piece Act/ Mirror	Notch mirror line
9	Construct the outer layer of the skirt in front piece	1. Create/Ln/ 2 Pt/ 2 Pt 2. Create/Ln/ 2 Pt/ Perp on Ln 3. Create/Ln/ Digitized 4. Create/Piece/ Trace	9-2, Beg: 13,0 cm 9-10, End: 5,0 cm Midpoint Dist: 4,0 cm Midpoint Dist: 2,0 cm Piece Name:
10	Extract the separate pieces from the assembled drawing	Create/Piece/ Trace	Piece Name:

1	2	3	4
11	Shape the short puff sleeve	Advanced/Pleats/ Tapered Pleat	Spread value: 2 x 1,5 cm
12	Construct the neckline and the sleeve hem facings	Create/ Piece/ Facing	Width: 3,0 cm
13	Add seam allowance and hem	Advanced/Seam/ Define	1,0 cm 2,0 cm
14	Place notches for assembling the details	Create/Notch/ Standard Advanced/Seam/ Regular Corner	

**Table 2.** Technological sequence map for manufacture the Model 6. Watermelon.

№	Name of the operation	Symbol	Stitch type	Comments
1	2	3	4	5
<b>01.00</b>	<b>Top Front</b>			
01.01	Overedge the seam allowances		504	
<b>02.00</b>	<b>Top back</b>			
02.01	Overedge the seam allowances		504	
<b>03.00</b>	<b>Skirt</b>			
03.01	Overedge the hem allowances, middle line and the side seams		504	
03.02	Stitch a decorative seam on the hem		301	With bar-tack
03.03	Sew the pieces of the front part in the side seams and waist of the dress		301	Without bar-tack
03.04	Sew the back middle seam to the marking		301	With bar-tack
03.05	Press the seam 03.04		Steam iron	
03.06	Sew the side seams		401.504	With bar-tack
03.07	Press the seam 03.06		Steam iron	
<b>04.00</b>	<b>Sleeves</b>			
04.01	Overedge the hem		504	
04.02	Sew the folds		301	Without bar-tack
04.03	Sew the inner seam of the sleeve		401.504	
04.04	Press the seam 04.03		Steam iron	
04.05	Sew the hem		301	With bar-tack
<b>05.00</b>	<b>Neckline</b>			
05.01	Fuse the neckline facings		Steam iron	
05.02	Overedge the facings		504	
05.03	Assembly the pieces of the neckline facings		301	With bar-tack
05.04	Press the seam 05.03		Steam iron	

1	2	3	4	5
<b>06.00</b>	<b>ASSEMBLY</b>			
06.01	Sew the shoulders and the side seams		301	With bar-tack
06.02	Press the seam 06.01		Steam iron	
06.03	Sew the top part and the skirt		401.504	
06.04	Press the seam 06.03		Steam iron	
06.05	Stitch a decorative seam on the waist of the dress		301	With bar-tack
06.06	Sew a zipper		301	With bar-tack
06.07	Assembly the facing and the neckline		301	With bar-tack
06.08	Press the seam 06.07 with a edge		Steam iron	
06.09	Stitch a decorative seam on the neckline		301	With bar-tack
06.10	Assembly the sleeves and the armhole		401.504	
06.11	Press the seam 06.10		Steam iron	
<b>07.00</b>	<b>FINISHING</b>			
07.01	Threads and chalk cleaning		Handwork	Handwork
07.02	Final ironing		Steam iron	

### 2.3 Technology for manufacture

The chosen children's art dresses, for which there are automatically developed patterns, are to be sewn. At the Table 2 is presented an example technological sequence map for manufacture a physical sample of the Model 6. Watermelon. Photos of some of the finished garments ("Watermelon", "Cat" and "Avocado") are shown in Fig. 5.

### 2.4 Areas of application of clothing from the collection

- ✓ children's birthdays, children's parties;
- ✓ celebrations in kindergarten and in the primary group at school;
- ✓ children's amateur performances, theater, masquerade balls.

## 3 Conclusions

In the present article, 20 unique models of children's art clothing inspired by children's imaginary world have been created. An educational effect on the child's character has been achieved. The applied part of the development includes fashion sketches of the designed clothes, technical and construction drawings, algorithms for computer aided pattern making, technological and operational maps.

The selected five models, for which patterns have been automatically developed, are to be sewn and their perception by a children's audience will be studied. The results of the present work open a field for further creative developments. The designed constructions can be used for modelling a wide range of clothing for children.





Fig. 5. Photos of the physical samples of the Styles “Watermelon”, “Cat” and “Avocado”.

This work has been accomplished with financial support by the Grant № 211XTД0002-02 Design and constructive – technological development for children’s art clothing.

## References

1. Rangelova, R., Concepts in designing children's clothing, doctors' thesis, NBU, Sofia (2014)
2. Atanasova, R., M. Pavlova, D. Sofronova, *Design and construction-technological concept for children's clothing*, PEPM'2018 with international participation, book of papers, ISSN: 1314-5371, pp. 394- 402, Sozopol, (201)8.
3. <https://skullbliss.com/blogs/news/animal-symbolism>
4. <http://firealpaca.com/>
5. Petrov, H., N. Petrov, N. Panova, *Apparel Pattern Making Part I*, Technica, Sofia (2006)
6. Without author, *User's guide AccuMark Professional Edition V10.0*, Gerber Technology Inc., a Business Unit of Gerber Scientific International (2015)

# Development of boutique denim clothing by the "upcycling" method

Magdalena Pavlova<sup>1,\*</sup>

<sup>1</sup>Technical University of Sofia, Department of Textiles, 1000 Sofia, Bulgaria

**Abstract.** In the present article have been developed denim models for women's figures with deviations from the conditionally nominal sizes, using the method of re-creative use - upcycling, in pursuit of motivation to reduce the textile waste from the sewing industry. A combination of three approaches is used: a concept for a boutique vision when creating the design of the models, as an attraction for each user; upcycling as an idea for reusing sewing products; moulage method in the development of the construction of clothing, based on a classic basic construction. To confirm the results, physical samples of the products were made. The research and creative activity is aimed towards realization of a design and construction-technological concept of denim clothing, which is the most common clothing used by absolutely all age groups, from babies to centenarians and is present in both the prêt à porter and haute couture. This makes the production of denim products, one of the most voluminous and polluting in the textile industry.

## 1 Introduction

Overproduction and the rapid development of the industry worldwide are causing catastrophic damage to the environment and the planet. Various world organizations are developing new methods of clean production led by the motto "Save the planet". The fashion industry is the second most polluting industry after the oil industry, worldwide. Therefore, the fashion designers empathic to protecting the environment for future generations should engage in solving these problems. For this purpose, they create bio or eco fashion, use recycled raw materials and reused textiles, create "upcycling" clothing, etc. Creative reuse has grown significantly in countries such as the United States, where in recent years the number of products labeled "upcycled" has increased by between 300% and 900% [1]. The proposed approach opens a market niche with the possibility of Internet-based small business and is aimed towards developing of an active attitude to global environmental problems, both for designers and clothing users.

In search of motivation to reduce the textile waste from the garment industry, denim models have been developed [2], using a combination of three approaches: a concept for a boutique vision of the design; upcycling as an idea for reusing sewing products; moulage method in the development of clothing design, based on a classic basic design for women's

---

\*Corresponding author: : [mpavlova@tu-sofia.bg](mailto:mpavlova@tu-sofia.bg)

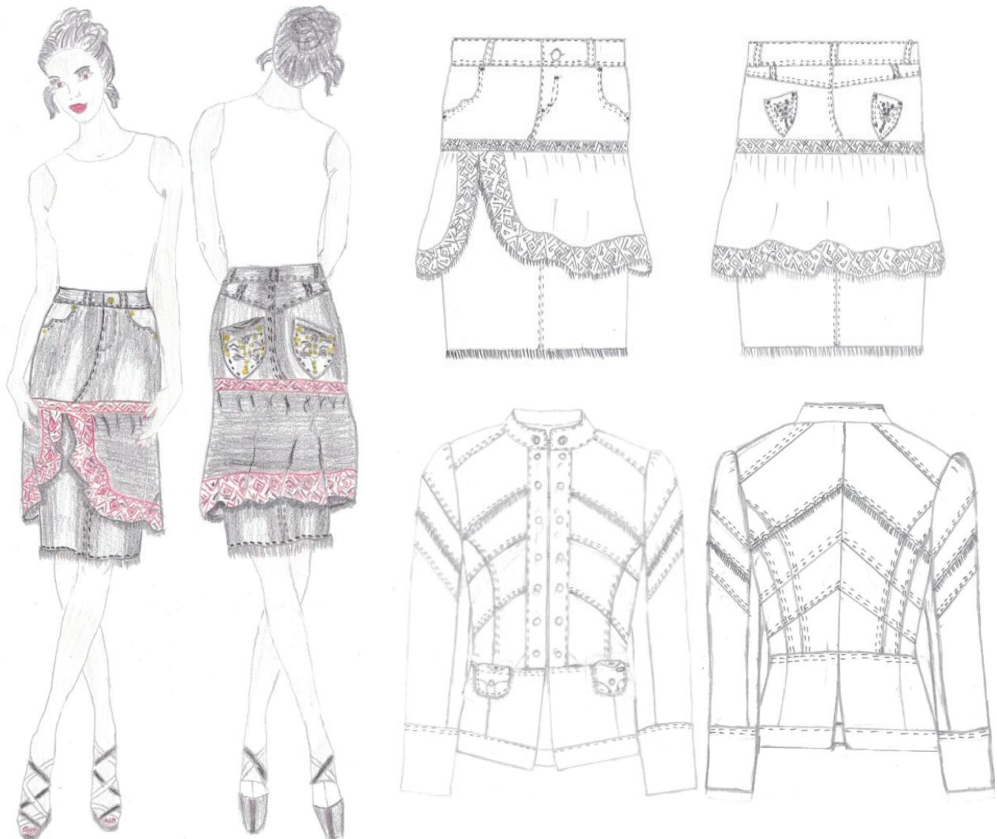
figures with deviations from the conditionally nominal sizes [3]. Upcycling or creative reuse to increase the value of the original product by changing and / or adding a personal view to the design of an already manufactured and used product [1]. The upcycling resources are used for as long as possible. Maximum value is extracted out of them, afterwards they are recovered several times, unlike the model purchase - use - disposal as waste. Upcycling as a method of clothing transformation is one of the solutions for sustainable living.

According to the moulage method [4], [5], the patterns are obtained directly from the human body or from a mannequin torso, by applying pieces of fabric or paper on its surface, after which the contours of the individual details are outlined in accordance with the model. The final shaping is done during the cutting and sewing. Several tests and corrections are mandatory.

## 2 Methods and Results

### 2.1 Development of models

Using the above combination of methods, two models of women's clothing were designed - a skirt and a jacket. Sketches of the designed products are presented on Fig.1.



**Fig. 1.** Fashion sketches and technical drawings of the designed clothes

The first model is a women's skirt in a straight silhouette, with a length above the knee and a gathered element along the hips, covered by ethnic motifs. The fastening is central

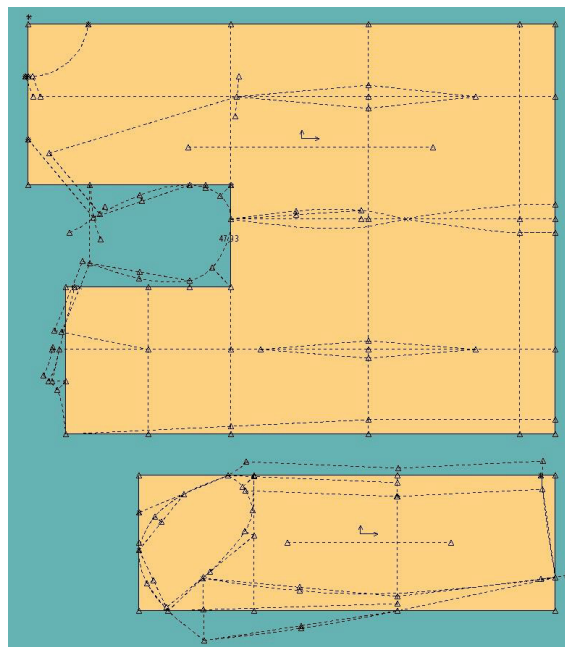
with a zipper and a button. The waist line is shaped with a belt and five loops. The side pockets are in shape. A triangular yoke is made on the back side. The pockets are externally attached with embroidered floral motifs.

The second model is a women's jacket in a semi-fitted silhouette with a length to the hip line, cut at the waist, with attached a long two seam sleeves. The front part is structurally divided in two along the waist line. The waist darts are transformed into princess seams. The design is completed by inclined decorative pieces in the front and back, which allow the use of multicoloured pieces. Along the waist in the front part there are 2 externally sewn pockets with a rounded shape. The fastening is by means of seven wire buttons, as the front parts touch frontally and are decorated with metal buttons. The back part has middle seam. A slit is made in the bottom part. The jacket has a collar with rounded edges. Three pairs of denim trousers in different colours were used for the production of the model - light blue, dark blue and black.

## 2.2 Development of clothing construction

The proposed combined approach, for creative reuse of clothing, is illustrated by creating two models of denim. Four jeans in different colours have been recycled. The designed clothing is made in two different ways, using the moulage method.

According to the first one the lady's skirt is formed directly on the human body, after the preliminary sketch, using direct cuts, outlining, fixing with pins and manual sewing. The finishing is done after undressing the products. A trial dressing is made to make further corrections, if necessary. The cycle is repeated until the desired result is achieved. Accepted corrections are fixed by stitches, according to the selected technology.

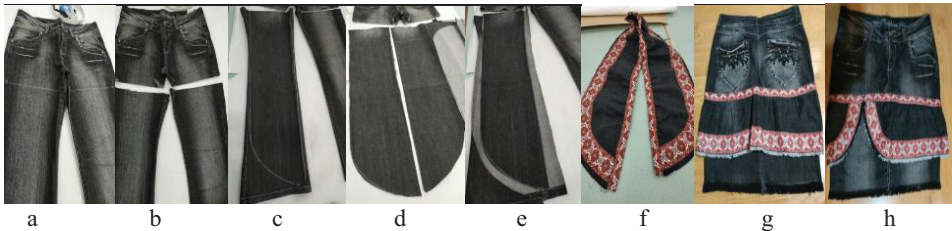


**Fig. 2.** Pattern making of the women's jacket - back, front and two seam sleeve

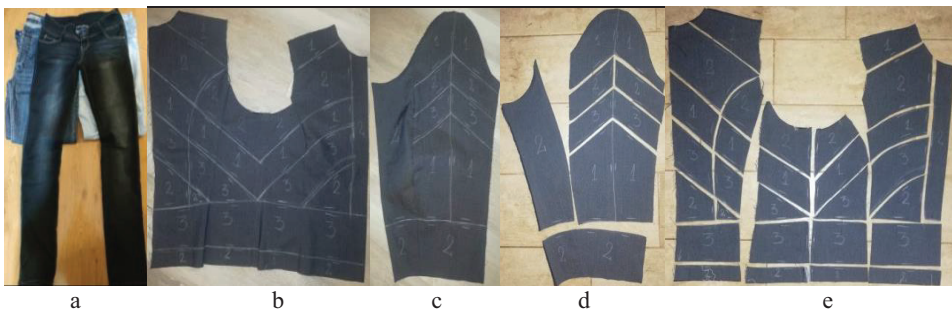
The women's jacket is developed by combining a base pattern according to a classical computational-analytical method and modeling as per the moulage method, following the "upcycling" principle. The product is modeled on the base construction, afterwards it is

formed directly on the torso, according to the preliminary sketch. For the purpose has been developed a basic construction of a jacket in a semi-fitted silhouette. The initial construction is made out of textile waste. After several consecutive tests on a human body, the patterns are outlined and the details are tailored. The basic construction is developed for a female figure of standard size 48 (164/96/104). The horizontal structural sections are dimensioned with the following ease values along the main structural lines: along the chest line 8.0 cm, along the waist line 8.0 cm, along the hip line 7.0 cm. The calculated front balance height is 5.2 cm. The functional dependences for calculating the structural dimensions are according to [6]. The take away value in the middle back is 2.0 cm. The additional length for gathering of the sleeve, obtained geometrically, is 3.7 cm. The functionality [7] of the specialized clothing software AccuMark, version V10 of the company Gerber Technology, USA were used for the pattern making of the construction. An algorithm for automated construction has been developed. The output pieces - back, front and two seam sleeve are presented in Fig. 2. They are used as a initial stage for moulage.

Both products - skirt and jacket are obtained by transforming women's denim pants with an elastomeric component (Fig. 3a, 4a).



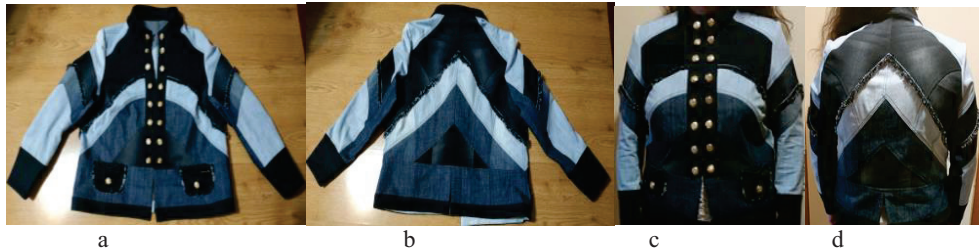
**Fig. 3.** Photos of selected stages of the sequence for transforming the pants into a lady's skirt



**Fig. 4.** Final adjustments, marking the details on the textile waste and cutting the patterns



**Fig. 5.** Laying the production patterns on the jeans and cutting the details of the jacket



**Fig. 6.** Photos of the women's jacket, developed by the "upcycling" method

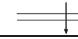
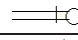
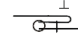
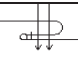
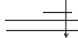
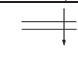
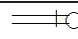
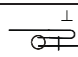
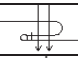
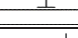
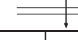

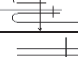
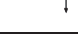
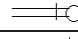
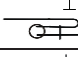
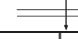
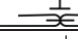
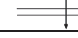
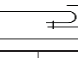
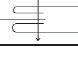
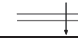
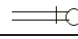
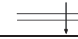

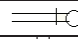
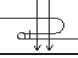
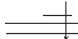
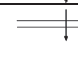
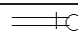
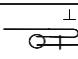
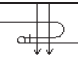
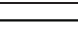
The models are presented with fashion sketches and technical drawings on Fig. 1. The stepwise transformation is illustrated by the photographic material on Fig. 3 a-h for the skirt and on Fig. 4a-e, Fig. 5 a-c. The final outlook of the women's jacket is presented face and back on Fig. 6 a - d. The sequence for transformation and production of the lady's skirt and lady's jacket is presented in details in Table 1 and Table 2.

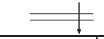
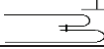

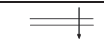
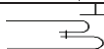
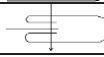


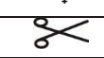

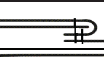
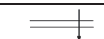
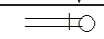
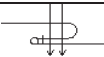
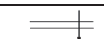
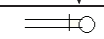
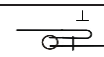
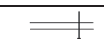
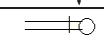
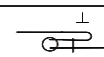
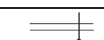
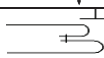
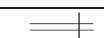

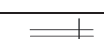
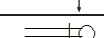
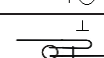
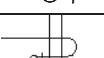


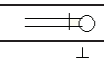
**Table 1.** Technological sequence map for transforming and manufacture a lady's skirt

№	Name of the operation	Symbol	Stitch type	Comments
1	2	3	4	5
1	Outlining and cutting the details		Handwork	
2	Overedge the band		504	
3	Sew the parts for front bottom, back and band		2x301	With bar-tack
4	Sew the front middle seam in the area below the zipper		301	in the direction of the right front
5	Sew the back middle seam		301	in the direction of the right back
6	Sew the middle of the gathered element		401.504	With bar-tack
7	Sew the decorative band at 1 cm from the hem of the gathered element		2x301	With bar-tack
8	Reinforce the seam under the band		301	Without bar-tack
9	Set up the gathering of the gathered element		301	
10	Sew the decorative band and the gathered element		2x301	With bar-tack
11	Outline and cut the the gathered element		Handwork	Handwork
12	Sew the front and back bottom pieces		401x504	With bar-tack
13	Sew the top and bottom part		401x504	With bar-tack
14	Pressing the 13		Steam iron	
15	Define the position of the gathered element			On the body
16	Sew the gathered element		301	With bar-tack
17	Reinforce the seam 2 cm from the hem		301	
18	Unweave the hem of the gathered element		Handwork	Handwork
19	Threads and chalk cleaning		Handwork	Handwork
20	Final ironing		Steam iron	

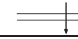
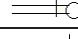
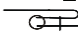
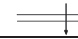


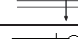
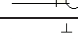
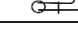

**Table 2.** Technological sequence map for transforming and manufacture a lady's jacket

№	Name of the operation	Symbol	Stitch type	Comments
1	2	3	4	6
<b>00.00</b>	<b>Cutting</b>			
<b>00.01</b>	Numbering		Handwork	Handwork
<b>00.02</b>	Fuse the top and bottom collar, plastron		Steam iron	
<b>01.00</b>	<b>FRONT</b>			

01.01	Sew the component pieces		301	With bar-tack
01.02	Overedge the seam allowances		504	
01.03	Pressing the 01. 02		Steam iron	
01.04	Reinforce the seam on the diagonal seams		302	
01.05	Unweave the seam allowance		Handwork	1 cm
01.06	Making a decorative seam		213	Put in a thread
01.07	Sew the front middle and the front side part		301	With bar-tack
01.08	Overedge the seam allowances		504	
01.09	Pressing the 01. 08		Steam iron	
01.10	Making a decorative seam		302	
01.11	Fold and press of the plastron		Steam iron	
01.12	Sew the front piece and the plastron		301	With bar-tack
01.13	Pressing the 01.12		Steam iron	
01.14	Closing seam of the plastron		301	Without bar-tack
01.15	Sew the bottom front middle and the front side part		301	With bar-tack
01.16	Overedge the seam allowances		504	
01.17	Pressing the 01. 16		Steam iron	
01.18	Sew the pieces of the hem band		301	Without bar-tack
01.19	Pressing the 01. 18		Steam iron	
01.20	Sew the two bands		301	With bar-tack
01.21	Press with the edge		Steam iron	The edge towards the inner band
01.22	Attach the band with a top seam		301	
02.00	<b>BACK</b>			
02.01	Sew the component pieces		301	Without bar-tack
02.02	Overedge the seam allowances		504	
02.03	Sew the back middle seam		301	With bar-tack
02.04	Sew the middle and the side part		301	With bar-tack
02.05	Overedge the seam allowancesca		504	
02.06	Making a decorative seam		302	
02.07	Unweave the seam allowance		Handwork	1 cm
02.08	Making a decorative seam		213	Put in a thread
02.09	Sew the back middle and back side part		301	With bar-tack
02.10	Overedge the seam allowances		504	
02.11	Pressing the 02. 10		Steam iron	Towards the back middle
02.12	Make a decorative seam on the assembly seams		302	
02.13	Overedge the seam allowances		504	

02.14	Sew the slit		301	With bar-tack
02.15	Press with a edge		Steam iron	
02.16	Sew the pieces of the bands		301	Without bar-tack
02.17	Assembly the bands		301	With bar-tack
02.18	Press with a edge		Steam iron	
02.19	Close the band with a top seam		301	
03.00	<b>COLLAR</b>			
03.01	Assembly the inner and upper collar		301	With bar-tack
03.02	Sew a reinforcing seam		301	
03.03	Cut the seam allowance		Handwork	Handwork
03.04	Turn the collar to the face side		Handwork	Handwork
03.05	Pressing the 03. 04		Steam iron	The edge towards the inner collar
04.00	<b>SLEEVES</b>			
04.01	Sew the component pieces		301	Without bar-tack
04.02	Overedge the seam allowances		504	
04.03	Making a decorative seam		302	
04.04	Sew the elbow seam		301	With bar-tack
04.05	Overedge the seam allowances		504	
04.06	Lies on one side and press the ellbow seam		Steam iron	
04.07	Sew the inner seam of the sleeve		301	With bar-tack
04.08	Overedge the operation 04.07		504	
04.09	Lies on one side and press the inner seam		Steam iron	
04.10	Assembly the inner and upper cuff		301	With bar-tack
04.11	Turn the cuff to the face side and press with a edge		Steam iron	towards the inner cuff
04.12	Sew the inner cuff and the sleeve		301	With bar-tack
04.13	Closing seam of the cuff		302	With bar-tack
05.00	<b>ASSEMBLY</b>			
05.01	Sew the shoulders and the side seams		301	Without bar-tack
05.02	Overedge the seam allowances		504	
05.03	Lies on one side and press the assembly seams		Steam iron	
05.04	Making a decorative seam of the shoulders		302	With bar-tack
05.05	Sew the front bottom pieces and the back		301	Without bar-tack
05.06	Overedge the seam allowances		504	
05.07	Lies on one side and press the assembly seams		Steam iron	



05.08	Sew the top and bottom part		301	Without bar-tack
05.09	Overedge the seam allowances		504	
05.10	Lies on one side and press the assembly seams		Steam iron	
05.11	Sew the front and the pocket		301	decorative seam
05.12	Unweave the seam allowance of the pocket		Handwork	1 cm
05.13	Assembly the collar and the neck line		301	With bar-tack
05.14	Pressing the 05. 13		Steam iron	
05.15	Assembly the sleeves and armhole		301	With bar-tack
05.16	Overedge the seam allowances		504	
05.17	Press the armhole		Steam iron	
06.00	<b>Finishing</b>			
06.01	Mark the place of the buttons		Handwork	Handwork
06.02	Sew the buttons		Handwork	Handwork, 25p
06.03	Threads and chalk cleaning		Handwork	Handwork
06.04	Final ironing		Steam iron	

### 3 Conclusions

The article proposes a creative method for reducing textile waste from the sewing industry. A women's skirt and a women's jacket of denim clothing has been created. A combination of three approaches is used: a concept for a boutique vision when creating the design of the models, as an attraction for each user; upcycling as an idea for reusing sewing products; moulage method in the development of the construction of clothing, based on a classic basic construction. The effect is also enhanced by the focus on denim products, whose production is one of the largest in the textile industry. To confirm the results, physical samples of the products were made.

The proposed approach opens a market niche with the possibility of Internet-based small business and is aimed towards developing of an active attitude to global environmental problems, both for designers and clothing users.

### References

- <https://intercongreen.com/2010/02/17/recycling-vs-upcycling-what-is-the-difference/>
- Nencheva M., *Anti-consumer approach to create denim clothes using the principle of upcycling and mulage*, Diploma thesis, Sliven (2020)
- Atanasova, R., D. Kasabova, *Design of mass customized women's clothing*, National Textile Conference 2014, Book of reports, ISBN: 978-954-91951-2-5, pp. 223-232, Sofia (2014)
- <https://www.universityoffashion.com/>
- Pavlova, M., R. Atanasova, *Developing a creative method for reuse of clothing*, E3S Web Conference, Vol. 207, <https://doi.org/10.1051/e3sconf/202020703006>, PEPM'2020, (2020)
- Petrov, Hr., *Apparel Pattern Making*, TU-Sofia, Sofia (2009)
- Without author, *User's guide AccuMark Professional Edition V10.0*, Gerber Technology Inc., a Business Unit of Gerber Scientific International (2015)
- <https://textilebeat.com/wp-content/uploads/2014/12/Global-apparel-fibre-consumption-vs-population-FINAL.jpg>

# Methods for personal cooling in hot environment used in clothing and wearables

Atanas Vasilev<sup>1,\*</sup>, Radostina A. Angelova, and Rositsa Velichkova

<sup>1</sup>Technical University of Sofia, Department of Hydroaerodynamics and Hydraulic Machines, 1000 Sofia, Bulgaria

**Abstract.** The use of an efficient personal cooling system in hot environments is becoming increasingly popular, as the increased air temperature provokes thermophysiological discomfort, heat stress, reduced productivity and could lead to several health issues. Different methods and devices for personal and local cooling have been developed over the years. The paper summarises the cooling methods applied in clothing and wearable items: phase-change materials, Peltier elements, evaporative cooling, water cooling and hybrid cooling. The local vs total (of the whole body) cooling is examined. The passive and active colling are analysed in terms of advantages, disadvantages and application.

## 1 Introduction

In recent years, more and more attention is paid to personal cooling, which allows local cooling of the body or parts of it in a hot environment. The use of an efficient personal cooling system is becoming increasingly popular, but it is known that there have been developments since the early twentieth century [1]. Heat stress is a serious problem, potentially dangerous to the health of workers who perform activities in hot outdoor and indoor environments: in the mining industry, construction, non-ferrous metal foundries, fire safety, military activities, the production of bricks and tiles, glassmaking, smelting of metals and alloys, cosmonautics [2-6].

The natural cooling of the human body is done by sweating. It is a thermophysiological reaction to reduce the temperature of the body's core to 37 °C in a hot environment so as not to jeopardize the proper functioning of internal organs, and the physical and mental state of man [7]. However, when it is necessary to wear protective clothing (firefighters, founders, welders), due to the presence of textile layers (system of layers), sweat fails to cool the human body sufficiently through the natural process of heat and moisture transfer [3, 8-9]. Therefore, lack of adequate cooling (often possible only through the head) can have serious consequences for the workers' productivity and health.

That is why people who work in high-temperature conditions have to rely on personal cooling devices increasingly. These devices are expected to reduce heat stress and fatigue and improve productivity and thermophysiological comfort. Indoors, personal cooling

---

\* Corresponding author: [atanasvasilev9@gmail.com](mailto:atanasvasilev9@gmail.com)

devices can completely replace HVAC systems in specific situations where the energy costs outweigh their usefulness. On the other hand, the presence of HVAC systems that allow the simultaneous maintenance of the thermal comfort of a large number of occupants (usually at a lower cost) is a kind of constraint on the development of devices and methods of personal cooling. Outdoors, however, personal cooling is the only option.

Over the years, various personal methods and devices for local cooling have been developed. These are mainly cooling clothing items aimed to reduce heat load and tailored to gender, workload, and the other work or protective clothing [10-13]. The most used products are vests or full suits [5, 10, 14-16]. They are active when the garments utilise external cooling sources: electrical components, additional cooling elements and units, and forced blows [3, 6, 8-9, 13, 15]. Passive items are based on applying phase-change materials, frozen gels, ice [2, 5, 11, 16].

The paper summarises the existing methods for cooling the human body using clothing and textile wearables in a hot environment. Passive and active cooling are considered together with local and total cooling of the human body. Furthermore, advantages, disadvantages and application of different methods are discussed.

## 2 Working in a hot environment

According to the definition of the Canadian Center for Occupational Health and Safety [17], an increase in temperature above 27 °C and relative humidity above 60% is considered a hot environment. The presumption is that an essential part of people feels comfortable at an air temperature of 20 °C to 27 °C and relative humidity of 35% to 60%. The systematic review in [18] has involved in its analysis of the hot environment all studies conducted in air temperature above 25 °C.

Even though the environment is hot, it only causes thermal discomfort, as long as the body's thermoregulatory system effectively copes with excess heat. If the core temperature rises even by 2-3 °C, the body still retains its functionality [17]. However, side effects can occur that reduce performance, damage health and could even lead to death. Working in such an environment poses a serious threat to human health because physical fatigue also increases due to the rise in body temperature and dehydration. Fatigue can lead to injuries and accidents at work. There is also a loss of concentration, which which can provoke injuries and accidents at work [7].

Such working conditions require a different work regime, including frequent breaks to prevent potential consequences for workers.

## 3 Personal cooling in the hot environment

Personal cooling is related to the cooling of the individual in a hot environment, regardless of the presence or absence of HVAC systems (for indoor environments, including means of transport). It can be provided by personal technical devices, for example, a mini fan connected to the computer. Wearable devices that are connected to and move with the human body can also be used.

Local cooling, in many cases, is synonymous with personal cooling, including in research publications. However, it is associated with cooling parts of the human body: e.g. head, nape, torso therefore, personal cooling items can be *local* if they provide cooling of a part of the body or *total* if they cool the whole body. Of course, both local and total cooling effect the thermoregulatory system, causing reactions in the whole body.

### 3.1 Phase-change materials

Phase-change materials (PCMs) are a passive cooling medium used for local cooling. PCMs are mainly incorporated in clothing items and wearable devices (collars, helmets), worn on the upper part of the human body, namely the torso and the head [5, 11, 16, 19]. PCMs are in the form of separate segments (packages), which facilitates their use and their easy replacement. As a part of the protective workwear, the PCM segments do not cause any discomfort. The weight of a cooling vest with PCMs in most cases is up to 3 kg. [11, 16].

Frozen gels, paraffin and salts are mainly used as phase-change materials. For cooling, they are used in their frozen state and have efficiency until the respective material melts. PCMs have a number that indicates the material's melting temperature: i.e. PCM5, PCM10, PCM 15 [16]. Figure 1 shows a microscope view of polyester fibres with incorporated PCM (courtesy of ©Outlast Technologies GmbH).

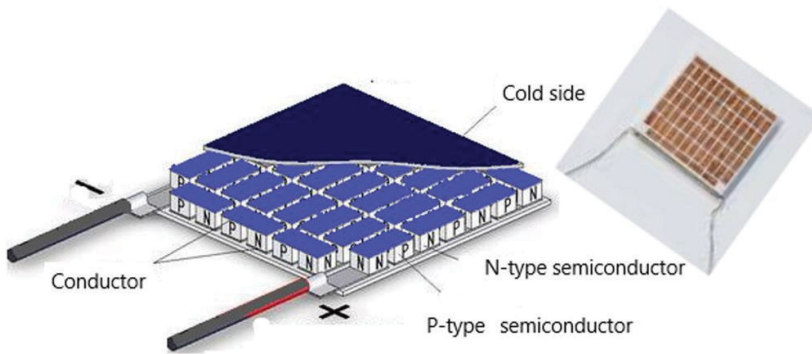


Fig. 1. Polyester fibres with PCM (courtesy of ©Outlast Technologies GmbH)

The application of PCMs in clothing and wearables for personal cooling in hot environments is very large. Belonging to the passive cooling methods, it is one of the most commonly used in various work environments, sports and other physical activities due to easy maintenance and relatively good efficiency over time.

### 3.2 Peltier elements

The Peltier element is a semiconductor composed of a large number of semiconductor pairs of two different materials – Fig. 2. When voltage is applied to one side of the element, it is heated while the other is cooled. This makes it a universal source of heat and cooling.



**Fig. 2.** Peltier element

Peltier elements are mainly used for cooling: the heat received from its heated surface is removed through a fan. Being a high-efficiency tool, they are common in cooling systems with a negligibly small volume. This is one of the most common methods for active cooling, used in clothing and wearables for both local and total cooling of the human body. There are design ideas for local stationary cooling in a closed system with a cold water carrier and total cooling in a mobile suit with a system of fans and built-in air duct elements [3, 8, 20].

### 3.3 Evaporative cooling

Evaporative cooling is an active cooling technique. Evaporative cooling vests have a built-in evaporative microenvironment, created in an intermediate layer, located between the cooling vest and human skin. The vests are focused on cooling the back of the torso. The released by the human body sweat is absorbed into highly hygroscopic layers. Thanks to the forced introduction of hot air from the environment with the help of small fans, sweat evaporates, thus assuring the cooling process.

Two types of evaporative cooling vests have been developed – a single evaporative cooling channel vest and a Maisotsenko cycle (M-cycle) vest [9]. They differ mainly in that the M-cycle technique uses two channels: a dry and evaporative channel. The M-cycle provides faster evaporation and thus better cooling because the sweat absorbed in the hygroscopic layer is subjected to double heating – once by the human body and a second time by the air, which once entered the inlet channel begins to give off heat. The formation of two channels is done by using a thin conductive fabric to transfer heat from the inlet channel to the outlet [9]. Figure 3 shows the design of the evaporative cooling vest (courtesy of ©TechNiche LLC).

### 3.4 Water cooling

Water cooling is another type of personal cooling methods designed to cool both locally or the whole body. The system is active, using a cold carrier – a mix of ice and water.

The water cooling wearables (suits or vests) are equipped with a backpack tank of water and ice mixture. The tank is well insulated to minimize the impact of weather conditions on its efficiency over time. The suit or vest is supplied with water via hoses running throughout the garment and are integrated into it – Fig. 4. The used water circulates forcibly with the help of a pump powered by a portable battery. The cooling clothing item is made

of highly elastic textile materials, making it comfortable to wear without affecting human motions [15].



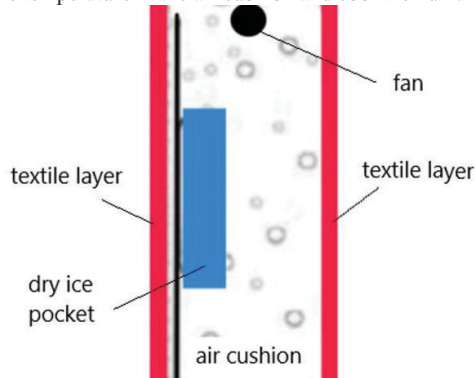
**Fig. 3.** Evaporative cooling vest (courtesy of ©TechNiche LLC)



**Fig. 4.** Water cooling suit (courtesy of ©BatoryHeatedClothing.com)

### 3.5 Hybrid cooling

The hybrid personal cooling systems belong to the active cooling methods and are focused on cooling the whole body. They use dry ice and air ventilation [9]. The textile layers for the suits are specially selected to be with close to zero permeability. An almost hermetically sealed volume is obtained inside the suit, which volume can be defined as an air cushion between the human body and the hot environment – Fig. 5. Dry ice is placed in specially designed pockets. In addition, fans are used to move the air around the pockets with ice. Thus, they reduce the temperature in the air cushion and cool the human body.



**Fig. 5.** Hybrid cooling principle

## 4 Passive vs active cooling clothing and wearables

The passive cooling clothing items and wearables are among the most common personal cooling devices. Their design is relatively simple. The clothes are made so that the installation and replacement of the cooling source are rapid and easy; in most cases, there are additional pockets in which the cooling elements are placed. If the environment does not require constant cooling of the human body, passive clothing and wearables find more application than active ones.

The main disadvantage of the passive cooling methods is that the cooling elements depend on additional cooling devices – refrigerators or freezers, in which to store before their operation. Another disadvantage is that they ensure local cooling since the cooling source is fixed in a particular area. That is why passive cooling clothing and wearables are not particularly preferred and are not widely used in hot environments with constantly high temperatures. In addition, local cooling can impair the comfort of the wearer. Last but not least condensation appears when the cooling packages melt, which is also a disadvantage. The efficiency of the active colling clothing and wearables is significantly higher, and their application is wider than the passive cooling clothing and wearables because of the applied working principle. The cooling is done by a system of hoses, a circulating pump, fans and a cooling source, which increases the cooling efficiency. Thanks to these components, the cooling is not localized on a specific area but is evenly distributed and covers the entire area of the cooling garment.

The main disadvantage of the active cooling method is that a single failure in the cooling system may require replacing the entire cooling item. In most cases, the components used in the system are embedded in the various layers of the clothing system, and their replacement is tedious, if possible, at all. The power source also limits the efficiency.

From the point of view of maintenance, passive cooling clothing and wearables are far easier to maintain and clean than active ones. The reason is that the cooling elements are easily removed. With active cooling vests and suits, due to the many components in them, maintenance and cleaning must be carried out with great care; otherwise, damage to the cooling system could occur during washing. For example, in cooling clothing with a built-in hose used to circulate the coolant, detergent may get inside the hose if the inlet and outlet remain open when washing. It could reduce the cooling efficiency during operation and even damage a component of the cooling system.

## 5 Local vs total cooling clothing and wearables

The considered examples showed that the cooling clothing are local (vests) and total (suits). The wearables (collars, scarves, helmets) are used for local cooling only.

The vests are very practical, light and comfortable and much more used than cooling suits. However, due to their limited size, they cannot cover a large part of the human body, leading to thermal discomfort or thermal stress.

Suits are far more preferred in work environments where the human body needs constant protection against high temperatures because, unlike vests, they cover almost the entire body and the possibility of thermal discomfort or hot stress is avoided.

## 6 Conclusions

Different solutions related to the personal cooling of the human body in a hot environment have been presented. The existing cooling methods, applied in clothing and wearable items:

PCMs, Peltier elements, evaporative cooling, water cooling and hybrid cooling, were summarised and discussed. The local vs total cooling was examined. The passive and active cooling was analysed in terms of benefits, disadvantages and application.

The paper is supported by a PhD project grant from the Technical University of Sofia.

## References

1. C.A. Wellman, Body-ventilating apparatus (US Patent 776003, 1904).
2. Y. Yang, J. Stapleton, B.T. Diagne, G.P. Kenny, C.Q. Lan, C. Q., *Appl Therm Eng*, **47**, 18-24 (2012).
3. M. D'Angelo, J. D'Angelo, M. Almajali, K. Lafdi, A. Delort, M. Elmansori, *Energ Conserve Manage*, **79**, 140-145 (2013).
4. M. Morrissey, F. Wang, *Air and water perfusion-based personal cooling systems (PCSs) to protect against heat stress in protective clothing* (Woodhead Publishing, 2014).
5. M. Itani, D. Ouahrani, N. Ghaddar, K. Ghali, W. Chakroun, *Build Environ*, **107**, 29-42 (2016).
6. C. Al Sayed, L. Vinches, S. Hallé, *Therm Sci Eng Prog*, **11**, 1-7 (2019).
7. R.A. Angelova, *Environmental Exposures and Human Health Challenges* (IGI Global, 2019).
8. I. Sahta, I. Baltina, J. Blums, V. Jurkans, *The control of human thermal comfort by the smart clothing*. In SHS Web of Conferences (Vol. 10, p. 00040). EDP Sciences (2014).
9. R. Raad, M. Itani, N. Ghaddar, K. Ghali, *Int J Therm Sci*, **142**, 1-13 (2019).
10. Y. Yang, J. Stapleton, B.T. Diagne, G.P. Kenny, C.Q. Lan, *Appl Therm Eng*, **47**, 18-24 (2012).
11. F. Mneimneh, C. Moussalem, N. Ghaddar, K. Ghali, I. Omeis, *J Therm Biol*, **91**, 102634 (2020).
12. R. Iwata, T. Kawamura, Y. Hosokawa, L. Chang, K. Suzuki, I. Muraoka, *J Therm Biol*, **94**, 102746 (2020).
13. S. Del Ferraro, T. Falcone, B.M. Rondinone, V. Molinaro, *Int J Ind Ergonom*, **75**, 102895 (2020).
14. T. Yoshida, H. Shin-ya, S. Nakai, H. Ishii, H. Tsuneoka, *The effect of water-perfused suits and vests on body cooling during exercise in a hot environment* (Elsevier Ergonomics Book Series 2005).
15. F. Wang, C.S.W. Chow, Q. Zheng, Y. Ke, B. Yang, X. Zheng, ... H. Zhou, *Energ Buildings*, **205**, 109561 (2019).
16. H. Pourghayoomi, H. Dehghan, M.J. Tarrahi, *Health Scope*, **9**(2) (2020).
17. S. Munten, S. Dorman, D. Gagnon, *Guide to thermal stress in the workplace* (Laurentian University, ON Canada, 2021).
18. A. Ruddock, B. Robbins, G. Tew, L. Bourke, A. Purvis, *Sports Med*, **47**, 517-532, (2017).
19. M. Zhao, C. Gao, F. Wang, K. Kuklane, I. Holmer, J. Li, *Text Res J*, **83**, 418-425 (2013).
20. H. Yang, B. Cao, Y. Ju, Y. Zhu, *Energ Buildings*, **198**, 528-541 (2019).



# Modification of Leather Surface Using Low-Pressure Plasma and Antimicrobial Reagent

Sanja Ercegović Ražić<sup>1,\*</sup>, Jadranka Akalović<sup>1</sup>, Tomislav Ivanković<sup>2</sup>, Anja Ludaš<sup>1</sup> and Katarina Ištef<sup>1</sup>

<sup>1</sup>University of Zagreb, Faculty of Textile Technology, Department of Materials, Fibers and Textile Testing, Prilaz baruna Filipovića 28a, 10000 Zagreb, Croatia

<sup>2</sup>University of Zagreb, Faculty of Science, Department of Biology, Rooseveltov trg 6 10000 Zagreb, Croatia

**Abstract.** Investigations, which are related to plasma efficiency on the treated leather surface, are significant in the development of ecologically and economically friendly processes in obtaining material of desired functional properties. Through the pretreatments using plasma different chemical-physical reactions in the surface layer of treated leather are occurred resulting in improved reactivity. In this paper, modification and functionalization of bovine leather using 1,2,3,4-butanetracarboxylic acid and chitosan were explored. Pretreatments of leather samples were realised using argon and oxygen plasma to assess various influence of chemically reactive oxygen and inert argon gas. Two different bovine leathers - chrome tanned leather and leather tanned with synthetic tanning agent (Cr-free) were chosen for treatments. Analyse of the surface morphology was conducted with SEM microscopy, while the chemical changes using ATR-FTIR spectroscopy. Antimicrobial effectiveness of treated leather was tested with qualitative Agar diffusion plate test against two bacterial *Staphylococcus aureus* and *Klebsiella pneumoniae*. Obtained results indicated how applied oxygen and argon plasma pretreatments in optimized process conditions contribute to the improvement of tested functional properties. Achieved surface changes positively affected on leather surface reactivity and antimicrobial effectiveness, particularly Cr-free leather.

## 1. Introduction

The leather industry is one of the huge polluters of the environment, because of that it is important to develop environmentally friendly procedures. A major problem is the proven treatments, which are mainly carried out by conventional procedures, and are most often very harmful to the environment. The use of plasma as a medium for property modification is an acceptable technique because its application could completely replace, or at least shorten the processing time and use of large amounts of water and chemicals in order to achieve the desired properties of leather product. The main advantages of cold plasmas are

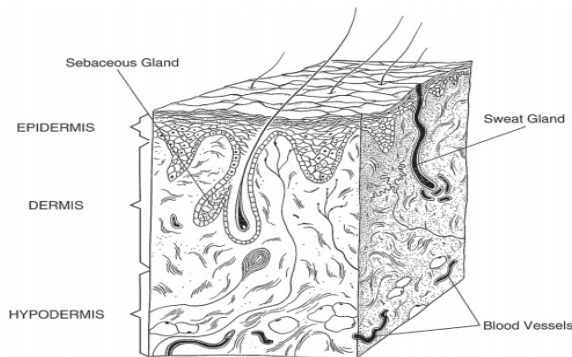
---

\* Corresponding author: [sanja.ercegovic@ttf.unizg.hr](mailto:sanja.ercegovic@ttf.unizg.hr)

applicability to all kinds of materials without negative effects on the basic properties of the material, without high consumption of chemicals, water and energy. Plasma treatment impact to the modification surface layer of the treated leather, resulting in the surface cleaning and its activation thus achieving better hydrophilicity (absorptivity) for some new chemical reactions. At low-pressure plasma, it is possible to apply chemical agents in monomeric form, which have the ability to polymerize with the substrate, whereby cleavage or crosslinking of the agents on the surface can take place, in order to achieve and /or improve the functional properties [1].

Microorganisms have a significant, often negative impact on human health in the form of the development of unpleasant odours, stains and fungal diseases, so today there are a very large number of different antimicrobial agents. Recently, it has become important as an antimicrobial agent gaining chitosan due to its excellent biocompatibility and biodegradability, excellent antimicrobial properties and great availability in nature. Therefore, it was used in this work as an antimicrobial agent with environmentally friendly technology of cold low-pressure plasma on cowhide, which is coated with various agents in the production phase. The prepared chitosan solution was applied to treated bovine leather by the method of horizontal spraying of the agent with the aim of achieving antimicrobial efficacy against targeted gram-positive *Staphylococcus aureus* and gram-negative *Klebsiella pneumoniae* bacterial species [2, 3].

Leather making is one of the oldest human crafts present in history for more than 3000 years. Humans used the leather of slaughtered animals to protect their bodies from the weather and injuries, and gradually for other purposes, such as making boats, tents, and other products [4]. The leather is one of the fundamental importance to the animal because it has various physiological functions, the most important of which are the regulation of body temperature, storage of nutrients, protection and excretion of waste products [5]. The waterproof layer of the leather acts as a barrier against various infections, preventing the absorption of water from the outside and the loss of water from the inside. Animal leather consists of the three main layers: epidermis, dermis and hypodermis. Dermis contains intertwined collagen fibers, which represent the most important layer of raw leather for obtaining the finished product, while the remaining two layers (epidermis and hypodermis) are removed during the processes (Fig. 1.) [5, 6].



**Fig. 1.** Cross section of animal leather [6]

Finished leather is a product that is created by processing of raw animal leather in the tanning process by various means, of which the most widely used are chrome tanning, during which it becomes more durable and applicable. Tanning agents are agents that

chemically react with the collagen molecule that builds the leather structure, stabilizing the triple helical structure of the collagen core, thus achieving leather resistance to chemical, thermal, and microbiological degradation. It has a complex morphological structure and its processing is extremely complex and requires the implementation of many process steps, of which the emphasis is on tanning in which it acquires its characteristic and unique properties and can be used for different purposes [5-7].

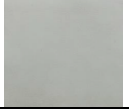
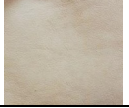
The emphasis of this paper is an introducing of environmentally friendly processes of the surface modification of semi-processed bovine tanned leathers, by application of plasma and ecological bio-agent chitosan, in order to achieve satisfactory functional (antimicrobial) properties of treated samples. The main goal is to achieve the desired properties by using of environmentally friendly processes with the lowest possible consumption of energy, water and chemicals to maximally preserve natural resources, with the purpose of protecting the environment and human health.

## 2. Materials and Methods

### 2.1 Material

The tests were carried out on two different semi-processed bovine leathers - chrome tanned leather and leather tanned with synthetic tanning agent (Cr-free). The basic characteristics of the tested leather samples are shown in Table 1.

**Table 1.** Basic characteristics of the examined leather samples

Sample name and label	Thickness [mm]	Sample description	Sample face appearance
Chrome tanned leather (sample label: <i>Cr-leather</i> )	1,1 - 1,3 mm	semi-processed bovine chrome tanned and hydrophobic leather full of natural face	
Leather tanned with synthetic tanning agent (sample label: <i>Cr-free leather</i> )	1,1 - 1,3 mm	semi-processed cowhide with a full natural face, synthetically tanned; not hydrophobic	

### 2.2. Methods of treatments

#### 2.2.1 Plasma pretreatment

Plasma pretreatments were realized using oxygen and argon gases (high purity 99.998%, by Messer) at a defined parameters of pressure and gas flow rate, at constant frequency of 40 kHz in a low-pressure plasma system (NANO LF, Diener electronic), Table 2. For determination of the effect of exposure time and power on leather surface properties, time of 10, 20 or 40 minutes under 500 and 800 W were explored. All samples were dried at 50 °C for 24 hours prior to plasma pretreatment to remove the moisture. Plasma pretreated samples were treated with BTCA immediately upon completion of pretreatment.

**Table 2.** Plasma pretreatment conditions

Sample label	Gas	Time, t [min]	Power, P [W]	Pressure, p [Pa]	Gas flow, q [cm <sup>3</sup> /min]	lxd [mm]
<i>Cr-leather</i>	oxygen	20	500	32	220	100x100
<i>Cr-leather</i>	oxygen	20	800			
<i>Cr-free leather</i>	oxygen	10	500			
<i>Cr-free leather</i>	oxygen	10	800			
<i>Cr-leather</i>	argon	40	800			
<i>Cr-free leather</i>	argon	40	500			

\* Frequency of low-pressure plasma system is constant - 40 kHz.

### 2.2.2 Treatment with BTCA

Polymerization process directly in the plasma chamber, was used with BTCA as reagent (in monomer bottle) at a pressure of 50 Pa, gas flow of 200 cm<sup>3</sup>/min and frequency of 40 kHz in a plasma system. The effects of exposure time for 30 minutes under the power of 100 W, on the polymerization rate were explored.

### 2.2.3 Spraying method with Chitosan

Second part of the experiment was realised using 1% chitosan (C<sub>56</sub>H<sub>103</sub>N<sub>9</sub>O<sub>39</sub>, medium molecular weight 100-300 kDa) solution on the plasma pretreated and BTCA treated leather samples by spraying method for achievement of antibacterial effectiveness. For enhanced deposition process of antibacterial agent, leather was sprayed with chitosan solution for 5 second and dried at 65 °C for 15 minutes.

## 2.3 Methods of Analysis

### 2.3.1 Surface morphological analysis

Surface changes of morphology were analysed using scanning electron microscope (SEM) (type JEOL LV-6060) at 100x and 2000x magnifications. The scanning electron microscope works by using a focused electron beam to scan the surface of the test sample to give information about the characteristics of the sample surface. When the electron beam is focused on the sample, various interactions occur, such as the emission of secondary and return primary electrons. A beam of electrons erupts electrons that are part of the cause atoms. The electron energies from the sample are collected and measured by detectors, and a pseudotwodimensional image is created with the help of a microprocessor. In order to obtain conductivity, samples were coated with gold for 20 minutes, using a sputter coater prior to analysis [8].

### 2.3.2 Chemical changes

The chemical changes were analysed using ATR-FTIR spectroscopy (Attenuated Total Reflectance-Fourier Transform Infrared Spectroscopy). Infrared spectroscopy is based on the interaction between IR radiation and molecules, i.e. groups of two or more atoms connected by a chemical bond. The material absorbs infrared radiation, and the amount of absorbed radiation is measured as a function of energy that can be expressed in the form of frequency. IR radiation is absorbed only if its frequency coincides with the vibration frequency of the molecular bond. The absorbed radiation is reflected as a "jump" on the spectrogram. The analysis of the samples on the device was performed by the method of

Attenuated Total Reflectance (ATR), in which the IR light was completely reflected when it reached the surface of the ATR crystal. When the sample is placed on the crystal surface, the IR beam penetrates the sample to a certain depth depending on the angle of incidence of the beam and the refractive index of the ATR crystal, as well as the type of sample [9].

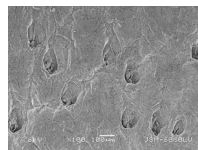
### 2.3.3 Antimicrobial efficacy

Antimicrobial effectiveness of treated leather samples was conducted using qualitative Agar diffusion plate test against two bacterial species *Staphylococcus aureus* (ATCC 25 923) and *Klebsiella pneumonia* (ATCC 11 296). The test procedure for antimicrobial efficacy of treated samples was performed in accordance with the standard HRN EN ISO 20645:2008, as well as the final assessment of antibacterial activity included the inhibition zone and the growth of the bacteria under the specimen.

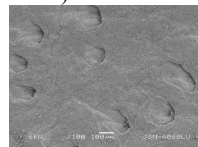
## 3. Results and discussion

### 3.1 SEM analysis of leather surface

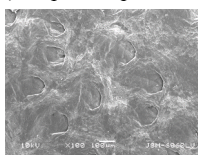
Based on the obtained images taken by scanning electron microscopy, the surface morphology characteristic of tested samples with observable follicles visible at a magnification of 100x is observed (Fig.2 a-d). By comparing images of the leather surface before and after pretreatment with O<sub>2</sub> plasma at a magnification of 2000x, a certain cleaning of the surface with residual surface "damage" of the face is observed (Fig. 2. b1). After treatment with polycarboxylic acid (BTCA) and chitosan on the pretreated surface with oxygen plasma (Fig. 2. c1 and d1), a slight smoothing and covering of the damaged parts with the applied agent was observed, which may indicate crosslinking of polycarboxylic acid on the sample surface and bonding.



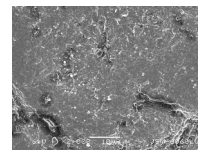
a) untreated



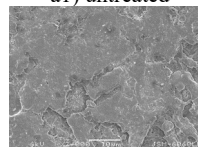
b) O<sub>2</sub> plasma pretreated



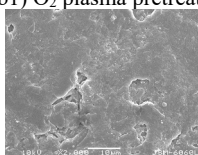
c) O<sub>2</sub>/BTCA treatment



a1) untreated



b1) O<sub>2</sub> plasma pretreated

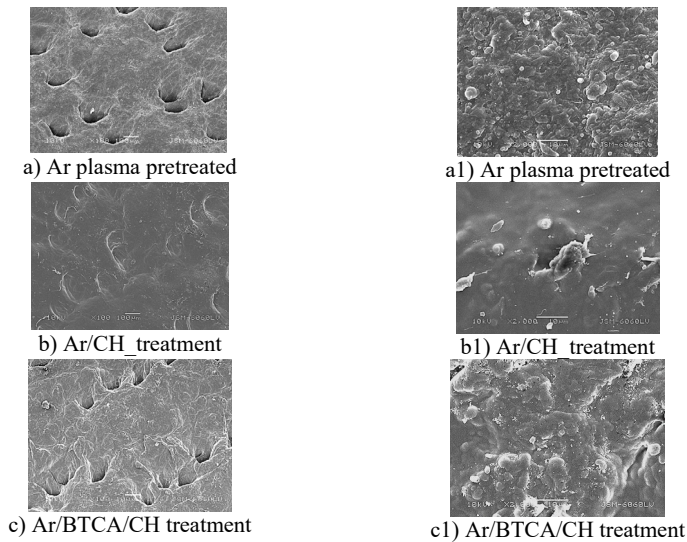


c1) O<sub>2</sub>/BTCA treatment



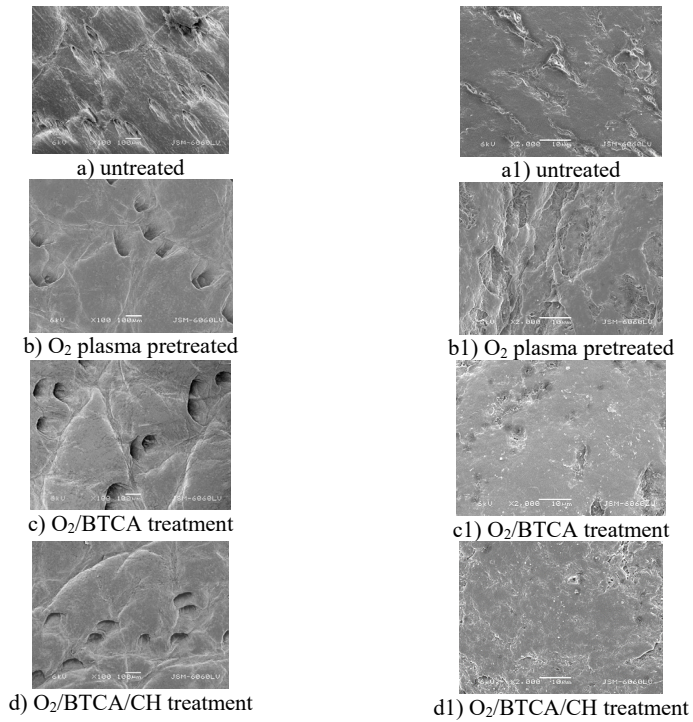
**Fig. 2.** SEM images of chrome tanned leather with 100x (left) and 2000x (right) magnifications: a, a1) untreated; b, b1) O<sub>2</sub> plasma pretreated; c, c1) O<sub>2</sub>/BTCA treatment and d, d1) O<sub>2</sub>/BTCA/CH treatment

By analysing microscopic images of chromium tanned samples, after pretreatment with argon plasma, granular segments are visible on the surface of tested sample, and the surface is rougher with more pronounced and open follicles. Treatment with chitosan after pretreatment with Ar plasma makes the surface smooth and the follicles are closed (Fig. 3. b and b1). After treatments with BTCA and chitosan, an increased amount of agent is observed on the leather surface (Fig. 3. c1).



**Fig. 3.** SEM images of a chromium tanned leather sample with magnifications of 100x (left) and 2000x (right): a, a1) argon plasma; b, b1) Ar/CH treatment and c, c1) Ar/ BTCA/CH treatment

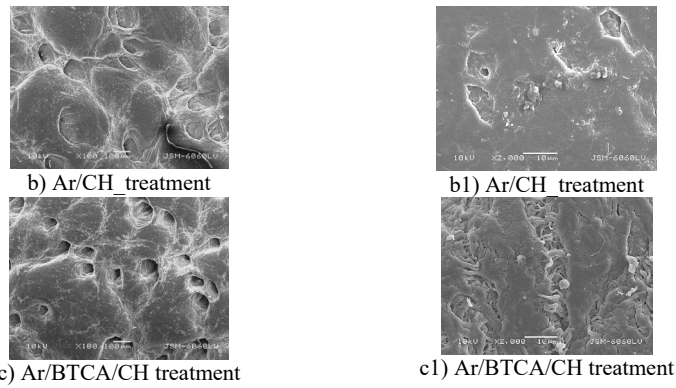
By analysing the surface of the tanned sample with synthetic tanning agent, after pretreatment with oxygen plasma (Fig. 4), the surface of the sample was cleaned of present impurities visible on the untreated sample (Fig. 4. a1), but also additionally "damaged" surface layer (face) below which collagen fibres (Fig. 4. b1). After the treatments with BTCA and chitosan, the surface is closed, smoothed and covered with the visible content of the applied agent (Fig. 4. c1, d1).



**Fig. 4.** SEM images of synthetic tanned leather with 100x (left) and 2000x (right) magnifications: a, a1) untreated; b, b1) O<sub>2</sub> plasma pre-treated; c, c1) O<sub>2</sub>/BTCA treatment and d, d1) O<sub>2</sub>/BTCA/CH treatment

By microscopic analysis of the surface of the tanned sample with synthetic tanning agent, after pretreatment with argon plasma, the surface of the sample is more open in the presence of surface craters formed due to the action of argon gas (Fig. 5. b1). After application of the crosslinking agent BTCA and antibacterial agent chitosan, the agents bound to the collagen fibres of the sample, which is visible at image with magnification of 2000x after treatment Ar/BTCA/CH (Fig. 5. c1).

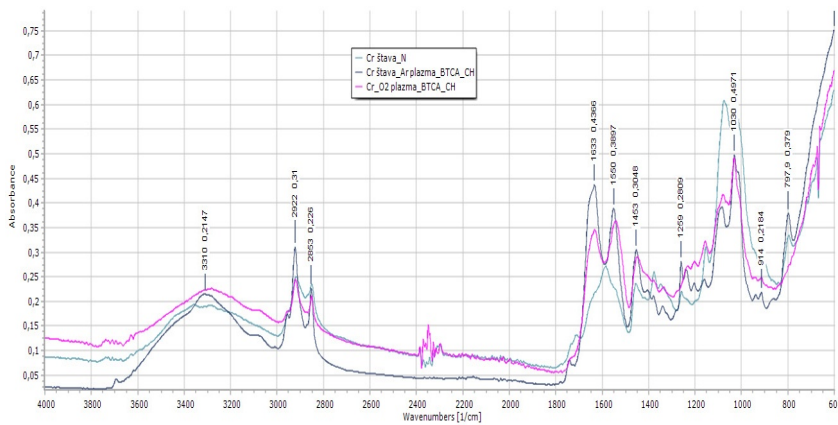




**Fig. 5.** SEM images of synthetic tanned leather with 100x (left) and 2000x (right) magnifications: a, a1) argon plasma; b, b1) Ar/CH treatment and c, c1) Ar/BTCA/CH treatment

### 3.2 Results of FTIR-ATR functional group analysis

The chemical structure of the surface of untreated and treated samples was analysed, i.e. the presence of characteristic wave bands (peaks) corresponding to functional groups. For better comparison, each graph shows the spectra of untreated samples and the spectra of samples after plasma pretreatments/BTCA and chitosan treatments in the spectral range of the mean IR spectrum from  $4000\text{ cm}^{-1}$  to  $600\text{ cm}^{-1}$ .



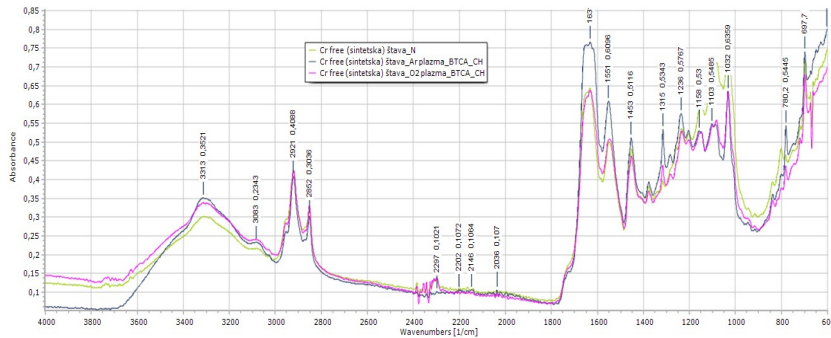
**Fig. 6.** Absorption FTIR spectra of chromium tanned leather sample before and after treatment with  $\text{O}_2$  or Ar/BTCA/CH

By comparing the spectra shown in Fig. 6., the intensity of the absorption bands of the treated samples is observed in relation to the untreated ones at  $2922\text{ cm}^{-1}$ ,  $1633\text{ cm}^{-1}$ ,  $1550\text{ cm}^{-1}$ ,  $1453\text{ cm}^{-1}$  and  $797\text{ cm}^{-1}$ , which indicate that intense vibrations occur on the  $-\text{NH}$ ,  $-\text{NH}_2$ ,  $-\text{CH}$ ,  $-\text{CH}_2$  groups and  $-\text{C}=\text{O}$  groups, which show that polycarboxylic acid (BTCA) and chitosan are very likely to bind to the substrate surface. The presence of absorption



peaks of the treated samples at  $1633\text{ cm}^{-1}$  and  $1550\text{ cm}^{-1}$ , which are not present in the untreated sample, and which correspond to the  $\text{-C=O}$  and  $\text{-NH}_2$  groups is observed. That may indicate the binding of chitosan to the substrate surface. There is also a decrease in the intensity of the absorption peak at  $1030\text{ cm}^{-1}$ , which indicates reduced tensile vibrations in the  $\text{-C=O}$  group [10-13].

The FTIR-ATR spectrum of the tanned sample with synthetic tanning agent (Fig. 7.) has marked absorption bands in the spectral range at characteristic wavenumbers where at  $3311\text{ cm}^{-1}$  and  $3083\text{ cm}^{-1}$  they indicate tensile vibrations  $\text{-NH}$  group of amino acids, at  $2921\text{ cm}^{-1}$   $\text{-CH}$  asymmetric deformation vibrations, at  $1630\text{ cm}^{-1}$  tensile vibrations  $\text{-C=O}$  group. The higher intensity of the absorption bands of the processed samples was expressed at wavenumbers at  $2921\text{ cm}^{-1}$  for  $\text{-CH}$  groups, at  $2852\text{ cm}^{-1}$   $\text{-CH}_2$  groups, at  $1630\text{ cm}^{-1}$  for  $\text{-C=O}$  groups, at  $1551\text{ cm}^{-1}$  for  $\text{-NH}_2$  deformation vibrations, at  $1315\text{ cm}^{-1}$  for  $\text{-COC-}$  tensile vibrations, at  $1236\text{ cm}^{-1}$  for  $\text{-C=O}$  groups and at  $780\text{ cm}^{-1}$  for aromatic  $\text{-CH}$  groups. The intensity of the absorption bands of the sample treated with argon plasma, with BTCA and chitosan is higher at  $1630\text{ cm}^{-1}$ ,  $1551\text{ cm}^{-1}$  and  $780\text{ cm}^{-1}$ , which may indicate better binding of chitosan and BTCA to the substrate after pretreatment with argon plasma. The intensity of the absorption bands at the wavenumbers at  $1158\text{ cm}^{-1}$ ,  $1103\text{ cm}^{-1}$  and  $1032\text{ cm}^{-1}$ , which indicate reduced vibrations at  $\text{-C=O}$ , and  $\text{-CH}$  groups, was reduced [10-13].



**Fig. 7.** Absorption FTIR spectra of a synthetic tanned leather sample before and after treatment with  $\text{O}_2$  or Ar/BTCA/CH

### 3.3 Antibacterial activity against selected bacteria

The results of antimicrobial efficacy of untreated and treated leather samples against specified bacteria *Staphylococcus aureus* and *Klebsiella pneumoniae* are shown in Table 3.

**Table 3.** Antibacterial activity of untreated and treated leather samples.

Sample label	Treatment	Growth under the specimen	Assessment*
<i>Staphylococcus aureus</i>			
<i>Cr-leather</i>	Untreated	slight	limit of efficacy
	$\text{O}_2$ /BTCA/CH	none	good effect
	Ar/BTCA/CH	slight	limit of efficacy
<i>Cr-free leather</i>	Untreated	none	good effect
	$\text{O}_2$ /BTCA/CH	none	good effect

	Ar/BTCA/CH	none	good effect
<i>Klebsiella pneumoniae</i>			
<i>Cr-leather</i>	Untreated	none	good effect
	O <sub>2</sub> /BTCA/CH	none	good effect
	Ar/BTCA/CH	medium	insufficient effect
<i>Cr-free leather</i>	Untreated	none	good effect
	O <sub>2</sub> /BTCA/CH	none	good effect
	Ar/BTCA/CH	none	good effect

\*Assessment is based on HRN EN ISO 20645:2008 - "Determination of antibacterial activity - Agar diffusion plate test", where "good effect" is described as "no growth" under the specimen, "limit of efficacy" as "slight growth (only some restricted colonies or growth nearly totally suppressed)" under the specimen and "insufficient effect" is described as "growth" of bacterial colonies under the specimen.

Both of samples show a good effect against *Staphylococcus aureus* after treatments. Tanned sample with synthetic tanning agent show significant antimicrobial activity prior to plasma pretreatment and treatment with agents (BTCA and chitosan). In the untreated chromium tanned sample there is a slight growth and without present zone of inhibition, which indicates that the antimicrobial effect is limited. Although, after treatment with plasmas and agents, zone of inhibition is not evident, bacterial growth below the sample is not present indicating good antimicrobial effect. The chromium tanned sample after pretreatment with argon plasma and treatment with the agents resulting in growing of tested bacteria, and it's assumed that no chitosan particles have bound to its surface, or the sample is contaminated during the antibacterial testing.

The obtained results in which the antimicrobial effect of the treated leather samples against the negative bacteria *Klebsiella pneumoniae* were tested show a generally good antimicrobial effect, which is manifested without bacterial growth and without a visible zone of bacterial inhibition. Slightly poorer results are shown by the chromium tanned sample after pretreatment with argon plasma and treatment with agents whose presence reduced its antimicrobial efficacy.

#### 4. Conclusions

Morphological changes of leather samples after pretreatment with oxygen and argon plasma were confirmed by analysis of SEM images where the 'cleaning' of the surfaces of the chromium tanned and Cr-free tanned sample is visible. After treatment with polycarboxylic acid (BTCA) and chitosan on pretreated plasma surfaces, a slight smoothing and covering of the damaged parts with applied agents is visible, which may indicate on crosslinking of polycarboxylic acid on the sample surface and binding of chitosan particles.

By analyzing the chemical structure of the surfaces of untreated and treated samples using FTIR-ATR spectroscopy, absorption peaks at 1630 cm<sup>-1</sup> and 1550 cm<sup>-1</sup> corresponding to the -C=O and -NH<sub>2</sub> groups are observed. An increase in the intensity of the absorption peaks may indicate the binding of chitosan to the surface of the substrate.

The applied treatments achieved satisfactory antimicrobial efficacy of both tested leather samples, especially the Cr-free tanned sample after pretreatment with oxygen and argon plasma and treatment with chitosan as antibacterial agent.

This work has been fully supported by the Croatian Science Foundation under the project (IP-2016-06-5278). Work (SEM analysis) was also financed by Slovenian Finance Agency, Slovenia (Infrastructure Centre RIC UL-NTF).

## References

1. Kaygusuz, M. et al.: Modification of Leather Surface with Atmospheric Pressure Plasma and Nano-Finishing, *Polymer-Plastics Technology and Engineering*, **57** (2018) 4, 260-268, ISSN 2574-0881.
2. Li, Q., E. T. Dunn, E. W. Grandmaison, M. F. A. Goosen: Applications and properties of chitosan, *Journal of Bioactive and Compatible Polymers*, **7** (1992) 370-397
3. Rinaudo, M.: Chitin and chitosan: Properties and applications, *Progress in Polymer Science*, **31** (2006) 603-632
4. Reed, R: Science for students of leather technology, Pergamon Press Ltd., Headington Hill Hall, Oxford (1966) **5**, 134-138
5. Nazer, D.W., Al-Sa'ed, R.M., Siebel, M.A.: Reducing the environmental impact of the unhairing-liming process in the leather tanning industry, *Journal of Cleaner Production*, **14** (2006) 65 – 74
6. Sizeland, K.: Nanostructure and physical properties of collagen biomaterials, Doctoral thesis, Massey University, Manawatu, New Zealand, 2015
7. Štěpánová, V. et al.: Surface modification of natural leather using diffuse ambient air plasma, *International Journal of Adhesion and Adhesives*, **77** (2017) 198-203, ISSN 01437496.
8. Mršić, G. & Žugaj, S.: Analiza GSR čestica upotrebom elektronskog mikroskopa (SEM/EDX), *Policija i sigurnost*, **16** (2008) 3-4, 179-200.
9. Zofka, A., Maliszewska, D., Maliszewski, M., Boratynski, J.: Application of FTIR method to examine the polymer content in the modified bitumen and to assess susceptibility of bitumen to ageing, *Roads and Bridges – Drogi i Mosty*, **14** (2015) 163 – 174
10. Hedberg, Y.S., Lidén, C., Odnevall Wallinder, I.: Correlation between bulk- and surface chemistry of Cr-tanned leather and the release of Cr(III) and Cr(VI), *Journal of Hazardous Materials* **280** (2014) 654–661
11. Falcão, L., Araújo M.E.M.: Application of ATR–FTIR spectroscopy to the analysis of tannins in historic leathers: The case study of the upholstery from the 19th century Portuguese Royal Train, *Vibrational Spectroscopy* **74** (2014) 98–103
12. Nashy E.H.A., Osman, O., Mahmoud, A.A., Ibrahim, M: Molecular spectroscopic study for suggested mechanism of chrome tanned leather, *Spectrochimica Acta Part A* **88** (2012) 171– 176
13. Tite, T., Miu, L., Giurginca, M., Meghea, A.: Evaluation of degradation of parchment leather by FT-IR and UV-VIS-NIR spectroscopy, *Revista de Chimie* **57** (5) (2006) 466-471.

# Tangram based technology for clothing design

*Boryana Georgieva-Gushtanova*<sup>1\*</sup>

<sup>1</sup>Technical University of Sofia, Faculty of Mechanical Engineering, Department of Engineering Design, Bulgaria

**Abstract.** The trends in the society regarding environment protection and more optimized production are reason for the research of the author in this direction. The technology of the item connect with the stamina of the product. Within the report, there is an author's development for series of clothing presented in the context of the steady design. Using zero-waste technology aims the improvement of the functional characteristics, as it is being experiment with different textile materials like artificial leather, cotton, wool, spandex and others. The design through transformation of square into other figure through cutting connect with the Chinese tangram game. Problems are included, such as construction, functional, and aesthetic character, as well social and ecological aspect.

## 1 Introduction

Eco fashion is a fairly small segment of the fashion industry at present, but it is among the fastest growing ones. The ethical and eco fashion are fashion trends dealing with the proper allocation of the resources that already have for the sake of protecting the Planet Earth. These trends also seek a more rational method of operation in the fashion industry. Design, produce and dispose of clothes have a huge impact on the environment. Their production requires toxic chemicals and leads to climate change, and the public in general does not know where and how to recycle them [1].

### 1.1 Tangram

The Tangram is a dissection puzzle consisting of seven flat polygons, called tans, which are put together to form shapes. It is reputed to have been invented in China sometime around the late 18th century and then carried over to America and Europe by trading ships shortly after. It is one of the most widely recognized dissection puzzles in the world and has been used for various purposes including amusement, art, and education.

The objective is to replicate a pattern (given only an outline) generally found in a puzzle book using all seven pieces without overlap. Alternatively the tans can be used to create original minimalist designs that are either appreciated for their inherent aesthetic merits or as the basis for challenging others to replicate its outline.

---

\* Corresponding author: [info.bobbyhobby@gmail.com](mailto:info.bobbyhobby@gmail.com)

This article discusses the possibilities for zero waste clothing design by applying the principle of the Tangram [2].

## 1.2 Tangram elements

The seven polygons (Fig. 1) are: 2 large right triangles (hypotenuse 1, sides  $\sqrt{2}/2$ , area  $1/4$ ), 1 medium right triangle (hypotenuse  $\sqrt{2}/2$ , sides  $1/2$ , area  $1/8$ ), 2 small right triangles (hypotenuse  $1/2$ , sides  $\sqrt{2}/4$ , area  $1/16$ ), 1 square (sides  $\sqrt{2}/4$ , area  $1/8$ ), 1 parallelogram (sides of  $1/2$  and  $\sqrt{2}/4$ , height of  $1/4$ , area  $1/8$ ). Of these seven pieces, the parallelogram is unique in that it has no reflection symmetry but only rotational symmetry, and so its mirror image can be obtained only by flipping it over. Thus, it is the only piece that may need to be flipped when forming certain shapes.

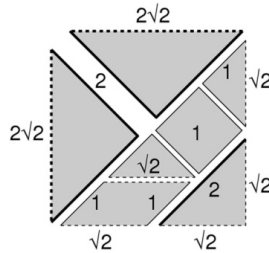


Fig. 1. Tangram seven tans.

## 1.3 Zero-waste design

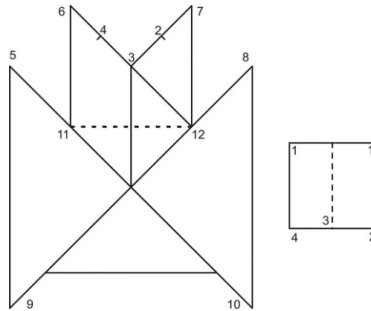
The principle of full utilization of fabrics has been known ever since ancient times. Traditional kimonos in Japan are still made based on that principle because of the high cost of silk [3]. The aim is to ensure its complete use by placing the elements very sparingly on the fabric so that no waste is generated. Globally, numerous designers are working on this problem by proposing solutions that cut the fabric into either identical or different pieces along the lines of regular or irregular grids. These pieces are then assembled and creases and frills are made by using the residual pieces for decoration of the items [4, 5], the principles of origami [6, 7], cutting the fabric into strips which are interwoven in a certain order [8], or 3D printing. These solutions for saving materials and achievement of zero-waste have been also successfully applied in the production of furniture [9], lighting fixtures and home textiles [10].

## 2 The experiment

The possible solution is the use of the traditional Tangram, which constitutes a square. Just one glance over the game is sufficient to notice numerous possibilities for using the proposed shapes for clothing elements. The style would be different from the style of clothing that can be achieved by traditional garment construction. The shapes used in the game are more suitable for outerwear, blouses and loose cut skirts. Constructing pants by using this method would be a particular challenge. As part of this first experiment, three pieces of clothing of the same construction will be made, however, textile of different characteristics will be used in order to change the appearance of the clothing [11]. A piece of outerwear clothing and two dresses will be made in order to study the behavior of zero waste construction when using different materials.

## 2.1 Construction

The output shape for cutting will be a square, the side of which will be equal to the width of the roll of fabric. The selected textiles will be of the most common width of 140-150 cm, where this range does not have any particular effect on the final product. The positioning of the elements of the cut is presented on Fig. 2. The cut follows the principle of axial symmetry along the vertical axis of the model. This principle has been selected based on logical reasoning and it is also present in traditional garment construction. The two large right triangles are placed at the two sides of the axis of symmetry, the medium right triangle is positioned symmetrically at the two sides of the axis and, in order to obtain two more symmetric details, the two small right triangles are connected so that they look like a parallelogram. In addition, a hood for the clothing is made by using the square of the Tangram.



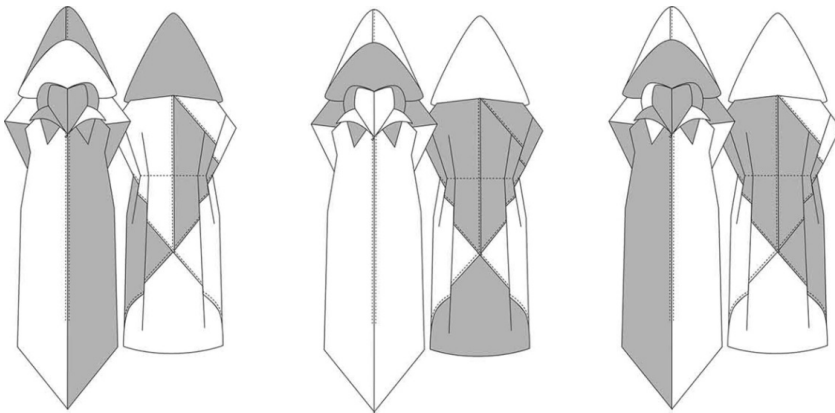
**Fig. 2.** The positioning of the elements of the cut.

## 2.2 Variations of models

After connection of the details a mannequin is used for this flat shape and the clothing is adjusted to the body based on the moulage technique. We attempt to vertically align lines 5-9 and 8-10. Diversity of the clothing front line can be achieved by using different fastening methods, such as a zipper, buttons, etc. A variation of the bust size can be achieved when joining the edges at points 5, 6, 7 and 8 by their different intertwining. Along the 11-12 line at the back (near the waist), the model can be changed by making frills with an elastic band, a cord, etc. Different types and sizes of pleats and peplums can be made.

## 2.3 Possibilities of using double-faced and patterned fabrics

Depending on the choice of textile and the clearly oriented patterns of the fabric, such as stripes or chequered pattern, a large variety of designs may be obtained by focusing on the detail orientation. Another possibility for development of a different design is the selection of double-faced fabric. Models made of it can be worn on either side and the faces of the details can also be interchanged, as shown on the drawing on Fig. 3. These two possibilities can be seen to some extent in Model 1 (Fig.4). Additional variety may be obtained from the method of connection of the details – by overlapping, lock stitch or decorative stitches. They can be connected with different types of braids and bias strips or colored threads. The choice of strips and threads in contrasting colors will put emphasis on the innovative construction.

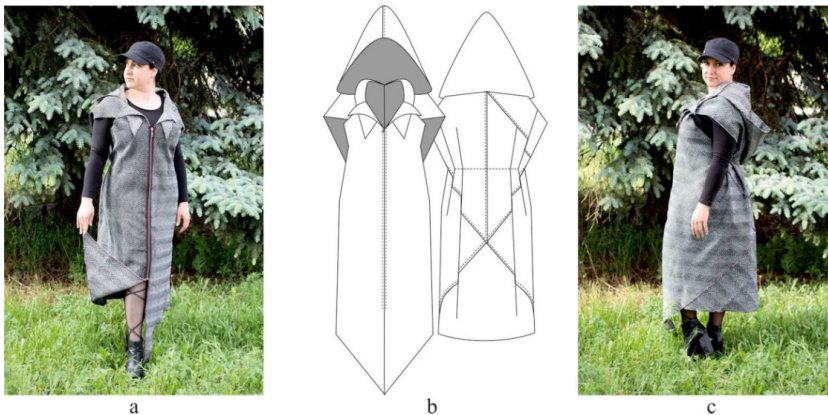


**Fig. 2.** Interchanged details – more different visions of the same cut on Model 1.

### 3 One cut behind three different garments

#### 3.1 Model 1

For the experiment with Model 1 (Fig. 4), which is a vest made of fabric for upholstery, twill weave (composition 100% polyester), which makes it look like a striped model. The model has a large hood. When the hood is on the head, it takes the shape of a triangle and gently falls on the shoulders. When it is taken off, its top reaches the waist. The edges of the details are finished with overlock machine and are connected with a red thread through a zigzag stitch. The intertwining of the corners at points 5, 6, 7 and 8 forms an interesting detail that looks like a lapel. The model is sleeveless, with covered shoulders, and it is fastened with a zipper. Its length is mid-calf and the corners of the large triangles at the front reach the ankle. The back of the model is fitted along the 11-12 line by using four peplums positioned symmetrically – two on each side.



**Fig. 4.** Model 1: a) Front view with detail that looks like a lapel; b) Flat sketch; c) Large hood and peplums.

### 3.2 Model 2

For the experiment with Model 2 (Fig.5), dual layer BlackOut fabric with woven black yarn (textile for curtains, composition 100% polyester) has been used. This is a heavy weight fabric which forms soft creases in the presence of frills. The model constitutes a calf length sleeveless dress. The dress is sewn at the front and no fastening has been designed. The entire dress is decorated with frills with ornamental and functional purpose. The details are connected with lock stitch finished with overlock machine. The frills are made by using threaded cords with stops. The frills along the neckline allow some adjustment of the bust size. The waist circumference can be adjusted with a cord threaded along the 11-12 line (Fig. 2). There is a threaded cord along the edge and the central line of the hood, which allow transformation of the hood into a generously pleated collar. A cord threaded along the lower hem of the skirt completely changes the silhouette. The cord channels are made by folding the edges of the details, whereas the ones along the 11-12 line is made using a bias strip.

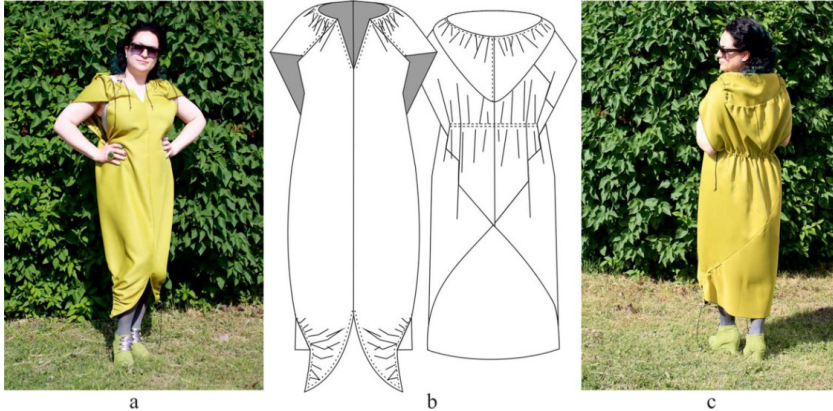
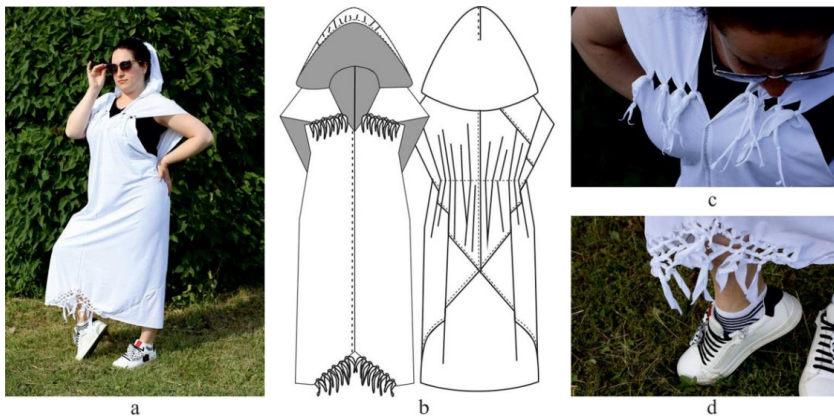


Fig. 5. Model 2: a) Front view; b) Flat sketch; c) Back view

### 3.3 Model 3

Spandex has been used for the experiment with Model 3 (Fig. 6). It is a mid-calf sleeveless sports dress. The details of the model are connected by overlapping, as in Model 1. This leaves the stitches visible and they serve as an additional engaging element in the design because of the property of the spandex to roll at the edges. The details do not need finishing and the edges are left as they are. They can be decorated with ornamental stitches. No fastening has been designed and the dress is closed with a front seam from the neckline to the knees. The corners of the triangles at the neckline fall freely and can be tied in different combinations of knots. The hood has a frill along the edge made by sewing an elastic band. The same frill has been made along the 11-12 line (Fig. 2). The corners of the large triangles which reach the ankle at the front side can also be modified by tying different knots.





**Fig. 6.** Model 3: a) Finished model with hood; b) Flat sketch; c) Knots on the neck; d) Knots on the front side.

## 4 Conclusion

The items are suitable for people of different height and weight, however, they need to be customized based on the moulage technique. The length of the entire item from the shoulder to the edges of the triangles at the front is 120 cm and the length of the back is 100 cm. If the corners on the front side in Model 1 make movement difficult, they can be sewn and folded in any direction, which would reduce the length of the item. For the dresses, this length can be adjusted by the frills and knots. The waist circumference of the item, without the frills, is 130 cm, and the openings for the arms are about 70 cm.

The additional materials used for all three models are bias strips, elastic bands, cords, caps and stops. These are materials that are nearly 100% utilized and can be adopted by the zero-waste clothing production technology.

Given that the entire width of the roll of fabric is used, its end is cut in a straight line and the additional materials are offered per linear meter, therefore the goal is achieved and the proposed design is implemented zero-waste.

The fact that the clothes allow them to adapt to a wider range of bodies makes them a sustainable design.

Despite the great possibility for use by people of different build and height, this type of design may be relatively difficult to adopt in certain spheres, for examples the ones that require very formal style. However, the future of the planet and our willingness to conserve it suggests that innovative methods for clothing production will be increasingly adopted and the new look will be accepted more widely.

## References

1. D. Thomas, *Fashionopolis: Why What We Wear Matters*, Penguin Books, ISBN: 978-073-522-403-2, (2020)
2. S. Loyd, *The Book of Tangrams: 700 Puzzles*, Dover Publications, ISBN: 978-048-683-386-6, (2019)
3. K. Nitnai, *Kimono Design: An Introduction to Textiles and Patterns*, Tuttle Publishing, ISBN: 978-480-531-428-9, (2017)

4. R. Atanasova, Women's clothing with eco design features, *E3S Web of Conferences*, 207, 03005, (2020)
5. T. Rissanen, H. McQuillan, *Zero Waste Fashion Design*, Bloomsbury Visual Arts, ISBN: 978-135-009-483-3, (2018)
6. B. Georgieva-Gushtanova, Origami based technology for handbag production, *Proceedings of the 15th International Conference Standardization, Prototypes and Quality, Turkey*, ISBN: 978-975-374-247-4, 273-279, (2019)
7. <https://www.isseymiyake.com/>
8. <https://www.behance.net/CarlosVillamil>
9. G. Chervendinev, E. Ochkova-Dimitrova, Possibilities of using cad products and parametric design in the sculpture (project "torch of knowledge"), *Proceedings of the Jubilee Scientific Conference, "Angel Kanchev" University of Ruse, Bulgaria*, ISSN: 131-133-21, **54**, 237, (2015)
10. E. Ochkova-Dimitrova, The surface as form-formation factor (project „lamp“), *Proceedings of the XV National Conference with International Participation on Lighting BulLigh* ISSN: 131-407-87, 244, (2014)
11. M. Panchev, Using the possibility of inorganic nano solution for special gentrification, *Proceedings of Scientific conference of FPEPM Technical University of Sofia*, **2**, 250, (2015)

# Application of ICT in the Online Education of Apparel Design and Production within the framework of ICT-TEX project

*Hassan Saeed<sup>1</sup>, Yordan Kyosev<sup>1</sup>, Radka Atanasova<sup>2</sup>, Angel Terziev<sup>2</sup>, and Carla Hertleer<sup>3</sup>*

<sup>1</sup>Technische Universität Dresden, Institute of Textile Machinery and High-Performance Material Technology (ITM), Dresden, Germany

<sup>2</sup>Technical University of Sofia, Faculty of Power Engineering and Power Machines, Sofia, Bulgaria

<sup>3</sup>AUTEX/ Ghent University, Zwijnaarde, Belgium

**Abstract.** One of the key lessons learned during the pandemic of COVID-19 is that the digital education and adaptation of Information and Communication Technologies (ICT) should not be viewed as an island on its own but should be considered as an integral part of all education and training. The ICT-TEX project is an EU-funded project which aims to integrate ICT in online education of textile and clothing. Within the framework of this project, deficiency areas have been identified with a comprehensive survey conducted across the project partner countries. A new course curriculum has been developed based on desk research, field research, surveys, and Gap Analysis. Eight modules (around 16 courses) according to the needs of the textile and clothing industry (TCI) will be developed within the framework of the project. This paper discusses the methodology of applying ICT in new course content for Apparel Design and Production which is a pilot course and serves as a benchmark for further development of other courses.

## 1 Introduction

The textile industry is a traditional and leading industrial sector in Europe with around 160.000 companies, mostly small and medium-sized niche players [1]. They produce high-quality and innovative products and focus on creativity and outstanding customer service. Therefore, the next generation textile industry workers must be well educated and have the required competencies and skills. The ICT-TEX (ICT in Textile and Clothing Higher Education and Business) project presented in this paper, is an Erasmus+ Knowledge Alliance aiming to improve the competencies in Information Communication Technology (ICT) for people working in the field of the Textile and Clothing Industry (TCI). This is done by developing syllabuses for various textile subareas that will be provided through an online platform on the project website and made available to all interested parties.

## **2 Methods and Results**

### **2.1 The ICT-TEX project in general**

The ICT-TEX project is an Erasmus+ Knowledge Alliance, an EU program aiming to strengthen Europe's innovation capacity and foster innovation in higher education by setting up transnational and result-driven activities between higher education institutions and businesses. In this ICT-TEX project, 12 geographically spread partners collaborate to achieve this goal, forming a balanced group of universities, companies, and non-profit organizations active in the textiles and clothing areas. The Project Coordinator is the Technical University of Sofia, Faculty of Power Engineering and Power Machines, Bulgaria. The project commenced on 1 January 2020 and will run for 3 years.

ICT technologies such as CAD, CAM, CAE, and PLM systems have developed more and more admission into the Textile and Clothing Industry, thus requiring personnel with a higher level of ICT skills is becoming important than before. The project aims at developing a curriculum of 'Information Technology in Design of Textile and Clothing' to improve the knowledge and skills of students, teachers, and staff. At first, the current situation was evaluated by distributing a survey amongst companies in Europe to determine the needs and requirements in terms of ICT and entrepreneurial skills. At the next stage, a gap analysis was performed from survey results and desk analysis to get a clear view of what is required. These insights were used to develop an adapted curriculum. The areas dealt with within the project are Design and Production of Knitwear; Design & Production of Woven Fabrics; Design & Production of Technical and Intelligent Textiles; Industrial Engineering, Quality Control & Management, and Finishing, Printing & Functionalization. After that, the pilot syllabuses are developed for Entrepreneurship, ICT - Digital Skills, and Apparel Design & Production. The last-mentioned module will be extensively described in this paper.

### **2.2 Preliminary work on the pilot Module of Apparel Design and Production**

The TCI companies of the EU are facing a shortage of experts in their fields. Therefore, developing necessary competencies and skills for the existing workforce and attracting qualified young experts of the next generation has become a priority for these companies. The textile industry is in pressing need of human resources because a great part (about 40%) is expected to retire in the next few years, and it is not attractive to young people who prefer ICT in general but are not aware that ICT is widely applied in the textile industry [1].

To design a new course curriculum and its content, two research approaches were adopted to understand the need for Apparel Design and Production. During the first approach called 'desk research' led by TU Dresden, the changes and needs of industry were studied and changes taking place in apparel design and production were researched. During the second approach of 'field research', a comprehensive survey questionnaire was developed by the mutual collaboration of consortium to understand the needs of TCI.

#### **2.2.1 Desk Research**

Due to changing policies of the EU, UN policies for environmental protection, corporate social responsibility for sustainable development, the technology has continuously developed for TCI businesses. To understand the state of the art and innovative character of Apparel Design and Production, an analysis of the subject area is performed. Clothing production has doubled in the last two decades, driven by the growing

middle-class population across the globe and due to fast fashion [3][4]. Due to quicker style changes and an increased number of collections per year and often at a lower price, the clothing industry is showing growth in terms of sales. The technological process of conventional apparel design and production processes can be divided mainly into two parts. The first one is the design part and the second involves the production of clothing.

### 2.2.1.1 Apparel Design

Applications of CAD/CAM made their first appearance in the clothing cutting room in the 1970s. Nowadays interactive garment CAD techniques provide garment enterprises with fashion design, pattern making, pattern grading, and marker making. Compared to manual operations, the techniques automate repetitive time-consuming tasks, shorten the product development cycle, improve product quality and respond more quickly to the customer's market, thus the techniques are widely utilized and play a significant role in mass production in the apparel industry [5].

Pattern making is the art of designing patterns by making templates from which clothing and industrial items can be sewn. A pattern making process realizes the imagination of the designer from sketching to the real product. Pattern makers are also called "Technical Designers". The aesthetic appearance, correct fit, and drape attributes of a garment depend significantly on garment-making process. Pattern making is considered the first step in garment production [6]. While making a garment as per design, production patterns are used to trace the various garment parts onto fabric before cutting and assembling. The digital pattern developing process has two paths. One path develops apparel according to traditional 2D pattern making technology [7]. There are three methods: parametric design, traditional grading technique, and pattern generating based on artificial intelligence. Another path develops patterns through surface flattening directly from an individual 3D apparel model. Applying this parametric method can largely improve the efficiency of pattern design or pattern alteration.

Traditional sample creation involves time-consuming manual fittings and re-fittings [8]. With the advancements in virtual reality applications, the garment industry has strived for new developments. 3D virtual try-on brings a whole new level of efficiency to the design department by combining the latest in 3D rendering technology with powerful, proven pattern production software. A large range of techniques is selected and organized into several key modules (digital human modelling, 3D garment design and modification, numerical integration of draping, 2D pattern generation, geometric details modelling, parallel computation, and GPU acceleration) which form the core of a 3D garment design technology platform [9].

The clothing industry increasingly prefers to use computer-aided design (CAD) techniques for both fashion design and pattern creation as it offers greater efficiency and time-saving solutions to many complicated tasks as well as facilitating Internet-based communication amongst designers, manufactures, and retailers. Specialized 2D CAD software, including packages such as cad.assyst (Assyst), Modaris (Lectra), Accumark 2D (Gerber), PDS 2D (Optitex), Master Pattern Design (PAD System), TUKAcad (Tukatech), GRAFIS (Software Dr. K. Friedrich), AudacesApparel (Audaces), COAT (COAT- EDV-Systeme) and Fashion CAD (Cad Cam Solutions), support geometrical pattern drafting from first principles using only anthropometric measurements of the target size and shape. In today's apparel industry, the designs are generally made in digital form with the help of CAD software [5].

The most advanced 3D applications available today combine patterns with fabric physical properties, appearance, and stitching lines to simulate how the fabric will fall or drape in form of a garment. 3D body scanning machines take all the millions of points of a company's

fit model to create an avatar of the same body, which can then be used to accurately predict the ease and tightness of a garment [2].

The user can then adjust the pattern pieces in the 2D pattern making application and view them in the 3D application to re-simulate and once again check the fit. These modifications are easily transferred to paper patterns for fine-tuning. Today's 3D applications include automatic functions specifically designed to allow trained technical designers to adjust 2D patterns [10]. To check if the fit of the pattern is correct, the prototyping on that basis is done to check if the product is suitable for bulk production. It is usually an iterative work, which is performed until the desired results are achieved. An increasingly used alternative is the 3D fit simulation where the fabric properties are given to material in a software environment and 2D patterns are digitally sewn and draped on an avatar. In this way, the prototyping work is reduced to save time and resources. Modern 3D CAD software also offers 3D visualization during motion which makes the product realization even more realistic during the design phase [9]. There are several 3D CAD solutions providers in the market, but Clo3D, Modaris v8, Tuka3D, and 3D Vidya are mostly used.

### 2.2.1.2 Apparel Production

The apparel production starts from getting prepared for cutting the fabric layers in required pattern. The process of cutting starts from the lay planning for cutting. The cutting lay plan or commonly known as a marker is generated in a way that maximum efficiency of fabric lay is achieved to reduce the fabric wastage as much as possible. This cutting lay planning is carried out in combination with 2D CAD software which was prior used to design pattern pieces. The cutting is performed either manually or computerized in apparel production. The efficiency and accuracy of computerized cutting are much more than manual cutting. The use of manual or computerized technologies depends on factors like required garment production, the complexity of cut parts, type of material, labor costs and return on investment of technology acquisition. The sewing department in apparel production involves most of human resources than any other department of clothing production. There are three main production systems in practice in apparel production known as progressive bundle system, unit production system, and modular production system. The selection of production system used in apparel manufacturing is depending upon the type of garments produced and the investment made into the process. Digitalization is pushing towards the unit production system because it provides real-time information of production flow.

Types of sewing machines in sewing production depend upon the type of product being produced and its functional requirements. Automatic sewing operations are performed in the sewing industry for the reproducibility of sewing operations to realize mass production. These sewing machine automations are usually performed on operations like Pocket setter, Pattern seamer, Bartacks machines, Buttonholes machines, J-stitch (on zipper fly), Leather patches seamers, Belt Loop attaching machines, etc. In sewing production, the machine features like needle positioning during and after sewing operation, automatic thread trimmers, and the location of sewing at the seam start and end are also important for production efficiency, because it can facilitate the sewing operator by reducing work fatigues and also reduce the later work during apparel finishing. Sewing machinery manufacturers are presenting their concepts sewing stations using a universal robot working with a machine operator side by side and feeding multiple machines [11]. This is a tendency that can be observed in the future due to decreasing prices of robot technology and increasing labor costs.

The use of ICT in the clothing industry is taking importance with passing time. To keep the sewing production line in full view of managers and production supervisors, German sewing machine manufacturer Dürkopp Adler has presented its Qondac system, which keeps

the record of each stage of the production stage and its efficiency in real-time and keep therecord of machine maintenance. The productivity of sewing machines and their status can be analyzed and machines can be maintained virtually. The interface can be connected with the ERP system of the organization e.g., SAP to exchange the status of production to other relative departments [12]

After the sewing has been finished, the garment goes to the finishing department where it is prepared for final shipment. The use of automatic universal finisher for shirts and pants is used to perform pressing. The use of simple pressing with steam function leaves burn/shiny marks on the fabric surface, which are more visible on fabrics with darker shades. With automatic finisher, different programs can be chosen according to the type of material and finish required. The digital database can be developed which can be retrieved, whenever the same material, fabric construction, material composition is processed in mass production. The company Veit GmbH is a market leader in finishing technology. Its Tunnel Finisher can replace manual tasks and improve production and labor costs [13]. Despite the advantages of automatic finishers on manual pressing, the comparison of the price is also important. A simple pressing station is way cheaper than the automatic finisher. Factors like labor cost and energy conservation are chosen while choosing between the technologies used.

### 2.2.2 Field research (GAP Analysis)

Understanding the educational needs in the future means knowing the current practices of the TCI business and respectively its historical background. The work has been done through desk analyses, historical evidence, and case studies in the past. Additionally, a preliminary questionnaire was prepared to provide appropriate business information for the analysis. Feedbacks from TCI enterprises were gathered. The GAP Analysis combined with the desk analysis served as the basis for the development of elaborated curriculum, syllabuses, and study materials.

The GAP analysis is essential for the implementation of the other work packages of the project too. In this way, the syllabuses and curriculum will meet the future needs of skilled and motivated workers for the TCI enterprises.

The GAP analysis was divided into three main stages:

- Description of the technological processes in the TCI enterprises: it was helpful to identify the difference between TCI product specialization, for instance: clothing, weaving, knitting, etc.
- Historical analysis of the technology changes in TCI enterprises: it allowed us to understand future steps in the development of the technology.
- Staff needs assessment: it defined the best employee and their current and future technological competencies, knowledge, and skills.

Some interesting results from the GAP Analysis regarding the course of "Apparel design and Production" are below. The detailed results are available online at the project website [14].

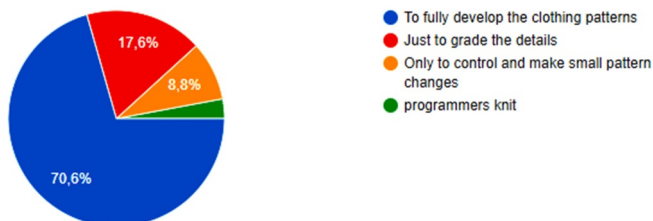


Fig. 1. What skills should patternmakers have in your company?

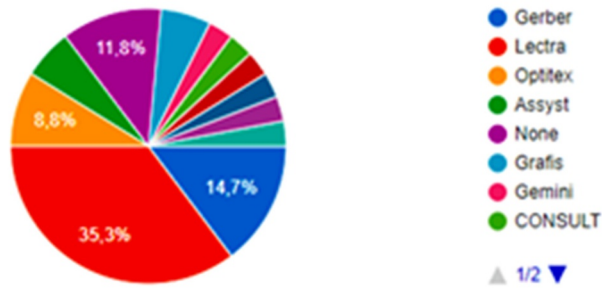


Fig. 2. What CAD systems do your company pattern makers work with?

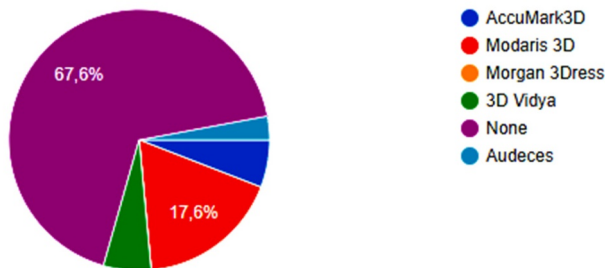


Fig. 3. What 3D Visualization and Fit accuracy software does your company use?

The survey results provided an interesting insight into the general practices of the European clothing industry. For example, it can be seen from the survey results that more than 2/3<sup>rd</sup> of participants said that they do not use any sort of 3D CAD software for visualization and fit simulation at all. This is a very interesting finding that also shows great room for improvement. The 3D visualization and fit simulation can reduce the iterative product prototyping procedure and reduce the lead times from product realization to product manufacturing.

Based on GAP Analysis conducted there is following skills need assessment for the use of ICT in general:

- To operate with advanced/automated production systems; to manage integrated systems for the exchange of information between different production processes also integrating internet of things; to improve the integration level of CAD/CAM and ERP systems;
- Knowledge and ability to apply and manage:
  - Radio Frequency ID (RFID) task;
  - Sensors and Internet of Things coupled with new software;
  - Augmented Virtual Reality (AVR);
  - Block-chains and Artificial Intelligence.
- Ability to use ERP systems to better manage production planning and control, supply chain, logistics, costumers' relationships, workloads, and work distribution, environmental impact, quality;
- Ability to use advanced design software, i.e., software able to detect contours and body shapes for tailor-making designs;



- Ability to use specialized software and analyze big data to study current market trends and predicts the future ones;
- Ability to use marketing techniques and tools to better targeting specific consumer categories and groups;
- Ability to use social media to engage and interact with customers and influence their buying behaviors.

### **2.3 Overview and presentation of the syllabuses of courses of Apparel Design and Production**

Based on the desk research and field research results obtained through GAP analysis, the new course curriculum objectives were designed and a new course curriculum is developed. The course of Apparel Design and Production was subdivided into three main courses.

1. 2D CAD Pattern Making;
2. 3D CAD Simulation;
3. Apparel Production.

The details and objectives which are aimed to be achieved within the framework of the ICT-TEX project are explained for each course.

#### *2.3.1 2D CAD Pattern Making*

Today's clothing industry is moving toward using advanced technology in designing and pattern-drafting. Clothing companies continuously seek new solutions for saving time in product development and generally increasing efficiency in activities ranging from, the design process through the manufacturing process. Such programs can enhance communication, ease flow, production, and cost-effectiveness at all stages. 2D CAD Pattern Making is a knowledge-intensive and creative course that will lead learners across different pattern making techniques taking into consideration materials, colors, and styles combination. Lessons are taught using specialized CAD software (AccuMark by Gerber Technology, Modaris by Lectra).

Following topics will be covered from the course of 2D CAD Pattern Making.

- Introduction to CAD functionalities
- Modelling techniques for different garments
- Symmetry and asymmetry principles
- Algorithms for pattern making of basic apparel constructions
- Computer grading of details
- Algorithms for pattern making of specific garment elements
- Design of gathered elements

#### *2.3.2 3D CAD Simulation*

Three-dimensional (3D) virtual prototyping is getting increasingly important for apparel design. Based on the utilization of 3D CAD simulation, product development in the clothing industry becomes faster and faster. The integration of 3D CAD systems for garment design leads to higher accurate cloth fitting. During the course, the participants will be guided to create virtual garments from fashion design ideas analyzing the principal aspects of 3D simulation by using specific software.

The following topics will be covered from the course of 3D CAD simulation.

- Introduction of 3D simulation;

- Virtual fit simulation in CLO 3D;
- 3D virtual model.

### 2.3.3 ICT in Apparel Production

The garment industry invariably goes through short fashion cycles. To survive in the market, regular innovations in color, style, design, fabric, finish, and fit are needed. Automated machinery and IT solutions are keys in such a scenario. Automations for cutting, sewing, buttonholes, CAD/CAM for pattern making, etc., have brought down the cost of production considerably. Garment companies now focus on technology to be productive and cost-effective at the same time, which means a skilled and constantly technically updated workforce. The course is focused on the analysis of the interconnections between innovative technologies and standard production processes to equip learners with relevant skills and knowledge.

Following topics will be covered from the course of ICT in Apparel Production:

- Sewing machines;
- Spreading/cutting;
- Finishing;
- Production systems;
- Automation in apparel production;
- Material management and work planning;
- Welding technologies.

## 3 Conclusions

A great deal of effort has been made to understand the needs of TCI businesses and HEI's have developed the new curriculum of different courses including Apparel Design and Production. The developed courses will cater to the needs of the staff of TCI businesses and will be freely available online on the project platform. Various interactivities have been developed where the learners will interact with the latest course content, with teachers, and with other learners and improve their online learning experience.

ICT-TEX is funded under the Erasmus+ Program of the European Commission [Project Number:612248-EPP-1-2019-1-BG-EPPKA2-KA]. This publication reflects the views only of the author, and the Commission cannot be held responsible for any use which may be made of the information contained therein.

## References

1. EURATEX, "Euratex annual report", June 2020.
2. Fibre2Fashion, "A glimpse of 3-D body scanning technology in the apparel industry," 2008. [Online]. Available: <https://www.fibre2fashion.com/industry-article/2980/a-glimpse-of-3-d-body-scanning-technology-in-the-apparel-industry>.
3. Euromonitor International, "Euromonitor International Apparel & Footwear (volume sales trends 2005–2015)," 2016.
4. S. Herrmann, "A new textiles economy: redesigning fashion's future," *Ellen MacArthur Foundation*. p. 150, 2017.
5. Y. Xiu and Z.-K. Wan, "A survey on pattern making technologies in Garment CAD," in *IEEE Conference Anthology*, 2013, pp. 1–6, doi: 10.1109/ANTHOLOGY.2013.6784694.

6. D. B. Datta and P. Seal, "Various approaches in pattern making for garment sector," *Journal of Textile Engineering & Fashion Technology*, vol. 4, no. 1. 2018, doi: 10.15406/jteft.2018.04.00118.
7. H. Petrov, "Pattern Making of Clothing," TU Sofia, 2009.
8. Gerber Technologies, "Accumark-Next generation pattern design software for the fashion and apparel industry." [Online]. Available: <https://www.gerbertechnology.com/fashion-apparel/design/accumark/>.
9. Y.-J. Liu, D.-L. Zhang, and M. M.-F. Yuen, "A survey on CAD methods in 3D garment design," *Comput. Ind.*, vol. 61, no. 6, pp. 576–593, 2010, doi: <https://doi.org/10.1016/j.compind.2010.03.007>.
10. Lectra, "What is Modaris." [Online]. Available: <https://www.lectra.com/en/products/modaris-expert>.
11. M. Suh, "Automated Cutting & Sewing Developments," 2020. [Online]. Available: <https://www.textileworld.com/textile-world/features/2020/03/automated-cutting-sewing-developments/>.
12. Dürkopp Adler GmbH, "The Digital Sewing Factory becomes reality." [Online]. Available: <https://www.duerkopp-adler.com/en/main/news/QONDAC>.
13. Veit GmbH, "Tunnel Finisher 8657." [Online]. Available: <https://www.veit.de/en/products/tunnel-finisher/tunnel-finisher-veit-8657/>.
14. V. Guagliumi, "Developing requirement of TCI technologies," 2020.

# GA-tuning of Multivariable PID Controller for Electrohydraulic Load-Sensing Servo System

*Alexander Mitov*<sup>1,\*</sup>, *Tsonyo Slavov*<sup>2</sup>, *Jordan Kralev*<sup>2</sup> and *Ilcho Angelov*<sup>1</sup>

<sup>1</sup>Technical University of Sofia, Dept. of Hydroaerodynamics and Hydraulic Machines, Kliment Ohridski blvd. №8, Bulgaria

<sup>2</sup>Technical University of Sofia, Dept. of Systems and Control, Kliment Ohridski blvd. №8, Bulgaria

**Abstract.** The main purpose of this article is to present the design, optimal setting and experimental study of a multivariable PID controller supposed for electrohydraulic power steering system with load-sensing function. The set of the controller is performed through an optimization procedure based on a genetic algorithm. The PID controller is embedded into a microcontroller for mobile machinery used in laboratory test rig for investigation of an electrohydraulic servo steering system. Results obtained in conditions of physical experiment and numerical simulation with the optimally tuned PID controller are presented. An analysis of the control performance, as well as some features of the used method for setting the PID controller.

## 1 Introduction

Recently, there has been a development of hydraulic drives, which can be summarized in two main directions: the first direction is to introduce digital control, and the second to improve their load-sensitive function. The main architectures of hydraulic systems with load-sensing function are relatively well studied, as well as their selection depending on the desired functionality of the driven machine. In a number of applications of the hydraulic drive, however, the two directions of development are combined, and the ultimate goal is to increase the energy efficiency of the entire electrohydraulic system. Achieving this ultimate goal is impossible without an effective control system [1]. The introduction of digital control in almost all applications of hydraulic drives necessitated the use of embedded control systems. In this aspect, the behavior of the whole system strongly depends on the embedded controller. When there are limitations to the architecture of the hydraulic system (i.e. it is solved), then efforts are focused on achieving high levels of control performance. It could be tentatively assumed that such a case is observed in electrohydraulic servo systems for power steering of mobile machines.

The task of controlling electrohydraulic servo systems in most of their variants can be solved by a classical PID control law obtained from an adequate model and set by an appropriate algorithm [2]. Evidenced by a number of studies and developments by other authors. Rather, efforts are focused on developing the methods and tuning algorithms used

---

\* Corresponding author: [a\\_mitov@tu-sofia.bg](mailto:a_mitov@tu-sofia.bg)

in them. One of the modern algorithms used for optimal setting of PID controllers is the so-called Genetic algorithm (GA). In [3] an improved genetic algorithm (IGA) to search for the optimal PID gains for robotic excavator trajectory control is proposed.

The authors have accumulated experience in the design and implementation of robust embedded controllers with application not only in electrohydraulic drive systems. Their previous developments have studied various types, both conventional and multivariable controllers of electrohydraulic systems for power steering systems without load-sensing. The present study focuses on a load-sensing power steering system. For this purpose, a state space model of the system is derived on the basis of an identification procedure based on experimental data shown in detail in [4]. The PID controller implements the state-space model of the electro-hydraulic servo actuator system to control the movable surface of space vehicle are presented in [5] and genetic algorithm (GA) is used to optimize the controller gain parameters. In [6] proposes the tuning method by GA which approached the optimal PID parameters so that it can increase the efficiency control of the electro-hydraulic servo valve system. A similar approach has been used in [7]. However, all these mentioned developments use the Ziegler-Nichols method to determine the initial values for of the PID controller gains, which is again a classical approach for single input single output system (SISO). In the present work, this approach for determining the initial conditions is inapplicable because the system under study is a multivariable which is represented as single input and multiple output (SIMO).

The main purpose of this article is to present the design, optimal setting and experimental study of a multivariable PID controller designed for electrohydraulic power steering system with load sensitivity. The set of the controller is performed through an optimization procedure based on a GA. The PID controller is embedded into a microcontroller for mobile machinery used in laboratory test rig for investigation of a electrohydraulic servo steering system. Results obtained in conditions of physical experiment and numerical simulation with the optimally tuned PID controller are presented. An analysis of the control performance, as well as some features of the used method for setting the PID controller.

## 2 Hardware description

The authors have designed and realized a new laboratory test rig for investigation of LS servo system applicable for power steering low-speed mobile machines. The hydraulic circuit diagram of the system synthesis on the laboratory model is depicted in Fig.1. The detailed description of the studied system is presented in a previous paper [4].

## 3 Identified model

To obtain a model of electrohydraulic servo system the two analytical modelling and system identification approaches can be used [9]. In our case, due to the lack of information about numerical value of parameters of internal units of electrohydraulic steering system, the identification approach is preferred. The additional advantages of models determined by "black box" identification are that the description of noises, actuators and sensor dynamics are obtained. For that reason, we chose to estimate numerical model of the plant by system identification procedure which is detail presented in [4]. It is assumed that the dynamics of electro-hydraulic steering system may be described in sufficiently wide operating range by linear discrete time stochastic state space model

$$x(k+1) = Ax(k) + Bu(k) + Ke(k) \quad (1)$$

$$y(k) = Cx(k) + Du(k) + e(k), \quad (2)$$

where  $x = [x_1 \ x_2 \ \dots \ x_n]^T$  is a state vector,  $u$  is a control signal that is a voltage applied to the control input of PVE,  $y = [y_{LVDT} \ y_{pos}]^T$  is output signals ( $y_{LVDT}$  is output of LVDT sensor and  $y_{pos}$  is a cylinder piston position),  $e(k) = [e_1 \ e_2]^T$  is a residual vector ( $e_1$  and  $e_2$  are residuals respect to the LVDT and cylinder position respectively).  $A, B, C, D$  and  $K$  are the matrices (model parameters) with appropriate dimensions.

The state space models (1) of various orders are estimated. Model parameters are determined by model predictive error method for estimation of state space model. In estimation, the observable canonical form of state space model (1) is used. The best results are obtained with model of 4<sup>th</sup> order. The values of estimated parameters are

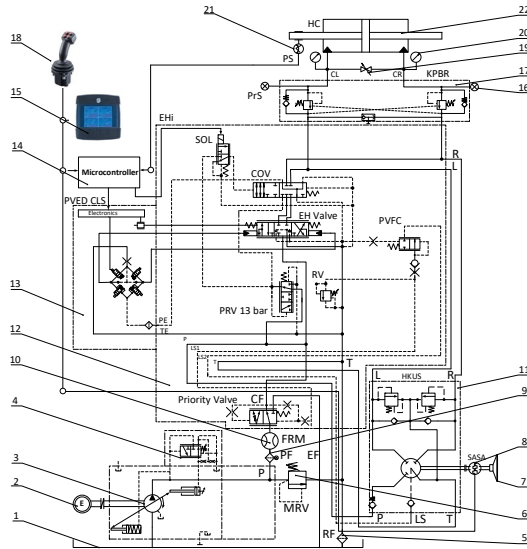
$$A = \begin{pmatrix} 0 & 1 & 0 & 0 \\ -2.1432 & 2.1207 & 1.4618 & -1.4624 \\ 0 & 0 & 0 & 1 \\ -0.3563 & -0.3524 & 0.0464 & 0.9532 \end{pmatrix}, \tag{3}$$

$$B = 10^{-5} \begin{pmatrix} 0.0231 \\ 0.4533 \\ 0.2308 \\ -0.4971 \end{pmatrix}, C = \begin{pmatrix} 1 & 0 & 0 & 0 \\ 0 & 0 & 1 & 0 \end{pmatrix},$$

$$D = \begin{pmatrix} 0 \\ 0 \end{pmatrix}, K = \begin{pmatrix} 1.5999 & -0.0031 \\ 1.7777 & -0.0084 \\ -0.5023 & 0.9847 \\ -1.4377 & 0.9866 \end{pmatrix}$$

and covariance matrix

$$M(ee^T) = \begin{pmatrix} 0.0039 & -0.0007 \\ -0.0007 & 0.4739 \end{pmatrix}.$$



**Fig.1.** Hydraulic circuit diagram of a new laboratory test rig.

### 4 GA tuning of multivariable PID controller

The block scheme of control system is presented in Fig.2. The design of PID controller is based on the model (3).

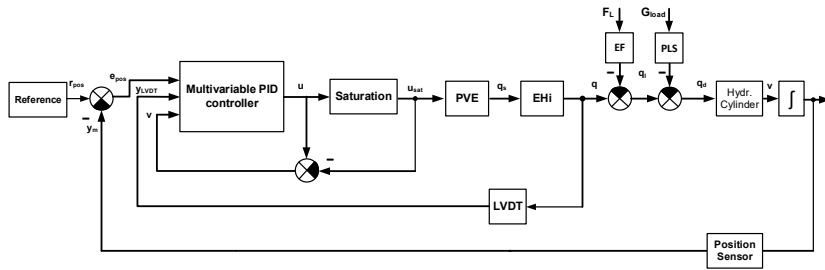


Fig.2. Block Scheme of control system.

The description of popular in practice single input single output parallel PID controller with low pass filter in derivative term and anti-wind up mechanism is given by

$$u(s) = K_p (err(s) + \frac{T_d N_s}{s + N} err(s)) + (K_p K_i err(s) - k_w v(s)) \frac{1}{s}, v(s) = u(s) - u_{sat}(s), \quad (4)$$

where  $K_p$  is the proportional gain,  $K_i$  is the integral gain,  $T_d$  is the derivative time constant,  $N$  is the pole of the low pass filter,  $k_w$  is the conditional feedback gain used to realize anti wind up algorithm,  $err(s) = r(s) - y(s)$  is reference error. The  $u_{sat}(s)$  is saturated control signal which is obtained as

$$u_{sat} = \begin{cases} u(s), & u_{min} \leq u \leq u_{max} \\ u_{min}, & u < u_{min} \\ u_{max}, & u > u_{max} \end{cases}, \quad (5)$$

where  $u_{min}$  and  $u_{max}$  are minimal and maximal admissible values of control signal. In order to implement the PID controller in digital control device, the integral and derivative terms in equation (4) are discretized by first order forward difference and first order backward difference respectively. Thus, the discrete-time PID controller is described by

$$u(z) = K_p (e(z) + \frac{T_d N(z-1)}{(1 + NT_s)z - 1} e(z)) + (K_p K_i e(z) - k_w v(z)) \frac{T_s}{(z-1)}, \quad (6)$$

where  $T_s$  is a sample time. Based on equation (6) the multivariable PID controller for electrohydraulic load-sensing servo system is designed. It has three inputs and one output. The first input is position error  $e_{pos} = r_{pos} - y_{pos}$  and the second one is  $y_{LVDT}$ , where  $r_{pos}$  is reference for cylinder piston position. The third input is the signal form conditional feedback  $v$ . The designed discrete time multivariable PID controller is described by

$$u(z) = \begin{bmatrix} K_{p_{pos}} & K_{p_{LVDT}} & 0 \\ K_{p_{pos}} K_{i_{pos}} \frac{T_s}{(z-1)} & 0 & \frac{T_s}{(z-1)} \\ \frac{K_{p_{pos}} T_{d_{pos}} N_{pos} (z-1)}{(1+N_{pos} T_s)z-1} & \frac{K_{p_{LVDT}} T_{d_{LVDT}} N_{LVDT} (z-1)}{(1+N_{LVDT} T_s)z-1} & 0 \end{bmatrix} \begin{bmatrix} e_{pos}(z) \\ -y_{LVDT}(z) \\ v(z) \end{bmatrix} \begin{bmatrix} 1 \\ 1 \\ 1 \end{bmatrix}, \quad (7)$$

where  $T_s = 0.01s$ ,  $u_{min} = -5000, u_{max} = 5000$  which are used to evaluate signal  $v$  according to equation (5).  $K_{p_{pos}}, K_{p_{LVDT}}, K_{i_{pos}}, T_{d_{pos}}, T_{d_{LVDT}}$  are controller parameters and poles of low pass filters are chosen as  $N_{pos} = \frac{T_{d_{pos}}}{5}, N_{LVDT} = \frac{T_{d_{LVDT}}}{5}$ . As can be seen from equation (7) for feedback of cylinder piston position the PID control law is used, whereas for feedback of LVDT sensor the PD control law is implemented. The design problem of PID controller (7) for model (3) is to find the vector with unknown parameters  $\theta = [K_{p_{pos}} \ K_{p_{LVDT}} \ K_{i_{pos}} \ T_{d_{pos}} \ T_{d_{LVDT}}]^T$ , which provide desired control system performance. A useful method to obtain parameters is optimal tuning. The performance index to be minimized, is given by

$$\min_{\theta} J(\theta), J(\theta) = \sum_{i=0}^{N^*} e_{pos}^2(i, \theta) + R \sum_{i=0}^{N^*} u^2(i, \theta), \quad (8)$$

where the weighting coefficient  $R = 0.001$  is experimentally chosen in order to obtain acceptable form of control signal. The unconstrained optimization problem (8) can be solved by various classical and modern methods [10]. In case of objective functions with several local minima's a methods for global optimization such as firefly optimization, simulated annealing, pattern search and genetic algorithm are preferred. The last one is especially suitable in case of unknown initial parameters, which is the case in this paper. The genetic algorithm is based on the natural selection, which is a method that drives biological evolution. The block scheme of genetic algorithm is depicted in Fig.3.

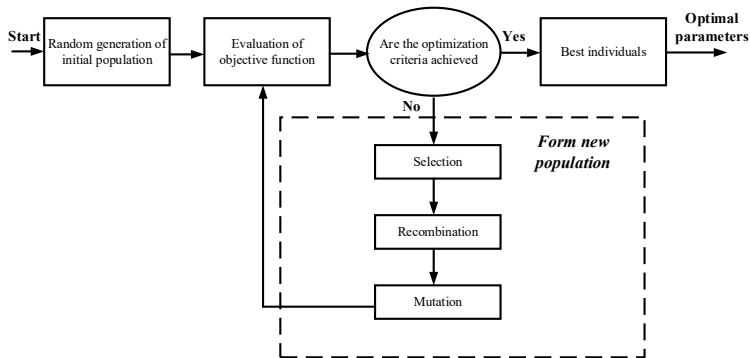


Fig.3. Block scheme of genetic algorithm.



In the beginning, the GA randomly generates initial population of  $n$  individuals (chromosomes). Then, it evaluates the objective function for initial population. In the next step, the individuals are ranked and their fitness is obtained. The algorithm for selection of individuals chooses ones for reproduction, based on their relative fitness. In this manner, the most fitted individuals are used for reproduction. Selected individuals are then recombined. To form children, the parents are crossed over with cross over probability. Then mutation is applied with determinate probability. The aim of mutation is to prevent falling of all solutions in the population into a local minimum. The crossover and mutation operators are realized to yield improved children for the next generations. The objective and fitness functions for new individuals are calculated again. The new generated population is used for a further run of the algorithm. Due to random generation of initial population, to achieve global optimum it is recommended to run several times the optimization procedure. Then one can use the best solution.

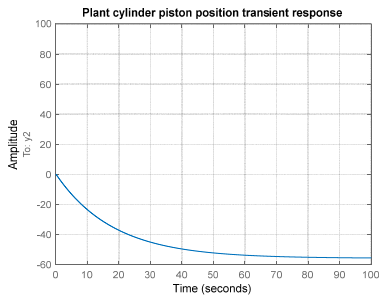
The optimization problem (8) is solved by *MATLAB*<sup>®</sup> function *ga*. The 15 runs of GA procedure with initial population of 100 individuals and option 'vectorized' for fitness function are performed. The obtained PID controller parameters and the value of objective function are presented in Table 1. In every run the optimization procedure stops due to that the average change in value of objective function is less than defined tolerance, which means that global or local minimum is achieved. The values of objective function for all runs are almost the same, which indicates that achieved optimum is global minimum. The values of  $K_{p_{pos}}$  and  $K_{i_{pos}}$  for all runs are close too.

**Table 1.** PID controller parameters.

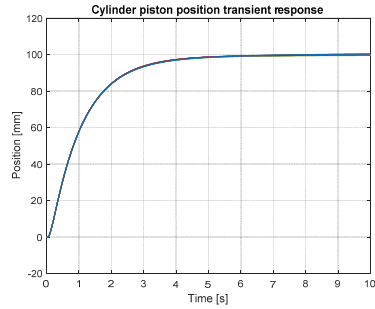
Run	$J(\theta)$	$K_{p_{pos}}$	$K_{p_{LVDT}}$	$K_{i_{pos}}$	$T_{d_{pos}}$	$T_{d_{LVDT}}$
1	$1.293778 \times 10^6$	-26.8670	-6.5600	0.0570	0.5680	0.0090
2	$1.2937649 \times 10^6$	-26.7690	-0.0090	0.0570	0.6000	0.1030
3	$1.295076 \times 10^6$	-25.2080	-0.1250	0.0690	0.8560	0.3760
4	$1.2939273 \times 10^6$	-26.7540	-0.0250	0.0590	0.6270	0.0490
5	$1.293454 \times 10^6$	-25.6950	-0.3980	0.0620	0.7930	-0.0460
6	$1.2938889 \times 10^6$	-26.5890	0.002	0.0590	0.6330	0.0330
7	$1.2940965 \times 10^6$	-26.2380	-8.8190	0.0610	0.6830	-0.0460
8	$1.2954078 \times 10^6$	-25.0060	-12.5890	0.0710	0.8630	0.0800
9	$1.2955409 \times 10^6$	-24.7330	-16.2500	0.0720	0.9040	0.2780
10	$1.2936065 \times 10^6$	-27.1200	-0.0020	0.0550	0.5410	0.0140
11	$1.2936983 \times 10^6$	-26.8200	-7.7190	0.0560	0.5740	0.0020
12	$1.2934437 \times 10^6$	-27.5520	-0.0310	0.0520	0.4550	6.7350
13	$1.2942432 \times 10^6$	-25.9000	-0.5020	0.0620	0.7530	0.2650
14	$1.2938759 \times 10^6$	-26.6070	-7.9130	0.0580	0.6180	0.0050
15	$1.2958139 \times 10^6$	-24.5170	-13.7200	0.0730	0.943	0.2270

In Fig.4 transient response of model (1) respect to cylinder piston position is presented. In Fig.5, Fig.6 and Fig.7 transient responses and control signal of control systems based on the multivariable PID controller with parameter values from Table 1 are depicted.

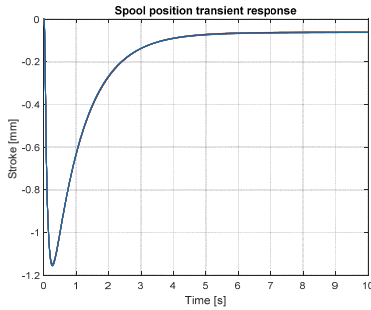
It is seen that the transient response of closed loop system is aperiodic and it is more 10 times faster than one for plant model. For all fifteen values of  $\theta$  (vector with PID controller parameters), transient responses and control signals are very close, which again approves that the obtained minimum is global. The control signal has admissible form and does not achieve its extremal values.



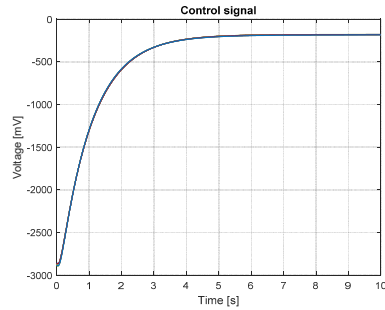
**Fig.4.** Plant cylinder piston position.



**Fig.5.** Control system cylinder piston position.



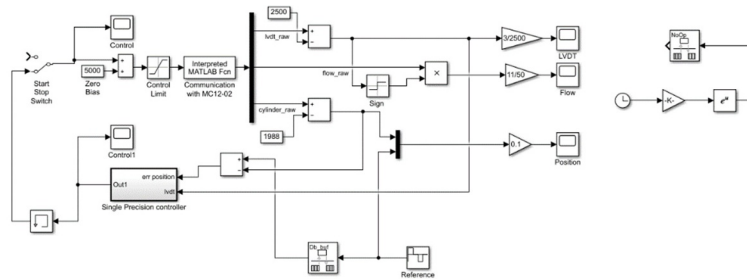
**Fig.6.** LVDT.



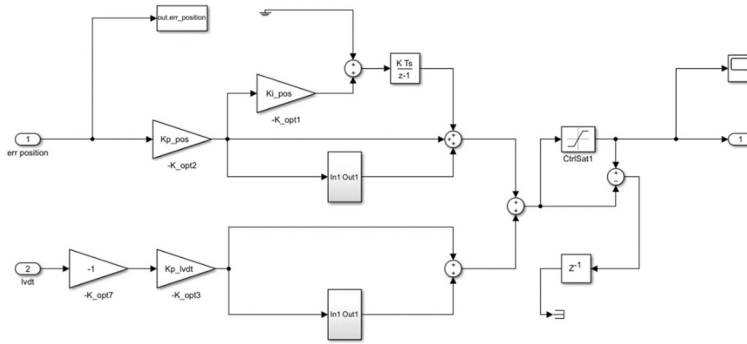
**Fig.7.** Control signal.

### 5 Comparison of simulation and experimental results

The tuned PID controller is embedded into the microcontroller of test rig for experimental investigation of electrohydraulic servo steering system. The implementation of controller is realized through real-time Simulink<sup>®</sup> program which is presented in Fig. 8 [10]. The main block of the model structure is a *Single Precision Controller* which is a subsystem for representation of the multivariable PID controller after GA-tuning. The subsystem structure is depicted in Fig.9.



**Fig.8.** Simulink<sup>®</sup> model for controller implementation.



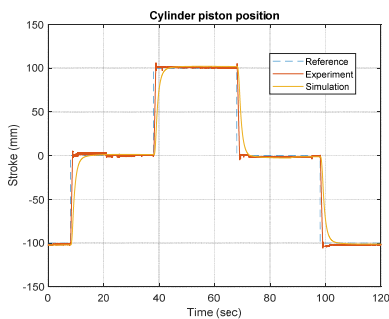
**Fig.9.** Subsystem of embedded multivariable PID controller.

The control performance is investigated based on several physical experiment. During the experimental tests we set a constant value (5MPa) of pressure load in the both chambers of the servo cylinder via counter-balance valves, which are incorporated in the hydraulic block and realized a load system.

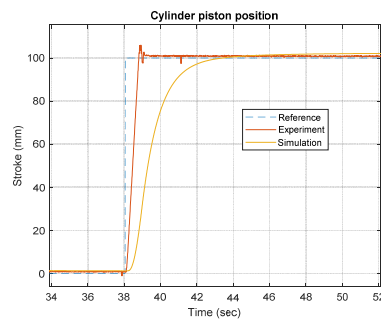
Figure 10 compares the experimental and simulated cylinder reaction to the reference signal. The programmed reference trajectory is a rectangular signal which span the full range from -0.1 to 0.1 m with period of 30 seconds. For the experiments we've programmed 2<sup>nd</sup>, 3<sup>rd</sup> and 4<sup>th</sup> PID parameter tunings from the Table 1.

However, their performance is very similar so in the figures we show only the results from the 3<sup>rd</sup> parameter set. Interesting effect to be observed is that experimental response is several 3÷4 seconds faster than the simulated response. The experimental system with the designed PID controller demonstrates very good reference tracking with settling time around 1.5 seconds. From our other investigations on the test bench we can conclude that it is very hard to achieve such response with other control structures or heuristic manual tuning of the PID gains.

A more detailed view of the second stepwise transient is presented in Fig. 11. There is not overshoot in both simulated and experimental response. The experimental response can be classified as critic aperiodic due to its small ripple above the reference, which doesn't affect the closed-loop system performance for low speed steering applications. Both simulated and experimental systems keep steady state error very small around 1mm. An interesting observation about the experimental system is its small sensitivity to measurement noises even though the controller reaction is very fast.

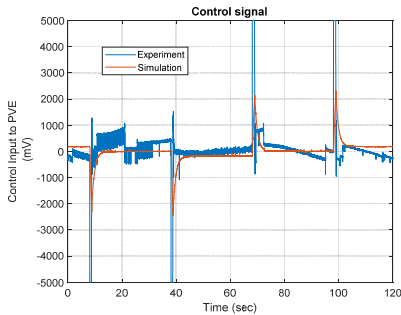


**Fig.10.** Transient response.

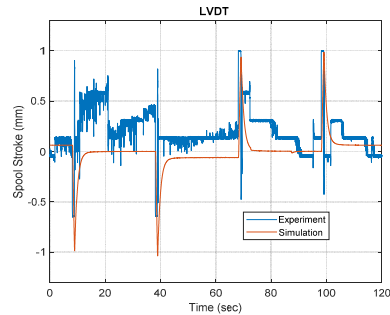


**Fig.11.** Detailed view of transient response.

Comparison the control signal of the simulated and experimental closed-loop system is depicted in Fig.12. Here we can note that the effect of the measurement noise is amplified in the experimental control signal, but its amplitude is not high enough to cause oscillation in the directional spool valve. For example if the noise amplitude was high enough to cause a change in spool direction beyond the zero point, that would have been demonstrated in the cylinder response. Another observation from the control signal is that during stepwise reference change the implemented controller reacts by applying maximal voltage to the PVE block. That guarantees an optimal response in terms of rising time because of the maximal cylinder velocity. However such movement can cause overshoot if not stopped at the right moment. The simulated system doesn't have such oscillations in the steady state control signal because sensor noise is not simulated.



**Fig.12.** Plant cylinder piston position.



**Fig.13.** Control system cylinder piston position.

Comparison between the experimental and simulated response of the directional spool valve is presented in Fig.13. Its motion is sensed by the LVDT sensor which detects the change in inductance caused by the spool movement. It is important to note that spool response is very fast, allowing fast execution of the calculated control signal. That is important to achieve an accurate cylinder positioning. Also the amplitude of the simulated and experimental LVDT signal is reaching same level. There is a steady state bias in the experimental signal which is due to mechanical zero bias an unidirectional spool spring element. However, these mechanical asymmetries doesn't impact the performance of the closed-loop system, and the controller compensates for them by automatically offsetting the spool position.

## 6 Conclusions

The article presents a modern method for tuning of multivariable PID controller designed for electrohydraulic servo system intended for load-sensing power steering. The method for setting of the controller parameters is essentially an optimization procedure using a genetic algorithm to minimize the performance index. The contribution of used method is that unlike other widely used methods for tuning of PID controllers, this allows multivariable controllers to be set. The description of the algorithm including its block diagram and the results for obtained PID controller parameters during the optimization procedure are presented in detail. The tuned PID controller is embedded into the microcontroller of test rig for experimental investigation of electrohydraulic servo steering system. The performance analysis is done based on comparison between experimental and simulation results, which are presented also.

## References

1. H. Merrit, *Hydraulic Control Systems*, John Wiley & Sons, Inc., ISBN 978-0-471-59617-2, (1967).
2. K. Aström, T. Hagglund, *PID Controllers: Theory, Design and Tuning*, Second Edition, ISBN 1-55617-516-7, United States of America, (1995).
3. H. Feng, C. Yin, W. Weng, W. Ma, J. Zhou, W. Jia, Z. Zhang, Robotic excavator trajectory control using an improved GA based PID controller. *Mechanical Systems and Signal Processing*, **105**, 153–168. doi:10.1016/j.ymssp.2017.12.014, (2018).
4. Al. Mitov, Ts. Slavov, J. Kralev, Il. Angelov, System Identification of Electro-Hydraulic Load-Sensing Servo System, 20th International Scientific Conference Engineering for Rural Development, ISSN 1691-5976, Jelgava, Latvia, (2021).
5. K. Elbayomy, J. Zongxia, Z. Huaqing, PID Controller Optimization by GA and Its Performances on the Electro-hydraulic Servo Control System, *Chinese Journal of Aeronautics*, **21**, 4, 378–384. doi:10.1016/s1000-9361(08)60049-7, (2008).
6. T. Samakwong, W. Assawinchaichote, PID Controller Design for Electro-hydraulic Servo Valve System with Genetic Algorithm, *Procedia Computer Science*, **86**, 91–94. doi:10.1016/j.procs.2016.05.023, (2016).
7. M. Hassan, N. Azubir, H. Nizam, S. Toha, B. Ibrahim, Optimal Design of Electric Power Assisted Steering System (EPAS) Using GA-PID Method, *Procedia Engineering*, **41**, 614–621. doi:10.1016/j.proeng.2012.07.220, (2012).
8. Danfoss Inc., Steering, EHi steering valve, Technical Information, BC00000379en-US0202, (2018).
9. L. Ljung, *System Identification: Theory for the User*. Prentice-Hall, Inc., Englewood Cliffs, NJ, 2nd edition, ISBN 978-0136566953, (1999).
10. G. Todorov, K. Kamberov, T. Ivanov, Parametric optimisation of resistance temperature detector design using validated virtual prototyping approach, *Case Studies in Thermal Engineering*, **28**, 1-9. doi:10.1016/j.csite.2021.101302 (2021).
11. Al. Mitov, Al., J. Kralev, Ts. Slavov, Il. Angelov, Model Predictive Control Design for Electro-hydraulic Power Steering Application, The 9th Mediterranean Conference on Embedded Computing - MECO'2020, ISBN 978-1-5386-5683-9, Montenegro, (2020).

# Design of direct acting differential pressure control valve test bench

Ognyan Bekriev <sup>1,\*</sup>, and Radoslav Asenov <sup>1</sup>

<sup>1</sup>Faculty of Power Engineering and Power Machines, "Department of Hydro-aerodynamics and Hydraulic Machines", Technical University of Sofia, 8 St. Kliment Ohridski Blvd, Bulgaria

**Abstract.** This article aims to acquaint readers with a designed test bench for direct acting differential pressure control valves. These control valves are used in district heating systems. The conformity of the construction of the test bench with the international standard IEC 60534-2-3:2015 is evaluated and the results of an experimental study of the control valve AVPB DN20 Kvs 6.3 PN16 are presented.

## 1. Introduction

One reason for the widespread use of control valves for differential pressure control, as a component of district heating network substations is the ability to improve the quality of local temperature control of the heat carrier to the internal installations of the users. This is achieved by adjusting the pressure drop on the control valve of the heating circuit and the heat exchanger or by adjusting the pressure drop on the control valve individually. The control valve authority factor "a", is generally defined as the ratio of the pressure drop across the fully open control valve "dPv" and pressure drop across whole circulation circuit "dPc" (Fig.1). In order to achieve quality control of the temperature in the heating system or in the domestic hot water system, it is necessary, the control valve authority factors of the selected control valve to be in the range from 0.5 to 1. This parameter is related to the deformations of the flow characteristic of the control valves, and thus to the ability of the electronic controllers in the substations to maintain the temperatures set point values, without significant deviations. The differential pressure control valve is also used for balancing the district heating network. This in turn leads to a reduction in the CHP power plant fuel consumption by decreasing the return temperature of the district heating network, and increasing the energy efficiency of the CHP power plant.

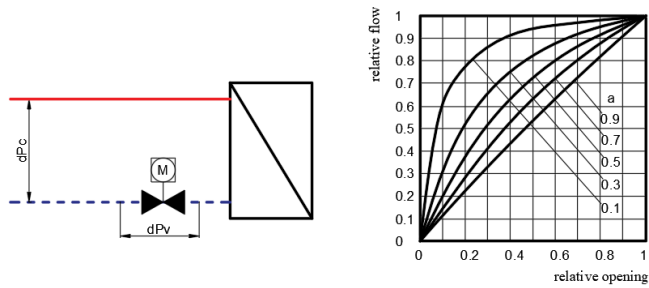
$$a = \frac{\text{differential pressure across the valve}}{\text{differential pressure across the circuit}} = \frac{dPv}{dPc} \quad (1)$$

where:

- a - control valve authority factor;
- dPv- differential pressure across the control valve Fig.1;
- dPc - differential pressure across the circuit Fig. 1.

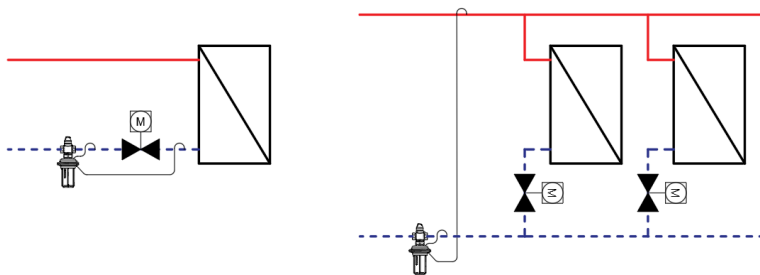
---

\* Corresponding author: [bekriev@tu-sofia.bg](mailto:bekriev@tu-sofia.bg)



**Fig. 1** An example of the influence of the authority factor on the flow characteristic.

In order to ensure a constant differential pressure (0.8 bar) for all of the heating circuits in district heating substation it is equipped with a differential pressure controller with a common range from 0.2 to 1 bar. There are a few variants of connection of impulse lines of the differential pressure control valve which are shown on the next Fig.2.



**Fig. 2** Differential pressure control valve connection options.

In the central district heating network of Sofia, the pulse lines of the differential pressure control valves are most often connected for control of the differential pressure in two parallel circuits. This stems from the compliance of the design of the district heating substations with the "Basic technical requirements for district heating stations with hot water for the city of Sofia" and "Changes and additions to the basic technical requirements for district heating stations with hot water for the city of Sofia", which contain general instructions for design of the subscriber stations for the district heating network of the city of Sofia.

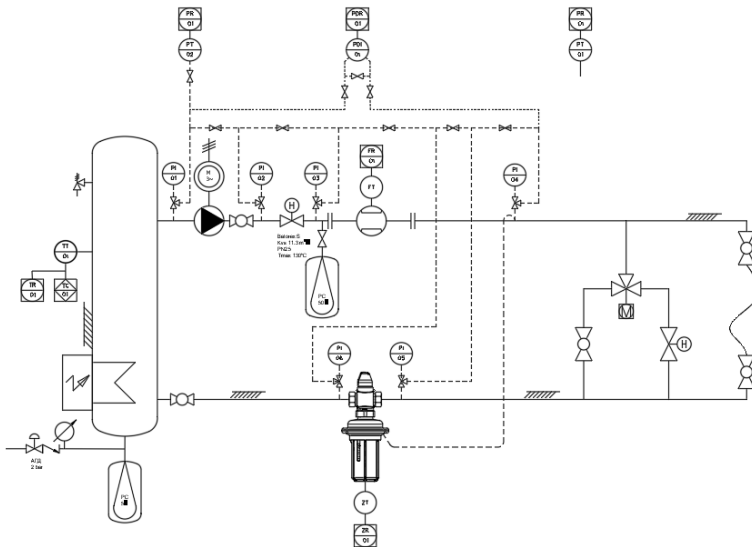
## 2. Construction of the test bench

The aim of the research is to study the characteristics of differential pressure control valves in the district heating network. The construction of the test bench can recreate a real working conditions. The test bench can be used for studying the operation of the control valves in static and dynamic mode of operation. To achieve a good repeatability of the test results, the construction of the laboratory test bench, have to meet some of the requirements of the international standard IEC 60534-2-3:2015:

- The length of the straight section before the control valve have to be at least  $18 \times D_n$ ;
- The length of the straight section after the control valve have to be at least  $7 \times D_n$ ;

- The flow measurement devices have to have an uncertainty of  $\pm 2\%$  and repeatability  $\pm 0.5\%$
- The accuracy of the temperature measurement devices be  $\pm 1\text{ }^{\circ}\text{C}$  or better;
- The device for measuring static pressure before and after the valve with uncertainty of  $\pm 2\%$ ;
- The location and dimensions of the nozzles for outputting a static pressure signal have to be as shown in the standard.

The next figure 3 presents a P&ID diagram of the laboratory test bench. It consists of the following main elements: buffer vessel, pump (WILO MHI 805-1), throttle valve, solenoid flow meter (PROMAG 33), three-way control valve, manual control valve (HERZ STRÖMAX-GR), differential pressure controller (AVPB DN20 Kvs6.3 PN16), automatic filling valve, safety valve, main expansion vessel, expansion vessel for network storage volume simulation, PLC controller (VISION V120 HMI), pressure transmitter, differential pressure transmitter (E+H PMP 70), electronic micrometric depth gauge (HBM 0..25.4mm  $\pm 0.01\text{ mm}$ ), electrical panel (not shown on Fig.3).



**Fig. 3** P&ID diagram.

### 3. Measuring instruments

The flow rate is measured with a magnetic inductive flow meter PROMAG 33 produced by E+H. The flow meter is selected to give a maximum accuracy at low flow rates, in accordance with the operating range of the studied differential pressure control valve. The flowmeter upstream and downstream straight pipe runs are in accordance with the manufacturer's requirements. The measurement accuracy is  $\pm 0.5\%$  and meets the requirements of the standard. The measuring range is from 0 to 6000 l/h.

The test bench is equipped with a pressure transmitter PMP70 produced by E+H. By switching the pulse lines, the operator can measure the static pressure at any point of the system. It allows pressure measurements with an accuracy of  $\pm 0.1\%$ , which satisfies the requirements of the standard.



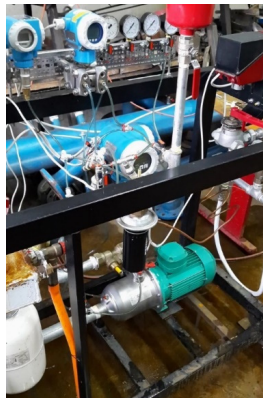
To ensure repeatability of results and high accuracy of measurements, the test bench is equipped with a precision differential pressure transmitter - PMD75 produced by E+H. It is mounted on a mounting frame that allows alignment and zero-point adjustment. Pulse lines can be switched quickly and easily with visual control for the presence of air bubbles. The measuring sensor is selected with a range that allows the measurement of any drop in differential pressure in the system, without the risk of overload and damage to the device.



**Fig. 4** Differential Pressure Transmitter - Deltabar PMD 75.

The test bench is equipped with a Pt100 type temperature sensor. It is used to measure the temperature of the working fluid and it is connected to fluid temperature control system to a Vision V120 PLC HMI controller. The controller performs the function of a self-adjusting PID controller with pulse width modulation. This allows the operator to set and control the temperature of the fluid in the system. Additionally, this function the PLC HMI controller is programmed to send an opening and closing signal to the actuator of the three-way control valve, with the possibility of controlling the opening and closing time. With this function the operator can do a dynamic simulations of real operation of the differential pressure control valve.

Two identical Honeywell pressure sensors PG-10 with a time constant of 5ms, are used to record the pressures before and after the differential pressure control valve during dynamic operation mode simulation. For this purpose, the recording of the rapidly changing pressure signal is performed with a two channel oscilloscope.

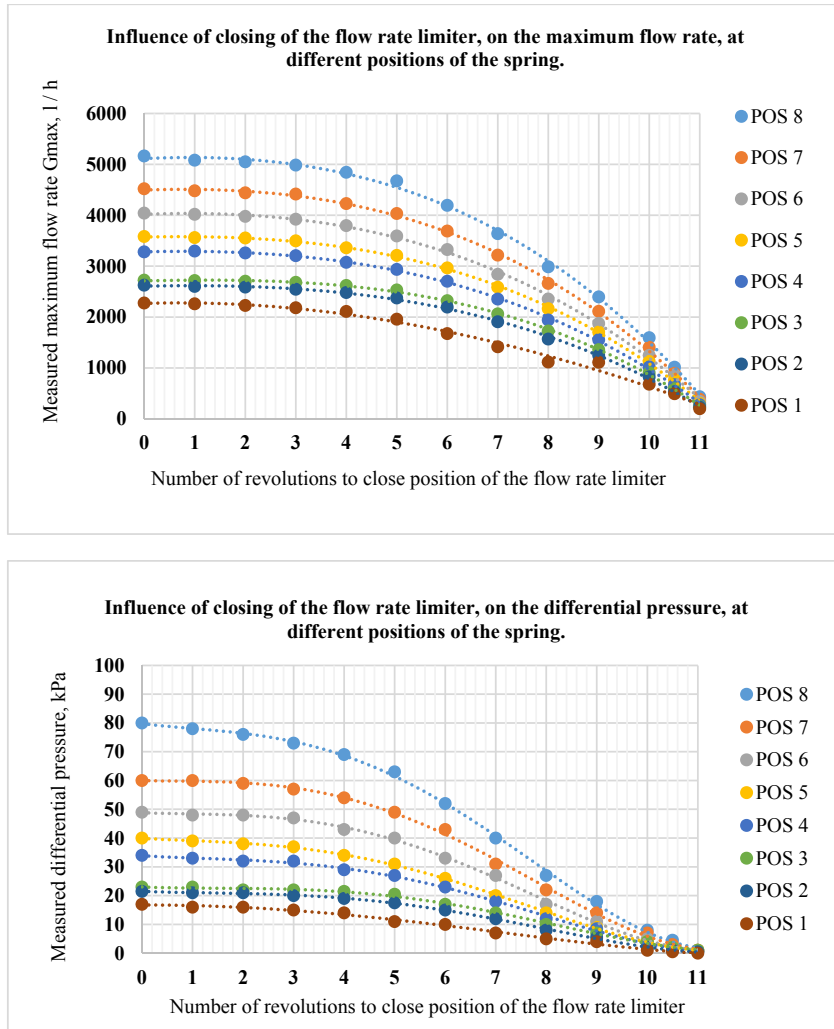


**Fig. 5** Image of the test bench.

To ensure safety during operation, the test bench is equipped with an electrical panel, a starter and a fuse for the pump. Power supply units for automatic and control measuring devices are installed in the panel. All terminal blocks are labeled and a preliminary functional test of the power supply of all devices has been performed.

## 4. Results

Using the test bench described above, several experiments were performed to investigate the characteristics of the AVPB DN20 Kvs 6.3 PN16 differential pressure control valve, Fig.6.



**Fig. 6** Results of a study of the operation of the flow rate limiter of the differential pressure control valve AVPB DN20 Kvs 6.3 PN16 produced by Danfoss.

The scale markings are used to establish always the same valve spring tension to adjust the differential pressure.

## 5. Conclusions

After the initial experiments with a differential pressure control valve AVPB DN20 Kvs 6.3 PN16, the following was achieved:

- The operator has the possibility to adjust the fluid flow in the specified range;
- The operator has the possibility to set and control the static pressure in the system;
- The operator has the possibility to accurately determine the pressure drops by manually switching the pulse lines;
- The operator has the possibility for accurate measurement of static pressure at different points after manual switching;
- The operator has the possibility to set and control the temperature in the system;
- The test bench has the possibility to simulate the characteristics of long heat transfer pipelines, with an effect of elasticity;
- A system for measuring and recording pressure in case of hydraulic shocks has been implemented, which can be simulated by changing the hydraulic stability in the system.

The test bench successfully recreates real working conditions and can be used to study the operation of differential pressure control valves.

## References

1. St. Stamov and collective, Handbook of heat supply and gas supply Part 2, 584, (2000)
2. Al. Kiriya, A. Asenov, Measurement of thermal, hydraulic and mechanical quantities, 260, (2006)
3. Matthias Altendorf and collective, Flow Handbook Endress+Houser, 456, (2004)
4. Danfoss, Differential pressure controller with flow limitation (PN 16) AVPB Data sheet

# Reduction of the Battery Capacity of Hybrid Electric Vehicle with the Help of Electrically Assisted Turbocharger

Milen Mihaylov<sup>1\*</sup>, Ivaylo Stoyanov<sup>2</sup>, and Teodor Iliev<sup>2</sup>

<sup>1</sup>BorgWarner Turbo Systems, GmbH, Kirchheimbolanden, Germany

<sup>2</sup>University of Ruse "Angel Kanchev", 7017 Ruse, Bulgaria

**Abstract.** In this manuscript, the reduction of the battery capacity of a hybrid electric vehicle with the help of electrically assisted turbochargers was analyzed. Using the battery for vehicle propulsion and the options for its recharging, it could be concluded, that the most efficient way would be to use the battery energy for boosting mainly through eTurbo™ and recharge the battery mainly with the traction motor in regenerative braking. Based on both steady-state and transient analysis it is clear, that for having the same dynamic HEV performance, the boosting with propulsion through ICE requires significantly less energy from the battery compared to the boosting through the traction motor. Therefore using the eTurbo™ as boosting device can lead to reduce the battery capacity and reduce fuel consumption and emission of the vehicle.

## 1 Introduction

Hybrid Electric Vehicles (HEV) are getting more and more popular as an alternative to the classic vehicle powertrains with a standard Internal Combustion Engine (ICE). There are two main reasons for this trend. The main reason is the reduction of CO<sub>2</sub>, which is supposed to be the main driver for the Earth's global warming. The second reason is the superior driving performance of the HEV in terms of faster vehicle acceleration, which is known as a "Fun to Drive". This is possible because the HEV powertrains combine two driving systems – ICE + Electrical Driving System (EDS). The energy source for EDS is a battery. The battery is one of the most innovative and expensive parts of the HEV powertrain and its capacity is essential for its cost and weight.

Hybrid vehicles allow many functionalities such as recuperation, starter-generator torque support, etc. [2]. In [3], a hybrid meta-heuristic algorithm for gear optimization based on certain criteria is proposed.

The modern ICEs are equipped with a turbocharger, which allows increasing their power density and reduction of fuel consumption. The consequence of the reduced fuel consumption is reduced CO<sub>2</sub> emissions [4, 5, 6]. Using a turbocharged engine as the main energy source of HEV powertrains allows using an Electrically Assisted Turbocharger – the so-called eTurbo™ – one of the most innovative products of BorgWarner. The eTurbo™

---

\* Corresponding author: [milenmihaylov@yahoo.com](mailto:milenmihaylov@yahoo.com)

incorporates three machines fitted on a common shaft – the two turbo machines compressor and turbine, which are the main part of the classical turbocharger, and additionally one electric machine. The electric machine is the innovative part of the eTurbo™.

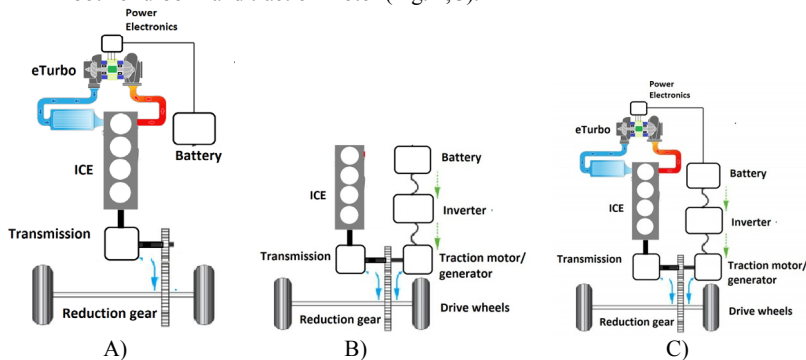
This paper shows that:

- HEV with ICE boosted only with eTurbo™ can offer the same Fun to Drive with lower battery capacity, compared to HEV with ICE boosted with classical turbocharger (without eTurbo™)+traction electric motor.
- If having the same battery capacity HEV with ICE boosted with eTurbo™ + traction electric motor will have the same Fun to Drive + lower fuel consumption and therefore lower CO<sub>2</sub> emissions.

## 2 Boosting Options inside HEV Powertrains

Depending on the way how the battery energy is used for boosting the HEV powertrains there are three options:

- boosting through the eTurbo™ - the battery boosts the powertrain through eTurbo™ and ICE (Fig. 1, A)
- boosting through the traction motor – the battery boosts the powertrain through the traction electric motor (Fig. 1, B)
- boosting through both eTurbo™ + traction motor – powertrain is boosted from both eTurbo™ and traction motor (Fig. 1,C).



**Fig. 1.** eTurbo boosting (A), EDS boosting (B), eTurbo + EDS boosting (C) [9]

The eTurbo™ boosting can be classified as indirect boosting, because first the ICE is boosted with the help of an additional boosting system and then the ICE boosts the HEV powertrain.

The traction motor boosting could be classified as direct boosting in the mild and power assist HEVs, because in these architectures the function of the traction motor is to support the ICE. The traction motor itself cannot power the vehicle alone. Therefore it has assisted or boosting function.

### 2.1. Boosting through the eTurbo™

As a part of the HEV powertrain, the ICE is always the main power source. Considering the standard vehicle powertrains, where ICE is the only power source, the term “boosting” is used for those ICEs, which have a system for forced air induction, commonly known as an air charging system, or just charging system. The charging system ensures engine power-

boosting function by supplying pressurized air with low temperature into the engine cylinder during the piston induction stroke. The high pressure and low temperature mean higher air density, which results in increased cycle air mass. More air means, that more fuel can be burned. More fuel means higher power from the same cylinder displacement.

Apart from the increased engine power density, some types of charging systems are offering additional side benefits like improved engine efficiency and reduced tailpipe emissions.

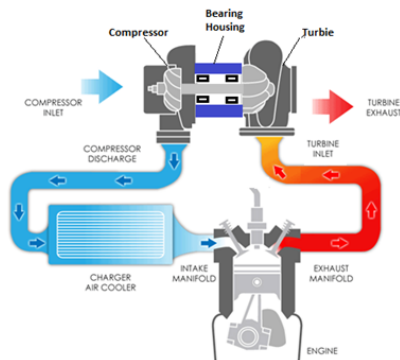
There are many types of charging systems used in the ICEs. The most common and popular one is the charging/boosting system with Exhaust Gas Turbocharger (EGT), known as Turbocharger or simply Turbo.

BorgWarner is a leading turbocharger supplier in the automotive market with more than 50% market share.

The term “turbo” comes from the fact, that the EGT incorporates turbomachines for accomplishing its boosting function. The term “Exhaust Gas” means, that the energy for the boosting is extracted from the engine exhaust, leaving the cylinder during the piston exhaust stroke.

### 2.1.1. Principal of turbocharging without electrical assistance (standard)

The principle of turbocharging is shown in Fig. 2.



**Fig. 2.** Principal of turbocharging

The turbocharger is a device, which incorporates two machines – compressor and turbine (Fig. 2). They are connected to a common shaft. The shaft is supported on a bearing system (sliding or rolling bearing), accommodated in the bearing housing between the compressor and the turbine.

From the engine exhaust manifold, connected to the turbine inlet, the exhaust gas flows from the engine cylinder to the turbine during the piston exhaust stroke. A turbine is a machine that converts part of the exhaust gas enthalpy into the mechanical power of the common shaft. The shaft transmits the mechanical power to the compressor. The compressor converts the mechanical power into enthalpy of the fresh air. As a result the pressure and temperature of the air rise. The compressor outlet is connected to the charge air cooler device, where the pressurized air is cooled down at constant pressure, before entering the engine cylinder during the piston induction stroke. The pressurized air with the lower temperature inside the cylinder has a higher density and therefore bigger air mass is trapped, compared to the case of a naturally aspirated engine (engine without a turbocharger). With more air, more fuel can be burned and therefore higher engine power

for the same engine displacement is achieved. Or if the engine displacement is reduced, with the help of the turbocharger a smaller engine can have the same power output, compared to a bigger engine without turbocharging. This is the so-called engine downsizing principle. The smaller engine has lower friction losses and can work more efficiently with less fuel consumption and fewer tailpipe emissions. The smaller engine is also cheaper and lighter, which is another advantage for the vehicle.

The main disadvantage of turbocharged engines is the slower response to the engine load. This means, that when the driver pushes the accelerator pedal the engine torque/power rise is delayed, and hence the vehicle acceleration has a certain delay. The reason for this is, that a certain time is needed for the turbine to collect exhaust gas and to convert its enthalpy to boost pressure in the intake manifold through the compressor. A certain time is necessary also the entire piping volume and charge air cooler between the compressor exist and engine cylinder to be filled to higher pressure, due to the compressibility of the air. And last but not least, the rotating components of the turbocharger – the compressor wheel and the turbine wheel have mass inertia, and to accelerate to higher speed, additional energy is necessary.

The vehicle acceleration demand appears more often at lower vehicle speed and lower engine speed when there is not a sufficient amount of exhaust gas for the turbine. To create sufficient power, the turbine is usually sized smaller, i.e. with less flow capacity. This helps for faster acceleration, but it is a drawback when the engine operates at higher speeds and loads. The turbine cannot permeate the entire exhaust flow amount, or if it permeates it the turbo shaft speed will rise above the mechanical limits, which will destroy the weakest rotating component. Additionally, the boost pressure control and engine load cannot be controlled. Therefore a protecting/regulating device is needed, which can be a turbine bypass valve, which releases part of the exhaust flow directly from the turbine inlet to the turbine outlet. This solves the engine control and prevents the turbocharger from overspeeding, but leads on the other hand to increased pressure inside the engine cylinder, which is not favorable for the engine combustion and gas exchange process and causes increased fuel consumption.

If the turbine is sized for higher flow capacity, then it will not create such high pressure in the engine cylinder, but then the vehicle acceleration and the “Fun to drive” will suffer at lower speeds. Therefore the turbine sizing is always a compromise.

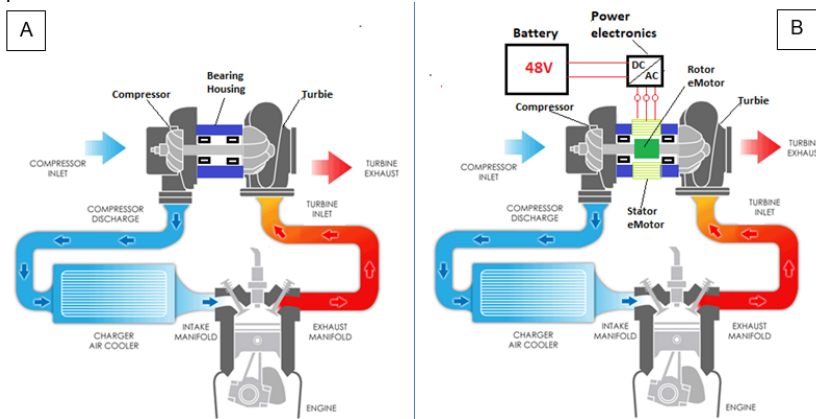
### *2.1.2. Principal of turbocharging with electrical assistance (eTurboTM)*

There are some ways how to minimize this compromise. A very popular and widely spread one is using the Variable Geometry Turbine (VTG), which is since decades in serial production. Or using multistage charging systems with more than one turbocharger connected in series or parallel and some others.

But in the case of HEV, there is accumulated electric energy stored in a battery. This energy could be used in several ways to boost the HEV. This is how the idea for electrically assisted turbochargers appears.

To the shaft of the classical turbocharger, (Fig. 3A, Fig.2), which has two turbomachines on a common shaft is fitted a third electric machine (Fig. 3B). There are several design concepts, but the most common one is with an electric machine fitted inside the bearing housing. This machine can work as an electric motor adding mechanical power to the shaft to support the turbine for driving the compressor, or to work as a generator, consuming mechanical energy from, when the turbine has excess power. In electric motor mode, electrical energy is provided to the motor from the battery of the HEV. In generator mode, the electric energy could be used directly for the traction electric motor(s) of the HEV or for recharging the battery.

Having an additional power device on the shaft as an electric motor, the compressor has additional support for acceleration and the turbine can be sized for higher flow capacity, which is beneficial for the engine combustion and gas exchange processes at higher engine speeds and loads.



**Fig. 3.** Principal of turbocharging without (A) and with (B) electrical assistance

This is how the eTurbo™ can use the electric energy from the battery to generate an additional boost on the ICE, which boosts the HEV powertrain for better vehicle dynamic performance and faster acceleration, and superior “Fun to drive”.

This is an indirect way of using the battery to boost the HEV powertrain. The battery energy is used from the Turbo™ motor to pressurize air through the compressor. The compressor boosts the ICE and the ICE then boosts the HEV powertrain. There are several energy transformation processes involved.

Having an additional power device on the shaft as a generator, the excess turbine power at higher engine speeds and loads could be harvested and utilized to generate electric energy for the needs of traction motor or for recharging the battery, instead of fully wasting it through bypass valve as it happens in case of the classic turbocharger.

The electric machine of eTurbo™ is a Permanent Magnet Synchronous Machine (PMSM) with permanent magnets inside the rotor.

A common view of BorgWarner eTurbo™ product with some product features and specifications is shown in Fig. 4 [7].



**Fig. 4.** A common view of BorgWarner eTurbo product [7]:

#### Product Features

Full performance 48 V architecture and HV\_2B and HV\_3 compliant high voltage architectures; Integrated and semi-integrated power electronics options including using engine coolant.

#### Specifications

Platform eTurbo - 48V 3kW ... 17kW; 400/800V 6... 34 kW peak. Versions: eB40. eB50. eB60 and eB80 samples with alternate motor length and voltage classes for each frame size



## 2.2. Boosting through traction motor(s)

It was shown, that the eTurbo™ is an indirect way of using the battery for HEV powertrain boosting while boosting through traction motor is a direct way. The battery energy is used to drive the traction electric motor(s) with only one energy conversion process from electrical to mechanical power.

Therefore one can assume that the boosting through the traction motor is more efficient and would need less energy from the battery and lower battery capacity for the same vehicle performance.

Jaguar Land Rover Limited in collaboration with BorgWarner Turbo Systems and MAHLE Powertrain Limited have performed an engine dyno test with an engine from Jaguar Land Rover engine equipped with BorgWarner eTurbo™ product. Based on the collected test data there is a possibility to calculate comparatively:

- what is the electric energy consumed from the eTurbo™ electric motor to achieve certain performance only through eTurbo™ boosting;
- what would be the electric energy consumed from the traction motor to achieve the same performance through traction motor boosting.

## 3 Engine test data

### 3.1. Engine test data at steady-state full load

The presented diagrams are obtained experimentally. The 2L Turbocharged gasoline engine of automotive manufacture Jaguar Land Rover was equipped with electrically assisted turbocharger designed, manufactured and supplied from the turbocharger supplier BorgWarner Turbo Systems. The engine test was performed at the testing facilities of the company MAHLE Powertrain. The steady state and the transient testing procedure are standard testing procedures for testing of turbocharged Internal Combustion Engines. That is why their test procedure were not in detail described. The terms “steady state full load” and “transient” with the given engine speeds describes both test fully. The main focus was to analyze the test data measured using a standard full load and transient test procedures in comparative way. In Fig.5 is shown the ICE full load torque curve and the eTurbo™ motor electrical power consumption. The blue lines are with deactivated eTurbo™ and the red lines are with activated eTurbo™. Let's consider the second operation point at an engine speed of 1200 rpm.

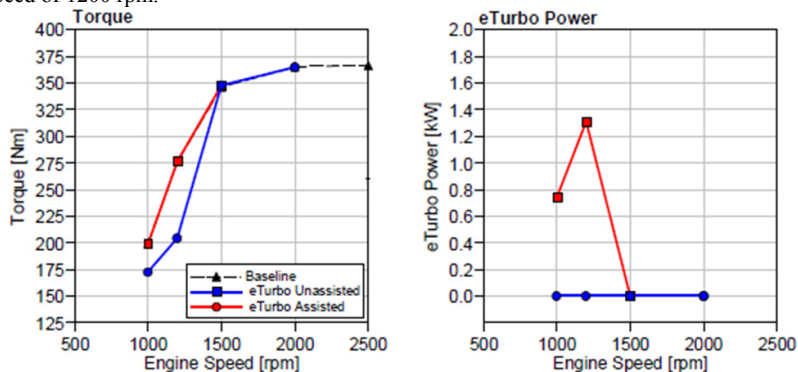


Fig. 5. Engine torque and eTurbo motor power [8]

Based on the ICE torque and ICE speed, ICE power is calculated for both cases with activated and deactivated eTurbo™. (Table 1).

**Table 1.** Calculated ICE speed and power.

	ICE speed	ICE Torque	ICE Power	eTurbo power
	rpm	Nm	kW	kW
eTurbo ON	1200	275	34.56	1.3
eTurbo OFF	1200	205	25.76	0

When the eTurbo™ is deactivated the boost pressure for the engine is created only from the energy of the exhaust gas through the turbine and compressor. The motor of the eTurbo™ is not active and does not generate shaft power. This corresponds to classical turbocharger operation without electrical assistance (Fig 3A). The boost pressure, which the turbocharger can create is enough for the engine to achieve 205 Nm or 25.76 kW of power.

When the eTurbo™ motor is activated with electric power from the battery, it supplies additional 1.3 kW power to the turbocharger shaft. With this additional power, the turbo speed increases and the compressor is capable to create higher boost pressure for the ICE. As a result, the torque of ICE rises from 205 Nm to 275 Nm (70 Nm torque rise) and the ICE power rises from 25.76 kW to 34.56 kW (8.8 kW power rise). In percentage, the engine power rises by 34.1%. In other words, for battery power of 1.3 kW, ICE provides 8.8 kW additional power for the vehicle.

In case that the vehicle is equipped 48V 50 Ah battery, this means accumulated energy in the battery is 2.4 kWh. Recommended battery Depth of Discharge (DoD) is 70%. This means, that the available energy for the eTurbo motor will be  $2.4 \text{ kWh} \times 70/100 = 1.68 \text{ kWh}$ . At a power consumption of 1.3 kW, eTurbo can work and boost the vehicle for approximately 1 hour and 18 minutes.

The task we set is, if the boosting function of the vehicle would be delivered only from the traction motor (Fig. 1B), to determine how much power would the traction motor need to boost the HEV powertrain with the same magnitude of 8.8 kW. The answer is easy and clear. The additional 8.8 kW instead of the ICE has to be delivered from the traction motor.

For the same 48 V, 50 Ah (2.4 kWh) battery discharged to the same 70% DoD the available energy for the traction motor will be theoretically the same 1.68 kWh. To deliver 8.8 kWh shaft power, assuming 95% traction motor efficiency and 97% power electronics efficiency it would consume  $8.8/0.95/0.97 = 9.55 \text{ kW}$ . With an energy of 1.68 kWh and 9.55 kW consumption, the battery would last approximately 11 min. But it would be less than 11 min, because with 9.55 kW discharging power the traction motor withdraws the battery with about 7.35 times higher current ( $9.55/1.3 = 7.35$ ) compared to the eTurbo™ motor, discharging the battery with 1.3 kW. At this higher current, the battery internal losses would be higher and the available energy to DoD =70% would be less than 1.68 kWh.

### 3.2. Engine test data at unsteady (transient) conditions

In Fig. 6A is shown the ICE transient performance, which represents the engine torque rise over time. For the vehicle, this means the acceleration process, when the driver steps on the gas pedal. The faster torque rise means faster vehicle acceleration. Several curves are shown. Each of them represents the ICE torque rise rate for different eTurbo™ motor shaft torque limits, starting from 0.2Nm to 1.6Nm.

Fig. 6B is shown the correspondent eTurbo™ motor electric power consumption. In Fig 6C with dotted line is shown the electric energy, which the eTurbo™ consumes for each torque limitation. This energy is the cumulative energy calculated as an integral of the data points from the eTurbo™ power curves in Fig. 6B.

For the analysis here let's take the case of the maximum ICE torque rise rate, at eTurbo™ shaft torque limit of 1.6 Nm. This is the red curve for which transient time is 0.6s. This will be compared to the baseline, which is the grey dashed curve, where eTurbo™ is switched off.

The cumulative energy, which the vehicle equipped with this ICE needs to accelerate for 0.6s (red acceleration curve on Fig. 6A with eTurbo™ shaft torque limit of 1.6 Nm), calculated as an integral over the acceleration time is 17.2 kJ =4.78 Wh. The eTurbo™ electric energy consumption from the battery is 6 kJ=1.67 Wh.

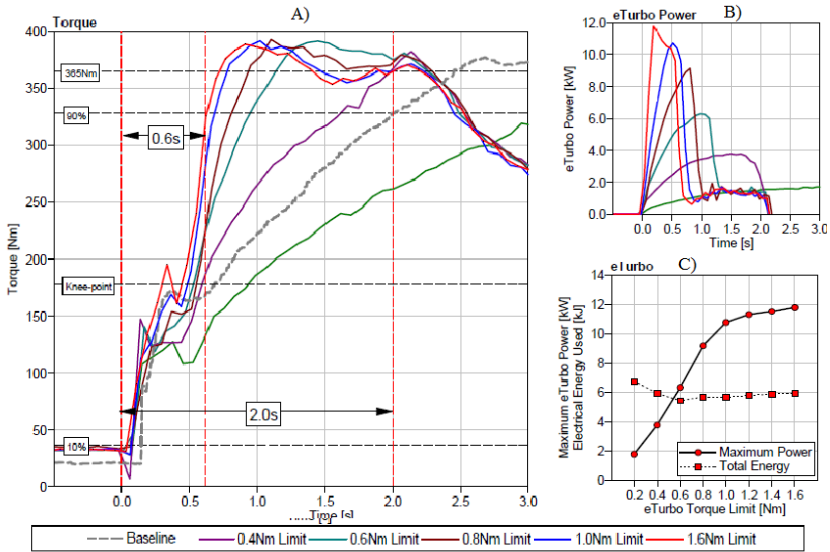


Fig. 6. Engine torque (A) and eTurbo™ motor power (B) and cumulative eTurbo™ energy (C) [8]

The cumulative energy, which the vehicle equipped with this ICE needed to accelerate for 2s (Baseline grey dashed curve on Fig. 6A, the eTurbo™ is switched off), calculated as an integral over the acceleration time is 57.3 kJ =15.93 Wh. The eTurbo™ electric energy consumption from the battery is 0 Wh (Table 2).

Table 1. Cumulative Energy for vehicle acceleration.

	Acceleration time, s	Cumulative Energy for vehicle acceleration, Wh	eTurbo™ energy consumption, Wh
eTurbo ON 1.6 Nm limit	0.6	4.78	1.66
eTurbo OFF	2	15.93	0

The eTurbo™ contributes to reducing the vehicle acceleration energy demand with 11.15 Wh from 15.93 to 4.78 Wh for the expense of 1.66 Wh energy consumed from the battery.

If a battery with the same capacity (48V 50Ah) is considered like for the steady-state calculations, the available energy for DoD of 70% is 1.68 kWh. With this energy amount, the eTurbo™ will support  $1.68/(1.66/1000)=1012$  vehicle acceleration events.

If the same vehicle acceleration in 0.6s is not supported from the eTurbo™, but from traction electric motor the energy for 1 acceleration event will be 15.93 Wh. With 1.68 kWh of battery energy, the traction motor would support  $1.68/(15.93/1000)=106$

acceleration events, which is almost 10 times less compared to the acceleration support from eTurbo™.

#### **4 Options for recharging the battery of HEV**

Having electric machines on the board of HEV, they are used not only in motor mode to boost or drive the vehicle but also in generator mode. The generated electric energy can be used to recharge the battery, which is mandatory for the HEV architectures, which are not Plug-In. They have to be designed in the way that the battery is recharged without an additional external energy source. Usually, the battery recharging energy in non-plug-in HEVs comes from the utilization of the vehicle braking energy. The classical friction brakes convert the vehicle kinetic energy during the braking process into heat energy, which is dissipated in the environment. Using the traction motors in generator mode, allows part of the braking energy to be converted into electrical and recharge the battery.

The eTurbo™ electric machine can also work in generator mode and generate electric energy from the excess exhaust gas energy of the ICE. This is another source available in HEVs to generate electric energy, which could be harvested through eTurbo™.

The advantage of using the eTurbo™ to generate electric energy is that it can be directly used to power the traction motor instead of storing it in the battery. The advantage in this case, that the energy losses for charging and discharging the battery can be avoided. This leads to a reduction of the battery cycles and longer battery life. Of course, charging the battery is also an option, but a less efficient one. On the other hand, using the eTurbo™ in generator mode has some disadvantages for the ICE combustion and gas exchange processes, which was explained earlier. But there are certain ICE operation conditions where using the eTurbo in generator mode is beneficial for the entire powertrain energy balance.

The advantage of using the traction motor in generator mode during the vehicle braking process is that it does not have any negative influence on other components (like the eTurbo™ in generator mode has on ICE). The more energy harvested from the braking process the better. In general, the traction motor is capable to generate more energy from the braking, compared to the eTurbo™ from the exhaust gas. The disadvantage of generation with traction motor is that this process takes place only during vehicle braking and the generated energy has to be stored in the battery and cannot be directly used for vehicle propulsion, because during the braking the propulsion is simply not needed. Like this, the generated electrical energy from the traction motor and its later usage for vehicle propulsion has to go through battery charging and discharging cycle, which is related to energy losses in the battery and the power electronics. In case that the battery has reached its 100% state of charge, the braking energy cannot be converted into electricity for charging the battery.

#### **5 Conclusion**

Based on both steady-state and transient analysis it is clear, that for having the same dynamic HEV performance (the same “Fun to Drive”), the boosting with propulsion through ICE requires significantly less energy from the battery compared to the boosting through the traction motor. Therefore using the eTurbo™ as boosting device can be an option to:

- reduce the battery capacity, which will have cost weight and packaging advantage for the vehicle
- reduce fuel consumption and emission if keeping the same battery capacity

Based on the analysis of the options for using the battery for vehicle propulsion and the options for its recharging, it could be concluded, that the most efficient way would be to use the battery energy for boosting mainly through eTurbo™ and recharge the battery mainly with the traction motor in regenerative braking. The most efficient way of utilizing the eTurbo™ generated electric energy is using it for direct vehicle propulsion instead of storing it in the battery and uses it later on.

## References

1. X. Feihong, P. Griefnow, F. Tidau, et al., Electric torque assist and supercharging of a downsized gasoline engine in a 48V mild-hybrid powertrain, *Proceedings of the Institution of Mechanical Engineers, Part D: Journal of Automobile Engineering*, November **3**, (2020), pp. 1245–1255, DOI: 10.1177/0954407020968956
2. C. Wu, K. Song, S. Li, H. Xie, Impact of Electrically Assisted Turbocharger on the Intake Oxygen Concentration and Its Disturbance Rejection Control for a Heavy-duty Diesel Engine. *Energies*. 2019; **12(15):3014**. DOI: 10.3390/en12153014
3. V. Kamboj, S. Saxena, K. Sandhu, Optimal Selection of Gear Ratio for Hybrid Electric Vehicles Using Modern Meta-Heuristics Search Algorithm, *E3S Web Conf.* **87 01006** (2019), DOI: 10.1051/e3sconf/20198701006
4. N. Connelly, D. George, A. Nix, and W. Generation and Analysis of Hybrid-Electric Vehicle Transmission Shift Schedules with a Torque Split Algorithm. *Journal of Transportation Technologies*, **10**, 21-49, (2020) DOI: 10.4236/jtts.2020.101003
5. L. Wang, S. Wang, and Z. Song, Control Strategy and Performance Simulation Study on Extended Range Electric Vehicle, *E3S Web Conf.*, **79** (2019) 03006, DOI: <https://doi.org/10.1051/e3sconf/20197903006>
6. A. Ekbote, M. Karvinkoppa, V. Bhojwani, and N. Patil, Comprehensive study on smart cooling techniques used for batteries, *E3S Web Conf.* **170 01028** (2020), DOI: 10.1051/e3sconf/202017001028
7. Electric Boosting Technologies – BorgWarner (<https://www.borgwarner.com>, 2021)
8. A. Cooper, M. Bassett, J. Hall, A. Harrington, et al., *HyPACE - Hybrid Petrol Advance Combustion Engine - Advanced Boosting System for Extended Stoichiometric Operation and Improved Dynamic Response*, (SAE Technical Paper 2019-01-0325, 2019), DOI: 10.4271/2019-01-0325.
9. H. Stanchev, *Types of hybrid electric cars (HEV). Advantages and disadvantages*, (in Bulgarian), University of Ruse (<http://cdo.uni-ruse.bg>, 2017)

# Experimental study of the accuracy of measuring of a central water meter

Ognyan Bekriev<sup>1,\*</sup> and Aleksandar Stanilov<sup>1</sup>

<sup>1</sup>Technical University of Sofia, Dept. of Hydroaerodynamics and Hydraulic Machines, Kliment Ohridski blvd. №8, Bulgaria

**Abstract.** The paper presents the results of a study of the error of a central water meter at different modes of water consumption. A stand has been designed for the purpose of the study and tests of the error of the water meter have been performed, in compliance with the requirements of Measuring Instruments (MID) Directive (2014/32/EU). The errors of the water meter have been determined in the area close to its start mode, which is not included in the area of inspection. The measuring errors have been also determined in specific operation modes with frequent starts and stops, associated with the flow of smaller water quantities. The study contains an analysis of the obtained differences in the accuracy of measurement during metrological verification of the water meter and reading on a real site. A quantitative estimate of the established losses in water metering is given.

## 1. Introduction

Water meters are measuring instruments designed for continuous measuring of the water quantity passing through them. They are equipped with a measuring device connected to a display. According to their purpose, water meters can be common central meters or control (individual) meters. Common central water meters are used for measuring water consumption in large consumers: residential buildings, public facilities and small companies. A common residential water meter is mounted at the entrance of building plumbing systems, and every consumer has an individual water meter. The type-size and the metrological characteristics of central and individual water meters are different because the central water meter must ensure the water flow at maximum consumption in the building. All water meters are subject to metrological inspection, which can be regular or following repair works. The frequency and the conditions of the inspection depend on the dimension-type and the rated consumption of the water meter. The requirements about the accuracy of measurement applicable for water meters are presented in an ordinance for measuring instruments [1]. The requirements of the Measuring Instruments (MID) Directive (2014/32/EU) [2] in force as of 30 June 2006 have also been included in the ordinance. Figure 1. shows the period of implementation of the directive for all EU member states.

---

\* Corresponding author: [astanilov@tu-sofia.bg](mailto:astanilov@tu-sofia.bg)

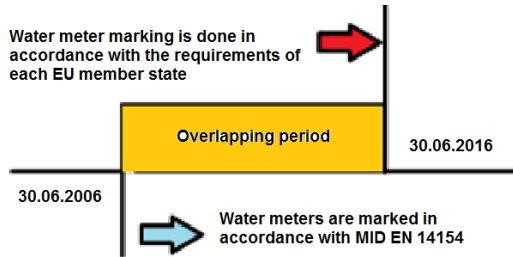


Fig. 1. Period of implementation of the directive MID/EN 14154.

The main metrological properties of water meters are:

Approved type of water meters manufactured before 30 June 2006	Water meters assessed as compatible and manufactured after 30 June 2016
Accuracy class of the water meter- A, B and C	Measuring range - R
Minimum flowrate - $Q_{min}$	Minimum flowrate - $Q_1$
Transitional flowrate - $Q_t$	Transitional flowrate- $Q_2$
Rated flowrate $Q_n$	Permanent flowrate - $Q_3$
Maximum flowrate - $Q_{max}$	Overload flowrate - $Q_4$

The permissible measuring error of water meters is directly dependant on the measuring range. The latter is limited by the minimum and maximum flowrate the water meter can measure. In addition, the error has different permissible values with regard to any initial, subsequent or post-repair inspection the water meter is subject to. In accordance with [1], the error for every water meter shall be determined at three test points.

Point	Approved-type water meters	Assessed compatibility water meters
1	$Q_{min} \pm 1,1 Q_{min}$	$Q_1 \pm 1,1 Q_1$
2	$Q_t \pm 1,1 Q_t$	$Q_2 \pm 1,1 Q_2$
3	$Q_{max} \pm 0,9 Q_{max}$	$Q_3 \pm 0,9 Q_3$

The areas where the error is determined for approved-type water meters and assessed compatibility water meters are presented in figure 2 and figure 3. The solid line shows the maximum permissible error for water meters in subsequent inspection and the dotted line shows the permissible error after repair works.

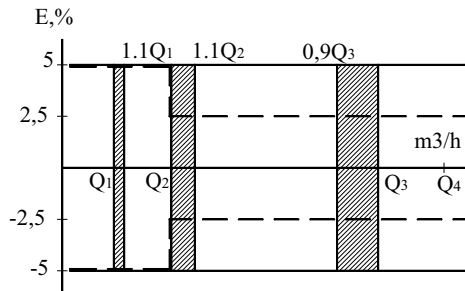
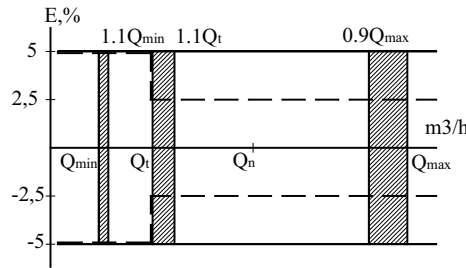
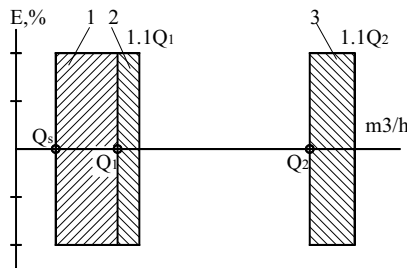


Fig. 2. Areas where the error is determined for approved - type water meters



**Fig. 3.** Areas where the error is determined for assessed compatibility water meters

Figure 2 and figure 3 show that water meters are initially inspected at flowrates ranging around  $Q_{min}$  or  $Q_t$ . For a normal central water meter, these ranges are several times bigger than the minimum ranges of the individual water meters mounted after them. As a result, it is possible to have water flows in the building, which will be measured with a higher error or will not be measured at all. That is why, this paper studies the error of a central building water meter, of assessed compatibility, within the following ranges: start mode 1 - ( $Q_s \div Q_t$ ), minimum flowrate zone 2 - ( $Q_t \div 1,1 Q_t$ ) and transitional flowrate zone 3 - ( $Q_2 \div 1,1 Q_2$ ) Figure 4.



**Fig. 4.** Test areas

The impact of the time of operation of the water meter for a given operational mode will also be assessed. To minimise the error caused by the smallest scale interval, it is required in laboratory testing to inspect the water meter for such quantity of water, for which that error shall not influence the test result. Furthermore, there is a requirement according to [1] that water meters inspection must provide a movement by at least one turnover of the smallest scale interval. Normally, one turnover of the smallest scale interval corresponds to 1l. In lowest operation modes, the testing time differs from the work time of the water meter in normal operational conditions. Therefore the second task of this paper is to establish if a difference exists in the measuring error depending on the time of operation.

The objectives of this work are:

- To perform a study of the error of a water meter in compliance with the requirements of Measuring Instruments (MID) Directive (2014/32/EU). The study's purpose is to show whether the water meter corresponds with the regulatory requirements.
- To perform tests about the error of the water meter at operation modes with debits close to its start mode 1 - ( $Q_s \div Q_t$ ). The reason for setting this objective is that several individual water meters are installed after the common central water meter. The individual

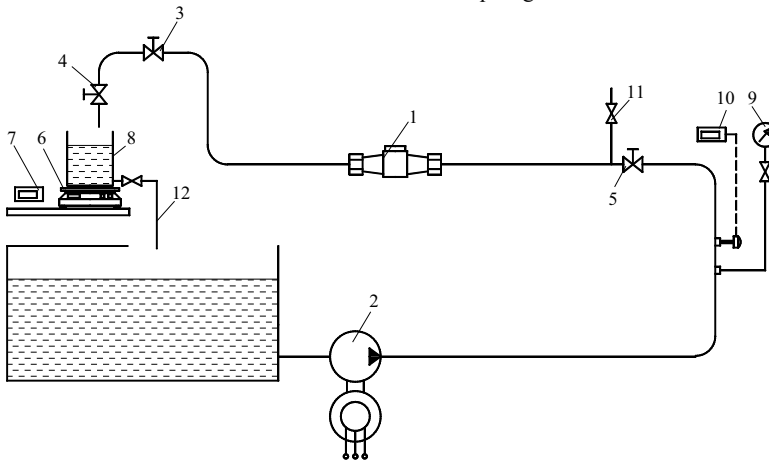


water meters have smaller dimension-types and their metrological properties allow them to let smaller flowrates. The smaller flowrates of the individual water meters get into the area of the central water meter's start mode.

- To study how the water volumes smaller than 1l flowing through the central water meter impact its metering results.

## 2. Experimental study

Figure 5 presents a diagram of a stand where tests are made on a central multi-jet water meter with the following metrological properties: Permanent flowrate  $Q_3=16m^3/h$ , measuring range  $R 100$ , horizontal mounting  $H$ , nominal diameter  $DN 40$ , and start flowrate determined by the manufacturer  $Q_s=56 l/h$ . The measuring instruments for measuring the main values are, as follows: a weighing scale 6 of the type B15T with a weighing range from 20g to 15 kg and equipped with a 12l weighing vessel has been used for measuring the quantity of water flowing through the water meter. Chronometer 7 has been used together with the scale to determine the flowrate (test mode). A thermometer 10 and a manometer 9 have been used to measure the water properties during the tests. A pumping unit 6 has been used to supply the stand with water. A valve 3 is responsible for setting the different modes. Valves 4 and 5 are only used to start and stop the water in the system. A straight section of 800mm has been provided through the water meter and the section after that is 400 mm. The measuring instruments used in the test have calibration certificates expiring in 2023.



**Fig. 5.** Diagram of a stand

The tests for determining the error of the water meter have been performed in the following order:

- Launch pumping unit 2 and set the respective mode by using valve 3 and chronometer 7.
- Close valve 4, reset the weighing scale and the chronometer and write down the indications of the water meter.
- Open valve 4 and starting the chronometer. When the vessel reaches 8 kg, close valve 4 and stop the chronometer.
- Register the indications of the weighing scale, the stopwatch and the water meter display. Three tests are performed for every flowrate.

The quantity of water used in the tests - 10 kg, has been chosen with regard to the smallest scale interval of the water meter corresponding to 50ml. Therefore the imported metering error will be 0.5%.

The error of the water meter is determined with the following relation:

$$E = \frac{V_W - V_e}{V_e} \cdot 100, \% \quad (1)$$

Where:

$E$  – Error of the water meter, %

$V_W$  – Volume, measured by the water meter,  $m^3$

$V_e$  – Volume, measured by the weighing scale,  $m^3$

$$V_e = \frac{m}{\rho} k, m^3 \quad (2)$$

$m$  – indication of the weighing scale,  $kg$ ;

$\kappa = 1.00106$  – coefficient of correction. The coefficient of correction  $\kappa$  is shown in [3], and measures the impact of the difference in the volumes of equal masses - water and reference weights, on the weighing scale indications.

$\rho$  - water density,  $kg/m^3$ ;

The density of the water is determined by measuring its temperature and using the following relation [3] :

$$\rho = 999,9197 - 0,000899T^{0,25} kg/m^3 \quad (3)$$

$T$  – temperature of the water,  $^{\circ}C$

The flowrate during the test is determined by using the following relation:

$$Q = \frac{V_e}{t}, m^3/s \quad (4)$$

$t$ - testing time,  $s$

The tests for determining the impact of time for the work of the water meter are performed in the following order:

- Launch the pumping unit and set it to the desired work mode. In this case, a work mode closer to the minimum is chosen  $Q_I \div I, I Q_I$ .
- Perform tests to determine the error in continuous work mode and work modes with interruptions at specific equal quantities  $V_n$  passing through the water meter for the same quantity of 10 kg. The specific quantities are, as follows: 10kg for the continuous test, and 2.5 kg for the measuring with 4 interruptions. These two tests comply with the requirements given in [1], in specific, there is a full movement of at least one turnover of the smallest scale interval of the water meter.

Tests are also performed to determine the error of the water meter with interruptions at smaller volumes, which do not correspond to a full movement of the smallest scale interval of the water meter. Those modes have been selected for equal volumes of 0.25 kg with 40 interruptions and 0.5 kg with 20 interruptions. When stopping and restarting the water meter, the indication arrow must have stopped completely before the next equal quantity is launched.

The tests are performed in the following order:

- After setting the test mode, the weighing scale should be reset and the starting indications of the water meter must be noted.
- Open valve 4 and monitor the indication of the weighing scale.
- When the weighing scale indicates the quantity pre-selected for the test, valve 4 should be closed and the testing team should wait until the water meter arrow stops moving completely, then open valve 4 and launch the next equal quantity. The tests continue until the total quantity of 10 kg has passed through the water meter.
- Note the indications of the weighing scale and the final indications of the water meter.

### 3. Results

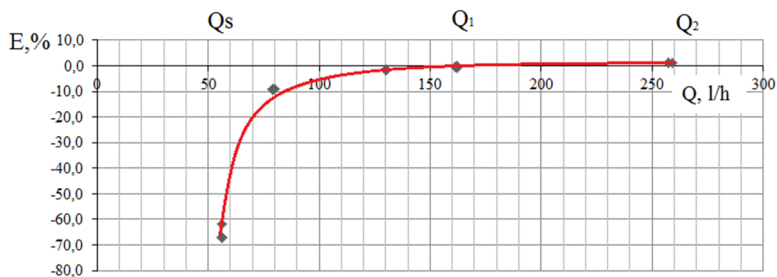
Determining the error of the water meter.

To determine the error of the water meter based on  $Q_3$  and  $R$  according to [1], two of the main test modes must be set – points 3 and 4 of table 1. The error of the central water meter between its starting mode  $Q_3$  and the minimum flowrate  $Q_1$  is also an object of interest. That is the reason to perform three measurements within that range.

**Table 1.** Test points.

Q <sub>3</sub> =16m <sup>3</sup> /h DN=40mm R100		
Setting the test points		
1,2 и 3	4	5
Q <sub>3</sub> ÷1,1 Q <sub>1</sub>	Q <sub>1</sub> ÷1,1 Q <sub>1</sub>	Q <sub>2</sub> ÷1,1 Q <sub>2</sub>
56 l/h	160÷176 l/h	256÷281,6 l/h

Figure 6 shows the diagram of the errors established during the test of the water meter in the selected modes. The diagram clearly shows that the error may reach 70% at modes close to the start mode. For a building plumbing system it is possible that the water meter works at an operation mode corresponding to the consumption of a smaller number of consumers.



**Fig. 6.** Diagram of the errors in the selected test points.

Determining the error of the water meter for a different number of start and stop cycles  $n$  for a measured volume of water of 10l.

Figure 7 shows the graphic relation of the error of the water meter for a continuous operation mode  $Q_1=161$  l/h established during the test. For that continuous flowrate, the error of the water meter has been established for the quantity of water of 10 l that flowed through it at 1, 2, 20 and 40 cycles. The diagram shows that the error increases when  $n$  increases. The

reason is that the water meter stops with a certain delay, which results in accumulation of the indications.

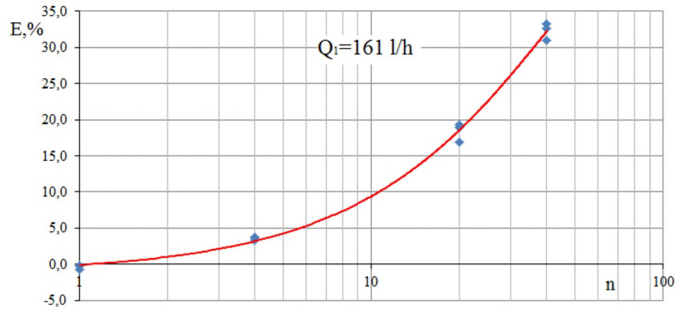


Fig. 7. Graph of errors during cyclic operation.

#### 4. Conclusion

On the grounds of the tests performed in the scope of the study, the following conclusions have been reached:

To make sure that the water meter corresponds with the requirements of Measuring Instruments (MID) Directive (2014/32/EU), we tested the water meter with the Weighing method. The metering error in that first test complied with the methodology, and namely  $\pm 5\%$ .

In modes close to the water meter's start mode, the measuring error is within the range from  $-60\%$  to  $-10\%$ . That means the water meter does not measure the full consumption.

The last test was performed to respond to the requirement that a water meter inspection must be made at a volume corresponding to the smallest scale interval, which usually is 1l. We performed tests with a volume of 10l passing through the water meter at a different number of cycles, and namely 1, 2, 20 and 40 cycles. We obtained a graphic dependence between the number of cycles and the error of the water meter. That test was carried out for a permanent flowrate corresponding to the minimum flowrate -  $Q_1$ . In that test, the measuring errors were within the range from 0,05% to 30%. The conclusion is that the frequent starts and stops result in higher metering while the metered quantity has not flown through the water meter in the same amount.

#### References

1. BS EN 14154-3:2005+A2:2011 Water meters. Test methods and equipment
2. Measuring instruments (MID) Directive (2014/32/EU)
3. EN 24185:1993 - Measurement of liquid flow in closed conduits - Weighing method (ISO 4185:1980)

# Investigations of a vertical axis wind turbine with frontal cylindrical guide vane unit

Valentin Obretenov<sup>1,†</sup> and Rossen Iliev<sup>1,\*</sup>

<sup>1</sup>Department of Hydroaerodynamics and Hydraulic Machines, Technical University of Sofia, Bulgaria

**Abstract.** The paper presents the results of an experimental study of a vertical wind turbine type Darrieus with frontal cylindrical guide vane unit. The main goal of the research is to analyze the influence of the geometry of a classical cylindrical guide vane unit on the active and passive zone of the wind turbine. The aerodynamic scheme is synthesized by a classic runner and frontal cylindrical guide vanes. Three different guiding devices of a model vertical wind turbine with frontally located guide vanes have been studied. Their influence on the characteristics of the turbine has been examined. The reasons of the differences in the characteristics of the three studied variants of the guiding devices are clarified by numerical study of the flow through the blade cascades of the guide vanes and the runner. The results of the study shows what is the reason for the positive effect of the cylindrical vane guide device on the wind turbine's runner.

## 1 Introduction

The idea for this study comes from the analysis of the streamlines and velocity vectors of the airflow through vertical axis wind turbine with cylindrical guide vane device[1]. It seems that the guide vanes acts more like as deflector rather than flow directing vane cascade. The results from the previous physical experiments conducted in HEHT Lab[2] in Technical University of Sofia, showed that the density of the guide vane cascade increases significantly the power coefficient of the wind turbine. That's because the guide vanes in the active zone directs the flow to the turbine's runner and improves the absorption of the kinetic energy. On other hand the guide vanes in the passive zone, acts like an energy absorbing shield that shades the runner's blades and eliminates the production of negative torque.

The task of the study is to analyze the influence of the reflecting and directing capabilities of a frontal guide vane device on the turbine performance. The rear guide vanes are removed from the aerodynamic scheme, since they don't significantly affect the power of the wind turbine[1]. This paper presents results of studies aimed at optimizing wind turbine efficiency.

---

<sup>†</sup> Died March 30, 2021

\* Corresponding author: [riliiev@tu-sofia.bg](mailto:riliiev@tu-sofia.bg)

## 2 Description of the test stand and the plan of the experiment

### 2.1 Test stand

In order to study in details the influence of the guiding vane cascade, three variants of frontal guiding devices are proposed.

First one (Fig.1) is consisted of sixteen frontally located guide vanes - 1. Their leading edge is oriented parallel to the velocity vector of the wind. Second one (Fig.2 (a)) differs only in the pitch angle of the vanes in the passive zone - 2. They are placed in such way that forms barrier. The last variant (Fig.2 (b)) is consisted of ten guide vanes mounted at their optimal pitch angle[2] and six vanes, placed in the same way as variant (b).

The axis of the guiding vanes - 1 are placed along the contour of a cylindrical surface with diameter  $D_{0gv} = 1.080$  m between two supporting static rings - 5. The vanes are part of cylindrical surface with radius of curvature  $r_1 = 0.1$  m. They have chord length  $l = 0.115$  m and height  $B_0 = 0.927$  m.

The runner's blades - 3 are mounted between two discs - 4 with axis placed on cylindrical surface with diameter  $D_{0r} = 0.8$  m. The blades are part of cylindrical surface with radius of curvature  $r_2 = 0.1$  m. They have chord length  $l = 0.150$  m and height  $H = 0.8$  m. The construction allows the change of the pitch angle -  $\varphi_r$  in wide range. The shaft of the turbine is mounted inside the static pipe - 7. The model wind turbine and the guiding device are mounted on the platform of stand №7C[3] in square aerodynamic tunnel - 6 with length of the sides  $D_t = 1.3$  m.

The wind velocity through the tunnel is generated by an axial fan driven by asynchronous electric motor[3]. It's speed is regulated by a frequency inverter which allows changing of the wind speed in wide range (up to 11 m/s). This completely covers the average velocities of the winds in most countries and makes the stand suitable for studying small scale wind turbines.

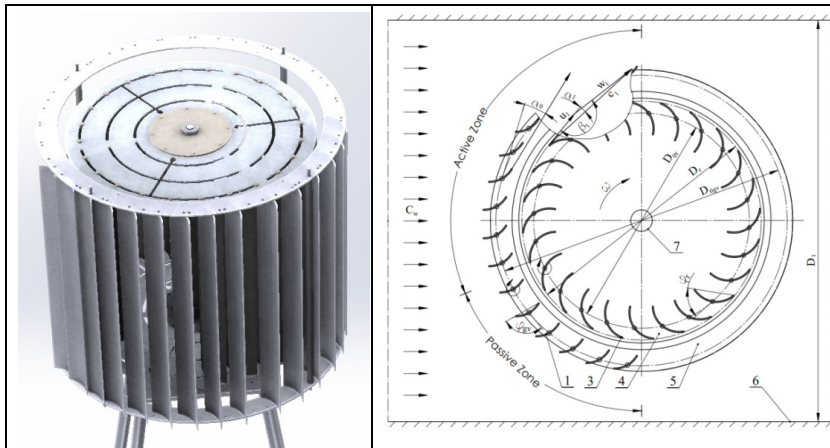
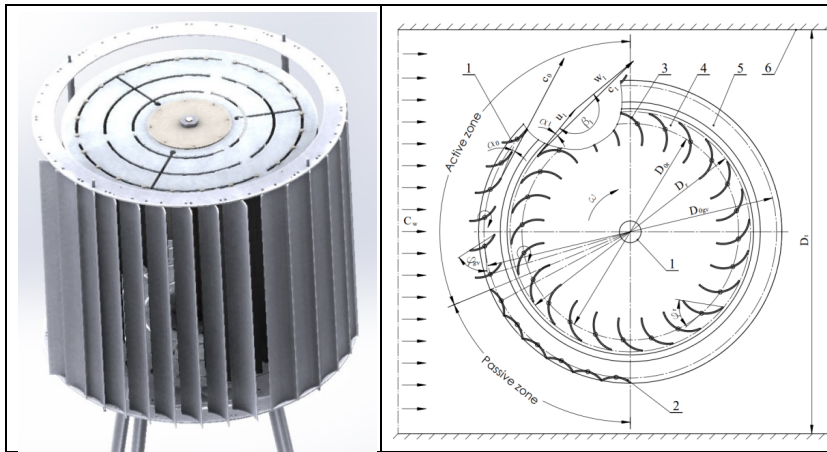
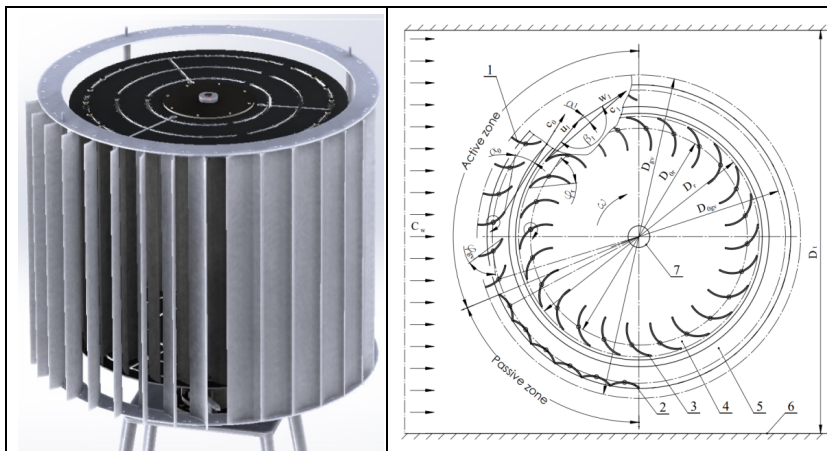


Fig. 1. Frontal guiding device (FGD) with frontal oriented guide vanes.



(a)



(b)

**Fig.2.** Frontal guiding device (FGD) with frontally oriented (a) and radially oriented (b) guide vanes in the active zone, with flipped guide vanes in the passive zone forming an absorbing shield.

## 2.2 Plan of the experiment

The study was conducted at optimal pitch angle of the guide vanes, calculated from planned physical experiment[1] and at five different pitch angles of the runner's blades around the optimal value. The objective function is the power coefficient (efficiency)  $C_p$  of the turbine:

$$C_p = \frac{P}{P_w}, \quad (1)$$

where  $P$  is the effective power on the shaft of the turbine (W) and  $P_w$  is the power of the airflow (W).

$$P = M_b \cdot \omega = M_b \cdot \frac{\pi \cdot n}{30} \quad (2)$$

$$P_w = \rho \cdot S \cdot \frac{C_w^3 \cdot S}{2} \quad (3)$$

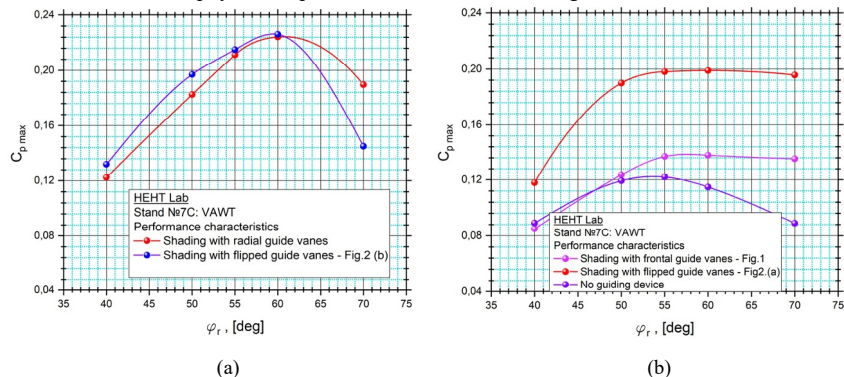
In the above equations  $M_b$  is the torque of the shaft (N.m),  $n$  is rotating speed of the turbine (rpm),  $\omega$  is the angular velocity (rad/s),  $S = D_{lr} \cdot H$  is the transverse area of the runner ( $m^2$ ), where  $D_{lr}$  is the outer diameter of the runner (m),  $H$  is the height the working blades (m) and  $C_w$  is the area-averaged airflow velocity (m/s).

The operating mode of the wind turbine is changed by mechanical brake system, which regulates smoothly the load on the turbine's shaft. The torque and the rotating speed values are automatically recorded in computer by process indicator and are averaged over time by specialized software, in order to eliminate the measurement error. The study is conducted at constant air velocity  $C_w = 7$  m/s, which is close to the average wind speed in the country.

The influence of the three different guiding cascades on the turbine efficiency will be determined by comparing the maximum values of the power coefficient  $C_p \max$  for each of the five pitch angles of the working blades.

### 3 Results

The results from the physical experiments are shown on the figures below.

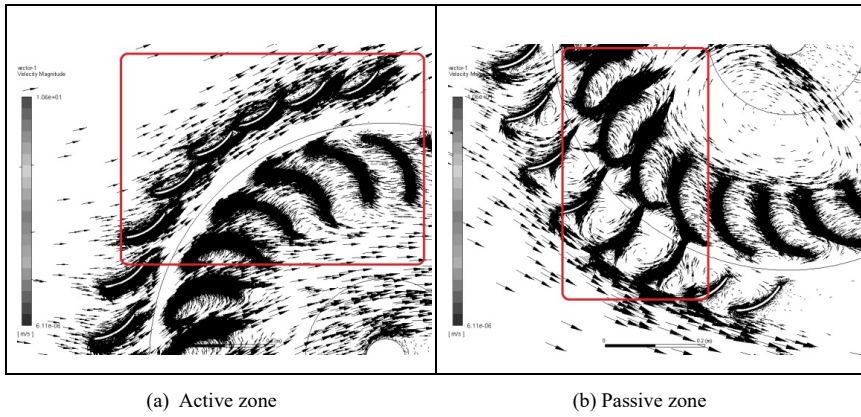


**Fig.3.** Characteristics of FGD with radial oriented (a) and frontal oriented (b) guide vanes.

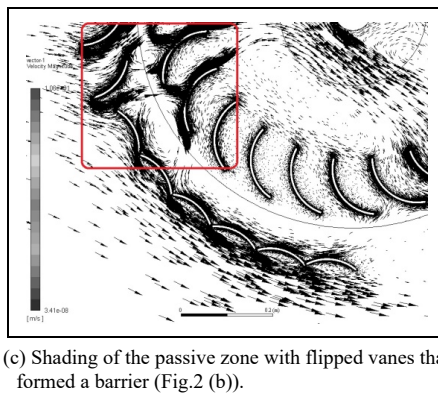
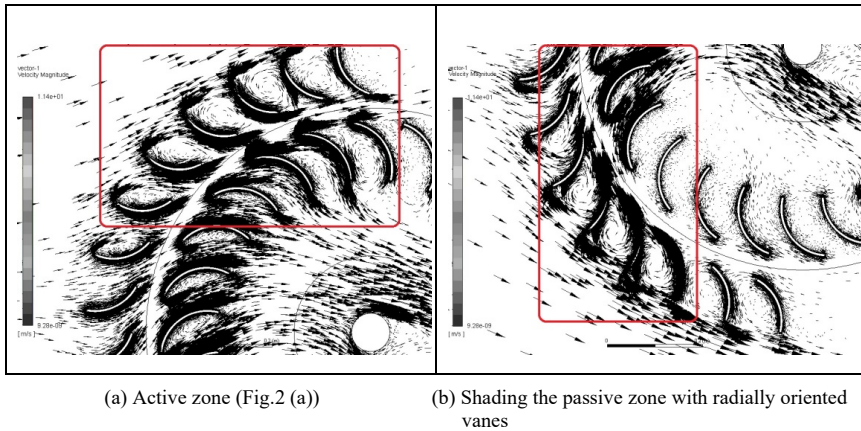
To clarify the airflow through the three types guiding cascades was performed a numerical study with the commercial software Ansys Fluent. The dimensions and grid parameters of the computational domains corresponds to the recommended values[4,5,6]. The far field velocity is set to 7 m/s and the environmental pressure inside the computational domains is set to 1 atm. The used turbulent model is k-omega SST with "The Moving Frame of Reference" (MFR)[7] approach.

The calculated velocity vectors of the flow through the active and passive zones for each of three variants are shown on Figs. 4 and 5 for the optimal operational modes of the wind turbine.



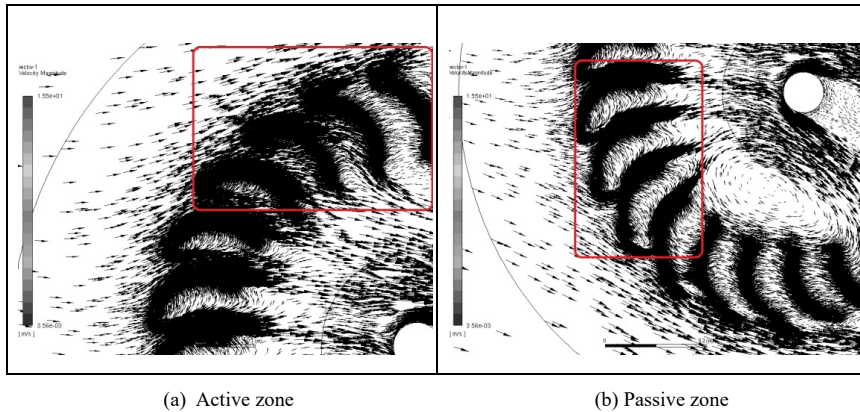


**Fig.4.** Airflow velocity vectors through the guiding device with frontal oriented guide vanes (Fig.1).



**Fig.5.** Airflow velocity vectors through the frontal guiding device (Fig.2).

On Fig. 6 for comparison is shown the flow through the runner without guiding device.



**Fig.6.** Airflow velocity vectors through the turbine's runner without guiding device.

#### 4 Analysis

1. Frontal guiding device with frontal oriented guide vanes increases the efficiency of the turbine up to 4.6%, compared to aerodynamic scheme without guiding device (Fig.1 and Fig.3 (b)). Larger deviations of the power coefficient  $C_p$  between these two schemes are observed at pitch angles  $\varphi_{tr}$  from  $50^0$  to  $70^0$ , while at pitch angles less than  $50^0$  the differences are insignificant. This can be explained by the fact that the guiding vanes in the active zone directs the airflow to the lower concave surface of the blades, especially at the high pitch angles. Thus, the drag force acting on the blades is increased and the blade cascade of the runner begins to work on the principle of the Savonius turbine. On other hand the shading of the passive zone with flipped guide vanes that forms barrier (Fig.3 (b)) increase the efficiency of the turbine with additional 6.4%. Thus, the overall efficiency reaches 19.6%. Graphs of these two guiding devices are similar and shifted relative to each other by almost 6% (except at pitch angle  $40^0$ ). They have almost constant  $C_{p\ max}$  at range of the pitch angle  $55^0$ - $70^0$ .
2. The shading of the passive zone with flipped guide vanes does not lead to significant differences in the power coefficient when using frontal guiding device with radially oriented blades (Fig.3 and Fig.6 (a),(b) and (c)). The  $C_p$  values at the optimal pitch angle are almost the same. The only noticeable difference of 4% is at  $\varphi_{run} = 70^0$  in favor of the variant on Fig.2 (b).
3. The frontal vanes (Fig. 1, Fig.4 (b)) lead part of the airflow in the passive zone, which partially decreases the negative torque. This explains why the power coefficient of turbine without guiding device is almost the same as the power coefficient of the turbine with frontal oriented guide vanes at pitch angles  $40^0$  -  $50^0$ .
4. The guide vanes placed radially at their optimal pitch angle directing the airflow to the active zone of the runner against the lower concave side of the blades – Fig.5 (a). The wind is repelled from the passive zone – Fig.5 (b). This improves the absorption of the kinetic energy and removes the production of negative torque at

the same time. When we flip the guide vanes in the passive zone (Fig.5 (c)) the repulsive effect is the same. This explains why there is no significant difference in the power coefficient between these two aerodynamic schemes (Fig.3 (a)).

5. In absence of guiding device the airflow attacking the runner blades at different angles, which decrease the effective power of the turbine – Fig.6. As a result of the free uncoordinated airflow, increased vortices are observed around the blades in the active and passive zone of the runner. The removed barrier in the passive zone of the wind turbine allows the airflow to attack freely the upper convex surface of the blades, which generates negative torque and decrease the power of the turbine's shaft.

## 5 Conclusions

- The reflection of the flow from the passive zone of the vertical wind turbine is the leading factor that increasing its efficiency. The directing of the flow in the active zone also increases the power coefficient but the benefits are 2.5 times lower.
- The classical cylindrical guiding device owes its high efficiency to the shading of the passive zone.
- Despite the existence of a number of alternative devices, the classical cylindrical guide vane unit is one of the most suitable options, as it does not create much frontal resistance and allows the airflow to pass through the vane cascade without huge volume losses.
- The high values of  $C_p$  for this type of wind turbines gives grounds for conducting more in-depth research in the field of frontal guiding devices in order to increase their efficiency.
- The use of frontal guiding device would justify the investments if is achieved independence from the wind direction relative to the periphery of the runner.

## References

1. V. Obretenov, R. Iliev. Determination of The Optimal Parameters of a Vertical Axis Wind Turbine with Cylindrical Guide Vane Unit. *6th International Symposium on EFEA*, Technical University of Sofia, (2021).
2. V. Obretenov, Ts. Tsalov. The new hydraulic laboratory at the Technical University of Sofia. Collection of scientific papers of the IX international scientific and technical conference „ *Hydraulic machines, hydraulic drives and hydropneumatic automation. Current status and development prospects* “, p. 79-87, St. Petersburg, (2016).
3. V. Obretenov, R.Iliev. A new model vertical axis wind turbine. Proceedings of the *Scientific Conference EMF`2018*, vol. **II**, p. 288-295, Sozopol, (2018) in Bulgarian.
4. R. Iliev. CFD analysis of performance characteristics of different Darrieus turbine runners. *E3S Web of Conferences*, vol. **207**. *25<sup>th</sup> Scientific Conference on PEPM*, Sozopol, (2020).
5. Almohammadi, K.M., D.B. Ingham, L. Ma, M. Pourkashan. Computational fluid dynamics (CFD) mesh independency techniques. *Energy*, vol. **58**, pp. 483-493, (2013).
6. Balduzzi, F., A. Bianchini, R. Maleci, G. Ferrara, L. Ferrari. Critical issues in the CFD simulation of Darrieus wind turbines. *Renew Energy* vol. **85**, p. 419-435, (2016).
7. R. Franzke, S. Sebben, T. B, E. Willeson. Evaluation of the Multiple Reference Frame Approach for the Modelling of an Axial Cooling Fan. *Energies*, vol. **12**, (2019)

# Modelling indoor pollutant distribution via passive scalar and virtual box approach

George Pitchurov<sup>1,\*</sup>, Detelin Markov<sup>1</sup>, Iskra Simova<sup>1</sup>, Rositsa Velichkova<sup>1</sup>, Peter Stankov<sup>1</sup>, Radostina Angelova<sup>1</sup>

<sup>1</sup>Dept. PEPM, Technical University of Sofia, Bulgaria

**Abstract.** The distribution of PM<sub>2.5</sub> around a thermal manikin with realistic female body shape in a naturally ventilated room has been modelled. The health risk (HR) due to inhalation of the PM<sub>2.5</sub> has been quantified by integrating the pollutants mass flux over the boundaries of a virtual box around the mannequin's head (the breathing zone). By the same approach HR is evaluated over the boundaries of another virtual box that surrounds the manikins body and defines the occupied zone. The paper focuses on the peculiarities of creating and meshing a virtual geometry, as well as on the application of user-defined functions (UDF) for defining a pollutant source within the room using Ansys Fluent modelling package.

## 1 Introduction

PM<sub>2.5</sub> readings are often included in air quality reports from environmental authorities and companies [1]. PM<sub>2.5</sub> refers to atmospheric particulate matter (PM) that has a diameter of less than 2.5 micrometres. The size of those particles makes them susceptible to easy inhalation into the lungs, where they can inflict damage. It is also possible that these particles agglomerate viruses or bacteria and transport them into the human body. According to WHO [2], the well-known coronavirus (SARS-CoV-2) can also adhere to aerosols and be transmitted to lungs via inhalation. This transport mechanism is also addressed in [3-6]. To model the pollutant distribution in the room the passive-scalar model is used, since particles are too tiny to impact the flow field and tend to spread like a cloud. In such case the Eulerian and Lagrangian methods offer similar accuracy in predicting the contaminant concentration using RANS equations [7].

To quantify the risk of a human subject inhaling a PM<sub>2.5</sub> pollutant, a virtual box approach was developed, where the subject head is surrounded by a box and the pollutants mass flux flowing through the box surfaces is calculated. Although it is possible to quantify surface fluxes in the post-processing level, the more robust solution is to create the box at the pre-processing level, i.e. during geometry creation. This required creation and manipulation of so-called virtual geometry in the mesh generator. This paper presents the steady-state emission and inhalation of pollutant PM<sub>2.5</sub>. To generate the pollutant in the room a user-defined function (UDF) approach was used, which allows the pollutant to be

---

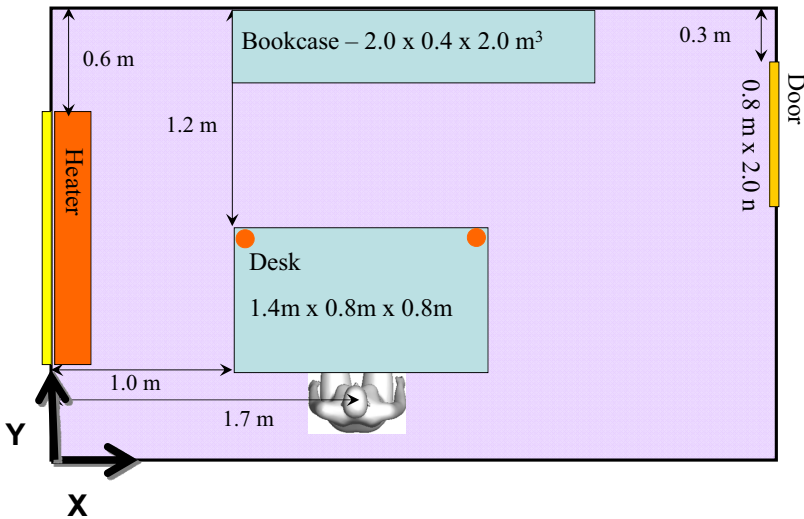
\* Corresponding author: [george@tu-sofia.bg](mailto:george@tu-sofia.bg)

generated at arbitrary point in the domain without the need to construct a dedicated pollutant source inlet during the geometry creation stage.

## 2 Problem formulation

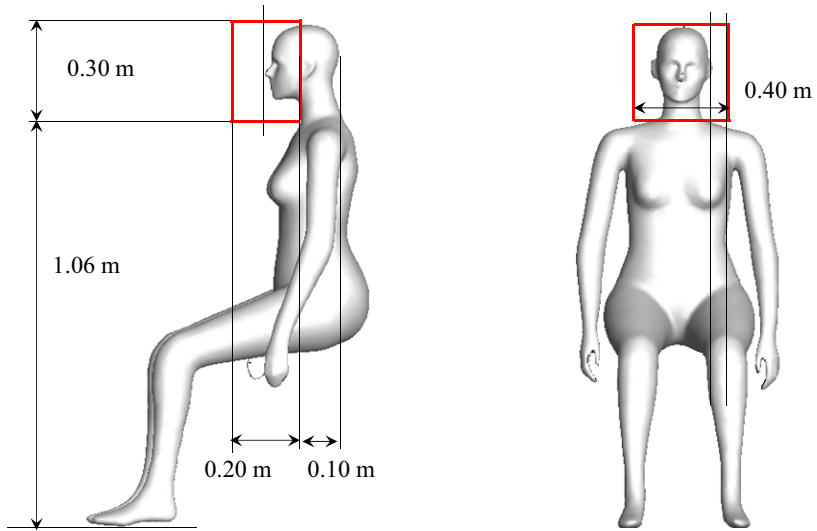
### 2.1 Geometry and computational mesh

A plan view of the simulated space is presented on Fig. 1. The room dimensions are 4m length, 2.5m width and 2.6m height. The room has a window on the external wall and a closed door with a slot underneath on the opposite wall. There is a heater below the window and a table behind which a seated mannequin reclines. The mannequin numerical model is created through a topographic scanning of a real mannequin body by [8] and has been successfully imported into a numerical simulation for example in [9]. The mannequin has been scanned in a stereolithographic format and then converted to three-dimensional primitives in ACIS format before being imported into the mesh generator. The mannequin together with the location and dimensions of the virtual box around the head (the head box) are shown on Fig. 2. A second virtual box is constructed around the body of the occupant (body box) to identify a so-called occupant zone.

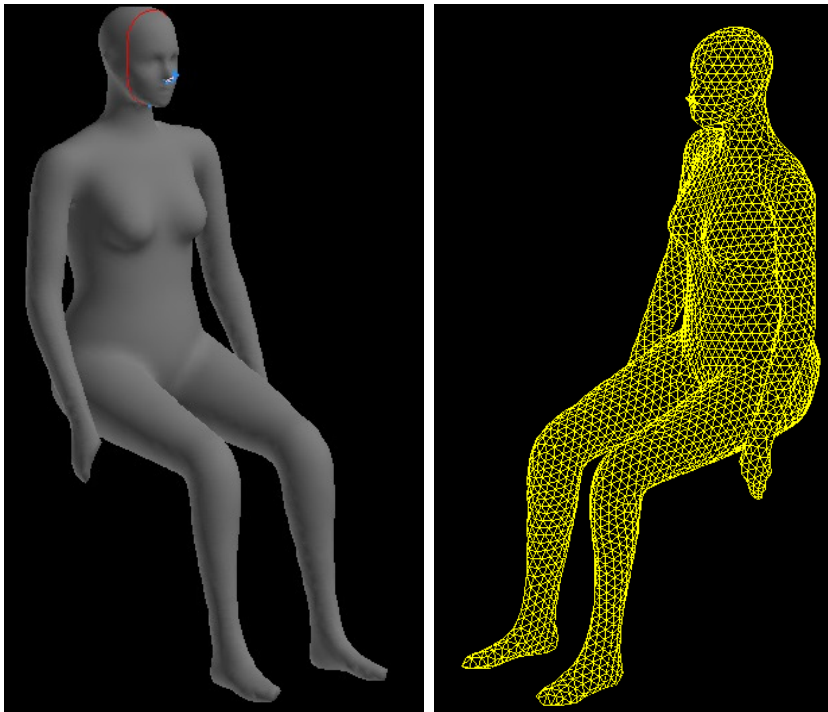


**Fig. 1.** Modeled enclosure with thermal mannequin.

The mesh was prepared with the Gambit mesh generator and consisted of 800 000 tetrahedral cells (tets). This choice of cell type was mainly dictated by the complicated geometry near the mannekin body. Tets also allow for gradual coarsening of the mesh away from the body and are practically the only way to accomplish refinement while preserving the mesh conformal. Upon import in the mesh generator, the head of the mannequin is split by the surfaces of the head box. The body surface is meshed with triangular elements and the nostrils are selected to define an outlet (Fig. 3). Even though the body is well represented by the mesh, local refinement was attempted based on constraining the angle between unit normal vectors of neighbouring mesh cells. This procedure however didn't prove successful in 3D case as much as in 2D, so it was abandoned.



**Fig. 2.** Digitalized mannequin and the head box dimensions



**Fig. 3.** Geometry and mesh of the mannequin body

## 2.2 Computational details

The computations were done with Ansys 16.2 version of the Fluent software package in parallel mode on up to 4 computational nodes. For modelling the mean effect of turbulence the realizable version of the k- $\epsilon$  model with enhanced wall treatment was used. The enhanced wall treatment models the wall effects by switching to low-Reynolds number model when the dimensionless wall distance  $y^+$  is lower than 5, and adopts wall function approach when  $y^+ > 30$ . In the region between these two limits a blending technique is employed. For modelling of the thermal effects on the flow the Boussinesq approach was used. The fluid is treated as incompressible, but allowing for buoyancy effects by introducing in the Z-momentum equation a source term proportional to a temperature difference and the thermal expansion coefficient of air. The Boussinesq approach is applicable when temperature difference between inlet and outlet are much lower in magnitude compared to the absolute temperature, which in the simulated cases was less than 1%. The radiative heat transfer was excluded from the simulation at this stage since it was assumed that the temperature difference were rather small for the radiative heat transfer to significantly change the velocity field that governs the pollutant transfer.

The SIMPLE pressure-velocity coupling was employed since fluid is incompressible (with respect to pressure). Momentum variables were discretized with a second-order upwind scheme and the scalar and temperature variables with a first-order. The first-order scheme has the property to be more conservative and to suppress solution oscillations beyond the physical limits of the variable.

The passive-scalar model is suitable for low pollutant concentrations, as discussed, however a proper treatment of the turbulent scalar diffusion is necessary, which has been ensured with the help of a user-defined function. For correct conservation of the pollutant it is also important to disable the scalar diffusion through the inlet. This is necessary since part of the scalar will leave the domain through the inlet via diffusion and the resulting mass flux at the outlet will not be equal to the one generated at the source. Pollutant distribution in the investigated space was calculated as a second step in a so-called frozen velocity field, after the flow field (velocity and temperature) has been converged.

## 2.3 Boundary conditions

Outdoor air enters through the whole window with a velocity of 0.01m/s which corresponds to a volume flow rate of 0.0112m<sup>3</sup>/s. The domain has two outlets: the first one is at the slot below the door and the second one is at the mannequin's nostrils. The door slot was extruded 1m further out of the domain to ensure fully developed flow and avoid recirculation. The door slot outlet pressure was fixed to zero, while the occupant's nostrils were assigned target mass flow rate of 0.12.10<sup>-3</sup> kg/s, which is roughly 1/100 of the room inflow. The boundary condition at the nostrils is still a static pressure, but it evolves dynamically based on the required mass flow rate.

For boundary conditions of pollutant a zero value was used on inlets. For the outlets a zero gradient (which corresponds to zero diffusive flux) was used. The zero gradient still allows a flow of pollutant, but assumes a fully developed flow. This is true for the slot outlet, but not so much for the mannequin nostrils, unless a deeper extrusion into the mannequin head is attempted. This wasn't done here because once the pollutant flux at the door slot is determined correctly, the mannequin nostrils flux will emerge naturally from mass conservation when the simulation converges.

To allow for proper mass conservation of pollutant, the inlet diffusion was disabled due to reasons discussed above, i.e. to disallow the flow of pollutant through the inlet. If the diffusion is not disabled, any non-zero gradient in the vicinity of the inlet will create flux

due to Fick's law and will let some pollutant to escape. This will create discrepancy between the pollutant flow rate at the outlets and the generation rate. In the rest of the domain the pollutant was of course allowed to diffuse. The diffusion coefficient of the pollutant was hard-linked to the turbulent momentum diffusion with a turbulent Prandtl number of 0.9. This modification is crucial for the realistic prediction of pollutant diffusion via turbulence.

Five pollutants were simultaneously simulated, three of them generated over the desk and two generated over the bookcase. The pollutant source coordinates are presented in Table 1. Source locations were assigned via a user-defined function (UDF), which scanned the numerical grid to find the cell closest to the pre-defined source location (appendix A). These cells were then assigned a pollutant source with a strength of  $1\text{E-}09$  kg/s. The advantage of using UDF instead of hard-fixing the location was the flexibility to change the pollutant location without modifying the mesh.

**Table 1** Diffusive sources of pollutant PM2.5

Pollutant	Coordinates [m]			Location
	X	Y	Z	
UDS0	1.6	1.2	0.85	Desk left
UDS1	2.0	1.31	0.85	Desk middle
UDS2	2.4	1.2	0.85	Desk right
UDS3	1.1	2.3	2.05	Bookcase
UDS4	2.9	2.3	2.05	Bookcase

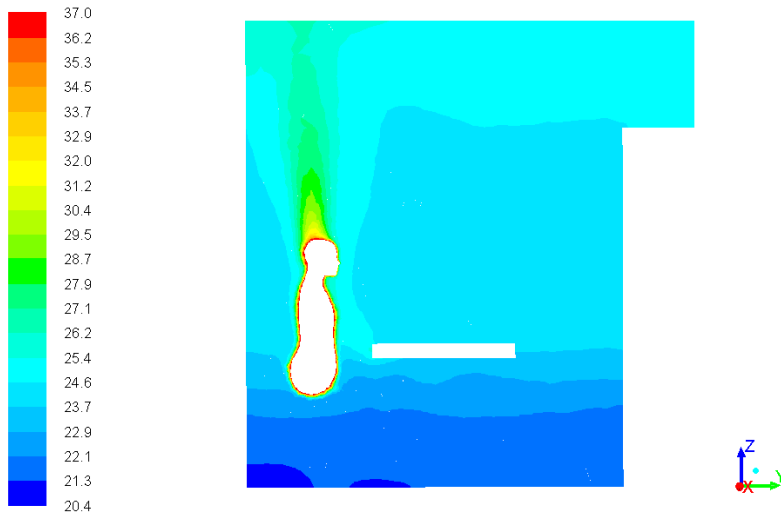
Regarding thermal boundary conditions the mannequin body surface was assigned a heat flux of  $70\text{W}/\text{m}^2$ . The heat output from heater was  $320\text{W}$ , which was split between its front and top surfaces. The inflow air temperature through the window was fixed at  $296\text{K}$ . All walls (incl. floor and ceiling) were adiabatic except for the one that separates the room from the outdoors, on which the window is installed. This wall was assigned a heat loss of  $100\text{W}/\text{m}^2$ .

### 3 Results and discussion

#### 3.1 Velocity and temperature

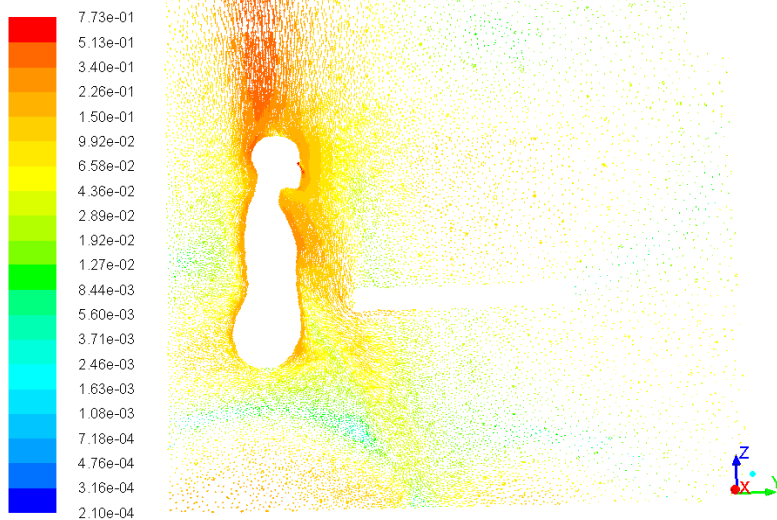
Richardson number for the flow was on the order of  $10^3$ , which indicates a much higher impact of natural compared to forced convection. The numerical results confirmed that the flow is dominated by the thermal plumes from mannequin and heater and not so much from the low-momentum flow through the window. Fig. 4 shows the temperature field in a plane cut through the mannequin, where the thermal plume is clearly visible.





**Fig. 4.** Temperature contours [°C] in a mid-plane through the mannequin.

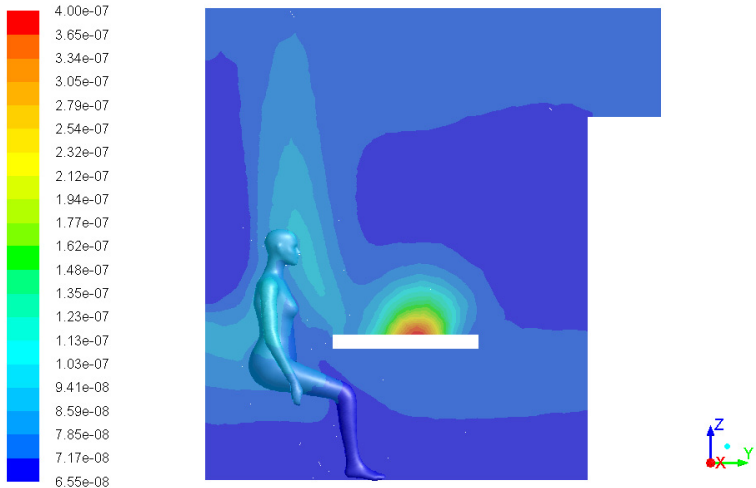
The resulting natural convection as predicted by the Boussinesq model is visualized by the velocity vector field in Fig. 5. Similar is the convective plume above the heater. This natural boundary layer cannot be penetrated by external airflows in the studied setup. This has the consequence that this layer can protect the person from contamination transported by external flows, which is the underlying principle of displacement ventilation [10]. However, if a contaminant source is located at the beginning of the boundary layer then the layer will entrain it and will transport the contaminant to the breathing zone.



**Fig. 5.** Velocity vectors in a mid-plane through the mannequin.

### 3.2 Contaminants

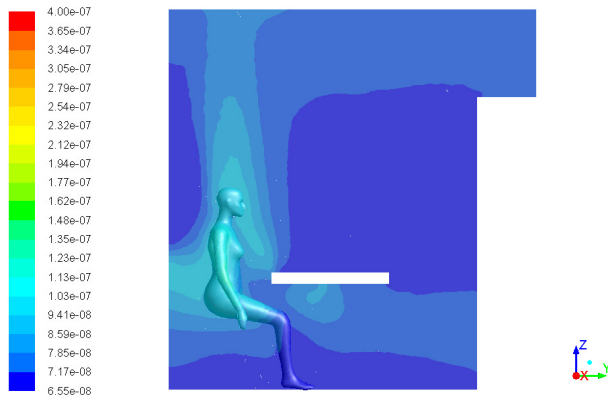
The mid-plane view from the previous section is used in Fig. 6 through Fig. 10 to show the distribution of contaminants for the five sources listed in Table 1. In the absence of strong flows near the contaminant source the contaminant is transported by turbulent diffusion, as can be seen for example in UDS0 in Fig. 6. The contaminant is further entrained by the thermal convective plume created by the heated human body and transported most likely to the breathing zone. To determine the pollutant concentration in the breathing zone the head box pollutant concentration is needed. It is visualized in Fig. 11 through Fig. 15 for the five simulated contaminants.



**Fig. 6.** Mass fraction of pollutant UDS0 [kg/kg] in a vertical mid-plane through the mannequin



**Fig. 7.** Mass fraction of pollutant UDS1 [kg/kg] in a vertical mid-plane through the mannequin



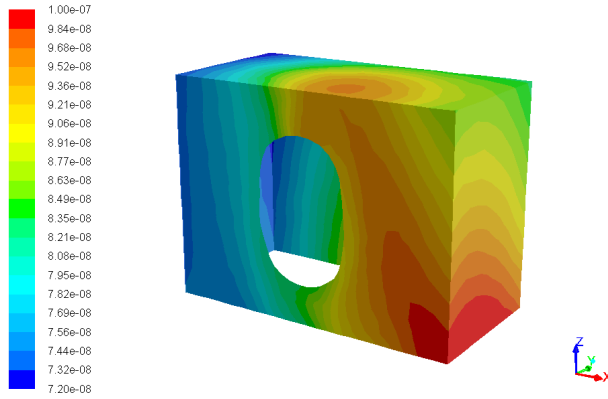
**Fig. 8.** Mass fraction of pollutant UDS2 [kg/kg] in a vertical mid-plane through the mannequin



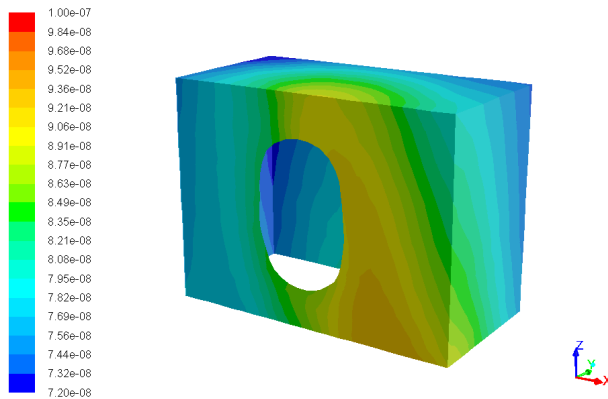
**Fig. 9.** Mass fraction of pollutant UDS3 [kg/kg] in a vertical mid-plane through the mannequin



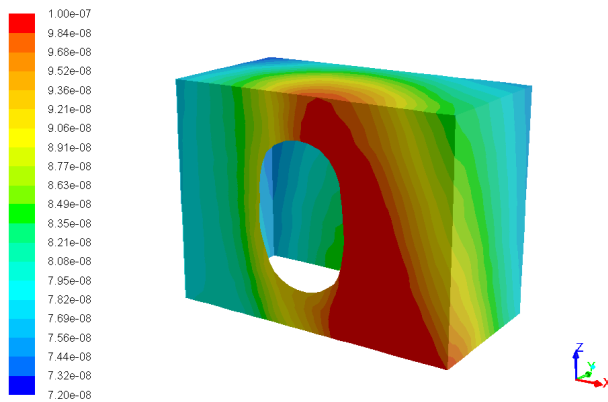
**Fig. 10.** Mass fraction of pollutant UDS4 [kg/kg] in a vertical mid-plane through the mannequin



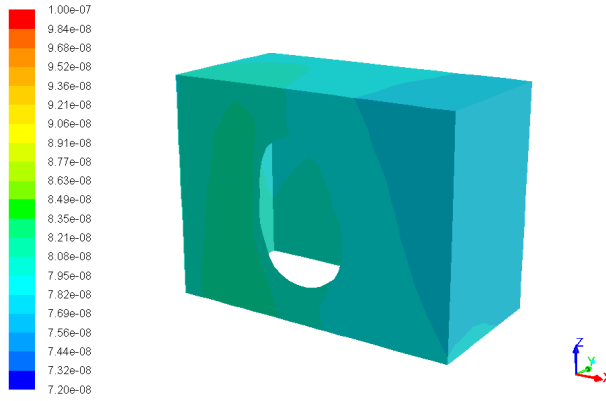
**Fig. 11.** Mass fraction of pollutant UDS0 [kg/kg] over the virtual mannequin head-box.



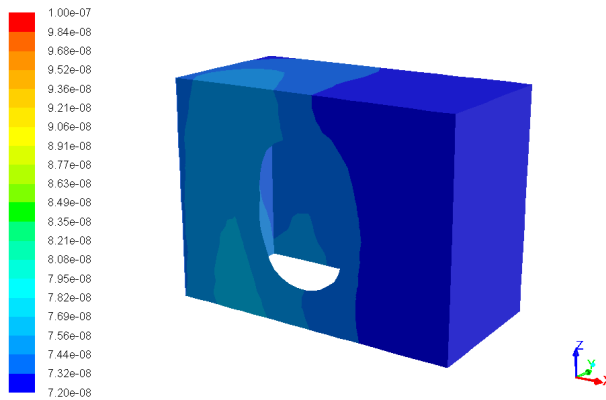
**Fig. 12.** Mass fraction of pollutant UDS1 [kg/kg] over the virtual mannequin head-box.



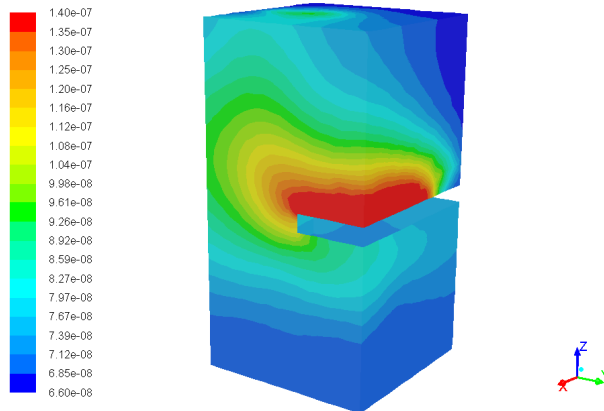
**Fig. 13.** Mass fraction of pollutant UDS2 [kg/kg] over the virtual mannequin head-box.



**Fig. 14.** Mass fraction of pollutant UDS3 [kg/kg] over the virtual mannequin head-box.

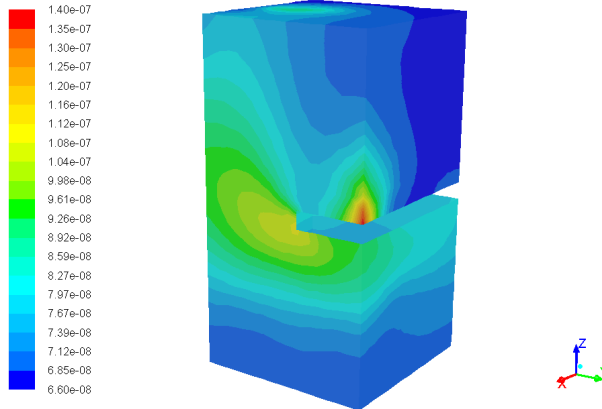


**Fig. 15.** Mass fraction of pollutant UDS4 [kg/kg] over the virtual mannequin head-box.

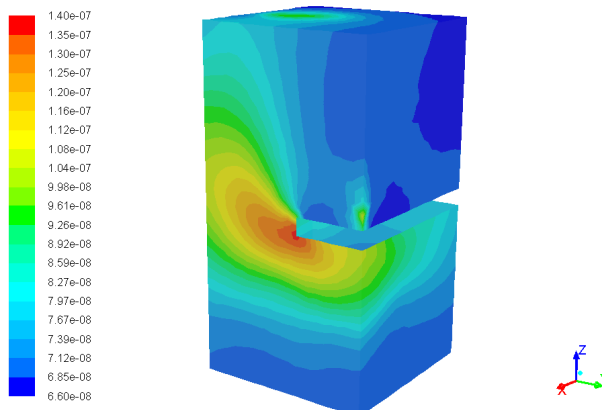


**Fig. 16.** Mass fraction of pollutant UDS0 [kg/kg] over the virtual body-box

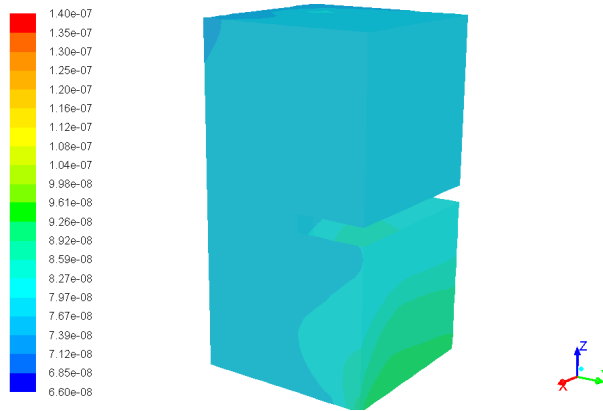
Fig. 16 through Fig. 20 depict the mass fraction of pollutant over the surface of the virtual body box. What is to be noted is the higher gradient of pollutant when the latter is located on the desk, i.e. close to the considered virtual surface. Being close to the surface prohibits the contaminant from mixing before entering the body box. On the other hand contaminants located further have sufficient time and space to mix and dilute. As a result the contaminants generated from the bookcase offer much uniform concentration over the body-box surface. The overall quantity of contaminant entering the body box however is rather equal between contaminants and independent on the location, which will become clear in a later analysis.



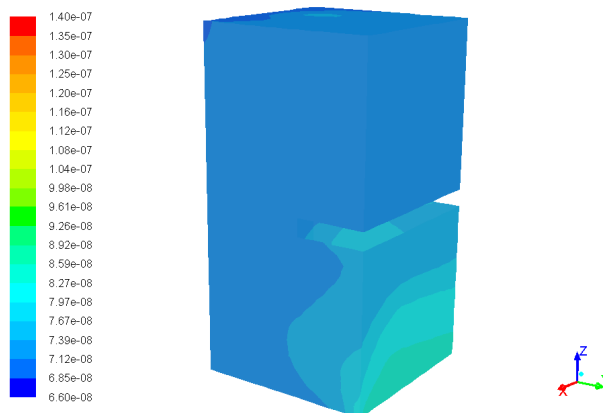
**Fig. 17.** Mass fraction of pollutant UDS1 [kg/kg] over the virtual body-box



**Fig. 18.** Mass fraction of pollutant UDS2 [kg/kg] over the virtual body-box



**Fig. 19.** Mass fraction of pollutant UDS3 [kg/kg] over the virtual body-box



**Fig. 20.** Mass fraction of pollutant UDS4 [kg/kg] over the virtual body-box

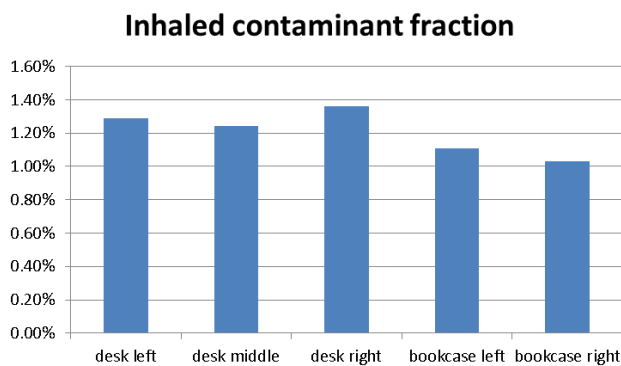
Concentration alone can not determine uniquely the inhaled pollutant quantity as the latter is an integral of the concentration by the air mass flowrate over the box surface. That means zones with high concentration may not lead to higher inhalation if not enough air flows through them and vice versa—a small segment with high concentration may increase the inhaled quantity significantly if enough air is transported through it. Table 2 presents the net flow rate of the five pollutants through the surface of both boxes (the head and body box), as well as the flowrate and mass fraction over the mannequin nose during inhalation mode. The table also presents normalized quantities obtained by dividing the corresponding flow rates by the source strength ( $1.10^{-9}$  kg/s). In this way it becomes visible what fraction of the emitted contaminant actually enters the occupied and the breathing zone. It should be noted that the flow rate is calculated as an integral of the velocity over the surface area, i.e. it represents the convective flux of the pollutant through the area. However, concentration gradients in the vicinity will also contribute to a diffusive flux, which is not accounted for in this calculus due to software limitations. Although the door outlet was extruded to provide for zero diffusive flux, any internal surface of the domain, over which integral balance is calculated, will also be subject to a diffusive flux, which is not accounted

for. This will explain certain discrepancy observed between the flow rates through the boxes compared to inhaled flow rates.

The inhaled fraction of contaminant is calculated by dividing the contaminant flowrate through the nose by the emission rate from the source. The result is depicted on Fig. 21 as a percentage, showing that roughly 1% from the generated contaminant is inhaled by the person. It is seen that contaminant sources closer to the occupant generally result in higher inhaled fraction. The observed difference between inhaled fractions is however not so large and is not proportional to the proximity of the pollutant source. The likely reason is that turbulent mixing in the room would homogenize the pollutant and thus smear out the difference between the different pollutant setups. Fig. 22 depicts the turbulent diffusion coefficient of pollutant in a room mid-plane. The coefficient is calculated from the turbulent viscosity and a turbulent Prandtl number of 0.9 for all contaminants alike. The figure shows high value of diffusion coefficient in the majority of the room and thus a strong mixing augmented by turbulence. This will reduce the difference between the different pollutant flowrates at the sampled surfaces.

**Table 2** Flowrates and mass fraction of pollutant PM2.5

	UDS0	UDS1	UDS2	UDS3	UDS4
<b>Flowrate headbox [kg/s]</b>	4.52E-11	3.10E-11	3.97E-11	1.66E-11	1.54E-11
<b>Normalized flowrate headbox [-]</b>	4.52E-02	3.10E-02	3.97E-02	1.66E-02	1.54E-02
<b>Flowrate bodybox [kg/s]</b>	1.75E-10	9.67E-11	5.08E-11	9.30E-11	8.64E-11
<b>Normalized flowrate bodybox [-]</b>	1.75E-01	9.67E-02	5.08E-02	9.30E-02	8.64E-02
<b>Flowrate nose [kg/s]</b>	1.29E-11	1.24E-11	1.36E-11	1.11E-11	1.03E-11
<b>Normalized flowrate nose [-]</b>	1.29E-02	1.24E-02	1.36E-02	1.11E-02	1.03E-02
<b>Nose mass fraction [kg/kg]</b>	9.20E-08	8.84E-08	9.73E-08	7.92E-08	7.37E-08



**Fig. 21.** Fraction of inhaled contaminant as a percentage from the contaminant emission rate in the room.



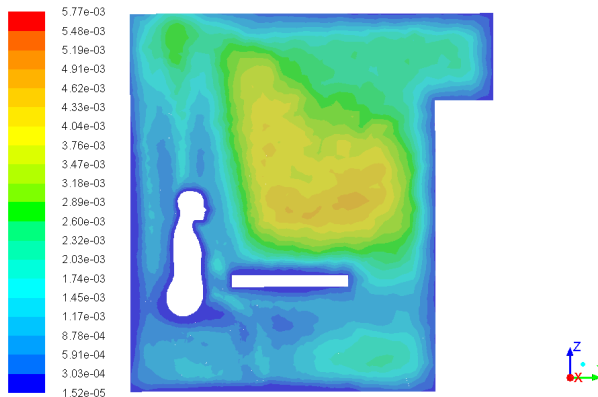


Fig. 22. Turbulent diffusion coefficient of contaminant [kg/m.s]

## 4 Conclusion

Inhalation risk of PM<sub>2.5</sub> was estimated by introducing 5 contaminants in a naturally ventilated room and calculating the percentage of contaminant inhaled by a thermal mannequin. Breathing zone and occupied zone have been analysed by introducing a head and body box as a virtual geometry in the simulation. Inhalation risk evaluated with the means of both the head box and the body box could be different than the inhalation risk calculated by the inhaled pollutant flux through the nostrils of the mannequin. Inhalation risk turned to be not much dependant on contaminant source distance, but this was due to the well mixed room airflow. The mixing was augmented by thermal plumes created by the heated mannequin body and a room heater. Concentration gradients, although not so big, impacted the accuracy of contaminant mass flow estimation through the virtual box surfaces, because gradients contribute to an extra diffusive mass flux. As a result, risk estimates were more credible when using the inhaled mass flow rate of contaminant. Because the room air was rather well mixed, the contaminant flow rate ratio was close to the airflow ratio between the mannequin nose and the room outlet, or roughly 1:100. In a poorly mixed case the result would likely be different, and thus the result will depend on both the flow field and contaminant location.

This work was supported by the European Regional Development Fund within the Operational Programme “Science and Education for Smart Growth 2014 - 2020” under the Project CoE “National center of mechatronics and clean technologies “BG05M2OP001-1.001-0008”.

## APPENDIX A. User-defined function (UDF) for Ansys Fluent to generate a scalar contaminant at user-defined location in the room.

```
#include "udf.h"

#define NUM_POINTS 5
real source = 1.0e-9 ; // [kg/s]
```

```

//Declare an array of structured data type, which contains the point
coordinates x, distance to desired location r, cell volume, and cell
identifier c
struct
{ float x[3],r,volume;
  int c;} p[NUM_POINTS];

DEFINE_EXECUTE_ON_LOADING(source_locations, libname)
{
  Domain *d ;
  Thread *t ;
  cell_t c ;
  float x[ND_ND], distance ;
  int i ;

  // Source coordinates
  p[0].x[0] = 1.6;  p[0].x[1] = 1.20;  p[0].x[2] = 0.85;
  p[1].x[0] = 2.0;  p[1].x[1] = 1.31;  p[1].x[2] = 0.85;
  p[2].x[0] = 2.4;  p[2].x[1] = 1.20;  p[2].x[2] = 0.85;
  p[3].x[0] = 1.1;  p[3].x[1] = 2.30;  p[3].x[2] = 2.05;
  p[4].x[0] = 2.9;  p[4].x[1] = 2.30;  p[4].x[2] = 2.05;

  //initialize the distance variable
  for (i = 0; i < NUM_POINTS; i++)
  {
    p[i].r=1000 ;
  }

  d=Get_Domain(1) ;

  // Locate the cells closest to the source coordinates
  thread_loop_c(t,d)
  {
    begin_c_loop(c,t)
    C_CENTROID(x,c,t);
    for (i = 0; i < NUM_POINTS; i++)
    {
      distance=sqrt( (p[i].x[0]-x[0])*(p[i].x[0]-x[0]) + (p[i].x[1]-
x[1])*(p[i].x[1]-x[1]) + (p[i].x[2]-x[2])*(p[i].x[2]-x[2]) );
      if (p[i].r >= distance)
      {
        p[i].r = distance;
        p[i].c = c;
        p[i].volume = C_VOLUME(c,t);
      }
    }
    end_c_loop(c,t)
  }
  for (i = 0; i < NUM_POINTS; i++)
  {
    Message("source %d: volume: %.8e cell: %d distance: %.4e \n", i,
p[i].volume, p[i].c, p[i].r);
  }
}

```

```

// define source for the cell whose identifier was determined from previous
function
DEFINE_SOURCE(UDS0,c,t,dS,eqn)
{
  real UDSsource = 0;
  if (c == p[0].c) // if cell is the source cell
  {
    float x[ND_ND];
    C_CENTROID(x,c,t);
    UDSsource = source / p[0].volume; // source is assigned with dimension
kg/(s.m3)
    printf("setting mass source for UDS0 on cell %d x=%.4e, y=%.4e, z=%.4e
\n",c, x[0],x[1],x[2] );
  }
  dS[eqn] = 0;
  return UDSsource;
}

// repeat DEFINE_SOURCE for the other contaminants

```

## References

1. Bliss Air, <https://blissair.com/what-is-pm-2-5.htm>
2. World health organization <https://www.who.int/emergencies/diseases/novel-coronavirus-2019/question-and-answers-hub/q-a-detail/coronavirus-disease-covid-19-how-is-it-transmitted>
3. Yu, Y. X., Sun, L., Yao, K., Lou, X. T., Liang, X., Zhao, B. W., ... & Zhang, H. (2020). Consideration and prevention for the aerosol transmission of 2019 novel coronavirus. [Zhonghua yan ke za zhi] Chinese journal of ophthalmology, 56, E008-E008.
4. Lv, J., Gao, J., Wu, B., Yao, M., Yang, Y., Chai, T., & Li, N. (2021). Aerosol Transmission of Coronavirus and Influenza Virus of Animal Origin. *Frontiers in Veterinary Science*, 8, 109.
5. Azimi, P., Keshavarz, Z., Laurent, J. G. C., Stephens, B., & Allen, J. G. (2021). Mechanistic transmission modeling of COVID-19 on the Diamond Princess cruise ship demonstrates the importance of aerosol transmission. *Proceedings of the National Academy of Sciences*, 118(8).
6. Amirav, I., & Newhouse, M. T. (2020). Transmission of coronavirus by nebulizer: a serious, underappreciated risk. *Cmaj*, 192(13), E346-E346.
7. Zhang, Z. and Chen, Q. 2007. "Comparison of the Eulerian and Lagrangian methods for predicting particle transport in enclosed spaces," *Atmospheric Environment*, 41(25), 5236-5248.
8. Nielsen P. V., Murakami S., Kato S., Topp C., et al., Benchmark Tests for a Computer Simulated Person, ISSN 1395-7953 R0307, Department of Building, Technology and Structural Engineering, Aalborg University, 2003, <http://cfd-benchmarks.com/>
9. Pichurov G., P. Stankov, Integration of thermophysiological body model in CFD, *Cent. Eur. J. Eng.*, 3(3), 2013, 513-521, DOI: 10.2478/s13531-012-0071-8
10. Xing, Huijuan, Andy Hatton, and Hazim B. Awbi. "A study of the air quality in the breathing zone in a room with displacement ventilation." *Building and environment* 36.7 (2001): 809-820.

# Parameters influencing the droplet formation in a focusing microfluidic channel

Emil Grigorov<sup>1,\*</sup>, Jordan A. Denev<sup>2</sup>, Boris Kirov<sup>3</sup> and Vassil Galabov<sup>3</sup>

<sup>1</sup> Faculty of German Engineering Education and Industrial Management (FDIBA), Technical University of Sofia, "Sveti Kliment Ohridski" 8, 1756, Bulgaria

<sup>2</sup> Steinbuch Centre for Computing, Karlsruhe Institute of Technology, Hermann-von-Helmholtz-Platz 1, 76344 Eggenstein-Leopoldshafen, Germany

<sup>3</sup> Department of Industrial Automation, Technical University of Sofia, 1756 Sofia, Bulgaria

**Abstract.** In the present work a detailed numerical study of the parameters influencing the droplet formation in a flow-focusing microfluidic device are made. First, an extensive verification of the simulations with data from the literature is carried out. Influence of parameters like viscosity and inflow velocity are compared with the results from literature showing a good agreement. Some differences are attributed to the different numerical techniques used: in the present work a pure volume-of-fluid method is used, while in the reference study this method is combined with the level-set method. As a second step of the verification of the present model, a comparison with experimental data from the literature was carried out which shows a very good agreement. After the verification was completed, eight new simulations are carried out covering a wide range of velocities of the continuous phase  $u_c$ . In these simulations the velocity of the discrete phase  $u_d$  remains unchanged. The variation of the continuous phase velocity reveals that with increasing the value of  $u_c$ , respectively the value of the capillary number  $Ca$ , the droplet length reaches a point of saturation, i.e. a point where the droplet length does not decrease any more. For the present setup this saturation occurs for  $Ca > 0,03$ . On the other hand, when the velocity of the continuous phase goes towards very low values ( $Ca < 0,01$  for the present setup), the droplet size increases significantly. Further, it was found that for increasing capillary numbers  $Ca$  above a value around 0,015 for water/oil and above 0,025 for water + 40% glycerol / oil systems, a transmission from the dripping towards the jetting regimes of droplet formation occurs. It was shown that when the viscosity of the continuous phase increases, higher total pressure jumps in the droplet occur, also leading to the formation of smaller droplets.

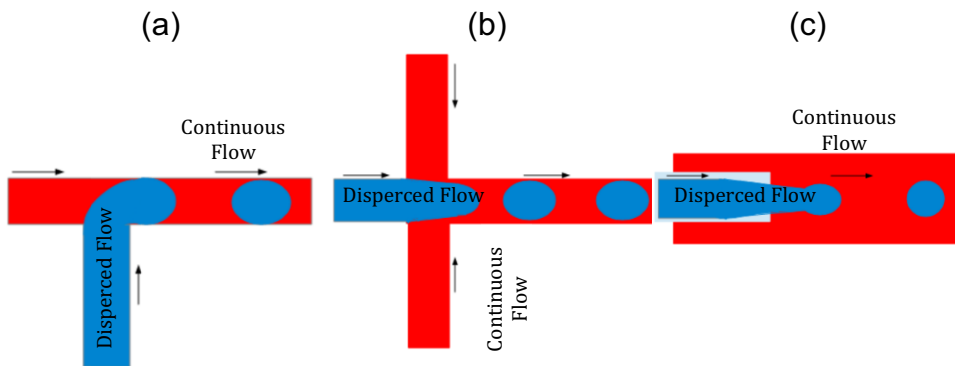
## 1 Introduction

---

\* Corresponding author: [egrigorov@fdiba.tu-sofia.bg](mailto:egrigorov@fdiba.tu-sofia.bg)

In recent years, microfluidic devices have emerged as a novel tool for the realization of different biological, chemical and medical processes. The decreased reagents volumes, usually in the nano/picolitres range, can significantly reduce reaction times, costs and energy consumption for certain processes [1]. Droplet-based microfluidics is a novel technique, which allows the encapsulation of different chemical or biological compounds into single picolitre-droplets. This makes it possible for the isolation and control of individual reactions, protecting them from their surroundings and unwanted interactions with other components. These small microreactors have allowed an easily implementable and relatively cheap approach for a broad range of processes including cell lysis [2], DNA purification [3], polymerase chain reaction (PCR) [4] and other. Therefore, understanding the mechanisms behind droplet generation is crucial for the control and efficiency of a droplet-based microfluidic system.

Droplets formation usually occurs when two immiscible liquids intersect each other. The process is achieved either by active (using electric fields) or by passive (using pressure-driven flow and channel geometry) methods. The specific design of the microfluidic channels makes it possible for a dispersed phase, usually water, to be sheared by another continuous phase (hydrocarbon oils, fluorocarbon oils etc. [5]) and to produce uniform-sized drops. Different geometry designs are possible, the most frequently used in the praxis are shown in Figure 1: T-junction [6-7] (a), flow-focusing [8-9] (b), and co-flowing [10] (c). The present work studies devices working on the flow-focusing principle.



**Fig 1.** Different geometrical designs for the droplet formation in microfluidic channels : (a) Flow-focusing, (b) T-Junction, (c) Co-flow.

Prior knowledge of droplet size, shape, formation frequency or pressure drop are usually required for the work with devices based on droplet-based microfluidic. Several experimental studies have already investigated the mechanisms behind droplet generation in microfluidic channels [11-15]. Those measurements give an adequate information about the needs of a certain experimental setup; it is not possible however, to include the influence of all effective parameters on the system. A feasible way to collect in advanced the needed information is by utilizing a predictive CFD model. A couple of numerical studies on droplet-based microfluidics were carried out in the past few years making use of different numerical methods (level set (LS) [16], Lattice Boltzmann method (LBM) [17-18] and other).

In this article the droplet formation in a flow-focusing microfluidic channel is investigated numerically by utilizing the volume of fluid (VOF) method. First, we validate our results with data from numerical and experimental studies from the literature. In a second part, using the same geometry as in [19], a parameter study is carried out. It consists of eight

new velocities of the continuous phase while at the same time the velocity of the dispersed phase was kept unchanged. Thus, the critical capillary number  $Ca$ , where the transition between the dripping and the jetting regimes occurs, can be determined. The pressure variation along the center line of the channel for the two flow regimes, is presented and discussed.

## 2 Mathematical model, geometrical setup, boundary conditions and numerical details

In the present study three-dimensional simulations of droplet formation in a flow-focusing geometry as shown in Fig. 2 are carried out. The two immiscible fluids, water and oil as well as their interface, are modelled by the Volume of fluid (VOF) technique. In this Eulerian method, the fluid flow is treated as a continuum. The phase fraction parameter,  $\alpha$ , indicates the presence of each phase in every control volume of the domain. The surface tension force is distributed near the interface as a body force in the Navier-Stokes equations.

The system of coupled partial differential equation consists of the continuity equation (Eqn.1) the momentum balance equation (Eqn. 2), and the phase fraction equation for  $\alpha$  (Eqn. 3) becomes:

$$\frac{\partial \rho}{\partial t} + \nabla \cdot (\rho \mathbf{U}) = 0 \quad (1)$$

$$\frac{\partial (\rho \mathbf{U})}{\partial t} + \nabla \cdot (\rho \mathbf{U} \mathbf{U}) = -\nabla p + \nabla \cdot (\mu [\nabla \mathbf{U} + \nabla \mathbf{U}^T]) + \mathbf{F}_s \quad (2)$$

$$\frac{\partial (\rho \alpha)}{\partial t} + \nabla \cdot (\rho \alpha \mathbf{U}) = 0 \quad (3)$$

In the equations above,  $\mathbf{U}$  is the velocity vector field and  $p$  is the pressure field.  $\mathbf{F}_s$  represents the surface tension force and is defined as shown in Eqn. 4 and is nonzero only at the interface between the two phases:

$$\mathbf{F}_s = \sigma \kappa (\nabla \alpha) \quad (4)$$

Here  $\kappa$  represents the curvature ( $\kappa = \nabla \cdot (\nabla \alpha / |\nabla \alpha|)$ ). Only one such transport equation (Eqn. 3) is solved since the volume fraction of the other phase can be inferred from the limitation:

$$\alpha_c + \alpha_d = 1 \quad (5)$$

where the index 'c' stands for continuous and 'd' for dispersed phase. The viscosity  $\mu$  and the density  $\rho$  are based on the weighted average of the phase fraction:

$$\mu = \alpha \mu_c + (1 - \alpha) \mu_d \quad (6)$$

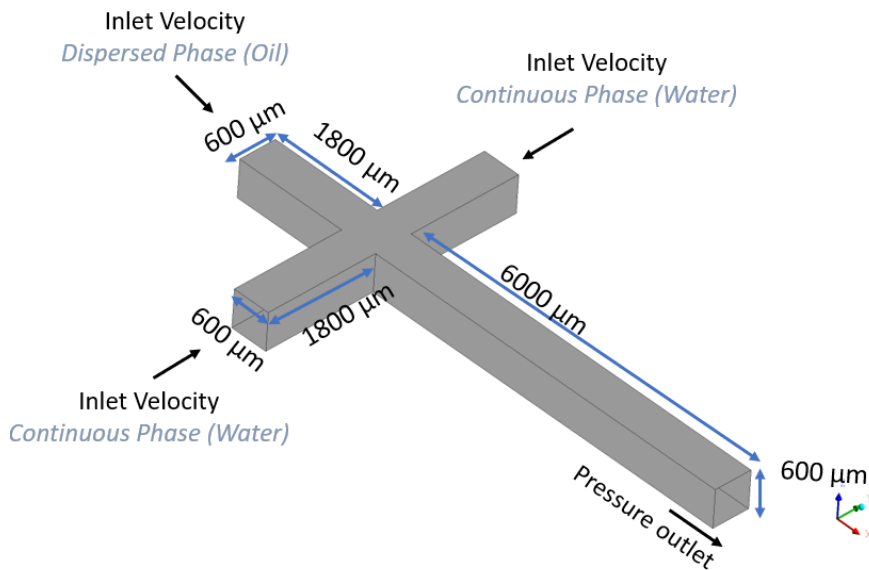
$$\rho = \alpha \rho_c + (1 - \alpha) \rho_d \quad (7)$$

In order to verify the results from the VOF method, a geometry of a flow-focusing microchannel, already investigated by Sontti and Atta [19] is considered. The lengths and dimensions of the square cross-section, the inlet and outlet channels are presented in Figure 2.

The continuous phase (water/water + 40% glycerol) is introduced through the two side channels and the dispersed phase (oil: octane +2,5% SPAN 80) is entered from the main (central) channel. Table 1 summarizes the physical properties of the two oil-water systems considered for the verification of the model and the later calculations in our work. As in [19], the information is obtained from the experimental results of Yao et al. [20].

**Table 1.** Physical Properties of Continues and Dispersed Phases.

Fluid	Density - $\rho$ [kg/m <sup>3</sup> ]	Viscosity - $\mu$ [mPas]
Water	995,4	0,89
Water + 40% Glycerol	1090,4	3,32
Oil (Octane 2,5+5% span 80)	689,9	0,53



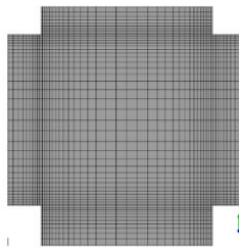
**Fig 2.** Model geometry, dimensions and boundary conditions for the present verification - following Sontti and Atta [19].

A finite volume method based CFD solver from ANSYS Fluent 16 with the implemented Volume of Fluid technique is used to solve the system of time-dependent partial differential equations. For the boundary conditions, constant velocity block profile was utilized for both continuous and dispersed phase inlets. The phase fraction  $\alpha$  is set to  $\alpha = 0$  at the two inlets of the continuous phase and  $\alpha = 1$  at the inlet of the dispersed phase. The walls of the channels were considered as fully wetted by the continuous phase, therefore the contact angle was set as zero at the walls. No slip boundary conditions are applied at the walls. Pressure boundary was specified at the outlet of the main channel. Table 2 summarizes the varied boundary conditions for each case investigated. The first two cases serve as a verification of our model. All other cases are completely different from [19] and cover a large range of new velocities for the continuous phase. The purpose is to investigate in detail how these velocities influence the flow regimes (dripping (D) or jetting (J)), which will be introduced in the following sections. The inlet velocity of the dispersed phase (oil) was kept constant at  $u_d = 0,0185$  m/s for all 10 cases.

**Table 2.** Boundary conditions varied for the investigation of droplet formation in the present work. In column 1: (D) means dripping regime, (J) means jetting regime.

Case & regime	Continuous phase	Inlet velocity of the continuous phase, $u_c$ [m/s]	Surface tension, $\sigma$ [mN/m]	Notes
1 (D)	Water	0,01850	5,37	Verification
2 (D)	Water + 40 % glycerol	0,01850	5,04	Verification
3 (D)	Water	0,00925	5,37	New $u_c$
4 (D)	Water + 40 % glycerol	0,00925	5,04	New $u_c$
5 (J)	Water	0,07400	5,37	New $u_c$
6 (J)	Water + 40 % glycerol	0,07400	5,04	New $u_c$
7 (J)	Water	0,10000	5,37	New $u_c$
8 (J)	Water + 40 % glycerol	0,03700	5,04	New $u_c$
9 (J)	Water	0,14000	5,37	New $u_c$
10 (J)	Water + 40 % glycerol	0,05100	5,04	New $u_c$

Making use of the mesh sensitivity analysis made by Sontti and Atta [19], we considered a near wall mesh refinement with a first row of thickness of  $6 \mu\text{m}$  and continuing with a 13% size increase towards the middle of the channel. The middle elements reach  $35 \mu\text{m}$  length size, and an overall of 390 000 elements are required for the hexahedral equidistant mesh. Figure 3 shows a zoomed view of the hexahedral elements in the cross region where the two fluids meet.



**Fig 3.** Zoomed view of the hexahedral elements in the cross region where the two fluids meet

A variable time step and a fixed Courant number ( $Co = 0,25$ ) were considered for solving equations 1-3.

## 3 Results and discussion

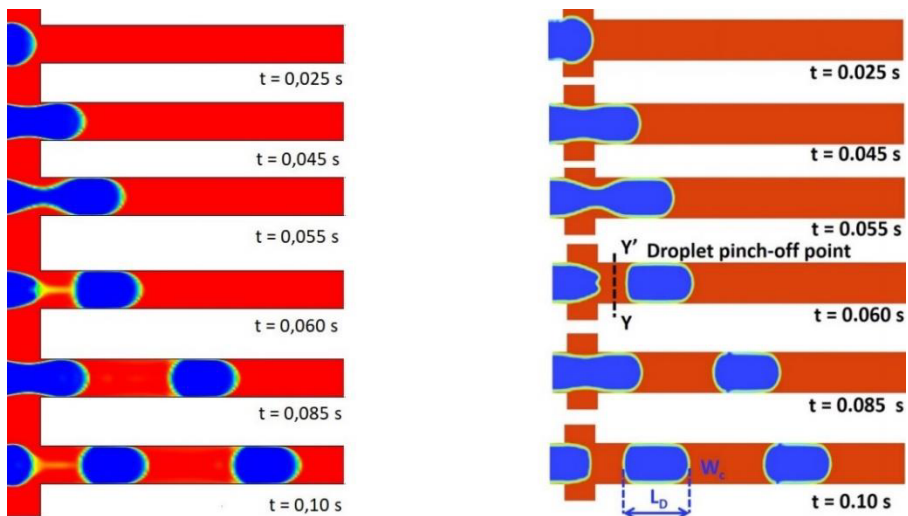
### 3.1 Verification and experimental comparison

As mentioned before, in order to examine the efficiency of the VOF model, first a verification of the results with the work of Sontti and Atta [19] is made. The authors of [19] utilized a combination of the VOF and LV (Level Set) methods, which compared to the pure showed more accurate methodology in capturing the interface between the two fluids. A detailed comparison between the VOF and the CLSVOF models is made by Keshavarzi et al. [21]. As a next step, a visual comparison with the experimental work of Wu et al. [22] was carried out, in order to further confirm the accuracy of the model.



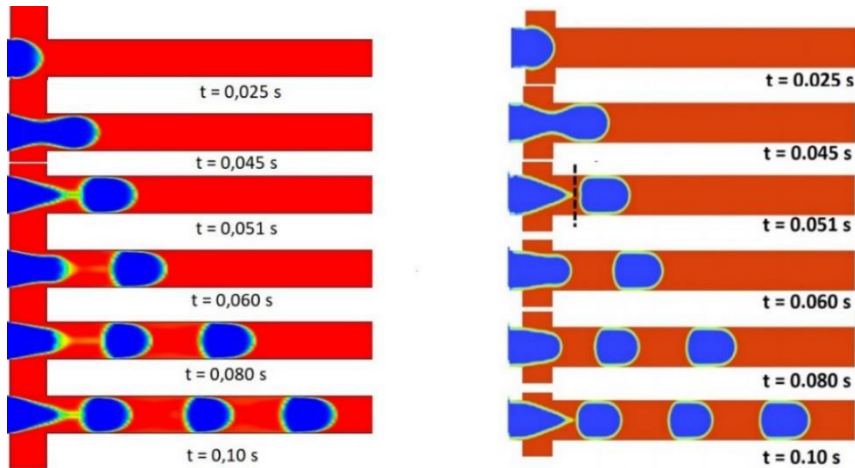
For our verification, cases 1 and 2 from Table 3 are considered and compared with identical simulations from [19].

Figure 4 shows the comparison of the droplet formation in the middle plane of the domains through time in the two studies for case 1. Both results show very close time scales regarding the generation of oil (blue) in water (red) droplets. The whole process can be divided into three stages. In the first, so-called filling stage (0,020s – 0,040s), the dispersed phase is injected into the main channel. At some point the growing oil-front blocks the flow from the side channels causing the upstream pressure to increase until it reaches a critical value where the continuous phase begins to squeeze the interface [23]. In the second stage (0,040s – 0,055s) the dispersed phase (oil) is still being injected into the droplet at a constant flow rate, while the neck starts to collapse. This accelerates the last pinch-off stage, in which droplet detaching occurs (around 0,060s). The three stages described above form, the so-called dripping regime in a microfluidic device [24].



**Fig. 4.** Comparison of the droplet formation in our work (left) and Sontti and Atta [19] (right) for case 1. Results from [19] are reproduced with permission

Similar observations are made in the second case (case 2 of Table 2), in which water +40% glycerol is utilized as continuous phase. The comparison is shown in Fig. 5. For this case the generated droplets have smaller volumes and higher formation frequencies compared to pure water (case 1). At the same operating condition for oil-water+40% glycerol system, an earlier droplet breakup (0,051 s) is also observed. This is due to the higher shear force, 'cutting' the droplet, connected with the higher viscosity of the red colored fluid in the second case. A larger difference in viscosity makes it possible to increase the shear at the boundary between the fluids thus increasing the generation frequencies.



**Fig. 5.** Comparison of the droplet formation in our work (left) and Sontti and Atta [19] (right) for case 2. Results from [19] are reproduced with permission.

A quantitative comparison of the two cases considered is also carried out and summarized in Table 3. The nondimensional droplet length with respect to channel width ( $= L_D/W_c$ ) and the droplet volume  $V_D$  are utilized for this purpose. For the calculation of  $V_D$  Equation 8 is used, with  $f$  standing for the frequency of droplet formation in Hertz and  $Q_d$  being the volume flow rate of the dispersed phase:

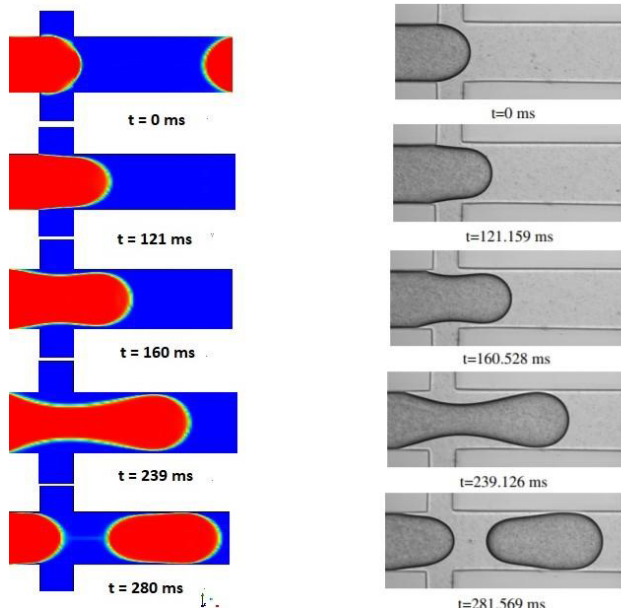
$$V_D = \frac{Q_d}{f} . \quad (8)$$

**Table 3.** Quantitative comparison of the results in our work with the work of Sontti and Atta

Parameter	Water / Oil			Water + 40% Glycerol / Oil		
	Our work	Sontti & Atta [19]	Rel. error [%]	Our work	Sontti & Atta [19]	Rel. error [%]
$L_D/W$	1,92	2,12	9,5	1,34	1,46	8,8
Droplet Volume [nL]	257	298	13,6	152	175	14,2

A relative difference of around 13-14% is observed for the volume of the generated droplets and around 10% for their length with respect to the channel width. This is in a reasonably good agreement with the CLSVOF method presented in [19], as the VOF technique often tends to smear the step profile of the interface over several mesh cells because of numerical diffusion, as it has been demonstrated in [22].

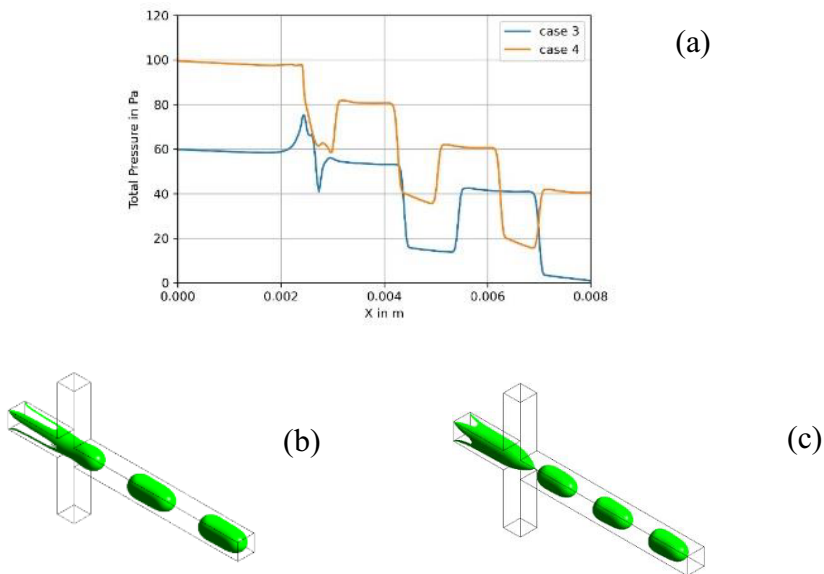
To further confirm the accuracy of the utilized VOF method, an additional comparison with the experimental work of Wu et al [22] was carried out. Numerical simulations were performed with the same fluid properties and channel dimensions, considered by the mentioned authors. Figure 6 demonstrates the visual comparison of droplet development. Here, the velocity of the continuous phase is  $u_c = 0,00252$  m/s, the velocity of the discrete phase -  $u_d = 0,00084$  m/s and the surface tension is  $\sigma = 30$  mN/m.



**Fig. 6.** Comparison of the droplet formation in our work (left) and the experimental work of Wu et al. [22] (right) Reproduced with permission.

### 3.2 Influence of continuous phase velocity and significance of the capillary number for the transition of regimes

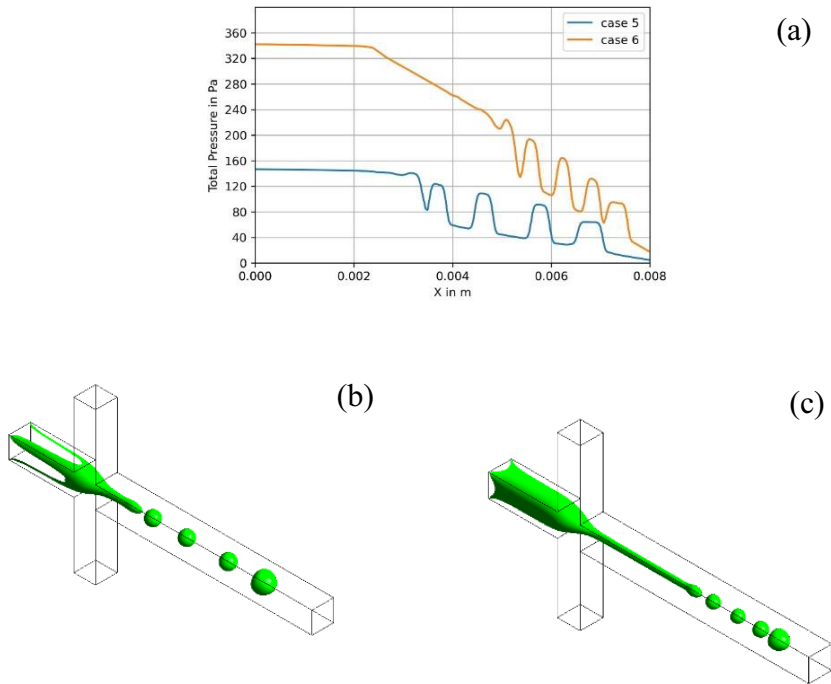
In order to understand better how droplet size for the flow-focusing microdroplet generator could be controlled more precisely, eight additional cases with varied continuous phase velocities (at constant dispersed flow rate of  $u_d = 0,0185$  m/s) were carried out, extending the range of simulated values by Sontti and Atta [19]. First, the value of  $u_c$  was decreased two times, compared to cases 1 and 2, to further evaluate the characteristics of the drops in the dripping regime (cases 3 and 4 from Table 2). Figure 7(a) shows the pressure variation along the center line of the channel for these two cases. Due to the increase in the internal friction of the continuous phase in case 4, a bigger total pressure in the domain (around 40%) is observed when compared to case 3. In any pressure profile, each peak and its width indicate a droplet position and shape, respectively. Due to their smaller size and hence, larger surface curvatures, the droplets from case 4 have on average approx. 15% higher pressure differences with their surrounding compared to case 3.



**Fig. 7** Comparison of case 3 and 4 from Table 2: (a) the total pressure profiles along the channel centerline ; (b) a three dimensional iso-surface evolution of droplet shapes for case 3; (c) a three dimensional iso-surface evolution of droplet shapes for case 4

Similar to cases 1 and 2, the droplet length in cases 3 and 4 decreases with increasing continuous phase viscosity, when comparing the three-dimensional iso-surface evolutions. As seen in Figure 7(b) and Figure 7(c) both cases are again in the dripping flow regime, described in section 3.1.

In the next step the velocity of the continuous phase is increased four times, compared to cases 1 and 2 (again for  $u_d = 0,0185$  m/s). This way we were able to further investigate the effect of  $u_c$  on the droplets and answer the question if the dripping regime take up even at higher velocity values. Compared to Figure 7, even larger differences in the total pressure can be seen between cases 5 and 6; these are shown in Figure 8(a). The bigger curvature radii lead to bigger resulting capillarity forces and hence, to three times higher pressure differences between the inside and the outside of the droplets as compared to cases 3 and 4. A noticeable pressure gradient across the droplet itself can also be seen. This is due to the difference in radius of curvature from back to nose of a droplet, shown also in the theoretical analysis made by Abiev et al. [25]. From Figures 8(b) and 8(c) a clear change in the shape and size of droplets is visible. Due to the increased “cutting” shear force on the dispersed phase, droplet length and volume for case 6 (when compared to case 5) decrease and higher formation frequencies occur. In this, so called jetting regime, a long-suspended column of the disperse fluid flows in the central channel as shown in Figures 8(b) and 8(c). The breakup of drops does not occur due to shear stress but due to the pressure drop across the emerging drop [26].



**Fig. 8** Comparison of case 5 and 6 from Table 2: (a) the total pressure profiles along the channel centerline ; (b) a three dimensional iso-surface evolution of droplet shapes for case 5; (c) a three dimensional iso-surface evolution of droplet shapes for case 6

The question where the transition from the dripping to the jetting regimes occurs has been discussed in the literature [27]. One of the critical parameters thoroughly investigated in droplet producing microfluidic devices is the capillary number, described in Equation 9:

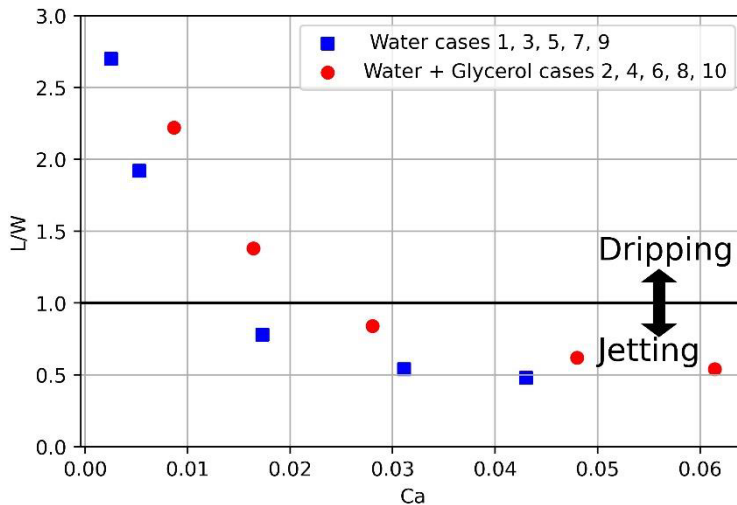
$$Ca = \frac{u_c \mu_c}{\sigma} \quad (9)$$

where  $\mu_c$  is the dynamic viscosity of the continuous phase. The number identifies the ratio of viscous to interfacial forces. For low capillary numbers, capillary forces dominate and therefore big droplets will be formed, whereas for high capillary numbers viscous forces generate small drops, increasing their surface energy. Similar to the Reynolds ( $Re$ ) number, the  $Ca$  number can be used to determine a transition point between two flow regimes. One way to do this is to show the geometrical changes in the generated droplets as a function of  $Ca$ . Figure 9 shows the non-dimensional length of the droplets for the 10 cases as a function of the Capillary number. In the Figure it can be seen that the largest changes of the drop size occur up to  $Ca \approx 0,02$ . The Figure shows that for even larger  $Ca$  numbers ( $Ca > 0,03$ ) the droplet size stagnates, i.e. it does not change significantly. Such a qualitative behavior is observed also in other studies with other geometries (e.g. Figure 6 from [28]).

At the left-hand side of the figure, the size of the droplets increases significantly when the  $Ca$  value decreases under the value 0,01.

Figure 9 allows clarifying the position of the transition point between the two regimes. The flow change appears where the droplet length  $L$  becomes smaller than the channel width

$W$ . For water (blue) this value is around  $Ca \approx 0,015$  and for water + 40 % glycerol (red) it is  $Ca \approx 0,025$ . The blue and red symbols show the same qualitative trend: larger slope for smaller  $Ca$  numbers and an almost constant droplet size for larger  $Ca$  numbers. The difference in the transition points of the two fluids is attributed to the different fluid properties. Although the  $Ca$  number of the continuous phase is the most important parameter that indicates the transition, there are other properties (viscosity of the dispersed phase, surface tension) which also influence the flow regimes.



**Fig. 9** The nondimensional droplet length with respect to channel width as a function of  $Ca$

It is important to note that for the definition of the  $Ca$  number, the average domain velocity - and not the inlet velocity - of the continuous phase was utilized. Table 4 summarizes the averaged domain values for the continuous phase which are used in Equation 9 and Fig. 9.

**Table 4** Average domain velocities for the 10 cases, utilized to calculate the  $Ca$  number

Case	Average $u_c$ in the domain
1	0,031
2	0,025
3	0,015
4	0,013
5	0,104
6	0,093
7	0,187
8	0,042
9	0,259
10	0,072

## 4 Conclusion

In this work the droplet generation in a flow-focusing microfluidic device has been investigated. The continuous phase (water, or water + 40 % glycerol) was introduced through the two side channels and the dispersed phase (oil: octane +2,5% SPAN 80) was entered from the main channel. For all simulations the VOF method was utilized. In the first part, a verification of the technique with the results from Sontti and Atta [19] has been made. Here, two cases were simulated, in the first, pure water was used as a continuous phase, and in the second - water+40 % glycerol which leads to increased viscosity. A good agreement between the two works, with maximum differences of 13% is found which are attributed mainly to the different numerical techniques. To further confirm the accuracy of the utilized VOF method, an additional comparison with the experimental work of Wu et al [22] was carried out which shows a very good agreement.

In the second part of the presented study, the influence of velocities of the continuous phase on the droplet formation is investigated. Two main flow regimes are observed – dripping and jetting, which are distinguished by the size of the droplet (for jetting, the droplets are smaller than the width of the channel). The transition between these regimes is investigated. This is done for a wide range of velocities  $u_c$  ( $0,1400 \text{ m/s} > u_c > 0,00925 \text{ m/s}$ ). The large number of studied regimes enabled the following main observations for the investigated setup:

- At very large velocities  $u_c$  ( $Ca > 0,03$ ) droplet size reaches a point of saturation, hence droplets do not decrease their size with increasing velocity  $u_c$  any more.
- At very small velocities  $u_c$ , ( $Ca < 0,01$ ) the observation is that droplet size still increases strongly with decreasing velocity.
- There is a critical  $Ca$  number, which serves as a transition point between the two described flow regimes (dripping and jetting). For the cases with water as a continuous phase, a critical value around  $Ca \approx 0,015$  is observed, whereas for the cases with water + 40 % glycerol it is  $Ca \approx 0,025$ . This difference is due to the influence of the dispersed phase properties.
- It was found that at higher flow rates (velocities) higher total pressures and pressure jumps in the droplets occur, also leading to the formation of smaller drops. The same effect was observed with increasing continuous phase viscosity.

As a whole, the present study shows that the VOF method is a reliable technique for the simulation and prediction of droplet generation in flow-focusing channels. It will allow the future study of other diverse setups and of various fluid combinations.

## References

1. N. Nguyen, S. Wereley, *Fundamentals and Applications of Microfluidics*; Artech House Publishing: Norwood, MA, USA, (2007)
2. E. Grigorov, B. Kirov, M.B. Marinov, V. Galabov, *Micromachines* **12**, 498 (2021)
3. Y. Xu, Z. Zhang, Z. Zhou, X. Han, X. Liu, *Micromachines*, **11**, 187 (2020)
4. B.K. Madhusudan, G. Sanket, *Eng. Res. Express* **2**, 042001 (2020)
5. N. Shembekar, C. Chaipan, R. Utharala, C. A. Merten, *Lab Chip*, **16**, 1314-1331 (2016)
6. T. Thorsen, R. W. Roberts, F. H. Arnold, S. R. Quake, *Phys. Rev. Lett.*, **86**, 4163 — 4166 (2001)
7. W. Zeng, H. Fu, *IEEE 8th International Conference on Fluid Power and Mechatronics (FPM)*, 1190-1196 (2019)

8. S. L. Anna, N. Bontoux, H. A. Stone, *Appl. Phys. Lett.*, **82**, 364 —366 (2003)
9. L. Yobas, S. Martens, W. L. Ong, N. Ranganathan, *Lab Chip*, **6**, 1073 —1079 (2006)
10. C. Cramer, P. Fischer, E. J. Windhab *Chem. Eng. Sci.*, **59**, 3045 —3058 (2004)
11. L. Mazutis, J. Gilbert, W. Ung, *Nat Protoc* **8**, 870–891 (2013).
12. M. A. Bijarchi, A. Favakeh, S. Alborzi, M. B. Shafii, *Sensors and Actuators B: Chemical*, 329, (2021)
13. Y. Zhang, L. Wang, *Nanoscale and Microscale Thermophysical Engineering*, **13:4**, 228-242 (2009)
14. W. Lan, S. Li, G. Luo, *Chem.Eng. Sc.*, **134**, 76-85, (2015)
15. Y. Lu, T. Fu, C. Zhu, Y. Ma, H. Z. Li, *Chem. Eng. Sc.*, **105**, 213-219, (2014)
16. W. Lan, S. Li, Y. Wang, G. Luo, *Ind. Eng. Chem. Res.*, **53**, 4913 (2014)
17. Y. Li, M. Jain, Y. Ma, Nandakumar, *Soft Matter*, **11**, 3884 (2015)
18. A. Gupta, H. S. Matharoo, D. Makkar, R. Kumar, *Comput. Fluids*, **100**, 218 (2018)
19. S. Sontti, A. Atta, *Ind. Eng. Chem. Res* **59**, 3702–3716 (2020)
20. C. Yao, Y. Liu, C. Xu, S. Zhao, G. Chen, *AIChE J.*, **64**, 346 (2018)
21. G. Keshavarzi, G.H. Yeoh, T. Barber, *The Journal of Comput. Mult. Flows*. **5(1)**, 43-55 (2013)
22. L. Wu, M. Tsutahara, L. S. Kim, M. Ha, *Int. J. Multiphase Flow*, **34**, 852 (2008)
23. P.A. Romero, A.R. Abate, *Lab Chip*, **12**, 5130-5132 (2012)
24. X. Chen, T. Glawdel, N. Cui, *Microfluid Nanofluid* **18**, 1341–1353 (2015).
25. R.Sh. Abiev, *Chemical Engineering Science*, Volume **174**, 403-412 (2017)
26. N.M. Kovalchuk, M. Sagisaka, K. Steponavicius, *Microfluid Nanofluid*, **23**, 103 (2019).
27. X. Chen, T. Glawdel, N. Cui, *Microfluid Nanofluid* **18**, 1341–1353 (2015).
28. S.K. Moon, I.W. Cheong, S.W. Choi, *Colloids and Surfaces A: Phys. And Eng. Aspects*, **454**, 84-88 (2014)



# The influence of the structure of laminar flows on the characteristics of equipment

Vasyl Arsirii<sup>1,\*</sup>, Oleg Kravchenko<sup>2</sup>, Bohdan Savchuk<sup>3</sup>, and Olena Arsirii<sup>4</sup>

<sup>1,4</sup> Odessa State Polytechnic University, 65044 Shevchenko av. 1, Ukraine

<sup>2</sup>National University "Odessa Maritime Academy" 8, Didrikhson str., Odessa,65029, Ukraine

<sup>3</sup>Odessa State Academy of Building and Architecture, 65029 Didrichson str 4, Ukraine

**Abstract.** The new method of visual diagnostics of liquid motion processes in physical models showed a high degree of the flow structure organization. Visual pictures made it possible to develop a hydraulic experiment to reveal the dimensions of the transverse structure in the form of layers and zones of flow separation from the channel walls. Visual diagnostics is the basis for comprehensive equipment design. Visual studies of the flow structure provide information for improving equipment by changing the geometry of the flow paths. Hydraulic studies show the change in the resistance of the equipment channels. Based on the results of visual and hydraulic studies, the wave character of the distribution of the pulsation velocity components was revealed. The regularities of the velocity distribution allow predicting the minimum or maximum values of the resistances of the flow paths of the equipment.

**Keywords:** Visualization; flow structures; laminar mode; resistance.

## 1 Introduction

The main task of mechanics of liquids and gases is to calculate the hydrodynamic parameters of the operation of various devices. Studying the patterns of flow organization in technological systems is the key to solving many problems. Despite the fact that this science has been forming for more than a century, Feynman's lectures on physics formulated an urgent problem in the design of equipment: "There is a very old physical problem common to many branches of activity and science. This is not a problem of searching for new elementary particles ... in its simplest form. There is a problem of what pressure P needed to move a given amount of water through the pipe? And no one based only on the laws and on the properties of water itself, does not know

---

\* Corresponding author: [vasily.arsiry@gmail.com](mailto:vasily.arsiry@gmail.com)

how to answer this question "[1]. That is, the imperfection of theoretical models and laws of hydrodynamics is one of the most pressing problems of technical progress. For example, energy consumption for compression and movement of deformable media is 5-15% in power engineering. Therefore, the main task of the models of fluid and gas mechanics is to offer the designer methods for improving hydro- and aerosystems to reduce resistance and accordingly increase the amount of transported water at a given initial pressure. Modern ideas about the movement of liquids and gases are based on the concept of turbulence [2]. The equations describing the turbulent flow provide only the averaged parameters of speed and pressure. The main cause of these problems is the optical transparency of liquids and gases (water, air, oil and gas), so their flow structure is not available for study [3, 4].

The visual diagnosis of the flow is especially important in the visualization and analysis of the dynamic processes. Therefore, an important task is the development of informative visualization methods, as well as methods for analyzing visual images to decipher the distribution fields of real hydrodynamic parameters. The study of the structure in the flow parts can be the key to solving many problems of various kinds in both technological and biological systems [5, 6].

**Object** of the article: presentation of a complex method for solving problems of optimization of hydrodynamic parameters of devices, which includes two stages. The first stage is the visualization of flows for the structure during the movement of liquids and gases. The second stage is optimization of the geometry of the flow paths to improve the hydraulic devices of the devices.

## 2 Well-known models of hydrodynamic processes

The hydrodynamic models are based on the results of a large number of scientific researches. Most often, the dependences of the dynamic indicators (flow rate) on the initial potentials (pressure) are studied with average value of their pulsation components. Several important experiments can be allocated for the presentation of modern models of the dynamic processes of liquids and gases.

D. Mendeleev in 1880 determined the regularities of calculating pressure losses in the flow paths to overcome resistance: at low speeds, they increase linearly with speed; at high speeds, losses are proportional to the square of the speed. The idea is also formulated that the main processes occur at the boundary layer and a model of roughness was proposed. Difficulties in obtaining information about processes within flows and uncertainties in measuring the parameters of fluid motion have led to the creation of models of flow continuity and averaging of parameters. Most of the studies are still related to the processes of separation of flows from the walls of channels [7]. However, it was the complex experiments of Reynolds (1883), where visual and hydraulic studies were combined, that became the most productive for understanding the dynamic processes of fluids. Visual studies made it possible to record two fundamentally different modes of movement. At low velocities, the introduction of a dye into the flow does not change the jet thickness, which indicates minimal diffusion [8]. That is, adjacent layers do not mix at low speeds. This flow mode was called laminar. With an increase in the flow rate, a mode occurs when the dye is rapidly mixed.

Such a mode is called turbulent or chaotic. Comprehensive Reynolds studies made it possible to develop a well-predicted value of the critical Reynolds number  $Re_{cr} = 2320$ , which characterizes the transition from a layered flow to a chaotic one. Only after Reynolds comprehensive research it became possible to investigate and correctly represent the values of resistances  $R$  for calculating pressure losses in channels at different flow mode. Poiseuille's experiments made it possible to develop a formula for calculating the resistance values for the laminar mode.

$$R = 64 / Re \quad (1)$$

The Poiseuille's on the Nikuradze diagram (1933) curve shows the decrease in resistances  $R$  with an increase in the Reynolds number in the range  $Re < 2320$ . Blasius's experiments made it possible to develop a formula for calculating the values of resistance  $R$  in channels with smooth walls (roughness  $\Delta = 0$ ) for a turbulent mode.

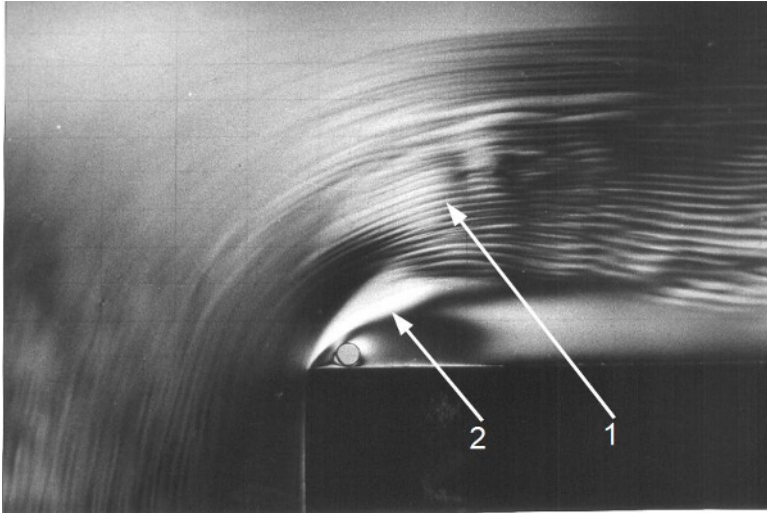
$$R = 0,3164 / Re^{0,25} \quad (2)$$

On Nikuradze diagram, the Blasius curve is also one line of decrease in  $R$  in the range of Reynolds numbers  $Re > 2320$ .

### 3 Method of flow structure visual diagnostics

The article presents a new method for improving the parameters of power equipment operation by visualizing the processes of fluid movement in special physical models. The method of the flows structure visual diagnostics (*FSVD*) makes it possible to reveal the structure of flows of liquids or gases not only at the walls arias of the channels, but also the layers inside the flow, that are not mixed [8]. New knowledge about the structure of flows makes it possible to improve the geometry of the channels to improve the energy performance of equipment by reducing the resistance of the flow paths.

Method *FSVD* can be used as the first stage of designing new or improving known flow parts of equipment. The visualization of flows is carried out in special physical models with the characteristic dimensions of the flow paths. An optically active liquid (based on vanadium oxide  $V_2O_5$ ) moves in the model. The speed of movement is consistent with the speed in a real device according to the Reynolds number. Elongated vanadium oxide molecules are oriented in the flow in accordance with velocity gradients. The stresses in the flow associated with the velocity gradients in polarized light are reflected by the change in the intensity of the illumination of the flow pattern in the entire field of the model. Light areas indicate positive velocity gradients, dark areas show negative gradients. Thus, visualization characterizes the field or the complete picture of instantaneous velocity values. Figure 1 shows the result of visual studies of liquid or gas flow in a  $90^\circ$  turn.



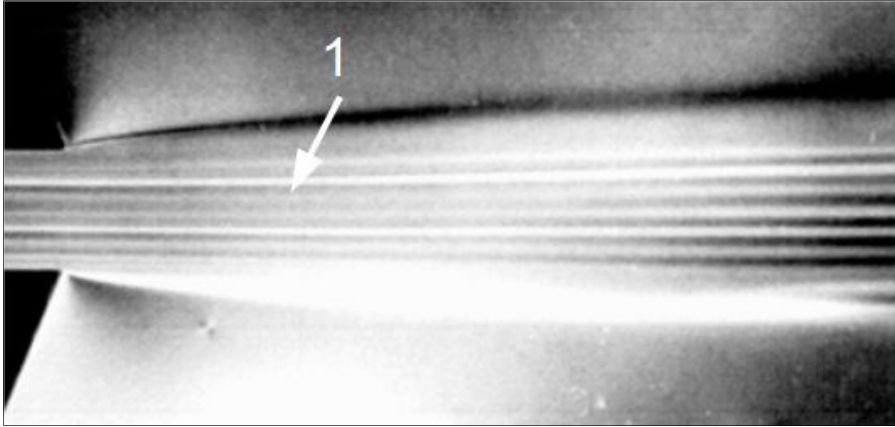
- 1 – Lines in the channel cross-section that have a stable structure;  
2 – The boundaries of flow separation from the channel walls.

**Fig. 1.** Image of the structure of flow in a  $90^\circ$  turn.

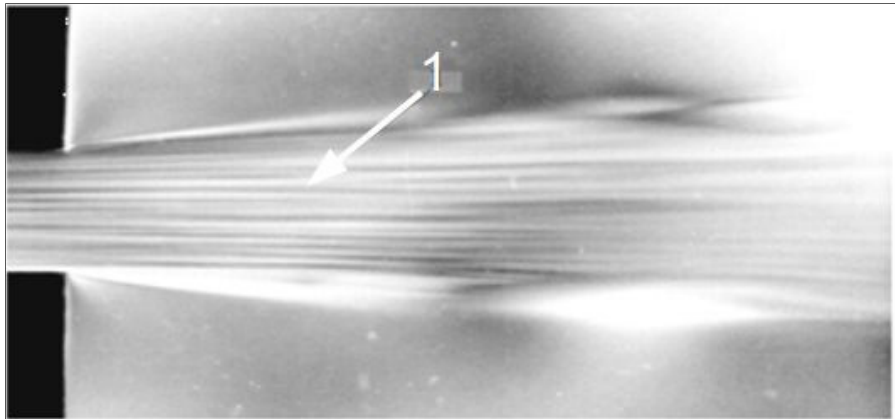
The visualization revealed lines in the channel cross-section that have a stable structure. In the figure, one can clearly distinguish also the boundaries of flow separation from the channel walls. Visual diagnostic of flows can be considered the first stage of design. In the second stage, you can improve the geometry of the channels to optimize the energy parameters of the equipment. At the second stage, you can improve the geometry of the channels to optimize the energy parameters of the equipment. To reduce the resistance of the flow paths, it is sufficient to eliminate the dissipative zones by replacing them with inserts, as well as by optimizing the placement of the identified layers.

#### 4 Visual studies of the laminar flow structure

The experience of visual studies of flows in physical models shows that the movement of fluids under certain combinations of geometric and hydraulic parameters has a stable structure both in the transverse and longitudinal sections. The article presents the results of studies of transverse flow structures only. In fig. 2 shows the results of visual diagnostics of the structure of a laminar jet in a flooded space. A physics experiment using the *FSVD* method at low Reynolds numbers shows layers that have minimal diffusion and therefore a stable cross-sectional structure.



a.



b.

a) the structure of the laminar stream ( $Re = 1700$ )

b) the structure of the laminar stream ( $Re = 2100$ )

1 - transverse structures (streamlines);

**Fig. 2.** Image of the structure of a laminar stream.

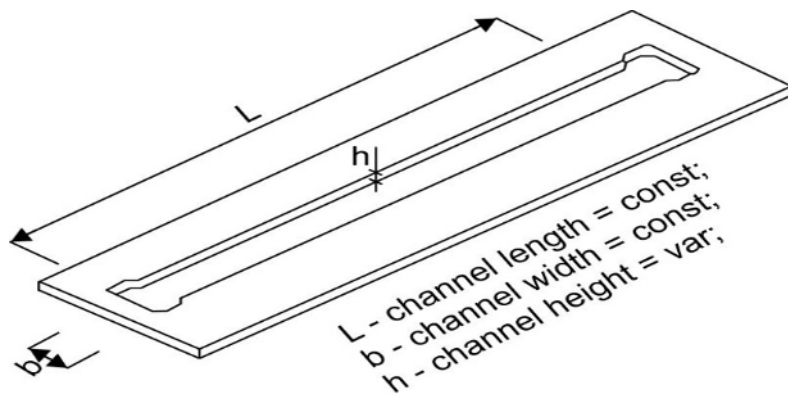
Light and dark stripes are clearly visible in the laminar jet image. Stable dimensions made it possible to determine the frequency of changes in illumination. The distance between the peaks or extrema of the illumination of the light stripes (or dark stripes) is  $\lambda = 0.52$  mm. Thus,  $\lambda$  is the wavelength of the periodic nature of the distribution of the revealed structure of the illumination intensity.

## 5 Hydraulic studies of laminar flow structure

Visual pictures of the stable nature of the structure of the flow of a laminar flow made it possible to develop and conduct a series of hydraulic experiments. The hydraulic experiment is the second stage in the study of the structure of the laminar flow. It is

necessary to answer whether there is a correspondence (correlation) between the visual patterns of the flow structure and the change in velocity in the cross section of the laminar flow. That is, the size of the wave character of the distribution of the optical density of the bands from light to dark and again to light correspond to the dimensions of the wave character of the change in the real velocity of the flow layers in the cross section at a given constant initial pressure  $P_1$ .

For the hydraulic experiment, 8 models in the form of thin sheets of getinax of different thickness were made simultaneously on the machine (bench). A channel was cut in all sheets, in which the length  $l$  and width  $b$  remained constant. In the experiments, only the channel height  $h$  was changed. (Fig. 3). Twelve experiments were carried out in which one or several models were clamped between two absolutely smooth plates with water inlet and outlet manifolds.

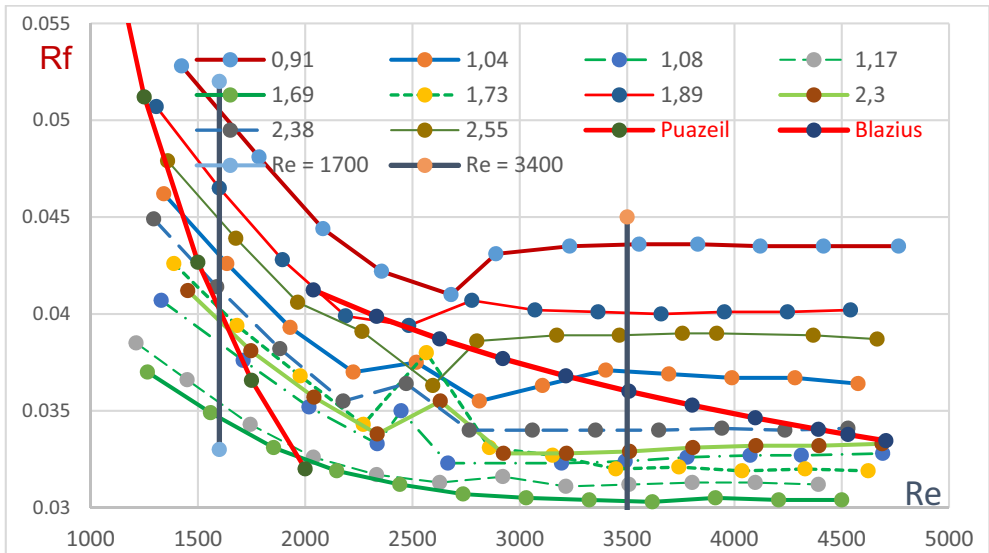


**Fig. 3.** Model for study of dependence  $\lambda = f(Re, h)$

In each experiment, the pressure  $P_1$  was varied discretely in the inlet manifold. In this case, two parameters were measured: pressure  $P_1$  and water flow rate to calculate the velocity  $V$  in the channel. The measured parameters of velocity and pressure made it possible to calculate the resistant coefficients  $R$  in 12 variants of straight channels with a change in height in the range  $h = 0.9 \div 2.55$  mm, as well as a change in the Reynolds number  $Re$  of each individual experiment. The results of hydraulic experiments are shown in Fig. 4 in the form of 12 dependences of the channel resistances on the Reynolds number  $\lambda = f(Re)$ .

The walls of the channels had a smooth surface (roughness  $\Delta = 0$ mm); therefore, the results obtained can be compared with the Poiseuille's and Blasius's formulas. Deviations of the hydraulic friction coefficient  $R$  from the values calculated by the Blasius formula (at  $Re > 2500$ ) are  $\Delta R = \pm 16\%$ . At  $Re < 2320$ , the deviations of the resistances from the values calculated by the Poiseuille formula are more than  $\Delta R = \pm 20\%$ .

Analysis of the parameters of hydraulic experiments showed that a linear change in the height of the channels in the range  $h = 0.9 \div 2.55$  mm corresponds to the wave nature of the change in the resistance  $R$  of the channels..



**Fig. 4.** Results of the study of the dependence  $R = f(Re, h)$ .

The wavelength of the resistance changes  $\lambda_R$  coincided with the value of the wavelength  $\lambda_L$  of the change in the optical density of the bands in the visual images of the laminar flow structure in Fig. 2. The analysis of the experimental results showed that for a given value of the Reynolds number ( $Re = \text{const}$ ), the linear change in the channel height  $h$  [mm] corresponds to the wave character of the change in resistance with a wavelength  $\lambda_R = 0.52$  mm.

The results of hydraulic experiments are in good correlate with the wave character of the change in the optical density of the bands in the visual images of the laminar flow structure in Fig. 2 with a wavelength  $\lambda_L = 0.52$  mm. The results presented in Figure 2 eliminate the problem of measurement uncertainty in many laminar flow studies. However, the resistance  $R$  is only a coefficient of proportionality between the main parameters of the movement of liquids: pressure  $P$  and speed  $V$ . Therefore, the results obtained are best interpreted as follows. For the range of channel transverse dimensions  $h = 0.91 \div 2.55$  mm, it is possible to determine the channel dimensions in which, at a given initial pressure  $P_1$ , the velocity value will be greater than the average velocity calculated by the Poiseuille formulas (laminar mode) or Blasius formulas (turbulent mode). To determine the size of the channel, where the speed will be higher than the average, you can use the formula 3:

$$b_{V_{max}} = n\lambda + 0.25\lambda \quad (3)$$

$n$  – multiple of wavelengths  $\lambda$ .

If necessary, you can solve the inverse problem of ensuring maximum resistance, for example, when designing the dimensions of seals. In this case, the channel size can be calculated using the formula 4:

$$b_{Vmin} = n\lambda + 0.75\lambda \quad (4)$$

The patterns distribution of transverse structures can be used in the design of flow paths for the movement of liquids and gases. An odd number of half-waves of pulsating velocity components  $\Delta V$  corresponds to the positive influence of transverse structures; an even number of half-waves corresponds to the dissipative effect of the distribution of the velocity components and generates the maximum flow pulsations at the channel wall.

The results of hydraulic experiments have confirmed the presence of a flows structure that have a positive or negative effect on the speed of movement of liquids or gases. However, it is easiest to identify the flows structure by visual research. The results of visual and hydraulic experiments by A. Losievsky (1933) can be called a similar method for improving flow paths or channels. Layers or transverse structures of river flows were identified visually. Models explaining the nature of the transverse flow structures allowed M. Velikanov (1936) to put forward a hypothesis that the internal flow structure is inherent in any motion of liquids and gases [12]. Experience in improving various power equipment over the past 20 years [8] showed the promise of designing flow paths with an additional stage of visualization of the flow structure. However, the flow structure model is still little used in the design of technical devices.

## Conclusions

The designing of equipment, the operation of which is associated with the movement of liquids and gases, has a number of problems. Often, the real productivity of the equipment is less than that calculated by the known formulas. The negative phenomena are noise, vibration.

The main reason for the difficulties in eliminating problems and negative phenomena is the lack of informative research methods for studying flows. It is the physical visual studies of flows that can provide new methods for designing more efficient equipment. The article presents a method for solving problems of optimization of hydrodynamic parameters in various devices, which includes two stages. The first stage is the visualization of flows to reveal the structure during the movement of liquids and gases. The second stage is optimization of the geometry of the flow paths based on the identified organization of the flow structure to reduce the resistance of the flow paths and improve the operating parameters of power equipment.

The method of visual diagnostics of the flow structure made it possible to reveal the wave character of the distribution of the pulsation velocity components in the cross section of channels with stable parameters both in space and in time. An odd number of half-waves of transverse structures have a positive effect on an increase in the flow rate at a given pressure, an even number of half-waves increases energy dissipation and other negative phenomena.



## References

1. Feynman Richard. *The Feynman Lectures on Physics Vol I* (2012)
2. Loytsyansky L. G. *Mechanics of fluid and gas: textbook for universities*. Moscow: Bustard, 840 p. (2003)
3. Chashechkin Yu.D., Mitkin V.V. A visual study on flow pattern around the strip moving uniformly in a continuously stratified fluid, *J. of Visualization*. V. 7. No. 2. P. 127–134. (2004)
4. Prokhorov V.E., Chashechkin Yu.D. Visualization and acoustic sounding of the fine structure of a stratified flow behind a vertical plate, *Fluid Dynamics*. V. 48. No. 6. P. 722–733. (2013)
5. Van Dyke. *An album of fluid motion*. / Stanford, California: The Parabolic Press. (1982)
6. Brian J. Cantwell. Organised motion in turbulent flow., *Ann. Rev. Fluid Mech.* – 1981. – Vol. 13. – P. 457-515. (1981)
7. Davletshin I.A. Space Time Structure and Drag in Round Pipe with Periodic Flow Rate Pulsation, Miheev N.I., Romanov D.I. // *Proc. 13th Int. Conf. On the Methods of Aerophysical Research*. Pt 1. – Novosibirsk: Publ. House “Parallel”.– P.88-93 (2007)
8. Arsiry VasyI, Reconstruction of turbomachines on the basis of the flow structure visual diagnostics ARSIRI VasyI, KRAVCHENKO Oleg., *International Journal Mechanics and Mechanical Engineering*, 2018. Volume 22. Number 2, P 405-414 ISSN: 1428-1511 e-ISSN: 2354-0192 (2018)
9. Abdul Rahim A. Khaled. Modelling and Theoretical Analysis of Laminar Flow and Heat Transfer in Various Protruding-Edged Plate Systems, *Journal of Electronics Cooling and Thermal Control* Vol.5 No.3, September 16, (2015)
10. Nikulin A., Moita A.S., Khliyeva O. Effect of Al<sub>2</sub>O<sub>3</sub> nanoparticles on laminar, transient and turbulent flow of isopropyl alcohol, *International Journal of Heat and Mass Transfer*. Vol. 130. P. 1032-1044. (2019)
11. Khliyeva O., Ryabikin S., Lukianov N., Zhelezny V. Experimental study of heat exchange and hydrodynamics at the laminar flow of nanocoolant based on propylene glycol and Al<sub>2</sub>O<sub>3</sub> nanoparticles, *Eastern european journal of enterprise technologies*. Vol. 1/8 (85). P. 4-12. (2017)
12. Velikanov M.A. Dynamics of channel flows. Part 1 (Flow Structures) – P.323 (1954)

# Modularity design of the bamboo plastic fiber forming machine

Nguyen Thanh Nam<sup>1,\*</sup>, and Nguyen Hoang Hiep<sup>2</sup>

<sup>1</sup>Faculty of Mechanical Engineering, Industrial University of Ho Chi Minh City, Vietnam

<sup>2</sup>Faculty of Mechanical Engineering, Vinh Long University of Technology and Education

**Abstract:** Currently, the research on the application of bamboo wood plastic fibers to 3D printing technology in Vietnam is limited. Almost all studies mainly focus on the application of natural polymers (wood, rubber, coir.) but ignore a rich natural polymer source, popular in Vietnam: bamboo. In addition, the quality of wood plastic fibers applied in 3D printing technology has not responded to the requirements of consumers. The durability of 3D printed parts that is based on wood plastic fibers is not high. Surface gloss of parts after implementation is still rough. During the 3D printing process of wood plastic fibers material, the nozzle is still always clogged due to the blockage of wood pulp. Therefore, the study of technology and equipment for the fabrication of bamboo wood fibers and research on the effect of technological parameters on the finished bamboo-wood-plastic fiber properties is necessary and should be urgently carried out. The paper proposes a new approach to structure modularization of the bamboo wood plastic fiber forming machine by using mostly standard parts, thus improving the quality and reducing the cost of the machine and bamboo wood plastic fiber material for the 3D printer.

## 1 Introduction

Currently, the event of the global warming is evident, so scientists have studied a variety of green and environmentally friendly materials to restrict partly the human serious problem. Naturally derived composites are being studied more and more, not only because they could limit the environmental pollution but also prevent the depletion of natural resources due to over exploitation [1].

Wood plastic composite (WPC) that is a new type of composite material, including wood pulp and its constituent resin, is recommended as a logical solution with the addition of some additives or compatible substances. WPC has many superior features than natural wood, one of them is corrosion resistance, rot, termites and unabsorbed water to the fibers inside [2]. An alkaline treatment of wood pulp or plastic as Polylactic Acid (PLA) also increases the water resistance of the WPC, however, this reduces its mechanical properties.

Nowadays, FDM technology is the most popular 3D printing technology in which the process of extruding molten plastic material in a nozzle and then forming layers that will form a block structure after solidification. Because the machining principle of FDM

---

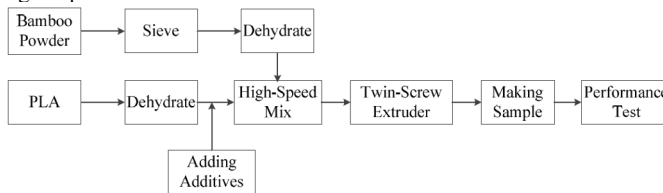
\* Corresponding author: [nguyenthanhnam@iuh.edu.vn](mailto:nguyenthanhnam@iuh.edu.vn)

technology is extremely simple, it applies to many different materials, and green composite is an extremely potential material. Scientists have conducted a lot of researches on creating fiber-like green composite products used in this technology, and they are often called wood-based plastic fibers.

In the study [3], the authors used pineapple fibers, banana peel fibers and bamboo fibers to create wood-based plastic fiber sheets based on epoxy. Composite is made of high mechanical properties, suitable for many industries and they also have the advantage of being low cost and easy to degrade.

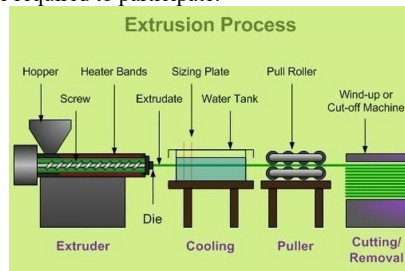
In the study [4], the authors presented an overview of the process of creating wood plastic fibers from the extrusion process that is applied to the material additive technology. They also presented the opportunities and challenges of green composite fibers from extruders in the application of 3D printing technology.

In the study [5], the researchers made an overview of the machines as well as materials, used in the production of bamboo wood plastic fibers. They also proposed all the requirements for 3D printed bamboo wood plastic fibers to have good product quality: the diameter of plastic fibers must be in the range of 1.75-1.8mm; maximum particle size is 0.27-0.3mm, if it is bigger as about 0.4mm, it will cause nozzle jamming; the suitable machining temperature is about 180<sup>o</sup>.



**Fig. 1.** The process of creating bamboo plastic fiber for 3D printer [5]

In the process of producing bamboo wood plastic fibers, as discussed above, there are many machines that are required to participate.

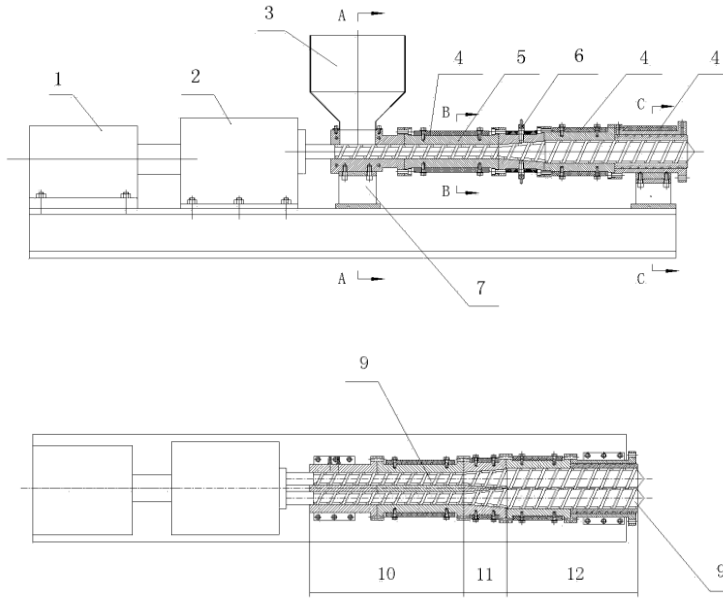


**Fig. 2.** Schema of basic machines for the production of bamboo plastic fiber [6]

Currently, with the strong development of composite materials technology, scientists increasingly focus on the development and application of green composites in industrial and civil fields. The application of natural wood fibers in the composite forming process with polymers to synthesize outstanding properties of wood fibers such as durability, hardness... and polymer properties such as water resistance, flexibility... With the advancement of 3D printing technology, scientists have also studied the creation of wood plastic fibers applied in this technology, initially creating basic products.

3D printed bamboo resin fiber forming process: treated bamboo powder (20%), PP (52.5%), and PLA (22.5%) are mixed with maleated polypropylene (MAPP) (5%) with

High speed mixer for 8 minutes. This mixture is then fed into a 2-screw extruder to produce wood-plastic pellets. From there, these bamboo wood plastic pellets are fed into a single screw extruder to form the product [7].



**Fig. 3.** Structure of extruding bamboo plastic fiber machine with double screw of [8]

Figure 3 shows the construction of the single-screw extruder of the invention [8]. All the 2-screw extruder parts are cited as in the following: 1: Electric motor; 2: Gearbox reducer; 3: Feeding hopper; 4: Thermistor heating; 5: Extruder housing; 6: Cooling water drainage; 7: Support structure; 8: Machine base; 9: 2-screw extrusion; 10: Feeding area; 11: Melting area; Region 12: Flow stable area. The extrusion by two screws facilitates the polymer flows along only one direction, limiting backflow. In addition, due to the properties of 2-screws, the material is mixed more efficiently than extruding with one-screw. The 2-screw structure is also studied by the authors, with the first design, one screw has a normal structure while the other is joined by 3 small screws in 3 divided regions above. That structure is logical to replace the extruded screw much more when it was damaged.

The authors mention the functional structure in which there are two extruders' screws with different sizes, but one screw that extends through all three regions, one that extends only through the last two regions. This helps to reduce the screw material and costs of machine. In the other side, it improves also the productivity because the feed area only needs to pre-melt the material, so one screw is also possible.

The above studies displayed preliminary processing methods of performing bamboo wood plastic fibers as well as the advantages and limitations of bamboo wood plastic fibers, but there has not been an innovated technology to develop products in practice. Therefore, it is necessary to develop new technology to create bamboo-wood plastic fiber, improve quality and reduce product costs.

## 2 The structure analysis method

### 2.1 Description the system

Setting up the diagram of the relation between function and structure of the machine [9], [10].

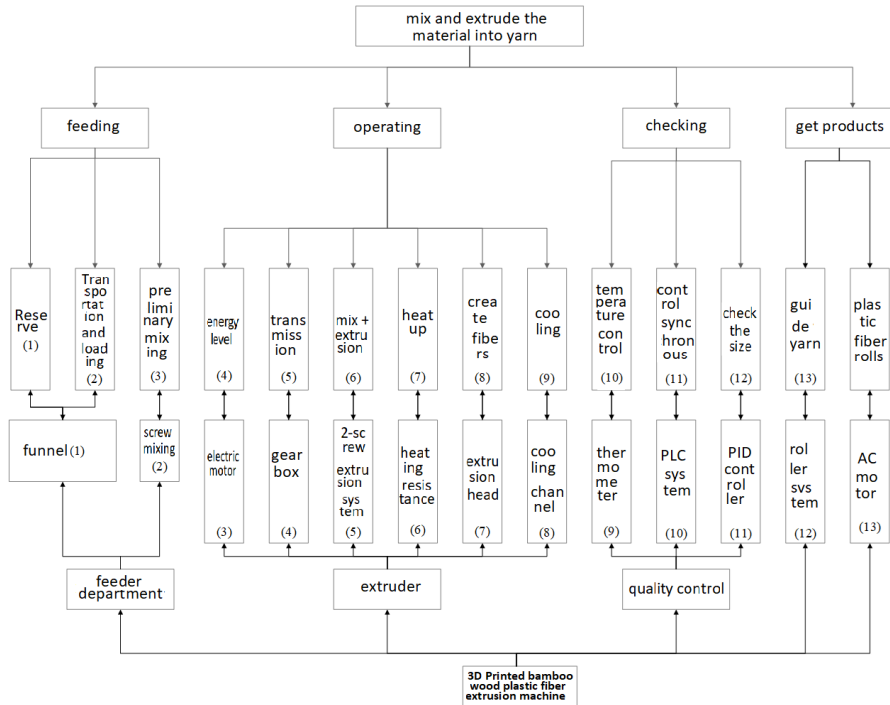


Fig. 4. Schema of the relation between Function and Structure of the machine design [11]

The system composes:

- (1) Storing and feeding hopper.
- (2) Preliminary mixing by screw.
- (3) Power supply by electric motor.
- (4) Transmission by gearbox, spur gear transmission and coupling.
- (5) Mixing and extruding wood plastic mixture by twin extrusion screw in cylinder.
- (6) Application of thermal strip to melt the resin.
- (7) Creating yarn by the extruder,
- (8) Cooling system to cool the hot extruded plastic fibers,
- (9) Temperature control by sensors,
- (10) Control and synchronization by PLC system,
- (11) Check dimension by PID system,
- (12) Leading bamboo wood plastic fiber by roller system,
- (13) An AC motor for winding the filament.

When starting the system, the plastic particles and bamboo powder are fed to the hopper where they are properly quantified and pre-mixed in the feed hopper by a mixing screw that

received the rotation from the motor via gear transmission and flexible shaft. Reversing twin-screw extrusion system is installed to increase the mixing efficiency. The partial heating of the screws is carried out by solenoid heating strips and a water' cooling system is also included to prevent overheating. During the extrusion process, the temperature is controlled by a thermal sensor and a PLC system. After getting out of the extrusion die head, bamboo plastic fiber will be checked size by PID system and then finished plastic fibers will be brought out by a roller system with cooling channels to stabilize their texture and surface. Finally, they are rolled into coils by an AC motor.

## 2.2 System module analysis

The primary analysis of modules that has the purpose of distinguishing to the main modules (machine detail cluster) of the machine, makes decision whether to combine these details into one module or whether different ones.

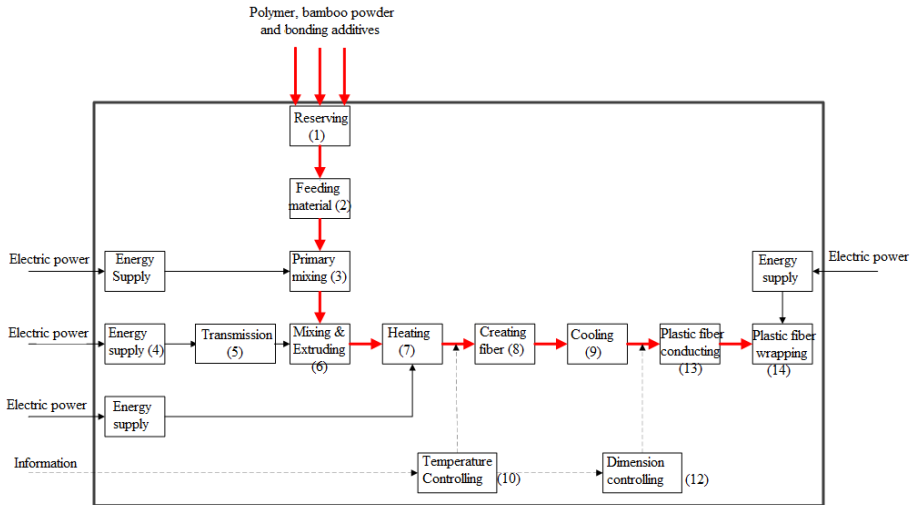


Fig. 5. Schema of primary arrangement and basic components in the system

## 2.3 Structure module analysis

Figure 5 displays the schematic analysis of the primary structure of the future machine. The structures after analysis are arranged in the direction of material flow from feeding to production. Figure 4 shows the basic functional-structure relationship diagram of the machine, in which functions are served by a set of components that can be called a "module". The power supply function is a special function that is included in each module.

The main function of the "Bamboo Wood Plastic Extrusion Machine for 3D Printer" is to perform the following processes: feeding, extruding and winding. The finished yarn is shown in Figure 6.

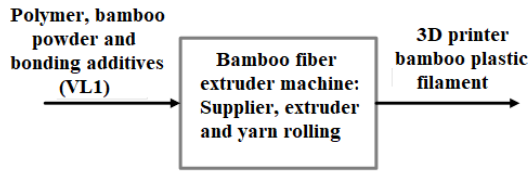


Fig. 6. Flowchart of general functions

When passing among the system, VL1 is supplied energy to change phase as well as to interact each other. After passing through all the components, it will vary in quantity and density, with or without synthesis with other materials. System-level parameters (SLP) between components are compared based on incoming and outgoing materials, material density synthesis and the variation.

The components in the system are then arranged in order to match the direction of movement of the material (Figure 7), in which the controller is temporarily removed from the system for easy analysis. The materials include bamboo powder, plastic beads and additives enters to the system through the fiber extrusion section. After being extruded into yarn, it will be rolled by the finished yarn winding unit.

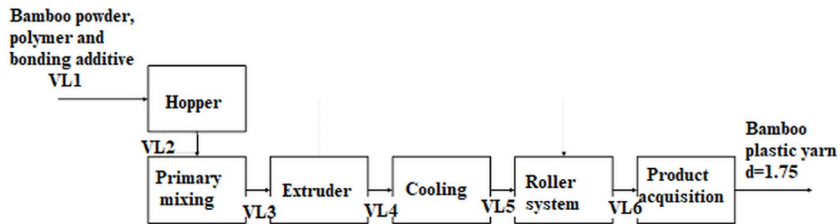


Fig. 7. Flowchart of function

Based on the functional flow diagram we determine the input and output relationships and compare them in the difference in size, similarity between materials or energy sources.

Components	Designation	Input	Output	Boundary condition I/O	Type of function
Hopper	P	VL1	VL2	VL1=VL2	Sub ordinary
Primary mixing module	TSC	VL2	VL3	VL2<VL3	
Electric motor	DCD	VL3	VL4	VL3<VL4	Main
Gear	BR				Main
Twin-screw & cylinder	TVD				Main
Heating	GN				Main
Extruder nozzle	DD				main

Components	Designation	Input	Output	Boundary condition I/O	Type of function
Cooling system	KLM	VL4	VL5	VL4<VL5	main
Rolled system	CL	VL5	VL6	VL5=VL6	main
Product acquisition	TSP				

## 2.4 Properties of the products

The technical parameters of “3D printed bamboo filament extrusion machine” are arranged in structural order. Based on the layout and state interaction between parts, the structural physics of the machine is divided to. In the schematic list of component pairs in a groups that have the relation of Serial connection, direct Interaction, homogeneity of material, compound effect, variable material, the pairs o groups do not appear in the comprehension map is considered to have the opposite properties. Note: N.T - Serial; S.S - Parallel; T.T - Direct interaction; T.R - Separating; T.T - Direct; G.T - Indirect; T.D - Impact; K.T.D - No impact.

The 1 to1 relationship of the components in the system is described via a System Level Specification (SLS). The requirements of SLS are located at the bottom of the hierarchical SLS diagram. Relationship are assigned to "1" if they exist, inversely to "0". The results of the basic component comparison process in the plastic filament extruder system are described in Table 1.

**Table 1.** The relation between structure and function

Detail/module		Physical Structure				Function			
		Arrangement		Position		Energy		Transmission	
		NT	SS	TT	TR	TT	GT	TD	KTD
P	TSC	1	0	1	0	0	1	0	1
	DCD	0	1	0	1	0	1	0	1
	BR	0	1	0	1	0	1	0	1
	TVD	0	1	0	1	0	1	0	1
	GN	0	1	0	1	0	1	0	1
	DD	0	1	0	1	0	1	0	1
	KLM	0	1	0	1	0	1	0	1
	CL	0	1	0	1	0	1	0	1
TSP	0	1	0	1	0	1	0	1	
TSC	DCD	0	1	0	1	0	1	0	1
	BR	0	1	0	1	0	1	0	1
	TVD	0	1	0	1	0	1	0	1
	GN	0	1	0	1	0	1	0	1
	DD	0	1	0	1	0	1	0	1
	KLM	0	1	0	1	0	1	0	1
	CL	0	1	0	1	0	1	0	1
TSP	0	1	0	1	0	1	0	1	
DCD	BR	1	0	1	0	1	0	1	0



	<b>TVD</b>	1	0	1	0	1	0	1	0
	<b>GN</b>	1	0	1	0	1	0	1	0
	<b>DD</b>	1	0	1	0	1	0	1	0
	<b>KLM</b>	0	1	0	1	0	1	0	1
	<b>CL</b>	0	1	0	1	0	1	0	1
	<b>TSP</b>	0	1	0	1	0	1	0	1
<b>BR</b>	<b>TVD</b>	1	0	1	0	1	0	1	0
	<b>GN</b>	1	0	1	0	1	0	1	0
	<b>DD</b>	1	0	1	0	1	0	1	0
	<b>KLM</b>	0	1	0	1	0	1	0	1
	<b>CL</b>	0	1	0	1	0	1	0	1
	<b>TSP</b>	0	1	0	1	0	1	0	1
<b>TVD</b>	<b>GN</b>	0	1	1	0	1	0	1	0
	<b>DD</b>	1	0	1	0	1	0	1	0
	<b>KLM</b>	0	1	0	1	0	1	0	1
	<b>CL</b>	0	1	0	1	0	1	0	1
	<b>TSP</b>	0	1	0	1	0	1	0	1
<b>GN</b>	<b>DD</b>	0	1	1	0	1	0	1	0
	<b>KLM</b>	0	1	0	1	0	1	0	1
	<b>CL</b>	0	1	0	1	0	1	0	1
	<b>TSP</b>	0	1	0	1	0	1	0	1
<b>DD</b>	<b>KLM</b>	0	1	0	1	0	1	0	1
	<b>CL</b>	0	1	0	1	0	1	0	1
	<b>TSP</b>	0	1	0	1	0	1	0	1
<b>KLM</b>	<b>CL</b>	1	0	0	1	1	0	1	0
	<b>TSP</b>	1	0	0	1	1	0	1	0
<b>CL</b>	<b>TSP</b>	1	0	0	1	1	0	1	0

The impact of System Level Specification (SLS) to the General Function Requirements (GFR):

Determining the impact of SLS on GFR is to identify properties that could have a positive or negative impact on the general function of the system. Relationships are more clearly defined, the easier to develop the texture of the product and to achieve a high level of satisfaction to the customers requirements as well as all the recommended specification.

The impact of SLS is determined on customers requirements by the following questions such as:

- What happens to GFR with or without any SLS in the system?
- What kind of effects of SLS will cause GFR?

All the answers of the above questions will help to determine the impact of SLS on GFR.

The impact of SLS on GFR is evaluated on the customer requirements where decisive factors are functional assurance, product size and operational productivity. The sequential layout of the components facilitates the ability of application of the product... In addition, the serial arrangement ensures the compactness of the product and while not having any effect on the performance, productivity. The parallel layout is suitable for the compact size of the product, while also having a positive effect on work efficiency when multiple machines are working at the same time.

Direct interaction between details does not affect the performance of the system. Direct interaction has a positive effect on the level of compactness, the closer the details are, the

more compact the product is. In addition, direct interaction aids also the performance when materials are directly transported.

Separate components make the maintenance easier, but it increases the sizes and has a negative impact on the compactness. The homogeneity and impurity of the material has positive effect on the performance of the product, due to the requirement of transportation, synthesis or modification of the material. Homogeneous materials have a positive impact on performance since the operation only has to handle the same materials from input to output.

The modification of material ensures the workability and has no effect on product size or performance of the system. In the other hand, the non-impacting that has no effect on workability or size of the product, has also a positive effect on performance as it does not take energy to impact on materials.

Once the questions are answered, the effects are listed in Table 2, based on the values:

- (-1) = Negative impact

- (0) = No impact or the impact is not clear, not determined.

- (+1) = Positive effects

The negative impact of SLS on GFR causes the undesirable results when SLS is present in the system because it will restrict and reduce the level of compliance with specifications and customer requirements. Positive effects will create the desirable results to the GFR to ensure the satisfaction of the specifications of the products and the requirements of the customers. An SLS has no effect if it neither supports nor impedes the implementation of the overall functionality.

**Table 2.** The effect of the relation between SLS and GFR [12]

SLS	Requirement of general function			Weight	
	Assure the workability	Compact	Performance		
N.T	1	1	0	1	Function
S.S	0	0	1	1	Compact
T.T	0	1	1	1	Performance
T.R	0	-1	0		
T.T	1	1	1	1	Function
G.T	1	0	-1	1	Compact
T.D	1	0	0	1	Performance
K.T.D	1	0	0		

### 3 Results and Discussion

#### 3.1 Calculation of matrix of similarity

Matrices of similarity are used to determine the degree of coherence among the different components in the system. The similarity matrix is established based on the similarity indices, which are the result of 3-matrix multiplication: SLS, effect of SLS on GFR, Weight of GFR. Each value in the similarity matrix represents a 1 to 1 relationship between the components of the system. Calculations were performed by Microsoft® Excel software and listed the results in the tables below.

**Table 3.** Matrix of Similarity of structure

		Matrix of similarity of structure								
	P	TSC	DCD	BR	TVD	GN	DD	KLM	CL	TSP
P	0	4	0	0	0	0	0	0	0	0
TSC	4	0	0	0	0	0	0	0	0	0
DCD	0	0	0	4	4	4	4	0	0	0
BR	0	0	4	0	4	4	4	0	0	0
TVD	0	0	4	4	0	3	4	0	0	0
GN	0	0	4	4	3	0	3	0	0	0
DD	0	0	4	4	4	3	0	0	0	0
KLM	0	0	0	0	0	0	0	0	1	1
CL	0	0	0	0	0	0	0	1	0	1
TSP	0	0	0	0	0	0	0	1	1	0

**Table 4.** Matrix of similarity of function

		Matrix of similarity of function								
	P	TSC	DCD	BR	TVD	GN	DD	KLM	CL	TSP
P	0	1	1	1	1	1	1	1	1	1
TSC	1	0	1	1	1	1	1	1	1	1
DCD	1	1	0	4	4	4	4	1	1	1
BR	1	1	4	0	4	4	4	1	1	1
TVD	1	1	4	4	0	4	4	1	1	1
GN	1	1	4	4	4	0	4	1	1	1
DD	1	1	4	4	4	4	0	1	1	1
KLM	1	1	1	1	1	1	1	0	4	4
CL	1	1	1	1	1	1	1	4	0	4
TSP	1	1	1	1	1	1	1	4	4	0

**Table 5.** Matrix of general similarity

		Matrix of general similarity								
	P	TSC	DCD	BR	TVD	GN	DD	KLM	CL	TSP
P	0	5	1	1	1	1	1	1	1	1
TSC	5	0	1	1	1	1	1	1	1	1
DCD	1	1	0	8	8	8	8	1	1	1
BR	1	1	8	0	8	8	8	1	1	1
TVD	1	1	8	8	0	7	8	1	1	1
GN	1	1	8	8	7	0	7	1	1	1
DD	1	1	8	8	8	7	0	1	1	1
KLM	1	1	1	1	1	1	1	0	5	5
CL	1	1	1	1	1	1	1	5	0	5
TSP	1	1	1	1	1	1	1	5	5	0

### 3.2 Group of components of modules

When the number of components in the system not too large, using Cluster Identification Algorithm (CIA) to arrange similar matrices into independent modules. The results are shown in the tables below.

Table 6. Module of structure

Module of structure										
	P	TSC	DCD	BR	TVD	GN	DD	KLM	CL	TSP
P	0	4	0	0	0	0	0	0	0	0
TSC	4	0	0	0	0	0	0	0	0	0
DCD	0	0	0	4	4	4	4	0	0	0
BR	0	0	4	0	4	4	4	0	0	0
TVD	0	0	4	4	0	3	4	0	0	0
GN	0	0	4	4	3	0	3	0	0	0
DD	0	0	4	4	4	3	0	0	0	0
KLM	0	0	0	0	0	0	0	0	1	1
CL	0	0	0	0	0	0	0	1	0	1
TSP	0	0	0	0	0	0	0	1	1	0

Table 7. Module of function

Module of function										
	P	TSC	DCD	BR	TVD	GN	DD	KLM	CL	TSP
P	0	1	1	1	1	1	1	1	1	1
TSC	1	0	1	1	1	1	1	1	1	1
DCD	1	1	0	4	4	4	4	1	1	1
BR	1	1	4	0	4	4	4	1	1	1
TVD	1	1	4	4	0	4	4	1	1	1
GN	1	1	4	4	4	0	4	1	1	1
DD	1	1	4	4	4	4	0	1	1	1
KLM	1	1	1	1	1	1	1	0	4	4
CL	1	1	1	1	1	1	1	4	0	4
TSP	1	1	1	1	1	1	1	4	4	0

Table 8. Synthetic module

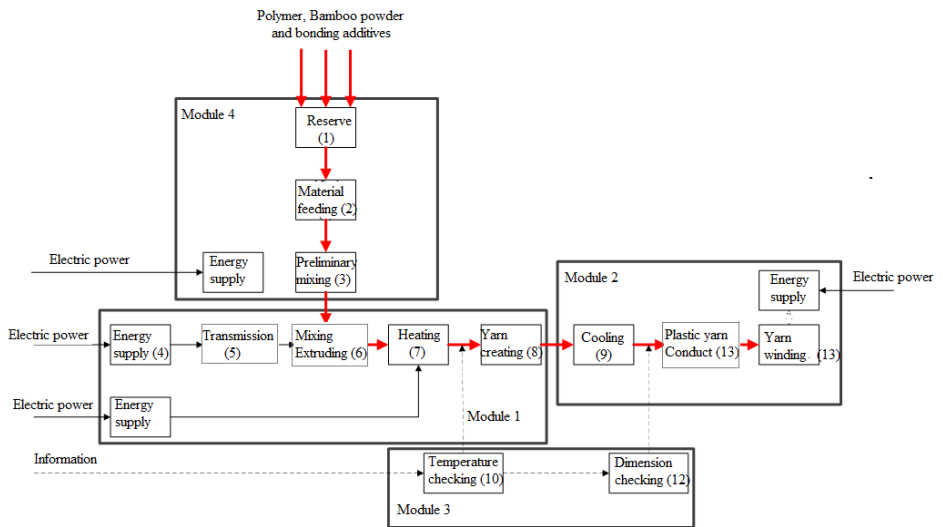
Synthetic module										
	P	TSC	DCD	BR	TVD	GN	DD	KLM	CL	TSP
P	0	5	1	1	1	1	1	1	1	1
TSC	5	0	1	1	1	1	1	1	1	1
DCD	1	1	0	8	8	8	8	1	1	1
BR	1	1	8	0	8	8	8	1	1	1
TVD	1	1	8	8	0	7	8	1	1	1
GN	1	1	8	8	7	0	7	1	1	1
DD	1	1	8	8	8	7	0	1	1	1
KLM	1	1	1	1	1	1	1	0	5	5
CL	1	1	1	1	1	1	1	5	0	5
TSP	1	1	1	1	1	1	1	5	5	0

Components with a degree of cohesion (high similarity index) are grouped into a group that can be considered a module. The other components that are outside the established group due to low degree of association with each other and for groups, are relative and indirectly related. There are also some components that have similar indices for one or more other components that are well above the floor value, perform the function of linking components or having relative relationships of interactions or materials. The results show that there are 3 modules of physical structure, including feed, extruder, control and cooling and 4 function modules.

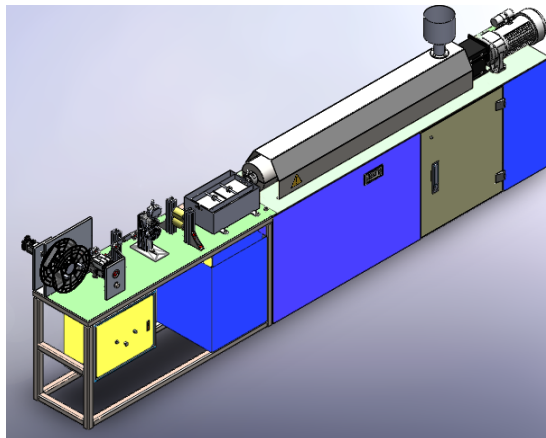
Based on the synthetic module matrix, we can divide the designed machine into 4 modules:

- *Module 1*: Extrusion module: Electric motor gearbox; Flexible coupling; Cylindrical gear. Twin screw facing outwards; Extrusion head; Cylinder; Heating solenoid.

- *Module II*: Product acquisition module: Controlled servo motor; Flexible coupling; Plastic fiber reel; Roller system; Cooling channel.
- *Module III*: Control module: Temperature sensor; PID system; PLC system.
- *Module IV*: Feeding Module: Hopper; AC motor mixer; Mixers.



**Fig. 8.** Layout of modules of the designed machine



**Fig. 9.** General model of the machine

## 4 Conclusion

With the application of Cluster Identification Algorithm (CIA) in modular approach to design the bamboo plastic fiber forming machine we can achieve reasonable design gain lot of advantages: satisfy customers; requirements, efficient in working, high performance and competitive price. In the other hand, it helps designers reduce design time and fabrication costs because there are many mechanical parts to choose from on the market. We hope that the research has a valuable position in the modern design.

## References

1. S. S. Muthu. *Green Composites: Sustainable Raw Materials* (Springer Nature, Singapore, 2019).
2. N. Stark, *Influence of Moisture Absorption on Mechanical Properties of Wood Flour-Polypropylene Composites*, Journal of Thermoplastic Composite Materials, **14**(2001).
3. K. Yuvaraj, M.P. Thirumoorthy, S. Ramalingam, C. Ravikumar, R. Swaminathan, *Mechanical properties of pineapple, banana and bamboo fiber reinforced epoxy hybrid composite systta*, International Journal of Research in Engineering and Managta ent [IJRTA], vol 1, no 1, pp. 270-276, 2019.
4. L. Chaunier, S. Guessasma, S. Belhabib, G.D. Valle, D. Lourdin, E. Leroy, *Material extrusion of plant biopolymers: Opportunities & challenges for 3D printing*, Additive Manufacturing, 21, (2018).
5. D. Zhao, X. Cai, G. Shou, Y. Gu, P. Wang, *Study on the Preparation of Bamboo Plastic Composite Intend for Additive Manufacturing*, Key Engineering Materials, Vol. 667 (2016).
6. 3d printing for beginners. How to make DIY Filament for your 3D Printer, 2018, [Online]. Available: [http://3dprintingforbeginners.com/wp-content/uploads/2014/05/How-to-make-DIY-Filament-for-your-3D-Printer\\_Download.pdf](http://3dprintingforbeginners.com/wp-content/uploads/2014/05/How-to-make-DIY-Filament-for-your-3D-Printer_Download.pdf). [Access on Jan 10, 2019].
7. H. Long, Z. Wu, Q. Dong, Y. Shen, W. Zhou, Y. Luo, C. Zhang, X. Dong, *Mechanical and Thermal Properties of Bamboo Fiber Reinforced Polypropylene/Polylactic Acid Composites for 3D Printing*, Polymer Engineering & Science, Vol. 59 (2019).
8. Double-screw extrusion machine, CN204123647U, 2014.
9. N. T. Nam. *Mechanical Design Process*, VNU HCM Press, Ho Chi Minh City, 2014.
10. A. Svetlin, K.D. Le, H.H. Nguyen, H.Q.H. Nguyen, and H.Q. Hoang, *A Design of Plastic-Bamboo Fiber Extruder Machine for 3D Printe*, Applied Mechanics and Materials, Vol. 902 (2020).
11. N.H. Hiep, *The manufacturing technology of bamboo-plastic-fibers for 3D printers*, Master thesis, 2020.
12. A.K. Kamrani, S.M. Salhieh. *Product Design for Modularity*, Springer US, 2002.

# A Research on The Formability of PVC Sheet in Single Point Incremental Forming (SPIF) Technology

Nguyen Thanh Nam <sup>1,\*</sup>, Nguyen Hoang Hiep<sup>2</sup>, Nguyen Tan Hung<sup>3</sup>, Tran Trong Hy<sup>4</sup>, Ho Huu Han<sup>5</sup>

<sup>1</sup>Faculty of Mechanical Engineering, Industrial University of Ho Chi Minh City, Vietnam

<sup>2</sup>Faculty of Mechanical Engineering, Vinh Long University of Technology Education

<sup>3</sup>Cao Thang Technical College

<sup>4</sup>Faculty of Mechanical Engineering, Ho Chi Minh City University of Technology, Vietnam

<sup>5</sup>Saigon Technology University (STU), Faculty of Mechanical Engineering, Vietnam

**Abstract:** Nowadays Single Point Incremental Forming (SPIF) is really a new technology of forming metal sheet after its formation and long development in about five decades. Although it was invented in, 1967 by Leszak, an American inventor, but the applications of the innovative technology have just been popular from 1990 because of the advance of controlling technology. This technology is especially adapted to small batch, unique or single productions. In almost all cases, the workpiece material sheets are metal such as aluminum alloys, bronze, mild steel, stainless steel and even Titanium with lot of researches, papers and thesis... Nonmetal sheets are rarely applied in this technology because of rare application. Nowadays, on the rise of the development of composite materials such as, PVC, thermoplastic resins... that have been a lot of applications on living life and technology. In this paper, we dedicate all of our work in the examination some parameters of forming that influence on the deformable ability of PVC plastic by empirical method under the support of DOE and Minitab software. This paper also provides our own experiences in forming PVC sheet that we had performed in the recent decade.

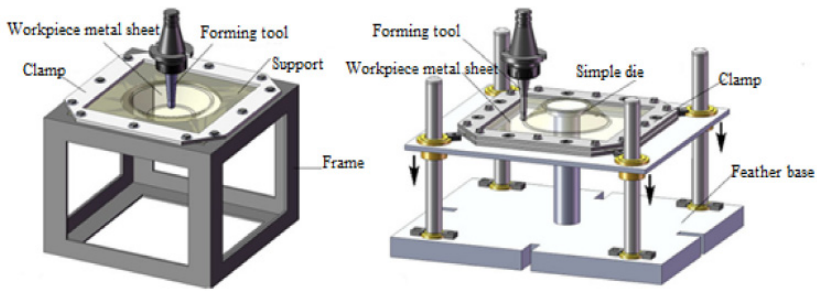
## 1 INTRODUCTION

In Single Point Incremental Forming (SPIF) technology, the non-cutter tool applies the forming forces on only one side of the sheet workpiece to form concave shapes on workpiece sheet. Beside SPIF there is Two Point Incremental Forming (TPIF) wherein the tools apply forces on both sides of the workpiece that could be formed complex convex and concave surfaces on model as shown in Figure 1. They are 2 branches of a state-of-the-art sheet forming without die technology invented by Leszak in 1967 [1] under the terminology of Incremental Forming Sheet (ISF). This forming sheet technology is suitable only for single

---

\* Corresponding author: [nguyenthanhnam@iuh.edu.vn](mailto:nguyenthanhnam@iuh.edu.vn)

or small batch production. Two branches of ISF: Single point Incremental Forming (SPIF) and Two Point Incremental Forming (TPIF) are illustrated in Figure 1.



**Fig. 1** a. Single Point Incremental Forming (SPIF) b. Two Point Incremental Forming (TPIF) [2]

At the beginning, this method is applied for forming metal sheets, but with the bloom of plastic or PVC based materials there are also researches of ISF for PVC material. In paper [3], the authors research the post-forming properties of thermoplastic polymer. Their results show that the post-ISF-process tensile properties is decreased, and the strain is increased in their experiment ranges. In research [4], the authors present the new methodology to find plastic flow and failure in the PVC sheets forming by the ISF process. These research helps us to clarify how plastic deform under ISF process, also help us know the modification of mechanical properties. But these studies only deal with basic parameters and do not study the effect of temperature, an important technological parameter, on the ISF processes. Therefore, we need to understand the influence of temperature parameter on this process, which is also the main goal of this study.

### 1.1 Mechanical properties of PVC

The mechanical properties of PVC sheet are given in Table 1 [5].

**Table 1.** Typical Properties of PVC [5]

<b>TYPICAL PROPERTIES of PVC and CPVC</b>			
<b>ASTM or UL test</b>	<b>Property</b>	<b>PVC</b>	<b>CPVC</b>
<b>PHYSICAL</b>			
D792	Density (lb/in <sup>3</sup> )	0.051	0.055
	(g/cm <sup>3</sup> )	1.41	1.52
D570	Water Absorption, 24 hrs (%)	0	0.04
<b>MECHANICAL</b>			
D638	Tensile Strength (psi)	7,500	8,200
D638	Tensile Modulus (psi)	411,000	430,000
D638	Tensile Elongation at Break (%)	-	27
D790	Flexural Strength (psi)	12,800	15,000
D790	Flexural Modulus (psi)	481,000	410,000
D785	Hardness	115 (Rockwell R)	121 (Rockwell R)
D256	IZOD Notched Impact (ft-lb/in)	1.0	1.6

### 1.2 Selection of model of experiment

The deformability of a material stands for by the angle  $\alpha$  that is made by the tangent at the forming point on the workpiece sheet and the horizontal line at this point. The deeper the position of formed point the bigger of the forming angle. According to a lot of researches,



this deformable angle depends on each sheet material and ways of forming and it cannot pass its limitation value of about  $80^\circ$  [6]. In order to examine exactly the angle by experimental process, almost all researches on SPIF technology also select the model on figure 2 because at any random torn point M, we could measure the depth  $z$  and deduce the deformable angle by this formula:  $\alpha = \arccos\left(\frac{R-z}{R}\right)$ . In the current time, standard market plates of PVC sheet are provided by dimension of 1000x2000, so in saving material we selected a square workpiece of 250x250 with no remain stub. After subtraction of the meadow the remained working circle is  $\varnothing 200$ .

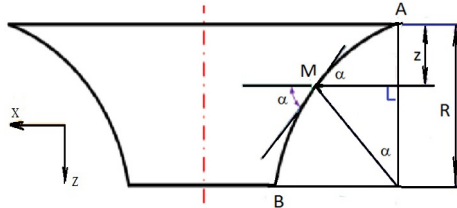


Fig. 2: SPIF model used in experiment

## 2 Design of Experiment on The Formability of PVC Sheet in SPIF

### 2.1 Selection of investigated forming parameters and method of design of experiment (DOE)

In our work, there are many forming parameters that influence to the formability of the metal sheet workpiece such as diameter of tool  $d$ , the vertical feed rate  $\Delta z$ , the velocity of tool in horizontal plane  $v$  and the temperature  $T$  of PVC sheet when forming. By our own experiment, properties and ability of specialist SPIF machine (figure 2) and based on DOE we selected of 2 limited values of 4 variable input parameters that are suitable to the properties of machine, tool and PVC sheet:

- The vertical feed rate after each orbit  $\Delta z = 0,4 - 1,2$  mm,
- The diameter of tool  $d = 6 - 12$  mm
- The velocity of tool in horizontal plane  $v = 1000 - 2500$  mm/min
- The temperature  $T$  of PVC sheet when forming  $T = 30^\circ - 60^\circ$  (according to [5] the maximum working temperature of PVC is only  $140^\circ\text{F}$  or  $60^\circ\text{C}$ )

Beside 4 above parameters we selected 3 constant values:

- The thickness of workpiece sheet is 2mm the popular thickness of almost all PVC sheet in market.
- The number of revolutions per minute  $n = 900$  rpm.
- SAE 40 oil is selected as lubricant at ambient temperature in South of Vietnam ( $30^\circ\text{C}$ ) as lowest and  $60^\circ\text{C}$  as selected high temperature.

In the purpose of saving effort in experiment according to [6] there are many experiments involve the study of the effects of 4 factors we could apply the factorial designs that is most efficient for this type of experiment. By a factorial DOE with 4 factors, each factor has 2 levels the number of experiments in forming model is  $N = 2^{k-p} = 2^{4-1} = 8$ ,

Wherein:

- $N$ : the number of forming model,
- $k = 4$  is number of factors,
- $p = 1$ , number of replaced factor,

The number of iteration [7]:  $m = t^2 \cdot s^2 / \Delta^2 = 2,145$ , selected value is 3. Finally, the total number of experiments is  $N \cdot m = 8 \cdot 3 = 24$ . Table 2 illustrates all limited value and coded of 4 influential parameters.

**Table 2.** Table of natural and coded influential parameters

Parameters			Limited value			
Nominal name	Symbol		Lowest	Highest	Mean value	Variable range to mean value
	Natural	Coded				
Vertical feed rate (mm)	$\Delta z$	x1	0.4	1.2	0.8	0.4
Diameter of tool (mm)	D	x2	6	12	9	3
Velocity of tool in horizontal plane (mm/min)	F	x3	1000	2500	1750	750
Forming temperature, °C	T	x4	30	60	45	15

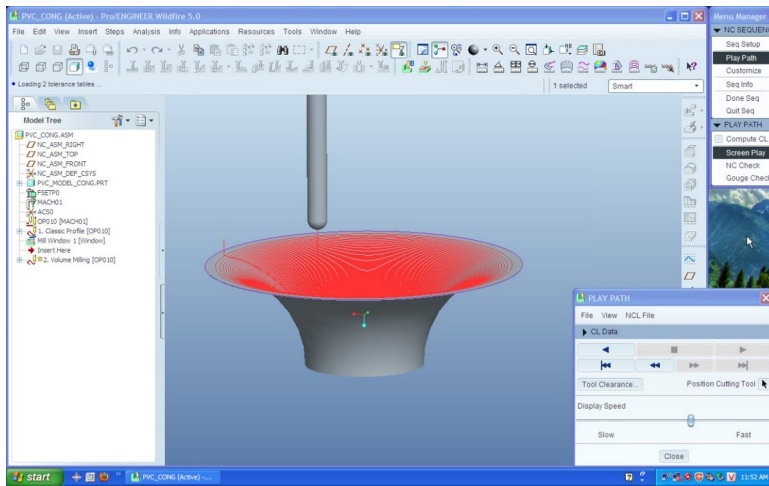
The temperature T (x4) was selected as the replaced parameter so we could perform the matrix of partial factors as in the following table.

**Table 3:** Table of coding parameters in Partial factor DOE

N <sub>0</sub>	x1	x2	x3	x4=x1x2x3
1	-1	-1	-1	-1
2	+1	-1	-1	+1
3	-1	+1	-1	+1
4	+1	+1	-1	-1
5	-1	-1	+1	+1
6	+1	-1	+1	-1
7	-1	+1	+1	-1
8	+1	+1	+1	+1

## 2.2. Simulation of the SPIF process by ProEngineer to guess the experimental result

The simulation of SPIF process has to perform with the same value of experimental process but have no iteration because there are no influential random parameters such as in experiment. All the properties of PVC are adapted from table 1 to ProEngineer when simulating. One of the results is displayed in figure 4 that confirms the application of SPIF for PVC sheet.



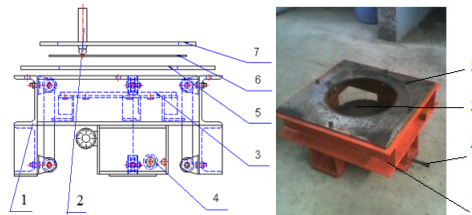
**Fig. 3:** A result of SPIF PVC model by Pro/E with  $h=60\text{mm}$ ,  $\varnothing=200\text{mm}$

### 2.3 Specialized SPIF machine, Clamping & heating feature, and tool to perform PVC models

All traditional CNC milling machine could be used to perform all the experimental PVC models. Fortunately, by the previous projects we already manufactured a specialized SPIF machine so all of our experiments of forming on PVC model were performed in a specialized SPIF machine in the CAD-CAM workshop of DCSELAB. The material of the tool (pestle) is high-speed steel (HSS) with a cylindrical shank and a no-cutting edge spherical end tip as shown in figure 4. In order to control the temperature of the PVC sheet when forming 24 models, we designed and manufactured a typical feature that has two functions: clamping and controlling the limited temperature for the PVC sheet. All the structures of clamping and controlling heat are displayed in figure 5.



**Fig. 4:** a. Specialized SPIF machine of DCSELAB; b. Self-manufactured tools and Standard bores collets



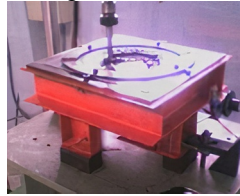
**Fig. 5:** a. Drawing of clamping and controlling heat feature b. Manufactured feature  
1. Frame of feature, 2. Tool, 3. Flexible thermostat, 4 adjustable control knob 5. Model support  
6. PVC workpiece sheet, 7. Clamp plate

There are 2 regimes of heating: 30°C thermostat is off, 60°C thermostat is on.

### 3 PERFORMING, MEASURING AND treatment the results OF PVC MODELS

#### 3.1 Performing and measuring PVC models for the deformability

PVC sheet with thickness of 2mm are cut and bend into workpiece of 250x250 (mm) and clamped in feature to be formed as in figure 6.



**Fig. 6:** Forming PVC model on integrated future at DCSELAB workshop [6]

The formed PVC models that are formed to reach torn point are measured and statistical are illustrated in figure 7.



**Fig. 7:** PVC model are formed to get torn lines or failures to reach a biggest angle of deformation [6]

#### 3.2 Treatment the result

The values of deformable angle are displayed in table 4 and calculated the mean value in table 5.

**Table 4:** Coarse result of deformable angle of forming of 24 models in 3 times of iteration

N <sup>0</sup>	Influential parameters				Results of $\alpha_{\max}$		
	$\Delta z$ (mm) x1	d (mm) x2	v (mm/min) x4	T (°C) x4	y1	y2	y3
1	0,4	6	1000	30	50		
2	0,4	6	1000	30		53	
3	0,4	6	1000	30			53
4	1,2	6	1000	60	65		
5	1,2	6	1000	60		63	
6	1,2	6	1000	60			63
7	0,4	12	1000	60	65		
8	0,4	12	1000	60		65	
9	0,4	12	1000	60			66
10	1,2	12	1000	30	60		
11	1,2	12	1000	30		63	
12	1,2	12	1000	30			60
13	0,4	6	2500	60	65		
14	0,4	6	2500	60		65	
15	0,4	6	2500	60			65
16	1,2	6	2500	30	65		
17	1,2	6	2500	30		62	
18	1,2	6	2500	30			62
19	0,4	12	2500	30	55		
20	0,4	12	2500	30		57	
21	0,4	12	2500	30			57
22	1,2	12	2500	60	65		
23	1,2	12	2500	60		68	
24	1,2	12	2500	60			66

**Table 5:** Mean deformable angle ready for statistics

N <sub>0</sub>	x1	x2	x3	x4=x1x2x3	$\bar{y} = \alpha_{\max}$
1	-1	-1	-1	-1	52,00
2	+1	-1	-1	+1	63,67
3	-1	+1	-1	+1	65,33
4	+1	+1	-1	-1	61,00
5	-1	-1	+1	+1	65,00
6	+1	-1	+1	-1	63,00
7	-1	+1	+1	-1	56,33
8	+1	+1	+1	+1	66,33

From the result in table 5, we could deduce the following regression equation of the deformability of the PVC sheets:

The regression equation of deformable angle in encoding shape:

$$y = 61,5833 + 1,9167x_1 + 0,6667.x_2 + 1,0833x_3 - 2.x_2x_3 + 3,5.x_4$$

After decoding, we get the regression equation of deformable angle:

$$\alpha = 20,6117 + 28,0625.\Delta z + 0,555.d + 0,001223.v - 0,5.d.v + 0,75.T \quad (1)$$

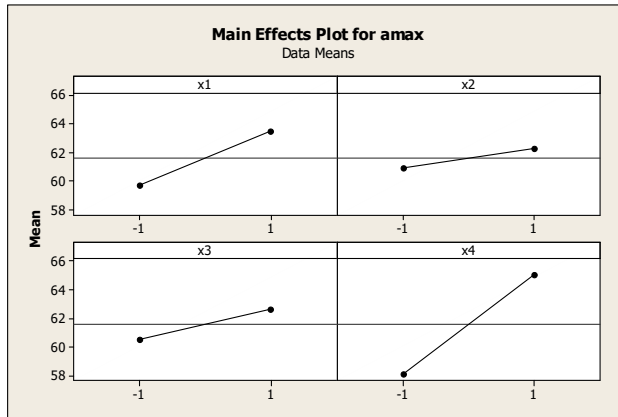
Wherein:

- $\Delta z$ : The vertical feed rate in mm,
- $D$ : The diameter of tool in mm
- $V$ : The velocity of tool in horizontal plane in mm/min
- $T$ : The temperature  $T$  of PVC sheet when forming in  $^{\circ}\text{C}$

The regression equation of angle of deformation  $\alpha$  was checked by Minitab® 15.1.30.0 software with the model results.

$$S = 1,3911 \quad R\text{-Sq} = 93,69\% \quad R\text{-Sq}(\text{pred}) = 91,93\% \quad R\text{-Sq}(\text{adj}) = 88,78\%$$

The result shows the reliability of the equation (1). With the  $R\text{-Sq}$ ,  $R\text{-Sq}(\text{pred})$  and  $R\text{-Sq}(\text{adj})$  value are all greater than 85% [7], meaning the regression equation are fit to the data. The Minitab diagram shows the effect of 4 input parameters to the deformable angle  $\alpha$  in figure 8.



**Fig. 8:** Effects of 4 parameters on angle of deformability of PVC sheet

In examining the diagram in figure 8 we confirm that 4 parameters are also proportional to the angle  $\alpha$  wherein the effect of  $x_4$  (stands for temperature  $T$ ) is greatest. So in order to increase the deformability of PVC we should increase all 4 parameters especially the temperature  $T$ . However, according to [5] the maximum operating temperature of PVC is  $140^{\circ}\text{F} = 60^{\circ}\text{C}$  so  $60^{\circ}\text{C}$  is the maximum temperature that we could selected.

## 4 CONCLUSIONS

Finally, in one word we conclude an essential points: The formability of PVC sheet is proportional to all 4 selected influential parameters such as the vertical feed rate  $\Delta z$ , the diameter of tool  $d$ , the velocity of tool  $v$  and the temperature  $T$  of PVC workpiece, therefore in order to increase the formability of PVC sheet we have to increase all of these parameters ( $\Delta z=1.2\text{mm}$ ;  $d=12\text{mm}$ ;  $v=2500\text{mm/min}$ ;  $T=60^{\circ}\text{C}$ ) and  $60^{\circ}\text{C}$  is the maximum temperature that we could selected.

## REFERENCES

1. E. Leszak. *Apparatus and Process for Incremental Dieless Forming*. Patent US3342051.
2. J. Jeswiet, F. Micari, G. Hirt, A. Bramley, J. Dufloy, J. Allwood. *Asymmetric Single Point Incremental Forming of Sheet Metal*, Springer US, 2005.

3. Wei H, Hussain G, Heidarshenas B, Alkahtani M, *Post-Forming Mechanical Properties of a Polymer sheet processed by Incremental Sheet Forming: Insights into Effects of Plastic Strain and Orientation and size of Specimen*, *Polymers*, 12(9), (2020).
4. S. A. Yonan, M. B. Silva, P. A. F. Martins, A. E. Tekkaya, *Plastic flow and failure in single point incremental forming of PVC sheets*, *EXPRESS Polym. Lett.*, Vol. 8, No 5, (2014).
5. *POLYVINYL CHLORIDE (PVC) PROPERTIES*, International Polymer Solutions Inc., iPolymer, <https://www.ipolymer.com/pdf/PVC.pdf>.
6. V. Tuyen, N. T. Nam, N. P. Anh, L. K. Dien, T. K. Nguyen and T. L. Tran, *A measure of Optimization of Parameters to Improve the Formability of Stainless-steel Sheet SUS 304 by SPIF Technology*, *Key Engineering Material*, Vol. 863, pp59-66 (2020).
7. D. C. Montgomery. *Design and Analysis of Experiment*, John Wiley & Sons, 2013.

# Modularity design of instant coffee powder packaging machine

Svetlin Antonov<sup>1</sup>, and L.K. Dien<sup>2,\*</sup>

<sup>1</sup>Technical university of Sofia, Faculty of telecommunications, Bulgaria

<sup>2</sup>Saigon Technology University (STU), Faculty of Mechanical Engineering, Vietnam

**Abstract.** For a long time, coffee has become a very popular drinks in over the world and Vietnam has been an coffee export country because of the quality of Vietnamese coffee is confirmed in the world. By the above reason, the question of coffee packaging for protection of its favor and transportation is considered one of the most important question. most products after the production process are fine packed in many different forms. Almost all products are especially packaged and quantified for convenient consumption depending on the form and texture of the product, there are different product packaging. Among the packaged products, instant coffee powder is the most packaged product. The coffee export market of Vietnam is very large in all around the world with the ranking of 4th. However, most instant coffee products in Vietnam are mainly invested by foreign companies with production lines system imported from foreign countries. This is the reason of the existence of the paper in which we mention on the design of a local instant coffee power with the application of the modular design.

## 1 Introduction

Modular design of mechanical products has developed rapidly in recent years [1]. By implementing the modular design, the enterprise can reduce cost and improve competitiveness largely. it is necessary to consider the modular design characteristics during the phase of product design, to facilitate product efficiency, shortening the supply cycle, improving product quality and reliability, reuse, upgrade and maintenance, and to make it easier to disassemble and recover [2, 3, 4]. At present, there is yet to be a very perfect and precise method which can solve the problems in modular design. Due to the trend of the diversification of customers' demands, small product batches with high varieties, modular design has been applied widely [5].

From the needs that are analysed above, it is necessary to modularize the design of product packaging machine. The design modular object is an instant coffee packaging machine.

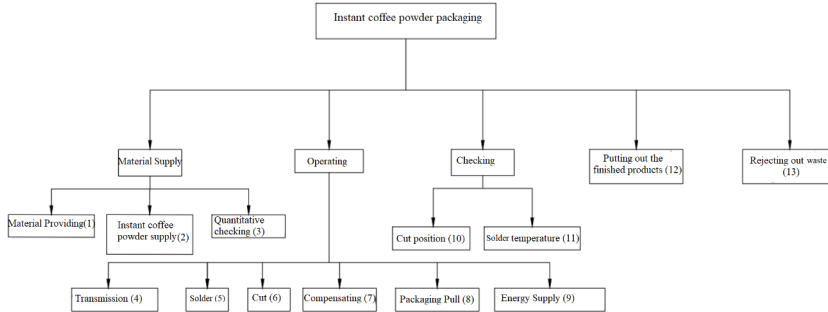
---

\* Corresponding author: [dien.lekhanh@stu.edu.vn](mailto:dien.lekhanh@stu.edu.vn)



## 2 Method of system design

To functional analysis for design products [6], from the above complete general functions, we analyze the sub-functions as the diagram that shows in Fig. 1.



**Fig. 1.** Schema of sub-function of the designed product.

First step is to propose some ideas for the design problem [6]: Deploying ideas for each function, combining ideas systematically, we get 04 ideas for instant coffee packaging machine as shown in Table 1.

**Table 1.** Implementation ideas for each function.

Function	Idea 1	Idea 2	Idea 3	Idea 4
Raw-material supply	Semi-automatic raw-material supply	Frequentative raw-material supply by hand	Automatic raw-material supply	Frequentative raw-material supply by hand
Quantify Gauge	Volume quantify by cup	Volume quantify by rotative barrel	Quantitative feeding by electrical control	Quantitative feeding by continuous weight feeding
Transmission	Mono electric motor system	Mono electric motor system	Two electric motor system	Two electric motor system
Welding	Roller system	Pushing rod system	Roller system	Pushing rod system
Cutting	Roller system	Pushing rod system	Roller system	Pushing rod system
Package compensating	Differentiel motor	Servo motor	Differentiel motor	Servo motor
Package pulling	Roller system	Roller-Pulley system	Roller system	Roller-Pulley system
Energy supply	3-phase motor	3-phase motor	3-phase motor	3-phase motor
Cutting position	Sensor	Switch journey	Sensor	Switch journey
Welding temperature	Solenoid-Sensor	Solenoid	Solenoid-Sensor	Heat Camera
Getting out the finished products	Receiving trough	Roller system	Receiving trough	Roller system
Getting out the waste	Receiving trough	Roller system	Receiving trough	Roller system

Pre-selection evaluation of ideas for design products [6]: Ideas are listed on the first horizontal row of the selection matrix. Selection criteria are arranged along the left column of the matrix. Choosing one of the above ideas as a standard one. Analysing one in these ideas that is compared with standard one according to the selection criteria and scored in the corresponding box (Table 2). From the above ideas we see that ideas 3 and 4 are feasible when design the product.

**Table 2.** Matrix of evaluation the ideas.

Creteria	Ideas			
	1(Standard)	2	3	4
Logical productivity	0	0	+	+
The quality of the product respond to the demands of customers	0	-	+	+
Acceptable qualitative error	-	0	+	+
Easy operating, high reability and longivity	0	0	+	+
Time of material supply and change type	0	0	+	+
Logical price	+	+	-	0
Environmental hygenic safety	0	0	0	0
Total score of +	1	1	5	5
Total score of 0	6	5	1	1
Total score of -	1	1	1	0
Final total score	0	0	4	5
Ranking	4	3	2	1
Continue?	No	No	Yes	Yes

Scoring for the final product design [6]: Decision matrix with additional weight column. Selection criteria are assigned a weight (in % value) which are determined by agreement of the design team. Analysing each idea that is compared with the standard one according to the selected criteria and scored in the corresponding box. Calculating the total score of each idea by the formula:

$$S_j = \sum_{i=1}^n r_{ij} \cdot w_i, \quad (1)$$

where:  $r_{ij}$  - the first criterion point of idea  $j$ ;  $w_i$  -the weight of the  $i^{\text{th}}$  criterion;  $n$  -total number of criteria;  $S_j$  - total score for idea  $j$ .

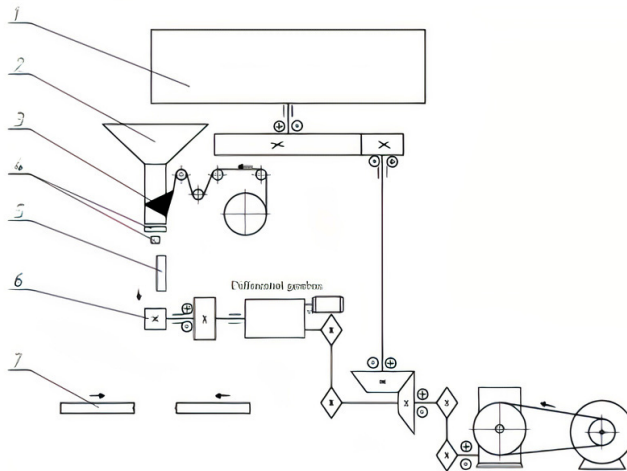
Ranking the ideas by total score is showed in Table 3.

**Table 3.** Matrix of scoring and selection of ideas.

Criteria	Weight (%)	Idea			
		3		4	
		Score		Score	
		Coarse	Multiplied to weight	Coarse	Multiplied to weight
Reasonable productivity	20	4	0,8	4	0,8
The quality of the	20	4	0,8	5	1

product respond to the demands of customers					
Acceptable qualitative error	10	4	0,4	4	0,4
Easy operating, high reability and longivity	10	3	0,3	3	0,3
Time of material supply and change type	10	3	0,3	3	0,3
Logical price	20	2	0,2	4	0,8
Environmental hygenic safety	10	3		0,3	
Total score	100	3.1		399	
ranking	1	2			
Continue?		No		Yes	

Based on the scoring matrix, we selected an idea as a design concept. The principle diagram is displayed in figure 2.



**Fig. 2.** Schema of theory of packaging machine.

Description of the system:

The motor drives the packaging pull assembly, the roll bag is fed to the shaft with the two end stoppers at its 2 ends (2), the bag head is pulled out through the guide rollers cluster (3) by the pull assembly rollers (5) and shaped by forming module (4) and at the same time it is welded by the vertical packaging module (6), then horizontally welded and packaging cut in the cluster (7). In the mean-while the motor also drives the metering assembly (1) to rotate the wheel quantifies through the measuring cups and down to the lower packaging through the hole that was created at product shaping assembly. The quantified material in the metering module falls into the shaped horizontal weld edge and a vertical weld edge packaging. Then the vertical welding module and the packaging cutting (7) welds the horizontal line and cut the packaging and finish the product (8). In case when the pull-out package is not long enough, the auxiliary engine will turn to the differential gearbox and pull out the packaging so that it can pack accurately according to the given data.

### 3 Results and discussion

After analysing customers' demands and choosing design ideas for the product [7] the next step is applying the design product modularization method to design the product system. Finally the combination of functional analysis diagrams and design concepts in one structural – functional power diagram is illustrated as follows:

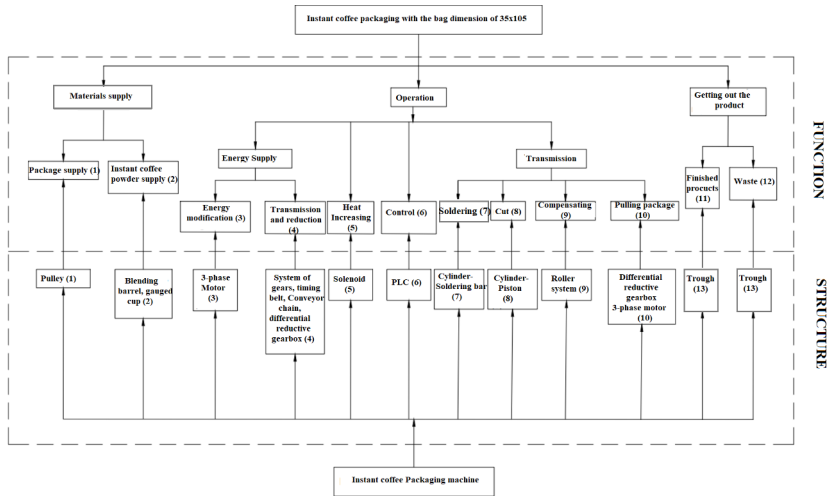


Fig. 3. Schema of structure and function.

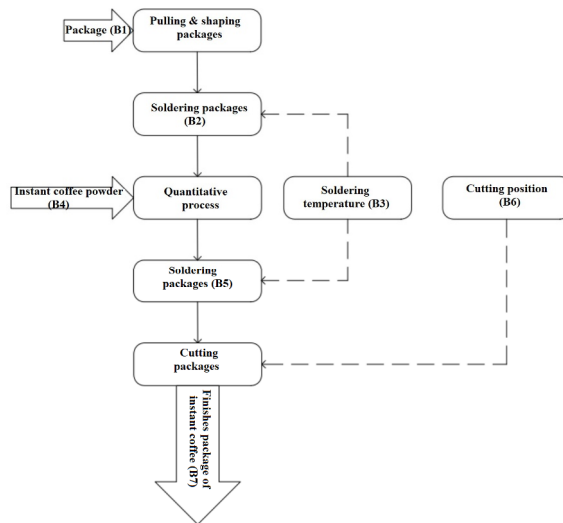


Fig. 4. Schema of process of general function of Instant Coffee Packaging Machine.

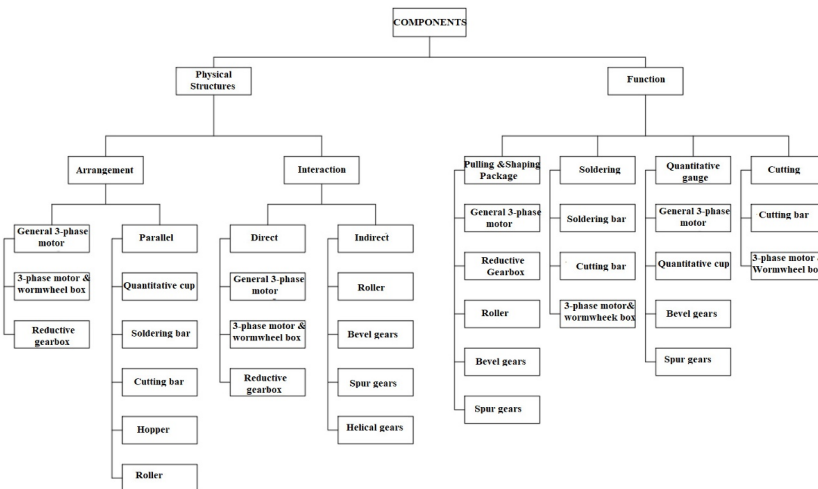
The main function of the machine is: raw materials supplying (instant coffee, packaging) and packaging into bags. The sub-functions are: providing the package in, shaping, soldering packages, pulling out and cutting packages.

List of the components and designation is shown in Table 4:

**Table 4.** Designation of components in instant powder coffee machine.

No	Components	Designation
1	Main 3-phase motor	DCC
2	3-phase motor gearbox	DCP
3	Reductive Gearbox	HGT
4	Chain transmission	BTX
5	Taper gear transmission	BRC
6	Spur gear transmission	BRT
7	Hopper	PTB
8	Roller for rolling package	CLK
9	Soldering bar	THX
10	Cutting bar	TKX
11	Quantitative cup	CDL

The system-level specifications of the products are arranged in a hierarchical structure [7] in which the physical structure is divided by the arrangement and the interactive state (direct, indirect), while the functional structure is divided by the flow of energy, materials and information (Figure 5).



**Fig. 5.** Schema of the relation among details and modules in the designed machine.

Establishing the relationships among the details in a system [7] through system properties of physical structure and function (Table 5), number 1 represents interaction, 0 represents no relationship system.

**Table 5.** The relation among details and modules in the designed machine.

Detail/ module	Structure				Function				
	Arrangement		Position		KD	HB	DL	CB	
	NT	SS	TT	TR					
<b>D C C</b>	<i>DCP</i>	1	0	1	0	1	0	1	0
	<i>HGT</i>	1	0	1	0	1	0	0	0
	<i>BTX</i>	0	0	1	1	1	0	0	0
	<i>BRC</i>	0	0	0	1	1	0	1	0
	<i>BRT</i>	0	0	0	1	1	0	1	0
	<i>PTB</i>	0	0	0	0	0	0	1	0
	<i>CLK</i>	0	0	1	0	1	0	0	0
	<i>THX</i>	0	0	0	0	0	1	0	0
	<i>TKX</i>	0	0	0	0	0	0	0	1
<i>CDL</i>	0	0	0	0	0	0	1	0	
<b>D C P</b>	<i>HGT</i>	1	0	1	0	1	0	0	0
	<i>BTX</i>	0	0	1	1	1	0	0	0
	<i>BRC</i>	0	0	1	0	1	0	1	0
	<i>BRT</i>	0	0	0	1	1	0	1	0
	<i>PTB</i>	0	0	0	0	0	0	1	0
	<i>CLK</i>	0	0	1	0	1	0	0	0
	<i>THX</i>	0	0	0	0	0	1	0	0
	<i>TKX</i>	0	0	0	0	0	0	0	1
<i>CDL</i>	0	0	0	0	0	0	1	0	
<b>H G T</b>	<i>BTX</i>	0	0	1	1	1	0	0	0
	<i>BRC</i>	0	0	1	0	1	0	1	0
	<i>BRT</i>	0	0	0	1	1	0	1	0
	<i>PTB</i>	0	0	0	0	0	0	1	0
	<i>CLK</i>	0	0	1	0	1	0	0	0
	<i>THX</i>	0	0	0	0	0	1	0	0
	<i>TKX</i>	0	0	0	0	0	0	0	1
	<i>CDL</i>	0	0	0	0	0	0	1	0
<b>B T X</b>	<i>BRC</i>	0	0	1	0	1	0	1	0
	<i>BRT</i>	0	0	0	1	1	0	1	0
	<i>PTB</i>	0	0	0	0	0	0	1	0
	<i>CLK</i>	0	0	1	0	1	0	0	0
	<i>THX</i>	0	0	0	0	0	1	0	0
	<i>TKX</i>	0	0	0	0	0	0	0	1
	<i>CDL</i>	0	0	0	0	0	0	1	0
<b>B R C</b>	<i>BRT</i>	0	0	0	1	1	0	1	0
	<i>PTB</i>	0	0	0	0	0	0	1	0
	<i>CLK</i>	0	0	1	0	1	0	0	0
	<i>THX</i>	0	0	0	0	0	1	0	0
	<i>TKX</i>	0	0	0	0	0	0	0	1
	<i>CDL</i>	0	0	0	0	0	0	1	0
<b>B R T</b>	<i>PTB</i>	0	0	0	0	0	0	1	0
	<i>CLK</i>	0	0	1	0	1	0	0	0
	<i>THX</i>	0	0	0	0	0	1	0	0
	<i>TKX</i>	0	0	0	0	0	0	0	1
	<i>CDL</i>	0	0	0	0	0	0	1	0
<b>P T B</b>	<i>CLK</i>	0	0	1	0	1	0	0	0
	<i>THX</i>	0	0	0	0	0	1	0	0
	<i>TKX</i>	0	0	0	0	0	0	0	1
	<i>CDL</i>	0	0	0	0	0	0	1	0

C L K	THX	0	0	0	0	0	1	0	0
	TKX	0	0	0	0	0	0	0	1
T H X	CDL	0	0	0	0	0	0	1	0
	TKX	0	0	0	0	0	0	0	1
T K X	CDL	0	0	0	0	0	0	1	0
	CDL	0	0	0	0	0	0	1	0

Where: NT – Serial; SS – Parallel; TT – Direct interactive; TR – Separate; KD – Pulling package in and forming; HB – Soldering packages; DL – Quantitative gauge, CB – Cutting packages.

Determining the degree of influence of System – Level Specification (SLS) on General Functional Requirements (GFR) [7]: To determine the effect of the designed machine performance on functional requirements, a relationship matrix between System – Level Specification (SLS) on General Functional Requirements (GFR):

- ✓ The desired impact value is 1;
- ✓ The value 0 stands for insignificant impact;
- ✓ The value -1 stands for the undesirable effect.

From the above ideas we could build a matrix of relationships between machine structure and importance factors (Table 6).

**Table 6.** Matrix of Relation between SLS and GFR.

<i>System – Level Specification (SLS)</i>	<i>Ease of Service</i>	<i>Compactness</i>	<i>Performance</i>
Serial	0	1	1
parallel	0	1	1
Contact each other	1	1	0
Separate each other	0	-1	1
Direct energy transferring	1	0	0
Indirect energy transferring	0	0	0
Reductive gearbox	0	0	0
Non-reductive gearbox	1	0	0
Weight	1	1	1

After applying the Cluster Identification Algorithm (CIA) [7], we determine the matrix of functional, structural and overall similarity:

**Table 7.** The structural similarity matrix.

	DCC	DCP	HGT	BTX	BRC	BRT	PTB	CLK	THX	TKX	CDL
DCC	4	4	2	2	0	0	0	0	0	0	0
DCP	4	4	2	2	0	0	0	0	0	0	0
HGT	4	4	2	2	0	0	0	0	0	0	0
BTX	2	2	2	2	0	0	0	0	0	0	0
BRC	2	2	2	0	2	1	0	0	0	0	0
RT	0	0	0	0	2	2	0	0	0	0	0
PTB	0	0	0	0	1	2	1	0	0	0	0
CLK	0	0	0	0	0	0	1	1	0	0	0
THX	0	0	0	0	0	0	0	1	0	0	0
TKX	0	0	0	0	0	0	0	0	0	2	2
CDL	0	0	0	0	0	0	0	0	0	2	2

**Table 8.** The functional similarity matrix.

	DCC	DCP	HGT	BTX	BRC	BRT	PTB	CLK	THX	TKX	CDL
DCC	1	1	1	0	1	0	0	0	0	0	0
DCP	1	1	1	1	0	0	0	0	0	0	0
HGT	1	1	1	1	1	0	0	0	0	0	0
BTX	0	1	1	1	1	0	0	0	0	0	0
BRC	1	0	1	1	1	1	0	0	0	0	0
RT	0	0	0	0	1	1	1	0	0	0	0
PTB	0	0	0	0	0	1	1	1	0	0	0
CLK	0	0	0	0	0	0	1	1	1	0	0
THX	0	0	0	0	0	0	0	1	1	0	0
TKX	0	0	0	0	0	0	0	0	0	1	1
CDL	0	0	0	0	0	0	0	0	0	1	1

**Table 9.** The general similarity matrix.

	DCC	DCP	HGT	BTX	BRC	BRT	PTB	CLK	THX	TKX	CDL
DCC	5	5	5	2	3	0	0	0	0	0	0
DCP	5	5	5	3	2	0	0	0	0	0	0
HGT	5	5	5	5	3	2	0	0	0	0	0
BTX	2	3	3	5	1	0	0	0	0	0	0
BRC	3	2	3	1	5	3	0	0	0	0	0
RT	0	0	0	0	3	3	3	0	0	0	0
PTB	0	0	0	0	0	3	5	2	0	0	0
CLK	0	0	0	0	0	0	2	5	3	0	0
THX	0	0	0	0	0	0	0	3	5	0	0
TKX	0	0	0	0	0	0	0	0	0	5	3
CDL	0	0	0	0	0	0	0	0	0	3	5

All the mechanical details of the designed machine are listed in the table below with the majority of standardized details available for easy purchase:

**Table 10.** Standardized details available for easy purchase.

<i>Mechanical details</i>	<b>Design for selection</b>	<b>Design for manufacturing</b>
3-phase motor	•	
Cylinder	•	
Roller bearings	•	
Position sensors	•	
Solenoids	•	
Chain transmission	•	
Belt transmission	•	
Gearbox	•	
Differential gearbox	•	
Spur gear transmission	•	
Bevel gear transmission	•	
PLC	•	
Flow control valve	•	
Pneumatic system	•	
Roller		•
Quantitative cup		•
Hopper		•
Keys		•
Machine frame		•
Machine chariot		•
Shafts		•
Driver	•	



### 3 Conclusion

The results of the paper illustrate that with the helping of modularity design method, the designer could perform his complicated works of design a machine that is efficiency respond all the technical demands, product quality and reliability, easy maintenance and logical price that could have a great competition. With the modular design, most of the clusters are designed for selection (purchasing from market), only seven parts are designed for manufacturing by our-self.

### 4 References

1. Báo cáo thị trường cà phê năm 2020, <https://cdn.vietnambiz.vn/171464876016439296/2021/1/20/a2012020-bao-cao-ca-phe-nam-2020-final-16111582854511351635957.pdf>. (2021).
2. PengjiaWanga, Yongxian Liua, S.K. Ongb, A.Y.C. Neeb, *Modular Design of Machine Tools to Facilitate Design for Disassembly and Remanufacturing*, 21st CIRP Conference on Life Cycle Engineering, Elsevier B.V (2014).
3. Qiuxiao Yang a, Kaibao Wang b, Mingzhu Zhang c, Li Zhao d, Su Hang and Ming Meng, *The Design and Research on Automatic Packaging Machine of the Strains*, International Conference on Management Science and Innovative Education (MSIE 2015), Atlantis Press (2015).
4. Zhihui Liu; Mengqi Li; Zhigang Chen; Zhiwei Lin; Xuemin Liu, *The automatic packaging machine design based on reconfigurable theory*, 2011 International Conference on Consumer Electronics, Communications and Networks (CECNet) (2011).
5. Rui Shang, Sheng Yuan Li, *The Study on CAD Technology of Reconfigurable and Module for Vertical Bag Packaging Machine*, Advanced Materials Research (2011).
6. Nguyễn Thanh Nam, *Giáo trình phương pháp thiết kế kỹ thuật*, Nhà xuất bản đại học quốc gia Tp. Hồ Chí Minh (2014).
7. A. K. Kamrani, S. M. Salhied, *Product design for modularity*, Second edition (2002).